THE UNIVERSITY OF HULL

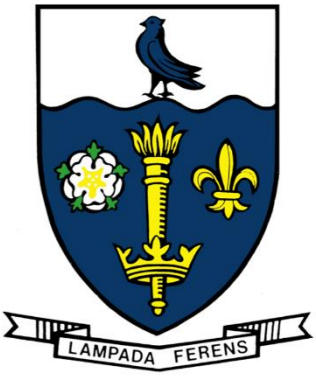

SYNTHESIS AND EVALUATION OF NOVEL POROUS MATERIALS FOR ENVIRONMENTAL REMEDIATION

being a Thesis submitted for the Degree of Doctor of Philosophy in

The University of Hull

By

Zahraa Hashim Athab Al-Mashaykhi

June 2019

Acknowledgement

First and foremost praises to Allah, who made this thesis possible and gave me the ability to proceed successfully. I would also like to thank all those people who contributed to this successful and helped me during my PhD study. Though it may not be enough express my thanks in few words to all those people, I would still like to give many, many thanks to all these people.

I would first like to express my sincere gratitude to my academic supervisors, Professor Gillian M Greenway and Dr. Jia Min Chin for their continued help, support and their valuable guidance. I really appreciate their careful and professional supervisions, which allowed me to gain a deep understanding in an area that I was not familiar with. Special thanks go to Dr Michael Reithofer for his help, suggestions and discussions on my project.

Also, I would like to acknowledge gratefully my colleagues in the Department of Chemistry and Biochemistry for their help and providing friendly environment for my research. My special thanks also go to Mr A. Sinclair, Mr Timothy S. Dunstan and Mr Ian Dobson for helping with scanning electron microscopy imaging and TGA.

I would like to express my warm and sincere thanks to my love of life my husband (Ahmed) and my beloved daughter (Malak) for their love, support and encouragement. Their support made the hard times easier and the good times wonderful. I owe my deepest gratitude to my mother, sister and brothers for their endless love, support and encouragement. Furthermore, I'm extending my gratitude and appreciation to my cousin who passed away during my PhD study for her encouragement and support.

Last but not least, my special thanks also go to the Iraqi Government/The Higher Committee for Education Development in Iraq (HCED-Iraq), the Iraqi Ministry of Higher Education and Scientific Research and the University of Babylon / Iraq for supporting me all financially. Finally, I would like to thank the Iraqi attaché in London and Ireland, for their help and support

Abstract

Porous materials have been widely used as adsorbents for water treatment due to their unique properties such as high surface area, excellent mechanical properties and good chemical stability. The work in this thesis aimed to develop novel porous materials for pollution remediation, with the focus being on materials that can be produced economically and environmentally friendly. The first part of this thesis covers two types of mesoporous carbon materials including mesoporous and magnetic mesoporous carbon materials which were fabricated through a soft templating method (Chapter 3). It has been shown that these porous carbon materials with monolithic form have high surface area, which is envisaged excellent adsorbent capacity. But there are some drawback which limit their use for water treatment as the preparation of these materials is time consuming, there are high operation cost and difficulties in regeneration and operation. Cellulose was considered as an attractive alternative material for preparation of porous materials for pollution remediation because it is naturally abundant, renewable, non-toxic and a low-cost biopolymer.

In the second part of this work a cellulose-based hydrogel was successfully synthesized using hydroxypropyl cellulose (HPC) with divinyl sulfone (DVS) as a chemical cross-linker via a modified temperature induced phase separation (TIPS) method (Chapter 4). The HPC hydrogel obtained was characterised and the results showed that the properties of this hydrogel depended on the gelation temperature. The FTIR results confirmed the chemical cross-linking between HPC and DVS. HPC hydrogel demonstrated a flexible behaviour without breakage under compression tests. In addition, there were good shape recovery properties upon adsorption of water. The morphology of the cross-linked HPC hydrogel showed an interconnected macroporous network structure, which allowed application for water purification.

Further work was then carried to develop a new and simple method to prepare a novel thermoresponsive HPC hydrogel with a graded pore size (Chapter 5). This method combined two approaches, varying the temperature between the upper and lower part of the hydrogel utilising the lower critical solution temperature (LCST) via the temperature induced phase separation (TIPS) method, which achieved a gradual change in pore geometry and pore size. The added inclusion of cryogenic treatment of the sample ensured a gradient porous HPC hydrogel was obtained with high permeability.

Double network (DN) hydrogels have a structure that can effectively improve the adsorption capacity as the second network can introduce more functional groups into

hydrogel structures, which is of great importance in the adsorption process due to improve the adsorption capacities. The DN hydrogels can also improve the mechanical strength of hydrogel materials, which makes it easier to regenerate. To this purpose, novel hybrid double networks hydrogel was prepared in this work via mixing two types of crosslinked polymers, these were covalently crosslinked HPC with DVS and ionically crosslinked alginate with calcium ions (Chapter 6). Alginate was selected to be the second network polymer as alginate has carboxylate functional groups that can be used to remove cationic pollutant by electrostatic interactions, thus improving the adsorption capacity of the HPC single network (HPC SN) hydrogel. SEM images of the double network produced s confirmed that the hydrogel was composed of two independently cross-linked networks with a homogeneous interconnecting porous structure. The mechanical tests on the DN hydrogel showed that it was much stronger compared with HPC SN hydrogel. The adsorption and filtration of organic pollutants by HPC hydrogel were investigated through dye adsorption experiments (Chapter 7). The results were showed a great ability of HPC hydrogel for selective adsorption towards MB dye. In order to evaluate the possibility of reuse of HPC hydrogel, the recyclability of these materials was examined. The obtained results indicated that the reusability of the HPC hydrogel was at some cycles without any loss in its sorption behaviour. Therefore, the HPC hydrogel can be a good reusable and economical adsorbent to remove the cationic species. It is important to note that HPC hydrogel column was further used for the first time for selective separation of dye mixtures by simple gravity filtration and the hydrogel can be re-used multiple times. Despite being one of the most promising types of porous materials for environmental applications, their low adsorption capacity is a significant disadvantage for their use in these applications. Adsorption of methylene blue dye (MB) on HPC/CA DN hydrogel was investigated through batch and column adsorption experiments and compared with HPC SN hydrogel (Chapter 7). The adsorption isotherms for both HPC SN and HPC/CA DN hydrogels fitted well with the Langmuir adsorption model and the maximum adsorption capacity of HPC/CA DN hydrogel was found to be 169.49 mg g^{-1}, which is larger than for the HPC SN hydrogel (112.35 mg g^{-1}). The results showed a significant pH-dependent equilibrium for the adsorption capacity of MB dye for both hydrogels in this study, which decreased dramatically with decreasing the pH of the MB dye solution. This meant that the MB-loaded HPC hydrogel could be easily regenerated under acidic conditions. The thermodynamic analysis of MB dye adsorption onto both HPC SN and HPC/CA DN hydrogels were also studied and the process was shown to be an exothermic and spontaneous process. An adsorption kinetic study was also carried out and the results

obtained showed that the adsorption of MB dye adsorption on both hydrogels was well described by the pseudo-second-order kinetic model. In the column study, the adsorbent reuse was investigated and the selective separation of a dye mixture was also studied through ten cycles. Both hydrogels columns showed efficient selective adsorbent for cationic dyes, with the removal of MB dye being very efficient, whilst extremely low removal of FL dye. However, the HPC/CA DN hydrogels column exhibited a higher adsorption capacity than HPC SN hydrogel due to the dual functional groups (hydroxyl and carboxyl groups) in HPC/CA DN hydrogel. Based on the selective adsorption towards cationic methylene blue over anionic sodium fluorescein dye, HPC SN and HPC/CA DN hydrogels columns could easily separate two dyes from aqueous solutions of dye mixtures by simple gravity filtration. Both HPC SN and HPC/CA DN hydrogel column showed high separation efficiency of more than 99%. It was also found that separation efficiency of the HPC SN decreased to 86% by the 10th cycle for this column, while no significant losses in the separation efficiency were detected even after ten cycles for the HPC/CA DN hydrogel column. These results show that the HPC/CA double network polymer hydrogels have great potential for improving the adsorption capacity with good reusability and would be a promising eco-friendly adsorbent for the treatment of dye wastewaters.

LIST OF POSTERS AND CERTIFICATES

Some of the results obtained in this work have been presented at the following events:

1. Poster presentation in the 8th PhD Experience Conference at the University of Hull on 12 July 2017. The poster was entitled “Porous Materials for Pollution Remediation”.
2. Poster presentation in PhD Colloquium on 24th Jan 2018 which was held in the department of chemistry and Biochemistry at the University of Hull. The poster was entitled “Hydroxypropyl Cellulose Hydrogels as Renewable Filters for Separation”.
3. Poster presentation in PhD Colloquium on 15th July 2019 which was held in the department of chemistry and Biochemistry at the University of Hull. The poster was entitled “Novel double network composite hydrogel based on hydroxypropyl cellulose and alginate for selective adsorption and separation of dyes from an aqueous solution”.
4. I attended of MERCIA meeting at Liverpool John Moores University in 14th December 2016.
5. I studied some of postgraduate and chemistry related modules and received 85 credits.

List of abbreviations

ATR-FTIR	Attenuated Total Reflectance Fourier Transform Infrared
BET surface area	Brunauer-Emmett-Teller surface area
CA	Calcium Alginate
CNF	Cellulose nanofibers
Cryo-SEM	Cryogenic scanning electron microscopy
Co/OMC	Cobalt-containing ordered mesoporous carbon
Col	Collagen
CVD	Chemical Vapor Deposition
DN	Double Network
DSC	Differential Scanning Calorimetry
DVS	Divinyl sulfone
EDX	Energy Dispersive X-Ray spectroscopy
EHEC	Ethyl hydroxyethyl cellulose
EISA	Evaporation-induced self-assembly method
Fe/OMC	Iron -containing ordered mesoporous carbon
FD	Freeze Drying
FGM	Functionally Gradient Material
FL	Fluorescein dye
GAD	Graphene/Alginate nanocomposite beads double network
GAS	Graphene/Alginate nanocomposite beads single network
G′	Storage modulus
G″	Loss modulus
HEC	Hydroxyethyl cellulose
H-DN hydrogels	Hierarchical structured DN hydrogels
HPC	Hydroxypropyl Cellulose
HPMC	Hydroxypropyl methylcellulose
IPN	Interpenetrating Polymer Network
LCST	Lower Critical Solution Temperature
MB	Methylene Blue dye
MC	Methyl cellulose
Ni/OMC	Nickel -containing ordered mesoporous carbon
NMMO	N-Methylmorpholine N-oxide
OMC	Ordered mesoporous carbon material

PAAm	Polyacrylamide
PAA	Polyacrylic acid
PAMPS	Poly (2-acrylamido-2-methylpropanesulfonic acid)
PEG	Poly ethylene glycol
Pluronic F127	Poly(ethylene oxide)- poly(propylene oxide)-poly(ethylene oxide) triblock copolymers (PEO-PPO-PEO)
PNIPAAm	Poly(N-isopropylacrylamide)
PS-P4VP	Polystyrene-block-poly (4- vinyl pyridine)
PVA	Polyvinyl al
SA	Sodium Alginate
SEM	Scanning Electron Microscopy
$ScCO_2$	Supercritical CO_2 drying
SN	Single Network
t_{AP}	Time after phase separation
t_{BP}	Time before phase separation
t_{DP}	Time during phase separation
TEOS	Tetraethyl orthosilicate
TGA	Thermogravimetric analysis
TIPS	Temperature-induced phase separation
XRD	X-Ray Diffraction
SN	Single Network
t_{AP}	Time after phase separation
t_{BP}	Time before phase separation
t_{DP}	Time during phase separation
XG	Xanthan gum

Contents

Chapter One

1. Introduction

1.1 Environmental pollution

The rapid development of industry has adversely influenced the environment due to resulting hazardous products called pollutants.[1] Generally, a pollutant has been defined as any substance that has the ability to impact negatively on the environment.[2] These pollutants have increased due to industrialization and human activities and take different forms such as sewage, waste or poisonous gas fumes and smoke released from factories and cars.[3] There are three major types of pollutions in the environment air pollution, water pollution, and soil pollution.[4-7] There are many reasons why pollution has caused a major impact on human life and the environment. First of all, the effect on people's health due to hazardous materials found in the food, water or air. Secondly, impact on the natural environment which later influences the animal's life, soil, water, and crops. Finally, damage the natural beauty by increasing the compound exhaust, dust, and smoke.[3] During the last three decades, the worldwide concern about the effect of environmental contamination on community health has been expanding especially the global anxiety of increasing various type of diseases. The World Health Organization (WHO) has assessed that 25% of the diseases confronting humanity are today due to long-term exposure to environmental contaminations.[8] Nevertheless, the majority of these diseases are not easily distinguished and may have been procured through childhood and exhibited later in adulthood.[9]

1.2 Types of pollutants in the environment

Environmental pollution typically arises from organic compounds, potentially toxic metals or a mixture of these materials. Organic pollutants are discharged into the environment through different sources, for example, petrochemical generation, burning fossil fuel, and waste. Technological advancement and industrial development have also led to increased release of these contaminants and represent a huge risk to the environment and general health.[10] Dyes are one of the main organic pollutants produced from the textile industry. [11]During the dyeing process, high levels of dissolved dyes remain unfixed on the textile and they are directly discharged into the water bodies. Most of the textile dyes are resistant to photodegradation, biodegradation and oxidizing agents.[12] The textile wastewater is inclined to pose serious threats to the environment if not treated correctly.[13] Coloured water affects the aquatic life as the dyes prevent sunlight

from diffusing through the water which inhibits the photosynthetic activity. In addition to that it can damage the natural beauty of the environment.[11] Another important type of water pollutants is potentially toxic metals, which are mostly coming from industrial waste. Toxic metals are found in nature, but anthropogenic activities can increase the concentration of these metals in the environment and especially in the water.[14] Toxic metals are a serious problem in the environment due to their negative impacts on the human and another organism. These metals for example lead (Pb), cadmium (Cd) and chromium (Cr), which are highly toxic to the environment and human health, causing possible damage to the liver, kidney, and cancer.[15]

1.3 Environmental remediation techniques

Environmental contamination anxiety has been increasing dramatically in the world over the years, because of the exponential development in human population and the changes in consumption and productivity behaviours. In addition, the development in the industry field leads to change the human lifestyles and increasing consumption of the resources. All these reasons have led to the rapid production of wastes, which in turn has brought the pollution of the air, water and soil.[16] In this case, there is a requirement for removal and treatment of these pollutants in order to mitigate their toxic effects and restore the ecology in polluted regions.

Remediation is a method of restoration or recycling of the contaminated environment to its normal condition by modifing the hazardous materials to safe products or taking them totally from the environment by using different treatment methods such as chemical, biological and physical methods.[17] Despite remediation processes being a good way to remove or treat pollutants from the environment, they rarely happen without negative side effects, which can be costly or cause destruction to the environment. Achieving effective environmental treatment methods relies not just on pollutants, removal and cost, but also external elements such as social and ecological factors, and political ramifications of the applied methods.[17]

Removal of organic pollutants from wastewater is the main challenge concerning environmental treatment.[18, 19] Several strategies have been used to treat the water from toxic organic contaminations such as chemical treatment,[20] biological treatment,[21, 22] physical filtrations,[23] and adsorption.[24] The adsorption technique is considered to be economical, active, and an ecologically method, as well as allowing different kinds of pollutants to be adsorbed while being reusable over numerous cycles. [25, 26]This method has been proven to be the most practical technique due to its simplicity and low cost of

deployment.[27] In this case, carbon materials have been widely used as adsorbent for removing pollutants from their aqueous solution because of their unique structure and large surface area.[28, 29]

Porous materials have been utilized as sorbents to separate oil from a mixture of oil and water by an easy and quick absorption process.[30] Typically, excellent sorbents should have a high capacity to absorb the oil, low density, high selectivity, and should be prepared from environmentally friendly materials. Adebajo *et al.*[31] has reported three main types of porous materials natural products, synthetic inorganic, and organic products can that be used as sorbents for the remediation process to remove pollutants. Hydrophobic aerogels may be suitable sorbents for removal of organic pollutants from water due to high surface area and low density.[32, 33] Additionally, heavy metals have become a significant problem environmental pollutants, adding urgency to their removal. Different methods such as filtration, ion exchange, membrane separation, adsorption, precipitation and biological approaches have been used for treating the wastewater.[34]

Of these methods, adsorption poses an attractive solution, particularly for dyes and heavy metals with high stability and resistance to degradation.[35] Further, the simplicity and low cost of deployment of dye removal by adsorption enhances its feasibility.[27] Activated carbons are generally the adsorbents most commonly used in adsorption process owing to their high surface area and adsorption capacity. However, there are a number of problems with their use, mainly related to the fact that regeneration is expensive and difficult, which limits their usage.[36, 37] Therefore, it is extremely important to investigate others type of adsorbents that should be sustainable, simple, inexpensive and highly effective for removing the heavy metals. Ideally, the sorbent is also reusable, allowing recovery of heavy metal sorbate from it. Hydrogels and aerogels as porous materials have recently received more attention as an economic adsorbent to treat the water from heavy metal ions.[38 39]

1.4. Porous materials

Porous materials are solid materials that contain voids in different shapes such as cavities, channels, or interstices. These materials can be classified depending on different criteria such as pore structure, shape, size and accessibility.[40] Firstly, porous materials are divided into three types depending on pore size: microporous (pore diameter < 2nm), mesoporous (pore diameter 2-50 nm) and macroporous (pore diameter >50 nm). Secondly, these materials classifications rely upon pore structure such as open and close voids according to how reachable the fluid is through the pore. Open pores are communicating with the outside surface of the material such as interconnected and blind pores. Interconnected pores have an open channel that starts at one position on the surface of materials and expands into various other positions in the surface. Blind pores have an opening to the surface just at one side and are closed from the other side. Open pores materials are desirable in most of the modern industrial applications such as filtration and purification which need these pores to be permeable for fluid. Closed pores involve non-interconnected pores which are completely isolated from outside the material. Closed porous materials are used mostly for thermal insulators. Figure 1.1 illustrates schematically the different types of pores in the porous materials.[41-43]Finally, classification of porous materials may also depend on pore arrangement. Porous materials may possess a regularly arranged pore system or random pore arrangements.

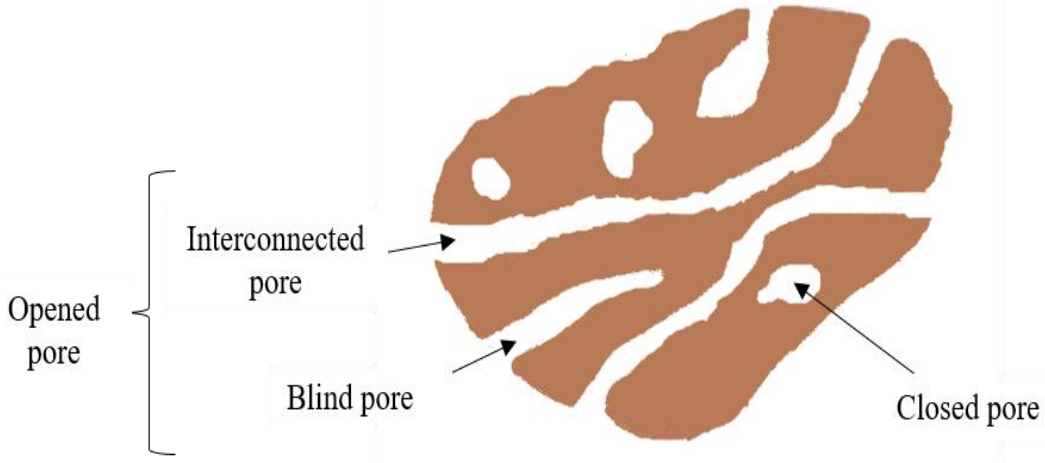

Figure 1.1. Schematic illustrates of cross-section of a porous solid materials. Redrawn from ref. 39.

1.4.1 Functionally Graded Porous Materials (FGM)

FGM is whereby the shape and size of the porous changes across the material. FGM could possess either a porosity density or pore size varying with respect to the three-dimensional position across the volume of the material. Hierarchically porous materials are present everywhere in nature, such as rocks, bone and plants.

Nature has provided a range of hierarchical porous materials with interconnecting multi-scale pores structure. An excellent example is in the human body which is made up functionally graded porosity materials such as bones and the teeth. The structure of bones and the teeth mainly contains a dense shell covering a spongy structure. This structure can provide high mechanical stability and excellent permeability, but, these are the most replaced human body parts, as a result of the natural ageing process or as a result of damage to these parts.[44] With the increasing requirements of industry, gradient porous materials have been shown to be useful in a wide range of applications in different areas, such as the biomedical and environmental fields. A porosity gradient functional materials is most commonly used in medical implants because their properties are very close to those of the parts they intend to replace, which helps to promote the new tissue growth with the desired mechanical properties.[45]

Functionally graded porous materials are mimicking the naturel system and are very important for the biomedical applications as the natural material intended to be replaced consists of functionally graded porosity, and the graded porosity would also help in the incorporation of the implant and the surrounding tissues. For instance, this type of FGM is seen in bone implants, where the larger pore sizes in the porosity functionally graded implants are to be implanted in the bone, in order to aid the bone ingrowth, while the smaller pores are useful for cartilage growth.[46, 47] Furthermore, gradient porous materials have an asymmetrical pore arrangement allowing for filtration materials with different pore sizes across the materials small and big pore size.[48]Materials with porosity gradient provide efficient separation and filtration characteristics due to their unique properties.[49] Filters with hierarchy porosity which decreasing pores size with depth have been shown to have a high separation efficiency than filters with uniform pores.[49] Commonly filters with regular pore size capture the majority of the contaminants in the top layer of the filter while leaving the rest relatively unused, leading to premature clogging and reduced filtration efficiency.[50] While filters whose porosity decreases with depth can improve filtration efficiency due to the small pores trapping small particles within and not just on the surface of the filter, thus, increase their efficiency due to the reduction of contaminant

concentration with depth. Furthermore, the big pores improve mechanical proprieties and enhanced permeability.[51, 52]

1.4.2. Preparation method of porous materials

Porous materials have attracted great attention as an important group of functional materials.[53] Recently, many approaches have been developed to fabricate porous materials, most of these methods adjust the chemical and physical parameters, such as post-treatment, phase separation and templating replication.[54-56] Figure 1.2 demonstrates some of the widely utilised approaches to produce porous materials. [55]

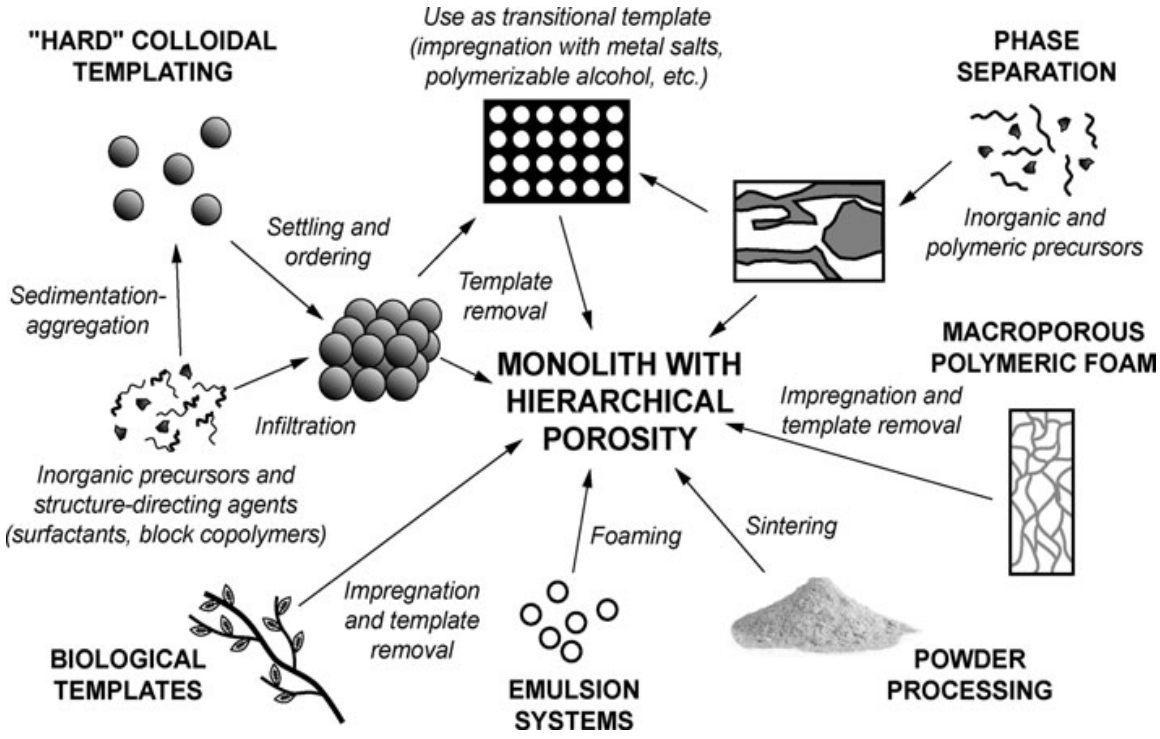

Figure 1.2. Schematic representation overview different synthetic strategies to prepare porous materials (Reproduced from P. Colombo et al 2010).[57]

Fabrication methods of porous materials including surfactant templating, colloidal crystal templating, biological templating, emulsion templating, polymer templating, breath figures, freeze-drying and supercritical fluid technology. Soft templates, are mainly used for the preparation of materials with mesoporous structures.[58] Colloidal crystal templating is an approach to fabricate porous materials, in which colloidal crystals are utilized as hard templates to create materials macroporous structure.[59, 60] Some other important strategies, such as emulsion templating and breath figure (BF) templating are also used to synthesize porous materials.[61-63] Additionally ice is used as a template to prepare

porous materials with interconnected pore channels by freeze-drying process.[64, 65] Supercritical fluid technology are effective approaches for processing and improving nanostructured porous materials.[66, 67]

The FGM with pore size gradient is prepared by changing the pore sizes or the pore shape, or both. The pore size gradation can be achieved by changing the powder particle sizes that are used at various positions in the material during the gradation development. It can also be produced by varying the production processing parameters by using different preparation conditions to produce the required porosity gradient.[68] FGM with multiscale pore size and porosity can be fabricated by either a stepwise (graded) or continuous (gradient) process.[69] The stepwise fabrication can be simply achieved by stacking material components into layers using a variety of methods, while in the continuous gradient structure the composition of material ingredients changes in a continuous way.[70] Production of gradient porous materials is more complicated than uniformly pore structures porous materials. Mainly, it requires further steps to introduce the gradient porosity structure.[71] Several approaches have been developed to fabricate a porous structure with a pore size gradient. For example, sintering of graded particles,[72] infiltration method,[73] multilayers multiple tape casting,[74] the emulsion centrifugation technique,[71] and ice-templating techniques.[69, 75] Most recently 3D printing technique has been also used to fabricate materials with gradient porosity.[76] Some of these techniques however have limitations because they are often time-consuming, size-limiting processes, not environmentally friendly, too costly, or just do not allow precise control over the final structure.[77, 78] Among these processes, the ice-templating method including freeze-drying and freeze casting can overcome many of these limitations. The method is simple and can be used with a variety of materials to control the porosity and is environmental friendly.[77-79] FGM also can be produced by varying the production processing parameters by using different preparation conditions to produce the required porosity gradient.[68]

1.4.3. Applications of porous materials

Porous materials have attracted massive scientific and technological interests over decades because of their unique properties including high surface area, chemical stability, and excellent accessibility.[80, 81] Molecules, atoms and ions can interact with the porous materials not only on the surface, but also inside the pores. Therefore, porous materials have been used in different area such as adsorption, separation, catalysis, ion exchange, etc. Currently, applications of porous materials are under rapid development.[81] Figure 1.3 demonstrates an overview of porous materials applications while the next part will present

briefly some of these applications. It concentrates on adsorption and filtration as these have been employed extensively in this thesis.

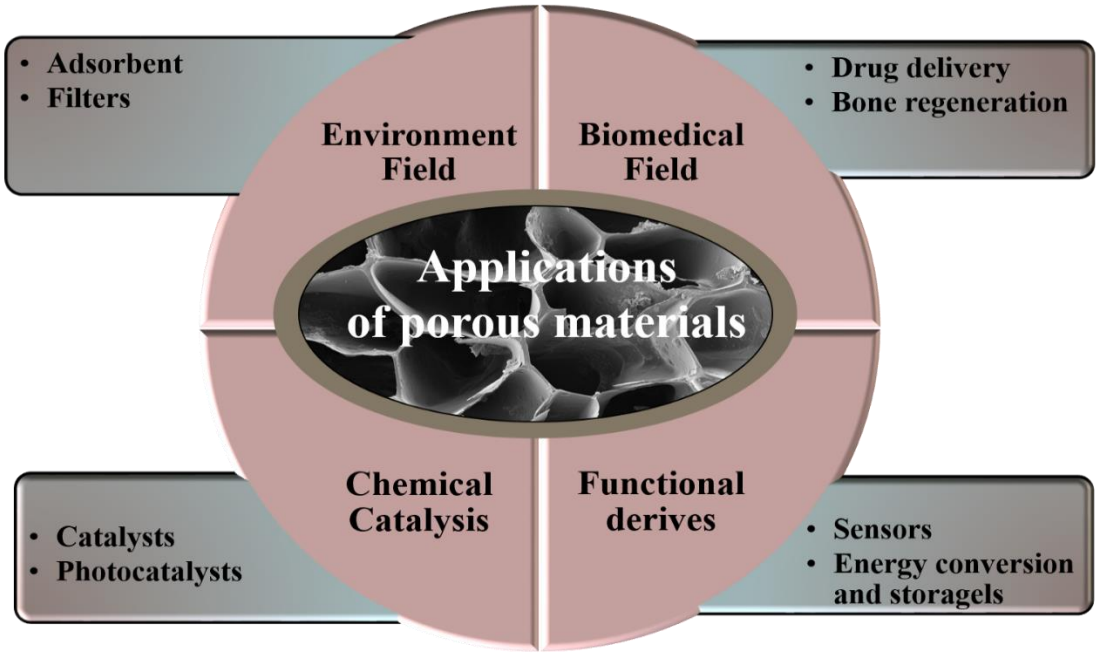

Figure 1.3. The illustration of the potential applications of porous materials

1.4.3.1. Porous materials for biomedicine

Because of the unique structure of porous materials which can provide special properties, these materials have earned important attention for biomedical applications, such as drug delivery, bone tissue engineering, and enzyme immobilization.[82-84] Thus, massive efforts have been made to fabricate porous biomaterials. Fabrication of porous materials for the biological applications needs to careful examine the porous structure found in nature and mimic of this structure to obtain synthetic materials that perform a role similar to that of natural porous materials.[53]

1.4.3.2. Porous materials for energy conversion and storage

Due to accelerating global energy consumption and growing environmental problems, there exists a need to develop renewable and clean energy source with the excellent potential. For example, fuel cells, metal-air batteries, Li-CO_2 batteries and dye-sensitized solar cells are of great importance.[85, 86] These types of sustainable energy technologies depend on numerous important reactions, involving CO_2 reduction reaction, oxygen reduction reaction, hydrogen evolution reaction and oxygen evolution reaction.[87] Porous materials are one of the man-made materials which can not only mimic the functions of

natural materials with a porous structures, but also have new properties; natural structures have been used as biotemplates for the design of materials for the functions of energy conversion, and storage.[88] Thereby, porous materials have been widely utilized in the solar and chemical energy conversion and storage field.[81, 88-90]

Firstly, the porous structures can increase the optical path length and promote dye molecular adsorption, therefore improving the light-harvesting ability, which can be effectively used as photoanodes for dye-sensitized solar cells. Secondly, porous materials are applicable to photocatalytic H_2 production, in which the separation and transfer of photogenerated electrons and holes can be effectively enhanced. Thirdly, these materials have been used in fuel cells, in which reactants flow into the cell and reaction products flow out. Electrical energy storage applications, including batteries such as lithium ion batteries are also among the applications that can profit from porous materials, because a hierarchically porous structure can facilitate charge transfer through the electrode/electrolyte interface and reduce the ion diffusion pathway.[53]

1.4.3.3. Porous materials for photocatalysis and catalysis

Porous materials have been received increasing attentions in catalysis and photocatalysis field. Since the presence of channels with macro size allows deep permitting of light and making the light scattering effect leading to the longer pathway of light for its higher utilization efficiency.[88] The incorporation of macropores into mesoporous architectures in the graded porosity materials can increase light scattering and potentially light harvesting, therefore improving photocatalytic efficiency.[91-93] Materials with multiple porosities levels from micro-, meso- to macro can provide accurate shape and size selectivity and catalytically active sites for molecules while the macropore system can decrease diffusion barriers and thus promote the mass transport.[94] Thus, hierarchically porous materials are applicable to photocatalytic and catalytic reactions.

1.4.3.4. Porous structures for sensing

Gas sensors play an essential role in environmental control monitoring chemical processes, and health and safety in the workplace. Many strategies have been applied to produce novel and effective gas sensors. Many metal oxide semiconductors, such as TiO_2, ZnO, Fe_2O_3, , have been developed as sensing materials for detection of numerous gaseous pollutant due to their fast response and high sensitivity.[95, 96] The chemical interaction between gas molecules and metal oxide semiconductors surface leads to observable changes which can be converted to suitable physical signal.[97] The properties

of these sensors based on semiconducting metal oxides are highly related to their shape, size, and surface conditions.[98]

Metal oxide semiconductors with porous structures have attracted much attention as sensors and many studies have focused on development of new structures for effective gas sensor applications, which control the morphology of semiconducting metal oxides with porous structures for gas-sensing performance.[99, 100] Porous structures provide a high surface area, which increases the adsorption sites and greatly facilitates gas diffusion inside the sensing material, thus improving gas response and sensitivity of the gas sensor.[101]

1.4.3.5. Porous materials for adsorption

Nowadays, huge amounts of chemical waste are being produced, which cause serious environmental problems. Water soluble pollutants, including heavy metal ions and dyes, and air pollutants such as volatile organic compounds (VOCs) can be easily adsorbed by the human body through drinking and breathing and is extremely harmful to human health due to their toxicity, which lead to many physical and mental diseases. Among various methods used for eliminating the chemical polutants in water, adsorption has been proven to be a successful method to remove a wide range of water pollutants because of the flexibility of the system, low energy and cheap operation costs.[102] Activated carbons are generally the most commonly adsorbents used in adsorption process owing to their high surface area and adsorption capacity. However, there are a number of problems with their use, mainly related to the fact that they are expensive and regeneration difficult, which limits their usage.[36, 37] In practice, the most researchers are focused to find adsorbents with a good stability and regeneration performance. Materials with porous structure are widely employed as adsorbents for removing harmful pollutants from the environment such as heavy metal ions and dyes.[39, 103] Among different materials used for adsorption heavy metals ions from wastewater, metal oxides with porous structures are engaging adsorbents owning to their thermal stability, high surface area and morphology structure.[104, 105] In addition, the interconnected porous system can simplify rapid transportation and diffusion of adsorbate molecules and promote access to the active sites.[106, 107] Metal oxides with porous structure showed a higher adsorption capability for heavy metal ion in comparison with the same metal oxide as nanomaterials powder.[108] Adsorbents which have been investigated for dyes removal include silica gel, activated carbon, synthetic polymers and even graphene oxide composites.[109]Besides, porous materials are applicable for removing of organic pollutants such as dyes owing to their

unique combination of chemical and physical properties.[110] Porous carbon materials are considered as promising candidates for adsorption of dye molecules due to their very high surface area and low cost compared with carbon materials as powder. For example, porous carbon with macroporosity have demonstrated higher adsorption capacity for methylene blue than the original carbon.[111]It is believed that the permeability of the adsorbate molecular to the internal surfaces in the porous structure is an important factor for improving the adsorption capacity of the porous materials.[104, 112]

1.4.3.6. Porous materials for separation

Filtration is a common separation method very widely utilized for many applications from dairy applications to high technology processing, which rely upon passing a gas or liquid through a column to make it pure. Many efforts have been made to develop the column technology due to the widespread development of gas and liquid chromatography for simple and quick separation.[113] To improve the efficiency of liquid chromatography, finely crushed particles have been used as packing materials for rising the number of theoretical plates. However, the columns packed with these fine particles required high pressure to pass the liquid at acceptable velocity. [114] In comparison with the small particle packed columns and monolithic columns with porous structures can provide better total efficiency due to their faster separation at low pressure.[115] Many types of materials have been used as porous filters such as paper and cloth. There are many specific properties required in porous materials to use as a filter such as high fluid permeability and high penetrating porosity, narrow pore size distribution, and high mechanical strength. High chemical stability is also required for some filters especially in chemical applications, which need filtration at high temperature.[116]

Porous monolithic silica materials have found markable application as separation media for high performance liquid chromatography (HPLC) due to their high permeability. The high efficiency is based on the high permeability and the fast equilibration of solutes between the stationary solid phase on the mesopore walls and the mobile liquid phase.[113] The mesopores structure in the monolith column increased the surface area to establish interaction between the solid surface and the liquid, while the macropores structure allow a facile drive of fluids through the column.[117]

1.5. Carbon porous materials

Porous carbon materials, as a big group of porous materials, have been studied due to their potential applications in environmental remediation, separation, catalysis, energy storage, adsorption and biomedicine.[118-126] Numerous researchers have been working on

the development of innovative carbon-based materials. Porous carbons materials include a broad spectrum of carbons ranging from microporous to mesoporous such as activated carbon, carbon nanotubes, mesoporous carbons, carbon particles, carbon aerogels, and carbon composites. The properties of each group of mesoporous carbons reflected by their porous structure and surface chemistry are influenced by both the nature of carbon precursors and the methods of carbonization and activation.

There are numerous carbon sources, for example, biomass,[127] natural graphite, thermosetting polymers, bio-waste, *etc.*, that have been researched for the preparation of different types of carbon materials. In particular, of the thermosetting polymers, phenolic resin-based polymers have been most commonly used due to their easy synthesis, cost effectiveness, and industrial attainability. In addition, they are highly versatile, having been adapted for the creation of various carbonaceous materials, for example, nanotubes,[128] mesoporous carbons materials,[129] and carbon aerogels.[130]

1.5.1. Synthesis

1.5.1.1 Hard-template synthesis of mesoporous carbon materials

Ordered mesoporous carbons (OMC) had opened a new section in the preparation of porous carbon materials and initiated one of the most common methods in the synthesis of OMC referred to as the "hard-templating method". [131-134] This route briefly includes three steps. Firstly, preparation of ordered mesoporous silica followed by filling the pores of the template with suitable carbon precursors. Following this, carbonization of the precursors and removal of the silica template are carried out. The resulting carbon materials are inverse replicas of the template and exhibit high surface area, large pore volume and ordered mesoporous. The adsorption properties of these materials can be easily tuned by using different silica mesostructures as templates. Figure 1.4 shows a simple scheme of the hard templating route.

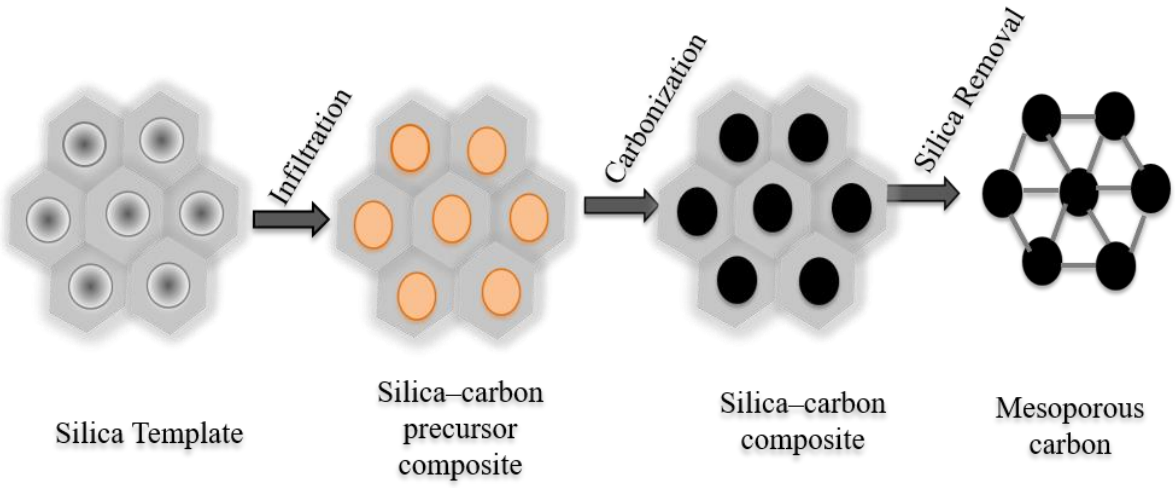

Figure 1.4. Hard-templating method for preparation of porous carbon materials.

Another strategy, which is more convenient for the synthesis of mesoporous carbon materials, includes colloidal crystals or colloidal silica particles as templates.[135-137] The many types of commercially available silica colloids allow creation of the pores in the carbon materials. This combination approach applies blending of colloidal silica particles with carbon sources to get the silica-carbon composite, which undergo carbonization and silica removal. Carbon materials synthesized by this method possess interconnected pores but the pore sizes are similar to that of the templating silica particles, and the pores are randomly arranged.[135, 136] Despite the fact that these strategies turned out to be exceptionally prevalent because of the potential properties of the carbon materials produced by these methods, they have vital drawbacks. Firstly, they have many synthetic steps and high cost due to the preparation of colloidal silica particles and silica porous. Moreover, using chemicals such as hydrofluoric acid (highly dangerous and limited to specially trained personnel) or sodium hydroxide solution (corrosive and environmentally unfriendly) for silica removal is undesirable and renders this method impractical for scale up.[138]

1.5.1.2. Soft -template synthesis of mesoporous carbon materials

Recently, the soft template method has been used for the synthesis of mesoporous carbon materials via self-assembly of organic carbon sources such as phenol, resorcinol, and phloroglucinol in the presence of formaldehyde as cross-linker and triblock copolymers. [139] Self-assembly of organic carbon sources such as phenolic resins and block copolymers

has opened another section in the preparation of mesoporous carbon materials using the soft template route.[140-142]

This new methodology exploits the advantage of the interaction between thermally-decomposable surfactants and thermosetting polymers to construct ordered polymer-polymer nanocomposites. Through initial heating, the thermally unstable soft template agent (triblock copolymer) is decomposed. Increasing the temperature carbonizes the thermosetting polymer to form the pore walls of porous carbon materials. Figure 1.5 shows a simple scheme of the soft template route for OMC preparation.

The soft templating method has fewer steps compared to the hard templating route. This method also avoids the use of hazardous materials, thereby decreasing the negative impact on the environment.[143]

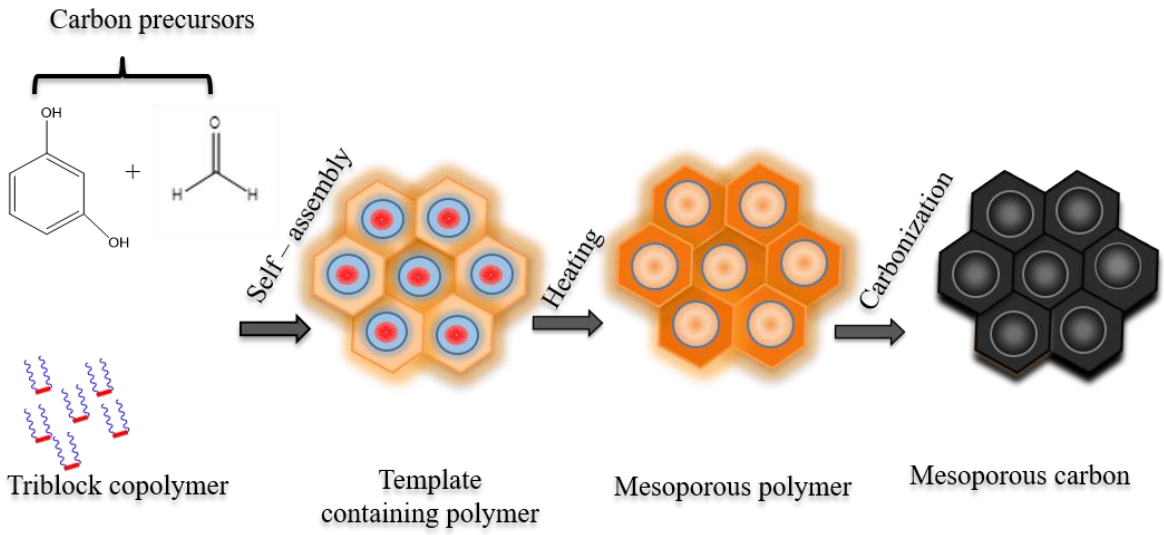

Figure 1.5. Schematic of the soft template route steps for preparation of OMC.

The soft template route was successfully used for the preparation of OMC films by using polystyrene-block-poly (4- vinyl pyridine) (PS-P4VP) as a templating agent.[140] Subsequently, surfactants such as poly(ethylene oxide)- poly(propylene oxide)-poly(ethylene oxide) triblock copolymers (PEO-PPO-PEO), which is ordinarily used for the synthesis of ordered mesoporous silica, were utilized instead as structure building agents for the preparation of OMC.[142, 144] Additionally, these research groups evolved two substitute synthesis ways not only for preparing OMC films but also for forming monoliths and fibres designs. The first group demonstrated a method to pre-polymerize phenol and formaldehyde under basic conditions.[144] Figure 1.6 show the schematic alkaline route of soft templating preparation. In contrast, the second group suggested

different routes that includes phloroglucinol and formaldehyde as a carbon precursor in acidic medium interact directly with the surfactant by self-assembly as a way to construct composite polymer.[142] Figure 1.7 shown the schematic acidic route of soft templating preparation.

The last strategy for synthesis of OMC has the main benefit of avoiding multi-steps for pre-polymerization to form resol and control the pH value for preparation under basic conditions.

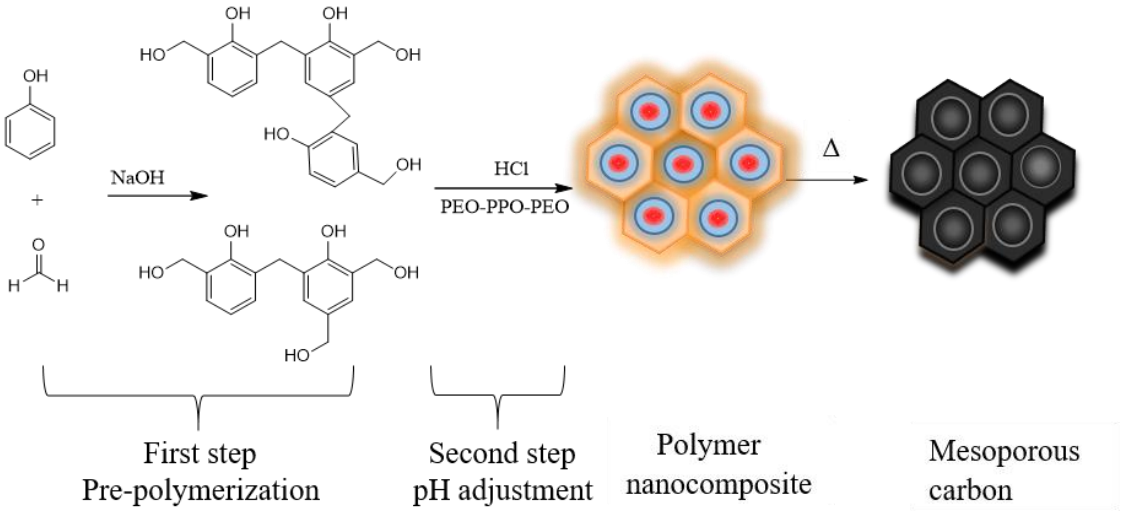

Figure 1.6. Alkaline route of soft templating preparation of ordered mesoporous carbon materials.

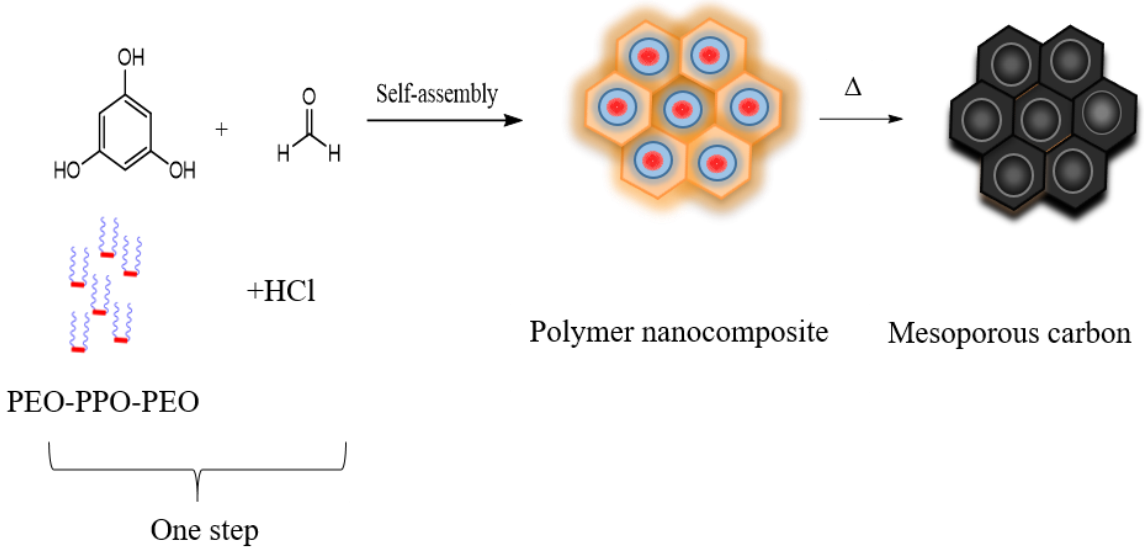

Figure 1.7. Acidic route of soft templating preparation of ordered mesoporous carbon materials.

Research on alternative soft templates has focused on the use of surfactants with different proportions of PEO/PPO blocks (F108, P123 and-and F127).[143, 144]

Mesostructures ranging from layers to continuous hexagonal, cubic, and body centered cubic structures can be obtained by raising the PEO-to-PPO proportion. Additionally, the formation of mesoporous carbon with bimodal pore sizes with a face centred cubic structure using amphiphilic triblock copolymer PPO53-PEO136-PPO53 was shown.[145]

Mostly, researchers have used resorcinol, phenol, phloroglucinol or even blends of these as carbon precursors because of their ability to form hydrogen bonding with the soft template.[146] Other reasons, which support phenolic resin more than other carbon sources, are their capacity for thermosetting, high carbon product after carbonization and great miscibility with copolymers utilised as a soft template.

Many polymeric sources, for example, urea formaldehyde,[147] and melamine,[148] were additionally studied as an option for the initially utilized phenolic resins. By incorporating carbon sources with heteroatoms, the surface chemistry of the resulting carbon-based sorbents can be tailored for different applications. For example, the urea-phenol-formaldehyde resin can form ordered mesoporous polymers containing nitrogen,[147] which is asserted to be a more effective adsorbent towards some pollutants such as heavy metal ions because of increased binding of metal ions and hydrophilicity of the polymeric surface.

Soft template route is the best method used for the synthesis of porous carbon materials due to well organized pore structure as well as specific morphologies. Carbon materials prepared by the soft template synthesis method differ from those prepared by other methods because of the mesostructure of the carbon formed after the carbonization process. Additionally, the synthesis conditions should be arranged before gelation accrues due to morphology development happen spontaneously. It was shown that the polymer design acquired after phase separation step could be simply utilized for the forming of carbon materials in different shapes such as fibers, films, and monoliths by using different methods and molds.[149, 150] Evaporation-induced self-assembly (EISA) technique is the most common method utilised for the synthesis of carbon monolith, but drawbacks include material shrinkage and crack formation, thus decreasing this technique's applicability.[151]To avoid the aforementioned drawbacks. A low temperature autoclaving (LTA) can be employed. This method led to producing highly ordered mesoporous carbon structure.[152]

1.5.2. Magnetic mesoporous carbon materials soft templating

Many applications such as catalysis, adsorption, energy storage and separation frequently require different types of mesoporous carbons, which contains inorganic species or carbon-inorganic nanocomposites. Inorganic species can be included into mesoporous carbons through their preparation process or by post-synthesis infiltration.[153, 154] Post-synthesis is frequently utilized, but its drawbacks include challenges in adjusting particle size and distribution; limitations in the loading of inorganic species; and possible pore blocking. However, these drawbacks are avoided when inorganic species are loaded through carbon synthesis. Therefore, many studies have been made to load inorganic species through the soft template,[155] and hard templating[155] preparation process of mesoporous carbons. Colloidal templating is appropriate for loading of inorganic nanoparticles into porous carbon materials as these particles can be simply co-assembled with silica colloids to shape a hard template.[155] Further, the colloidal templating route allows for a large quantity of inorganic nanoparticles of the required size and shape to be incorporated without influencing the pore size of the subsequent carbon composites; the latter is dictated by particles size of silica colloids.[156]

The disadvantage of this methodology is its restriction to nanoparticles, which can be influence removing the silica template. In contrast with the hard templating method, the soft templating preparation approach is more qualified for loading of inorganic nanoparticles and additionally for their development from suitable inorganic sources. In fact the direct addition of metal salts into preparation mixtures demonstrates an appropriate route for the construction of well scattered nanoparticles in the carbon framework. However at the same time, it is hard to adjust the size of these particles and the arrangement of the carbon mesostructure, which frequently gets to be microporous.[157]

In some early reports, it was demonstrated that tetraethyl orthosilicate (TEOS) could simply participate in the preparation of mesoporous carbon materials by self-assembly of organic species.[158, 159] Using hydrofluoric acid or sodium hydroxide solution to remove the silica and burn the carbon precursors resulted in mesoporous carbon and silica, respectively, which means uniform circulation of all species in the silica-carbon composites. In addition to that many other inorganic components such as nickel, iridium, and titanium element were prepared through self-assembly method of carbon materials and resulted ordered mesoporous carbon containing inorganic nanoparticles.[160]

Ordered mesoporous carbon materials with magnetic properties have a great interest in different applications.[161] The soft templating approach seems to be a good alternative to the hard templating technique for the synthesis of ordered mesoporous carbon materials

because it is a simple method and cost effective. Recently, an iron oxide containing mesoporous carbon was prepared by using resol and block copolymer as template and iron salt via evaporation-induced self-assembly (EISA) method.[162] It was demonstrated that the low Fe_2O_3 content in the carbon materials (for example, 9.0 wt %) had a high surface ranges (up to 590 m^2/g), pore size (~ 4.0 nm), and pore volumes (up to 0.48 cm^3/g). Increasing the Fe_2O_3 content gave excellent magnetic properties, but at the same time can decrease the pore volume and the Brunauer-Emmett-Teller surface area (BET surface area).

Nickel-containing mesoporous carbon composites have ferromagnetic properties, which means these materials can be used for magnetic separation.[163] Likewise, the metal-containing carbons with a cubic structure have been reported. The construction of cage forms rather than channels need varying preparation conditions, all these conditions can effect the growth of nickel nanoparticles, which showed approximately the same size (~20 nm) regardless of the quantity of nickel salt utilised in the preparation process.

In comparison, Wang and Dai [164] have reported that the increase the metal salt amount lead to increase the average size of Ni nanoparticles. There is some confirmation that the nanoparticles are composed on the external surface and within the carbon matrix of the hexagonal structure of ordered carbon. In addition to that, the produced Ni-carbon composites displayed desirble properties, for example, a high BET surface area (up to 660 m^2/g), ordered pores with a diameter approximately 7 nm, and a pore volume from 0.46 to 0.68 cm^3/g.

1.6. Hydrogel materials

Hydrogels are defined as three-dimensional (3D) polymer networks that are able to absorb large amounts of water and undergo swelling but stay insoluble because of chemical or physical crosslinks that connect the individual polymeric chains.[165] The polymers in hydrogels are connected together by either physical cross-linking (such as van der Waals forces, ionic interactions,[166] hydrogen bonds and /or crystallite associations,[167]) or chemical interactions by forming covalent bonding between the polymer chains.[168] Aerogels and cryogels can be obtained by drying the hydrogel by using supercritical or freeze drying methods.[169] Typically, hydrogels are divided into two groups, depending on their origin: biopolymer-based or synthetic. Hydrogel-based natural polymers involve polysaccharides such as cellulose, chitin, alginate and agarose and proteins such as gelatin and collagen. Synthetic polymers hydrogels are generally synthesised via chemical polymerization routes.[170, 171]

Different natural polymers, their derivatives or their salts have been utilised to create biopolymer based hydrogels, for example, starch,[172] cellulose,[173] chitin,[174] gelatin[175] and sodium alginate.[176] Biopolymer-based hydrogels have many applications, for instance, environmental applications as pollutant adsorbents (heavy metal ions[177]and dyes[178]) or, medical applications like in (drug delivery[179] and tissue engineering scaffolds[180]) and biosensors[181]*etc*.

1.6.1. Type of hydrogel

Hydrogels can be separated into two groups according to the physical and chemical interaction between the polymer chains.[182]

1.6.1.1. Physical hydrogels

Physical hydrogels are formed via cross-linking the polymer chains during dissolution of these polymers, for example, van der Waals forces, hydrogen bonding, electrostatic or hydrophobic associations.

1.6.1.2 Chemical hydrogels

A- Chemical cross-linking

Chemical hydrogels form by using chemical reagents capable of forming covenant bonds that link the polymer chains together in a three dimension network. Hydrogels formed by this type of cross-liking are stable gels due to these bonds. Covalent bond for the three-dimension network is mostly happened by use of chemical reagent as cross-linkers during the gelation processes. The mechanism of cross-linking interactions show that chemical cross-linkers for many biopolymers can be separated into two types. Firstly, there are esterifying agents involving carboxylic anhydrides and carboxylic (in this type cross-linkers lead to the construction of –COOR bonds). Secondly, there are etherifying agents involving epoxide, organochlorine, and vinyl compounds (in this type cross-linking involves the creation of R–O–R bonds).[183]

B- Irradiative cross-linking

Irradiation is a beneficial strategy for the forming of covalent bonding between polymer chains. The advantage of this strategy is the production of high purity hydrogel without using toxic crosslinker reagents, therefore, increasing the applications of this method in pharmaceutical and food industries. Nevertheless, the gel obtained by using γ-ray irradiation was shows very low yield, which is less than 30%.[184, 185] The gel yield could be increased in this method by electron beam (EB) irradiation in a vacuum. For instance,

the gel fraction extended to up to 55% after EB irradiation at 20 kGy, with increased the irradiation dose.[186]

Additionally , rather than low yield and a fluid result , some researchers obtained porous materials by using UV irradiation from (3 wt.%) concentration of the polymer in aqueous solutions for example methyl cellulose MC, hydroxyl ethyl cellulose HEC and hydroxyl propyl methylcellulose HPMC solutions using a photoinitiator (4-benzoylbenzyl) trimethylammonium chloride (BBTMAC).[187] Photo crosslinker must be added to the solution before irradiation to improve the gelation ability.[188] The polymer chains degrade with crosslinking through irradiation, particularly at low polymer concentration and high irradiation intensity resulting in broken network structures and lower tensile strength.[189]

1.6.2. Smart hydrogels

Smart hydrogels or intelligent gels terms refer to gels with stimuli-responsiveness.[190] Such gels show a response to environmental stimulus, which can produce changes in structures, shapes, colours, reaction rate, surface activities and electric and mechanics properties. Thus incorporating extra functionality to the gel.[191] Smart hydrogels can be separated into different groups depending on their sensitivity for varies stimulus such as temperature, pH, sound, light, electric field and magnetic field. Hydrogels can show exciting changes in their network structure, swelling behaviour, and mechanical properties in response to various external and internal stimuli.[192] External impetus has been created with the assistance of various stimuli producing by instruments, though internal impetus is delivered inside the body to adjust the construction changes in the network connection system of the polymer.[193] There are extensive studies on the pH-responsive and temperature-responsive hydrogels due to their wide applications, especially in medication field.

1.6.2.1. pH-responsive hydrogels

In pH-responsive hydrogels, changing the pH value by using weak acid or base may result in a conformational change in the swelling conduct and polymers solubility of the hydrogel materials when these ionic groups are connected to the polymer structure.[179] Minimal change in pH value can result in large responses in the cross section size of the polymeric systems. Anionic hydrogels swell at a pH over the pKa of the polymer due to an expansive osmotic swelling power. But the cationic hydrogels are swelling at lower pH.

1.6.2.2. Temperature-responsive hydrogels

Temperature is another factor that can affect the hydrogel behaviour. Temperature-responsive hydrogels display a phase transition behaviour at a specific temperature, which causes an unexpected change in the solvation case.[194] Thermoresponsive polymers divided into kinds: first type, depending have lower critical solution temperature (LCST) of the polymer solution, while the second type have the upper critical solution temperature (UCST). It is important to note that LCST is an entropic effect while UCST is an enthalpic effect as shown in Figure 1.8.

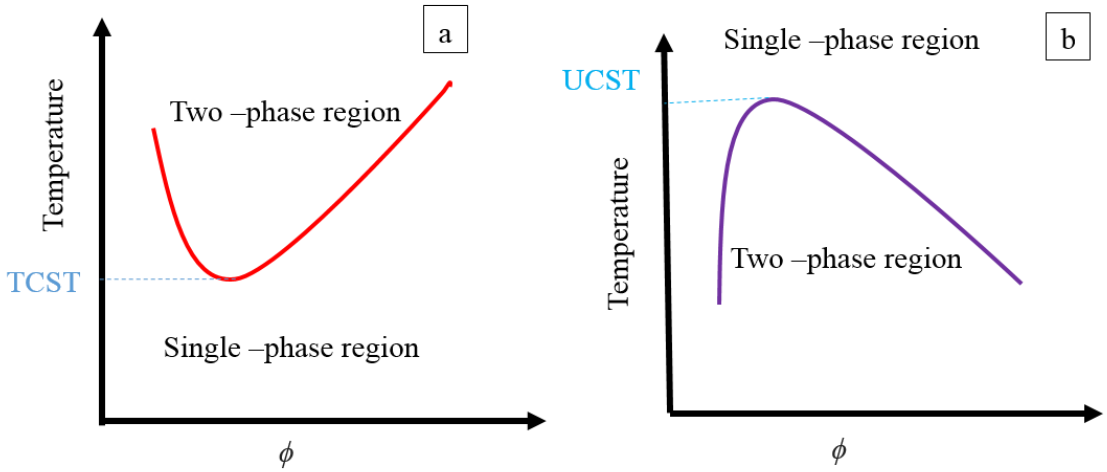

Figure 1.8. Temperature *vs.* polymer volume fraction, ϕ. Schematic explanation of phase diagrams for polymer solution at different temperature (**a**) LCST behaviour (**b**) UCST behaviour.[195]

LCST and UCST are below and above the critical temperature points respectively, which is the solvent and polymer completely unable to mix. For example, a polymer solution below the LCST is a homogeneous and clear solution while above the LCST seem to be cloudy. Therefore, the LCST also indicated to the cloud point of the polymer solution.[195] Particularly, considering the free energy of the system utilizing the Gibbs equation:

$$\Delta G = \Delta H - T\Delta S$$

(Where ΔG: change in Gibbs free energy, ΔH: the change in enthalpy, T : temperature and ΔS: the change in entropy) The main reason for phase separation when increasing the temperature is due to the change in entropy of the system. Specifically, the entropy is the main driving force in the water, which when the polymer is not in solution, the water has a higher entropy. This is also termed the "hydrophobic effect".[196, 197]

1.7. Aerogel materials

The term aerogel refers to porous materials produced by a substitution of the liquid in a gel network with air. The network structure in the precursor liquid gel phase is greatly in the resulting aerogel. Aerogels are very light materials due to their low density.[198] Additionally, aerogels have a huge surface area, low thermal conductivity,[198, 199] rendering aerogels unique. Aerogels have many applications, for example, as optical sensors and catalysts.[198, 200] In 1931 Samuel Kistler synthesised different type of aerogels by drying hydrogel materials including organic and inorganic aerogels, and Kistler established that this list of compounds might be developed inconclusively.[201]

In the late 1960s that innovative work of aerogels began because of the fast improvement of the sol - gel process.[198] These days, an expansive assortment of aerogel materials are accessible. These materials are synthesised from wet gel materials by using different drying strategies. Wet gels are acquired by the accumulation of colloidal particles (sol) in a 3D network (gel). For this situation, the sol-gel science is essential and allows adjust of the aerogel design.[198] Different type of aerogels has been synthesised such as silica aerogel,[198] chitosan aerogel,[202, 203]cellulose aerogel *etc*.[204]

1.7.1. Synthesis of aerogel materials

A wide range of aerogels have approximately the same synthesis route steps: sol–gel procedure, aging, and drying as shown in Figure 1.9. However, preparation of carbon aerogels has additional step, which is the carbonisation after drying step.[205] Many applications of aerogels rely upon the porous structure and the active groups on the surface of aerogels,[206] which are controllable during their preparation.

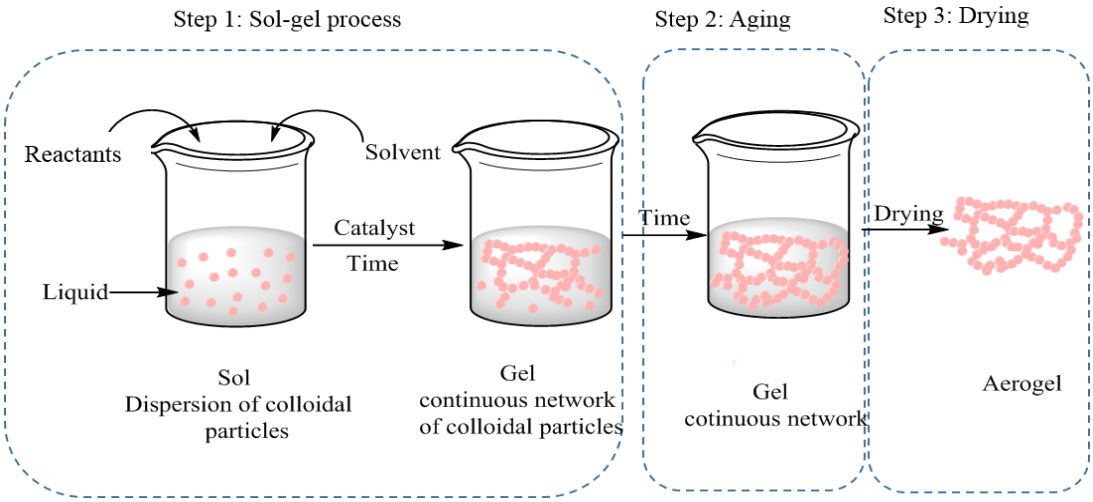

Figure 1.9. Schematic representation the general preparation method to prepare aerogels.[205]

1.7.1.1. Sol–gel process

All aerogels are synthesised by a sol-gel approach, but by various beginning precursors, performing and requirements.[206] Sol refers to an extremely dispersed solution of colloidal essential particles/monomers prepared to compose a blended solution including precursors, solvents, water, and catalysts resulting from polycondensation and hydrolysis reactions.

Colloidal particles associated with the structure of a three-dimensional network by adding chemical compounds as a cross linker or by changing the physical parameters of the reaction such as pH and temperature.[207] The creation of porous materials with three-dimensional structure is the most basic and determinant part of aerogel production. The wet gel name depends on the type of the liquid that filling the pore. For instance, hydrogel, acetogel, alcogel refer that the liquids fills pores are water, acetone, and alcohol respectively.[208] Hydrogels refer to gels that are generally synthesised from natural polymers that are subjected to the chemical and physical gelation in the water. Depending on rate of crosslinking and the development process, network clusters in the size range of 1–10 nm will be formed with either sol or gel morphology.[206, 209] Despite chemistry after the sol–gel procedure is different from one sort to another sort of gel. The sol–gel process is an adaptable procedure that allows tuning the gel nanostructure by changing the reaction conditions. Various parameters impact the sol–gel process and the organization of the network structure. These include the temperature, pH, concentration precursor, concentration and type of solvent, and the ratio between precursor, solvent, and water during the sol-gel process.[210, 211]

1.7.1.2 Aging

The chemical reaction is not complete upon gel formation by the sol –gel process.[212] The subsequent aging process further develops the network. Generally, the gelation solvent inside the pores may include reactive groups such as hydroxyl groups ($^{-}$OH) in addition to residual monomers which can further condense with the polymer network.[208]

Mostly, this process takes from some hours to days by immersion the gel in their initial sol solution or other convenient solvent under the adjusted conditions.[210] The main purpose of the aging process is to develop the mechanical properties of aerogels.[213] The aging process can be impacted by many parameters such as time, temperature and pH.[212, 214, 215] Additionally, textural properties change during an aging process such as surface area, porosity, and pore size.[216-218]

1.7.1.3 Drying

Drying gels or hydrogels without breaking the porous network structure is a crucial step during aerogel synthesis. Many drying techniques are utilised to dry the acquired wet gels, for example, supercritical drying,[219, 220] freeze drying.[221,222, 223] Freeze-drying and supercritical drying are the most typically used to produce aerogel with a monolithic shape.

A. Supercritical drying

The most suitable and active way to dry the hydrogels to obtain aerogels is removing the liquid inside the pores under the supercritical conditions since drying gives a crack free solid gel.[209] During supercritical drying, the gel is set inside the closed vessel with high pressure, whereby the temperature and pressure of vessel exceed the critical point (T_C, P_C) of the liquid filling the pores of gels. The critical drying method circumstances vary, relying upon the solvent used.[224, 225]Supercritical carbon dioxide is the most commonly utilized solvent Figure 1.10 shows carbon dioxide phase diagram showing the supercritical area and the supercritical drying pathway. Because of the moderate critical temperature in supercritical CO_2 ($ScCO_2$), drying is approximately equal 31 ºC, the usage of this drying strategy is more advantageous in contrast with the supercritical drying with other solvent. For example, the critical temperature in supercritical drying with ethanol equal 240 ºC.[203, 209, 226]

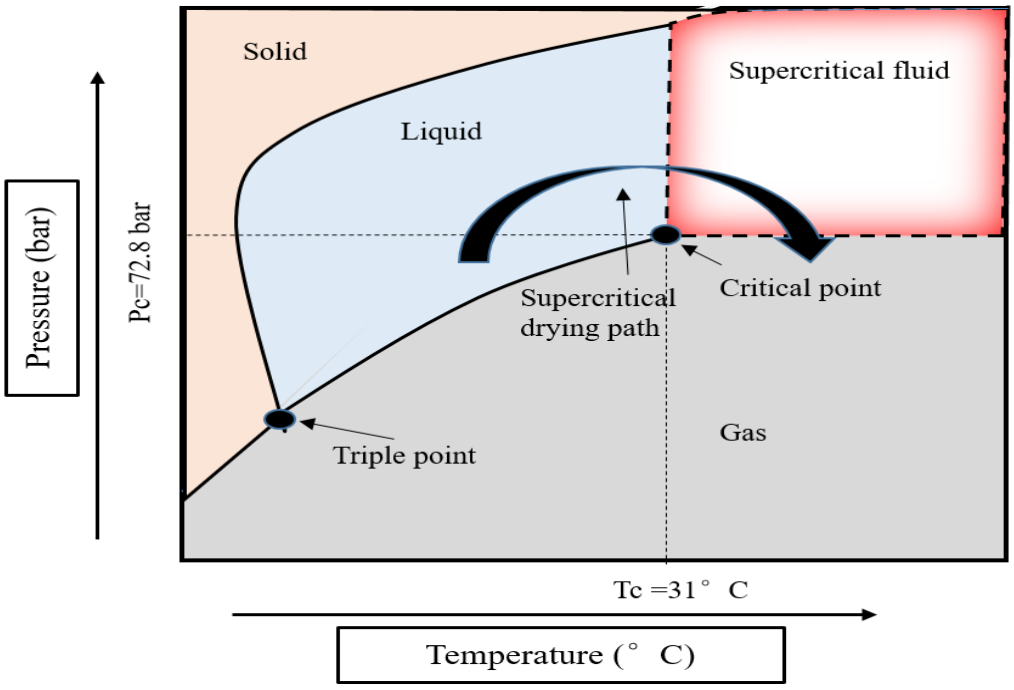

Figure 1.10. Carbon dioxide phase diagram showing the supercritical area and the supercritical drying pathway.[227]

B. Freeze drying

Freeze drying is an easy, low-cost and environmentally safe drying method which is used to synthesizes aerogel like materials with porous structures.[205]In this drying method, first of all, liquid is frozen inside the pores in gels and after that removed by sublimation under low-pressure Figure 1.11 shows the phase diagram of water and freeze drying pathway. The resulting products are termed cryogel .When compared to their aerogel counterparts produced by $ScCO_2$ drying, cryogels possess approximately 80%of aerogel porosity and 50% less surface area. The increasing the gel aging time can result in an aerogel with improved properties. Likewise, freezing rate is a significant parameter and connected with the ice crystals size and shape, which influences the pore structure in the aerogel. For example, a quick freezing rate produces small ice crystals and lead to aerogels with high surface area and small pore sizes. Cryogels tend to display macroporous structure , lower surface areas and greater degree of shrinkage compared to aerogels prepared by $ScCO_2$ extraction.[228]

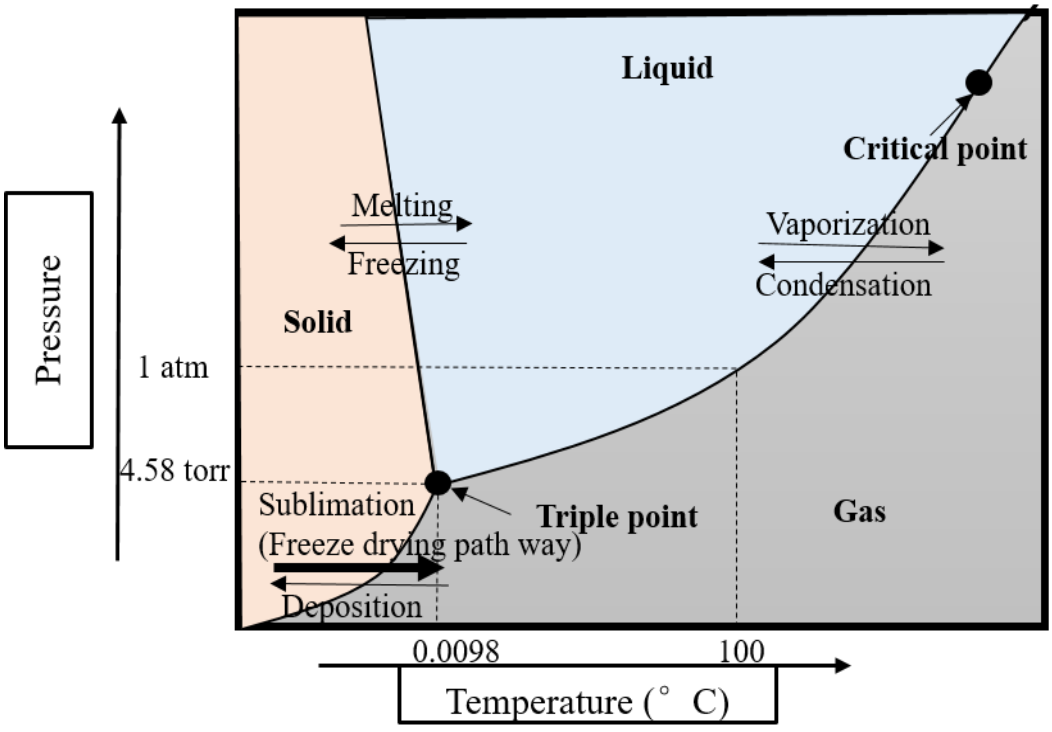

Figure 1.11. Water phase diagram showing the freeze drying pathway.[229]

1.7.2 Cellulose hydrogel and aerogels

Cellulose and its derivatives are the most important organic source used to synthesise hydrogels and aerogels materials due to their hydrophilicity, natural abundance, non-toxicity, and high stability.[183, 230] Cellulose is a natural polysaccharide and is the most abundant renewable substance on the earth. Nearly 1.5×10^{12} tonnes of cellulose are consumed every year in a pure structure in addition to lignocellulosic materials.[231, 232] It is commonly component available in all the plants cell wall and to a lesser degree in some organisms such as some type of bacteria, fungi, tunicates and algae.[233] Cellulose consists of long linear chains of D-glucose, which is connected by ß-1, 4-glycosidic bonds. Every cellulose chain consists of approximately several hundred to over ten thousand β (1-4) D-glucose units. Each unit involves three hydroxyl groups at C2, C3, and C6 positions which possess the common reactivity of primary and secondary alcohols. Figure 1.12 shows the general structure of cellulose.[234, 235]

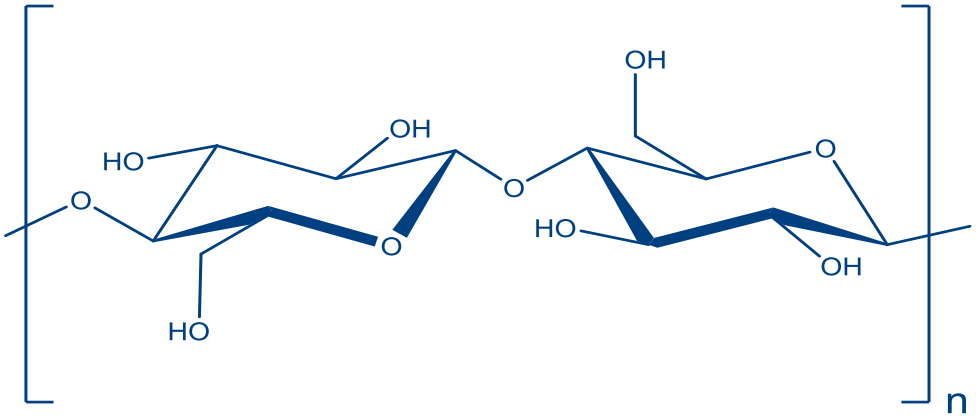

Figure 1.12. General chemical structure of cellulose.

The hydroxyl groups are capable of forming numerous hydrogen bonds with OH near chains and combining the chains together. Additionally, the chains bundle regularly to hard, stable crystalline shapes, which gives the combined chains considerably more strength and stability.[236] Extensive hydrogen bonding existent in cellulose contributes to making the cellulose insoluble in water. Hydrophobic modified cellulose is one of the largest members. When hydroxyl groups are substituted partly by methyl groups or hydroxypropyl groups, some hydrogen bonds are prevented and the resultant derivatives become water soluble.[237] Different cellulose derivatives have been synthesised by

etherification of the hydroxyl groups on D-glucose units of cellulose resulting in many water-soluble derivatives, for example, hydroxypropyl cellulose (HPC), methylcellulose (MC), hydroxyethyl cellulose (HEC), hydroxypropylmethylcellulose (HPMC) and ethyl hydroxyethyl cellulose (EHEC).[238, 239] Figure 1.13 shows the structure of cellulose derivatives.

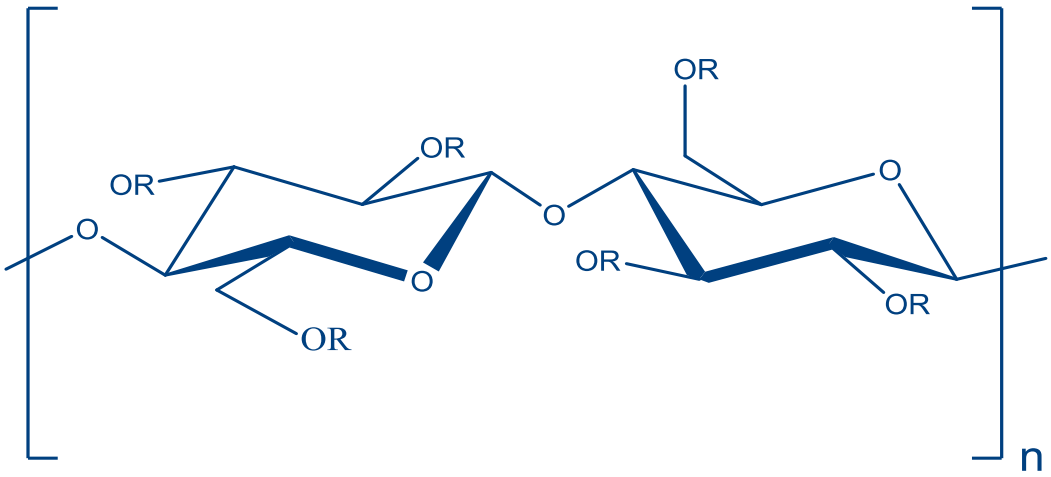

Figure 1.13. Structure of cellulose derivatives, where R =H or R=substituent from table 1.1.

Table 1.1. Structural formula of different cellulose derivatives.

No.	Cellulose derivatives	R
1	Methyl cellulose (MC)	$-CH_3$
2	Hydroxypropyl cellulose (HPC)	$-CH_2CH_2CH_2OH$
3	Hydroxyethyl cellulose (HEC)	$-CH_2CH_2OH$
4	Hydroxypropyl methyl cellulose (HPMC)	$-CH_3$ or $-CH_2CH(OH)CH_3$
5	Ethyl hydroxyethyl cellulose (EHEC)	$-CH_2CH_3$ or $-CH_2CH_2OH$

Cellulose aerogels are the oldest organic aerogels and the primary natural aerogels which were invented accompanying the birth of the silica aerogel.[240]The cellulose gels are shaped by dissolving and recreation of cellulose in an organic solvent or water.[241, 242] In addition, cellulose can possibly create porous structures with a very low density approximately less than 5 mg/ cm^3 and especially high porosity (more than 99%). The aerogels network structure have huge pores with pore size nanometer to micrometre scales.[243, 244]

In fact, the porous three dimensions structure of cellulose aerogels skeletons and the pore size can be changed from mesoporous to microporous by changing the concentration of cellulose in the starting hydrogel and by modifying their drying techniques.[244, 245]

In addition, Cai *et al*. have prepared natural aerogel with high purification, ultralight, and microstructure by utilizing cellulose nanofibrils.[246] The aerogel microstructure has a very high porosity with pore size extending from nanometers to micrometres and a density less than 0.0018 g/ cm^3. Chemical crosslinking between the native cellulose chains resulted in the very stable aerogel. The utilisation of natural materials such as biomass is a rising methodology for the generation of new mesoporous aerogel materials. The generation of aerogels from cheap and natural sources have received interest in the academic and industrial fields. Different materials, for example, bamboo leaf,[247] paper waste,[248] jute strands,[249] and rice straw [250] have been used to create cellulose aerogels. Nguyen et al. prepared an economical and flexible way for modifying cellulose aerogels from paper waste. The resulting cellulose aerogels have macroporous structure with density of approximately 0.04 g/ cm^3 and thermal conductivity of between 0.029 to 0.032W/m^1K^1 [251] Additionally, cellulose aerogels were prepared from bamboo leaf in acidic medium, which show low thermal conductivity and high surface area around 547.2 m^2 g^{-1}. [252] Moreover, cellulose aerogels has been prepared from cellulose materials that were defibrillated from rice straw cellulose and produced ultra-light aerogel with high porosity from 99.5% to 99.9%.[250] Many scientists have reported preparation of cellulose aerogels. These aerogels are synthesised via drying the hydrogels materials by supercritical carbon dioxide ($ScCO_2$) drying in a technique including prepare the hydrogel dry dissolution cellulose materials in a different solvents such as N-Methylmorpholine N-oxide NMMO,[253] sodium hydroxide,[254] NaOH/urea,[242] LiOH/Urea,[255] or aqueous calcium thiocyanate.[243] Then drying the produced gel by using supercritical CO_2 drying. This drying method able to produce cellulose aerogels without cracking the network structure due to using low critical pressure of CO_2 approximately 7.4 MPa and low temperature around 31 ºC. In addition, the properties of these materials have been studied and was demonstrated that they have small pore size, high surface area[242, 256] and unique mechanical properties.[255] Cellulose aerogels have been prepared by using others drying methods such as freeze drying.[243]

1.7.3. Alginate hydrogel

The alginate or salts of alginic acid as biopolymers have been attracted a great deal of attention owing to their unique properties.[257, 258] Alginate is one of the most naturally abundant biosynthesized materials isolated from the cell wall of brown algae. This polymer is hydrophilic and anionic polysaccharide composed of linear unbranched units of β 1,4-linked- - D-mannuronic acid (M) unites and α(1-4)-L-guluronic acid (G) unites.[259] In an alginate linear chain arranged in blocks of M and G unites sequence within the structure, the M and G unites are distributed in repeating M blocks G blocks and blocks of interspersed with regions containing alternating (MG blocks) sequences.[260] Figure 1.14 and Figure 1.15 show the chemical structure of alginate monomers and the possible sequences of (G) and (M) blocks in an alginate polymer respectively.

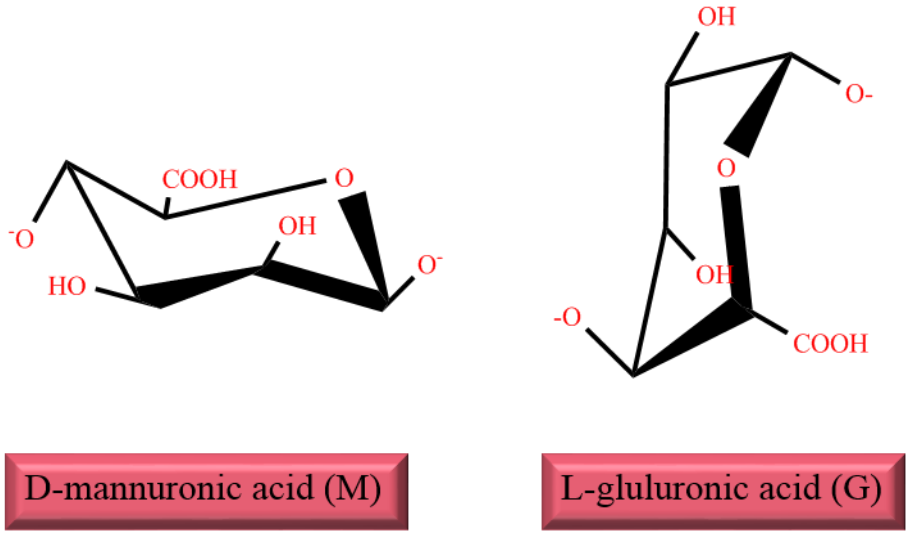

Figure 1.14. Chemical structure of alginate monomers: D-mannuronic acid and L-guluronic acid

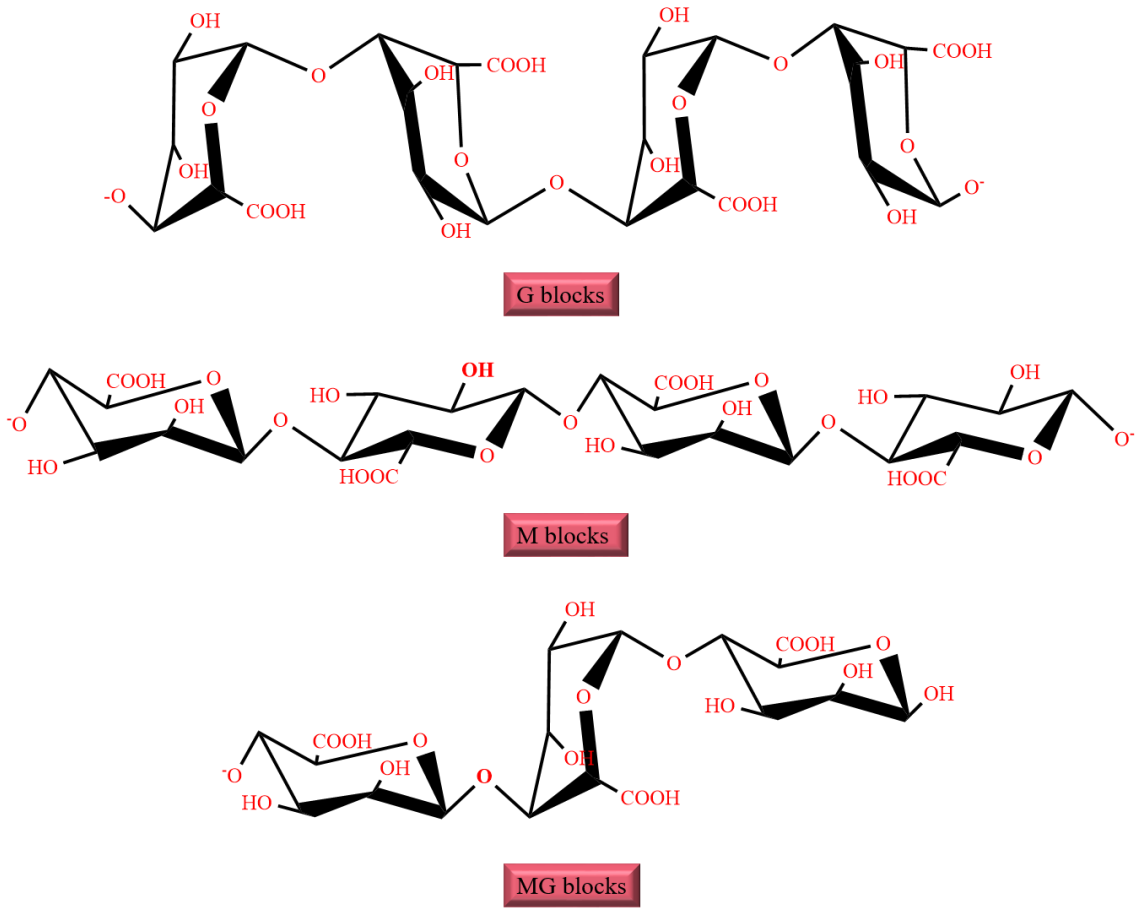

Figure 1.15. Possible sequences of L-guluronic acid (G) and D-mannuronic acid (M) residues in an alginate polymer. Redrawn from Ref.[258]

Alginate with monovalent ions (alkali metals and ammonium) are soluble and only enhance the viscosity, However, those with divalent or trivalent ions are insoluble.[261] Alginate solutions that able to form a gel in the presence of multivalent cations, as a result of creating ionic interchain associations due to the carboxylic functional groups along of the polymer chain.[260, 262] According to the "egg-box" model for alginate gelation, multivalent cations such as calcium, barium, and aluminium ions cooperatively bind with G blocks forming ionic crosslinks between alginate polymer chains.[261, 263] Therefore, the gel forming properties of alginates are derived from their capacity to bind a large number of multivalent ions and the gel strength is correlated with the proportion and length of the G blocks in the polymer chains.[264, 265]Figure 1.16 demonstrate diagrammatic representation of the multivalent ion salt bridges for formation of the alginate hydrogel.

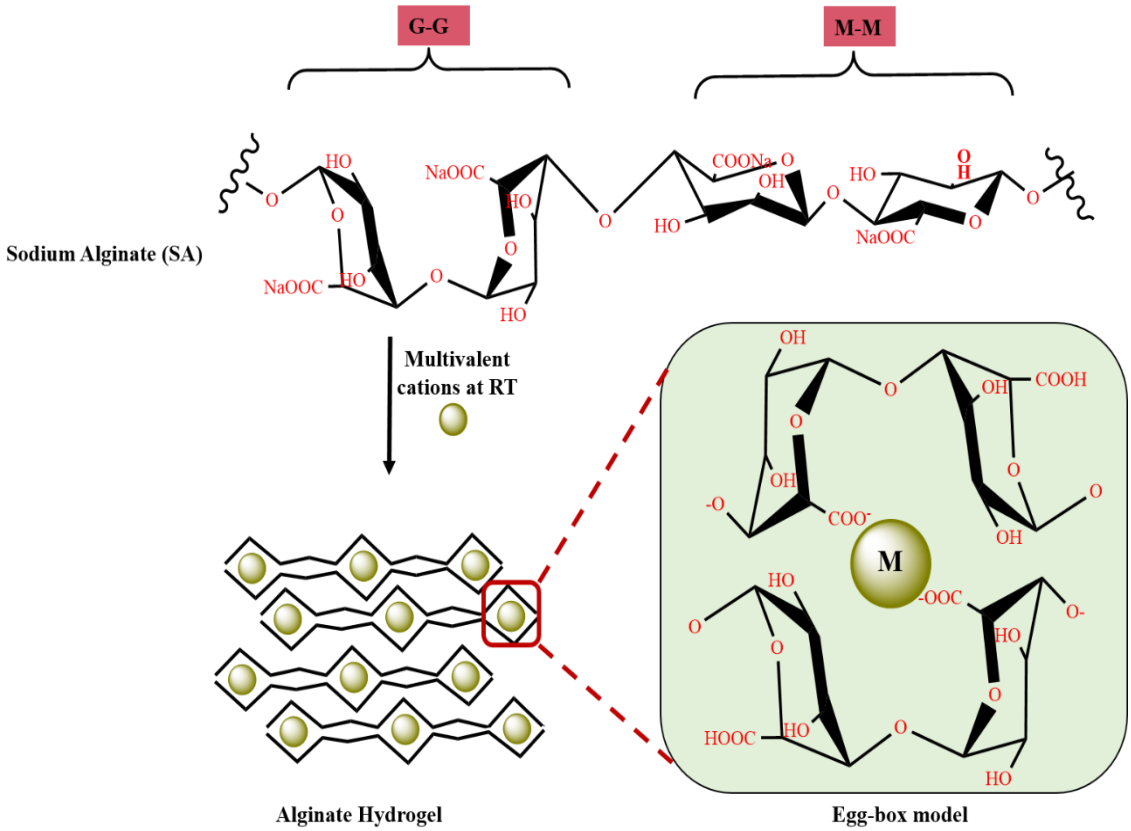

Figure 1.16. Mechanism of ionic interaction between alginate and multivalent cations at room temperature and formation of the alginate hydrogel by coordination of multivalent cations between alginate chains as per the ‘‘egg-box’’ model. Redrawn from Ref.[266]

1.8. Types of hydrogel network

Hydrogels comprise of either covalently or physically cross-linked network. The network components of hydrogels can be either synthetic or natural, as long as they absorb and maintain large quantities of water. Mainly, there are two kinds of hydrogel network depending on the number of networks in the hydrogel materials.

1.8.1. Single network (SN)

The chemical structure of single network hydrogel can result via one kind of polymer crosslinked by physical or chemical crosslinking. For example, the hydrogels forming by the polysaccharides materials such as cellulose, starch, alginate, and agarose.[207]

1.8.2. Double Network Hydrogel (DN hydrogel)

DN hydrogel is a type of Interpenetrating Polymer Network (IPN) hydrogel. This consists of two polymer networks in the absence of covalent linkages. [267, 268] The properties of the two networks are very different due to their network density, molecular

weight, cross-linking density and ridgidity.[269] The first polymer network is brittle and tightly cross-linked; the crosslinks serve as sacrificial bonds which dissipate energy. The second polymer network is loosely crosslinked and has the ability to be customisable and extended.[270, 271] Generally, DN hydrogels present superior properties in comparison with the corresponding single-network parent hydrogels.[272] DN hydrogels have also demonstrated extremely high mechanical strength and toughness with a high water content.[273, 271, 274] Gong and co-workers where the first group to study DN hydrogels in 2003.[271] It has been ~16 years since the first DN hydrogels were synthesised, this has resulted in a very fruitful research career where there have been numerous publications as a result of their work on the development of DN hydrogels.

1.8.2.1. Preparation methods for a DN hydrogel

1. Two-pot method

Firstly, DN hydrogels are usually synthesized via a classical method which includes a two-step polymerization process.[267, 271] The first step is to use strong polyelectrolytes to form a covalently cross-linked, rigid and brittle structure. Then, the first polyelectrolyte gel is immersed and swelled in a precursor solution containing the second network monomers, initiators and cross-linkers. Due to the high swelling nature of strong polyelectrolytes, the second network reactants will slowly diffuse into the first network. This results in a large volume expansion for the first network. Upon the swelling process, the second polymerization occurs to form a loosely cross-linked, soft, ductile and neutral second network within the first network as shown in Figure 1.17. This method, was widely used in the past to prepare the majority of DN hydrogels where both networks are chemically cross-linked and it has the advantage of being readily modified and adapted to accommodate different polymer systems.[275] This method involves swelling, diffusion and two polymerization processes, and is therefore very resource constrained as it requires a large excess of the second network materials (i.e. the second network monomers are in a 20–50 times excess, as compared to the first network monomers) to efficiently initiate the second polymerization and to form a strong network entanglement with the first network. The timescale required for a typical two-step method usually takes 1–2 days.

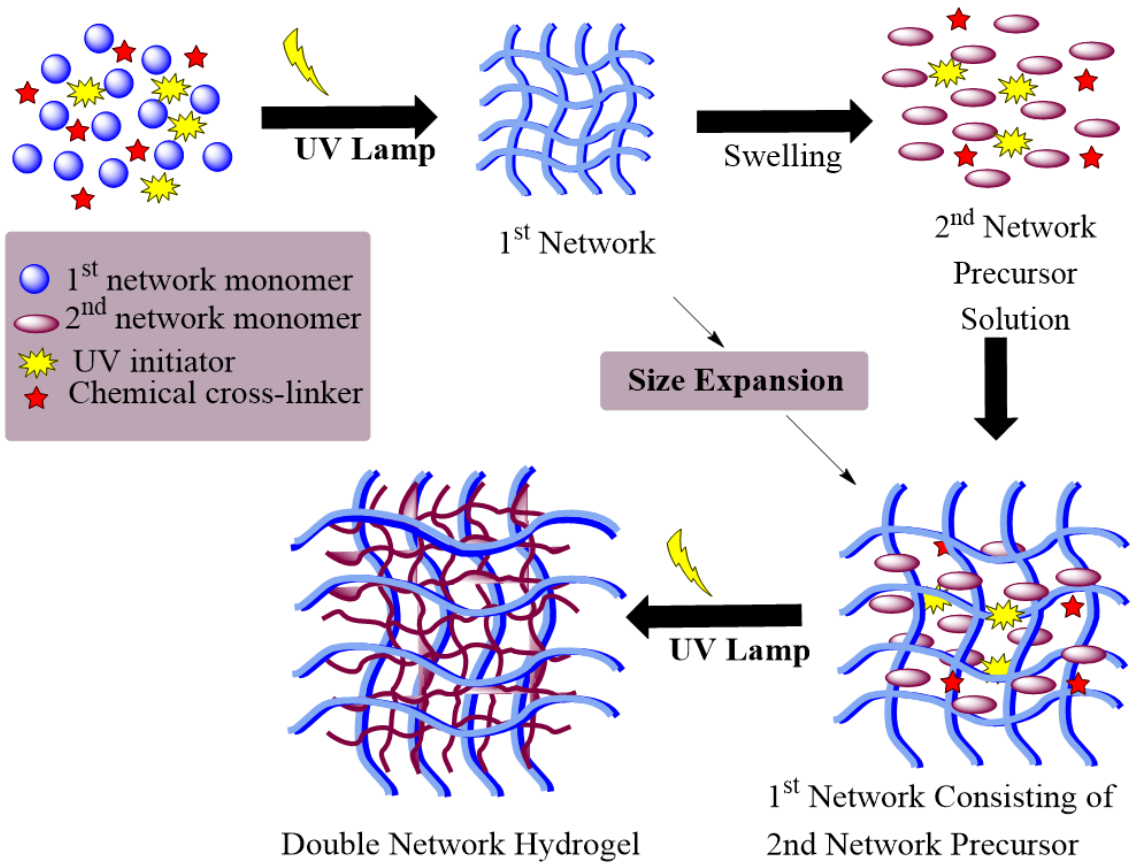

Figure 1.17. Two-step polymerization method to prepare chemically linked DN hydrogels.[275]

2. One-pot method

The classical methods have offered great generality and flexibility in the preparation of tough DN hydrogels. However, this method encounters some limitations. Firstly, the multi-step synthesis process is time-consuming, which involves a swelling process, diffusion, and two polymerization steps that demand 1–2 days to complete the whole synthesis. Secondly, conventional multi-step methods are unable to prepare complex shaped gels to meet specific applications in a straightforward approach. The chemically linked gel networks once formed can fracture, particularly the first network. This causes irreversible and permanent bond breaks, making the hydrogels very difficult to repair and recover from damage. It is also difficult to control the molar ratio of the two polymer components when the linkages are compromised.[275, 276] To overcome these limitations, Chen et al.[277] developed a novel and relatively simple one-pot method to synthesize a new type of hybrid physically–chemically cross-linked agar–polyacrylamide (agar–PAAm) DN hydrogels. These consist of two interpenetrating networks, the first being a hydrogen

bonded agar network and the second a covalently cross-linked PAAm network. Figure 1.18 displays schematic representing the one pot method for preparing DN hydrogels.

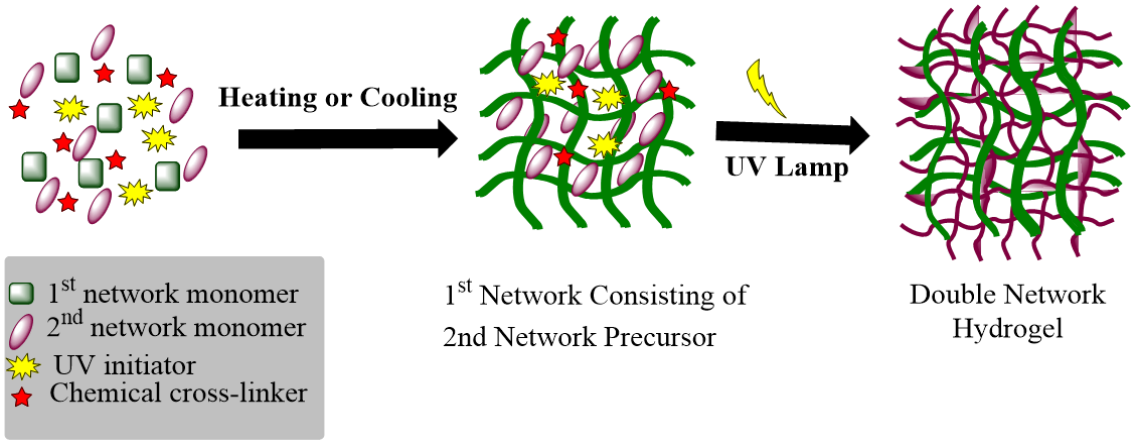

Figure 1.18. Schematic illustration of the one-pot method for preparing hybrid linked DN hydrogels with the first network being physically linked and the second network being chemically linked.[275]

The physically crosslinked agar network were formed first then the agar gel and other unreacted species in the same pot were photo-polymerized to form the second chemically cross-linked network of polyacrylamide (PAAm) this was found to penetrate into the first agar network. The resulting agar–PAAm DN hydrogels demonstrated their superior mechanical properties of stiffness, strength, toughness and fast recoverability. These were comparable to those of the chemically linked poly (2-acrylamido-2-methylpropanesulfonic acid)- polyacrylamide DN hydrogel (PAMPS–PAAm DN hydrogels). The agar-PAAm hydrogel also exhibited a unique free-shapeable property (formation of many complex geometrical shapes) this was also found to be improvement on the other hydrogel systems.

Contrasting the classical method for preparing chemically linked DN hydrogels, this'one-pot' method is developed for preparing hybrid physically chemically cross-linked DN hydrogels, particularly with specific selections for the first network polymers that possess reversible sol–gel property. Due to the one-pot method does not involve the swelling and diffusion processes, it can easily produce and optimize the DN hydrogels in a fast and controllable way. This preparation method is also far quicker as it only takes 1–2 hours to complete. This is opposed to the 1–2 days required for the multi-pot procedure mentioned previously.

1.8.2.2. Network structures of DN hydrogels

The different hydrogel preparation methods has created a wide variety of network structures in DN hydrogels preparation. Therefore, the hydrogels can be classified depending on the type of cross-linking in the both networks.

1. Chemically-chemically crosslinked networks

Mostly the chemically-chemically crosslinked networks DN hydrogels synthesized by the classical method involve multiple-step polymerization of different network polymers. As a result, these chemically linked DN gels appear heterogeneous in nature, however they have similar network structures and mechanical behaviours. As previously mentioned, Gong and co-workers prepared the first DN hydrogels. In particular, one of the systems was generated from two hydrophilic polymers separately crosslinked by two covalent bonds utilising a two-step method via free radical polymerization using poly(2-acrylamido-2-methylpropanesulfonic acid) (PAMPS) as the first network and polyacrylamide(PAAm) as the 2nd network. These hydrogels show a fracture resistance strength very high, as compared with other single network hydrogels which are prepared from these polymers.[271] Chang et al. have also synthesised a novel hydrogels composed of cellulose and poly(N-isopropylacrylamide) (PNIPAAm) with high mechanical strength and adjustable thermosensitivity. Cellulose hydrogels were prepared by chemically cross-linking cellulose in a NaOH/urea aqueous solution. This synthesis procedure developed the first network. The second network was subsequently obtained by in situ polymerization/cross-linking of N-isopropylacrylamide into the first network component, the cellulose hydrogel. This work created DN hydrogels, which combined the advantages of the natural polymer and synthesized PNIPAAm collectively into one system. This allowed the users to regulate temperature response and gave further improvements to the other physical properties.[267] Recently, Chen and others have reported a series of tough polyethylene glycol/collagen (PEG/Col) DN hydrogels, synthesised via a two-step strategy. PEG was introduced to form the initial network and to enhance the modulus of DN hydrogels, this was followed by addition of the collagen as the second network. The fracture strength of the PEG/Col DN hydrogels was found to increase by 9- to 12-fold compared with that of a singular PEG network hydrogel. Also, it was found to be stronger 48 times as compared to a Single Network (SN) of collagen.[278] DN hydrogel formed by two independent networks, both crosslinked by covalent bonds, the first possessing long chains, while the other having short chains, possesses various properties.[271] When the hydrogel is stretched, the short-chain network ruptures and

dissipates energy.[279] The rupture causes permanent destruction, where upon no repairs can take place. After the first loading, the hydrogel will not recover from the damage; on subsequent loadings, the breakage energy can be reduced.

2. Hybrid physically–chemically crosslinked networks

To overcome the issue mentioned above, the DN hydrogel can be created by different types of crosslinking. This impacts various physical properties such as enhanced toughness and improved strength. Hybrid DN hydrogels mostly physically cross-linked component (first network) and a chemically linked part (second network). The association forces between both networks and within the physical network are non-covalent linkages such as hydrophobic interactions, Van der Waals interactions, hydrogen bonding and electrostatic association. This is dependent on the intrinsic physicochemical properties of both individual polymers.[275]

Suo and co-workers have created DN hydrogels by mixing two types of cross-linked polymers which are covalently bound by polyacrylamide and ionically cross-linked with alginate have extremely stretchable and tough properties.[280] Alginate chains will form ionic linkages through multivalent inorganic cations (e.g., Ca^{2+}), resulting in an alginate based hydrogel. While for a polyacrylamide hydrogel, chains are formed by covalent crosslinks. DN hydrogels with both covalent and ionic cross-links enable recoverable energy dissipating mechanisms. When the hydrogel is stretched, the covalent crosslinking chains do not rupture, whereas the ionic cross-links will break and dissipate energy. The ionic crosslinks can restructure after a period of time after the first loading.[280, 281]

Chen *et al.* synthesized a different type of hybrid physically-chemically crosslinked Agar/PAM DN hydrogels using a one-pot method consisting of two interpenetrating networks of a hydrogen-bond linked agar network and a covalently crosslinked PAM network. The resulting Agar/PAM DN hydrogels exhibit superior mechanical properties such as stiffness and strength.[282] Liu *et al.* combined an ionically cross-linked κ-carrageenan network with a covalently cross-linked polyacrylamide network. Once again, this system was synthesised using a single pot approach, the resulting hydrogel possessed a high elastic modulus of 280 kPa.[283] Wang and co-workers developed a novel DN hydrogel with high mechanical and self-healing properties by a UV-initiated copolymerization of polyacrylic acid (PAA)-grafted quaternized cellulose (QCE) and polyvinyl alcohol (PVA). The PAA network was fabricated by inducing ferric coordination crosslinkers. These hydrogels have far superior mechanical and self-healing properties due to ionic bonding between Fe^{3+} and carboxylic groups in PAA hydrogels,

as well as hydrogen bonding between alcohol groups in the PVA molecules.[284] Xiang *et al*. fabricated hierarchical structured DN hydrogels (H-DN hydrogels) by inducing ferric co-ordination cross-linkers in the second network of the PAMPS/P(AAm–AAc) DN hydrogel.[285] Yan and co-workers constructed a Gelatin/Polyacrylamide (Gelatin/PAAm) DN hydrogels by combining thermo-reversible and physically cross-linked gelatin as the first network and covalently crosslinked PAAm as the second network. These systems presented high mechanical properties; this was attributed to effective energy dissipation due to the rupture mechanism of the gelatin network. [272] Baskan et al. prepared a tough Interpenetrating Polymer Network (IPN) hydrogels which are pH- and temperature sensitive. These were created by cross-linking acrylic acid (AAc) and N,N`-methylenebis (acrylamide) in F127 (PEO99-PPO65-PEO99) aqueous solutions. The F127 within the gel network slightly decreases the elastic modulus; meanwhile this revealed an increase in energy dissipation within the IPN hydrogel. Cyclic compression tests demonstrate large mechanical hysteresis in IPN hydrogels due ionic and hydrophobic interactions between individual F127 molecules. The energy dissipative mechanisms created by F127 lead to a beneficial mechanical performance effect as compared to the polyacrylic acid (PAAc) gel controls.[286] Recently, IPN gelatin-alginate hydrogels prepared by a combination of enzymatic and ionic cross-linking have been found to be an effective method to improve the functional properties of hydrogels. This dual process generates interpenetrating networks which have been found to be highly beneficial.[287]

3. Physically–physically crosslinked networks

Yuan et al. explored a physically cross-linked polyacrylamide/xanthan gum (PAM/XG) DN hydrogel and realised this could be a material that can exhibit high strength and toughness. This family of hydrogels were prepared via a one pot approach where upon the polymerization of acrylamide in a xanthan gum solution could be completed. This utilised hydrophobic associations and bivalent cations as the cross-linking agents for the first and second network, respectively. The non-chemically cross-linked PAM/XG DN hydrogels exhibited fracture stresses as high as 3.64 MPa (13 times higher than a pure PAM SN hydrogel) as well as compressive stresses at 99 % strain of more than 50 MPa.[288] Zhang and others designed a fully physically cross-linked DN hydrogel. The initial network was cross-linked using strong hydrophobic interactions. The amphiphilic triblock copolymer consisted of the hydrophobic end blocks of poly (butyl methacrylate) (PBMA) and hydrophilic mid-block of poly (methacrylic acid) (PMAA), making a PBMA- *b* -PMAA- *b* –PBMA structure. The linear polyacrylamide acted as the second

network. The amide groups on PAAm are able to form hydrogen bonds with the carboxylic acid groups on the hydrophilic mid-block (PMAA). The resulting hydrogen bonds acted as sacrificial sections for energy dissipation. This method provided a new way to design a tough hydrogel, however, the use of a large triblock copolymer could act as an obstacle and inhibit is use for wider applications.[289] Wei *et al.* demonstrated in their work physically cross-linked Agar/PAAm DN gels. The composition, consisting of a physical agar gel as the first network and a physical polyacrylamide (PAAm) gel as the second network, that were prepared by a one pot approach. Using this method, both of the networks are cross-linked by the resulting hydrogen bonds. The combination of these two systems gave high strength, rapid self-recovery, as well as self-healing properties. This indicates that fully physical Agar/PAAm DN hydrogels hold promising futures for potential bio-applications under physiological conditions.[290]

A novel class of physically cross-linked polyacrylamide based nanocomposite hydrogels reinforced with cellulose nanofibers (CNF) were fabricated using a radical polymerization approach. This was followed by further strengthening through ferric ions via strong ionic coordination interactions between Fe^{3+} and carboxyl on the surface of the CNFs. The resulting nanocomposite hydrogels show outstanding mechanical properties with a high stiffness and toughness, quick recovery and rejuvenation, this is attributed to the distinctive roles of the dual physical cross-linker.[291]

1.9. Applications of DN hydrogels for environmental remediation

There has been a growing interest in DN hydrogels due to their unique properties. [292] Their uses have been applied to various fields such as drug delivery,[293] tissue engineering[278, 294] and for the treatment of contaminated water. [295] Other applications such as the adsorption and separation of dyes and heavy metal ions by DN hydrogel as sorbents have been recently reported. Chauhan and Mahajan have followed the adsorption of some metal ions from an aqueous solution on DN hydrogels. This was prepared by the incorporation of cellulose derivatives into a poly (methacrylamide) (PMAAm) matrix. The authors observed that the adsorption capacity and mechanism of the metal ions were strongly influenced by the functional groups in the polymer networks. It was found that the adsorption capacity of these ions increased after the amide groups transformed into COO^- groups after partial hydrolysis.[296] Chu *et al.* fabricated PVA/polyacrylic acid gels absorbents which exhibit high heavy metal adsorption capacity and excellent reusability.[297] Due to the hydrogel possessing the ability to bind with some pollutants through inherent polar functional groups, these systems can be widely used in

contaminated water treatment applications. However, the regular hydrogels that are cross-linked by the conventional crosslinking agents can suffer from poor adsorption capacity and mechanical performance, thus limiting the scope of possible applications significantly.[298] To improve the adsorption capacity of hydrogel materials, various physical and chemical modifications are completed to obtain good porosity and an increase in the number of functional groups available.[299] In recent years, the three-dimensional DN hydrogel network has been studied. Zhuang *et al.* fabricated a new kind of porous graphene/alginate DN nanocomposite bead (GAD) and compared them with a single network composite of graphene/alginate nanocomposite beads (GAS). The results show that GAD have a higher specific surface area than GAS. Furthermore, both batch and column adsorption experiments indicated that GAD have a better potential than GAS to be applied as an adsorbent for the removal of organic pollutants.[300] Rui Xu and others have demonstrated that a new type of DN hydrogel, synthesised from poly (sodium acrylate) and graphene oxide can be utilised as an adsorbent with excellent mechanical strength and high adsorption capacity for toxic metal ions with good reusability.[301] This DN hydrogel is considered as an adsorbent mainly due to including the graphene oxide network structure which helps to improve the overall strength of the hydrogel. In addition, the existence of amino and oxygen-containing groups in the network provides numerous active sites for adsorbtion toxic metal ions.

1.10. Aims of current research

The overall aim of the project presented in this thesis was to develop novel porous materials for pollution remediation, with the focus being on materials that can be produced economically. The first part of this thesis was preparation and characterisation of mesoporous carbon materials including mesoporous carbon materials and magnetic mesoporous carbon materials through the soft templating method and characterisation these materials. Despite this preparation method was low cost and simple when compared to other methods, but there were some disadvantages that limit of use these materials for water treatment such as the preparation of these materials is time consuming, there are high operation cost and difficulties in regeneration. Cellulose was selected to be used for preparation of porous materials because it is naturally abundant, renewable, non-toxic and cost effective biopolymer. Hydroxypropyl cellulose was used to prepare highly porous hydrogel materials by chemical cross-linking using divinyl sulfone via the temperature induced phase separation (TIPS) method. The obtained HPC hydrogel were characterised by using Scanning Electron Microscopy (SEM), Energy Dispersive X-ray Spectroscopy

(EDX), Nitrogen sorption measurements (BET), Fourier Transform Infrared spectroscopy (FTIR), Thermogravimetric Analysis (TGA) and Differential Scanning Calorimetry (DSC) in order to investigate morphology of the HPC hydrogel, surface area, the crosslinking occurrence, their thermal stability respectively. Investigation the mechanical properties of the prepared HPC hydrogels via compression test and rheology measurements. Furthermore, controlling the mechanical properties of this hydrogel to the most desirable properties in our application by varying the gelation time before phase separation.

The objective of this thesis was also preparation and characterisation of permeable gradient porous HPC hydrogel with different pores size by combining two methods, which are variation the temperature between the upper and lower part of the hydrogel depends on the LCST and cryogenic treatment of the gradient porous hydrogel.

This work reported also preparation and characterisation of a novel hybrid double network hydrogel (HPC/CA DN) by a simple two-step synthetic route with both chemically and physically cross-linking comprising of hydroxypropyl cellulose (HPC) and calcium alginate (CA) respectively to improve the adsorption capacity and the mechanical properties of HPC hydrogel. The chemical cross-linked HPC hydrogel (the first network) was produced using DVS as chemical cross-linker during the same TIPS method, while the second network was formed by ionic crosslinking of alginate chains through multivalent inorganic cations (Ca^{2+}) to result in an alginate based hydrogel. Alginate was selected to be the second network polymer since alginate with a carboxylate function groups is a suitable agent to remove cationic pollutant by electrostatic interactions, which can improve the adsorption capacity of HPC SN hydrogel. In addition to that this polymer is naturally abundant, environmentally friendly, reusable and cost-effective materials.

The present study evaluates HPC SN and HPC/CA DN hydrogels as adsorbents for the adsorption of dyes from aqueous solution (using methylene blue and sodium fluorescein dyes as representative dye), and also use these hydrogel to form reusable columns for the adsorptive removal of cationic dye and investigate the selective separation of the two dyes from aqueous solutions of dye mixtures by simple gravity filtration, and then compare the adsorption capacity which of these materials is more effective in the adsorption and the separation of the dyes by varying different parameters. In this research also investigate the reusability of HPC SN and HPC/CA DN hydrogels columns to reduce operating costs.

1.11. References

1. M. M. Khin, A. S. Nair, V. J. Babu, R. Murugan and S. Ramakrishna, *Energy & Environmental Science*, 2012, **5**, 8075-8109.
2. O. A. Jones and R. L. Gomes, *Pollution: Causes Effects and Control (Harrison, RM, ed), Royal Society of Chemistry, London, UK p*, 2013, 1-28.
3. D. Briggs, *British Medical Bulletin*, 2003, **68**, 1-24.
4. A. Fuga, M. Saiki, M. P. Marcelli and P. H. Saldiva, *Environmental Pollution*, 2008, **151**, 334-340.
5. R. D Harikishore Kumar, *Journal of Environmental & Analytical Toxicology*, 2012.
6. R. P. Schwarzenbach, B. I. Escher, K. Fenner, T. B. Hofstetter, C. A. Johnson, U. Von Gunten and B. Wehrli, *Science*, 2006, **313**, 1072-1077.
7. L. Beesley, E. Moreno-Jiménez, J. L. Gomez-Eyles, E. Harris, B. Robinson and T. Sizmur, *Environmental pollution*, 2011, **159**, 3269-3282.
8. S. Wang, H. Sun, H.-M. Ang and M. Tadé, *Chemical engineering journal*, 2013, **226**, 336-347.
9. N. Kimani, *United Nations Environment Programme*, 2007, 1-31.
10. V. K. Gupta and T. A. Saleh, *Environmental Science and Pollution Research*, 2013, **20**, 2828-2843.
11. A. Ghaly, R. Ananthashankar, M. Alhattab and V. Ramakrishnan, *Journal of Chemical Engineering & Process Technology*, 2014, **5**, 1.
12. B. de Campos Ventura-Camargo and M. A. Marin-Morales, *Textiles and Light Industrial Science and Technology*, 2013.
13. B. Padhi, *International Journal of Environmental Sciences*, 2012, **3**, 940.
14. J. E. Andrews, P. Brimblecombe, T. D. Jickells, P. S. Liss and B. Reid, *An introduction to environmental chemistry*, John Wiley & Sons, 2013.
15. P. A. Amoyaw, M. Williams and X. R. Bu, *Journal of Hazardous Materials*, 2009, **170**, 22-26.
16. K. Foo and B. Hameed, *Journal of Hazardous Materials*, 2009, **171**, 54-60.
17. D. Oughton, *Journal of environmental radioactivity*, 2013, **119**, 21-25.
18. E. Unur, *Microporous and Mesoporous Materials*, 2013, **168**, 92-101.
19. S. J. Yang, J. H. Kang, H. Jung, T. Kim and C. R. Park, *Journal of Materials Chemistry A*, 2013, **1**, 9427-9432.
20. M. Hartmann, S. Kullmann and H. Keller, *Journal of Materials Chemistry*, 2010, **20**, 9002-9017.

21. J. D. Walker, R. R. Colwell and L. Petrakis, *Journal of Applied Microbiology*, 1975, **30**, 79-81.
22. A. Pasila, *Marine Pollution Bulletin*, 2004, **49**, 1006-1012.
23. W. Jian, A. Kitanaka, W. Nishijima, A. U. Baes and M. Okada, *Water Research*, 1999, **33**, 1857-1863.
24. M. J. Ayotamuno, R. B. Kogbara, S. O. T. Ogaji and S. D. Probert, *Applied Energy*, 2006, **83**, 1258-1264.
25. H. M. Choi and R. M. Cloud, *Environmental Science & Technology*, 1992, **26**, 772-776.
26. Z. Zhang, G. Sèbe, D. Rentsch, T. Zimmermann and P. Tingaut, *Chemistry of Materials*, 2014, **26**, 2659-2668.
27. K. Periasamy and C. Namasivayam, *Chemosphere*, 1996, **32**, 769-789.
28. L. Mouni, D. Merabet, A. Bouzaza and L. Belkhiri, *Desalination*, 2011, **276**, 148-153.
29. Y. Zheng, H. Niu, D. He, S. Wang, Y. Cai and S. Zhang, *Microporous and Mesoporous Materials*, 2019, **276**, 251-259.
30. Y. Li, X. Luo, S. Yang, X. Cao, Z. Wang, W. Shi and S. Zhang, *Journal of Agricultural and Food Chemistry*, 2014, **62**, 1492-1497.
31. M. O. Adebajo, R. L. Frost, J. T. Kloprogge, O. Carmody and S. Kokot, *Journal of Porous Materials*, 2003, **10**, 159-170.
32. S. Štandeker, Z. Novak and Ž. Knez, *Journal of Colloid and Interface Science*, 2007, **310**, 362-368.
33. J. G. Reynolds, P. R. Coronado and L. W. Hrubesh, *J. Non-Cryst. Solids*, 2001, **292**, 127-137.
34. C. Namasivayam and K. Ranganathan, *Environmental technology*, 1995, **16**, 851-860.
35. G. M. Shaul, T. J. Holdsworth, C. R. Dempsey and K. A. Dostal, *Chemosphere*, 1991, **22**, 107-119.
36. P. Cooper, *Journal of the Society of Dyers and Colourists*, 1993, **109**, 97-100.
37. M. S. El-Geundi, *Adsorption science & technology*, 1997, **15**, 777-787.
38. W. Li, S. Gao, L. Wu, S. Qiu, Y. Guo, X. Geng, M. Chen, S. Liao, C. Zhu and Y. Gong, *Scientific reports*, 2013, **3**.
39. G. Zhou, J. Luo, C. Liu, L. Chu and J. Crittenden, *Water research*, 2018, **131**, 246-254.
40. B. D. Zdravkov, J. J. Čermák, M. Šefara and J. Janků, *Central European Journal of Chemistry*, 2007, **5**, 385-395.
41. J. Rouquerol, D. Avnir, D. H. Everett, C. Fairbridge, M. Haynes, N. Pernicone, J. D. F. Ramsay, K. S. W. Sing and K. K. Unger, *GUIDELINES FOR THE CHARACTERIZATION OF POROUS SOLIDS*, 1994.

42. J. Rouquerol, D. Avnir, C. W. Fairbridge, D. H. Everett, J. H. Haynes, N. Pernicone, J. D. F. Ramsay, K. S. W. Sing and K. K. Unger, *Pure and Applied Chemistry*, 1994, **66**, 1739-1758.
43. K. Ishizaki, S. Komarneni and M. Nanko, *Porous Materials: Process technology and applications*, Springer science & business media, 2013.
44. J.-Y. Rho, L. Kuhn-Spearing and P. Zioupos, *Medical Engineering & Physics*, 1998, **20**, 92-102.
45. M. Castillo, J. J. Moore, F. D. Schowengerdt, R. A. Ayers, X. Zhang, M. Umakoshi, H. C. Yi and J. Y. Guigne, *Advances in Space Research*, 2003, **32**, 265-270.
46. X. Miao and D. Sun, *Materials*, 2009, **3**, 26-47.
47. D. Wise, D. Trantolo, D. Altobelli, M. Yaszemski, J. Gresser and E. Schwartz, *Journal*, 1995.
48. P. Liu and G.-F. Chen, *Porous materials: processing and applications*, Elsevier, 2014.
49. I. Vida-Simiti, N. Jumate, G. Thalmaier, N. Sechel and V. Moldovan, *Journal of Porous Materials*, 2012, **19**, 21-27.
50. S. Datta and S. Redner, *Physical Review E*, 1998, **58**, R1203.
51. S. Barg, D. Koch and G. Grathwohl, *Journal of the American Ceramic Society*, 2009, **92**, 2854-2860.
52. M. P. Dalwadi, I. M. Griffiths and M. Bruna, *Proceedings of the Royal Society A: Mathematical, Physical and Engineering Sciences*, 2015, **471**, 20150464.
53. M.-H. Sun, S.-Z. Huang, L.-H. Chen, Y. Li, X.-Y. Yang, Z.-Y. Yuan and B.-L. Su, *Chemical Society Reviews*, 2016, **45**, 3479-3563.
54. N. Annabi, J. W. Nichol, X. Zhong, C. Ji, S. Koshy, A. Khademhosseini and F. Dehghani, *Tissue Engineering Part B: Reviews*, 2010, **16**, 371-383.
55. C. Triantafillidis, M. S. Elsaesser and N. Huesing, *Chemical Society Reviews*, 2013, **42**, 3833-3846.
56. K. Huang, Z. Xing, L. Wang, X. Wu, W. Zhao, X. Qi, H. Wang and Z. Ju, *Journal of Materials Chemistry A*, 2018, **6**, 434-442.
57. P. Colombo, C. Vakifahmetoglu and S. Costacurta, *Journal of materials science*, 2010, **45**, 5425-5455.
58. Y. Mun, M. J. Kim, S.-A. Park, E. Lee, Y. Ye, S. Lee, Y.-T. Kim, S. Kim, O.-H. Kim and Y.-H. Cho, *Applied catalysis b: environmental*, 2018, **222**, 191-199.
59. Z.-Y. Yuan and B.-L. Su, *Journal of Materials Chemistry*, 2006, **16**, 663-677.
60. M. R. Benzigar, S. Joseph, A. V. Baskar, D. H. Park, G. Chandra, S. Umapathy, S. N. Talapaneni and A. Vinu, *Advanced Functional Materials*, 2018, **28**, 1803701.

61. R. Rezanavaz, C. J. Fee and S. Dimartino, *Journal of Applied Polymer Science*, 2018, **135**, 46295.
62. P. Escalé, L. Rubatat, L. Billon and M. Save, *European Polymer Journal*, 2012, **48**, 1001-1025.
63. L.-R. Lee, C.-T. Liu, H.-F. Tseng, K.-T. Lin, C.-W. Chu and J.-T. Chen, *Langmuir*, 2018.
64. H. Chen, Y. Ma, X. Lin, D. Yang, Z. Chen, X. Li, X. Lin, F. Pan and Z. Ma, *Ceramics International*, 2018.
65. X. Qian, P. Ren, X. Liu, Y. Du, H. Li, X. Shi and F. Ding, *Materials Letters*, 2018.
66. K. Matsuyama, *The Journal of Supercritical Fluids*, 2018, **134**, 197-203.
67. R. Sui and P. Charpentier, *Chemical reviews*, 2012, **112**, 3057-3082.
68. R. M. Mahamood and E. T. Akinlabi, in *Transactions on Engineering Technologies*, Springer, 2015, pp. 31-42.
69. X. Miao and D. Sun, *Materials*, 2010, **3**, 26-47.
70. M.-J. Suk, S. Choi, II, J.-S. Kim, Y. D. Kim and Y.-S. Kwon, *Metals and Materials International*, 2003, **9**, 599-603.
71. A. Ahmed, J. Smith and H. Zhang, *Chemical Communications*, 2011, **47**, 11754-11756.
72. M. Thieme, K.-P. Wieters, F. Bergner, D. Scharnweber, H. Worch, J. Ndop, T. Kim and W. Grill, *Journal of materials science: materials in medicine*, 2001, **12**, 225-231.
73. P. Chabera, A. Boczkowska, A. Witek and A. Oziębło, *Bulletin of the Polish Academy of Sciences Technical Sciences*, 2015, **63**, 193-199.
74. J. Werner, B. Linner-Krčmar, W. Friess and P. Greil, *Biomaterials*, 2002, **23**, 4285-4294.
75. K.-h. Zuo, D. Jiang and Y.-P. Zeng, 2011.
76. S. Sultan and A. P. Mathew, *Nanoscale*, 2018, **10**, 4421-4431.
77. S. Deville, E. Saiz and A. P. Tomsia, *Biomaterials*, 2006, **27**, 5480-5489.
78. S. Deville, E. Saiz, R. K. Nalla and A. P. Tomsia, *Science*, 2006, **311**, 515-518.
79. K. Pawelec, A. Husmann, S. M. Best and R. E. Cameron, *Applied Physics Reviews*, 2014, **1**, 021301.
80. M. E. Davis, *Nature*, 2002, **417**, 813-821.
81. S. Dutta, A. Bhaumik and K. C.-W. Wu, *Energy & Environmental Science*, 2014, **7**, 3574-3592.
82. K. Rezwan, Q. Chen, J. Blaker and A. R. Boccaccini, *Biomaterials*, 2006, **27**, 3413-3431.
83. A. Salerno, L. Verdolotti, M. Raucci, J. Saurina, C. Domingo, R. Lamanna, V. Iozzino and M. Lavorgna, *European Polymer Journal*, 2018, **99**, 230-239.
84. A. Khan and G. Kumaraswamy, *ACS Applied Nano Materials*, 2018.

85. N. S. Lewis and D. G. Nocera, *Proceedings of the National Academy of Sciences*, 2006, **103**, 15729-15735.
86. J. Zhang, Z. Xia and L. Dai, *Science advances*, 2015, **1**, e1500564.
87. C. Hu, Y. Xiao, Y. Zou and L. Dai, *Electrochemical Energy Reviews*, 2018, 1-29.
88. Y. Li, Z. Y. Fu and B. L. Su, *Advanced Functional Materials*, 2012, **22**, 4634-4667.
89. C. Wang, Y. V. Kaneti, Y. Bando, J. Lin, C. Liu, J. Li and Y. Yamauchi, *Materials Horizons*, 2018, **5**, 394-407.
90. C. Y. Lin, D. Zhang, Z. Zhao and Z. Xia, *Advanced Materials*, 2018, **30**, 1703646.
91. J. Yi, H. Y. Jeong, D. Y. Shin, C. Kim and S. J. Lee, *ChemCatChem*, 2018, **10**, 3974-3977.
92. Q. Sun, Z. Dai, X. Meng and F.-S. Xiao, *Chemical Society Reviews*, 2015, **44**, 6018-6034.
93. C. M. Parlett, K. Wilson and A. F. Lee, *Chemical Society Reviews*, 2013, **42**, 3876-3893.
94. L.-H. Chen, X.-Y. Li, J. C. Rooke, Y.-H. Zhang, X.-Y. Yang, Y. Tang, F.-S. Xiao and B.-L. Su, *Journal of Materials Chemistry*, 2012, **22**, 17381-17403.
95. T. Santhaveesuk, K. Shimanoe, K. Suematsu and S. Choopun, *physica status solidi (a)*, 2018, 1700784.
96. N. T. A. Thu, N. D. Cuong, D. Q. Khieu, P. C. Nam, N. Van Toan, C. M. Hung and N. Van Hieu, *Sensors and Actuators B: Chemical*, 2018, **255**, 3275-3283.
97. R. A. Potyrailo and V. M. Mirsky, *Chemical reviews*, 2008, **108**, 770-813.
98. X. Xia, J. Tu, Y. Zhang, X. Wang, C. Gu, X.-b. Zhao and H. J. Fan, *ACS nano*, 2012, **6**, 5531-5538.
99. T. Wagner, T. Sauerwald, C.-D. Kohl, T. Waitz, C. Weidmann and M. Tiemann, *Thin Solid Films*, 2009, **517**, 6170-6175.
100. R. Malik, V. K. Tomer, V. Chaudhary, M. S. Dahiya, S. Nehra, S. Duhan and K. Kailasam, *Sensors and Actuators B: Chemical*, 2018, **255**, 3564-3575.
101. J.-H. Jeun, D.-H. Kim and S.-H. Hong, *Materials Letters*, 2013, **105**, 58-61.
102. D. P. Serrano, G. Calleja, J. A. Botas and F. J. Gutierrez, *Industrial & engineering chemistry research*, 2004, **43**, 7010-7018.
103. Y. Lin, 2018.
104. M. Chee Kimling, N. Scales, T. L. Hanley and R. A. Caruso, *Environmental science & technology*, 2012, **46**, 7913-7920.
105. J. E. Efome, D. Rana, T. Matsuura and C. Q. Lan, *Chemical Engineering Journal*, 2018, **352**, 737-744.
106. G.-R. Li, D.-L. Qu, L. Arurault and Y.-X. Tong, *The Journal of Physical Chemistry C*, 2009, **113**, 1235-1241.

107. Z. Ye, H. Chen, X. Cui, J. Zhou and J. Shi, *Materials Letters*, 2009, **63**, 2303-2305.
108. J. Qian, Z. Chen, C. Liu, F. Wang, Y. Zhang and M. Wang, *Chinese science bulletin*, 2014, **59**, 3260-3265.
109. V. K. Gupta and Suhas, *Journal of Environmental Management*, 2009, **90**, 2313-2342.
110. M. C. Bruzzoniti, M. Appendini, L. Rivoira, B. Onida, M. Del Bubba, P. Jana and G. D. Sorarù, *Journal of the American Ceramic Society*, 2018, **101**, 821-830.
111. D. Liu, P. Yuan, D. Tan, H. Liu, T. Wang, M. Fan, J. Zhu and H. He, *Journal of colloid and interface science*, 2012, **388**, 176-184.
112. A. Ide, G. L. Drisko, N. Scales, V. Luca, C. H. Schiesser and R. A. Caruso, *Langmuir*, 2011, **27**, 12985-12995.
113. K. Nakanishi and N. Tanaka, *Accounts of Chemical Research*, 2007, **40**, 863-873.
114. B.-L. Su, C. Sanchez and X.-Y. Yang, *Hierarchically structured porous materials: from nanoscience to catalysis, separation, optics, energy, and life science*, John Wiley & Sons, 2012.
115. K. Cabrera, *Journal of separation science*, 2004, **27**, 843-852.
116. K. Ishizaki, S. Komarneni and M. Nanko, in *Porous Materials: Process technology and applications*, Springer US, Boston, MA, 1998, DOI: 10.1007/978-1-4615-5811-8_5, pp. 181-201.
117. J. Konishi, K. Fujita, K. Nakanishi, K. Hirao, K. Morisato, S. Miyazaki and M. Ohira, *Journal of Chromatography A*, 2009, **1216**, 7375-7383.
118. C. Liang, Z. Li and S. Dai, *Angewandte Chemie (International ed. in English)*, 2008, **47**, 3696-3717.
119. T. Y. Ma, L. Liu and Z. Y. Yuan, *Chemical Society Reviews*, 2013, **42**, 3977-4003.
120. L.-F. Chen, X.-D. Zhang, H.-W. Liang, M. Kong, Q.-F. Guan, P. Chen, Z.-Y. Wu and S.-H. Yu, *ACS Nano*, 2012, **6**, 7092-7102.
121. C. Merlet, B. Rotenberg, P. A. Madden, P. L. Taberna, P. Simon, Y. Gogotsi and M. Salanne, *Nature materials*, 2012, **11**, 306-310.
122. N. A. Travlou, C. Ushay, M. Seredych, E. Rodríguez-Castellón and T. J. Bandosz, *ACS Sensors*, 2016, **1**, 591-599.
123. P. Xiong, J. Zhu, L. Zhang and X. Wang, *Nanoscale Horizons*, 2016, DOI: 10.1039/C5NH00134J.
124. Y. Fang, D. Gu, Y. Zou, Z. Wu, F. Li, R. Che, Y. Deng, B. Tu and D. Zhao, *Angewandte Chemie-International Edition*, 2010, **49**, 7987-7991.
125. N. P. Wickramaratne, V. S. Perera, J. M. Ralph, S. D. Huang and M. Jaroniec, *Langmuir*, 2013, **29**, 4032-4038.

126. X. Jia, G. Zhang, T. Wang, X. Zhu, F. Yang, Y. Li, Y. Lu and F. Wei, *Journal of Materials Chemistry A*, 2015, **3**, 15738-15744.
127. Z. Ma, H. Zhang, Z. Yang, Y. Zhang, B. Yu and Z. Liu, *Journal of Materials Chemistry A*, 2014, **2**, 19324-19329.
128. B. Guo, X. Wang, P. F. Fulvio, M. Chi, S. M. Mahurin, X.-G. Sun and S. Dai, *Advanced Materials*, 2011, **23**, 4661-+.
129. J. Gorka, M. Jaroniec and W. L. Suchanek, *Nanoscale*, 2010, **2**, 2868-2872.
130. H. Tamon, H. Ishizaka, M. Mikami and M. Okazaki, *Carbon*, 1997, **35**, 791-796.
131. R. Ryoo, S. H. Joo and S. Jun, *The Journal of Physical Chemistry B*, 1999, **103**, 7743-7746.
132. R. Ryoo, S. H. Joo, M. Kruk and M. Jaroniec, *Advanced Materials*, 2001, **13**, 677-681.
133. J. Lee, J. Kim and T. Hyeon, *Advanced Materials*, 2006, **18**, 2073-2094.
134. S. J. Han and T. Hyeon, *Chemical Communications*, 1999, DOI: 10.1039/a905848f, 1955-1956.
135. J. Lee, S. Han and T. Hyeon, *Journal of Materials Chemistry*, 2004, **14**, 478-486.
136. A. A. Zakhidov, R. H. Baughman, Z. Iqbal, C. Cui, I. Khayrullin, S. O. Dantas, J. Marti and V. G. Ralchenko, *Science*, 1998, **282**, 897-901.
137. J.-S. Yu, S. Kang, S. B. Yoon and G. Chai, *Journal of the American Chemical Society*, 2002, **124**, 9382-9383.
138. S. Tanaka, N. Nishiyama, Y. Egashira and K. Ueyama, *Chemical Communications*, 2005, DOI: 10.1039/B501259G, 2125-2127.
139. L. Chuenchom, R. Kraehnert and B. M. Smarsly, *Soft Matter*, 2012, **8**, 10801-10812.
140. C. Liang, K. Hong, G. A. Guiochon, J. W. Mays and S. Dai, *Angewandte Chemie International Edition*, 2004, **43**, 5785-5789.
141. Y. Meng, D. Gu, F. Zhang, Y. Shi, H. Yang, Z. Li, C. Yu, B. Tu and D. Zhao, *Angewandte Chemie*, 2005, **117**, 7215-7221.
142. C. Liang and S. Dai, *Journal of the American Chemical Society*, 2006, **128**, 5316-5317.
143. C. Liu, L. Li, H. Song and X. Chen, *Chemical Communications*, 2007, 757-759.
144. Y. Meng, D. Gu, F. Zhang, Y. Shi, L. Cheng, D. Feng, Z. Wu, Z. Chen, Y. Wan and A. Stein, *Chemistry of materials*, 2006, **18**, 4447-4464.
145. Y. Huang, H. Cai, T. Yu, F. Zhang, F. Zhang, Y. Meng, D. Gu, Y. Wan, X. Sun and B. Tu, *Angewandte Chemie*, 2007, **119**, 1107-1111.
146. S. Tanaka, Y. Katayama, M. P. Tate, H. W. Hillhouse and Y. Miyake, *Journal of Materials Chemistry*, 2007, **17**, 3639-3645.

147. J. Yang, Y. Zhai, Y. Deng, D. Gu, Q. Li, Q. Wu, Y. Huang, B. Tu and D. Zhao, *Journal of colloid and interface science*, 2010, **342**, 579-585.
148. K. Kailasam, Y.-S. Jun, P. Katekomol, J. D. Epping, W. H. Hong and A. Thomas, *Chemistry of Materials*, 2009, **22**, 428-434.
149. J. Wang, H. Liu, J. Diao, X. Gu, H. Wang, J. Rong, B. Zong and D. S. Su, *Journal of Materials Chemistry A*, 2015, **3**, 2305-2313.
150. Y. Deng, Y. Cai, Z. Sun, D. Gu, J. Wei, W. Li, X. Guo, J. Yang and D. Zhao, *Advanced Functional Materials*, 2010, **20**, 3658-3665.
151. S. E. Elaigwu and G. M. Greenway, *Materials Letters*, 2014, **115**, 117-120.
152. L. Liu, F.-Y. Wang, G.-S. Shao and Z.-Y. Yuan, *Carbon*, 2010, **48**, 2089-2099.
153. M. Jaroniec, J. Gorka, J. Choma and A. Zawislak, *Carbon*, 2009, **47**, 3034-3040.
154. M. Jaroniec, J. Choma, J. Gorka and A. Zawislak, *Chemistry of Materials*, 2007, **20**, 1069-1075.
155. P. Gao, A. Wang, X. Wang and T. Zhang, *Chemistry of Materials*, 2008, **20**, 1881-1888.
156. Y. Kim, C.-Y. Cho, J.-H. Kang, Y.-S. Cho and J. H. Moon, *Langmuir*, 2012, **28**, 10543-10550.
157. M. Rojas-Cervantes, L. Alonso, J. Dıaz-Terán, A. López-Peinado, R. Martın-Aranda and V. Gómez-Serrano, *Carbon*, 2004, **42**, 1575-1582.
158. Y. Deng, T. Yu, Y. Wan, Y. Shi, Y. Meng, D. Gu, L. Zhang, Y. Huang, C. Liu and X. Wu, *Journal of the American Chemical Society*, 2007, **129**, 1690-1697.
159. R. Liu, Y. Shi, Y. Wan, Y. Meng, F. Zhang, D. Gu, Z. Chen, B. Tu and D. Zhao, *Journal of the American Chemical Society*, 2006, **128**, 11652-11662.
160. H. Wang, A. Wang, X. Wang and T. Zhang, *Chemical Communications*, 2008, 2565-2567.
161. J. Liu, S. Z. Qiao and Q. H. Hu, *Small*, 2011, **7**, 425-443.
162. Y. Zhai, Y. Dou, X. Liu, B. Tu and D. Zhao, *Journal of Materials Chemistry*, 2009, **19**, 3292-3300.
163. J. Yao, L. Li, H. Song, C. Liu and X. Chen, *Carbon*, 2009, **47**, 436-444.
164. X. Wang and S. Dai, *Adsorption*, 2009, **15**, 138-144.
165. N. A. Peppas, P. Bures, W. Leobandung and H. Ichikawa, *European Journal of Pharmaceutics and Biopharmaceutics*, 2000, **50**, 27-46.
166. X. Z. Shu and K. J. Zhu, *International Journal of Pharmaceutics*, 2002, **233**, 217-225.
167. S. Van Vlierberghe, P. Dubruel and E. Schacht, *Biomacromolecules*, 2011, **12**, 1387-1408.
168. W. E. Hennink and C. F. van Nostrum, *Advanced Drug Delivery Reviews*, 2002, **54**, 13-36.

169. N. Job, A. Thery, R. Pirard, J. Marien, L. Kocon, J. N. Rouzaud, F. Beguin and J. P. Pirard, *Carbon*, 2005, **43**, 2481-2494.
170. W. A. Petka, J. L. Harden, K. P. McGrath, D. Wirtz and D. A. Tirrell, *Science*, 1998, **281**, 389-392.
171. C. Wang, R. J. Stewart and J. KopeČek, *Nature*, 1999, **397**, 417-420.
172. C. Elvira, J. Mano, J. San Roman and R. Reis, *Biomaterials*, 2002, **23**, 1955-1966.
173. J. Zhou, C. Chang, R. Zhang and L. Zhang, *Macromolecular bioscience*, 2007, **7**, 804-809.
174. H. Tamura, H. Nagahama and S. Tokura, *Cellulose*, 2006, **13**, 357-364.
175. H.-W. Kang, Y. Tabata and Y. Ikada, *Biomaterials*, 1999, **20**, 1339-1344.
176. A. W. Chan, R. A. Whitney and R. J. Neufeld, *Biomacromolecules*, 2009, **10**, 609-616.
177. R.-S. Juang and R.-C. Shiau, *Journal of Membrane Science*, 2000, **165**, 159-167.
178. G. Li, Y. Du, Y. Tao, H. Deng, X. Luo and J. Yang, *Carbohydrate Polymers*, 2010, **82**, 706-713.
179. Y. Qiu and K. Park, *Advanced drug delivery reviews*, 2001, **53**, 321-339.
180. K. Y. Lee and D. J. Mooney, *Chemical reviews*, 2001, **101**, 1869-1880.
181. B. Adhikari and S. Majumdar, *Progress in polymer science*, 2004, **29**, 699-766.
182. A. C. Jen, M. C. Wake and A. G. Mikos, *Biotechnology and bioengineering*, 1996, **50**, 357-364.
183. X. Shen, J. L. Shamshina, P. Berton, G. Gurau and R. D. Rogers, *Green Chemistry*, 2016, **18**, 53-75.
184. M. Wang, L. Xu, M. Zhai, J. Peng, J. Li and G. Wei, *Carbohydrate polymers*, 2008, **74**, 498-503.
185. A. Kimura, N. Nagasawa and M. Taguchi, *Radiation Physics and Chemistry*, 2014, **103**, 216-221.
186. L. Zhao, H. Mitomo and F. Yosh, *Journal of Bioactive and Compatible Polymers*, 2008, **23**, 319-333.
187. P. Petrov, E. Petrova, R. Stamenova, C. B. Tsvetanov and G. Riess, *Polymer*, 2006, **47**, 6481-6484.
188. E. Velickova, E. Winkelhausen, S. Kuzmanova, M. Cvetkovska and C. Tsvetanov, *Reactive and Functional Polymers*, 2009, **69**, 688-693.
189. L. Zhao, H. Mitomo, N. Nagasawa, F. Yoshii and T. Kume, *Carbohydrate Polymers*, 2003, **51**, 169-175.
190. I. Roy and M. N. Gupta, *Chemistry & biology*, 2003, **10**, 1161-1171.
191. B. Kumar, A. K. Singh, R. K. Prasad, C. S. Singh and V. Dwivedi.

192. P. Gupta, K. Vermani and S. Garg, *Drug discovery today*, 2002, **7**, 569-579.
193. A. Gutowska, J. S. Bark, I. C. Kwon, Y. H. Bae, Y. Cha and S. W. Kim, *Journal of Controlled Release*, 1997, **48**, 141-148.
194. D. Schmaljohann, *Advanced drug delivery reviews*, 2006, **58**, 1655-1670.
195. M. A. Ward and T. K. Georgiou, *Polymers*, 2011, **3**, 1215-1242.
196. L. Klouda and A. G. Mikos, *European Journal of Pharmaceutics and Biopharmaceutics*, 2008, **68**, 34-45.
197. N. T. Southall, K. A. Dill and A. Haymet, *The Journal of Physical Chemistry B*, 2002, **106**, 521-533.
198. N. Husing and U. Schubert, *Angewandte Chemie-International Edition*, 1998, **37**, 23-45.
199. K. Kanamori, M. Aizawa, K. Nakanishi and T. Hanada, *Advanced Materials*, 2007, **19**, 1589-1593.
200. L. W. Hrubesh, *J. Non-Cryst. Solids*, 1998, **225**, 335-342.
201. S. S. Kistler, *Nature*, 1931, **127**, 741.
202. S. Takeshita and S. Yoda, *Chemistry of Materials*, 2015, **27**, 7569-7572.
203. X. Chang, D. Chen and X. Jiao, *The Journal of Physical Chemistry B*, 2008, **112**, 7721-7725.
204. F. Fischer, A. Rigacci, R. Pirard, S. Berthon-Fabry and P. Achard, *Polymer*, 2006, **47**, 7636-7645.
205. L. Zuo, Y. Zhang, L. Zhang, Y.-E. Miao, W. Fan and T. Liu, *Materials*, 2015, **8**, 6806-6848.
206. K. Sinkó, *Materials*, 2010, **3**, 704-740.
207. E. M. Ahmed, *Journal of advanced research*, 2015, **6**, 105-121.
208. D. Karami, *Journal of Petroleum Science and Technology*, 2018, **8**, 3-15.
209. H. Maleki, L. Durães and A. Portugal, *J. Non-Cryst. Solids*, 2014, **385**, 55-74.
210. A. V. Rao, G. Pajonk, U. K. Bangi, A. P. Rao and M. M. Koebel, in *Aerogels Handbook*, Springer, 2011, pp. 103-124.
211. C. J. Brinker and G. W. Scherer, *Sol-gel science: the physics and chemistry of sol-gel processing*, Academic press, 2013.
212. L. L. Hench and J. K. West, *Chemical Reviews*, 1990, **90**, 33-72.
213. M. A. Einarsrud, E. Nilsen, A. Rigacci, G. M. Pajonk, S. Buathier, D. Valette, M. Durant, B. Chevalier, P. Nitz and F. Ehrburger-Dolle, *J. Non-Cryst. Solids*, 2001, **285**, 1-7.
214. P. J. Davis, C. Jeffrey Brinker and D. M. Smith, *J. Non-Cryst. Solids*, 1992, **142**, 189-196.
215. D. J. Suh and T.-j. Park, *Journal of materials science letters*, 1997, **16**, 490-492.

216. D. Y. Nadargi, S. S. Latthe and A. V. Rao, *Journal of sol-gel science and technology*, 2009, **49**, 53-59.
217. R.-A. Strøm, Y. Masmoudi, A. Rigacci, G. Petermann, L. Gullberg, B. Chevalier and M.-A. Einarsrud, *Journal of sol-gel science and technology*, 2007, **41**, 291-298.
218. H. Maleki, L. Durães and A. Portugal, *Journal of Materials Chemistry A*, 2015, **3**, 1594-1600.
219. I. Smirnova and W. Arlt, *Journal of sol-gel science and technology*, 2003, **28**, 175-184.
220. G. Tkalec, M. Pantić, Z. Novak and Ž. Knez, *Journal of Materials Science*, 2015, **50**, 1-12.
221. H.-B. Chen, E. Hollinger, Y.-Z. Wang and D. A. Schiraldi, *Polymer*, 2014, **55**, 380-384.
222. L. Durães, T. Matias, R. Patrício and A. Portugal, *Materialwissenschaft und Werkstofftechnik*, 2013, **44**, 380-385.
223. J. Yang, S. Li, L. Yan, J. Liu and F. Wang, *Microporous and Mesoporous Materials*, 2010, **133**, 134-140.
224. K. Kawagishi, H. Saito, H. Furukawa and K. Horie, *Macromolecular rapid communications*, 2007, **28**, 96-100.
225. A. C. Pierre and A. Rigacci, in *Aerogels handbook*, Springer, 2011, pp. 21-45.
226. A. S. Dorcheh and M. Abbasi, *Journal of materials processing technology*, 2008, **199**, 10-26.
227. R. Halim, M. K. Danquah and P. A. Webley, *Biotechnology advances*, 2012, **30**, 709-732.
228. A. Pons, L. Casas, E. Estop, E. Molins, K. D. M. Harris and M. Xu, *J. Non-Cryst. Solids*, 2012, **358**, 461-469.
229. G. Nireesha, L. Divya, C. Sowmya, N. Venkateshan, M. N. Babu and V. Lavakumar, *International journal of novel trends in pharmaceutical sciences*, 2013, **3**, 87-98.
230. Z. Wang, S. Liu, Y. Matsumoto and S. Kuga, *Cellulose*, 2012, **19**, 393-399.
231. D. Klemm, B. Heublein, H. P. Fink and A. Bohn, *Angewandte Chemie International Edition*, 2005, **44**, 3358-3393.
232. S. Barthel and T. Heinze, *Green Chemistry*, 2006, **8**, 301-306.
233. R. E. Quiroz-Castañeda and J. L. Folch-Mallol, *Sustainable degradation of lignocellulosic biomass techniques, applications and commercialization. InTech*, 2013, 119-155.
234. Y. Habibi, L. A. Lucia and O. J. Rojas, *Chemical reviews*, 2010, **110**, 3479-3500.
235. B. Peng, N. Dhar, H. Liu and K. Tam, *The Canadian Journal of Chemical Engineering*, 2011, **89**, 1191-1206.
236. T. Shen and S. Gnanakaran, *Biophysical journal*, 2009, **96**, 3032-3040.

237. S. Jain, P. S. Sandhu, R. Malvi and B. Gupta, *Journal of Applied Pharmaceutical Science*, 2013, **3**, 139-144.
238. S. Jain, P. S. Sandhu, R. Malvi and B. Gupta, 2013.
239. C. Clasen and W. M. Kulicke, *Progress in Polymer Science*, 2001, **26**, 1839-1919.
240. S. Kistler, *The Journal of Physical Chemistry*, 1932, **36**, 52-64.
241. Z. Zhou, X. Zhang, C. Lu, L. Lan and G. Yuan, *RSC Advances*, 2014, **4**, 8966-8972.
242. J. Cai, S. Kimura, M. Wada, S. Kuga and L. Zhang, *ChemSusChem*, 2008, **1**, 149-154.
243. S. Hoepfner, L. Ratke and B. Milow, *Cellulose*, 2008, **15**, 121-129.
244. H. Jin, Y. Nishiyama, M. Wada and S. Kuga, *Colloids and Surfaces A: Physicochemical and Engineering Aspects*, 2004, **240**, 63-67.
245. J. Li, Y. Lu, D. Yang, Q. Sun, Y. Liu and H. Zhao, *Biomacromolecules*, 2011, **12**, 1860-1867.
246. H. Cai, S. Sharma, W. Liu, W. Mu, W. Liu, X. Zhang and Y. Deng, *Biomacromolecules*, 2014, **15**, 2540-2547.
247. K.-W. Kow, R. Yusoff, A. A. Aziz and E. Abdullah, *J. Non-Cryst. Solids*, 2014, **386**, 76-84.
248. S. T. Nguyen, J. Feng, N. T. Le, A. T. Le, N. Hoang, V. B. Tan and H. M. Duong, *Industrial & Engineering Chemistry Research*, 2013, **52**, 18386-18391.
249. J. Lin, L. Yu, F. Tian, N. Zhao, X. Li, F. Bian and J. Wang, *Carbohydrate polymers*, 2014, **109**, 35-43.
250. F. Jiang and Y.-L. Hsieh, *Journal of Materials Chemistry A*, 2014, **2**, 6337-6342.
251. S. T. Nguyen, J. Feng, S. K. Ng, J. P. Wong, V. B. Tan and H. M. Duong, *Colloids and Surfaces A: Physicochemical and Engineering Aspects*, 2014, **445**, 128-134.
252. K.-W. Kow, R. Yusoff, A. A. Aziz and E. Abdullah, *Applied Surface Science*, 2014, **301**, 161-172.
253. F. Liebner, A. Potthast, T. Rosenau, E. Haimer and M. Wendland, *Holzforschung*, 2008, **62**, 129-135.
254. R. Gavillon and T. Budtova, *Biomacromolecules*, 2008, **9**, 269-277.
255. J. Cai, S. Kimura, M. Wada and S. Kuga, *Biomacromolecules*, 2008, **10**, 87-94.
256. O. Aaltonen and O. Jauhiainen, *Carbohydrate Polymers*, 2009, **75**, 125-129.
257. S. Opasanon, P. Muangman and N. Namviriyachote, *International wound journal*, 2010, **7**, 467-471.
258. H. Daemi and M. Barikani, *Scientia Iranica*, 2012, **19**, 2023-2028.
259. A. Martinsen, G. Skjåk- Bræk and O. Smidsrød, *Biotechnology and bioengineering*, 1989, **33**, 79-89.

260. J. A. Rowley, G. Madlambayan and D. J. Mooney, *Biomaterials*, 1999, **20**, 45-53.
261. P. Lee and M. Rogers, *International Journal of Gastronomy and Food Science*, 2012, **1**, 96-100.
262. N. Mohammed, N. Grishkewich, R. M. Berry and K. C. Tam, *Cellulose*, 2015, **22**, 3725-3738.
263. J. P. Ibáñez and Y. Umetsu, *Hydrometallurgy*, 2002, **64**, 89-99.
264. F. Mancini and T. McHugh, *Food/Nahrung*, 2000, **44**, 152-157.
265. G. Skjåk-Bræk, H. Grasdalen and O. Smidsrød, *Carbohydrate polymers*, 1989, **10**, 31-54.
266. D. Kühbeck, J. Mayr, M. Häring, M. Hofmann, F. Quignard and D. D. Díaz, *New Journal of Chemistry*, 2015, **39**, 2306-2315.
267. C. Chang, K. Han and L. Zhang, *Polymers for Advanced Technologies*, 2011, **22**, 1329-1334.
268. T. Nakajima, H. Furukawa, Y. Tanaka, T. Kurokawa, Y. Osada and J. P. Gong, *Macromolecules*, 2009, **42**, 2184-2189.
269. M. A. Haque, T. Kurokawa and J. P. Gong, *Polymer*, 2012, **53**, 1805-1822.
270. R. E. Webber, C. Creton, H. R. Brown and J. P. Gong, *Macromolecules*, 2007, **40**, 2919-2927.
271. J. P. Gong, Y. Katsuyama, T. Kurokawa and Y. Osada, *Advanced Materials*, 2003, **15**, 1155-1158.
272. X. Yan, Q. Chen, L. Zhu, H. Chen, D. Wei, F. Chen, Z. Tang, J. Yang and J. Zheng, *Journal of Materials Chemistry B*, 2017, **5**, 7683-7691.
273. X. J. Liu, X. Y. Ren, S. Guan, H. Q. Li, Z. K. Song and G. H. Gao, *European Polymer Journal*, 2015, **73**, 149-161.
274. J. Wang, J. Wei, S. Su, J. Qiu and S. Wang, *Journal of Materials Science*, 2015, **50**, 5458-5465.
275. Q. Chen, H. Chen, L. Zhu and J. Zheng, *Journal of Materials Chemistry B*, 2015, **3**, 3654-3676.
276. T. Lin, Q. Bai, J. Peng, L. Xu, J. Li and M. Zhai, *Carbohydrate polymers*, 2018, **200**, 72-81.
277. Q. Chen, L. Zhu, C. Zhao, Q. Wang and J. Zheng, *Advanced materials*, 2013, **25**, 4171-4176.
278. J. X. Chen, J. Yuan, Y. L. Wu, P. Wang, P. Zhao, G. Z. Lv and J. H. Chen, *Journal of Biomedical Materials Research Part A*, 2018, **106**, 192-200.
279. Q. M. Yu, Y. Tanaka, H. Furukawa, T. Kurokawa and J. P. Gong, *Macromolecules*, 2009, **42**, 3852-3855.

280. J.-Y. Sun, X. Zhao, W. R. Illeperuma, O. Chaudhuri, K. H. Oh, D. J. Mooney, J. J. Vlassak and Z. Suo, *Nature*, 2012, **489**, 133.
281. K. J. Henderson, T. C. Zhou, K. J. Otim and K. R. Shull, *Macromolecules*, 2010, **43**, 6193-6201.
282. Q. Chen, L. Zhu, L. Huang, H. Chen, K. Xu, Y. Tan, P. Wang and J. Zheng, *Macromolecules*, 2014, **47**, 2140-2148.
283. S. Liu and L. Li, *ACS applied materials & interfaces*, 2016, **8**, 29749-29758.
284. Y. Wang, Z. Wang, K. Wu, J. Wu, G. Meng, Z. Liu and X. Guo, *Carbohydrate Polymers*, 2017, **168**, 112-120.
285. S. Xiang, W. Qian, T. Li, Y. Wang, M. Chen, P. Ma and W. Dong, *New Journal of Chemistry*, 2017, **41**, 14397-14402.
286. T. Baskan, D. C. Tuncaboylu and O. Okay, *Polymer*, 2013, **54**, 2979-2987.
287. Y. Niu, Q. Xia, N. Li, Z. Wang and L. L. Yu, *Food chemistry*, 2019, **270**, 223-228.
288. N. Yuan, L. Xu, H. Wang, Y. Fu, Z. Zhang, L. Liu, C. Wang, J. Zhao and J. Rong, *ACS applied materials & interfaces*, 2016, **8**, 34034-34044.
289. H. J. Zhang, T. L. Sun, A. K. Zhang, Y. Ikura, T. Nakajima, T. Nonoyama, T. Kurokawa, O. Ito, H. Ishitobi and J. P. Gong, *Advanced Materials*, 2016, **28**, 4884-4890.
290. D. Wei, J. Yang, L. Zhu, F. Chen, Z. Tang, G. Qin and Q. Chen, *Polymer Testing*, 2018, **69**, 167-174.
291. J. Niu, J. Wang, X. Dai, Z. Shao and X. Huang, *Carbohydrate polymers*, 2018, **193**, 73-81.
292. A. S. Hoffman, *Advanced drug delivery reviews*, 2012, **64**, 18-23.
293. S. Pacelli, P. Paolicelli, M. Avitabile, G. Varani, L. Di Muzio, S. Cesa, J. Tirillò, C. Bartuli, M. Nardoni and S. Petralito, *European Polymer Journal*, 2018, **104**, 184-193.
294. Z. Gu, K. Huang, Y. Luo, L. Zhang, T. Kuang, Z. Chen and G. Liao, *Wiley Interdisciplinary Reviews: Nanomedicine and Nanobiotechnology*, 2018, e1520.
295. G. Jing, L. Wang, H. Yu, W. A. Amer and L. Zhang, *Colloids and Surfaces A: Physicochemical and Engineering Aspects*, 2013, **416**, 86-94.
296. G. S. Chauhan and S. Mahajan, *Journal of Applied Polymer Science*, 2002, **86**, 667-671.
297. L. Chu, C. Liu, G. Zhou, R. Xu, Y. Tang, Z. Zeng and S. Luo, *Journal of hazardous materials*, 2015, **300**, 153-160.
298. U. Yildiz, Ö. F. Kemik and B. Hazer, *Journal of hazardous materials*, 2010, **183**, 521-532.
299. Y. Zhuang, F. Yu, J. Ma and J. Chen, *Journal of colloid and interface science*, 2017, **507**, 250-259.

300. Y. Zhuang, F. Yu, J. Chen and J. Ma, *Journal of Environmental Chemical Engineering*, 2016, **4**, 147-156.
301. R. Xu, G. Zhou, Y. Tang, L. Chu, C. Liu, Z. Zeng and S. Luo, *Chemical Engineering Journal*, 2015, **275**, 179-188.

Chapter Two

2. Experimental

This chapter provides an explanation of the materials and experimental methods used throughout this project. Moreover, the characterization techniques are described, which are used to investigate the chemical properties and show the structural of different porous materials prepared in this thesis.

2.1. Materials

2.1.1. Materials used to prepare ordered mesoporous carbon materials (OMC)

Resorcinol with 99% purity was used as carbon precursor, triblock copolymer pluronic F127 used as a soft template agent and had an average molecular weight of 12,600 these were purchased from Sigma-Aldrich. Formaldehyde (37%), used as a cross-linker agent to synthesize mesoporous carbon materials, was purchased from Scientific Fisher, UK. Absolute ethanol (≥99.8%) and hydrochloric acid (37%) were both analytical grade and purchased from Scientific Fisher, UK. Iron (III) nitrate (98%) was purchased from Scientific Fisher, UK. Cobalt (II) nitrate hexahydrate (98%) was purchased from Sigma-Aldrich and Nickel (II) nitrate hexahydrate (98%) was purchased from BDH. All these chemicals were used without any further purification.

2.1.2. Materials used to prepare of hydroxypropyl cellulose (HPC) aerogel and hydrogel and HPC/CA DN hydrogel.

Hydroxypropyl cellulose (HPC) powder has an average Mw~80,000 and average Mn~10,000 with 20 mesh particle size was purchased from Sigma-Aldrich and was used as received. Sodium alginate (SA), aluminum nitrate anhydrous and calcium chloride were also purchased from Sigma-Aldrich. Divinyl sulphone (DVS) 97% with 0.05% hydroquinone (used as a chemical cross-linker agent to prepare cellulose aerogel) and sodium hydroxide were purchased from Fisher Scientific, UK. Purified water was obtained from a Milli-Q reagent water system (Millipore, UK) by passing the water through an Elgastat Prima Reverse Osmosis Unit followed by a Millipore Milli-Q reagent water system consisting of one carbon filter and two ion-exchange filters this was utilized for all work.

2.1.3. Materials used in the adsorption process

Methylene blue dye (MB) was purchased from Lancaster Synthesis Ltd and fluorescein dye (acid yellow 73) (FL) was purchased from Sigma-Aldrich. Hydrochloric acid (HCl) was purchased from Fisher Scientific, United Kingdom. All chemicals were used without further purification purified water was utilized for all work.

2.2. Experimental methods

2.2.1. Synthesis of porous carbon materials

2.2.1.1. Synthesis of mesoporous carbon materials

Mesoporous carbon materials were prepared based on a modified version of the method described by Liu *et al*. [1] 1.65 g resorcinol (R) and 2.5 g Pluronic F127 were dissolved in 14 g of ethanol/ water mixture solvent (1/1 v/v %) under magnetic stirring at 25ºC temperature. This was followed by the addition of 0.23 g hydrochloric acid to the above solution after stirring for about 30 min and followed by stirring for 2 hours at room temperature (22±2 °C). The colour of the solution changed from colourless to light brown. After stirring for two hours, 2.3 g of formaldehyde (37%) was subsequently added dropwise to the solution under vigorously stirring. The reaction solution mixture was stirred for another two hours. The final homogeneous solution was kept standing for a further 72 hours for aging. In this period the solution turned cloudy and phase separated into two layers. The upper layer was composed of the solvents, and the bottom layer was rich in the polymer. Subsequently, the upper layer was removed while the lower layer was stirred for 12 hours until a sticky polymer was created. Then, the polymer was transferred to in different shaped moulds and cured at 85 ºC for 24 hours to remove the residual solvent. Finally, the dried polymer was carbonized in a tubular furnace under nitrogen gas by using a heating programme starting from 25 ºC to 400 ºC at a ramping rate of 1ºC/min while the temperature increased from 400 ºC to 800 ºC at a heating rate 5 ºC/min and kept at the final temperature for two hours. The resulting heat-treated composite material as prepared to be mesoporous carbon monolith.[1-4] Figure 2.1 shows the schematic illustration the preparation method of OMC materials and Figure 2.2 show photographs of the preparation stages of mesoporous carbon monolith

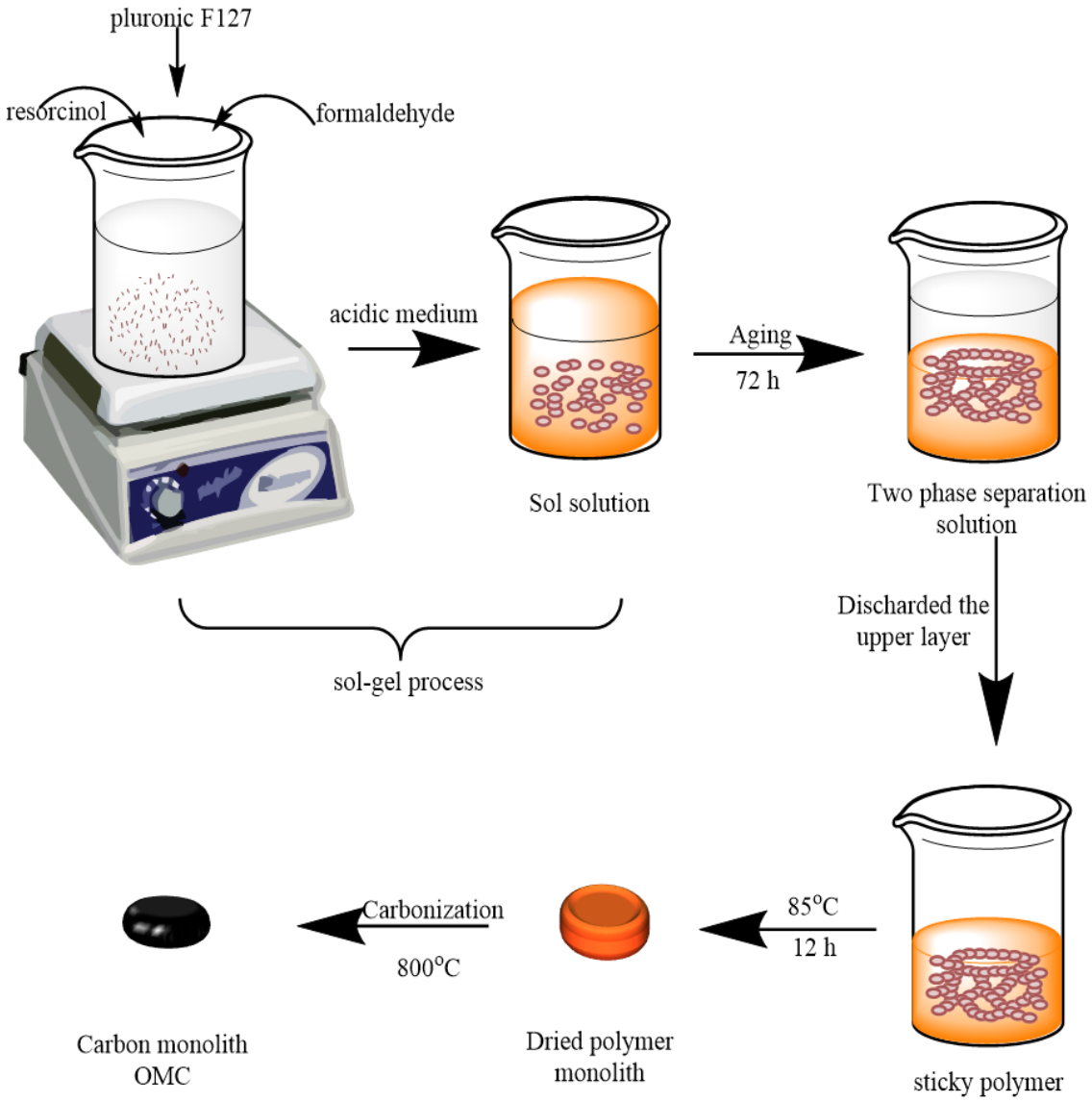

Figure 2.1. Schematic illustration the preparation of mesoporous carbon materials using the soft templating method

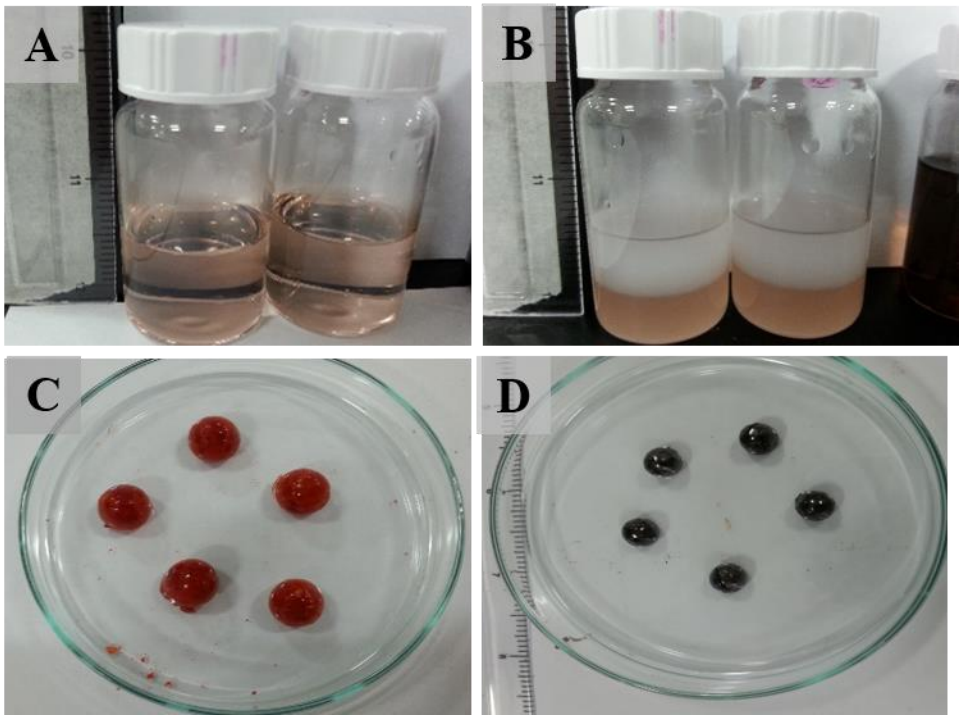

Figure 2.2. Photographs show the preparation steps of mesoporous carbon material (A) sol solution (B) phase separation solution after kept the sol solution for 72 hours (C) dried polymer monolith (D) carbon monolith.

2.2.1.2. Synthesis of magnetic mesoporous carbon materials

Magnetic ordered mesoporous carbon materials (OMC) were synthesized using resorcinol(R) and formaldehyde (F) as carbon precursor , Pluronic F127 as a soft template and various metal salts as a source of metals ions such as (hydrated iron nitrate ($Fe(NO_3)_3.9H_2O$), Cobalt(II) nitrate hexahydrate ($Co(NO_3)_2.6H_2O$) or Nickel(II) nitrate hexahydrate ($Ni(NO_3)_2.6H_2O$). The producing composite is formed as Fe/OMC, Co/OMC or Ni/OMC.

2.5 g of Pluronic F127 and 1.65 g resorcinol were dissolved completely in 14 g of mixture solvent was included (1/1 v/v%) ethanol/ water solution under magnetic stirring at room temperature (solution A). 0.3 g of $Fe(NO_3)_3.9H_2O$ was dissolved in 7 g of mixture solvent (1/1 v/v%) ethanol/water (solution B). When the colour of solution A turned light brown, solution B was subsequently dropped into it. After stirring for 2 hours, 2.3 ml of formaldehyde (37%) was added dropwise to the above solution under vigorously stirring. The reaction solution mixture was stirred for another 2 hours to form a homogenous solution. The metal source was utilized as a catalyst to adjust the pH value

for cross-linking between resorcinol and formaldehyde, because acid was generated by the hydrolysis of the metal iron salt. The final preparation steps of Fe/OMC was kept the same as blank OMC preparation method (Section 2.2.1.1).

Co/OMC and Ni/OMC were also prepared under the same conditions as those for the Fe/OMC OMCs, but with adding 0.23 ml of hydrochloric acid to the solution A to adjust the pH value and changing the hydrated iron nitrate ($Fe(NO_3)_3.9H_2O$) in solution B by Cobalt(II) nitrate hexahydrate ($Co(NO_3)_2.6H_2O$) and Nickel(II) nitrate hexahydrate ($Ni(NO_3)_2.6H_2O$) respectively .[3] Figure 2.3 shows a flow chart of the preparation steps of Fe/OMC, Co/OMC and Ni/OMC.

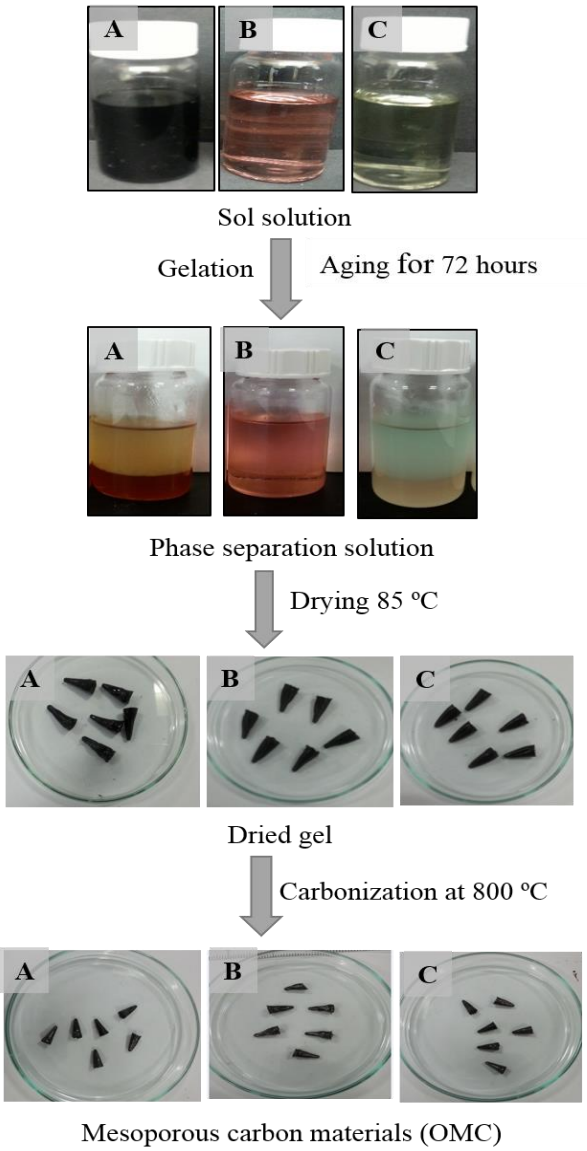

Figure 2.3. Flow chart of the preparation steps of Fe/OMC, Co/OMC and Ni/OMC with real images for (A) Fe/OMC (B) Co/OMC and (C) Ni/OMC.

2.2.2. Preparation of hydroxypropyl cellulose single network hydrogel and aerogels monolith and column

Hydroxypropyl cellulose aerogel was prepared by using divinyl sulfone (DVS) as a chemical cross-linker. The procedure for HPC hydrogel synthesis was based on a modified version of the method described by Harsh and Gehrke.[5, 6] 7.0 w/v % of hydroxypropyl cellulose (HPC) was dissolved in 0.01 M NaOH solution at room temperature (22±2 °C). After the solution became homogenous 1.3 w/v % divinyl sulfone (DVS) was added to the solution, and the reaction was mixed thoroughly for 2 min by using vortex mixture (Vortex-2 Genie). The initial crosslinking reaction occurred at room temperature (22±2 °C) for 3 hours. The sample was then placed in the water bath at the LCST for 6 hours and then was removed the sample from the water bath and was left at room temperature (below the LCST) for a further 24 hours according to the temperature induced phase separation (TIPS) method.[7] Afterwards the HPC hydrogel was washed with MilliQ-purified water to remove unreacted DVS. Finally, the last hydrogel product was frozen in liquid nitrogen and was directly transferred to the freeze dryer (VirTis SP SCIENTIFIC) to obtain the monolithic HPC aerogel material. Figure 2.4 shows a schematic representation of the preparation of HPC aerogel and Figure 2.5 shows real images representing HPC aerogel preparation stages. The freeze-drying diagram is shown in Figure 2.6. A hydroxypropyl cellulose hydrogel column was also prepared as described above, but the sol-gel solution was poured into a glass fritted funnel filtration during the initial crosslinking reaction with porosity grade of three or 20 mL, 20 mm diameter plastic syringes as moulds. Then in the final step, the column was washed by deionization water several times to remove the extra amount of DVS until the column become very white. This allowed the formation of columns which were then utilized for filtration experiment as hydrogel without drying. Figure 2.7 shows schematic representation the production of HPC hydrogel filtration column.

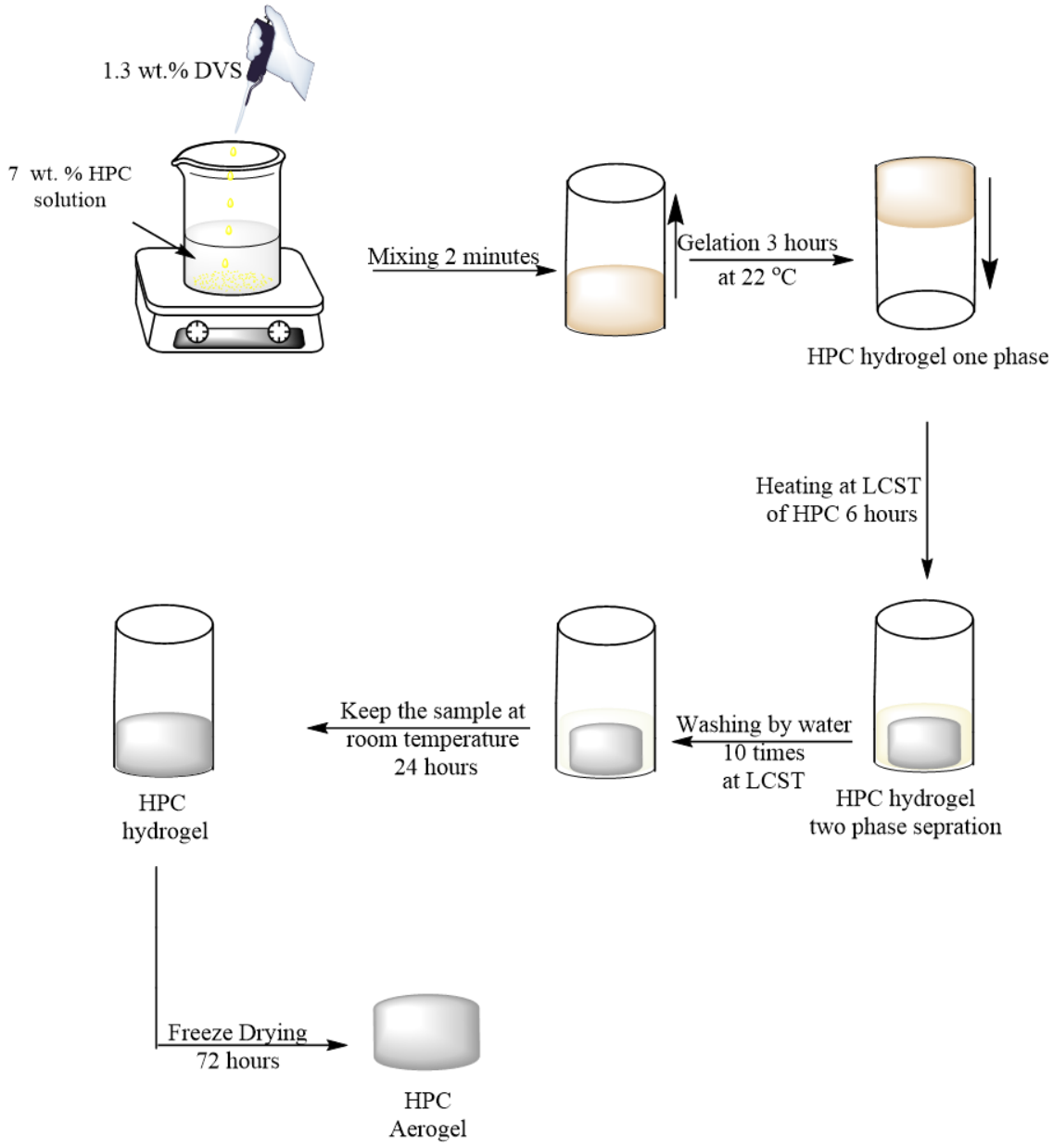

Figure 2.4. Schematic representation the preparation of HPC aerogel using TIPS method.

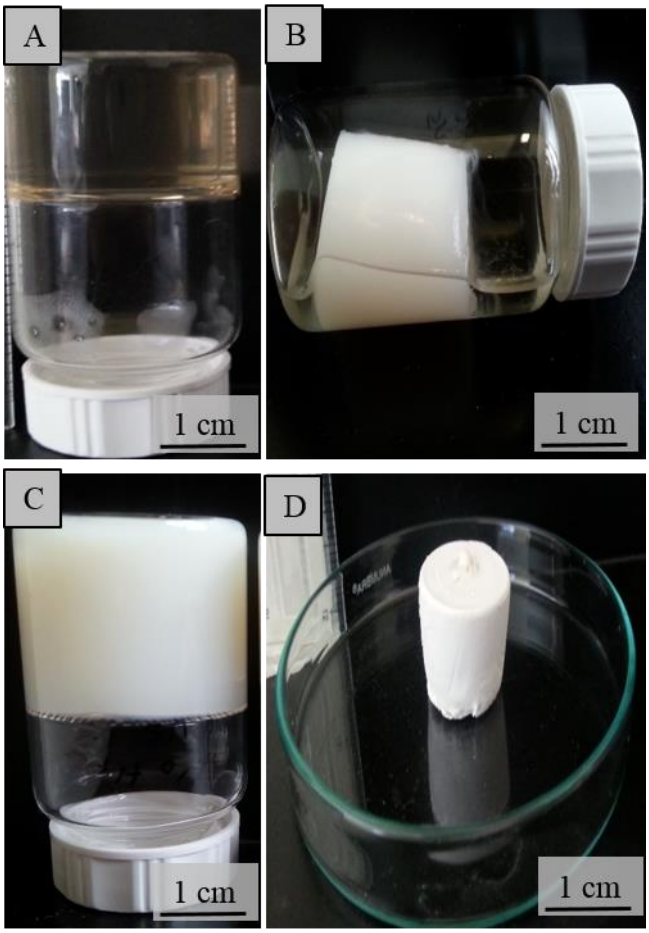

Figure 2.5. Images illustration the preparation stages of HPC aerogel (A) HPC hydrogel at room temperature for 3 hours (one phase) (B) HPC hydrogel at LCST for 6 hours (two phase separation) (C) HPC hydrogel at room temperature after heating at LCST (remixing of phases) (D) HPC aerogel after freeze-drying for 2 days.

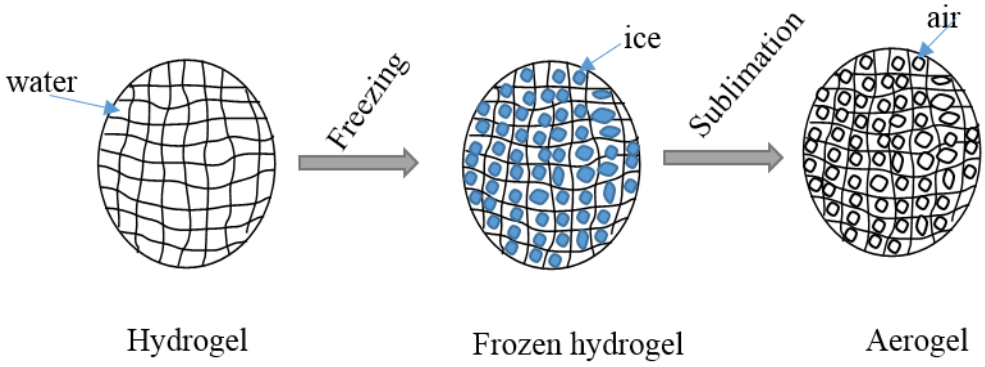

Figure 2.6. Schematic diagram shows the freeze-drying method.

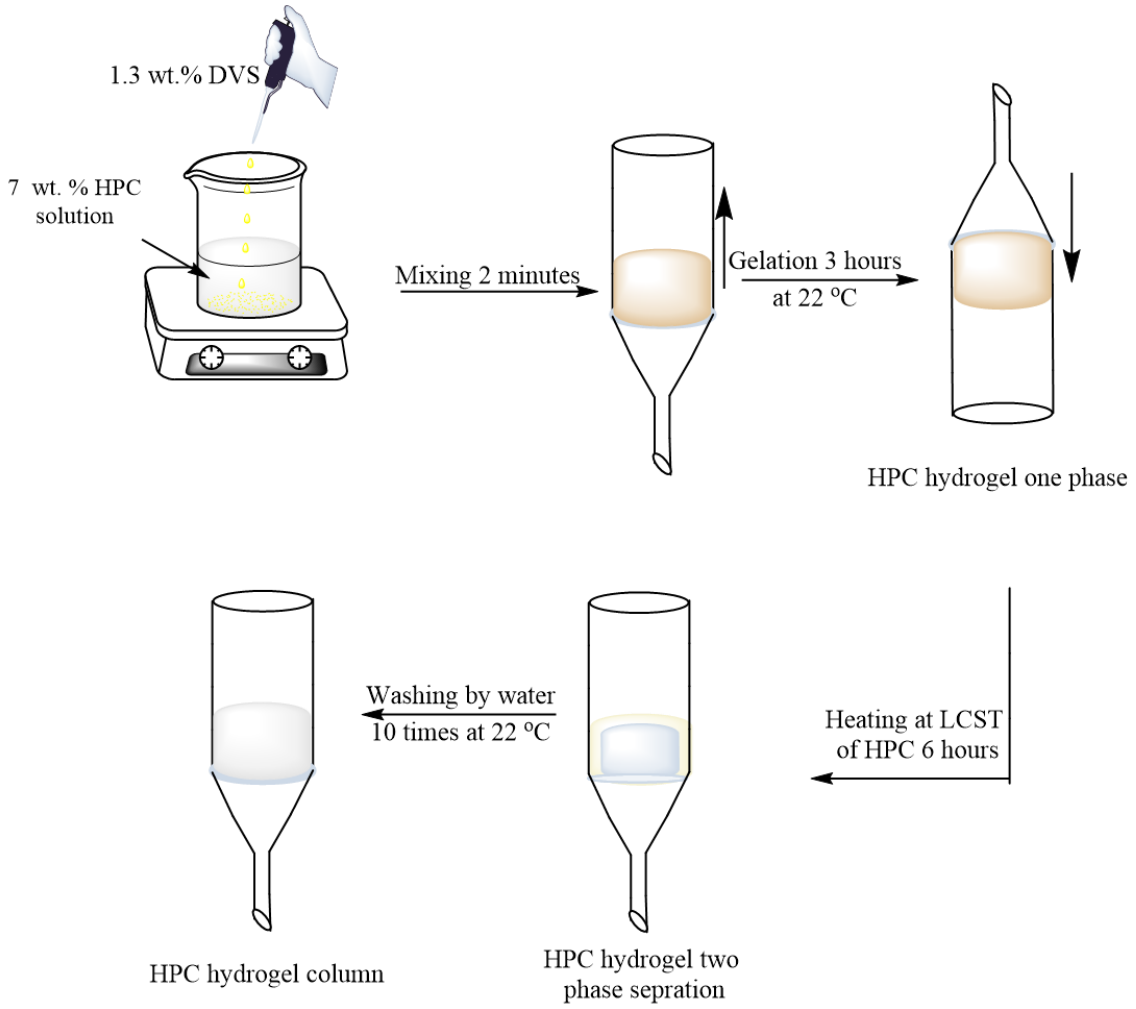

Figure 2.7. Schematic representation the preparation of HPC hydrogel column using the temperature induced phase separation TIPS method.

2.2.3. Preparation of graded porosity hydroxypropyl cellulose hydrogel and aerogels

A method was developed to create a HPC functionally graded porous materials, whereby the shape and size of the porous change across the material. This method exploited the LCST of the thermoresponsive HPC polymer to induce a graded porosity. HPC hydrogel and aerogel are synthesized and the graded porosity was achieved by varying the gelation temperature for the same sample. 7.0 wt. % of hydroxypropyl cellulose (HPC) was dissolved in 0.01 M NaOH solution at room temperature. After the solution became homogenous 1.3 wt. % divinyl sulfone (DVS) was added to the solution, and the reaction was mixed thoroughly for 2 min by using vortex mixture (Vortex-2 Genie). The initial cross-linking reaction occurred at room temperature for 3 hours. Then a selected portion

was placed in the water bath at LCST, and the second portion was kept outside the water level which it was at room temperature (below the LCST) for 6 hours. The sample was then removed from the water bath and left at room temperature for 24 hours according to the temperature induced phase separation (TIPS) method.[7] The hydrogel product was then frozen in liquid nitrogen and was directly transferred to the freeze dryer instrument to obtain the monolithic HPC aerogel with graded porosity. Figure 2.8 shows a schematic representation the preparation of graded HPC aerogel.

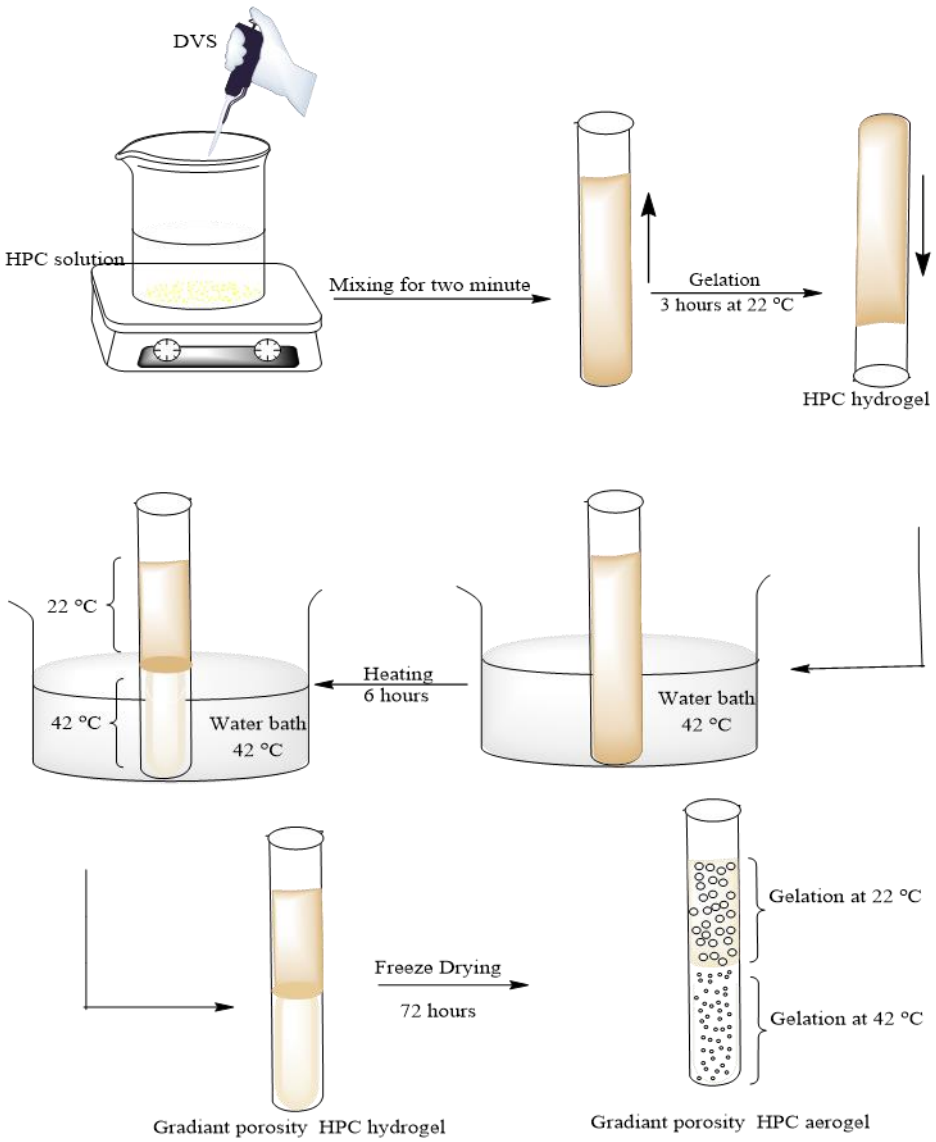

Figure 2.8. Schematic representation of the preparation of a graded porosity HPC aerogel using different gelation temperature.

2.1.2.4 Preparation of hydroxypropyl cellulose/calcium alginate double network (HPC/CA DN) hydrogels and aerogels

There is a number of approaches that could be used to prepare DN hydrogel materials. Various preparation methods has been used to reach our target synthesis HPC/SA DN hydrogels. Here two different methods have been tried to prepare HPC/CA DN hydrogel including one-pot method and two-pot method. First, the chemically and physically cross-linked HPC/CA DN hydrogels were synthesised in one step by mixing the two types of cross-linked polymer: ionically cross-linked sodium alginate (SA), and covalently cross-linked HPC. This was achieved by preparing the first network in the present the polymer of the second network, where the total concentration of HPC and SA was fixed at 7.0 % w/w. According to the gelation temperature of the above HPC SN hydrogels, different gelation temperatures below and at the LCST of HPC materials were used. Briefly, 6.0 % w/w of HPC and 1.0 % w/v SA was dissolved in 0.01 M NaOH solution at room temperature. After the solution became homogenous 1.3 % w/v divinyl sulfone (DVS) was added to the solution, and the reaction was mixed thoroughly for 2 min using a vortex mixer (Vortex-2 Genie). The sample was kept at room temperature for gelation and aging, which is below the LCST of HPC materials. Finally, the last hydrogel product was immersed in 50 mM $CaCl_2$ solution for 24 hours. The final hydrogel product was removed from the $CaCl_2$ solution and washed by deionization water several times to remove the extra amount of DVS and $CaCl_2$ and this method was labeled as method one (M1) as shown in Figure 2.9. An alternative way have used is just after the initial cross-linking reaction occurred at room temperature for 3 hours for pre-crosslinking the hydrogel was placed in a water bath at the LCST of HPC for 6 hours and during the phase separation of HPC hydrogel. This method was labeled as method two (M2) as shown in Figure 2.10.

Secondly, HPC/CA DN hydrogels were also synthesized by a novel two step method. In this method, the first network was synthesised in the absence the polymer of the second network and then the polymer of the second network was diffused into and after that cross-linked this polymer inside the first network. In addition, this approach was applied at two different gelation temperature depend on the LCST of HPC materials. The first step, HPC SN hydrogel was prepared as described above. The second step, HPC SN hydrogels were immersed in a 1 % w/v SA aqueous solution until equilibrium was reached for approximately 24 hours. Later, the ionic crosslinking was performed by removing the hydrogel from SA solution and immersing it in 50 mM $CaCl_2$ solution for 24 hours. The final hybrid HPC/CA DN hydrogels were removed from the $CaCl_2$ solution

and washed by deionization water several times to remove the extra $CaCl_2$. This method was labeled as method three (M3) as shown in the schematic in Figure 2.11. By varying the temperature at which the first network was immersed in the solution of the second network polymer can we control the permeability of this polymer inside the first network hydrogel. HPC SN hydrogel was completely prepared as mentioned above. The sample was then placed in the water bath at the LCST for 6 hours and during the phase separation of HPC hydrogel at this temperature the HPC hydrogel was washed by water for 10 times to remove unreacted DVS. The shrunken HPC hydrogel was then immersed in 1 % w/v SA aqueous solution at the same this temperature for another 3 hours. Then the sample was removed from the water bath and left at room temperature (below the LCST) for 24 hours. Subsequently, the last hydrogel product was removed from SA and impression in 50 mM $CaCl_2$ solution for 24 hours for ionic cross-linked of SA. Finally, the hydrogel was removed from the $CaCl_2$ solution and washed with deionization water several times to remove the extra $CaCl_2$. The hydrogel was then frozen in liquid nitrogen and directly transferred to the freeze-drying instrument to obtain the monolithic HPC/CA DN aerogel material. Figure 2.12 shows the schematic for the preparation of HPC/CA DN aerogel prepared by this approach and this method labeled as method four (M4).

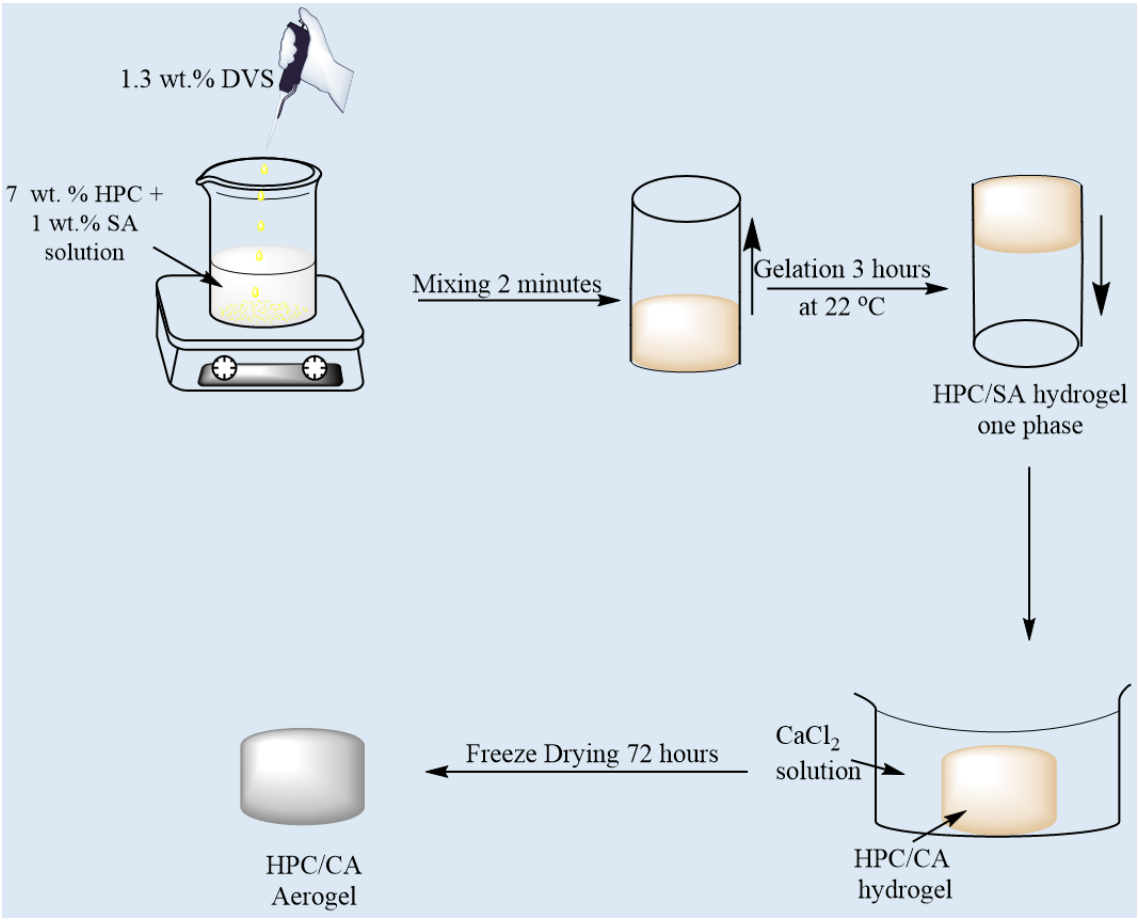

Figure 2.9. Schematic of the preparation of HPC/CA aerogel by one-pot method via mixing SA with HPC before added DVS solution and gelation at room temperature (22±1 °C) and after the hydrogel was formed complete the ionic cross-linked by $CaCl_2$ (M1).

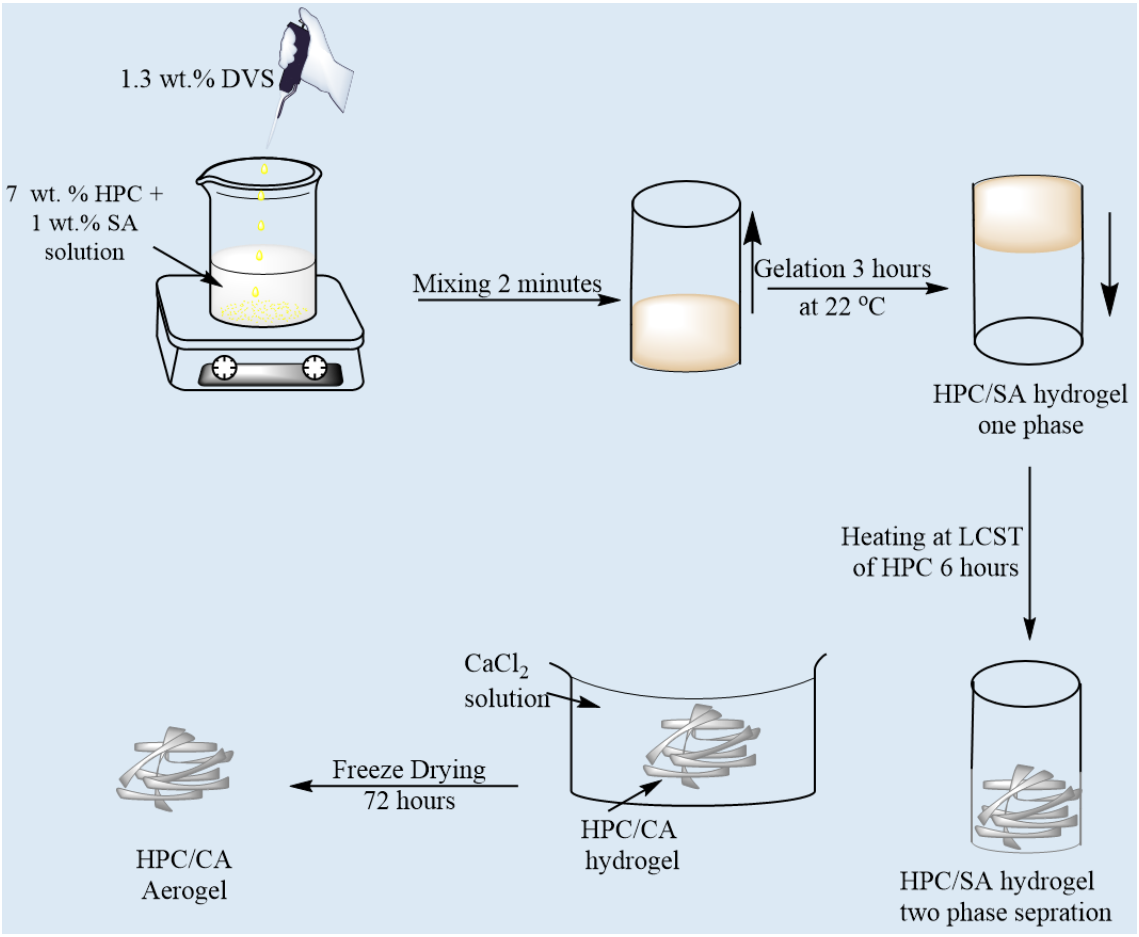

Figure 2.10. Schematic of the preparation of HPC/CA aerogel by one-pot method via mixing SA with HPC before added DVS solution and gelation at LCST and after the hydrogel was formed complete the ionic cross-linked by $CaCl_2$ (M2).

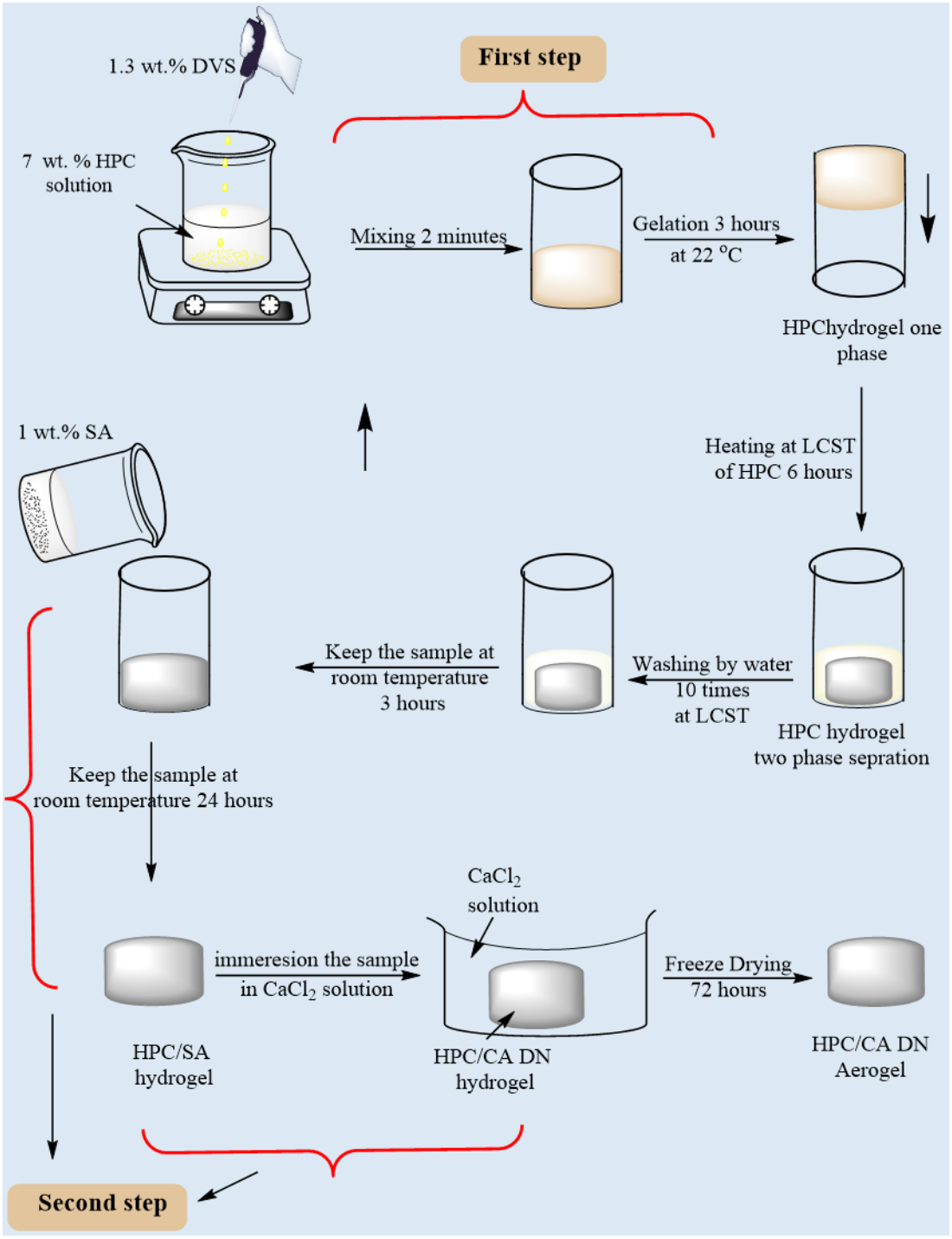

Figure 2.11. Schematic of the preparation of HPC/CA DN aerogel by using two pot method and added SA at a temperature below the LCST (22±1 °C) (M3).

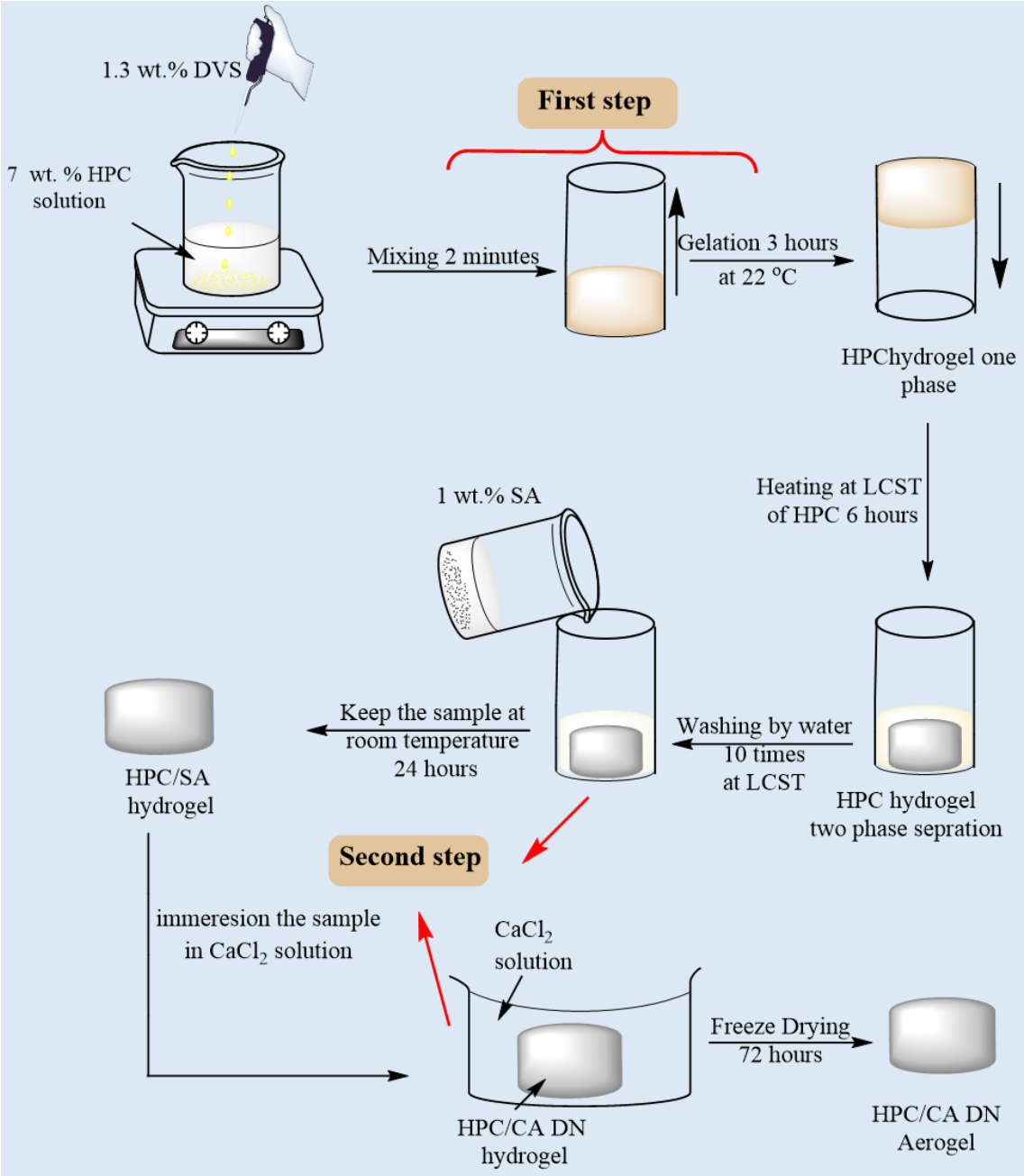

Figure 2.12. Schematic of the preparation of HPC/CA DN aerogel by using two pot method and added SA at LCST, which is during the phase separation of HPC SN hydrogel (M4).

2.3. Characterization of porous materials

2.3.1. Nitrogen sorption measurement

Textural properties such as specific surface area, pore size distribution and total pore volume for solid materials and specially for porous materials are very important in the determination of the quality and behavior of these materials in different applications, such as catalysts, separation, and adsorption. The BET (Brunauer–Emmett–Teller) surface area and porosity analyser has been used in the determination of the surface area and pore size distribution of different porous materials in this project, carbon monolith, HPC SN hydrogel and HPC/CA DN hydrogel by using nitrogen adsorption-desorption measurement. BET surface area was measured on a Micromeritics Tristar II 3000 (USA) BET-N_2 surface area analyser using N_2 gas adsorption analysis by stabilising at -196 ºC. Surface area is calculated from the volume of gas adsorbed onto the sample surface as a function of pressure. The sample was dried at a different temperature between 40-120 ºC for 12 hours for degassing the samples before carrying out the surface area analysis. The pore size distributions were calculated using the Barett-Joyner-Halenda (BJH) model. The sorption isotherms were compared with the typical types of sorption isotherms, which are found on all solid materials as can be seen in Figure 2.13.

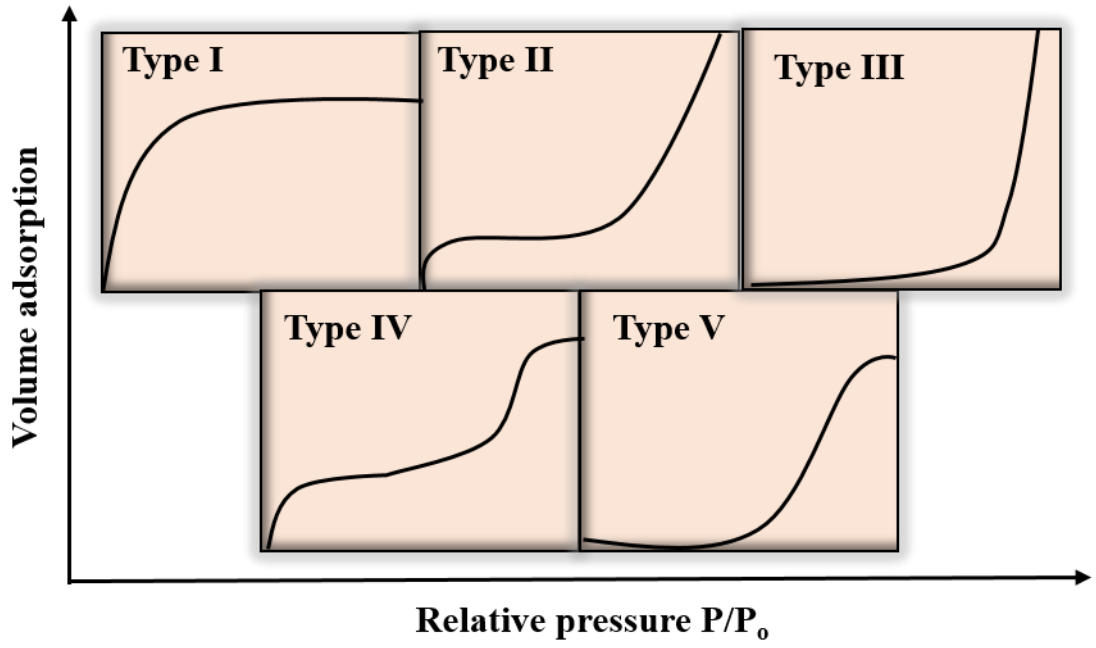

Figure 2.13. Typical five types of adsorption isotherms of solid materials. Redrawn from ref. 8.[8]

Type I is a Langmuir monolayer type, which is found for microporous materials.Type II is referred to as non-porous materials.Type III is non-porous materials and interaction between gas molecules is bigger than gas-solid interaction. Type IV is referred to mesoporous materials. Type V is porous materials and the gas molecules prefer to adsorb on the solid surface than to interact with other gas molecules.[8]

2.3.2. Scanning Electron Microscopy (SEM)

A scanning electron microscope is a type of electron microscope that produces images of a specimen by scanning it with a focused beam of electrons. The electrons interact with atoms in the sample, reflecting at different angles that can be noticed and that contain data about the morphology structure of the specimen. The scanning electron microscope (SEM) has been used in providing information about the structural morphologies of mesoporous carbon materials. It was also used to visualize the freeze-dried HPC and HPC/CA DN hydrogels. JEOL JSM-6480 LV SEM instrument was used to examine the surface morphology of these composites materials. Prior to SEM analysis, a fresh surface was created carefully by sharp knife to prevent crushing and collapse of the network structure of the sample and then stuck to a tab on an aluminum stub and sputter coated with gold to a thickness of ~ 2 nm The schematic diagram of SEM is shown in Figure 2.14.

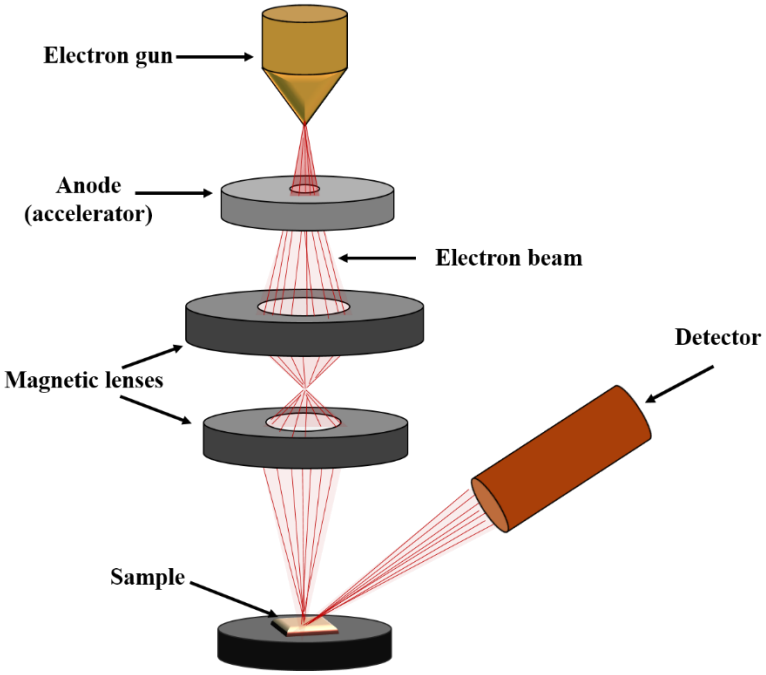

Figure 2.14. Schematic diagram of the scanning electron microscopy (SEM) Redrawn from ref.9.[9]

2.3.4. Cryogenic Scanning Electron Microscopy (Cryo-SEM)

In order to study in more detail the morphology structural of HPC hydrogels, the morphology under wet conditions were also observed using cryo-SEM. Cryo-Scanning electron microscopy (SEM) was carried out for HPC SN and HPC/CA DN hydrogels using a Zeiss Evo 60 SEM instrument. The sample was adhered onto an SEM stub and cooled with liquid nitrogen (~ -210 °C), then transferred onto a cryo-SEM cool stage in the preparation chamber at -140 °C. The sample was sectioned with a cold knife integrated into the chamber to create a fresh surface, then the ice was sublimed at -70 °C and 2–4 Pa for approximately 10 min. The sample was then sputter coated with Pt to a thickness of ~ 2 nm in the preparation chamber via an integrated sputter coater and then transferred into the SEM chamber of the Zeiss Evo 60 scanning electron microscope for imaging at a voltage of 15 kV, where it remained frozen during imaging.

2.2.4. Energy Dispersive X-Ray Spectroscopy (EDS)

Energy dispersive X-ray spectroscopy (EDS) using EDX system, which is coupled with JEOL JSM-6480 LV SEM instrument, was used for elemental data analysis. It can supply qualitative elemental analysis of elements present in a sample for up to a surface depth of several microns and can quantify the chemical ratio of these elements.

2.2.5. Powder X-Ray Diffraction (PXRD)

XRD is an important characterisation technique that gives detailed information about the crystallographic structure of solid materials, and chemical composition. Further characterization was done on to show that the crystal growth of mesoporous carbon materials, HPC and HPC/CA DN hydrogels. PXRD patterns were obtained by using X-ray diffraction technique (Siemens D5000 X-ray diffractometer with 0.15418 nm wavelength) using Cu Kα radiation with a 2θ range between 5° and 80°. Carbon monolith sample was prepared for measurement by crushing the sample into a fine powder, while the HPC and HPC/CA DN hydrogels samples were freeze-dried and chopped into powder.

2.2.6. Fourier Transform Infrared (FTIR) Analysis

IR spectroscopy was used to identify the functional groups involved in the prepared porous materials. FT-IR spectra were examined using Thermo Scientific Nicolet 380 FT-IR (Thermo Scientific, Hemel Hempstead, UK), supplied with attenuated total reflectance (ATR). ATR is one accessory to measure FTIR spectra where the samples were conected directly with the ATR diamond crystal, which has high refractive index at a certain angle. The IR beam will be reflected several times within the crystal and by measuring the

changes that occur in an internally reflected IR beam when the beam contact with the specimen.[10] Each sample was analyzed in the wavenumber range of 4000–500 cm^{-1} using 4 scans. Figure 2.15 illustrates a schematic representation of FTIR-ATR spectrometer.

.

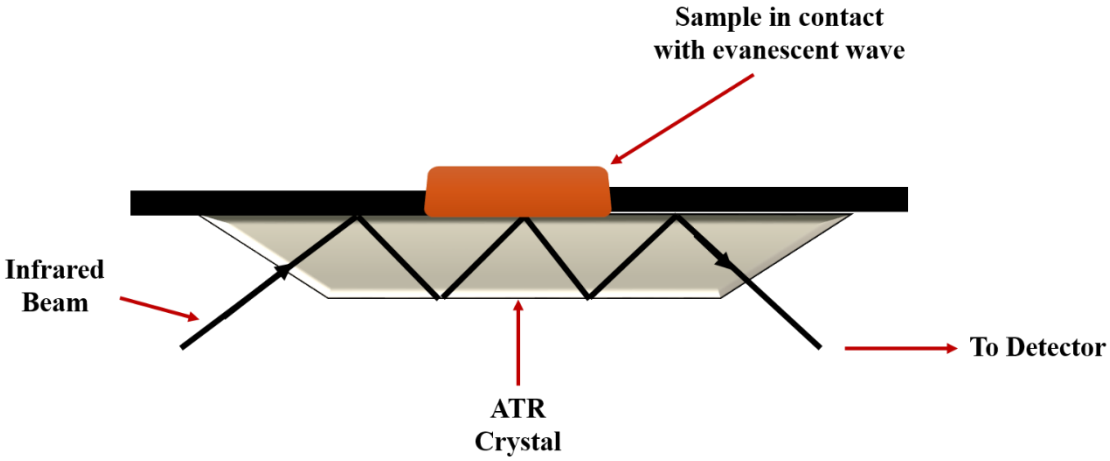

Figure 2.15. The schematic representation of the infrared beam reflected on the crystal - sample interface in FTIR-ATR spectrometer. Redrawn from ref. 10.[11]

2.2.7. Thermogravimetric analysis (TGA)

Thermal gravimetric analysis (TGA) was used to determine the thermal degradation of the sample by calculating the mass loss of a material as a function of temperature under nitrogen or air atmosphere. Thermogravimetric (TGA) measurements of both dried polymer and the carbon material for the same sample were studied using a Mettler Toledo TGA/DSC under air and N_2 atmosphere. Thermogravimetric profiles were recorded from 25 ºC to 900 ºC in flowing air at a heating rate of 10 ºC/min. TGA profiles provide information about template removal and the degree of template removal via observing the decomposition the template through weight change, incorporation of inorganic species through recording the weight of residue and by monitoring the combustion temperature of carbon materials. It was also used to determine the thermal properties of the dried HPC and HPC/CA DN hydrogels and to compare them with the original polymer before cross-linking. Thermogravimetric profiles were recorded from 25 ºC to 800 ºC in flowing air at a heating rate of 10 ºC/min and gas rate 60 ml/min.

2.2.8 Differential Scanning Calorimetry (DSC)

DSC measures the change in heat flow with increasing the temperature between the reference and the sample. This change will indicate some type of physical transition, such as a glass transition temperature of the polymer, and also show where the reaction will be

endothermic or exothermic. DSC measurements of both starting polymer and the FD-HPC hydrogel were investigated by using a Mettler Toledo DSC 30. DSC, analysis was carried out using Nitrogen gas as an inert gas in the temperature range between 25 and 300 °C, with a heating rate of 10 °C/min and gas rate 50 ml/min.

2.2.9 Mechanical properties measurement

2.2.9.1. Compression test

Compression test are used to determine material behaviour under compressive load by measuring fundamental parameters such as Young's Modulus and compressive. strength The mechanical properties for HPC SN, FD-HPC, and HPC/CA DN hydrogels were performed using Mark-10 with load cell series 5 (500 N load) with a cross head speed 1.2 mm/min. This test was examined under air and water environment for cylindrical samples with 10 mm height and 20 mm diameter. All tests were carried out at room temperature at around 20 ºC. Their compressional strength was taken as the force applied at the point of structural failure, normalised with the cross-sectional area of the sample. To make direct comparisons between materials, the specimen geometry and size must be accurate. Therefore, the dimensions of each sample are noted to compute stress and strain from load and displacement, respectively. Compression strain can be calculated using the following equation:

$$\varepsilon_e = \Delta L / L_o \qquad (2.1)$$

Where ε_e is the compressive strain; ΔL is the measured displacement and L_o is initial specimen length. Compression stress is calculated by using the equation:

$$\sigma_e = F/A \qquad (2.2)$$

Where σ is Compressive stress of the sample (in MPa); F is the applied load and A is the initial cross-sectional area of the sample (in mm^2). Young's modulus (E) was obtained from the gradient of the linear elastic region of the stress/strain plots or the ratio of the compression stress to compression strain in the axis:

$$E = \sigma e / \varepsilon e \qquad (2.3)$$

E has characterized the stiffness of material in units of force per unit area (N/m^2), or Pa).

2.2.9.2. Rheology

Rheological measurements of HPC SN and HPC/CA DN hydrogels were performed using a Bohlin CVO 120 rheometer (Malvern Instruments) using a 20 mm diameter parallel plate geometry and connected with a Peltier plate to control the temperature. Oscillatory tests and the storage modulus were done at different temperatures (25 °C, 35 °C, 45 °C and 55 °C and was measured at increasing shear stress from 10 - 400 Pa. The frequency used was constant and always 1 Hz. At each temperature, the sample was equilibrated for 30 seconds prior to being measured.

2.2.10. The measurement of magnetic susceptibility

Gouy method is the simplest method to study the magnetic properties of the solid materials by determining the magnetic susceptibility by using the Johnson-Matthey magnetic susceptibility balance. The mass Susceptibility was studied by using magnetic susceptibility balance, Sherwood Scientific, Cambridge, UK. This method was used to measuring the magnetic susceptibility of mesoporous carbon materials and metallic mesoporous carbon materials. The mass susceptibility was calculated in cgs to unite by the following question:

$$Xg = \frac{Cl(R - Ro)}{10^9\, m} \quad (2.4)$$

Where **l is** the sample length in the tube in cm; **m** the sample weight in g; **C** calibration constant; **R** the balance reading from the digital display when to place the sample tube in the instrument; **R_o** the balance reading from the digital display when the empty tube is in the instrument. The final mass susceptibility was converted to the SI unit by multiplying with conversion factors ($4\Pi \times 10^{-3}$).

2.2.11. Density and porosity

Hydrogel density was determined by measuring the weight and volume of FD-HPC hydrogel samples. The weight of an FD-HPC hydrogel was measured by an analytical balance (readability 0.0001 g, Analytical Balance, Denver SI-234, UK) and the dimensions of hydrogels were measured by a digital caliper at four different positions. Three samples were used for density measurement for hydrogels with the same gelation temperature, HPC and DVS concentration. Hydrogel porosity (P) or (θ) were calculated using the density of FD-HPC hydrogel (aerogel) ($\rho_{aerogel}$) and the density of wet HPC hydrogel ($\rho_{hydrogel}$) using the following equation:

$$P\% = 100 \times (1 - \rho_{aerogel} / \rho_{hydrogel}) \quad (2.5)$$

2.2.12. Swelling measurement

2.2.12.1. Equilibrium swelling ratio

The equilibrium swelling ratios of HPC hydrogels were measured for three HPC hydrogel samples with the same concentration of HPC and the chemical cross linker, but at different gelation temperature (at the lower critical solution temperature of (LCST), at room temperature, which is below the LCST (RT) and at RT, but then freezing (RTF).

The swelling ratio (SR) was measured by gravimetric analysis, from 5 to 50 °C with a 5 °C increment. Before each series of measurements, the hydrogels were stored in distilled water at 5 °C for 24 h. They were then transferred in a water bath at the desired temperature for 24 h. Before measurement, the excess of water at the surface of the sample was absorbed with a filter paper. SR is defined as the following equation:

$$SR = Ws/Wd \quad (2.6)$$

Where Ws is the weight of the equilibrated hydrogel at a given temperature and Wd is the weight of the hydrogel at 50 °C, in the dehydrated state.

2.2.12.2. Kinetics of deswelling and swelling

The deswelling kinetics of the above three samples were measured as well via gravimetry analysis. The equilibrated hydrogels, initially stored in distilled water at 15 °C for 24 h, were then transferred in 50 °C distilled water. They were then weighted at predetermined intervals of time: (1) every 30 s for the first 4 min; (2) then every 1 min for the next 3 min; (3) every 2 min for the next 8 min; (4) then every 5 min for the following 15 min; (5) and finally every 10 min for the last 30 min, for a total time of 60 min. As mentioned above, the excess of water at the surface of the gel was gently absorbed with filter paper before measuring the weight. The water retention ratio WR is defined as the following equation:

$$WR = (Wt/Wg) \times 100 \quad (2.7)$$

Here Wt is the weight of the hydrogel at a given time and Wg is the original weight of the hydrated hydrogel at 15 °C.

The swelling kinetics were also measured by gravimetry analysis. The hydrogels were first immersed in 15 °C distilled water, brought to equilibrium, and weighed (Wg). They were then plunged in 50 °C distilled water for 1 hour, until equilibrium in the dehydrated state was reached. They were then plunged back in 15°C distilled water and were weighted (Wt) at the same predetermined time intervals described previously in this

section. The excess of water at the surface of the sample was also absorbed with moistened filter paper before weighing. The water uptake ratio WU is calculated using the following equation.

$$WU = (Wt/Wg) \times 100 \quad (2.8)$$

Here Wt is the weight of the hydrogel at a given time and Wg is the original weight of the dehydration hydrogel at 50 °C.

2.3. Applications of HPC SN and HPC/CA DN hydrogels

2.3.1. Dye adsorption by HPC SN and HPC/CA DN hydrogels

2.3.1.1. Batch adsorption of methylene blue (MB) dye by using HPC and HPC/CA DN hydrogels as adsorbents

MB adsorption onto HPC SN and HPC/CA DN hydrogels was investigated via a batch method whereby the hydrogel (~0.3 g of HPC, 5 mL volume) were individually placed into separate conical flasks with 100 mL solutions of MB (5-40 mg L^{-1} concentrations). The samples were gently shaken in the dark condition at room temperature (22 ± 2 °C) using a platform shaker (Thermo Scientific, Compact Digital Mini Rotator) with a shaker speed of 100 rpm until the system reached equilibrium. All experiments were carried out in triplicate and the concentration of the MB dye solution before and during the adsorption process was determined by removing aliquots for double beam UV−vis spectrometry (Perkin Elmer Lambda Bio-10 UV-Vis spectrometer with UV WinLab v.6.0.4 software) at the maximum absorbance of MB dye (664 nm). The dye removal percentage of MB dye was calculated according to the following equation:

$$\%\ Removal = \frac{C(\mathrm{MB})_0 - C(\mathrm{MB})_t}{C(\mathrm{MB})_0} \times 100\% \quad (2.9)$$

Where $C(\mathrm{MB})_0$ and $C(\mathrm{MB})_t$ are the MB dye concentrations (in mg·L^{-1}) before and after shaking with HPC hydrogel at time *t*, respectively.

The removed quantity of MB dye adsorbed per unit mass of adsorbent at particular time Q_t and at equilibrium Q_e (mg.g^{-1}) were calculated using the equations below respectively:

$$Q_t = \frac{(C_0 - C_t)\,V}{M} \quad (2.10)$$

$$Q_e = \frac{(C_0 - C_e)\,V}{M} \quad (2.11)$$

Where C_o (mg L^{-1}) and C_t (mg L^{-1}) is the initial concentration of MB dye and concentration of MB dye at time t respectively, and C_e (mg L^{-1}). Is the equilibrium concentration, m and V are the mass of adsorbent (g) and the volume of dye solution (L).

Effect of pH

The effect of pH on the adsorption of MB dye from aqueous solution onto the HPC SN and HPC/CA DN hydrogels were performed using different pH value of the dye solutions at the range of (3.62-10.09). MB dye solution pH was pre-adjusted using drops of 0.01 M NaOH or 0.01 M HCl solutions. The experiment was carried out at room temperature (22±1 °C) using 40 $mg.L^{-1}$ adsorbate concentrations, and 0.3g of adsorbent dosage in 100 mL of adsorbate solution. The samples were gently shaken for 28 hours in the dark condition. This experiment was performed in triplicate to calculate the error bars are the standard deviation.

Adsorption isotherm

Study of adsorption isotherms was investigated using both Langmuir and Freundlich isotherms for adsorption of MB dye on the HPC SN and HPC/CA DN hydrogels. In the theoretical Langmuir model, it is assumed that the dye undergoes monolayer adsorption around the homogenous surface of the adsorbent and that there is no interaction between the adsorbate molecules.[12] The Langmuir isotherm parameters were evaluated using the following equation:

$$\frac{C_e}{Q_e} = \frac{1}{Q_{max}K_L} + \frac{C_e}{Q_{max}} \quad (2.12)$$

Where C_e (mg L^{-1}) is the equilibrium concentration of MB dye in solution, Q_e (mg g^{-1}) is the equilibrium capacity of MB on the adsorbent, Q_{max} (mg g^{-1}) is the maximum amount of MB on the adsorbent to form a complete monolayer on surface, K_L (L mg^{-1}) is the Langmuir constant that relates to the affinity of adsorption sites.[13]

The Freundlich model is an empirical model and more applicable at low adsorbate concentrations. In the theoretical Freundlich model, it is assumed that adsorption of dye occurs on a heterogeneous surface of the adsorbent, it suggests multilayer adsorption and there is an interaction between the adsorbate and adsorbent molecules depend on the electrostatic interaction between negative and positive charges.[14]

The Freundlich isotherm parameters were calculated using the following equation:

$$\log Q_e = \log K_F + \frac{1}{n}\log C_e \quad (2.13)$$

Where, Q_e (mg/g) is amounts of MB dye adsorbed at equilibrium, C_e (mg/L) is equilibrium MB dye concentration in the solution. K_F and (1/n) are Freundlich adsorption isotherm constants.

Thermodynamics studies

Temperature variation studies are very important in order to know whether an adsorption process is exothermic or endothermic, and where the processes are spontaneous or nonspontaneous. The thermodynamic parameters (Gibbs free energy ΔG°, enthalpy ΔH°, and entropy ΔS°) for the adsorption of MB dye onto both HPC SN and HPC/CA DN hydrogels were investigated. This experiment was carried out using 100 mL of MB dye solution (40 $mg.L^{-1}$) with 0.3 g of the hydrogels and the mixture was gently mixed for 28 hours by shaking at 100 rpm min^{-1} using (Stuart Shaking Incubator) at different temperatures 25, 35, 45and 55 °C. After each adsorption, 5 mL of the supernatant was taken without any further separation and were measured by UV−vis spectrometry (Perkin Elmer Lambda Bio-10 UV-Vis spectrometer with UV WinLab v.6.0.4 software) at the maximum absorbance of MB dye (664 nm) to determine the residual concentration of MB dye after adsorption process. Every experiment was triplicated under the same conditions.

The thermodynamic parameters of the adsorption processes of MB dye onto HPC SN and HPC/CA DN hydrogels were calculated using the following equations:

The equilibrium constant (*Keq*) of the adsorption processes can be evaluated using the following equation:[15]

$$K_{eq} = \frac{Q_{eq}}{C_{eq}} \quad (2.13)$$

Where Q_{eq} (mg g^{-1}) is the adsorption capacity of MB dye adsorbed at equilibrium and C_{eq} (mg L^{-1}) is the equilibrium concentration of MB dye.

The free energy change (ΔG°) of the adsorption process is given by the following equation:[16]

$$\Delta G^O = -RTlnK_{eq} \quad (2.14)$$

The van't Hoff equation gives the relationship between equilibrium constant (*Keq*) and temperature (*T*)

$$\Delta G^O = \Delta H^O - T\Delta S^O \quad (2.15)$$

$$\ln K_{eq} = \frac{\Delta S^O}{R} - \frac{\Delta H^O}{RT} \quad (2.16)$$

where q_{eq} (mg.g^{-1}) is the amount of MB dye adsorbed on the adsorbent from solution at equilibrium, C_{eq} (mg.L^{-1}) is the equilibrium concentration of metal ions in the solution, R (J.mol^{-1}.K^{-1}) is the gas constant 8.314, T (K) is the absolute temperature, Keq (L.g^{-1}) is the equilibrium constant of the adsorption, ΔG°, ΔH°, and ΔS° are the changes in the Gibbs free energy, enthalpy and entropy of the adsorption process respectively. The values of ΔH° and ΔS° were calculated from the linear graph which is plotted between ln *Keq* and 1/T.

Adsorption Kinetics

The pseudo-first-order, pseudo-second-order, and intraparticle diffusion models to establish the adsorption kinetic parameters of the adsorption process. These are the most commonly used models to describe the adsorption kinetics of organics such as dyes from aqueous solution on different adsorbents. To investigate MB dye adsorption kinetics on HPC SN and HPC/CA DN hydrogels, adsorption experiments were carried out using 100 mLof different concentrations of the dye in the range between (5- 40 mg.L^{-1}) with 0.3 g of adsorbent. The mixture was agitated on a shaker at 100 rpm under room temperature (22±1 °C). The samples were extracted at various time intervals and the residual concentration of MB dye was determined by UV spectrophotometer. The experimental data of adsorption were investigated firstly under pseudo first order and it is rate constant (k1) was calculated by using the following equation:[17]

$$\frac{1}{q_t} = \left(\frac{k_1}{k_d}\right)\left(\frac{1}{t}\right) + \frac{1}{q_e} \quad (2.17)$$

Where q_{eq} and q_t are the amount of MB dye adsorbed per unit mass of the adsorbent (mg/g) at equilibrium and time t (mins) respectively, k_1 (min^{-1}) is the first-order rate constant. By plotting $1/q_t$ against $1/t$, the values of $k1$ and q_{eq} can be calculated from the slope and intercept of the graph. The pseudo-second-order rate was calculated by using the following equation,which is cited by Yuh-Shan Ho :[18]

$$\frac{t}{q_t} = \frac{1}{k_2 q_e^2} + \frac{t}{q_e} \quad (2.18)$$

Where q_{eq} and q_t are the amount of MB due adsorbed per unit mass of the adsorbent (mg/g) at equilibrium and time t (mins) respectively, k_2 (g mg^{-1} min^{-1}) is the pseudo-second- order

rate constant. By plotting t/q_t against t, the second-order sorption rate constant k_2, and q_{eq} can be calculated from the slope and intercept of the graph. The intraparticle diffusion model was calculated by using the following equation:[19]

$$q_t = k_p t^{1/2} + C \quad (2.19)$$

Where q_t (mg/g) is the amount of MB dye adsorbed at time t (mins), k_p (mg g^{-1} $min^{-1/2}$) is the intraparticle diffusion rate constant, C (mg/g) is the intercept when q_t is plotted against $t^{1/2}$.

2.3.1.2. Filtration adsorption of MB dye by HPC SN and HPC/CA DN hydrogel columns

Methylene Blue (MB) and Sodium Fluorescein (FL) dyes were used as model pollutants to investigate the dye uptake characteristics of HPC SN and HPC/CA DN hydrogel columns. MB and FL are cationic and anionic dyes, respectively, and their chemical structures are shown in Figure 2.16. Elution experiments were carried out at room temperature (22 ± 2 °C) with these columns, which prepared in 20 mL syringe barrels. MB and FL dye solutions were eluted through these hydrogel columns and the dye concentration of the eluent collected in 10 mL fractions was determined via UV-Vis spectroscopy over the wavelength range 350-750 nm.

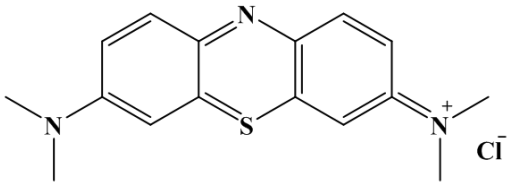

Methylene Blue Dye (MB)

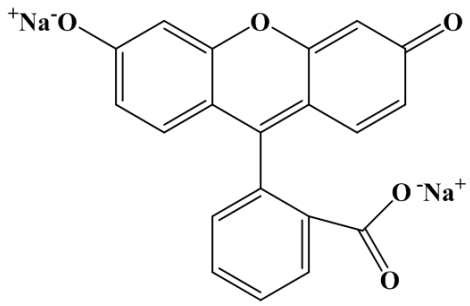

Sodium Fluorescein Dye (FL)

Figure 2.16. Drawings showing the molecular structures of Methylene Blue (MB) and Sodium Fluorescein (FL).

The regeneration of the dye-loaded HPC hydrogels was investigated. FL dye could be easily removed from the columns by elution with deionized water, whereas MB-loaded columns were regenerated by elution with 0.01 M aq. HCl, as column protonation

decreases electrostatic attraction between the column and the positively charged dye.[20] After elution of the adsorbed dye, the HPC hydrogel column was further washed with deionized water and reused for MB dye removal. The above dye separation experiment was repeated on the regenerated column to evaluate reusability.

2.3.2. Filtration Separation of MB/FL Mixed Dyes

Aqueous solution mixtures containing both MB and FL were prepared. 200 mL of this solution mixture was passed through the HPC SN and HPC/CA DN hydrogel columns by gravity filtration. The eluent was collected in 10 mL fractions and the dye concentration was determined via UV-Vis spectroscopy over the wavelength range 350-750 nm. Subsequently, each column was regenerated by washing firstly by deionized water to remove FL dye from the columns and then with 0.01 M aqueous HCl (20 mL) and finally with deionized water again (50 mL). The above dye separation experiment was repeated on the regenerated column to evaluate reusability. The adsorption/regeneration cycles were performed 10 times. The separation efficiency (S) is used to evaluate the separation ability by the following equation:

$$S\ (\%) = \frac{C(\mathbf{F})_f}{C(\mathbf{F})_f + C(\mathbf{MB})_f} \times 100\% \quad (2.20)$$

Where $C(MB)_f$ and $C(FL)_f$ are the concentration of MB and FL in the filtrate respectively.

2.4. References

1. L. Liu, F.-Y. Wang, G.-S. Shao and Z.-Y. Yuan, *Carbon*, 2010, **48**, 2089-2099.
2. J. Li, J. Gu, H. Li, Y. Liang, Y. Hao, X. Sun and L. Wang, *Microporous and Mesoporous Materials*, 2010, **128**, 144-149.
3. Z. Liu, Y. Song, Y. Yang, J. Mi and L. Deng, *Materials Research Bulletin*, 2012, **47**, 274-278.
4. S. E. Elaigwu, G. Kyriakou, T. J. Prior and G. M. Greenway, *Materials Letters*, 2014, **123**, 198-201.
5. D. C. Harsh and S. H. Gehrke, *Journal of controlled release*, 1991, **17**, 175-185.
6. K. Norihiro and H. Stevin, *Colloids and Surfaces B: Biointerfaces*, 2004, **38**, 191-196.
7. B. G. Kabra, S. H. Gehrke and R. J. Spontak, *Macromolecules*, 1998, **31**, 2166-2173.
8. S. Brunauer, L. S. Deming, W. E. Deming and E. Teller, *Journal of the American Chemical society*, 1940, **62**, 1723-1732.
9. B. Inkson, in *Materials characterization using nondestructive evaluation (NDE) methods*, Elsevier, 2016, pp. 17-43.
10. R. Minnes, M. Nissinmann, Y. Maizels, G. Gerlitz, A. Katzir and Y. Raichlin, *Scientific reports*, 2017, **7**, 4381.
11. Y. Shai, *Biochimica et Biophysica Acta (BBA)-Biomembranes*, 2013, **1828**, 2306-2313.
12. I. Langmuir, *Journal of the American Chemical society*, 1918, **40**, 1361-1403.
13. B. Hameed and M. El-Khaiary, *Journal of Hazardous Materials*, 2008, **159**, 574-579.
14. H. Freundlich, *J. Phys. Chem*, 1906, **57**, 1100-1107.
15. A. Kausar and H. N. Bhatti, *J Chem Soc Pak*, 2013, **35**, 1041-1052.
16. Y. Liu, *Journal of Chemical & Engineering Data*, 2009, **54**, 1981-1985.
17. A. Olgun and N. Atar, *Journal of Industrial and Engineering Chemistry*, 2012, **18**, 1751-1757.
18. Y.-S. Ho and G. McKay, *Process Safety and Environmental Protection*, 1998, **76**, 183-191.
19. W. J. Weber and J. C. Morris, *Journal of the Sanitary Engineering Division*, 1963, **89**, 31-60.
20. C. H. Chan, C. H. Chia, S. Zakaria, M. S. Sajab and S. X. Chin, *RSC Advances*, 2015, **5**, 18204-18212.

Chapter Three

3. Preparation and characterisation of mesoporous carbon materials

3.1 Introduction

Porous materials are solid materials that contain voids in different shapes such as cavities, channels, or interstices. These materials have been divided into various classifications. Firstly, porous materials are divided into three types depending on pore size microporous (pore diameter < 2nm), mesoporous (pore diameter 2-50 nm) and macroporous (pore diameter >50 nm). Secondly, these materials classifications rely upon pore structure such as open and close voids according to how reachable the fluid is through the pore. Open pores are addition classified into interconnected pores and blind pores. Interconnected pores have an open channel that starts at one position on the surface of materials and expands into the various positions in the surface. Blind pores have an opening to the surface just at one side and close from the other side. Closed pores involve non-interconnected pores that are completely isolated from the surface and their neighbors.[1, 2] Porous carbon materials, as a big group of porous materials, have been studied due to their potential applications in environmental remediation, separation, catalysis, energy storage, adsorption, and biomedicine.[3-11] Numerous researchers have been working on the development of innovative carbon-based materials. Porous carbons materials include a broad spectrum of carbons ranging from microporous to mesoporous such as activated carbon, carbon nanotubes, carbon particles, carbon aerogels, and carbon composites. The properties of each group of mesoporous carbons reflected by their porous structure and surface chemistry are influenced by both the nature of carbon precursors and the methods of carbonization and activation.

There are numerous carbon sources, for example, biomass[12], natural graphite, thermosetting polymers, bio-waste, etc., that have been researched for the preparation of different types of carbon materials. In particular, of the thermosetting polymers, phenolic resin-based polymers have been most commonly used due to their easy synthesis, cost effectiveness, and industrial attainability. In addition, they are highly versatile, having been adapted for the creation of various carbonaceous materials, for example, nanotubes [13], mesoporous carbons materials [14] and carbon aerogels. [15]

One of the most common methods in the synthesis of mesoporous carbon materials referred to as the “hard-templating method”. [16-19] This route briefly includes three steps.

Firstly, the preparation of ordered mesoporous silica followed by filling the pores of the template with suitable carbon precursors. Following this, carbonisation of the precursors and removal of the silica template is carried out. The resulting carbon materials are inverse replicas of the template and exhibit a high surface area, large pore volume and ordered mesopores. The adsorption properties of these materials can be easily tuned by using different silica mesostructure as templates. Despite the fact that these strategies have been widely used, they have a vital drawbacks. Firstly, they have several synthetic steps and are costly due to the preparation of the colloidal silica particles and silica porous. Moreover, using chemicals such as hydrofluoric acid (highly dangerous and limited to specially trained personnel) or sodium hydroxide solution (corrosive and environmentally unfriendly) for silica removal is undesirable and renders this method impractical for scale up.[20] Many researchers have therefore used a soft template method for the synthesis of mesoporous carbon materials via self-assembly of organic carbon sources such as phenol, resorcinol, and phloroglucinol in the presence of formaldehyde as a cross-linker and triblock copolymers.[21] Self-assembly of organic carbon sources such as phenolic resins and block copolymers has opened another option in the preparation of mesoporous carbon materials by using soft template route.[22-24] This methodology exploits the advantage of the interaction between thermally-decomposable surfactants and thermosetting polymers to construct ordered polymer-polymer nanocomposites. Through initial heating, the thermally unstable soft template agent (triblock copolymer) is decomposed. Increasing the temperature carbonizes the thermosetting polymer to form the pore walls of porous carbon materials. In the soft templating method, fewer steps are needed compared to the hard templating route. This method also avoids the use of hazardous materials, thereby decreasing the negative impact on the environment.[25]

Evaporation-induced self-assembly (EISA) technique is the most regular method utilized for the synthesis of carbon monolith, but drawbacks include material shrinkage and crack formation, thus decreasing this technique's applicability.[26] These materials can be carried out by different methods, firstly, varying the solvent system from mixture solvent containing water-ethanol at different ratio[27] to ethanol solvent [25]or completely aqueous solvent.[28] Secondly, changing the concentration of triblock copolymer or PEO/PPO ratio. Many applications require different types of mesopores carbons, which are containing inorganic species or carbon-inorganic nanocomposites such as catalysis, adsorption, energy storage, and separation.

Inorganic species can be included in mesoporous carbons through their preparation process or by post-synthesis infiltration.[29, 30] Post-synthesis is frequently utilized, but its

drawbacks include challenges in adjusting particle size and distribution, limitations in the loading of inorganic species, and possible pore blocking; however, these drawbacks are avoided when inorganic species are loaded through the carbon preparation process. Therefore, many studies have been made to load inorganic species through the soft template preparation process of mesoporous carbons.[31]

The aim of this chapter was the synthesis and characterization of various types of materials including blank mesoporous carbon materials and magnetic mesoporous carbon materials such as Fe/OMC, Co/OMC and Ni/OMC by using the soft template method. Resorcinol and formaldehyde were used as the carbon precursor and triblock copolymer Pluronic F127 as the templating agent in acidic conditions. The synthesized material was characterised using Scanning Electron Microscopy (SEM), Brunauer-Emmett-Teller nitrogen sorption measurements (BET), powder X-Ray Diffraction (PXRD), Fourier Transform Infrared spectroscopy (FTIR), and Thermogravimetric Analysis (TGA).

3.2 Results

3.2.1 Blank ordered mesoporous carbon materials

The soft template route was used to synthesise mesoporous carbon materials. The synthesis mechanism reflected the strong interaction between the reaction substances as shown in Figure 3.1.

The formation of mesoporous carbon monolith involves two steps. Firstly, polymerization gradually happens between the resorcinol and formaldehyde to form soluble oligomers (RF) with plenty of hydroxyl groups. The main reactions between the phenolic monomer and formaldehyde form covalent crosslinks through an addition reaction to produce methylene and hydroxymethyl bridges.[32] Secondly, the hydroxyl groups are able to interact with the surfactant triblock copolymer (pluronic F127) by hydrogen bonding.[24] The use of resorcinol and formaldehyde as a carbon precursor is vital for the successful association of organic–organic mesostructured due to it having a number of hydroxyl groups, which can interact strongly with Pluronic F127 by formation of hydrogen bonds.

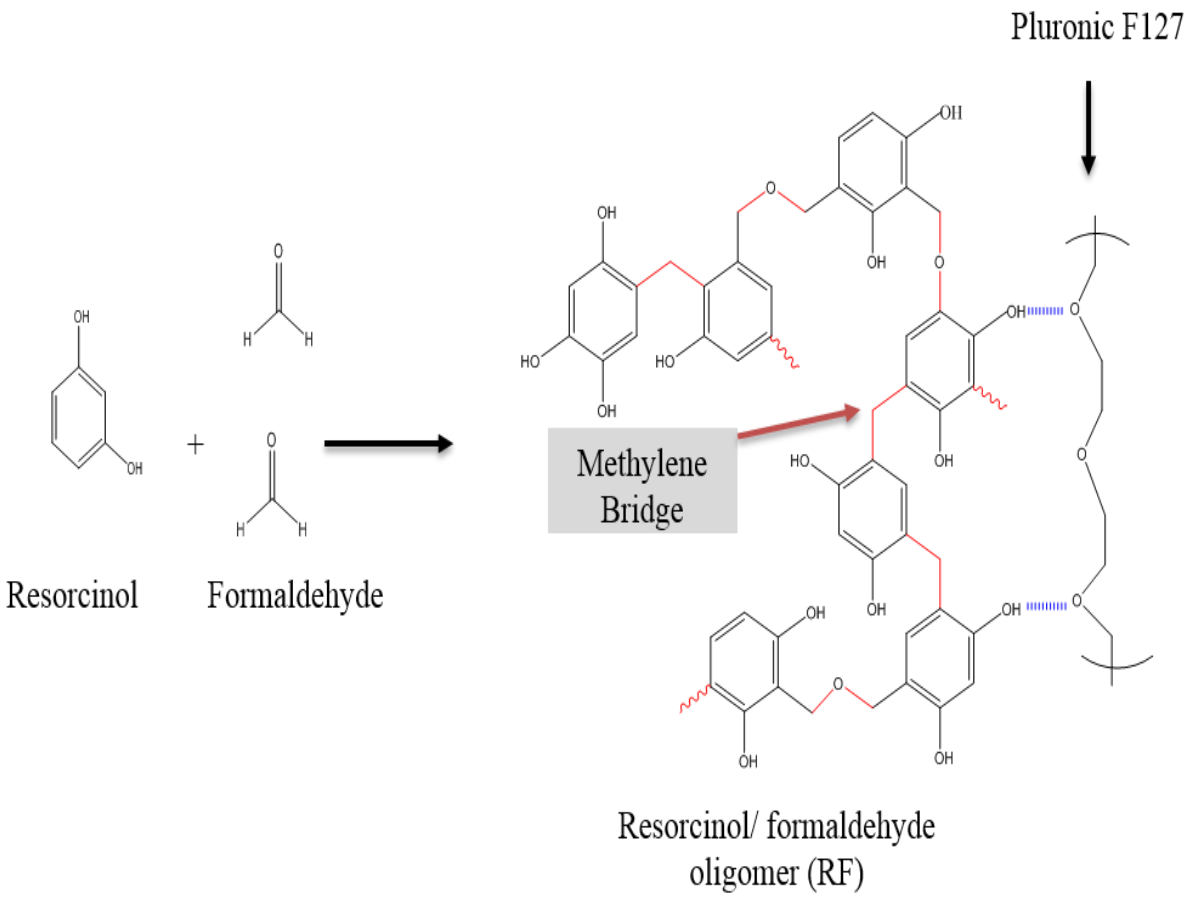

Figure 3.1. Schematic of the reaction of resorcinol with formaldehyde and interaction between the F127 and the hydroxyl group in the RF via hydrogen bonding.

The carbon monoliths obtained after carbonisation at 800 ºC for two hours are shown in Figure 3.2 (B). The polymer monoliths can be shaped in different forms depending on the shape of the moulds. It can be seen that the polymer monolith show shrinkage after carbonisation. It is evident from that the photographs that a large shrinkage occurred through the carbonisation process. The volume decreased by approximately 50% after carbonisation and the colour changed from orange to black, but the monolithic morphology was still maintained.

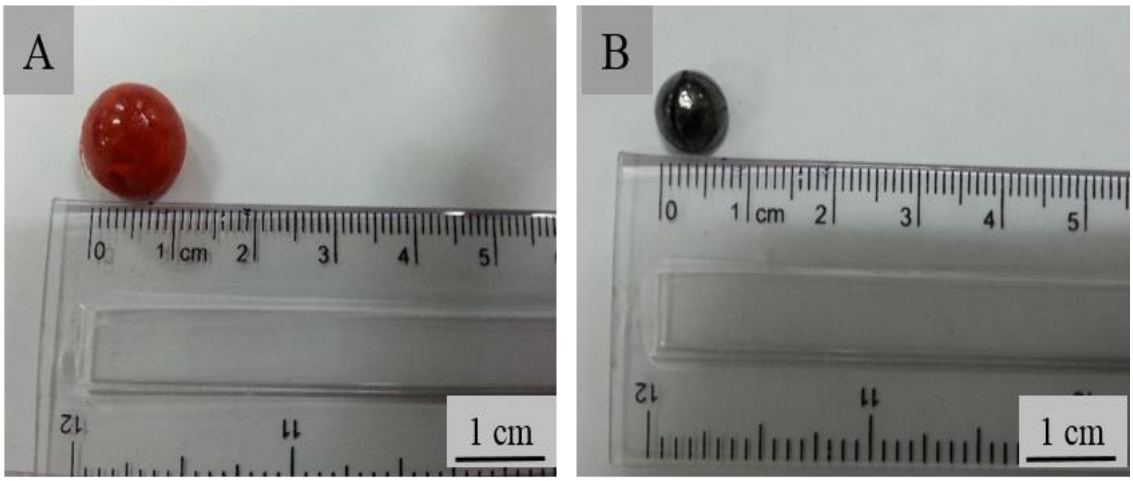

Figure 3.2. Photographic images of synthesised (A) polymer monolith (B) carbon monolith using resorcinol and formaldehyde as a carbon precursor.

3.2.2 SEM Analysis

Scanning electron microscopy (SEM) provided information about the structural morphologies of the different materials. The SEM images of polymer monolith and blank ordered mesoporous carbon monolith (OMC) are shown in Figure 3.3 A and B respectively. The SEM image of the polymer monolith showed a smooth surface and confirmed that this material non-porous (at the magnifications imaged), but the SEM of carbon material prepared by carbonisation of the same polymer monolith at 800 ºC shows pores with different sizes. These pores result from the decomposition of the soft template (triblock copolymer F127) and the carbonisation the polymer at a high temperature with the carbon precursor stayed as a wall of these pores.[33]

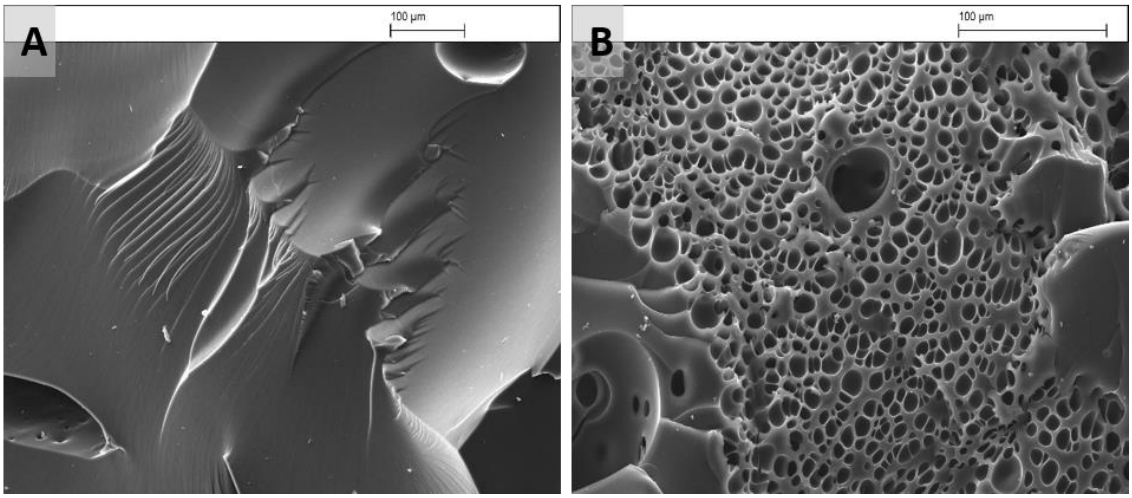

Figure 3.3. Scanning Electron Microscopy (SEM) images of (A) the polymer monolith (B) the ordered mesoporous carbon monolith OMC.

3.2.1.1. BET surface area analysis

The BET (Brunauer–Emmett–Teller) surface area and porosity analyser was used in the determination of the surface area and porosity of polymer monolith and carbon monolith using nitrogen sorption measurements.

Figures 3.4 shows the N_2 adsorption-desorption isotherms of the polymer monolith. The polymer monolith showed a Type II isotherm, which is a typical isotherm for a non-porous material.[34] The sorption isotherm of OMC shown in Figure 3.5 demonstrated a Type-IV isotherm, which is a characteristic exhibited by mesoporous materials.[35] The pore size distribution shown of the carbon monolith is in Figure 3.6. It has a narrow pore size distribution with average 7.6 nm and BET specific surface area of 635±6 m^2/g which is in the mesopore range. The increase in the amount of gas adsorbed at relative low pressures ($P/P_o < 0.1$) for the carbon monolith confirms the presence of the micropores in the framework.[36]

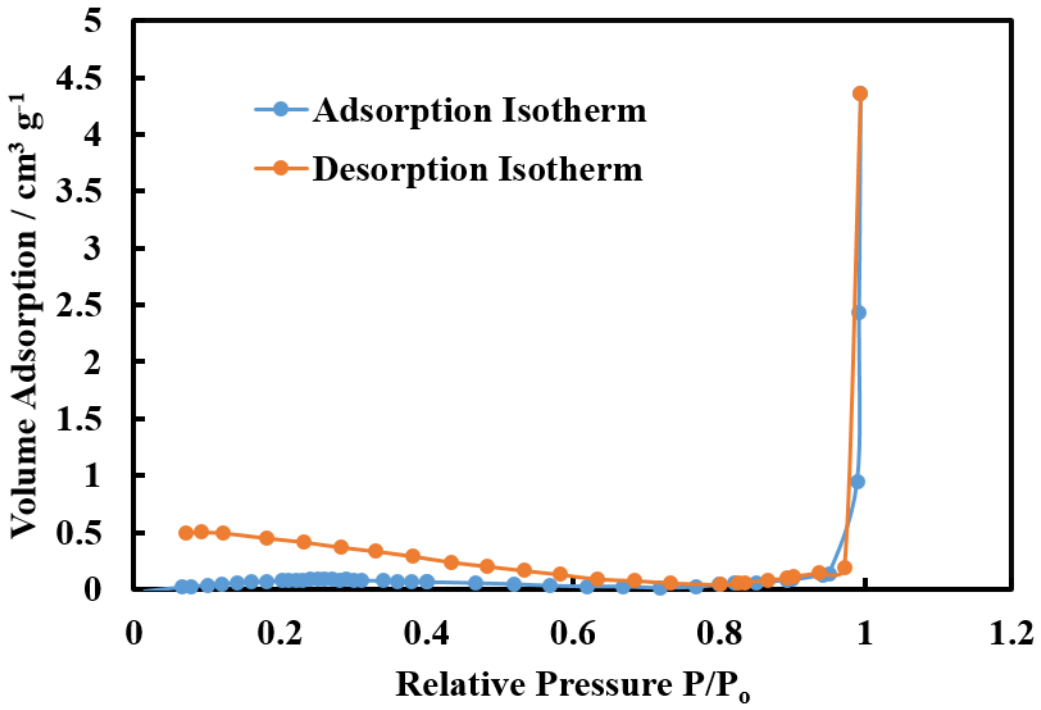

Figure 3.4. N_2 adsorption-desorption isotherm of the polymer monolith.

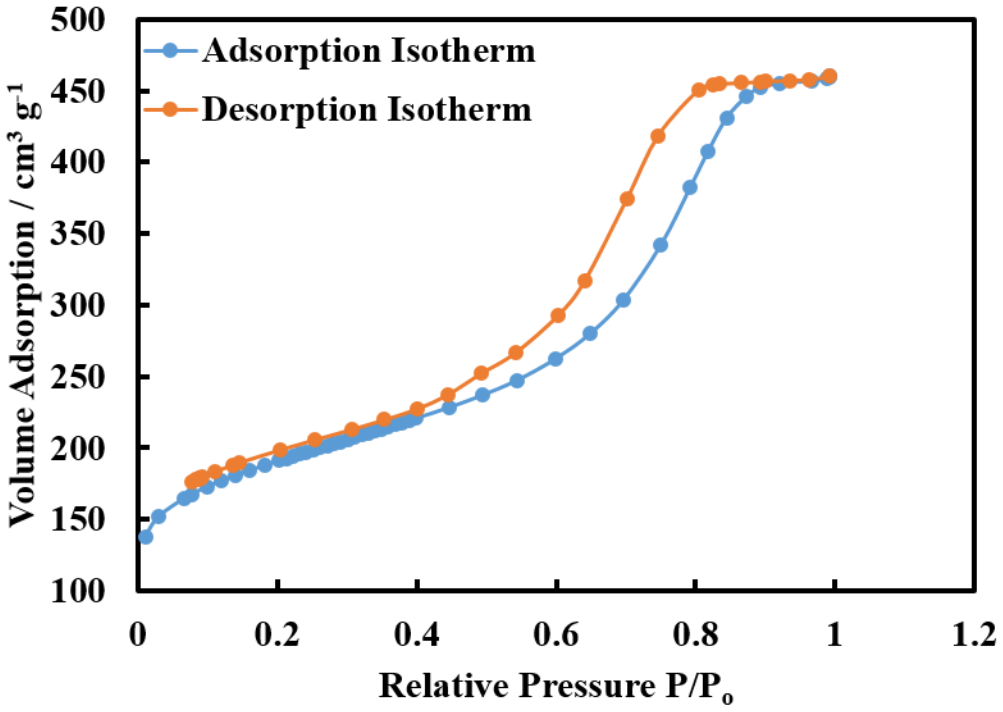

Figure 3.5. N_2 adsorption-desorption isotherm for carbon monolith.

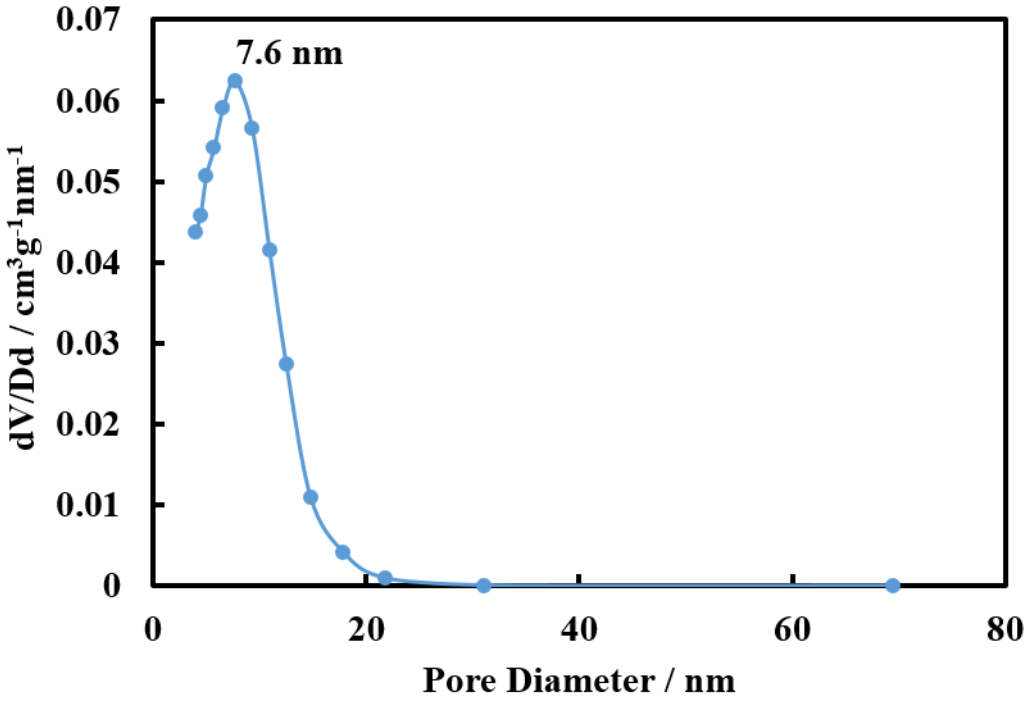

Figure 3.6: Pore size distribution for carbon monolith.

3.2.1.2. ATR-FTIR analysis

ATR-FTIR provided an further information into the chemical composition of the carbon materials. Figure 3.7 shows the ATR-FTIR spectra of the polymer monolith (red) and mesoporous carbon materials (blue). The spectra have various shapes, referring to an evident change in the network structure due to the carbonisation process. The main functional groups determined from the previous literature.[35, 36]

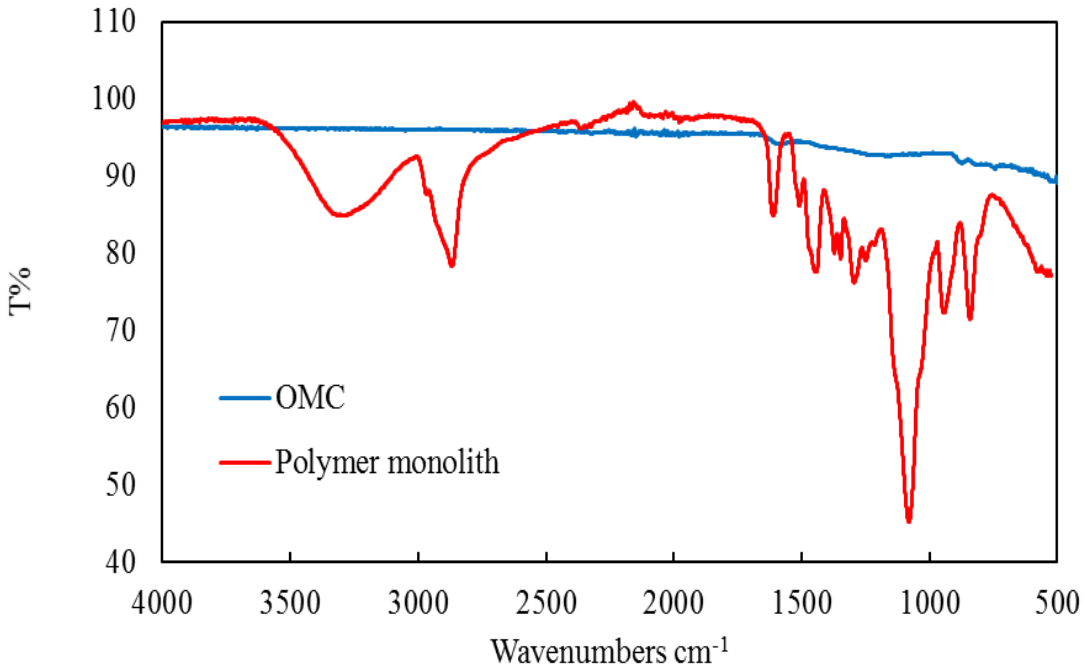

Figure 3.7. ATR-FTIR spectra of the polymer monolith (red) and the porous carbon materials (blue), showing the changes in the spectra due to the decomposition of the template during the carbonisation the polymer at 800 ºC.

A wide band at approximately 3600-3000 cm^{-1} is indicative of –OH stretching, due to a number of phenolic groups in the polymer. The peak at approximately 1600-1400 cm^{-1} is due to the C-C stretching vibration of the aromatic ring structure of phenolic resin produced by resorcinol and formaldehyde. There are two peaks at approximately 3000-2800 and 1200-950 cm^{-1} which could be appointed to the C-H and C-O stretching vibrations due to the triblock copolymer F127 and the aromatic C-H due to aromatic ring of phenolic resin. These peaks can be seen to be have disappeared after carbonisation. This will be due to decomposition of F127 at temperature above 400 ºC.

3.2.1.3. Powder X-Ray Diffraction (PXRD)

Powder X-Ray Diffraction (PXRD) affords information regarding the crystallinity of the carbon materials. Figure 3.8 shows the wide-angle XRD patterns of the carbon monolith. This clearly shows a peak at 24° (2θ), together with another broad peak at 44° (2θ) and a weak peak at 78° (2θ) which correspond to diffractions from the (002), (100) and (110) planes of graphite respectively. These peaks represent different phases of graphite and reflections of the graphitic pore walls of the framework. Therefore, the wide-angle XRD pattern shows a higher degree of graphitization of the carbon framework.[36, 37]

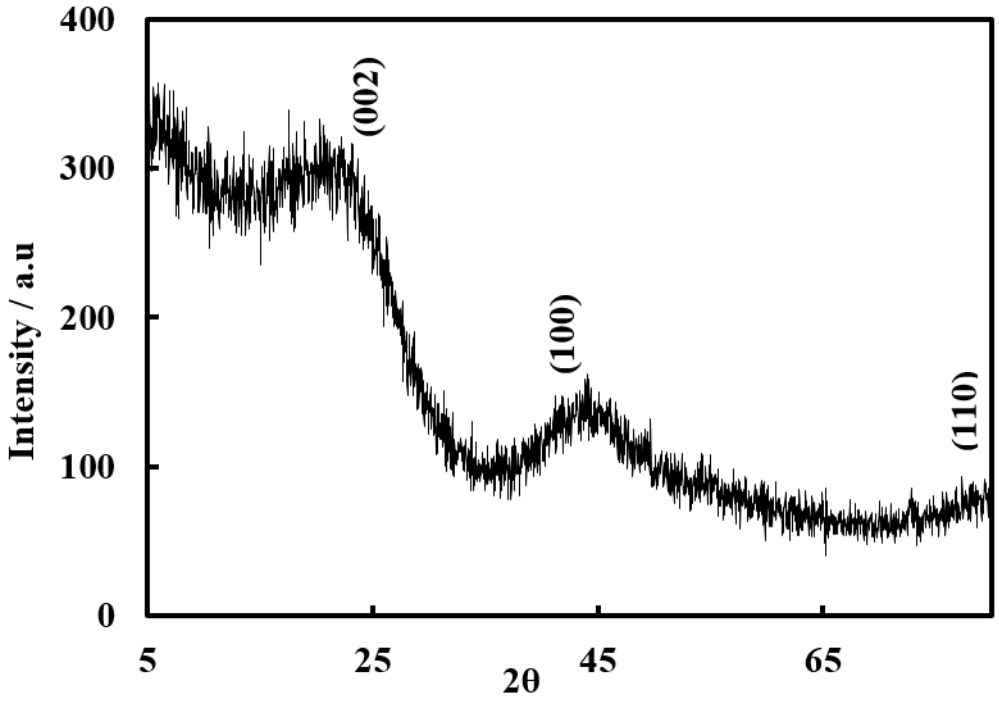

Figure 3.8. Wide-angle XRD patterns for the mesoporous carbon materials prepared by soft template method.

3.2.1.4. Energy dispersive X-ray spectrometry (EDX) analysis of the OMC

Surface EDX analysis was carried out on cross sections of the blank ordered mesoporous carbon materials as shown in Figure 3.9. EDX confirms the presence of high percentage of carbon element and a small percent of oxygen was also revealed in the mesoporous carbon sample, because of some surface oxidation.[38]

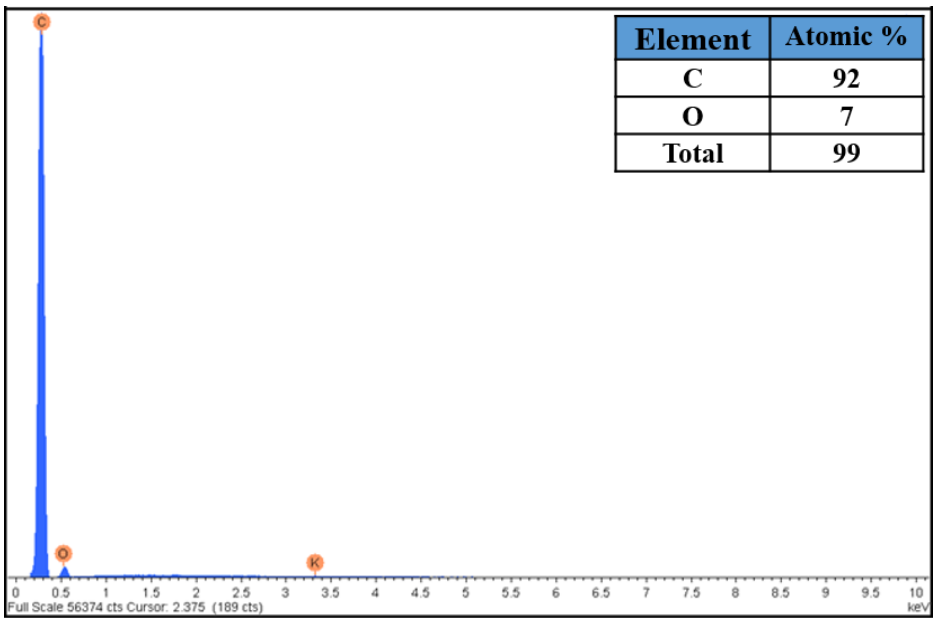

Figure 3.9. EDX spectra of the carbon monolith after carbonisation the polymer monolith at 800 ºC.

3.2.1.5. Thermogravimetric Analysis (TGA)

The TGA curves of the polymer monolith (red) and carbon monoliths (blue) under nitrogen flow are shown in Figure 3.10.

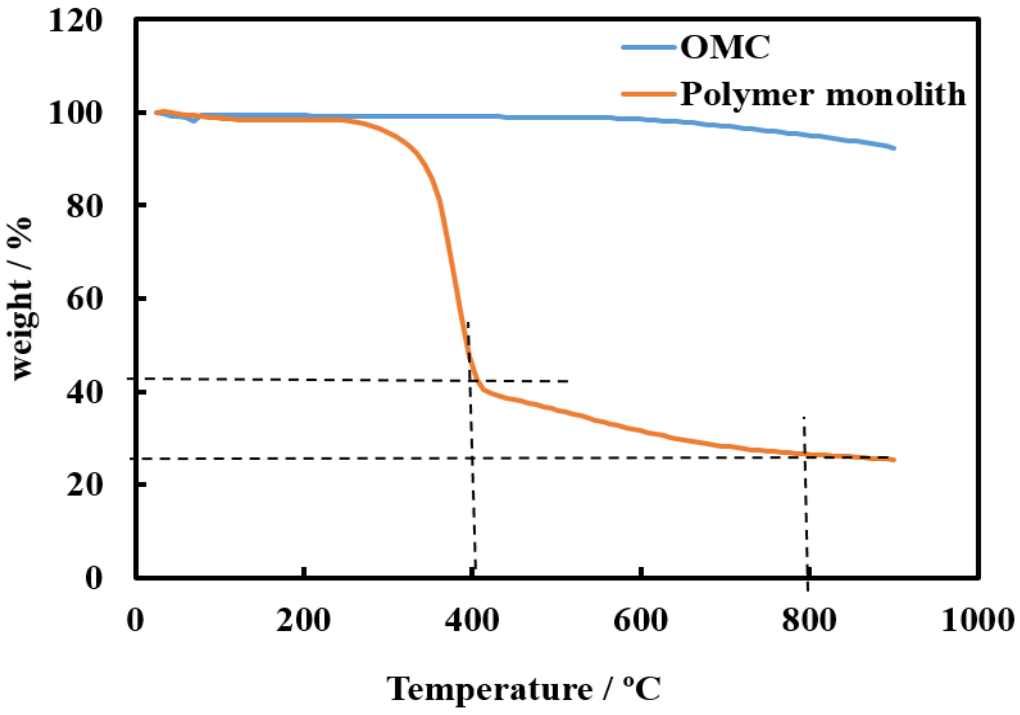

Figure 3.10. Thermal Gravimetric Analysis (TGA) of the polymer monolith (red) and the carbon monolith (blue).

The TGA curve of the polymer monolith containing phenolic resin and Pluronic F127 in the temperature range 300–400 ºC shows approximately 60% weight loss indicating that the soft template successfully decomposed during the carbonisation process. This is due to the decomposition of Pluronic F127 at this temperature range and the phenolic resin more thermally stable forming the mesopores walls in the carbon materials as reported in other literature.[39-41] Finally, approximately 24% of carbon residue was left at 800 ºC.

3.2.2. Magnetic ordered mesoporous carbon materials

The polymer monolith containing iron, cobalt, and nickel changed after carbonisation at the temperature of 800 ºC. The colour was transferred from very dark brown to black, and the size shrinks by around 35%. Figure 3.11 shows the photographic images of (A) Fe-polymer monolith (B) Fe –carbon monolith.

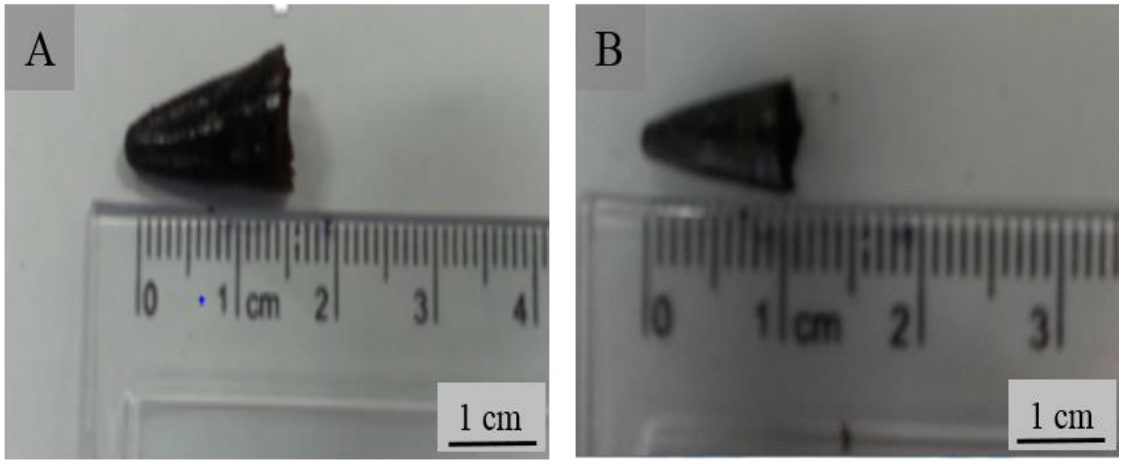

Figure 3.11. Photographic images of (A) Fe -polymer monolith (B) Fe-carbon monolith using resorcinol and formaldehyde as carbon precursor with the monolithic morphology was still maintained.

3.2.2.1. SEM Analysis

SEM analysis provided information about the structural morphologies of the different materials and SEM images of Fe, Co, Ni -polymer monolith and Fe/ OMC, Co/OMC and Ni/OMC are shown in Figure 3.12 A and B, 3.13 A and B, 3.14 A and B respectively.

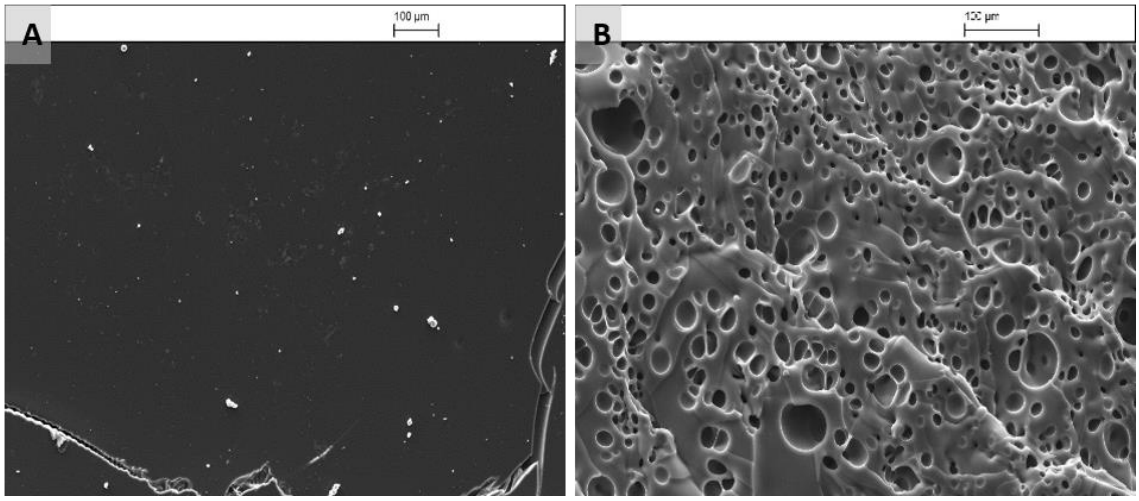

Figure 3.12. SEM images of (A) Fe-polymer monolith (B) Fe-ordered mesoporous carbon materials Fe/OMC.

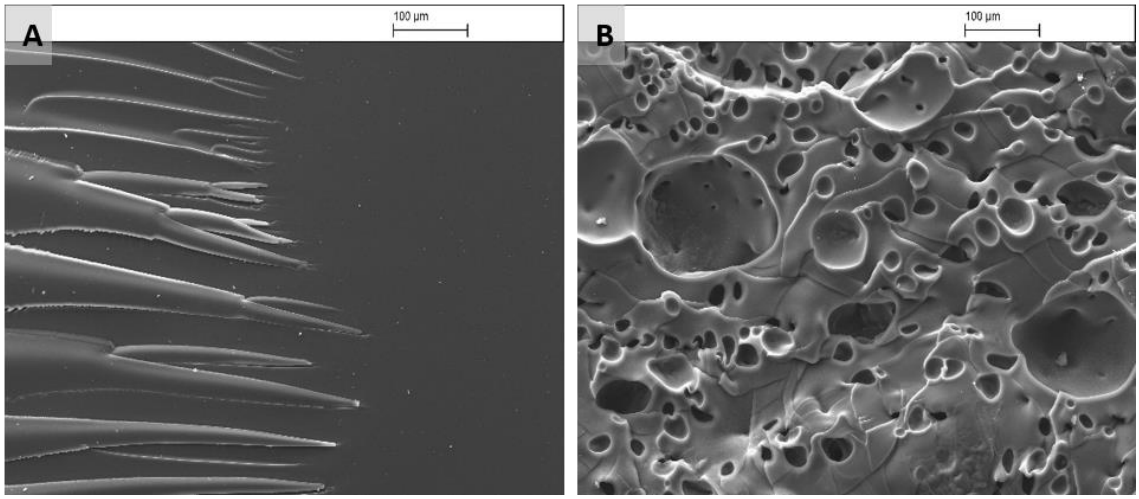

Figure 3.13. SEM images of (A) Co-polymer monolith (B) Co-ordered mesoporous carbon materials Co/OMC.

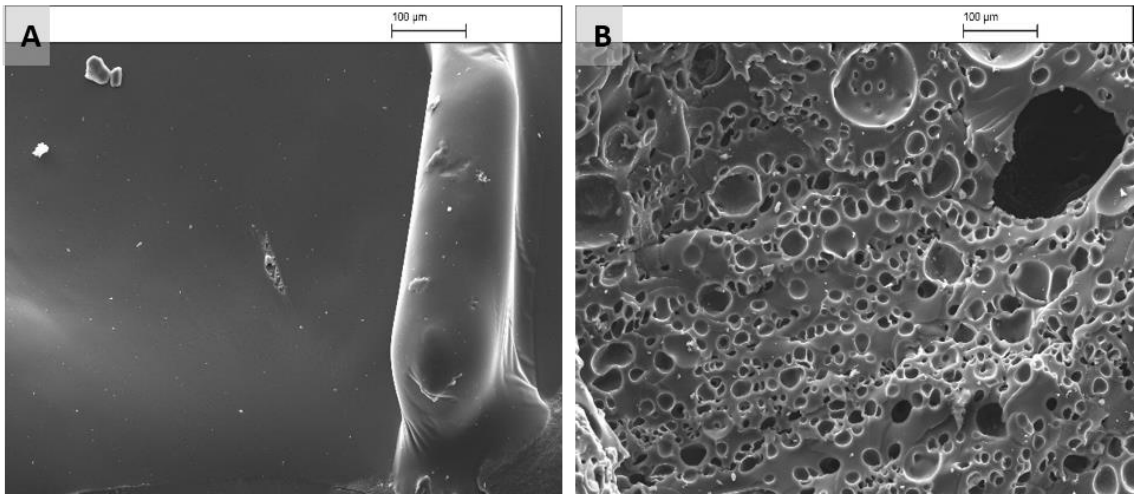

Figure 3.14. SEM images of (A) Ni-polymer monolith (B) Ni-ordered mesoporous carbon materials Ni/OMC.

Similar to the monoliths without metal loading SEM images of the polymer monoliths showed smooth surfaces and confirmed that the materials are non-porous, but the SEM of carbon material prepared by carbonisation of the same polymer monolith at 800 ºC shows porous materials with different pore size. These pores result from the decomposition of the soft template (triblock copolymer F127) through the carbonisation the polymer at a high temperature and the carbon precursor stayed as a wall of these pores.[33]

Figures 3.15, 3.16, and 3.17 show the higher magnification of Fe/OMC, Co/OMC and Ni/OMC respectively. Iron, cobalt and nickel nanoparticles can be observed on the surface and the walls of mesoporous carbon materials network.

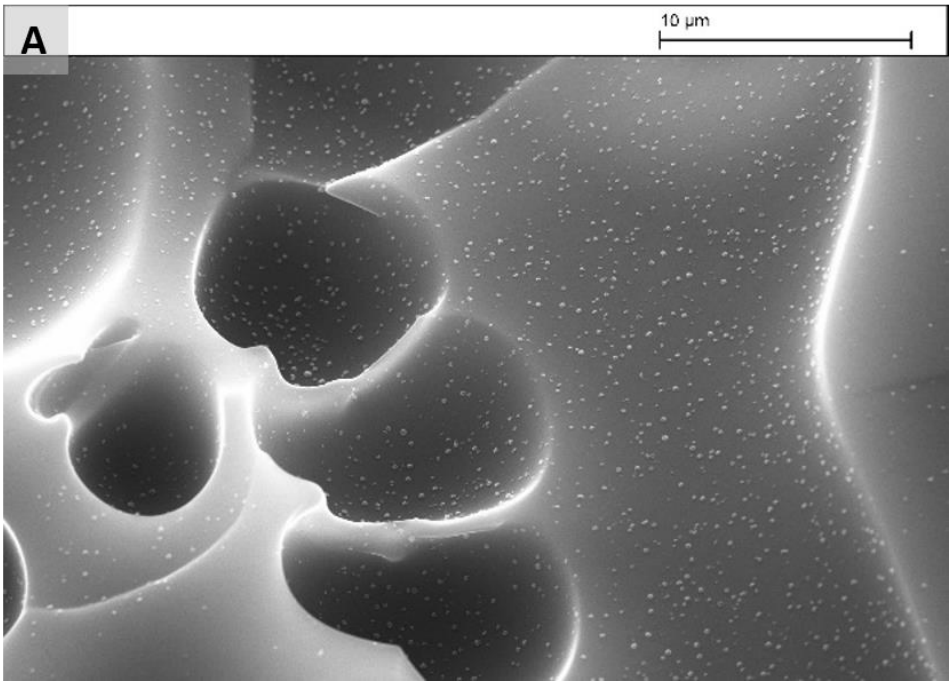

Figure 3.15. SEM images of Fe-ordered mesoporous carbon materials Fe/OMC

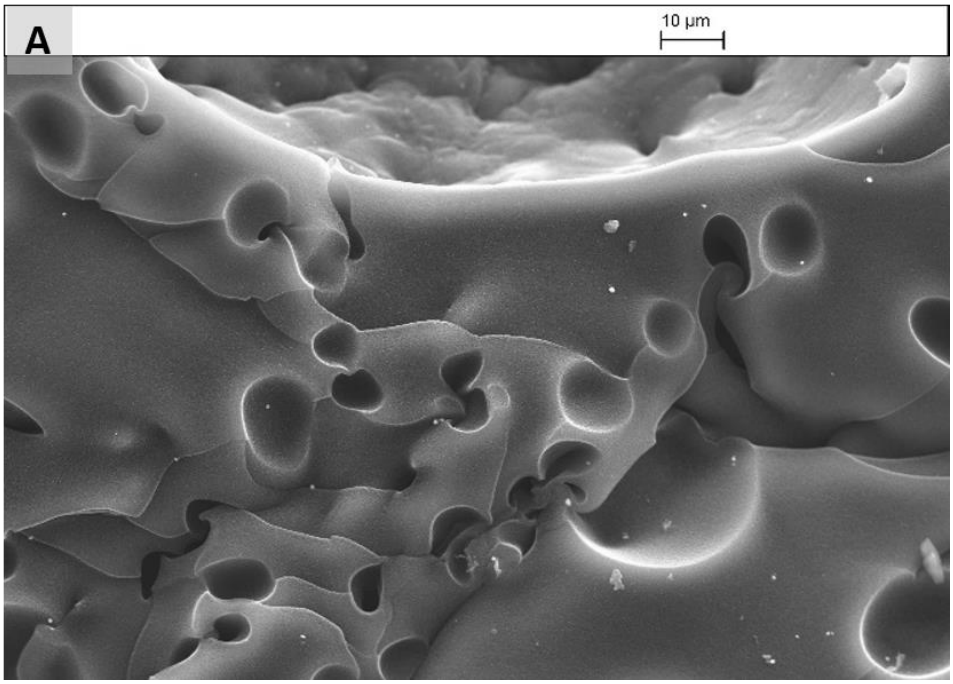

Figure 3.16. SEM images of Co-ordered mesoporous carbon materials Co/OMC

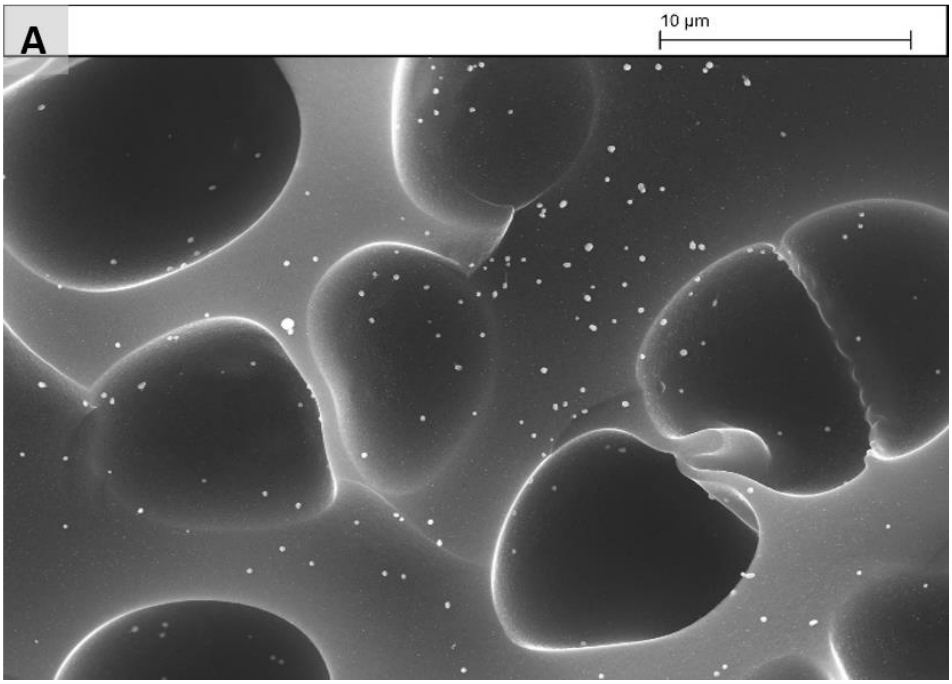

Figure 3.17. SEM images of Ni-ordered mesoporous carbon materials Ni/OMC

3.2.2.2. The energy dispersive X-ray spectrometry (EDX) analysis of the OMC

Energy dispersive X-ray (EDX) analysis was carried out on cross sections of the Fe/OMC, Co/OMC and Ni/OMC materials as shown in Figures 3.18, 3.19 and 3.20, respectively.

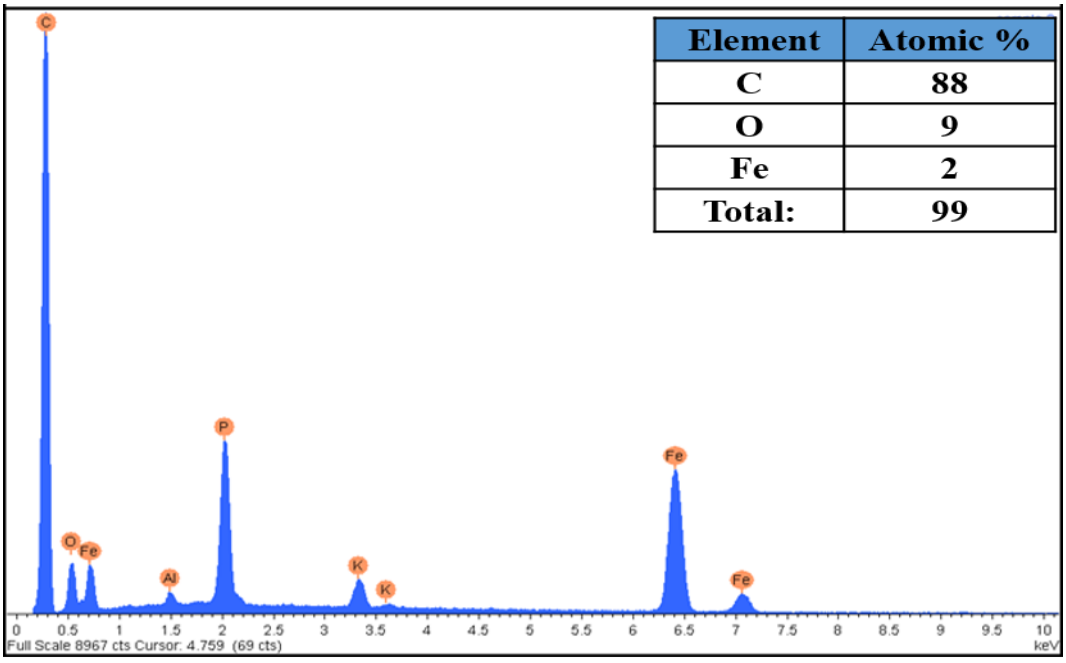

Element	Atomic %
C	88
O	9
Fe	2
Total:	99

Energy / KeV

Figure 3.18. EDX spectra of the Fe/OMC after carbonisation the Fe-polymer monolith at 800 ºC.

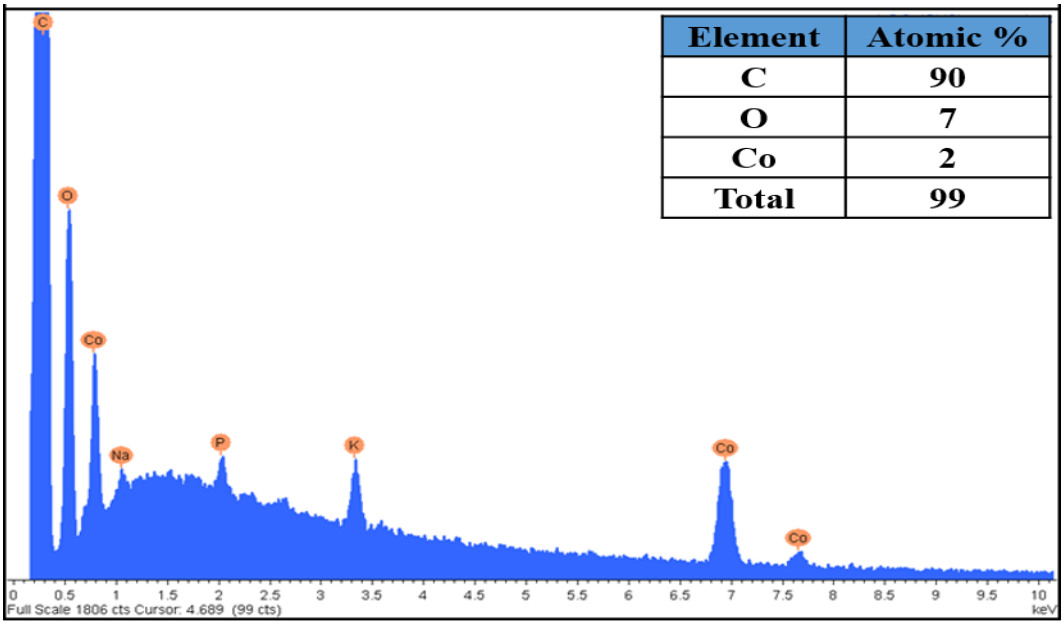

Element	Atomic %
C	90
O	7
Co	2
Total	99

Energy / KeV

Figure 3.19. EDX spectra of the Co/OMC after carbonisation the Co-polymer monolith at 800 ºC.

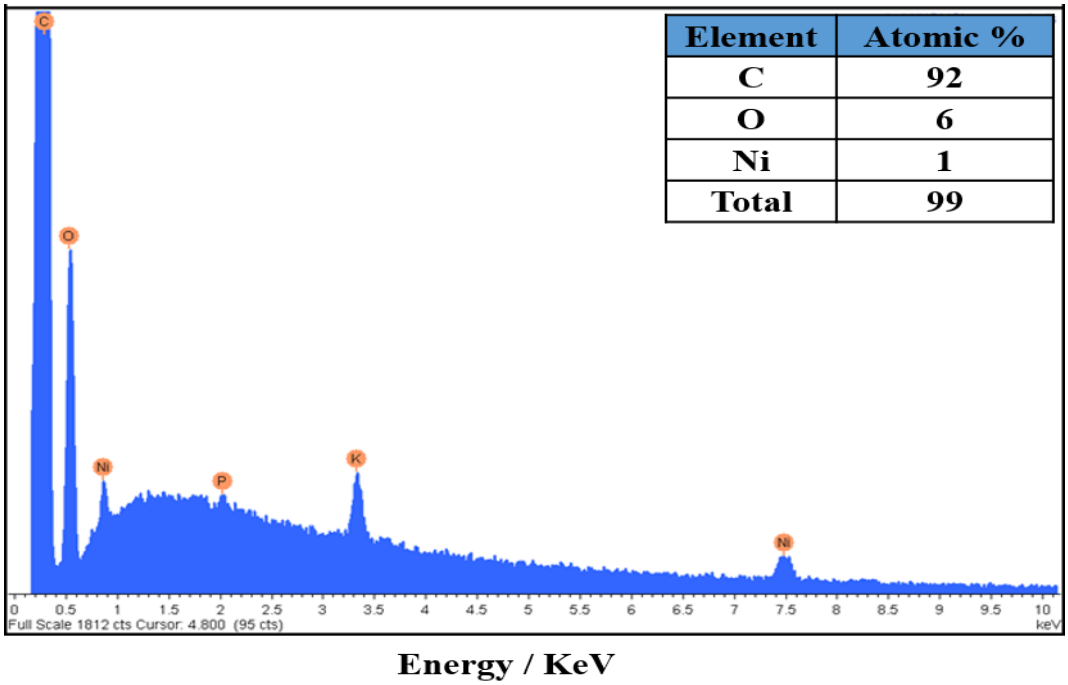

Element	Atomic %
C	92
O	6
Ni	1
Total	99

Figure 3.20. EDX spectra of the Ni/OMC after carbonisation the Ni-polymer monolith at 800 ºC.

EDX confirms the existence of high percentage of carbon element and a small percent of oxygen was also revealed in the carbon monolith sample, because of some surface oxidation.[38] In addition to that EDX analysis provided metals amount such as iron, cobalt and nickel in the mesoporous carbon materials network have prepared by soft template method. The EDX results complemented the SEM results above and clearly showed that metallic nanoparticles within the mesoporous carbon materials network.

3.2.2.3 BET surface area analysis

The BET surface area and porosity analyser were used to determine of the surface area and porosity of both the polymer monolith and carbon monolith using nitrogen sorption measurements. The nitrogen sorption measurements were performed on the polymer and carbon monoliths to provide further confirmation of changes in the material after the carbonisation process. The textural properties of these materials studied are summarised in Table 3.1. The results show high increased in the surface area for carbon monoliths as compared with the polymer monoliths. This is due to the removing of the soft template and generation pores. The pore size distribution and the BET surface area were decreased after loading metals on the carbon network structure.

Table 3.1. Textural characterization of the various carbon monoliths synthesized at 800 ºC.

Materials	BET Surface Area / m^2 g^{-1}	Pore Size / nm	Pore Volume / cm^3g^{-1}
Polymer monolith	0.48±0.08	-	-
OMC	635±6	7.66	0.67
Fe-polymer monolith	3.21±0.09	-	-
Fe-OMC	537±5	4.30	0.32
Co-polymer monolith	3.6±0.1	-	-
Co-OMC	434±7	4.28	0.22
Ni-polymer monolith	3.12±0.04	-	-
Ni-OMC	528±7	4.31	0.23

N_2 adsorption-desorption isotherms of the Fe, Co and Ni -polymer monolith showed a Type II isotherm, which is a typical isotherm for a non-porous material [34] as shown in Figure 3.21(A), 3.21(B) and 3.21(C). The polymer monolith surface seemed to be smoother on the surface as shown early in the SEM images (Figures 3.12, 3.13 and 3.14) that confirmed the low surface area of the solid polymer prior template removal by the carbonisation process.

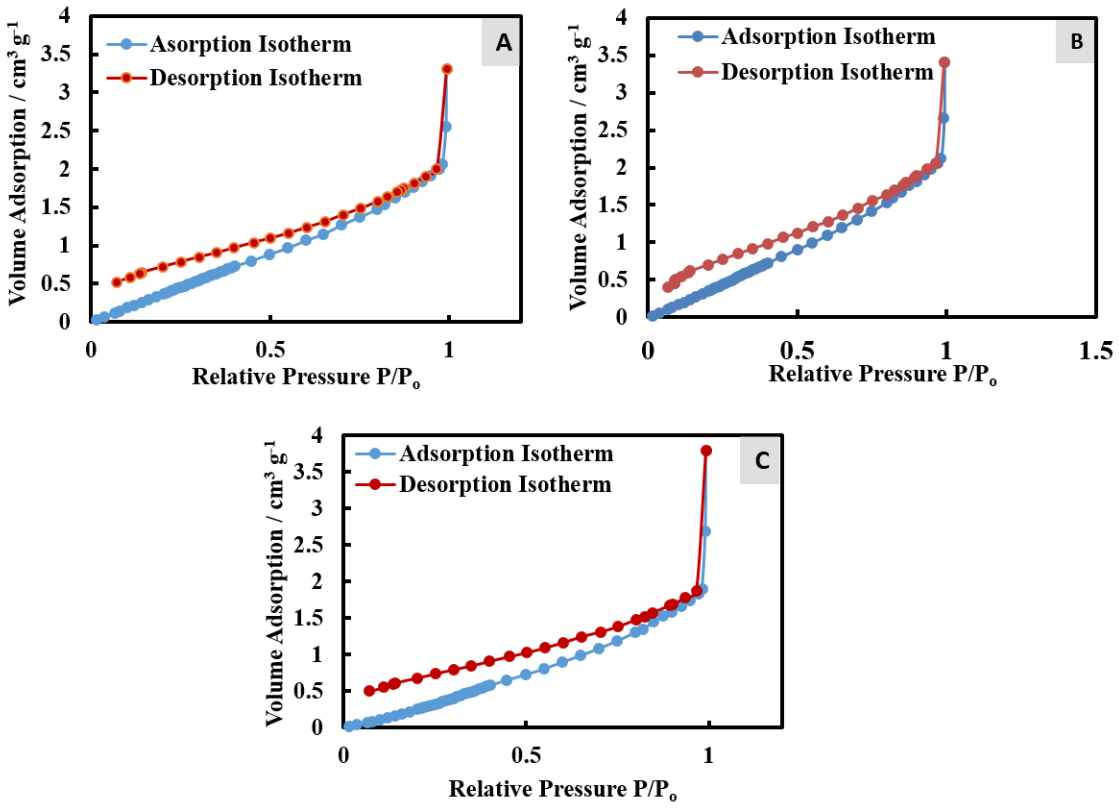

Figure 3.21. N_2 adsorption-desorption isotherms of (A) Fe-polymer monolith (B) Co-polymer monolith (C) Ni-polymer monolith.

The N_2 adsorption-desorption isotherms of Fe/OMC, Co/OMC and Ni/OMC are shown in Figure 3.22(A), 3.22(B) and 3.22(C) respectively. These isotherms demonstrated a type-IV isotherm, which is a characteristic exhibited by mesoporous materials.[35]

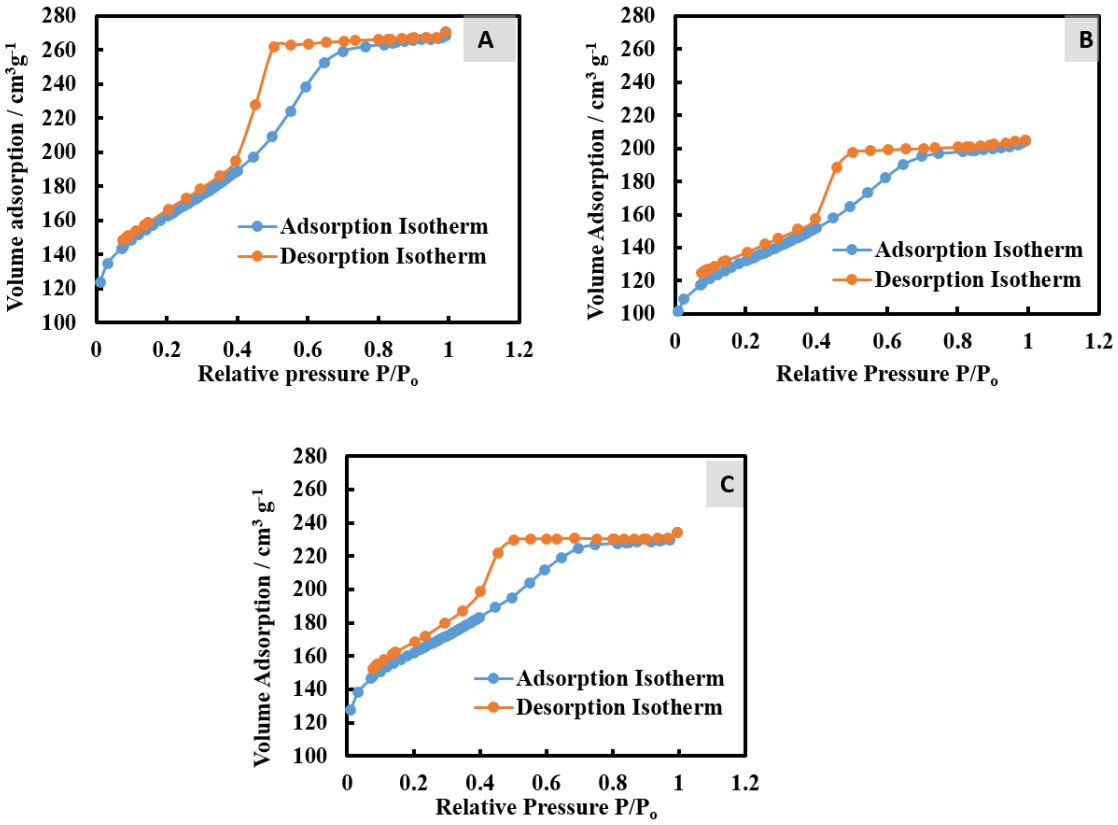

Figure 3.22. N_2 adsorption-desorption isotherm for (A) Fe-carbon monolith (B) Co-carbon monolith (C) Ni-carbon monolith.

Desorption isotherms for all the above materials have appeared more obvious that indicative of delayed capillary evaporation and the presence of constrictions in the mesoporous structure. At this point, it should be mentioned that the graphitic carbon generated during the carbonisation step is formed around the metal nanoparticles that act as a catalyst. The removal of these metallic nanoparticles gives rise to hollow graphitic carbon nanostructures such as capsules with entrances and other carbon structures with large voids. The constrictions associated to the entrances of these nanostructures are the cause of the observed delayed desorption.[42, 43]

The pore size distribution for Fe/OMC, Co/OMC and Ni/OMC shown in Figure 3.23 (A), 3.23 (B) and 3.23 (C) respectively, it has a narrow pore size distribution in the mesopore range center at 4.30 nm, 4.28 nm and 4.31 nm, respectively, also was agreement with the previous studies.[44, 45]

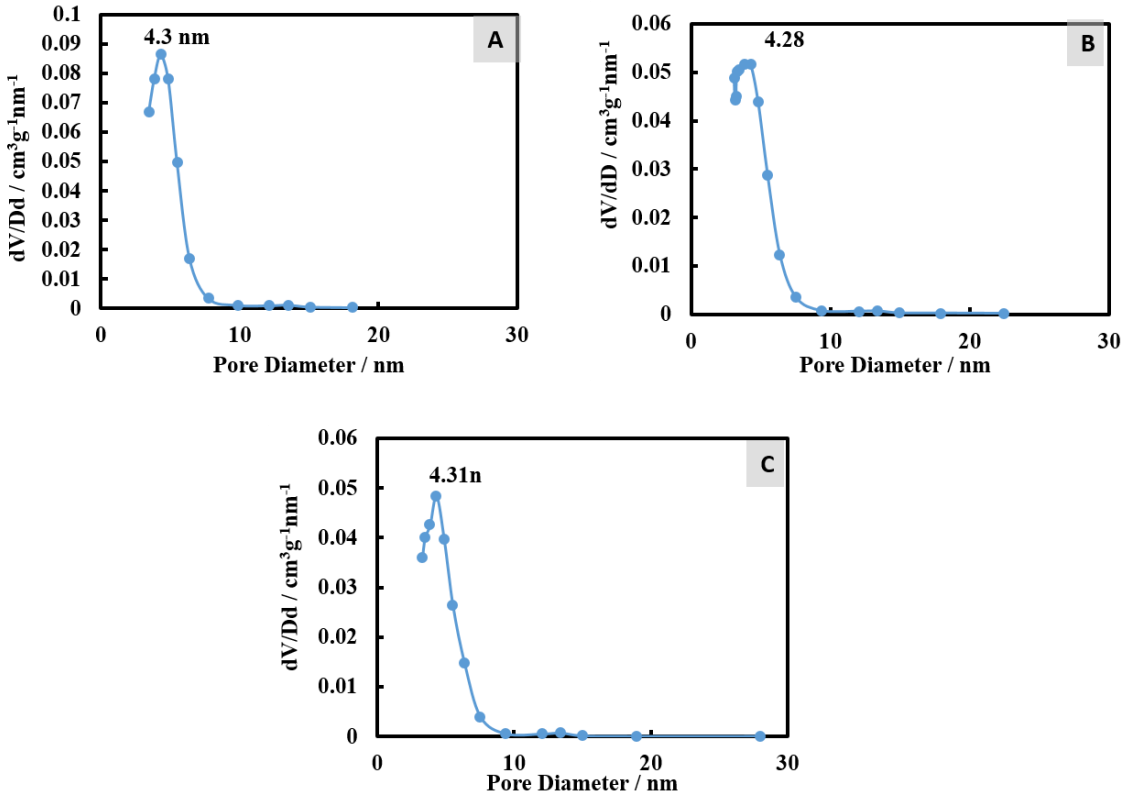

Figure 3.23. Pore size distribution which is in the mesopore range for (A) Fe/carbon monolith showing a narrow pore size of 4.3 nm; (B) Co-carbon monolith showing a narrow pore size of 4.2 nm; Ni-carbon monolith showing a narrow pore size of 4.3 nm.

Both the BET surface areas and the pore size distribution can be seen to decrease with incorporation of the magnetic metal on the mesoporous carbon material. The reduction in the surface area might be due to decrease the total amount of nitrogen gas adsorption on the composite sample as well as the effect of loading metals could blocking the pores, which led to reduce the pore size.

3.2.2.4 ATR-FTIR analysis

ATR-FTIR provided an additional information into the chemical composition of the carbon materials. Figures 3.24 (A), (B) and (C) show the ATR-FTIR spectra of the polymer monolith (blue) and mesoporous carbon materials (red) for Fe-OMC, Co-OMC and Ni-OMC respectively. In all these figures the red line represents the polymer, and the blue line represents the materials after carbonisation.The spectra have various shapes, referring an evident change in the network structure due to the carbonisation process. The main functional groups are summarised in Table 3.2 and determined to depend on the previous literature.[35, 36]

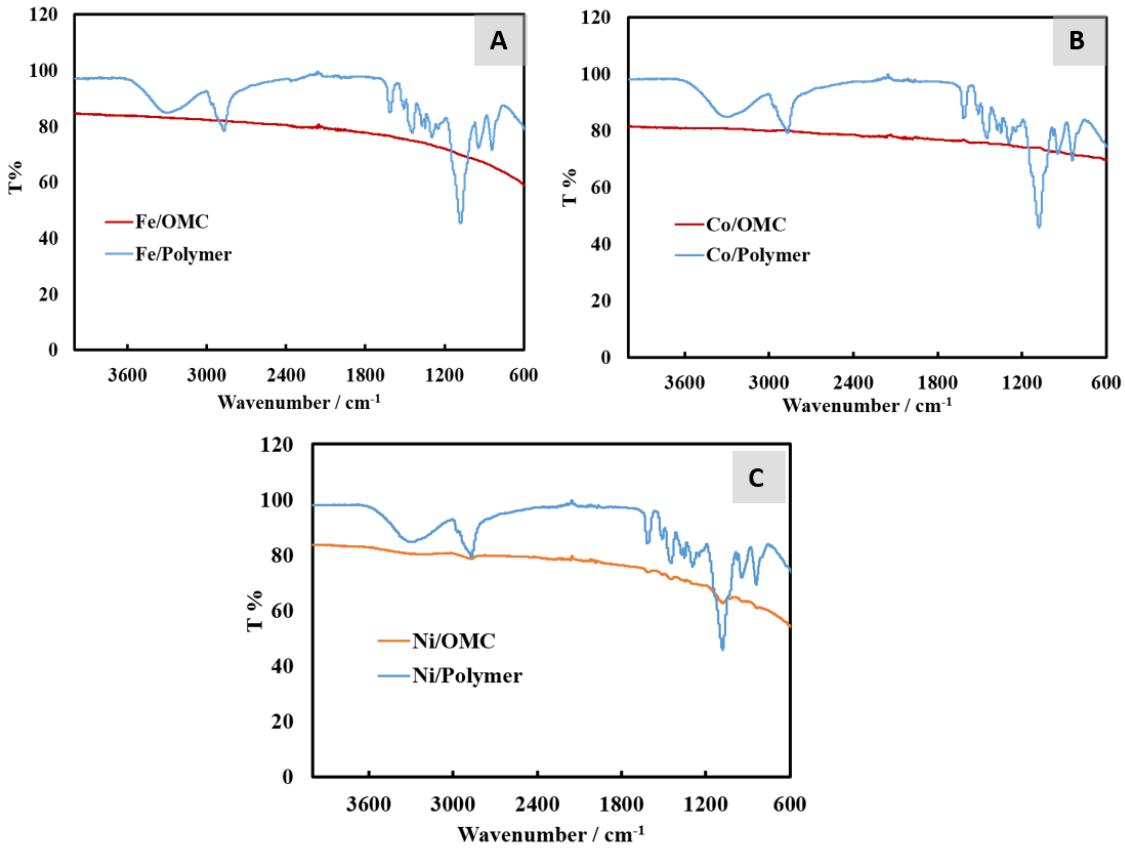

Figure 3.24. ATR-FTIR spectra of (A) Fe polymer and Fe-containing porous carbon materials; (B), Co-polymer and Co-containing porous carbon material; and (C) Ni polymer and Ni-containing porous carbon materials, the ATR-FTIR spectra of the polymer monolith (blue) and mesoporous carbon materials (red) , showing the changes in the spectra due to the decomposition of the template during the carbonisation the polymer at 800 ºC.

Wavenumber range / cm^{-1}	Functional group	Description
3600-3000	O-H stretching	Due to the presence of a large number of phenolic groups in the polymer monolith
3000-2800	C-H stretching	Due to the stretching vibrations of C-H bond in the triblock copolymer F127
1600-1400	C-C stretching	Due to the stretching vibration of tri-substituted aromatic ring structure of phenolic resin framework of the resorcinol-formaldehyde
1200-950	C-O stretching	Due to the stretching vibrations of C-O bond in the triblock copolymer F127
< 950	C-H bending	Due to aromatic C–H bending vibrations

A wide band existence at nearly 3600-3000 cm^{-1} is demonstrating of –OH stretching, due to a number of phenolic group in the polymer. The peak at approximately 1600-1400 cm^{-1} is because of the C-C stretching vibration of the aromatic ring structure of phenolic resin produced by resorcinol and formaldehyde. There are two peaks at nearly 3000-2800 and 1200-950 cm^{-1} which could be appointed to the C-H and C-O stretching vibrations due to the triblock copolymer F127. These peaks disappeared after carbonisation that means decomposition the triblock copolymer F127 due to increasing the temperature. The last peaks at around 950 cm^{-1} and below are because of aromatic C-H bending vibrations.

3.2.2.5 Powder X-Ray Diffraction (PXRD)

The XRD patterns in the wide-angle region (5º–80º) corresponding to the Fe/OMC composite prepared at 800ºC are shown in Figure 3.25.

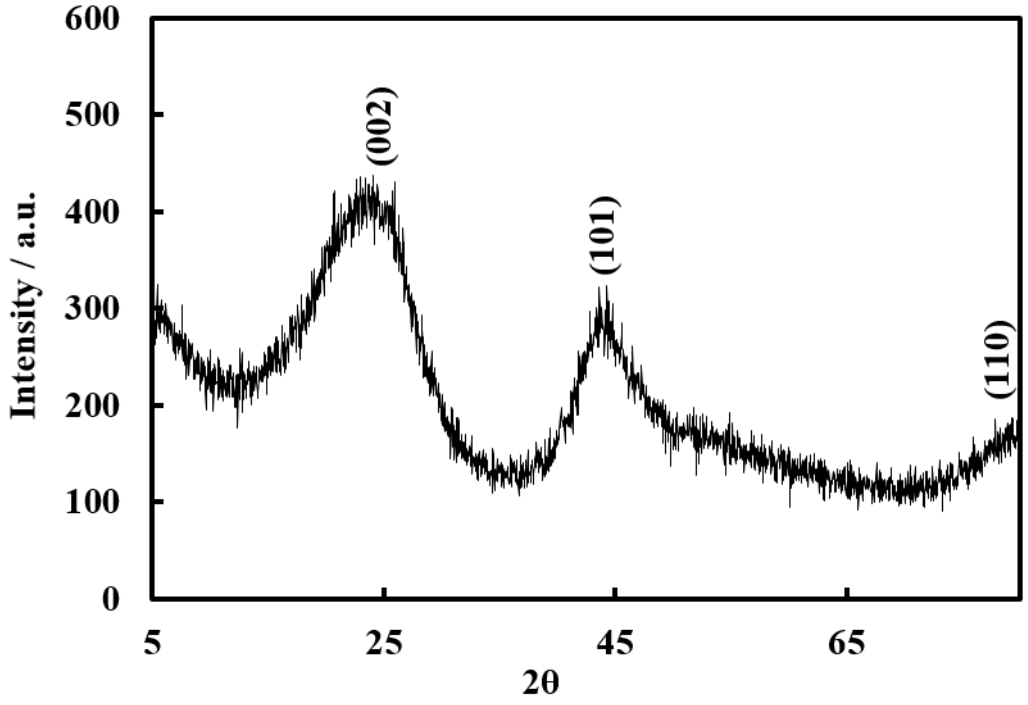

Figure 3.25. wide-angle XRD patterns of the Fe/OMC composite materials carbonisation at 800 ºC.

This Figure demonstrates a well resolved diffraction peak at 2θ =26.0° assigned to the (002) diffraction peak of the graphite structure In addition, a sharp peak at 2θ = 44.6° could be indexed to the (101) diffraction of body-centered cubic α-Fe.[46, 47] Furthermore, a peak at 2θ = 78° can be observed in the resulting Fe/OMC composites, which can be indexed to the (110) diffraction peak for typical graphite-like carbon.[43]The reduction of Fe^{3+} during the carbonisation treatment at high temperature under inert gas atmosphere could be the reason for the formation of Fe nanoparticles .[48] Metallic iron is not detected at 600 °C, however, iron, graphitic carbon are seen at 700 and 850 ºC. The results are indicate that higher temperature is in favor of the aggregation and growth of the metal nanoparticles. The results indicate that the prepared materials are graphitized during carbonisation at 800 ºC. [49]

XRD patterns for Co/OMC in the wide angle region (5–80°) shows broad diffraction peaks at 2θ=24° which can be assigned to the (002) diffractions and indicate carbon materials in graphite phase (see Figure 3.26). This Figure also shows three peaks at 2θ = 44.5°, 51.3° and 76.1° which can be assigned to the (111), (200) and (220) diffractions of the graphitic framework and assignable to Co are observed, which implies Co^{2+} was completely reduced to Co^0 with the face-centered cubic structure during the carbonization process at 800 ºC.

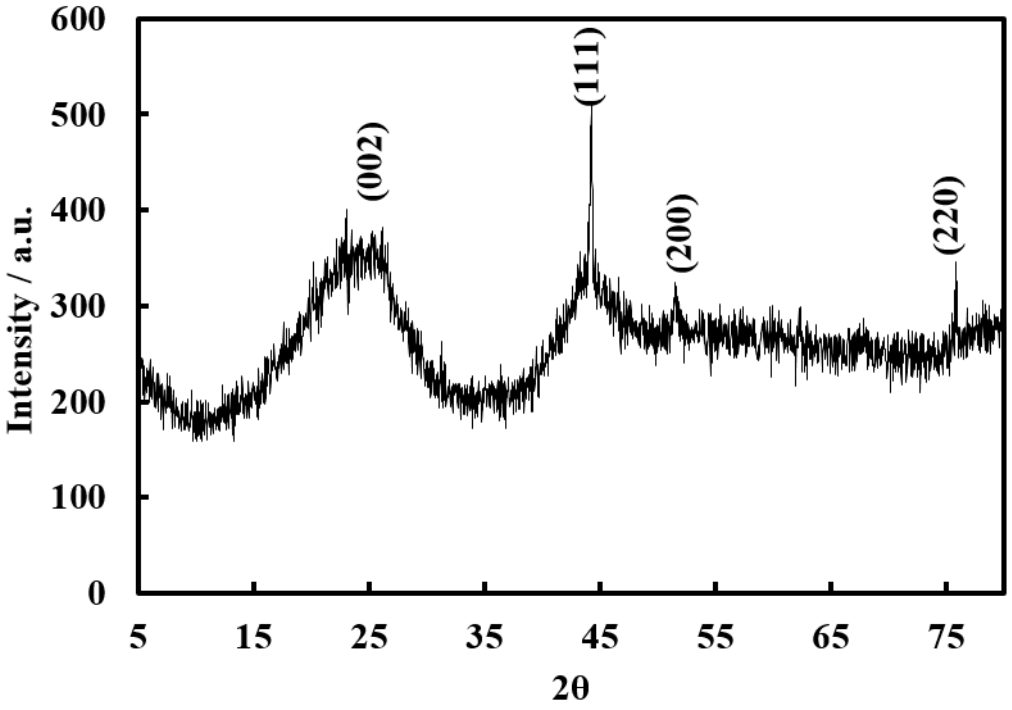

Figure 3.26. Wide-angle XRD patterns of the Co/OMC composite materials carbonisation at 800 ºC.

Wide-angle XRD patterns of the Ni/OMC composite materials after carbonisation at 800 ºC shows a broad peak at 2θ=26º, which can indicate to the (002) diffraction peak for graphite phase (see Figure 3.27). In addition, three sharp peaks at around 2θ= 43º, 54º and 78º, which can be assigned to the (111), (200), and (220) reflections of metallic nickel with the face-centred cubic structure.

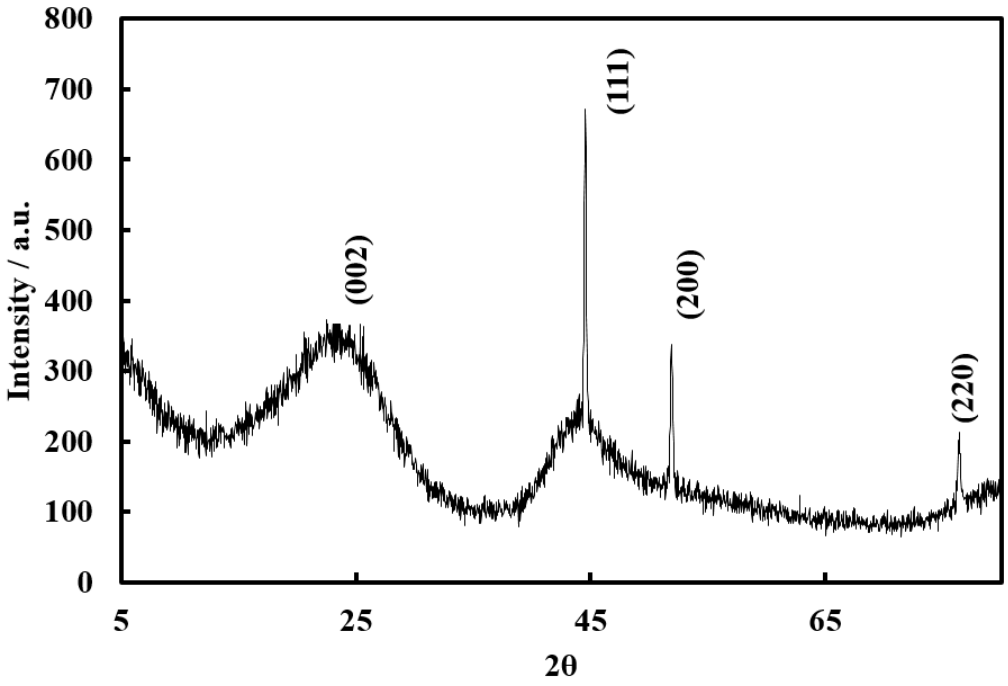

Figure 3.27. Wide-angle XRD patterns of the Ni/OMC composite materials carbonisation at 800 ºC.

The results investigate that the Ni^{2+} was totally reduced to Ni^{0} during the carbonisation process at 800 ºC.[50] The XRD patterns confirmed that the metal species were incorporated into highly dispersed nanoparticles in the OMC network structure.

3.2.2.6 Thermogravimetric Analysis (TGA)

The TGA curves of the Fe, Co, Ni -polymer monolith (red) and Fe/OMC, Co/OMC, and Ni/OMC (blue) under nitrogen flow are shown in Figures 3.28 (A), (B) and (C) respectively. The TGA curve of the polymer monolith containing phenolic resin, Pluronic F127 and metal sources for all these materials show major weight loss in a range between 60 % to 65% in the temperature centered at 400 ºC and was approximately similar to the blank OMC.

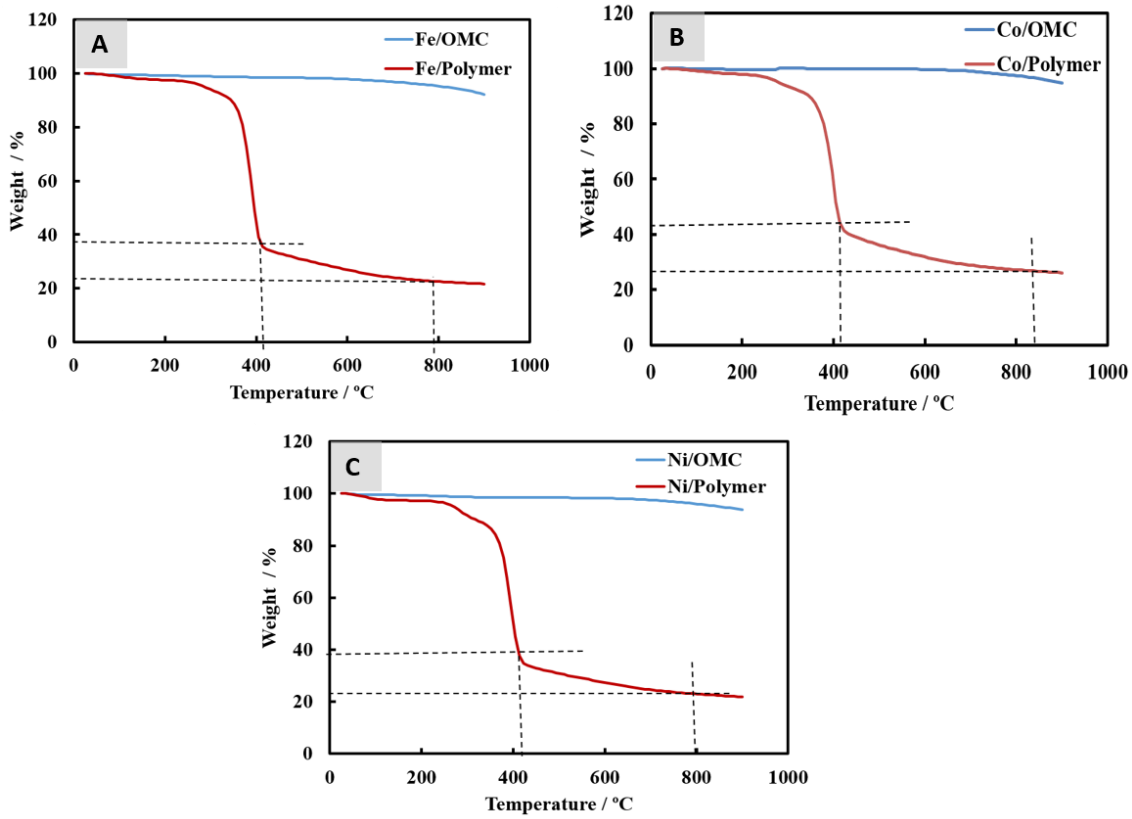

Figure 3.28. Thermal Gravimetric Analysis (TGA) graph recorded in N_2 atmosphere of (A) Fe-polymer monolith (red) and Fe/OMC (blue); (B) Co-polymer monolith (red) and Co/OMC (blue); (C) Ni-polymer monolith (red) and Ni/OMC carbon monolith (blue).

These results indicate that the major weight loss step is found in the temperature range of 350 - 400 ºC, which is due to the soft template (Pluronic F127) successfully decomposed at 400 ºC and forming mesopores which are happen in this temperature.[40] The carbonisation of RF resins starts above 400 °C because of RF more thermally stable forming the carbon materials with mesopores as reported in other literature.[39-41] Therefore, the carbonisation processes of mesoporous carbon materials synthesis via soft template method divided into two steps, first one at 400 °C for 6 h to remove the template, after that carbonisation the RF and reduction the metal salts to the nanoparticles phase at 800 °C for 6 h in a nitrogen flow. RF resins can convert to carbon with a high yield at high temperature in an inert gas. Finally, approximately carbon residue in the range between 25% to 30% was left at 800 ºC, and these results were agreement with the other studies.[41, 45] Thermal gravimetric analysis (TGA) of OMC and metallic OMC recorded under air (see Figure 3.29). The results show the combustion temperature of carbons shift to higher temperatures compared with blank OMC by 98, 168 and 98 ºC for the samples Fe/OMC, Co/OMC and Ni/OMC, respectively.

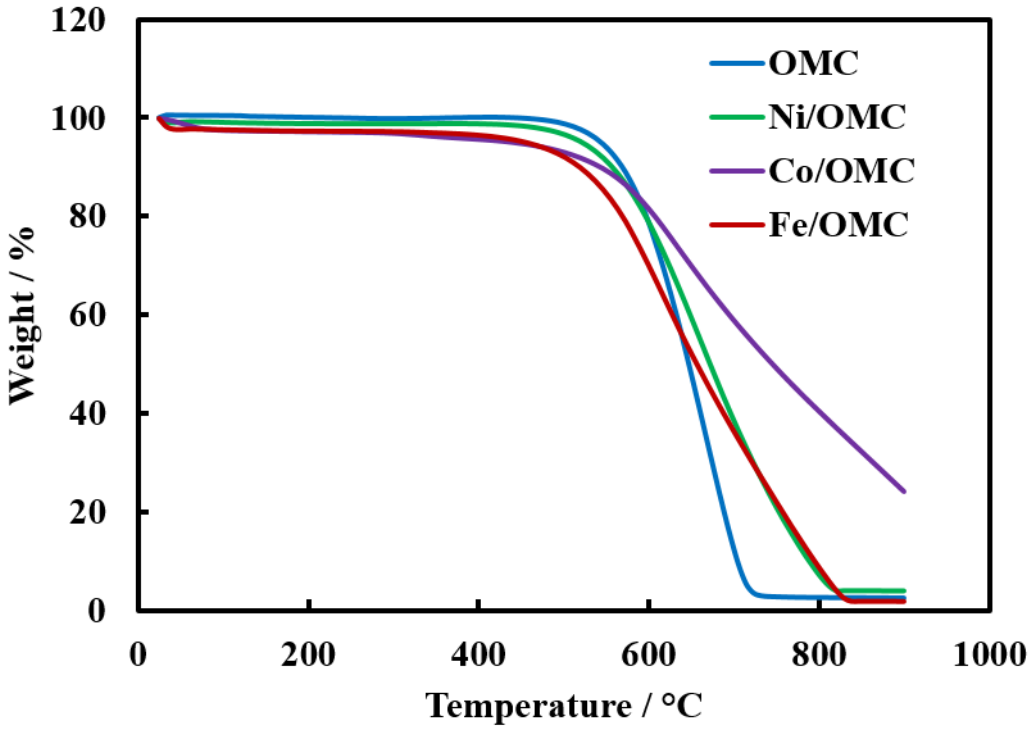

Figure 3.29. Thermal Gravimetric Analysis (TGA) graph recorded in air for OMC, Fe/OMC, Co/OMC and Ni/OMC.

It is clear that, as the present of metal content, the shifting the combustion temperature to the higher degree. This may be due to present the metals which may prevent diffuse the air to burn the carbon. The results indicate that metallic nanoparticles located in the Carbon Framework play as an oxidation-resistance agent, block the carbon frameworks from break down, which is agreement with the mesoporous titanium carbide carbon composites.[51] The TGA results demonstrated in Figure 3.29 confirmed the EDX result above mentioned and obviously exhibited that more than 90 % of these materials was carbon, wherein Fe, Co and Ni content calculated via EDX analysis.

3.2.2.7 Magnetic Properties of Nanocomposite Particles

The magnetic properties of blank OMC, Fe/OMC, Co/OMC and Ni/OMC were obtained using a magnetic susceptibility balance at 18 °C. The mass magnetic susceptibility of each mesoporous carbon materials is shows in Table 3.3.

Table 3.2. Magnetic properties of blank OMC and metallic OMC obtained from Johnson-Matthey balance at 18 °C.

Sample name	Mass magnatic susceptibility (Xg) m^3/kg	Mass susceptibility (Xg) m^3/kg standard of the element
OMC	$-4.44x10^{-9}$	C= $-6.3x10^{-9}$
Fe/OMC	$8.42x10^{-7}$	Fe =$276000x10^{-6}$
Co/OMC	$4.83x10^{-7}$	Co= $204000x10^{-6}$
Ni/OMC	$9.80x10^{-7}$	Ni= $68850x10^{-6}$

These results confirmed that the OMC had diamagnetic behaviour due to the negative value of mass susceptibility, while the positive value of mass susceptibility for Fe/OMC, Co/OMC and Ni/OMC indicated that these materials had paramagnetic behaviour. All species of metallic salt could be reduced to metallic nanoparticles during carbonisation at high temperature. The metals nanoparticles such as iron, cobalt and nickel can develop of the graphitic framework when they are heating at high temperature under inert gas.[52, 53] Carbon materials with magnetic properties have numbers of potential applications in nanotechnology.[54]

3.3 Conclusion

In this chapter mesoporous carbon materials (blank OMC) and their magnetic counterparts (Fe/OMC, Co/OMC and Ni/OMC) were successfully prepared using resorcinol and formaldehyde as carbon precursor and triblock copolymer F127 as the template via the soft templating method. Characterisation of these materials showed that the template during the carbonization process to form the pores in the carbon materials. In comparison with other methods to prepare mesoporous carbon monolith, this method is cost-effective and simple. The mesoporous carbon monoliths obtained have a high surface area, narrow pore size. The metal-containing OMC shown magnetic behaviour. The result confirmed that the blank mesoporous carbon material displays diamagnetic behaviour while Fe/OMC, Co/OMC and Ni/OMC have paramagnetic behaviour. Therefore, magnetic mesoporous carbon materials would have a potential use in a environmental remediation due to their facile separation and high selective adsorption capacity. However, the drawback of this method includes the need for carbonization and the resulting OMC show blind pores, which may be undesirable in the filtration.

References

1. J. Rouquerol, D. Avnir, D. H. Everett, C. Fairbridge, M. Haynes, N. Pernicone, J. D. F. Ramsay, K. S. W. Sing and K. K. Unger, *GUIDELINES FOR THE CHARACTERIZATION OF POROUS SOLIDS*, 1994.
2. J. Rouquerol, D. Avnir, C. W. Fairbridge, D. H. Everett, J. H. Haynes, N. Pernicone, J. D. F. Ramsay, K. S. W. Sing and K. K. Unger, *Pure and Applied Chemistry*, 1994, **66**, 1739-1758.
3. C. Liang, Z. Li and S. Dai, *Angewandte Chemie (International ed. in English)*, 2008, **47**, 3696-3717.
4. T. Y. Ma, L. Liu and Z. Y. Yuan, *Chemical Society Reviews*, 2013, **42**, 3977-4003.
5. L.-F. Chen, X.-D. Zhang, H.-W. Liang, M. Kong, Q.-F. Guan, P. Chen, Z.-Y. Wu and S.-H. Yu, *ACS Nano*, 2012, **6**, 7092-7102.
6. C. Merlet, B. Rotenberg, P. A. Madden, P. L. Taberna, P. Simon, Y. Gogotsi and M. Salanne, *Nature materials*, 2012, **11**, 306-310.
7. N. A. Travlou, C. Ushay, M. Seredych, E. Rodríguez-Castellón and T. J. Bandosz, *ACS Sensors*, 2016, **1**, 591-599.
8. P. Xiong, J. Zhu, L. Zhang and X. Wang, *Nanoscale Horizons*, 2016, DOI: 10.1039/C5NH00134J.
9. Y. Fang, D. Gu, Y. Zou, Z. Wu, F. Li, R. Che, Y. Deng, B. Tu and D. Zhao, *Angewandte Chemie-International Edition*, 2010, **49**, 7987-7991.
10. N. P. Wickramaratne, V. S. Perera, J. M. Ralph, S. D. Huang and M. Jaroniec, *Langmuir*, 2013, **29**, 4032-4038.
11. X. Jia, G. Zhang, T. Wang, X. Zhu, F. Yang, Y. Li, Y. Lu and F. Wei, *Journal of Materials Chemistry A*, 2015, **3**, 15738-15744.
12. Z. Ma, H. Zhang, Z. Yang, Y. Zhang, B. Yu and Z. Liu, *Journal of Materials Chemistry A*, 2014, **2**, 19324-19329.
13. B. Guo, X. Wang, P. F. Fulvio, M. Chi, S. M. Mahurin, X.-G. Sun and S. Dai, *Advanced Materials*, 2011, **23**, 4661-+.
14. J. Gorka, M. Jaroniec and W. L. Suchanek, *Nanoscale*, 2010, **2**, 2868-2872.
15. H. Tamon, H. Ishizaka, M. Mikami and M. Okazaki, *Carbon*, 1997, **35**, 791-796.
16. R. Ryoo, S. H. Joo and S. Jun, *The Journal of Physical Chemistry B*, 1999, **103**, 7743-7746.
17. R. Ryoo, S. H. Joo, M. Kruk and M. Jaroniec, *Advanced Materials*, 2001, **13**, 677-681.
18. J. Lee, J. Kim and T. Hyeon, *Advanced Materials*, 2006, **18**, 2073-2094.

19. S. J. Han and T. Hyeon, *Chemical Communications*, 1999, DOI: 10.1039/a905848f, 1955-1956.
20. S. Tanaka, N. Nishiyama, Y. Egashira and K. Ueyama, *Chemical Communications*, 2005, DOI: 10.1039/B501259G, 2125-2127.
21. L. Chuenchom, R. Kraehnert and B. M. Smarsly, *Soft Matter*, 2012, **8**, 10801-10812.
22. C. Liang, K. Hong, G. A. Guiochon, J. W. Mays and S. Dai, *Angewandte Chemie International Edition*, 2004, **43**, 5785-5789.
23. Y. Meng, D. Gu, F. Zhang, Y. Shi, H. Yang, Z. Li, C. Yu, B. Tu and D. Zhao, *Angewandte Chemie*, 2005, **117**, 7215-7221.
24. C. Liang and S. Dai, *Journal of the American Chemical Society*, 2006, **128**, 5316-5317.
25. C. Liu, L. Li, H. Song and X. Chen, *Chemical Communications*, 2007, 757-759.
26. S. E. Elaigwu and G. M. Greenway, *Materials Letters*, 2014, **115**, 117-120.
27. Y. Meng, D. Gu, F. Zhang, Y. Shi, L. Cheng, D. Feng, Z. Wu, Z. Chen, Y. Wan and A. Stein, *Chemistry of materials*, 2006, **18**, 4447-4464.
28. D. Gu, H. Bongard, Y. Meng, K. Miyasaka, O. Terasaki, F. Zhang, Y. Deng, Z. Wu, D. Feng, Y. Fang, B. Tu, F. Schüth and D. Zhao, *Chemistry of Materials*, 2010, **22**, 4828-4833.
29. M. Jaroniec, J. Gorka, J. Choma and A. Zawislak, *Carbon*, 2009, **47**, 3034-3040.
30. M. Jaroniec, J. Choma, J. Gorka and A. Zawislak, *Chemistry of Materials*, 2007, **20**, 1069-1075.
31. P. Gao, A. Wang, X. Wang and T. Zhang, *Chemistry of Materials*, 2008, **20**, 1881-1888.
32. R. Pekala, *Journal of Materials Science*, 1989, **24**, 3221-3227.
33. S. Tanaka, N. Nakatani, A. Doi and Y. Miyake, *Carbon*, 2011, **49**, 3184-3189.
34. K. S. Sing, *Pure and applied chemistry*, 1985, **57**, 603-619.
35. D. Liu, J.-H. Lei, L.-P. Guo and K.-J. Deng, *Carbon*, 2011, **49**, 2113-2119.
36. L. Liu, F.-Y. Wang, G.-S. Shao and Z.-Y. Yuan, *Carbon*, 2010, **48**, 2089-2099.
37. T. W. Kim, I. S. Park and R. Ryoo, *Angewandte Chemie*, 2003, **115**, 4511-4515.
38. E. Duffy, X. He, P. N. Nesterenko and B. Paull, *Journal of Materials Science*, 2015, **50**, 6245-6259.
39. S. Tanaka, A. Doi, N. Nakatani, Y. Katayama and Y. Miyake, *Carbon*, 2009, **47**, 2688-2698.

40. A.-H. Lu, B. Spliethoff and F. Schüth, *Chemistry of Materials*, 2008, **20**, 5314-5319.
41. S. E. Elaigwu, G. Kyriakou, T. J. Prior and G. M. Greenway, *Materials Letters*, 2014, **123**, 198-201.
42. M. Kruk, V. Antochshuk, J. R. Matos, L. P. Mercuri and M. Jaroniec, *Journal of the American Chemical Society*, 2002, **124**, 768-769.
43. M. Sevilla and A. B. Fuertes, *Carbon*, 2006, **44**, 468-474.
44. Z. Liu, Y. Song, Y. Yang, J. Mi and L. Deng, *Materials Research Bulletin*, 2012, **47**, 274-278.
45. M. Sevilla and A. B. Fuertes, *Carbon*, 2013, **56**, 155-166.
46. T.-M. Zhang, D.-L. Zhao, L. Yin and Z.-M. Shen, *Journal of Alloys and Compounds*, 2010, **508**, 147-151.
47. J. Li, J. Gu, H. Li, Y. Liang, Y. Hao, X. Sun and L. Wang, *Microporous and Mesoporous Materials*, 2010, **128**, 144-149.
48. N. F. Nejad, E. Shams and M. Amini, *Journal of Magnetism and Magnetic Materials*, 2015, **390**, 1-7.
49. G. Zhong, *Journal of Wuhan University of Technology-Mater. Sci. Ed.*, 2013, **28**, 668-672.
50. Y. Zhai, Y. Dou, X. Liu, S. S. Park, C.-S. Ha and D. Zhao, *Carbon*, 2011, **49**, 545-555.
51. T. Yu, Y. Deng, L. Wang, R. Liu, L. Zhang, B. Tu and D. Zhao, *Advanced Materials*, 2007, **19**, 2301-2306.
52. H. Song, X. Chen, X. Chen, S. Zhang and H. Li, *Carbon*, 2003, **41**, 3037-3046.
53. W. Weisweiler, N. Subramanian and B. Terwiesch, *Carbon*, 1971, **9**, 755-761.
54. B. Xu, J. Guo, X. Wang, X. Liu and H. Ichinose, *Carbon*, 2006, **44**, 2631-2634.

Chapter Four

4. Preparation and characterization of thermoresponsive hydroxypropyl cellulose (HPC) hydrogel and aerogel

4.1. Introduction

Hydrogels have become of great interest for many applications in all fields of technology and science.[1] Hydrogels are defined as insoluble cross-linked polymer networks with relatively hydrophilic properties that can absorb water 100 times more than their dry weight.[2] Hydrogels can be separated into two groups according to their chemical or physical behaviour of the cross-link connections.[3] Physical hydrogels are formed via cross-linking the polymer chains by physical connections during the dissolution of these polymers, for example, van der Waals forces hydrogen bonding, electrostatic or hydrophobic associations.[4] Chemical hydrogels are prepared by using chemical reagents as cross-linkers during the gelation process and these reagents are capable of forming covalent bonds their link the polymer chains together in three dimensional network.[5] Hydrogels formed by this type of cross-linking are stable gels under physiological conditions.[6] The mechanism of cross-linking with chemical cross-linkers can be separated into two types. Firstly, esterifying agents involving carboxylic anhydrides and carboxylic, in this type –COOR bonds are formed. Secondly, etherifying agents involving epoxide, organochlorine, and vinyl compounds, in this type of R–O–R bonds are formed.[7] Furthermore, the chemical hydrogels can be formed via photo crosslinking by using a UV irradiation strategy to produce high purity hydrogel without using toxic cross linker reagents.[5] Typically, hydrogels are produced from synthetic or natural polymers. Synthetic polymers that shape hydrogels are generally synthesised via chemical polymerization routes.[8, 9] Natural polymers including polysaccharides such as cellulose, chitin, alginate and agarose and proteins such as gelatin and collagen, have been used to fabricate hydrogel materials.[7] Compared with synthetic polymers, polysaccharides that are widely used for hydrogel formation, because they are naturally available, come from renewable sources are non-toxic and show a number of physical and chemical properties that make them suitable for a wide range of applications.[10] Cellulose and its derivatives are the most important organic source used to synthesise hydrogels and aerogels materials due to their hydrophilicity, natural abundance, non-toxicity, high stability and the increasing demand for biocompatible and environmentally friendly products.[7, 11, 12] Cellulose has abundant hydroxyl groups which can be used to form hydrogels simply

with unique properties and structures.[13] Cellulose hydrogels can be prepared from native cellulose directly through physical cross-linking by forming hydrogen bonding between the hydroxyl groups. However, the highly extended hydrogen bonding in cellulose contributes to making it insoluble in water. Cellulose, which is insoluble in water due to its extensive hydrogen bonding, can be rendered water soluble by etherification of some of its hydroxyl groups, such as with hydroxypropyl groups to form hydroxypropyl cellulose (HPC),[14, 15] thus allowing for aqueous processing of this material. Etherified cellulose can then form hydrogels - three-dimensional (3D) polymer networks that are able to absorb large amounts of water and yet retain their physical structure through chemical or physical crosslinks between individual polymeric chains.[16]Some hydrogels can be shown changes into their structures, shapes, colours, reaction rate, and mechanical properties due to response to environmental stimulus. This type of hydrogels named smart or intelligent hydrogels.[17] Smart hydrogels can be separated into different groups depending on their sensitivity for varies stimulus such as temperature, pH, sound, light and mechanical stimuli.[18-20] There are extensive studies on the pH-responsive and temperature-responsive hydrogels due to their wide applications, especially in the medication field. The temperature must be modified externally, but the pH changes happen inside the body of the hydrogel.[21] Temperature-responsive hydrogels display a phase transition behaviour at a specific temperature, which causes an unexpected change in the solvation case.[22] Thermoresponsive polymers depending on the lower critical solution temperature (LCST) of the polymer solution, Above the critical temperature points the solvent and polymer are unable to mix. For example, a polymer solution below the LCST is a homogeneous and clear solution while above the LCST seem to be cloudy. Therefore, the LCST also indicates the cloud point of the polymer solution.[23]

Hydroxypropyl cellulose (HPC) is one of the most important chemical derivatives of cellulose because of its high solubility in water.[24] When an aqueous solution of HPC is warmed up to about 42 ºC, a phase separation occurs leading to strong increase in turbidity (white suspension).[25] Below the LCST, HPC is dissolved in water while the side chains remain in a collapsed state on increasing the temperature up to its LCST value. HPC is cross-linkable by the chemical way[25, 26]as well as by photopolymerization.[25, 27] In the current chapter, anionic HPC hydrogels and aerogels with interconnected pores were fabricated using divinyl sulfone (DVS) as chemical cross-linker via a modified temperature induced phase separation (TIPS) method. The FD-HPC obtained was characterized in order to investigate morphology of the HPC hydrogel, surface area, the crosslinking occurrence, thermal stability and mechanical properties.

4.2. Results

4.2.1. HPC hydrogel and aerogel chemically crosslinked with DVS

A chemically cross-linked hydroxypropyl cellulose (HPC) hydrogel and aerogel was successfully synthesized using divinyl sulphone (DVS) as a crosslinker with more than 90% yield. Figures 4.1 and 4.2 illustrate the chemical reaction between HPC and DVS and schematic diagram representation the preparation of HPC hydrogel using DVS as chemical crosslinker respectively.

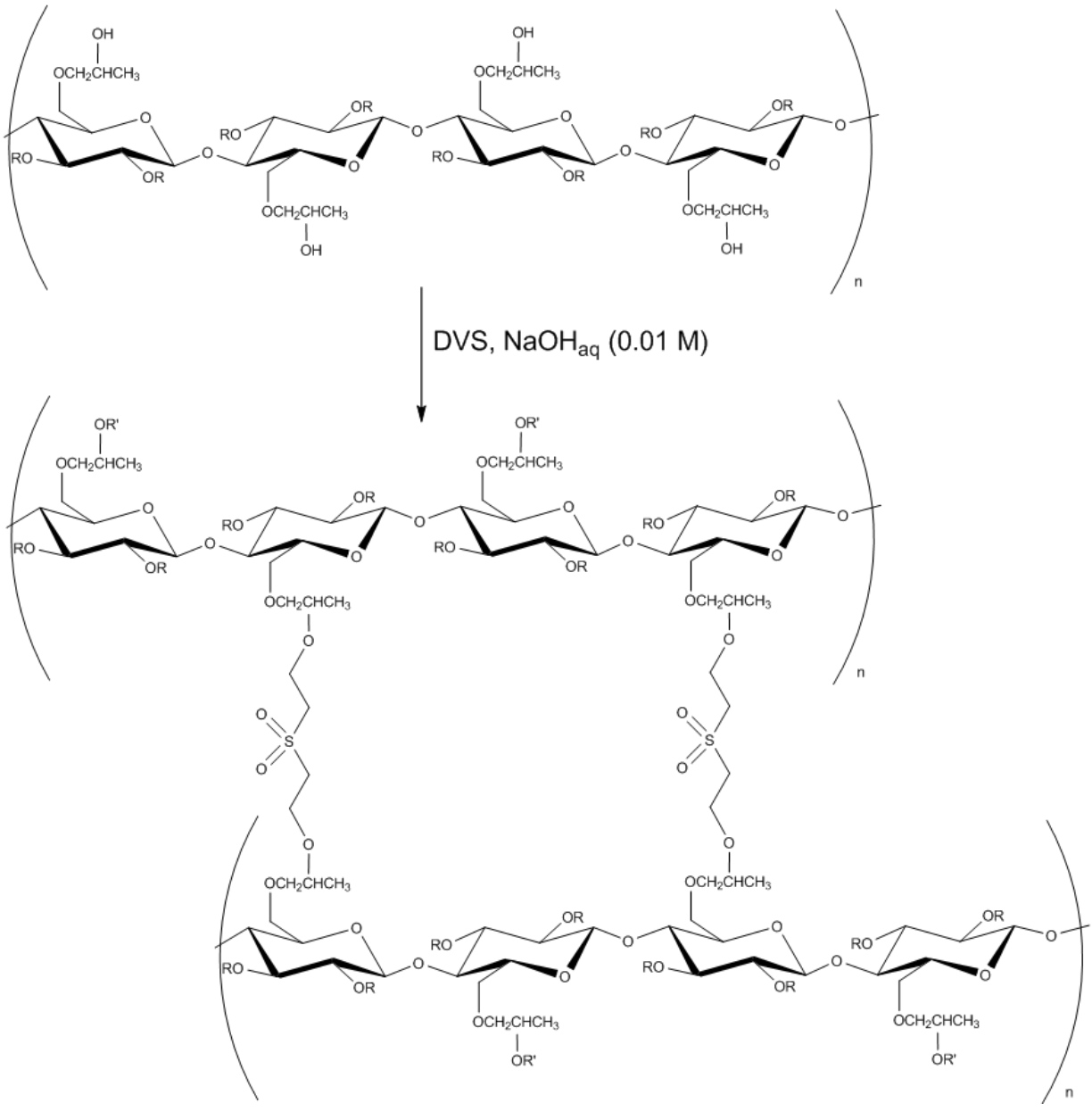

Figure 4.1. Chemical cross-linking process of HPC with DVS in basic medium.

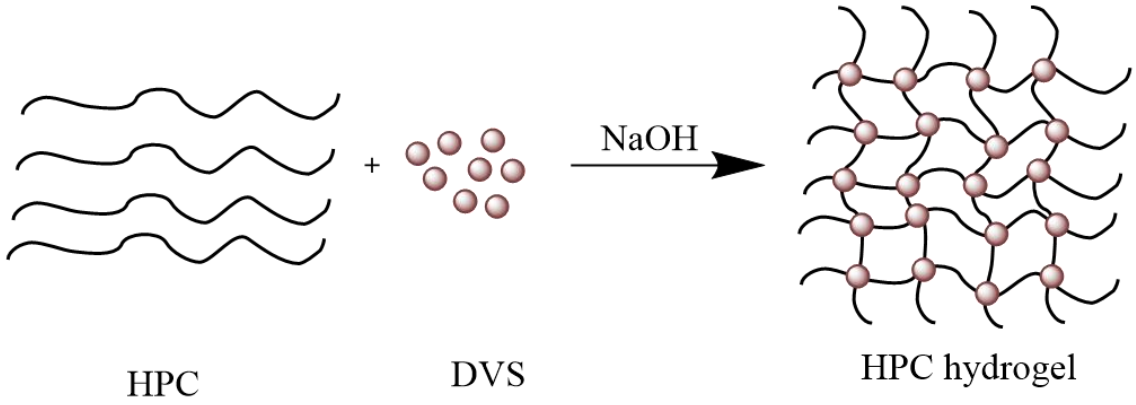

Figure 4.2. Schematic diagram representing the preparation of HPC hydrogel by using DVS as a chemical cross-linker.

4.2.2. Effect of temperature

HPC is a thermoresponsive polymer which exhibits a lower critical solution temperature (LCST) at around 42 ºC.[28] It is noteworthy that an aqueous solution of HPC is capable of rapid hydration-dehydration switching in response to temperature fluctuations around at 42 ºC. Below the LCST, the HPC chains hydrate to form an expanded structure due to its hydrophilicity. Conversely, at and above the LCST, the HPC chains dehydrate to form a shrunken structure. This property is due to entropic effects, which are magnified a the higher temperatures, the HPC chains collapse to a shrunken structure, thereby freeing the surrounding water molecules and might due to broken the hydrogen bonds between the HPC and surrounding water molecules at this temperature.[29] The chemical crosslinking of HPC with divinyl sulfone can be adjusted by controlling the gelation temperature.[30] Porous thermoresponsive hydrogels with unique morphologies were prepared by using the temperature induced phase separation (TIPS) method. The TIPS process has been used to synthesize porous foams from polymer solutions depending on the phase separation behaviour.[31] Figure 4.3 shows a scheme representing the TIPS method to prepare porous hydrogels.

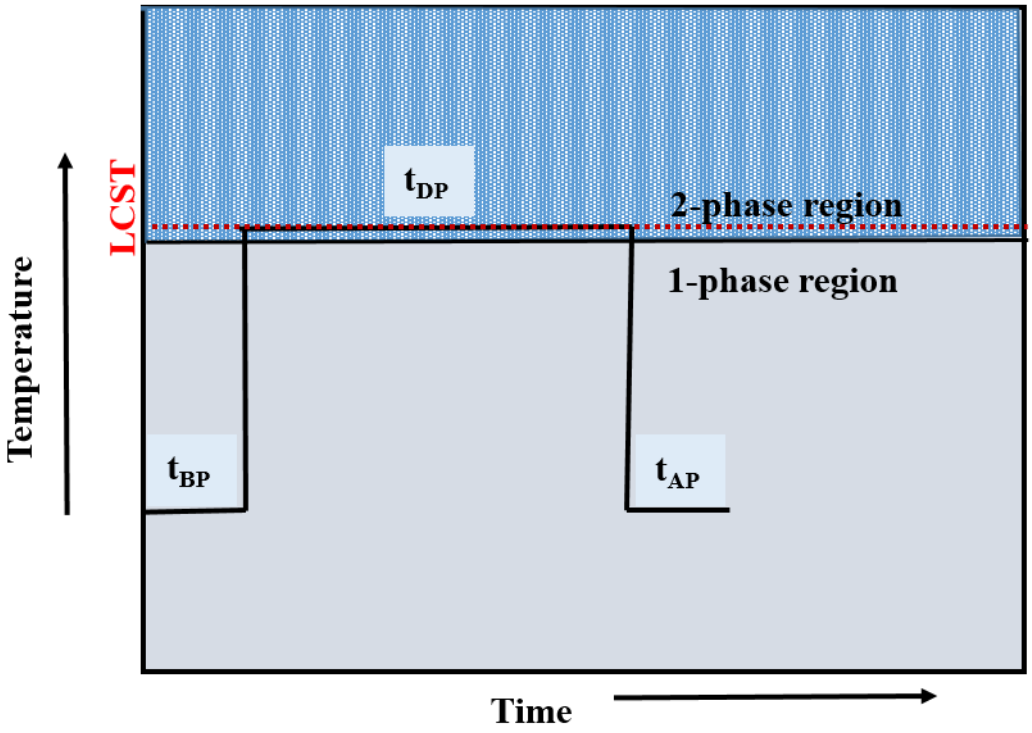

Figure 4.3. Schematic representation of the TIPS process for fabricating of HPC hydrogel, where t_{BP}, t_{DP} and t_{AB} refer to the reaction period before, during and after phase separation (Redrawn from Ref.41).[31]

Thermoresponsive HPC hydrogels and aerogels have been prepared according to the above method (as described in Chapter 2). Figure 4.4 shows photographic images of 7.0 w/v % HPC hydrogels gelation at different temperatures (A) at RT (22±2 ºC), which is below the LCST (B) by TIPS at 42 ºC (at LCST) (C) by TIPS at 52 ºC (above the LCST). HPC hydrogel which prepared at a temperature below the LCST, which shows a monolith HPC hydrogel with a light brown transparency colour. Whereas, the HPC hydrogel sample prepared via TIPS process shows white colour due to the HPC at the LCST turn to cloudy, which is named the cloud point. Figure 4.5 shows HPC aerogel formed by freeze-drying of HPC hydrogels that were prepared at different gelation temperatures. The hydrogel can be shaped depending on the shape of the mould. Figure 4.6 (A) shows photograph image of the HPC hydrogel and Figure 4.6 (B) demonstrate the HPC aerogel obtained after freeze drying of HPC hydrogel which confirms that the aerogel keeps the size and shape of the precursor hydrogel.

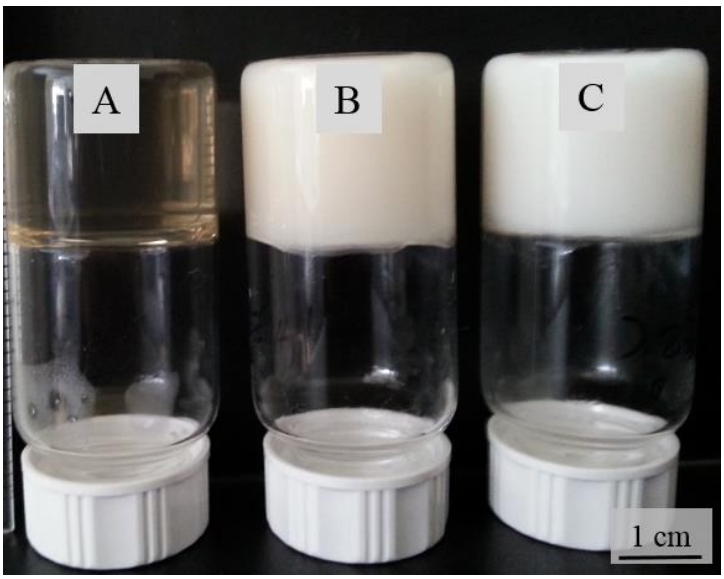

Figure 4.4. Photograph of HPC hydrogels prepared at different gelation temperature (A) at 22 ºC (below the LCST) (B) 42 ºC (at LCST) (C) 52 ºC (above the LCST).

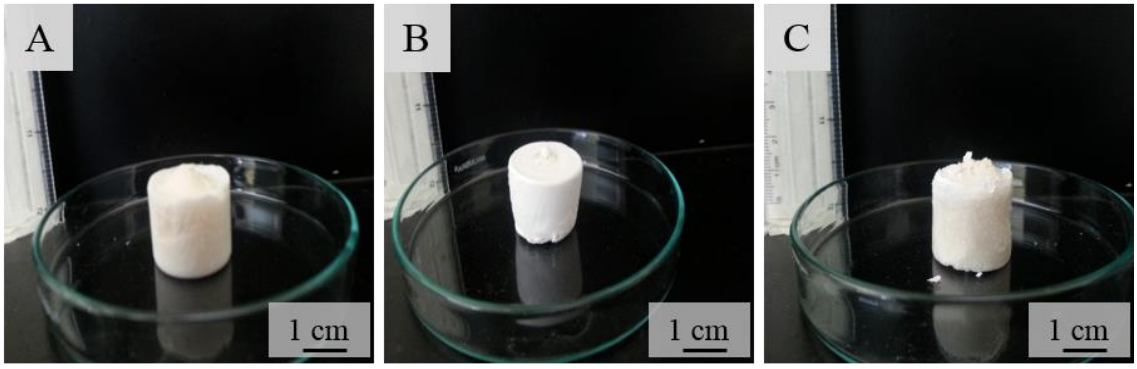

Figure 4.5. Photographic images of freeze-dried HPC aerogels whereby their corresponding hydrogel precursors were prepared at different temperatures (A) at room temperature (22±1 ºC) (below the LCST) (B) 42 ºC (at LCST) (C) 52 ºC (above the LCST).

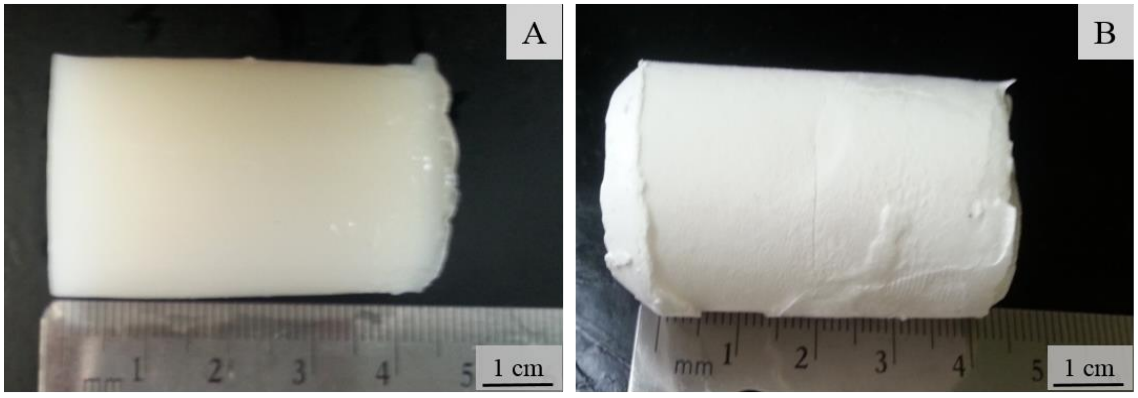

Figure 4.6. Photographs show (A) HPC hydrogel prepared from 7.0 w/v % HPC and 1.3 w/v % DVS at LCST temperature (B) HPC aerogel after freeze drying the hydrogel.

4.2.3. Morphology of FD-HPC hydrogel

SEM provided information about the structural morphologies of the different materials. The SEM images at different magnifications of freeze-dried (FD) HPC hydrogel prepared from 7.0 w/v % HPC and 1.3 w/v % DVS at different gelation temperatures are shown in Figures 4.7, 4.8 and 4.9 below LCST, at LCST and above LCST respectively. Figure 4.7 shows the SEM images of FD-HPC hydrogel prepared at temperature below the LCST. This hydrogel exhibits a macroporous structure with average pores size around (100 µm) .It can be also seen the pores shaped as honeycomb with a thick pores wall. Whereas, the SEM images of HPC hydrogel prepared at LCST by TIPS method show homogeneous dense interconnected pores with smallest pores size from 1 to 8 µm as represent in Figure 4.8. However, The SEM images of HPC hydrogel prepared at gelation temperature above the LCST show breakdown of the network structure as shown in Figure 4.9.

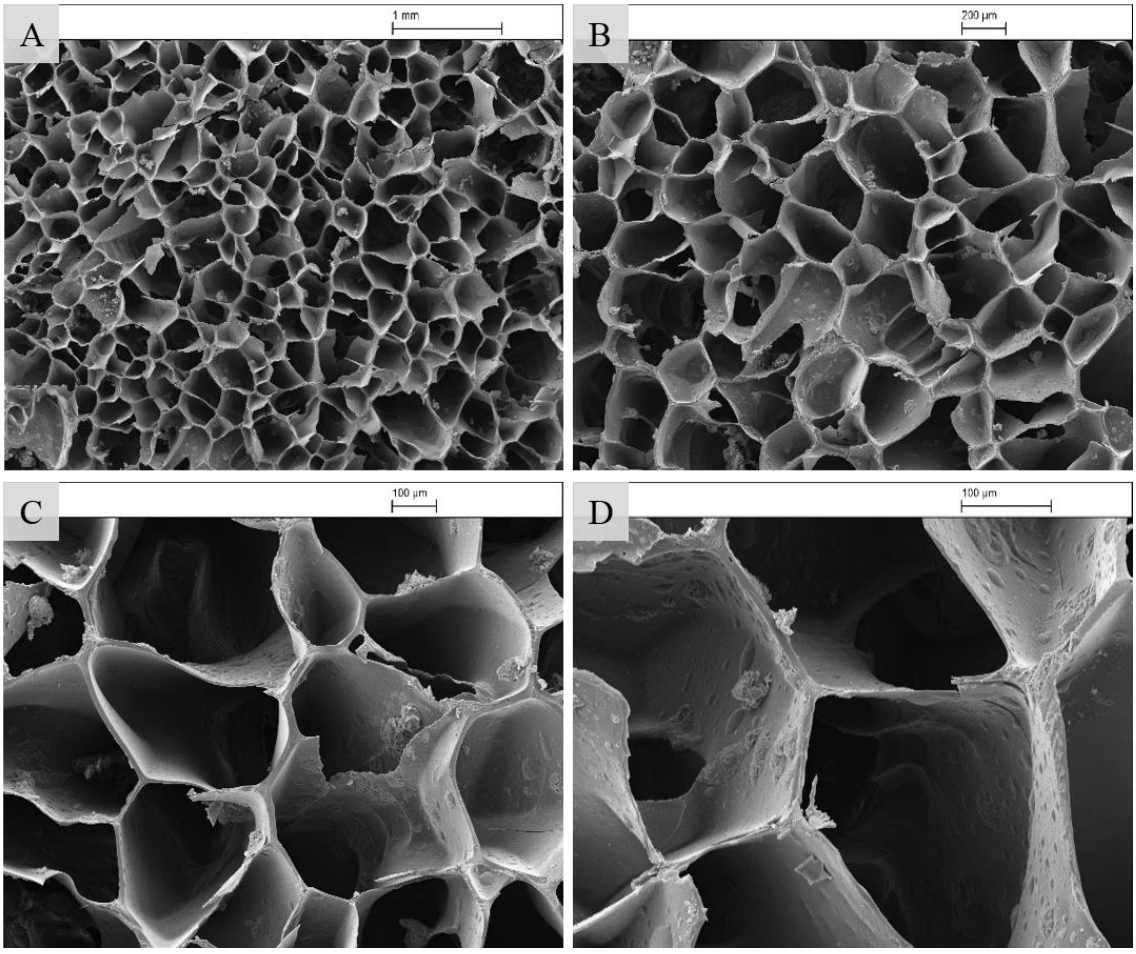

Figure 4.7. SEM images of FD-HPC hydrogels prepared by using 7.0 w/v % HPC and 1.3 w/v % DVS as crosslinker at room temperature (21±2 ºC) at different scales and magnifications (A) 1 mm (B) 200 µm (C) 100 µm (D) 100 µm.

It is clear from the SEM images in Figure 4.7 that the freeze-dried HPC hydrogel prepared at room temperature (21±2 ºC), which is below the LCST of HPC has a largely homogeneous porous structure with interconnecting channels. The results differ from previous studies reported, which are reported that the HPC hydrogels prepared at a temperature below the LCST are nonporous or porous with closed pores.[31, 32] Probably the main reason behind that the pore structure results from the growth of relatively large ice crystals and sublimation of these frozen water during the freeze-drying process.[33-35]

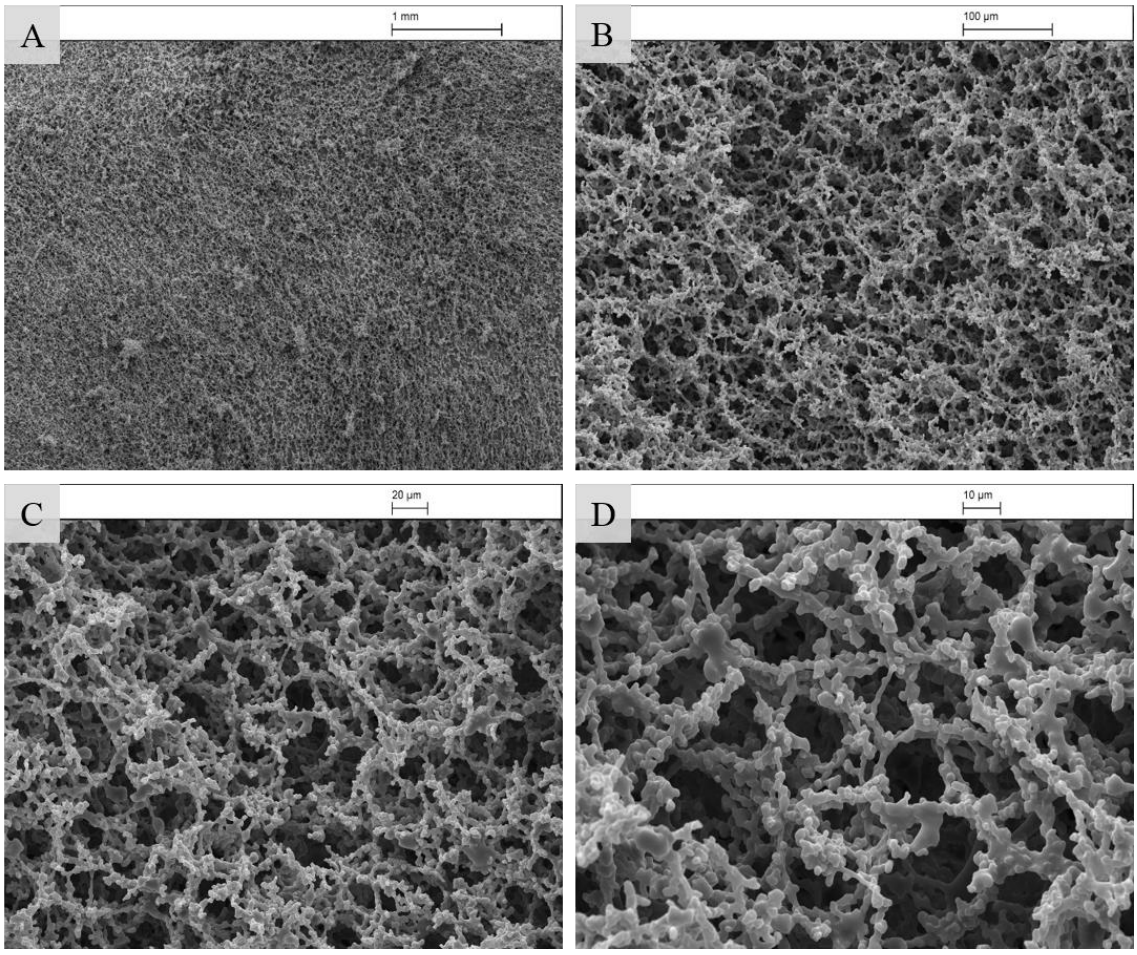

Figure 4.8. SEM images of FD-HPC hydrogel prepared by using 7.0 w/v % HPC and 1.3 w/v % DVS as crosslinker at 42 ºC (LCST of HPC) at different scales and magnifications (A) 1 mm (B) 100 µm (C) 20 µm and (D)10 µm.

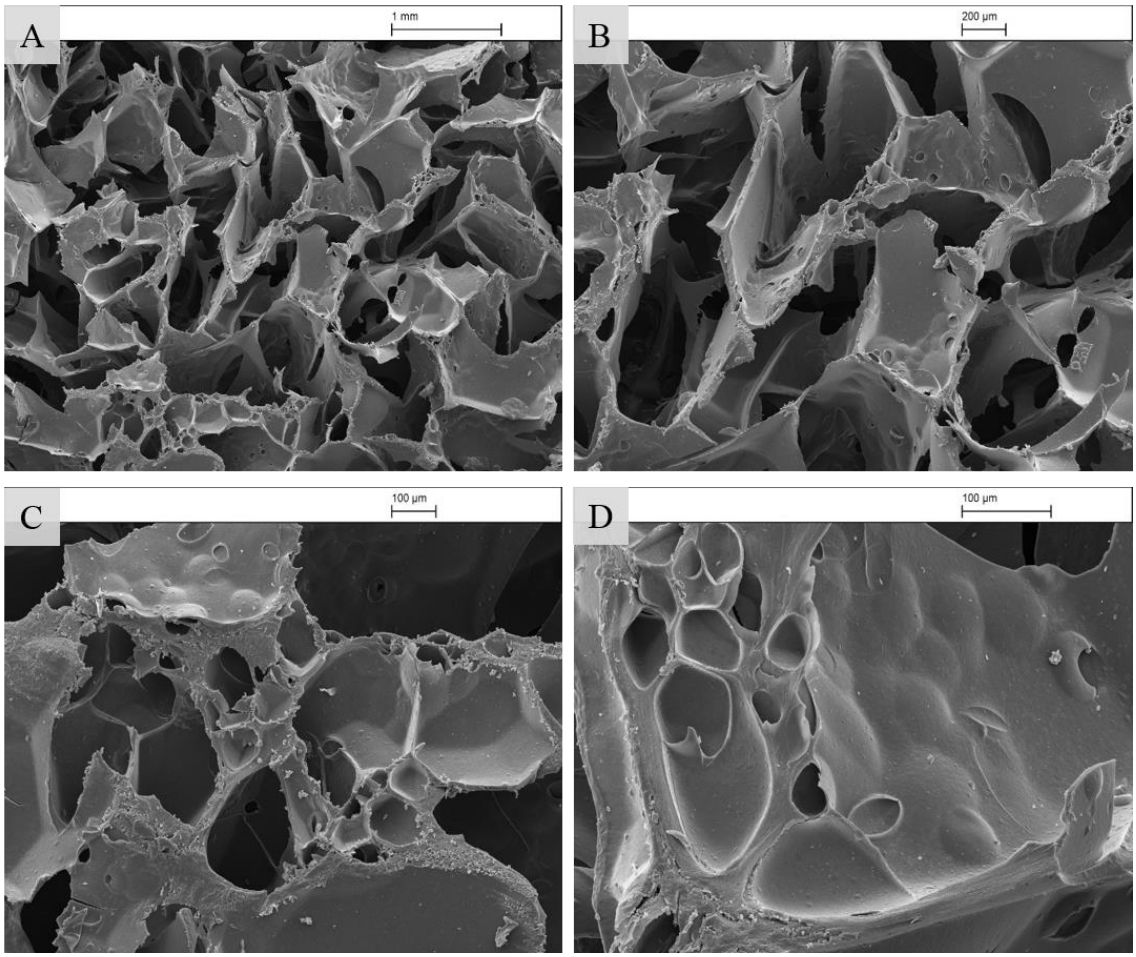

Figure 4.9. SEM images of FD-HPC hydrogel prepared by using 7.0 w/v % HPC and 1.3 w/v % DVS as crosslinker at 52 ºC (above LCST of HPC) at different scales and magnifications (A) 1 mm, (B) 200 µm, (C) 100 µm and (D) 100 µm.

These SEM images in Figure 4.8 clearly show the porous internal structure of the HPC aerogels that prepared at LCST temperature the macroporous structure from HPC crosslinked aerogel shows 3D interconnected network. The results indicate that the formed aerogels appeared to have homogeneous porous structures all over the cross-section. The sizes of the pores are about 1–8 µm in diameter. It is clear that the pores in the aerogels are consistent with those developed during spinodal decomposition in a typical TIPS method at the LCST and very different from the kinds of aerogels formed at above and below the LCST. Spinodal decomposition is a mechanism of rapid decomposition of the materials when it was changing from one thermodynamic phase to form two phase separation.[36] The SEM images of HPC aerogels prepared at gelation temperature above the LCST show breakdown of the network structure (Figure 4.9).

EDX spectra recorded on the selected area of FD-HPC hydrogel at different concentration of HPC are show in Figure 4.10. The results show the main element of the aerogels were found to be carbon, oxygen and sulphur. The present of sulphur peak indicates that the HPC reacted with DVS and formed covalent bonds with the sulfone group in the network structure. In addition, the results show HPC aerogels prepared by this method with high purity.

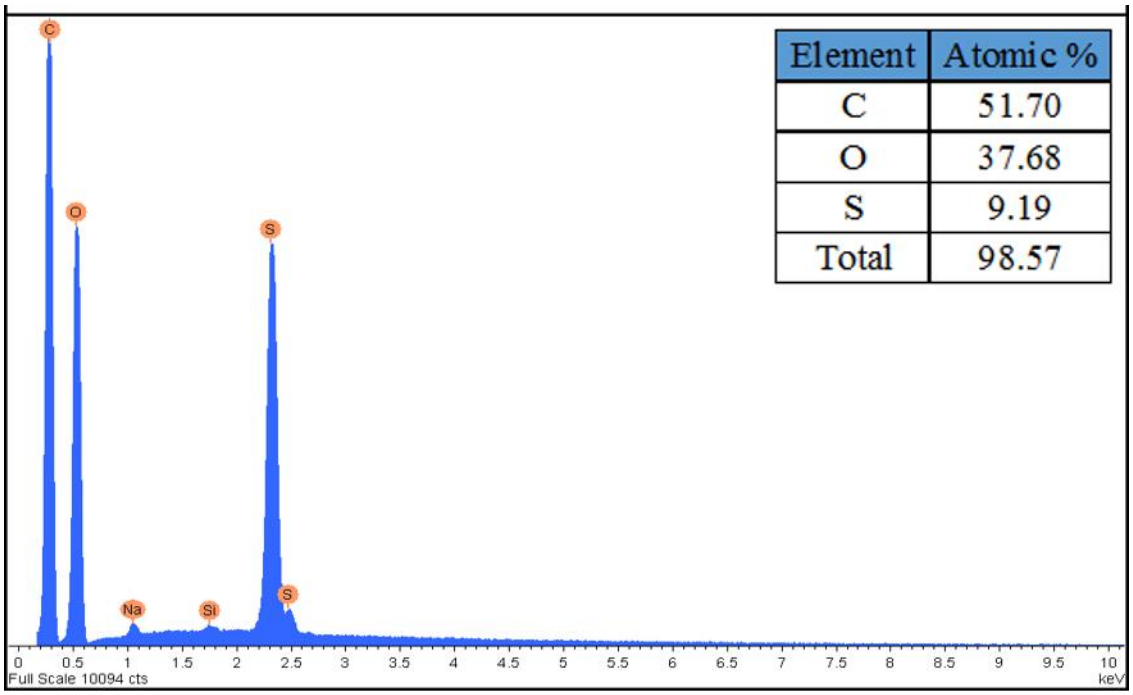

Element	Atomic %
C	51.70
O	37.68
S	9.19
Total	98.57

Figure 4.10. EDX spectra of the HPC aerogel prepared by using 7.0 w/v % HPC and 1.3 w/v % DVS at LCST after drying by freeze drying method.

Attempts were made to minimize the amount of DVS used due to the toxicity of DVS and the presence of unreacted DVS when 1.3 w/v % was utilized with 7.0 w/v % of HPC. Figure 4.11 shows SEM images of HPC aerogels at the LCST temperature of HPC with less DVS 0.5 w/v % with 7.0 w/v % of HPC. It can be seen that the homogeneous interconnected porous structures with bigger pores size when compared with 1.3 w/v % of DVS. This was due to decrease the crosslinking density between the HPC polymer chains.

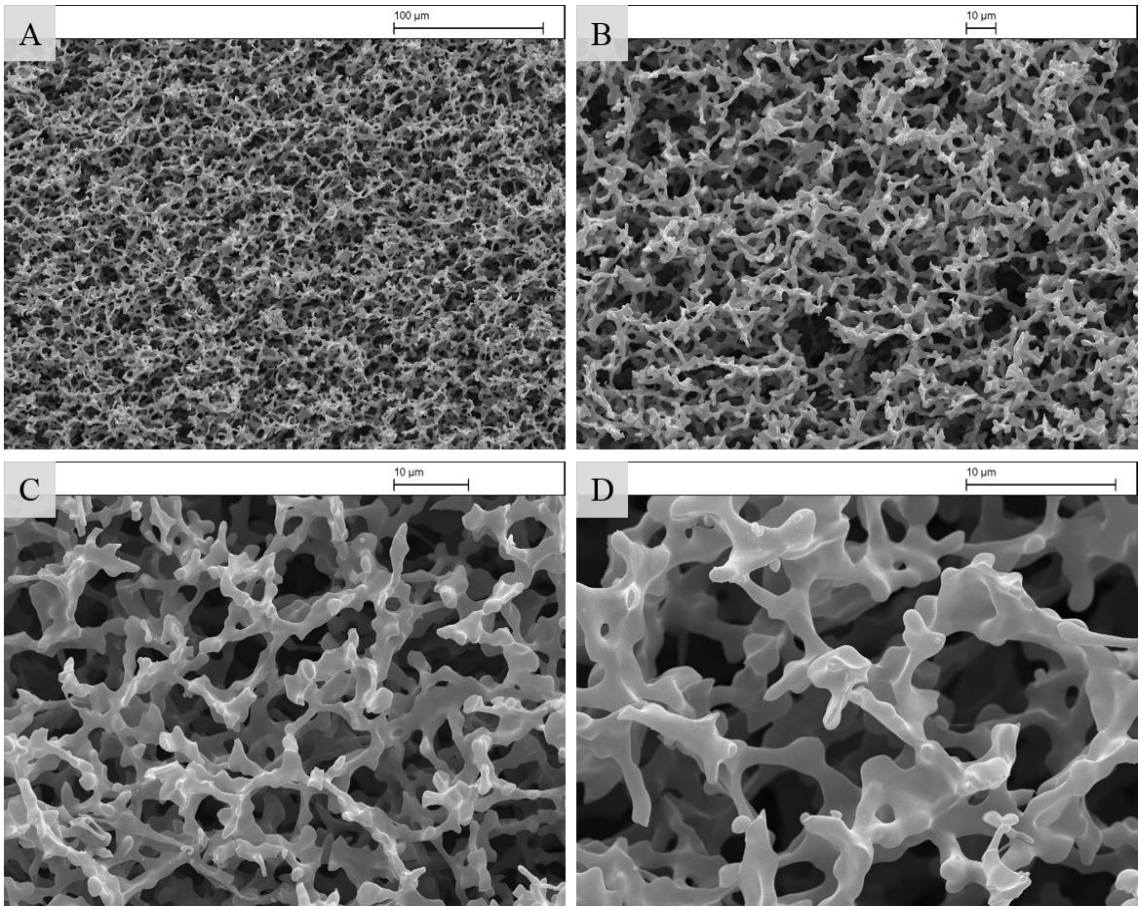

Figure 4.11. SEM images of FD-HPC hydrogel by using 7.0 w/v % HPC and 0.5 w/v % DVS as cross linker at the LCST of HPC at different scales and magnifications (A) 100 µm, (B) 10 µm, (C) 10 µm and (D) 10 µm.

In order to study effect of drying method on the network structure and the surface area of the HPC hydrogel, supercritical CO_2 drying was also used in addition to freeze drying method. This type of drying prevents the breakdown of the network structure of hydrogel materials where no capillary forces liquid-gas interfaces emerge, the latter being due to the surface tension of the liquid. A capillary pressure gradient appearing in the pore walls and being present during evaporative drying usually leads to the shrinkage most of the pores. Drying in supercritical conditions means a transformation of the liquid into a supercritical fluid with surface tension equal zero, and as a result, the porous structure remains intact. [37, 38] HPC hydrogel was dried by using the supercritical dryer with different solvent exchange which is ethanol and acetone. Figure 4.12 and 4.13 shows SEM images at different scales and magnifications of HPC aerogels prepared from 7.0 w/v % HPC and 1.3 w/v %DVS at LCST by TIPS method then dried using $ScCO_2$ drying with ethanol and acetone solvent exchange respectively.

From SEM images in Figures 4.12 shows the morphology structure and the pores size of HPC hydrogel dried by $ScCO_2$ using ethanol as solvent exchange was different from the hydrogel dried by using acetone as solvent exchange (Figure 4.13), which is show smaller pores size.

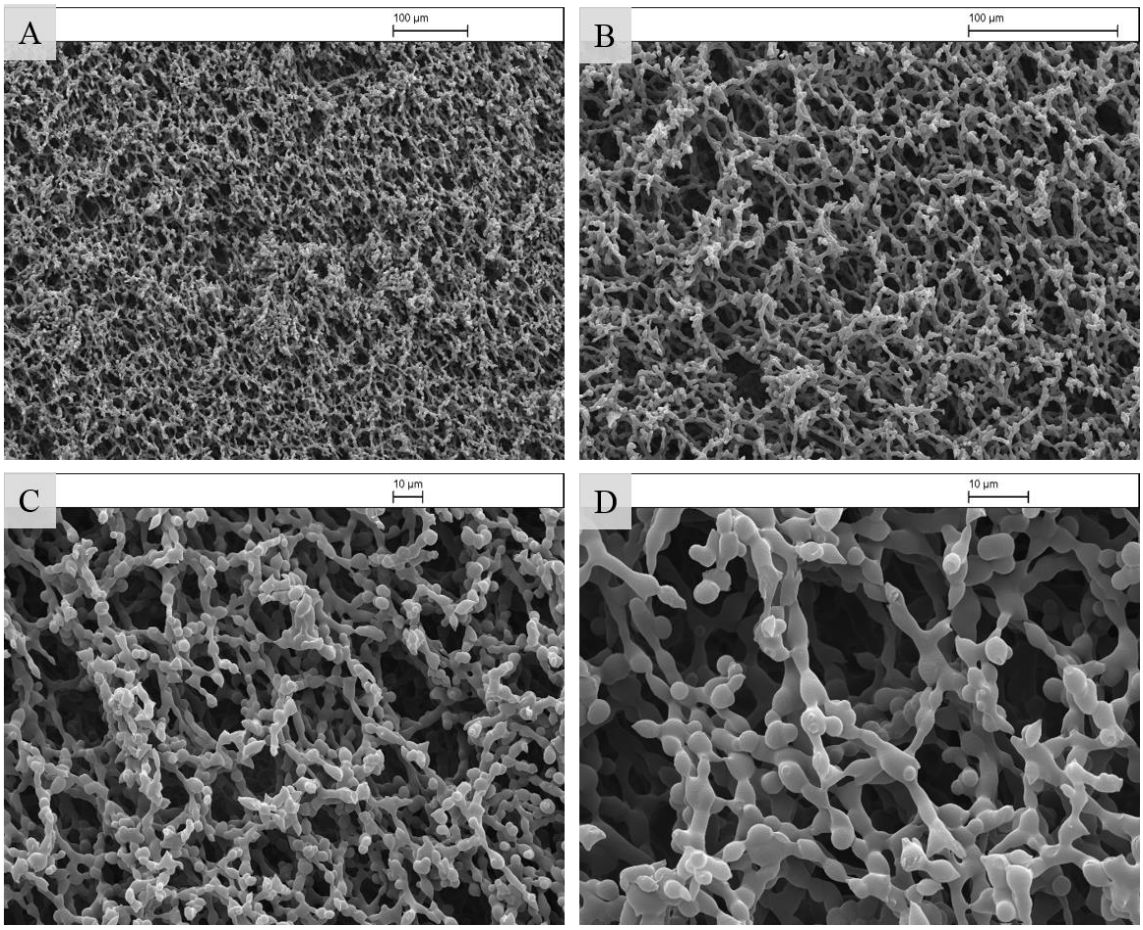

Figure 4.12. SEM images of $ScCO_2$ HPC aerogel (ethanol solvent exchange) prepared by using 7.0 w/v % HPC and 1.3 w/v % DVS as cross linker at LCST of HPC at different scales and magnifications (A) 100 µm, (B) 100 µm, (C) 10 µm and (D) 10 µm.

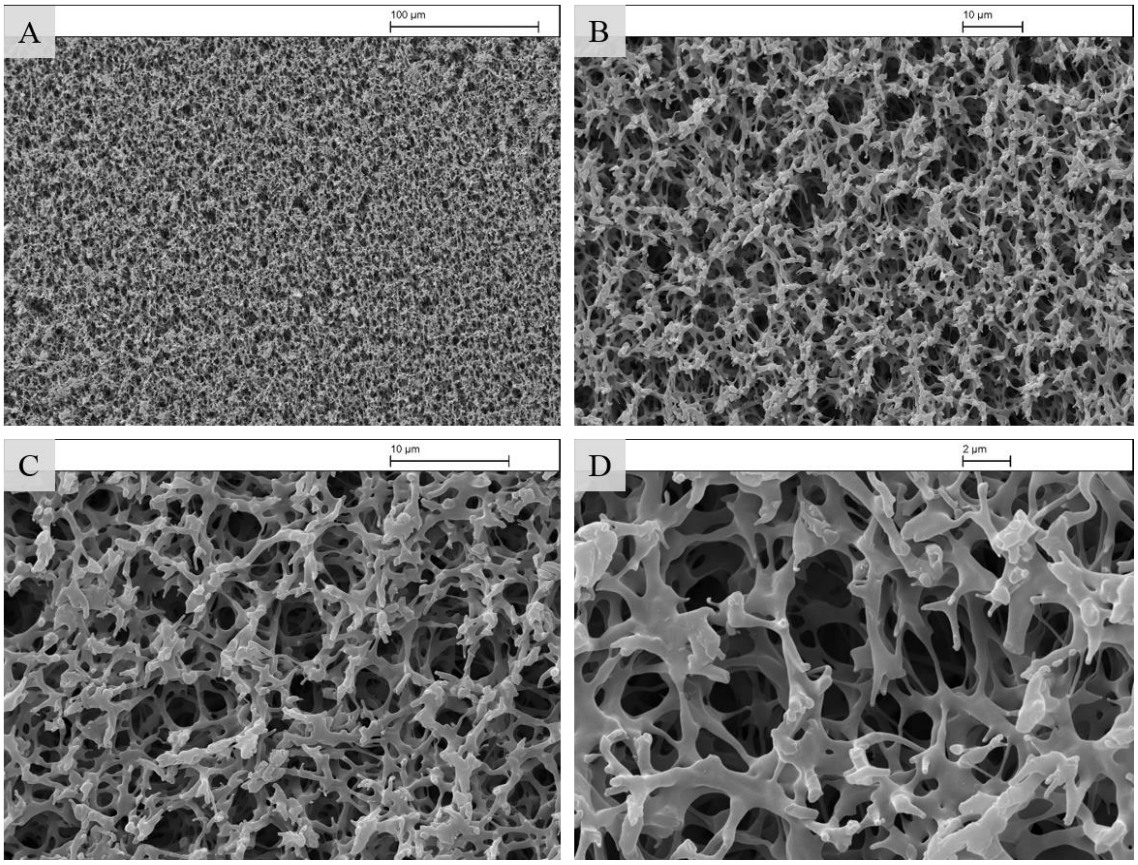

Figure 4.13. SEM images of $ScCO_2$ HPC aerogel (acetone solvent exchange) by using 7.0 w/v % HPC and 1.3 w/v % DVS as cross linker at LCST at different scales and magnifications (A) 100 µm, (B) 10 µm, (C) 10 µm and (D) 2 µm.

It is clear from the SEM images all the drying methods used in this study showed homogeneous porous structure without a broken network. However, the pore size is different with different drying methods. Supercritical $ScCO_2$ drying showed smaller pore size than freeze drying method. The reason behinds that in the FD drying method the forces caused by growing ice crystals formatted larger pores, while the supercritical CO_2 removes the solvent without any disturbing surface tension effects.[39] Furthermore, during solvent exchange might cause shrinkage in the network structure due to the competitive interactions between the organic solvent and the biopolymer.[40, 41] The SEM images also indicate that the solvent exchange used in the $ScCO_2$ dryer can affect the pore size of HPC aerogel. As a changes in pore size of HPC aerogel is seen when drying via $ScCO_2$ with acetone solvent exchange compared to using ethanol solvent exchange for the same sample. The effect of the type of solvent on the pore size is due to the different strengths of interactions that occur between the organic solvents and the HPC are strongly impacted by the abundance of OH^- groups.[42]

4.2.4. Density and porosity of FD-HPC hydrogel

The effect of initial parameters such as HPC concentration, gelation temperature and DVS concentration on the density and porosity of HPC aerogels were also studied.

Increasing the initial HPC concentration increased the density of the final HPC aerogels as shown in Figure 4.14. The average density ranged from 0.09 to 0.16 g/cm^3 for the aerogels synthesised from 2.0 to 10.0 w/v % of HPC. Figure 4.15 is a photograph of the light weight of the HPC aerogel material. Increasing the HPC concentration decreased the porosity of final FD-HPC hydrogel as shown in Figure 4.16. The average porosity of the FD-HPC hydrogels decreases from 95.6% to 78.5% when the initial concentration of HPC increases from 2.0 to 10.0% w/v. In fact, the initial concentration of HPC plays a major role in the development of the aerogel network structure. Increasing the concentration of the polymer would strengthen the structure, but significantly reduce the pore space and increase the density at the same time.[31, 43]

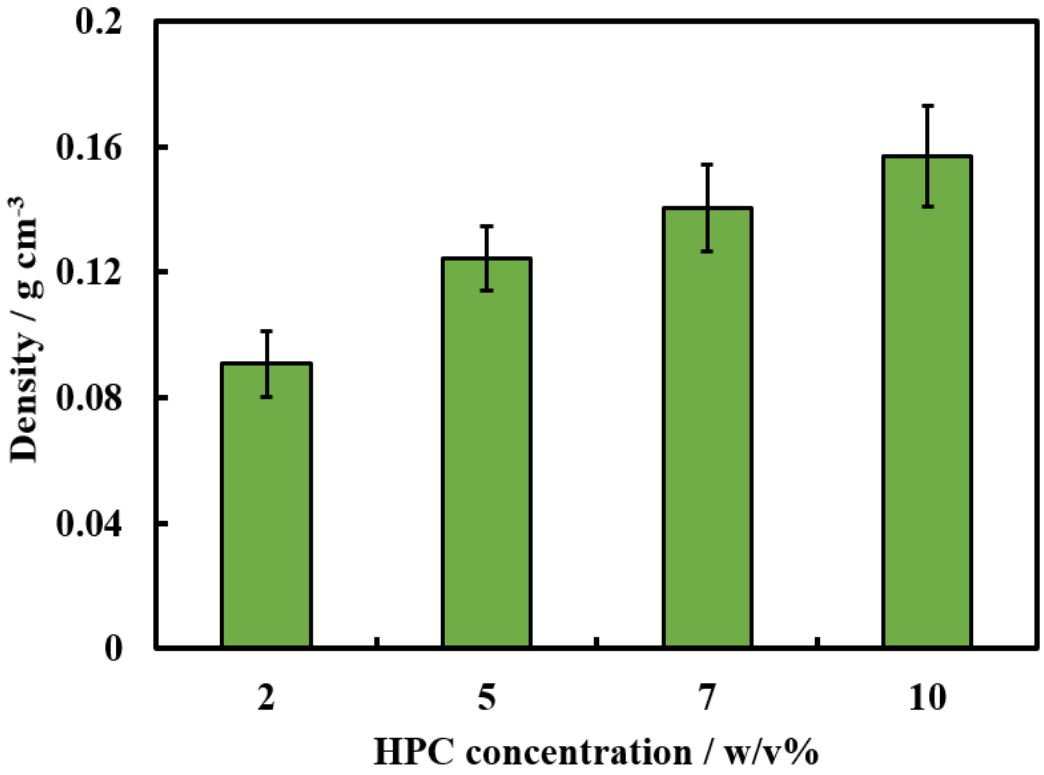

Figure 4.14. Effect of HPC concentration on the density of HPC aerogel gelation at LCST of HPC and drying by freeze drying method. Each data point is an average of three measurements and the error bars are the standard deviation.

Figure 4.15. Photograph image shows the light weight of HPC aerogel.

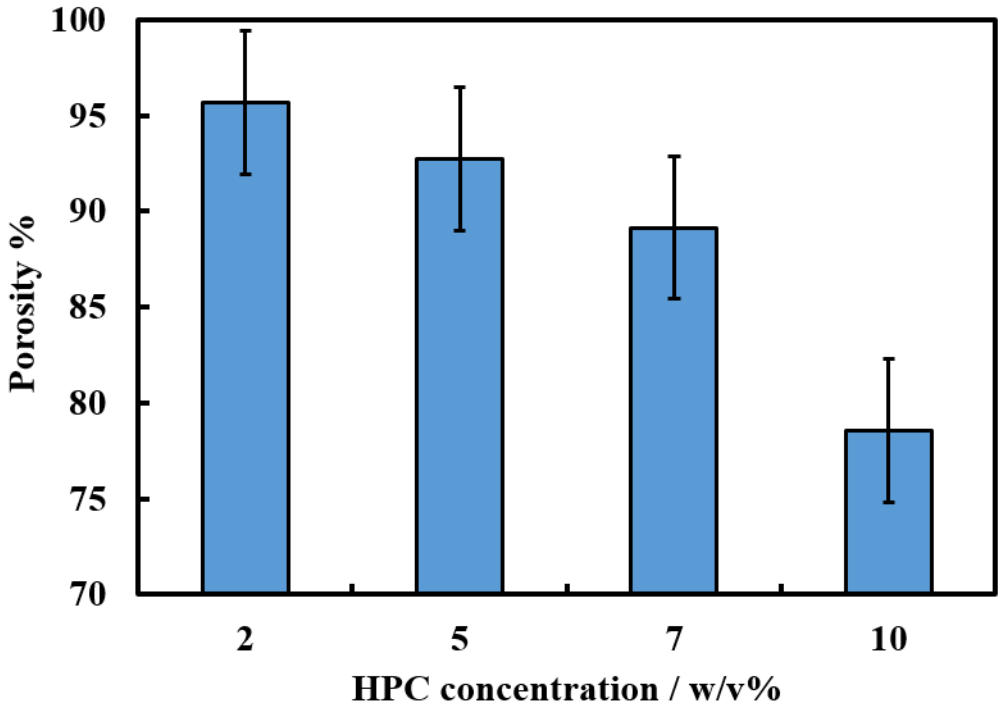

Figure 4.16. Effect of HPC concentration on the porosity of HPC aerogel gelation at LCST of HPC with the same concentration of DVS 1.3 w/v% and drying by freeze drying method. Each data point is an average of three measurements and the error bars represent the standard deviation.

Gelation temperature plays a significant role in the synthesis of HPC aerogels due to HPC polymer exhibit the LCST. In Figures 4.17 and 4.18 shows the effect of temperature on the density and porosity of HPC aerogels respectively. The density of the HPC aerogel increased from 0.089 g/cm^3 to 0.14 g/cm^3 when the gelation temperature increased from 22 ºC to 42 ºC as shown in Figure 4.17. Increasing the temperature above the LCST gave no further observable impact on the aerogel density. This is due to phase separation and development of the structure during spinodal decomposition, which happens at the LCST. SEM confirmed the breakdown of the porous structure at gelation temperature above the LCST.

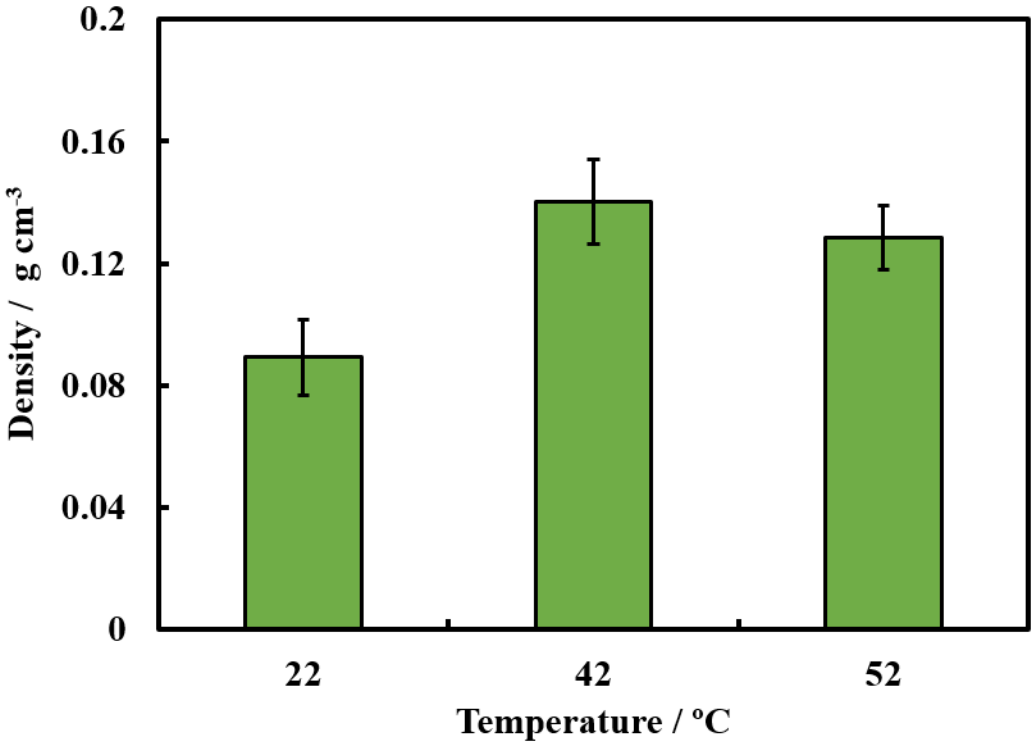

Figure 4.17. Effect of gelation temperature on the density of freeze drying HPC aerogel prepared by 7.0 w/v % HPC and 1.3 w/v % DVS. Each sample was measured in triplicate and the error bars are the standard deviation.

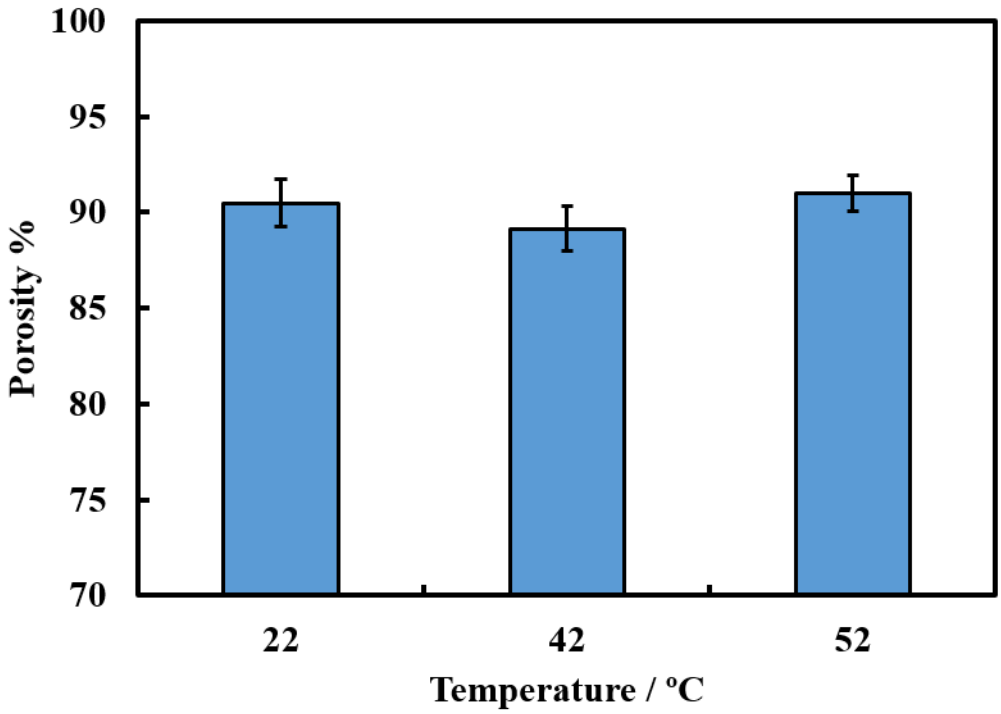

Figure 4.18. Effect of gelation temperature on the porosity of freeze drying HPC aerogel prepared by 7.0 w/v % HPC and 1.3 w/v % DVS. Each data point is an average of three measurements and the error bars are the standard deviation.

In fact, the amount of cross linker plays a major role in the development of the network structure of hydrogel materials. Increasing the cross-linker concentration increased the density of the final FD-HPC aerogels as shown in Figure 4.19. The average density ranged from 0.068 to 0.149 g/cm^3 for the aerogels synthesised from 0.5 to 2.0 w/v % of DVS. The effect of the amount of DVS on the porosity of HPC aerogels was investigated. As it can be seen in Figure 4.20 increasing DVS concentration from 0.5% w/v to 1.3% w/v decreased the porosity of FD-HPC hydrogels, but increased the amount of DVS to 2.0 w/v % causing no further decrease in the porosity.

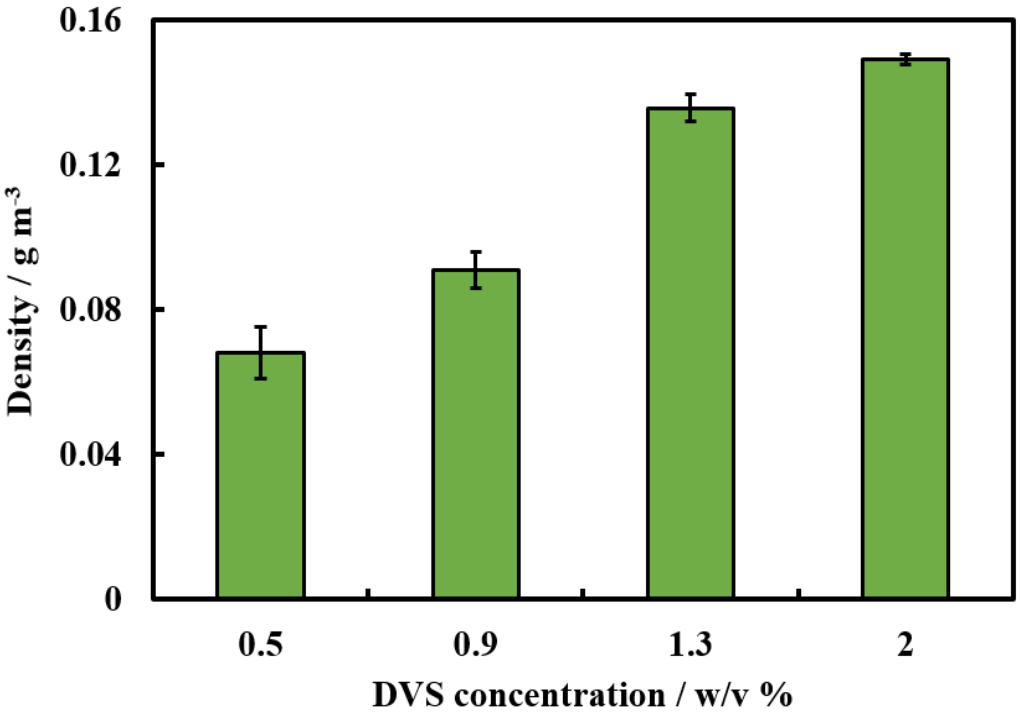

Figure 4.19. The effect of DVS concentration on the density of the freeze dried HPC aerogels prepared using 7.0 w/v % HPC at LCST. Each data point is an average of three measurements and the error bars are the standard deviation.

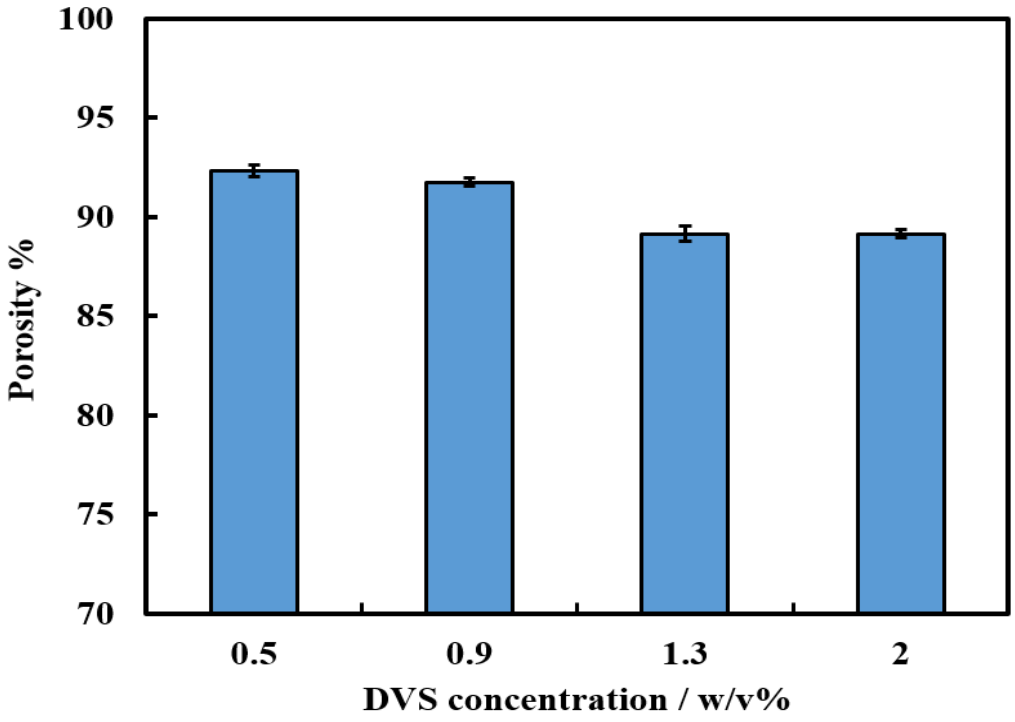

Figure 4.20. The effect of DVS concentration on the porosity of the freeze dried HPC aerogels prepared with 7.0 w/v % HPC at LCST. Each data point is an average of three measurements and the error bars are the standard deviation.

4.2.5. BET surface area analysis

The BET surface area and porosity analyser was used to determine of the surface area and porosity of the HPC aerogel using nitrogen sorption measurements. The textural properties of the HPC aerogel materials prepared with different gelation temperature are reported in Tables 4.1. The data show that the pore size of the HPC hydrogel prepared by TIPS method smaller than that of the HPC prepared at temperature below the LCST. However, the BET surface area show unexpected results, which surface area of the HPC hydrogel prepared below the LCST higher than the HPC hydrogel prepared by TIPS method.

Table 4.1. Textural characterization of the FD HPC aerogels prepared from 7.0 w/v % with 1.3 w/v % DVS at different gelation temperature

HPC w/v %	Gelation temperature T/°C	BET surface area $m^2 g^{-1}$	Pore size nm	Pore volume $cm^3 g^{-1}$
7.0	22	9.1±1.1	15.22	0.0155
7.0	42	5.2±0.2	9.20	0.0101
7.0	52	1.4±0.2	126.5	0.0015

Figure 4.21 displays the N_2 adsorption-desorption isotherms of the freeze dried HPC aerogel prepared from 7.0 w/v % HPC and 1.3 w/v % DVS at 22 ºC. Figure 4.22 shows the N_2 adsorption-desorption isotherms of the freeze dried HPC aerogel prepared from 7.0 w/v % HPC and 1.3 w/v % DVS by TIPS method. All the adsorption isotherms showed type IV according to IUPAC with a hysteresis loop in the range of 0.5–1 P/P_o, indicating the HPC aerogel had both mesoporous and macroporous structures.[44]

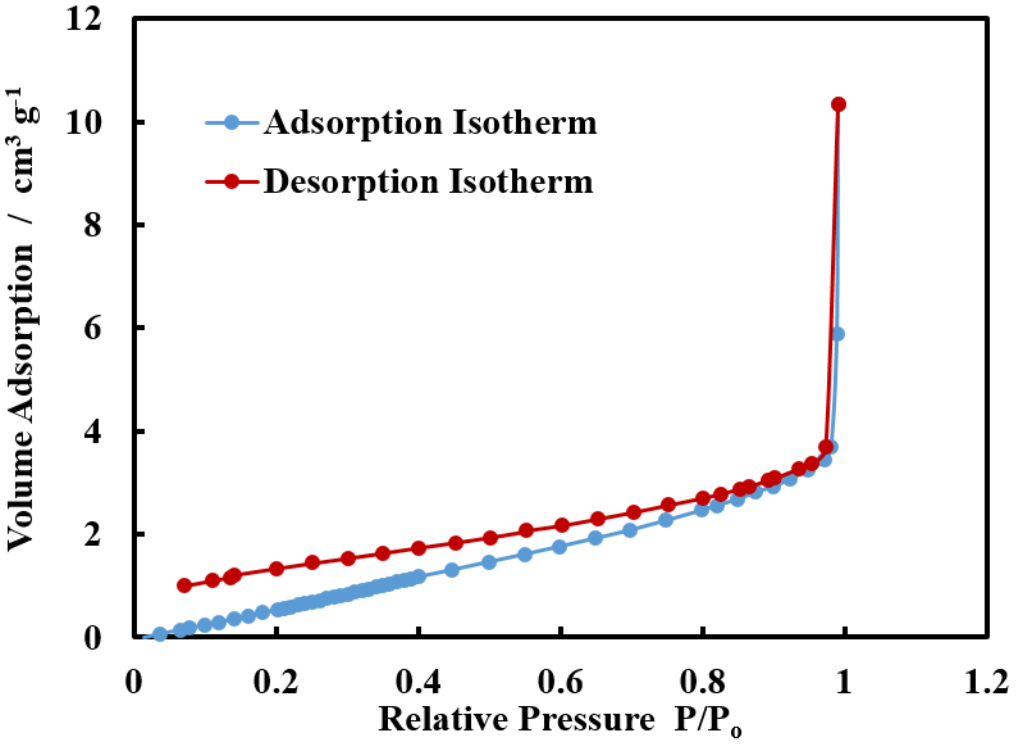

Figure 4.21. N_2 adsorption-desorption isotherm for HPC aerogel prepared by cross-linking 7.0 w/v % HPC and 1.3 w/v % DVS and gelation temperature below the LCST.

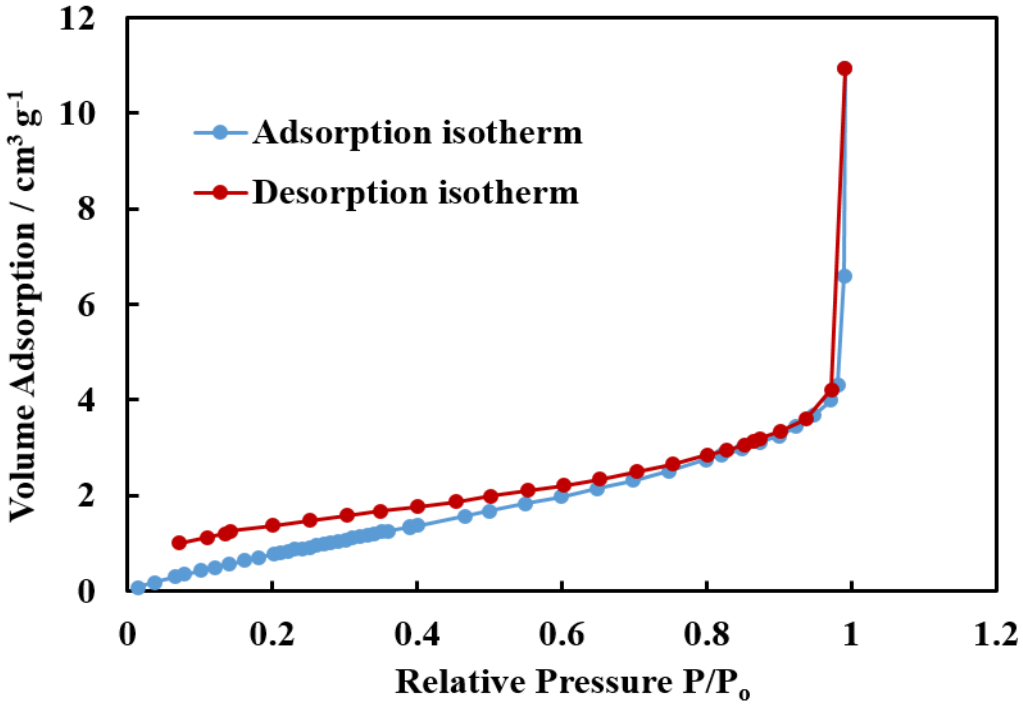

Figure 4.22. N_2 adsorption-desorption isotherm for HPC aerogel prepared by cross-linking 7.0 w/v % HPC and 1.3 w/v % DVS and gelation temperature 42 ºC by TIPS method and degassing at 40 °C.

The results obtained indicated that the BET surface area was different from previous studies.[45, 46] Furthermore, these results were unexpected and contrast with the scanning electron microscopy and the porosity/ density measurements for the same samples. The mean reasons behind that as mentioned in the literature the specific surface area of macropores materials obtained from nitrogen absorption method was approximately less than 1 m^2 /g, while for mesopores materials measured by the same method was about 220 m^2 /g .[38] This could be due to the pores being very big compared with the adsorbed layers, thus there is no difference between open surface adsorption and macropore adsorption. The second reason might be the HPC aerogel was still wet after freeze drying, therefore, the water molecules prevent the N_2 molecules to adsorb on the surface of HPC aerogel materials.

The BET surface area and pore size for the HPC aerogel dried by $ScCO_2$ dryer was also determined to show the effect of drying method on the morphology structure and pore size. The textural properties of the HPC aerogel materials dried with different method are reported in Tables 4.2. The results in Table 4.2 shows that the surface area of the HPC aerogel dried by $ScCO_2$ higher than freeze dried sample. The result demonstrated that the surface area of the HPC aerogel dried by $ScCO_2$ was 40 m^2/g, which is obviously higher than those of the freeze drying method (5.14 m^2/g). Figure 4.23 and 4.24 demonstrated N_2 adsorption-desorption isotherms of $ScCO_2$ drying HPC aerogel with ethanol and acetone solvent exchange respectively.

Table 4.2. Textural characterization of the HPC aerogels prepared from 7.0 w/v % with 1.3 w/v % DVS at LCST at different drying method

Drying types	BET surface area $m^2 g^{-1}$	Pore size nm	Pore volume $cm^3 g^{-1}$
FD	5.2±0.2	9.20	0.0101
$ScCO_2$ drying Ethanol solvent exchange	6.1±0.1	8.40	0.0109
$ScCO_2$ drying Acetone solvent exchange	40.6±1.0	5.05	0.0464

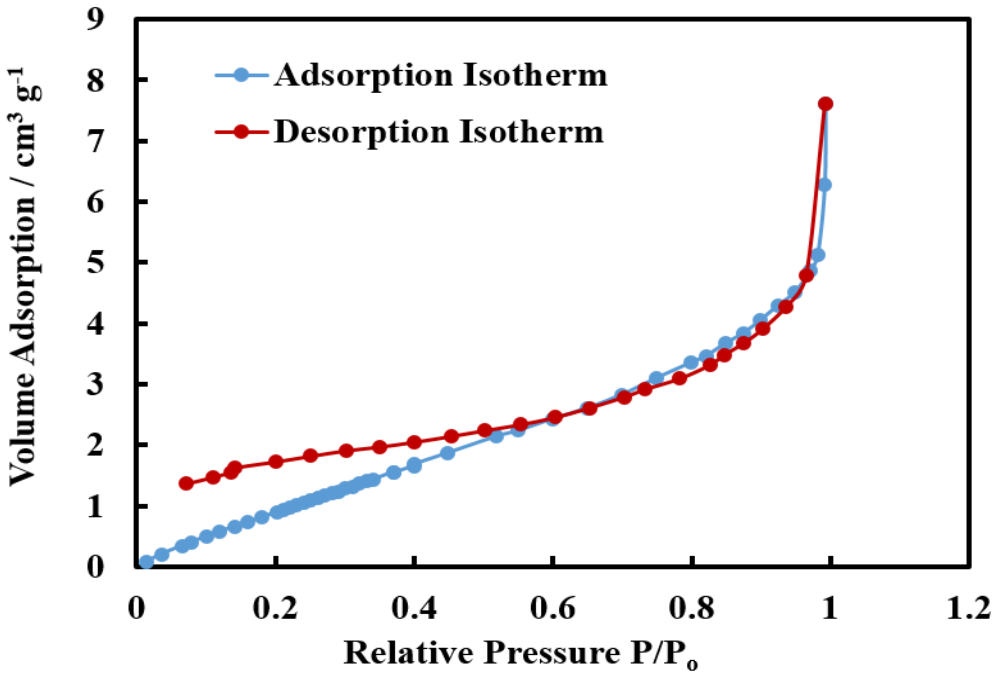

Figure 4.23. N_2 adsorption-desorption isotherm for HPC aerogel prepared by cross-linking 7.0 w/v % HPC and 1.3 w/v % DVS and gelation temperature at LCST and drying by $ScCO_2$ with ethanol solvent exchange.

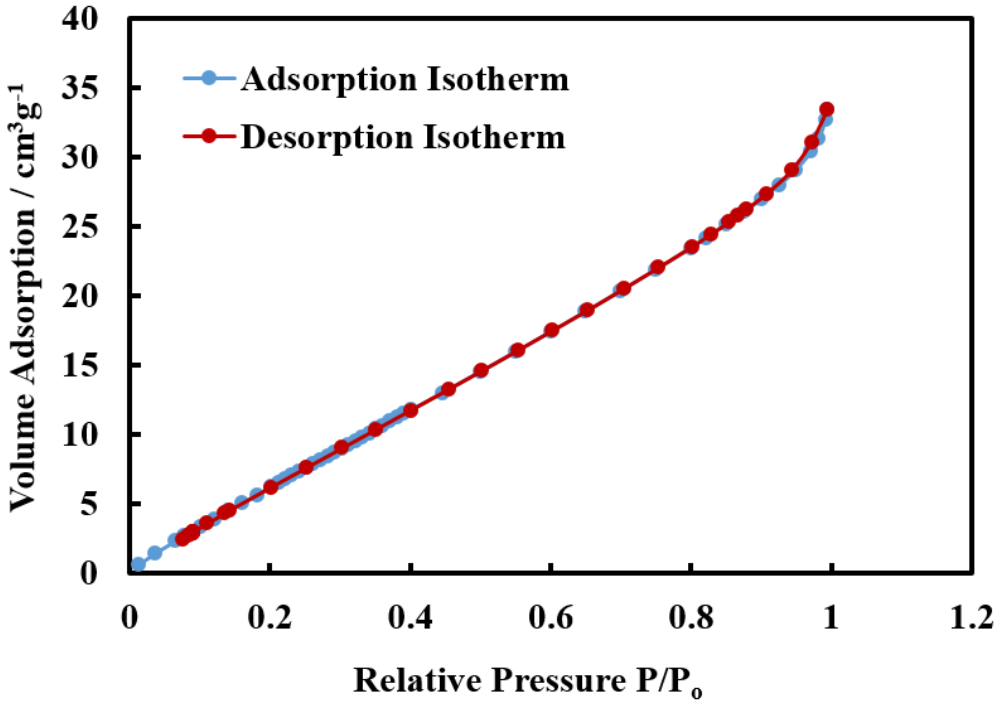

Figure 4.24. N_2 adsorption-desorption isotherm for HPC aerogel prepared by cross-linking 7.0 w/v % HPC and 1.3 w/v % DVS and gelation temperature 42 ºC and drying by $ScCO_2$ with acetone solvent exchange.

The HPC aerogel had a 3D macrostructure network with a specific surface area 5 to 40 m^2/g. The specific surface area of HPC aerogel dried by FD method was 5 m^2/g, while those of the HPC aerogel dried by $ScCO_2$ method with acetone solvent exchange was 40 m^2/g. This indicated the drying method effectived of on the surface area of the HPC aerogel as the drying methods can impact on the pore size. It was clearly seen in the BET surface area of HPC aerogels dried with the supercritical CO_2 method is higher than freeze drying method. Furthermore, the BET surface area was higher for the supercritical CO_2 with acetone solvent exchange compare to ethanol solvent exchange.

4.2.6. Fourier Transform Infrared Spectroscopy (FTIR)

ATR-FTIR provided a further investigation into the chemical cross-linking between the polymer chains by appearing new functional group after modification of the polymer. Figure 4.25 shows the ATR-FTIR spectra of the HPC before cross-linking (blue), HPC after cross linking and drying by freeze drying method (red) and the DVS spectrum (green).

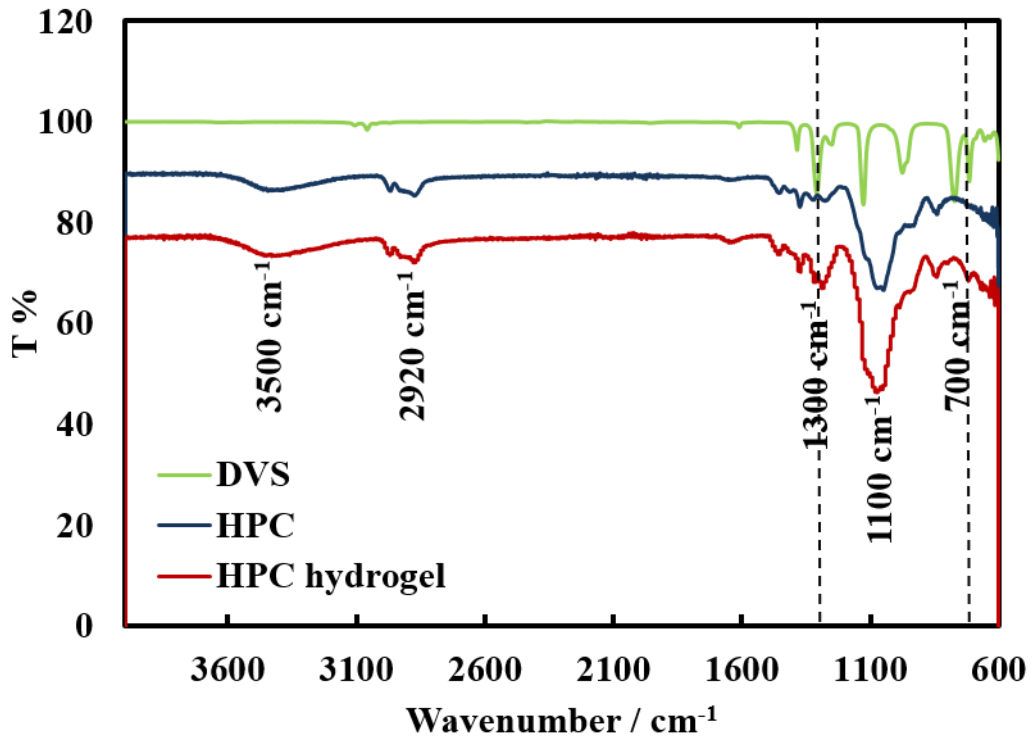

Figure 4.25. ATR-FTIR spectra of HPC (blue line) and HPC aerogel (red line), showing the changes in the spectra due to the cross-linking.

ATR-FTIR the spectra have a new absorption band, referring an evident change in the structure due to forming covalent bonds between the cellulose chains. HPC powder and hydrogel show broad peaks at 3300–3500 cm^{-1} were referred to (-OH) stretching due to a large number of hydroxyl groups on the HPC backbone. The peaks at 2920 cm^{-1} and

2880 cm^{-1} were assigned to (CH) stretching vibration. The sharp peaks at 1060–1150 correspond to the (C–O) and (C-O-C) stretching due to due to vibration from (C-O) in the aromatic ring in HPC. Furthermore, peak at 1450cm^{-1} referred to the (C-H) bending due to CH_2 groups. [47] HPC hydrogel spectra showed the appearance of new absorption bands at 1300 cm^{-1} after cross-linking of HPC with DVS. This band is attributed to the asymmetric stretching of S=O in the sulfone cross-linker. The symmetric stretching of S=O appears around 1130 cm^{-1}, thereby increasing the already large band present. A new absorption band at approximately 700 cm^{-1} corresponds to thioether CH_2S (CS) stretching.[48] These observations show that cross-linking has effectively taken place. It is obvious that no absorption bands for DVS in the cross-linked hydrogel, indicating the successful washing and removal of excess DVS, if any.

4.2.7. Thermal properties of HPC aerogel materials

4.2.7.1. Thermogravimetric analysis TGA of HPC aerogel materials

To compare the thermal decomposition profiles of DVS-crosslinked HPC against the HPC starting material, TGA was performed on FD-HPC hydrogels and HPC. Their thermal stability was measured using TGA under nitrogen gas flow, gas rate (60 ml/min) and heating rate (10 ºC /min). Figure 4.26 shows the TGA analysis of HPC powder (red line) and FD-crosslinked HPC hydrogel (blue line).

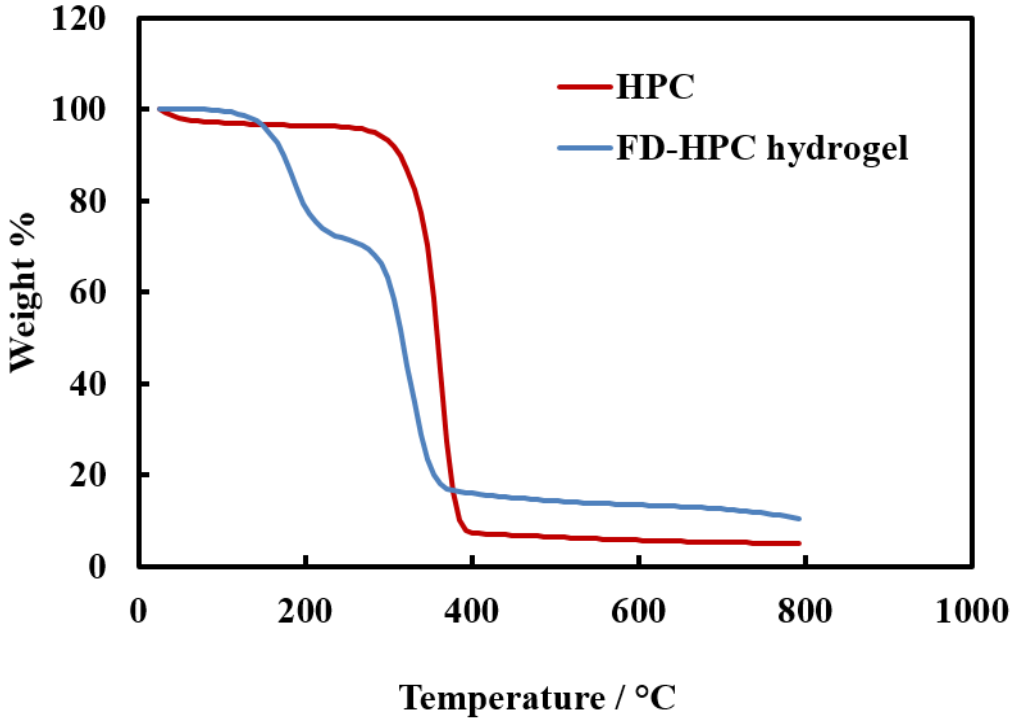

Figure 4.26. TGA curves of HPC aerogel after cross-linked by DVS (blue line) and HPC powder (red line).

In Figure 4.26, it is seen that the thermal decomposition of HPC that occurred at a temperature range of 200–400 °C which could be indicated to the depolymerisation and breakdown of glycosidic linkages of hydroxypropyl cellulose.[49] Whereas, the cross-linked HPC starts to show thermal degradation at around 140 °C, earlier than that of the HPC starting material. Which can be attribute this to breakdown to the degradation of the sulfone linkages. Other saccharide derivatives such as β-cyclodextrin also show earlier occurrence of thermal degradation after DVS cross-linking.[50]

4.2.7.2. Differential Scanning Calorimetry DSC

Differential Scanning Calorimetry (DSC) was used to identify any change in the heat flow with increasing the temperature of the starting HPC compared to the HPC aerogel. The DSC was used to show the chemical crosslinking between the polymer chains could change the glass transition temperature of the polymer. In Figure 4.27 different in endothermic peaks which are seen illustrate the phase transition of the HPC aerogel sample. First, for the HPC polymer (blue line) shows a broad low temperature endotherm at around 85˚C. Furthermore, a small discontinuity in the baseline at approximately 200°C, this could be considered to be the glass transitions of HPC.[51] While the DSC curve of HPC aerogel crosslinked by DVS (red line) another endothermic peak appears with increasing temperature. In addition, there are decreasing in the glass transitions of HPC to at around 152˚C. The observed change in endotherms may indicate the existence of chemical cross linking between HPC and DVS molecules, through–OH groups of HPC. This indicates that the thermal properties of HPC aerogel is changed by the chemical cross-linking.

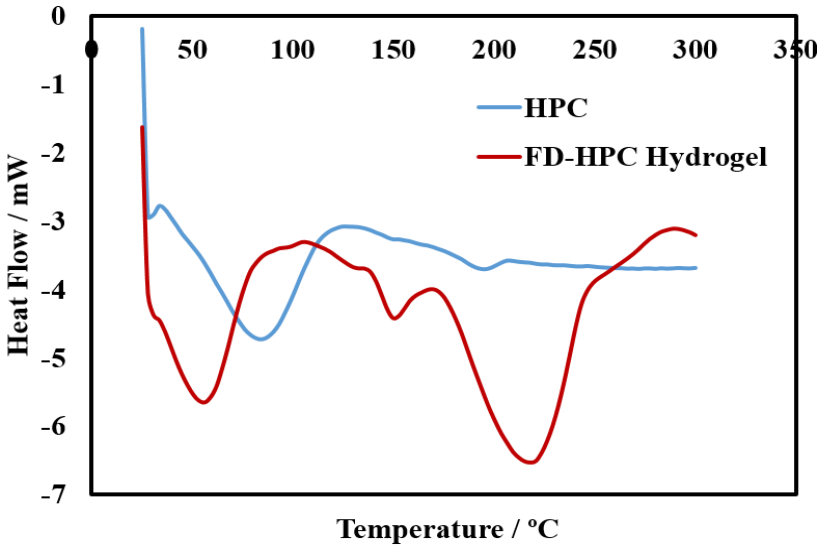

Figure 4.27. DSC curves of HPC aerogel after cross-linked by DVS (blue line) and HPC powder (red line).

4.2.8. X-ray diffraction analysis

Figure 4.28 depicts the XRD patterns of HPC powder and freeze-dried HPC hydrogel samples. The XRD showed a peak at proximately 2θ=20°. Another broad and diffused peak was observed at 2θ=45°. The diffraction pattern for HPC showed typical semi-crystalline nature of the polymer and is in agreement with other studies in the literature which show have suggested that HPC is semi-crystalline.[24, 52] The HPC aerogel showed similar semi-crystalline nature with a sharp peak at around 2θ=9°. The structure of the HPC aerogel is more crystalline and similar to the structure of the HPC polymer. Compared with the XRD pattern the intensity of HPC polymer shows an increased intensity of peak at around2θ=20° after cross-linked to form hydrogel.

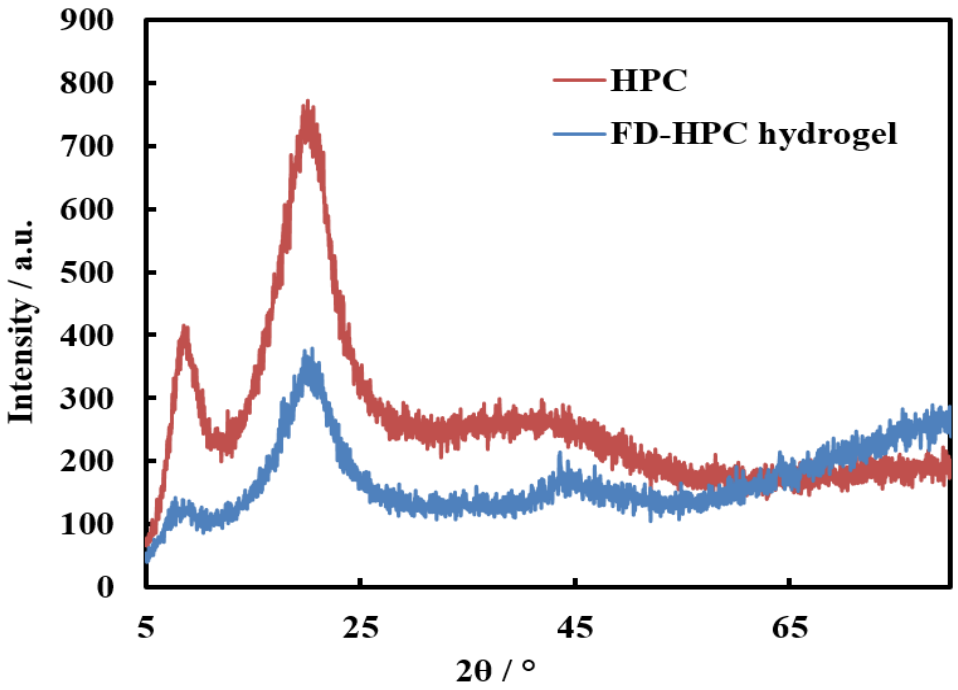

Figure 4.28. XRD patterns of HPC polymer and freeze-dried HPC hydrogel cross-linked via DVS

4.2.9. Mechanical testing of the HPC aerogel and hydrogel

4.2.9.1. Mechanical testing of the HPC aerogel

Preliminary studies of the mechanical properties of the HPC aerogels were performed using a compression test. The HPC cross-linked aerogels are flexible and not broken when compressed in an air environment as the chemical cross-linking remaines intact. Figure 4.29 shows the compressive stress-strain behaviour of the HPC aerogels in the air with a different concentration of HPC. The compressive strength of HPC aerogels increased with increased concentration of HPC and these results similar to the other study.[53] These

results indicate that aerogels prepared from higher concentrations of HPC would have a high chemical cross-linking and thus become harder than the lower concentration. The compressive stress of the HPC hydrogel prepared with 7.0 and 10.0 w/v % show gradually increased with increasing strain until the compressive strain was approximately 70%; above this point, it suddenly increased and showed typical ‘‘J’’ shape curves, indicating their high compressive strength.[54] While, the HPC hydrogel with 5.0 w/v% exhibits a lower compressive strength, which is undesirable in our application.

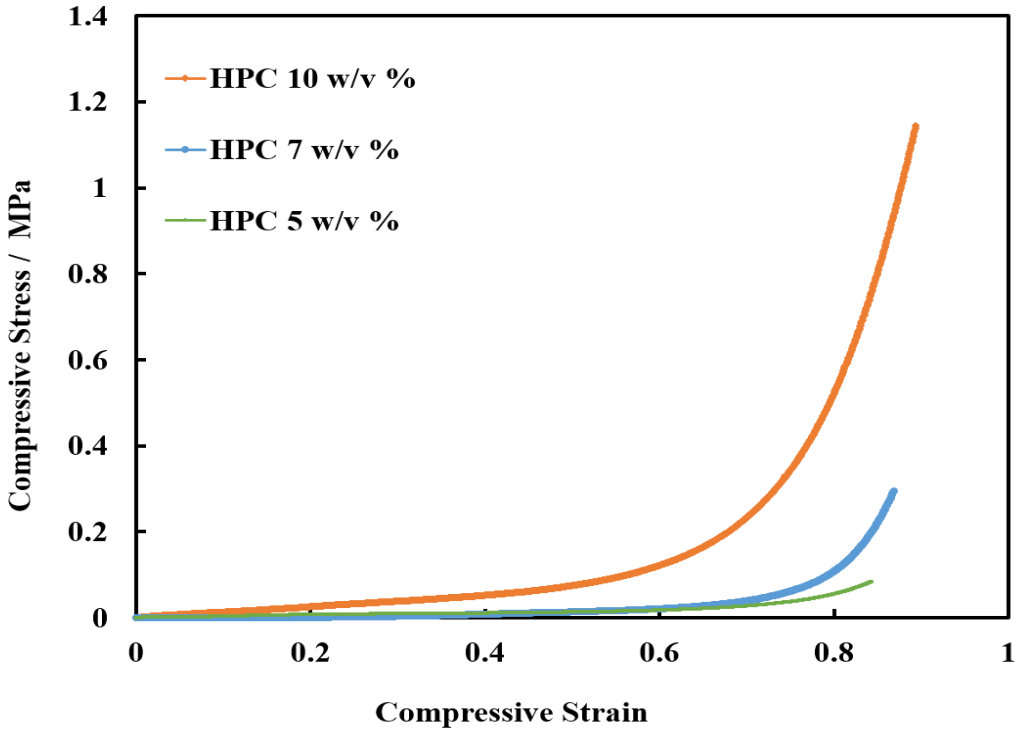

Figure 4.29. Compressive stress-strain curves of freeze drying HPC aerogels prepared from different concentration of HPC polymer 5.0, 7.0 and 10.0 w/v % with the constant concentration of the cross linker.

Young’s modulus is given in Figure 4.30 varies between 0.5-3.5 MPa for HPC aerogel monoliths for different HPC concentration. It was found that the Young modules increased with increasing the concentration of HPC polymer.

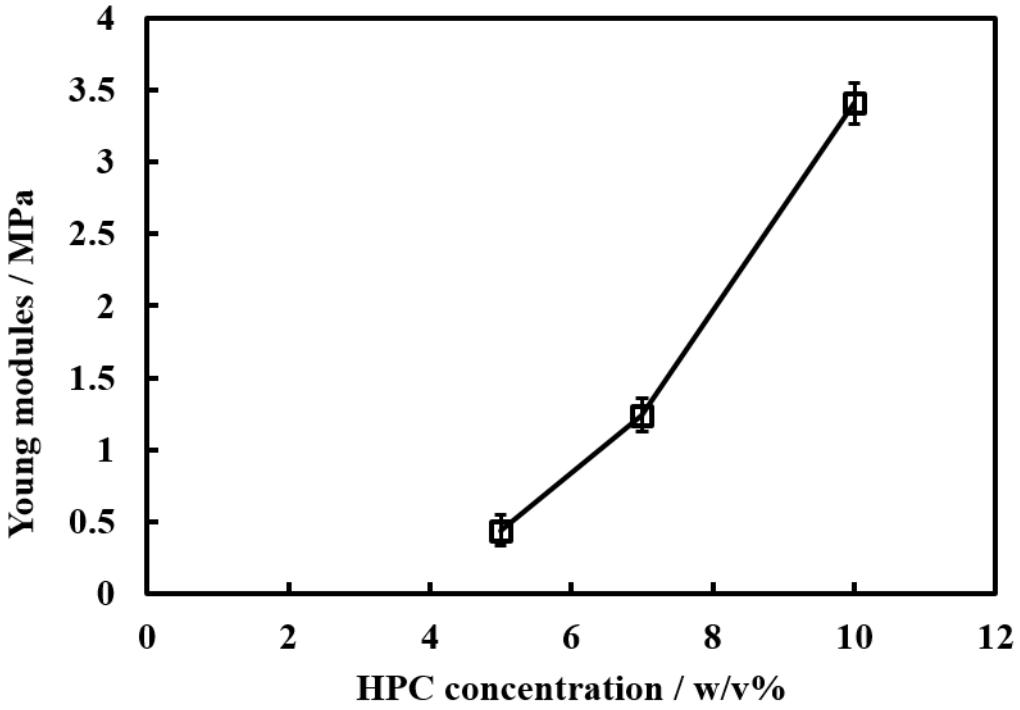

Figure 4.30. The effect of HPC concentration on the Young modules of HPC aerogel. Each data point is an average of three measurements and the error bars are the standard deviation.

The compression tests were carried out in both air and water environments. It can be seen in Figure 4.31 that the compression test of HPC aerogel showed higher compressive strength in the air environment rather than a compression test in a water environment. The reason behind this the HPC aerogel had many hydroxyl groups enabling to interact with water molecules by hydrogen bonds.

Figure 4.32 displays the compression test of HPC aerogel in the water environment in a number of cycles. The results show the elastic modulus decreased with time and the network structure was broken after 10 compression test cycles as shown in Figure 4.33 the photographic image of HPC aerogel in the water before and after 10 times compression. It can be seen the HPC hydrogel after one cycle of compression keeps the same size and shape without damage, while after 10 compression cycles show partially damaged.

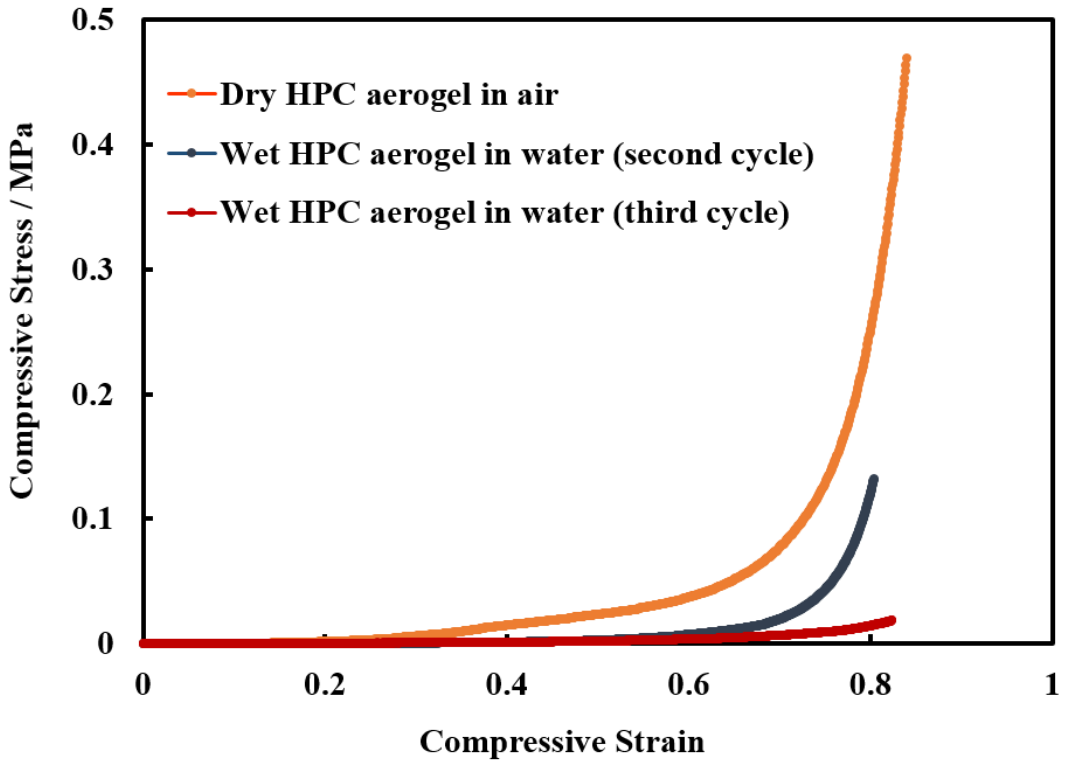

Figure 4.31. Compressive stress-strain curves of freeze drying HPC aerogels prepared from 7.0 w/v % HPC in the air and in water after 10 cycles.

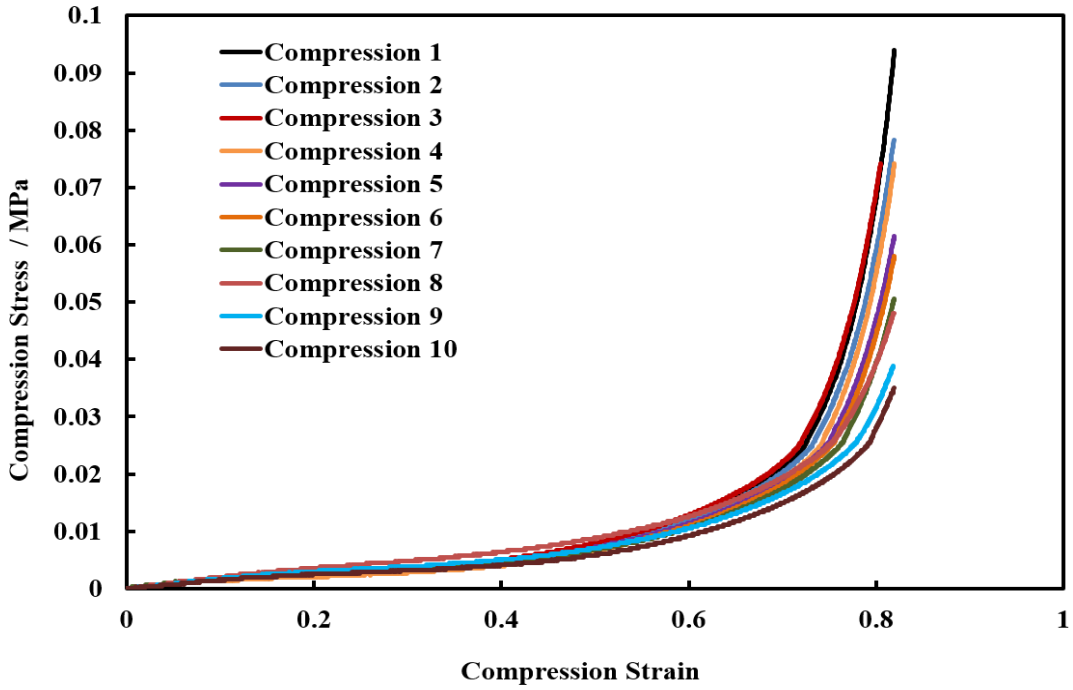

Figure 4.32. Compressive stress-strain curves of freeze drying HPC aerogels prepared from 7.0 w/v % HPC in the water after 10 cycles of compression test.

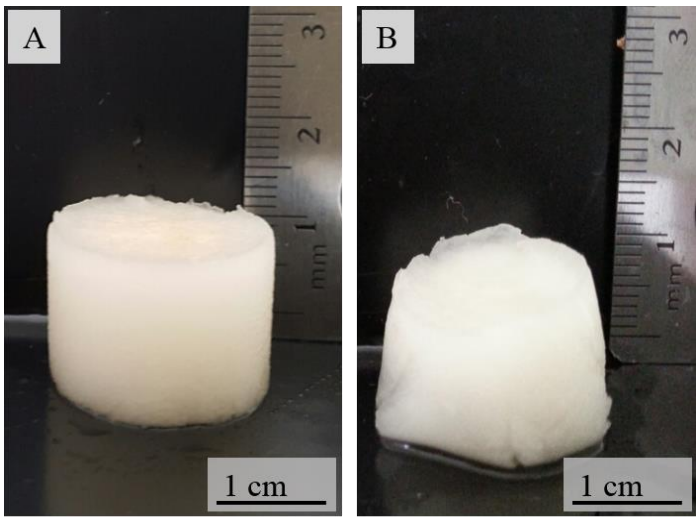

Figure 4.33. Photographs showing (A) HPC aerogel prepared by chemical cross- linking of 7.0 w/v % HPC and 1.3 w/v % DVS at LCST swollen by water after one cycle of compression test (B) after a number of cycles.

4.2.9.2. Mechanical testing of HPC hydrogel

Preliminary studies of the mechanical properties of the HPC hydrogel with different concentration of the starting polymer and crosslinker, different gelation temperature and pre-cross-linking time were studied using compression test.

4.2.9.2.1. Effect of HPC concentration

The initial HPC concentration plays a major role in the porosity and density of HPC hydrogel, it has also play a significant role in the development of hydrogel network structure and the mechanical properties of the produced hydrogel. The mechanical properties also affects by the gelation temperature due to HPC exhibited the LCST, which is keep the solution in the single-phase separation region of the phase diagram at temperature below the LCST or transfers the system into an unstable phase region at LCST due to spinodal decomposition of an initially homogeneous polymer solution occurs by moving into the unstable region and leads to two phase separation formation (which should produce interconnected structure desired). The mechanical tests have been studied at different HPC concentrations and temperature by moving from below the LCST into the unstable phase at LCST. The effects of HPC concentration on the compressive strength of HPC hydrogel is shown in Figure 4.34 for the sample prepared at LCST by TIPS method. The HPC hydrogel samples prepared at LCST showed a decrease in height of the sample and release the water from the sample network as a compressive load was applied. The Young modulus of HPC hydrogel (prepared at LCST) was calculated. The compression stress and strain curve of HPC hydrogel with various polymer concentration

and the Young modulus can be seen in Figures 4.35 and 4.36 respectively. The value of Young modulus increased from 0.03 MPa to 0.2 MPa with increase the HPC concentration from 5 w/v % to 10 w/v %. It can be seen that the compressive stress of HPC aerogels increased with increased concentration of HPC and these results are similar to other studies.[53] This coincides with the hypothesis that mechanical strength will increase with the incorporation of the polymer.

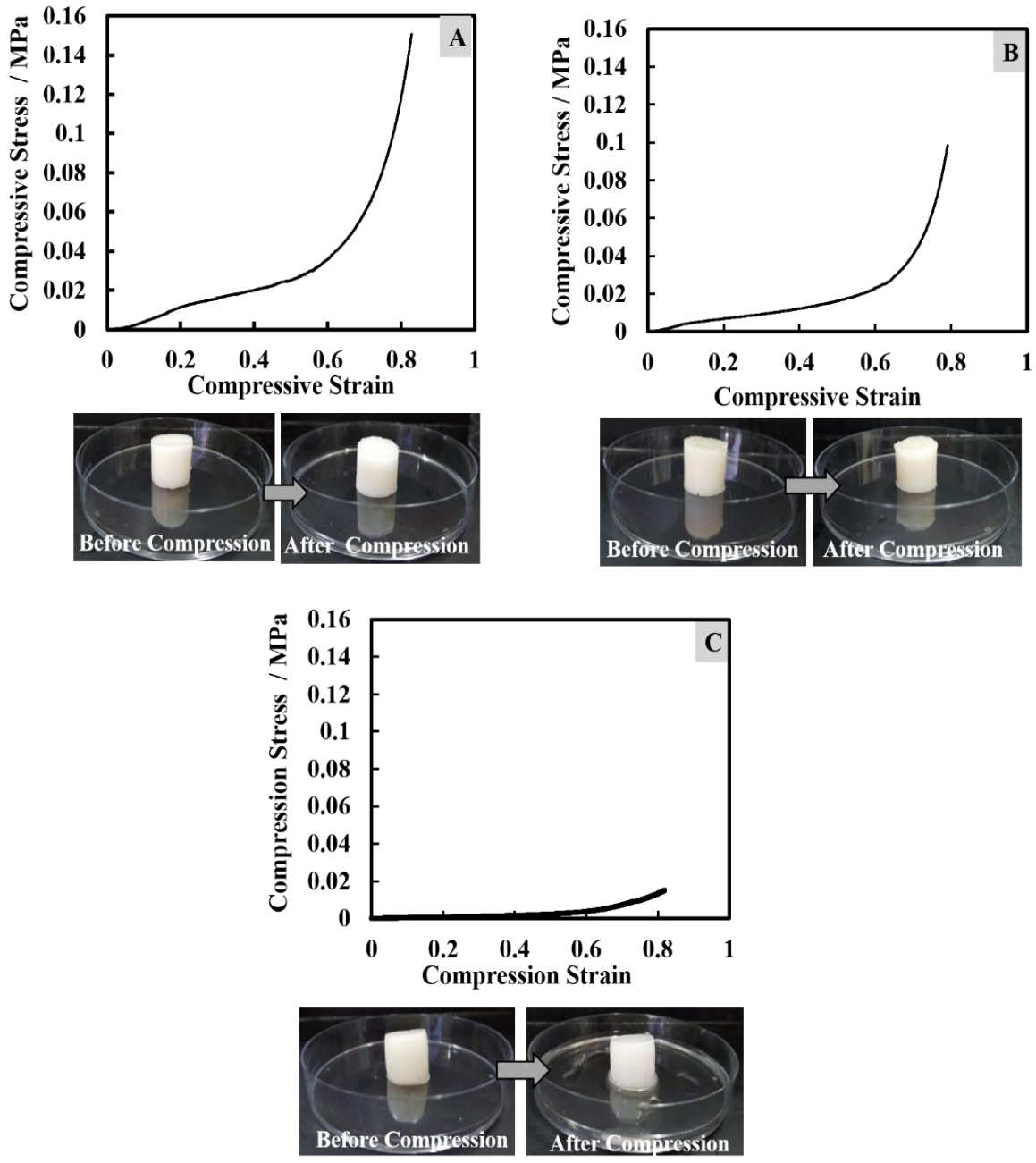

Figure 4.34. Compressive stress-strain curves of HPC hydrogel prepared from different concentration of HPC at LCST (A) 10.0 w/v % HPC (B) 7.0 w/v % HPC (C) 5.0 w/v % HPC.

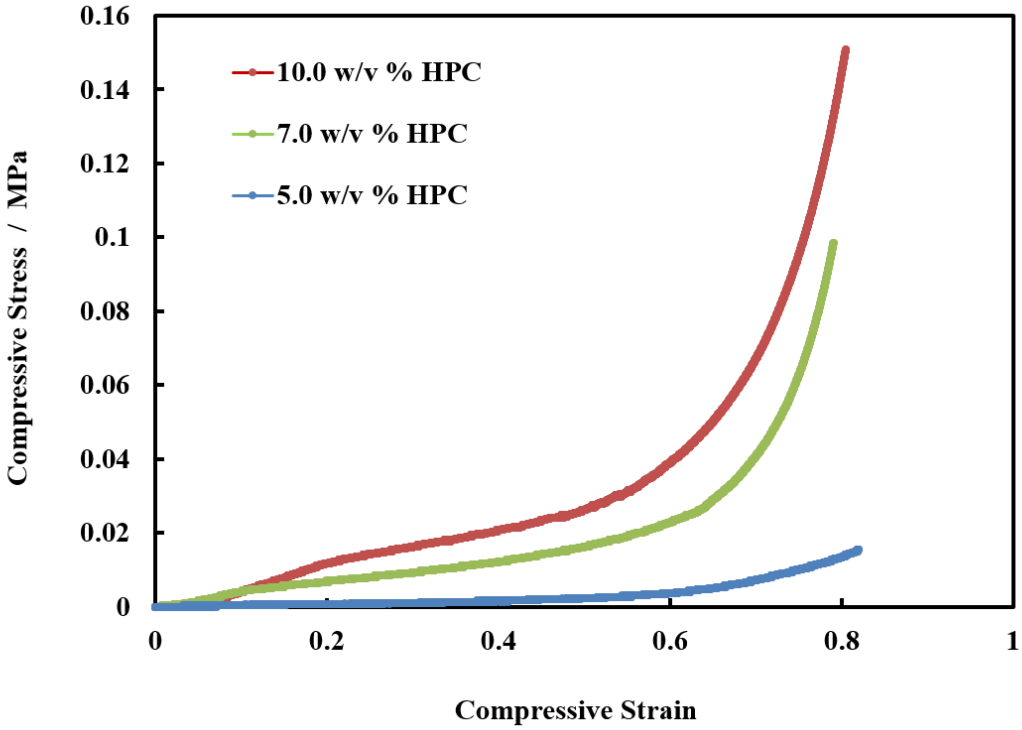

Figure 4.35. The variations of the compression stress and strain curve of HPC hydrogel with change the polymer concentration.

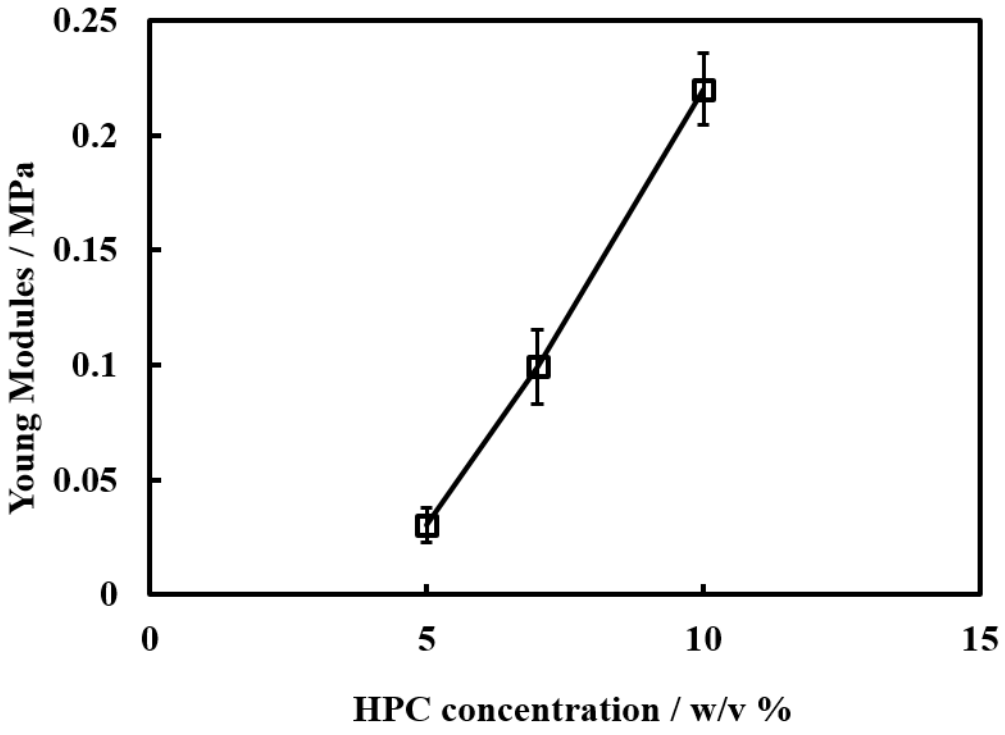

Figure 4.36. The effect of HPC concentration on the Young Modules of HPC hydrogel. Each data point is an average of three measurements and the error bars are the standard deviation.

Figure 4.37 for the HPC hydrogel with different concentration of HPC at a temperature below LCST. The HPC hydrogel prepared at a temperature below the LCST started to break into small particles under a compressive load. The value of the Young modulus was difficult to obtain.

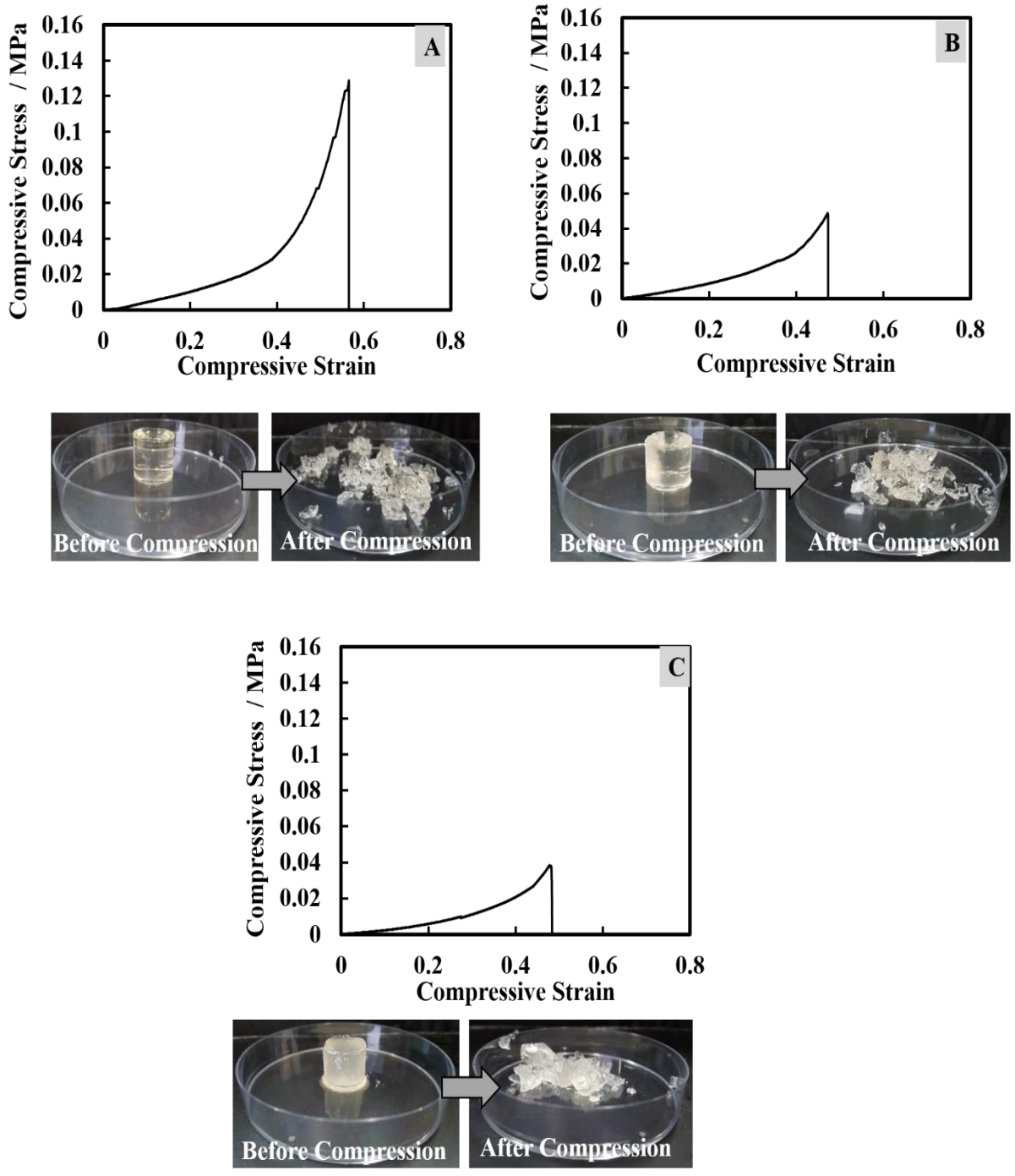

Figure 4.37. Compressive stress-strain curves of HPC hydrogel prepared from different concentration of HPC at temperature below the LCST (A) 10 wt. % HPC (B) 7.0 w/v % HPC (C) 5.0 w/v % HPC.

4.2.9.2.2. Effect of DVS concentration

The DVS cross-linker concentration and the gelation temperature are very important variables can affect the mechanical properties of HPC hydrogel. Figure 4.38 and 4.39 show the compressive stress-strain behavior of HPC hydrogel prepared at LCST at different concentration of DVS. Figure 4.40 shows the effect of DVS concentration on the Young modules of the produced hydrogel. As you can see in Figure 4.41 the compressive stress-strain behavior of HPC hydrogel prepared at below the LCST at different concentration of DVS.

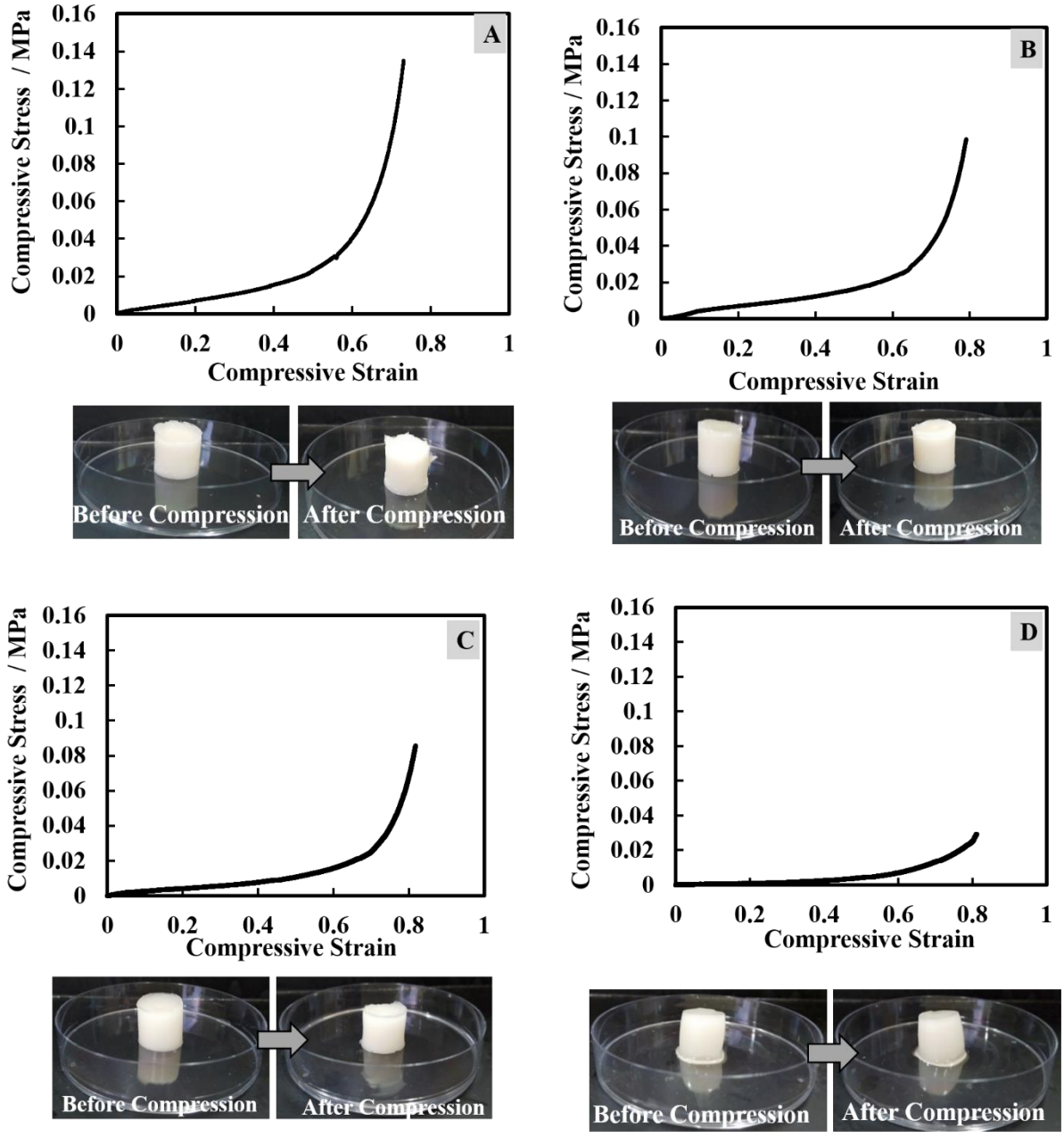

Figure 4.38. Compressive stress-strain curves of HPC hydrogel prepared from different concentrations of DVS at the LCST (A) 2.0 w/v % DVS (B) 1.3 w/v % DVS (C) 0.9 w/v % DVS and (D) 0.5 w/v % DVS.

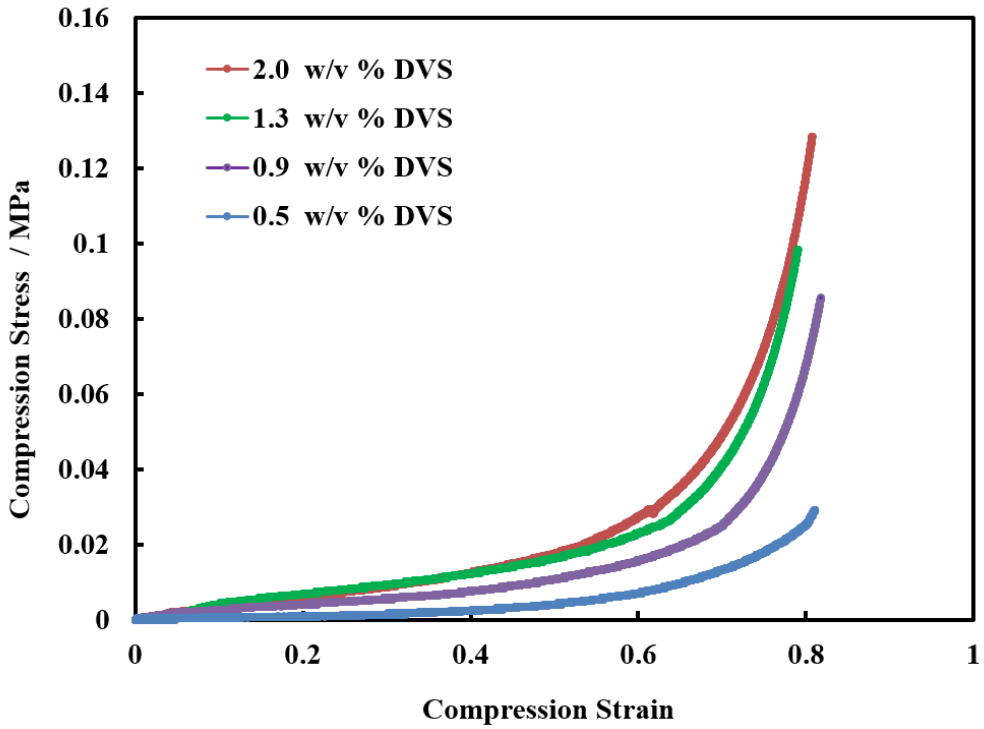

Figure 4.39. The variations of the compression stress and strain curve of HPC hydrogel with change the crosslinker concentration.

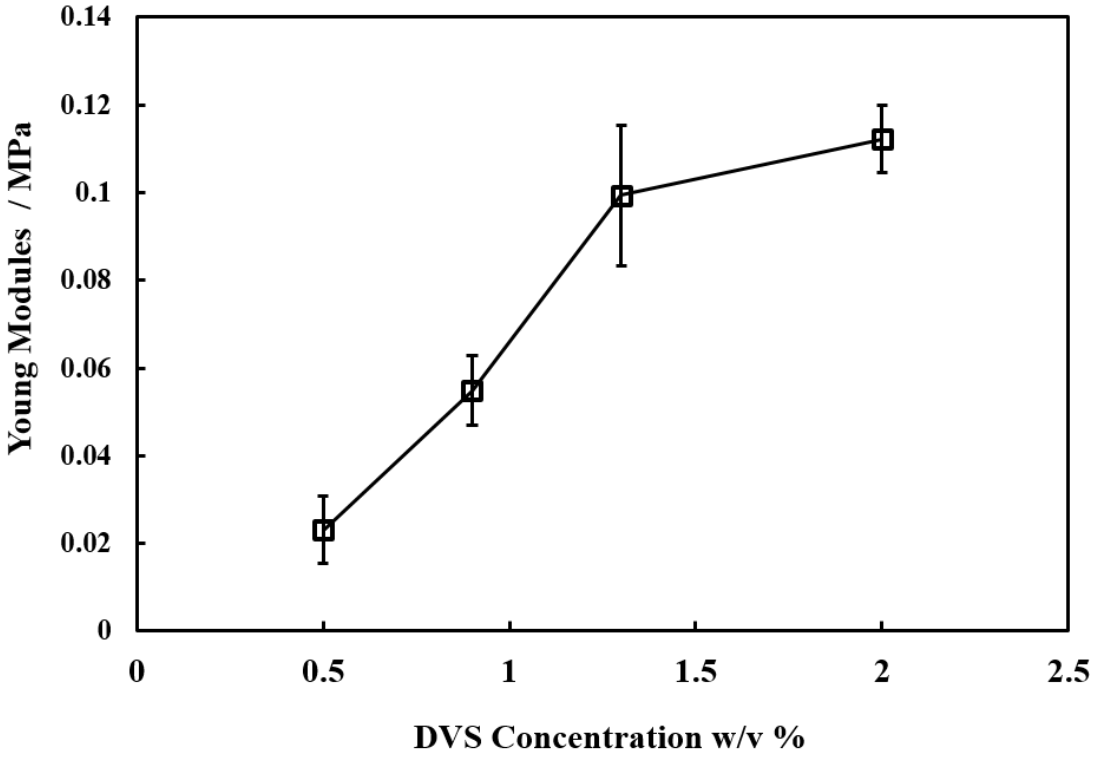

Figure 4.40. The effect of DVS concentration on the Young Modules of HPC hydrogel. Each data point is an average of three measurements and the error bars are the standard deviation.

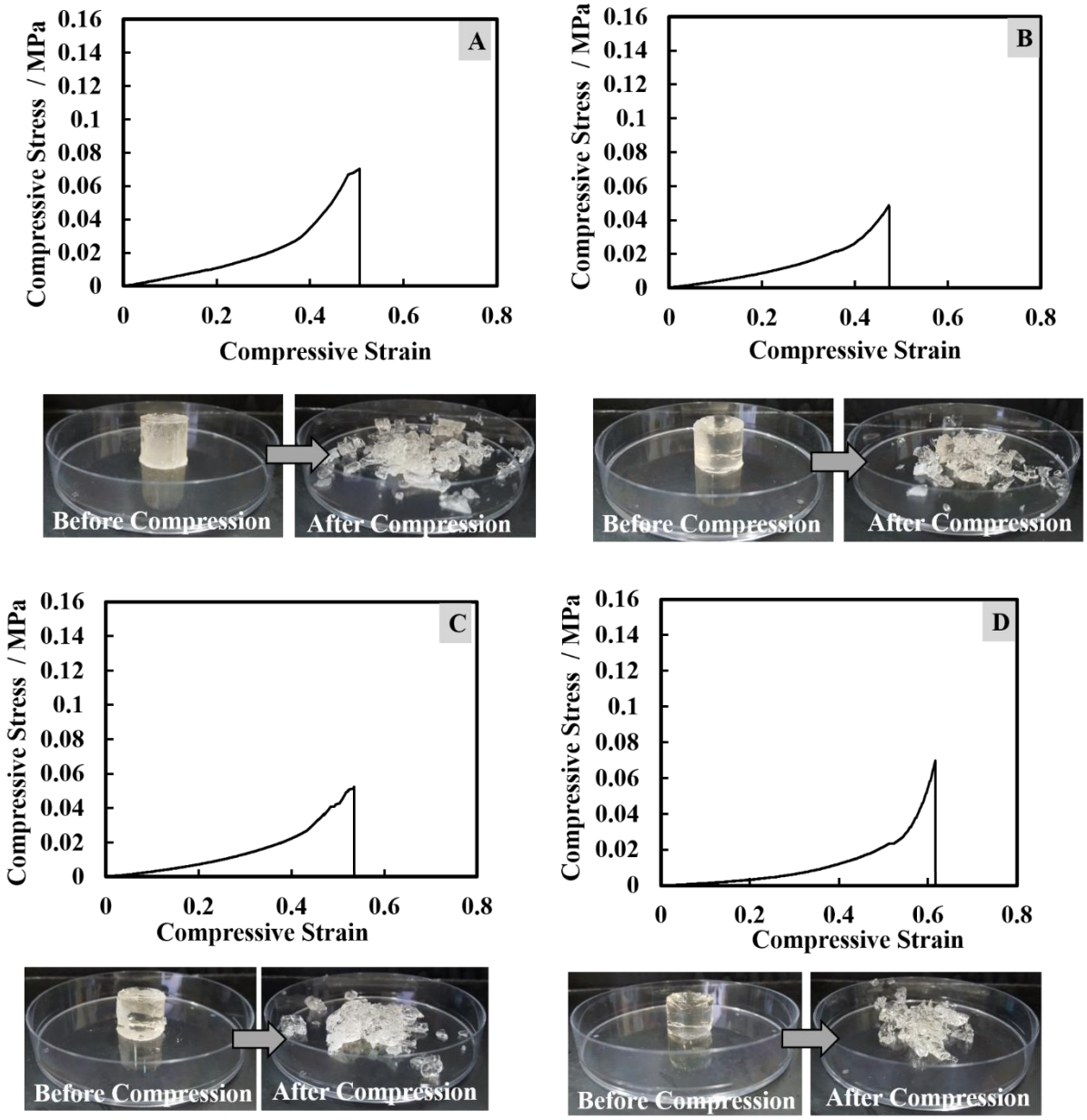

Figure 4.41. Compressive stress-strain curves of HPC hydrogel prepared from different concentrations of DVS at temperature below the LCST (A) 2.0 w/v % DVS (B) 1.3 w/v % DVS (C) 0.9 w/v % DVS and (D) 0.5 w/v % DVS.

It was observed that the compressive stress of HPC hydrogel increased with increased concentration of DVS. These results indicated that the hydrogel prepared from higher concentrations of DVS would have high chemical cross-linking would be harder than the lower concentration. The HPC cross-linked hydrogel prepared at LCST is flexible and not broken when compressed due to chemical cross-linking remained intact. The HPC hydrogel prepared at a temperature below the LCST was started to chip into small particles under a compressive load. Therefore, the value of Young modulus is difficult to

obtain. On the other hand, the HPC hydrogel samples which prepared at LCST show a decrease in height of the sample and released the water from the sample network as a compressive load is applied. The Young modulus of HPC hydrogel (prepared at LCST) was calculated. The value of Young modulus increased from to 0.02 MPa to 0.21 MPa with increasing the DVS concentration from 0.5 wt. % to 2.0 wt. %. The reason for that is when the polymer cross-linked is a high concentration of cross-linker, there could be more sites for crosslinkers to bond, which enhances the mechanical strength of the gel.

4.2.9.2.3. Effect of pre-crosslinking time

Effect of reaction time before phase separation (t_{BP}) on the mechanical properties have been studied. The cross-linking time before phase separation was changed from 0 to 7 hours while keeping the other parameters constant (HPC 7.0 w/v %, DVS 1.3 w/v % time during phase separation 6 hours). As seen in Figure 4.42 the colour of HPC hydrogel was changed with different pre-crosslinking time from 0 hours to 7 hours. It can be seen that the physical properties of the HPC hydrogel changed with change the reaction time before phase separation.The HPC hydrogel without pre-crosslinking time show weak hydrogel, while after 3 hours pre-crosslinking show stronger hydrogel. Figure 4.43 shows the compressive stress-strain curves of HPC hydrogel at different reaction time before phase separation from 1 to 7 hours.

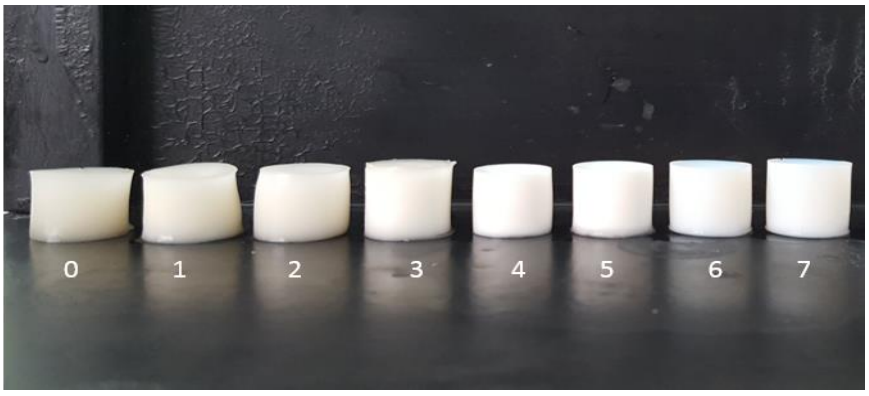

Figure 4.42. Photographic HPC hydrogels at the different pre-crosslinking time.

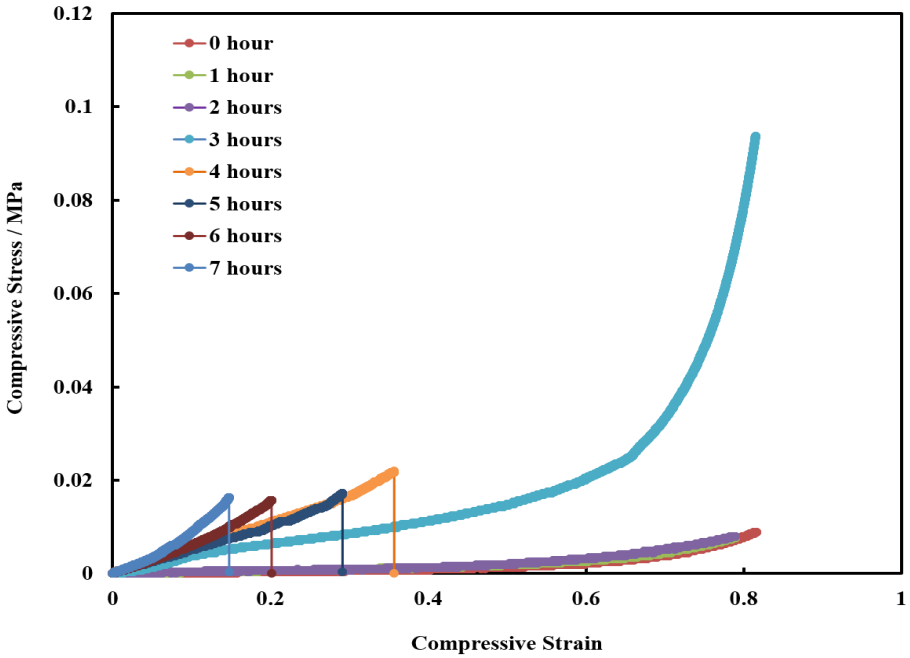

Figure 4.43. Compressive stress-strain curves of HPC hydrogel prepared from 7.0 w/v % HPC and 1.3 w/v % DVS with reaction time before phase separation from 1 to 7 hours.

HPC hydrogel at pre-crosslinking time from 0 to3 hours appear very soft with light brown colour, while at pre-crosslinking time from 4 to 7 the hydrogel begins to change to the white colour and has become stronger. The solution viscosity increased with increasing the reaction time before phase separation since the HPC chains become more and more cross-linked in the homogenous solution and that led to decline in the HPC chain mobility which decreases the rate of phase separation. As a result, the phase separation rate keeps on diminishing as the cross-linking reaction time before phase separation. Simultaneously, the crosslinking of polymer chains holds them into a three-dimensional structure, which may confine the space in which a polymer chain can move from other polymer chains during phase separation process.[31]

It is apparent that the mechanical properties have been affected strongly by the pre-cross linking time at a temperature below the LCST due to the level of crosslinking before phase separation will make polymer chains difficult to move from each other.

4.2.10. Shape recovery of HPC aerogel

The shape recovery ability of chemical cross-linking of HPC aerogel was tested. HPC aerogel caused variance in the shape after compressive deformation. Figure 4.44 shows the change in HPC aerogel after compression and after wetting the compressed sample.

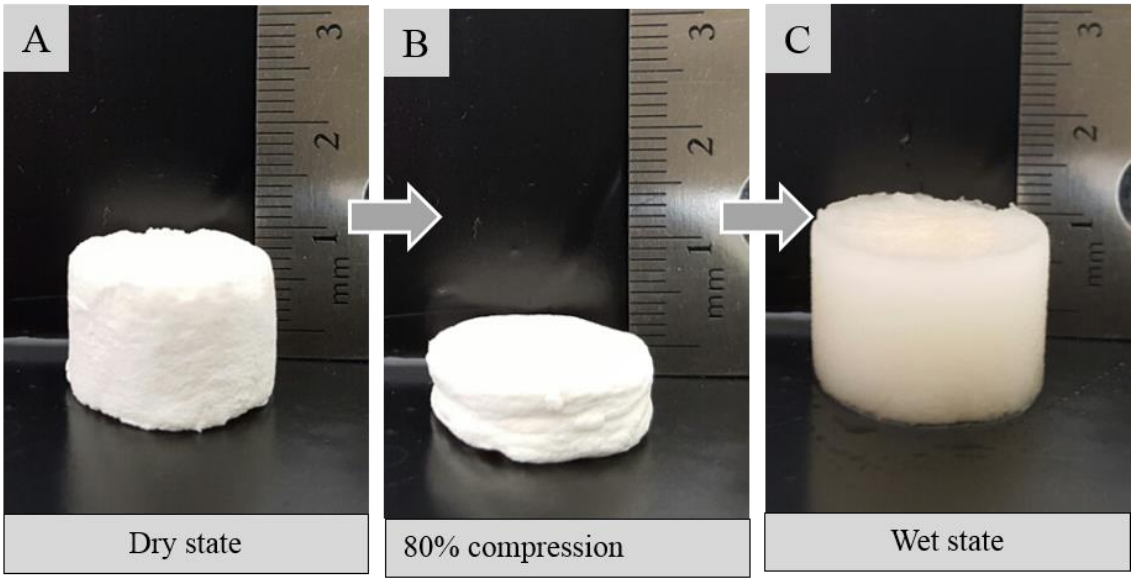

Figure 4.44. Photographs show shape recovery of HPC aerogel prepared by chemical crosslinking of 7.0 w/v % HPC and 1.3 w/v % DVS at 42 ºC (A) the original shape (B)compressed shape (C) wet shape after compressive.

As can be seen Figure 4.44 the compressed HPC aerogels stayed in compressed shape in the dry state, but after immersion it in the water the compressed HPC aerogel shape was immediately changed and showed substantially greater shape recovery properties. The HPC aerogel recovered to nearly 100% of the original shape within a few seconds after wetting due to the high absorption capacity of this material. It was clear that the HPC aerogel had excellent ductile behaviour, could be bent to large strains and subsequently expand back to nearly its original shape.

4.2.11. Swelling and deswelling behaviour of HPC hydrogel

4.2.11.1. The swelling ratio of HPC hydrogels

Cellulose hydrogels are able to change their volume when they are in contact with specific solvents, because of their excellent hydrophilic properties thus it has demonstrated a high swelling ratio.[55] The effect of preparation temperature on the swelling ratio of HPC hydrogels at different temperature and at constant pH, HPC and crosslinker concentration was investigated. Figure 4.45 shows photographic images of the swelling deswelling behaviour of the HPC hydrogels prepared with different gelation temperature, when the gel is transferred from 15 °C water to water at 50 °C. It can be seen that the HPC hydrogel prepared by TIPS method (LCST) shows obvious deswelling at 50 ºC when compared

with the HPC prepared at temperature below the LCST (RT), which is show negligible change towards changing the temperature. However, the HPC hydrogel prepared at RT shows marked change when freeing the sample in the liquid nitrogen before test the swelling properties (RTF).

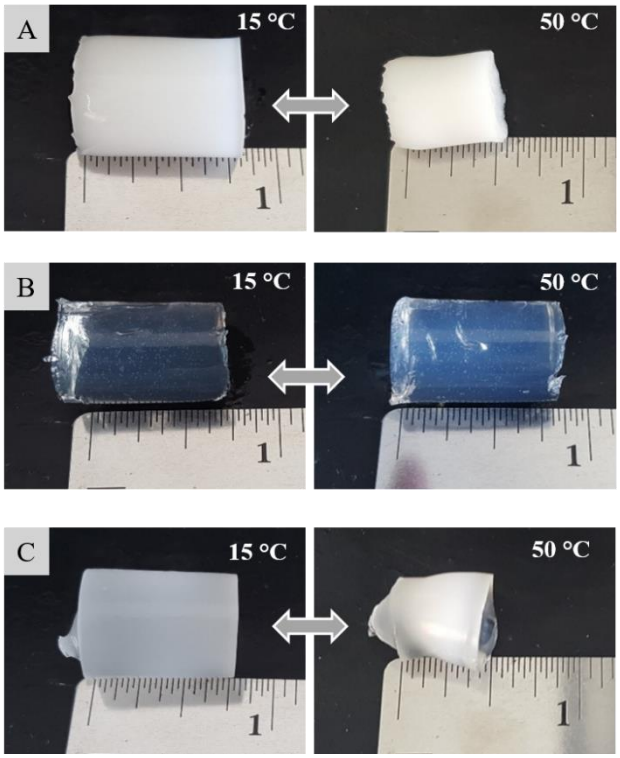

Figure 4.45. Photographic images HPC Hydrogel swelling deswelling when the gel is transferred from 15 °C water, below the HPC LCST, to water at 50 °C (above LCST), for porous HPC hydrogel (A) prepared at LCST (B) prepared at RT (below LCST) (C) prepared at RT (below LCST)and then frozen in the liquid nitrogen.

Figure 4.46 shows the Swelling Ratio (SR) as a function of temperature of the HPC hydrogels prepared at different gelation temperature which is at LCST by TIPS method (LCST), at temperature below the LCST (RT) and at temperature below the LCST then frozen by liquid nitrogen (RTF). As can be seen in Figure 4.46, the swelling ratio decrease with increase the temperature from 5 to 50 ºC with HPC hydrogel prepared at LCST. HPC hydrogel prepared at room temperature RT (22±2 ºC) showed constant swelling ratio with a change the temperature, but showed obvious deswelling with the same hydrogel, which prepared at room temperature but after preparation frozen in the liquid nitrogen RTF.

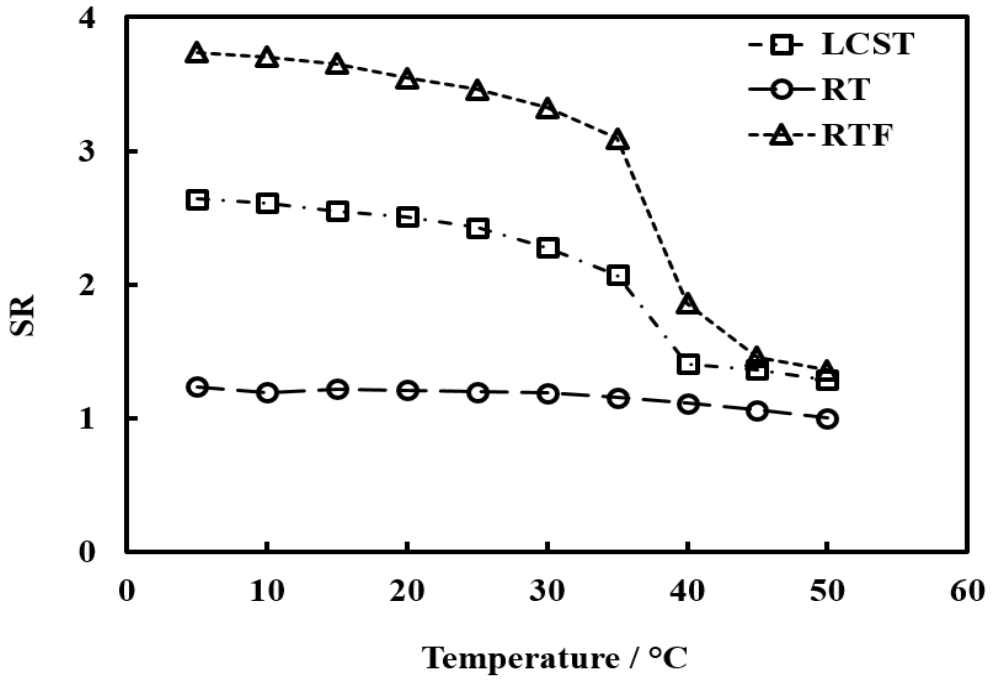

Figure 4.46. Swelling Ratio (SR) as a function of temperature of the HPC hydrogels prepared at different gelation temperature at LCST by TIPS method, at room temperature and at room temperature then freezing by liquid nitrogen.

At temperatures below LCST, the hydrogen bonds between the hydrophilic groups in polymer chains and water molecules are strong, which leads to good swelling properties of the HPC hydrogels in water. As the temperature is increased, these hydrogen bonds become weak and the hydrophobic interactions among hydrophobic side groups in the polymer chains become strong. At temperatures above LCST, hydrophobic interactions become dominant, and cause collapse and phase separation of the polymer chains. Therefore, as the temperature increased, the SR of HPC LCST and HPC RTF hydrogels decreases when the temperature is increased above the LCST due to the phase separation degree of HPC hydrogel is the greatest.[56] With increasing the temperature the deswelling level increased due to migration of water molecules from the gel phase to the surrounding water phase.[57] However, HPC RTF hydrogel quickly dehydrated and exhibited rapid deswelling with an increase in the temperature above the LCST might be the larger pores in the hydrogel matrix a reason for the rapid deswelling. Whereas HPC RT show no deswelling with an increase the temperature above the LCST. This might be because the water in this type of HPC hydrogel is prevented from diffusing out due to this hydrogel having a close porous structure as mentioned early in SEM images in this chapter (Figures 4.7 and 4.8) and the thick wall of this hydrogel did not allow loose the water to diffuse in or out easily. Generally, porous matrix in the hydrogel provides more space to accommodate water.[58, 59]

4.2.11.2. Kinetics of swelling and deswelling.

HPC hydrogel swelling kinetic were studied by measuring the degree of swelling with time. Figures 4.47 A and B depict the degree of deswelling and swelling as a function of time for HPC hydrogels based on different gelation temperature respectively. Figure 4.47 (A) shows deswelling kinetics of the HPC hydrogel with different preparation strategies at 50 ºC. HPC hydrogel prepared at room temperature then freezing by liquid nitrogen HPC RTF showed quick loss most of water after exposure to 50 ºC for 10 min. HPC LCST hydrogel exhibited a slower water loss in comparison with HPC RFT . However the HPC RT shows negligible loss of the water with increase in the temperature. Figure 4.47 (B) demonstrate reswelling kinetics of the HPC hydrogel at 15 ºC. HPC LCST hydrogel exhibited quicker and much water uptake in comparison with HPC RTF, whereas HPC RT shows slightly swelling with decrease the temperature below the LCST.

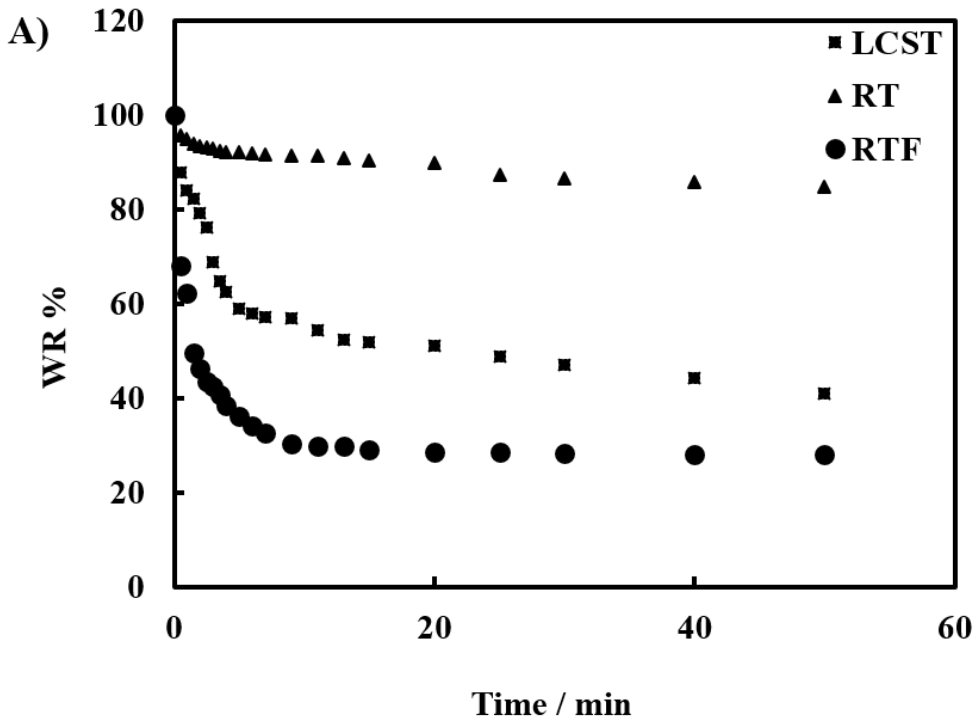

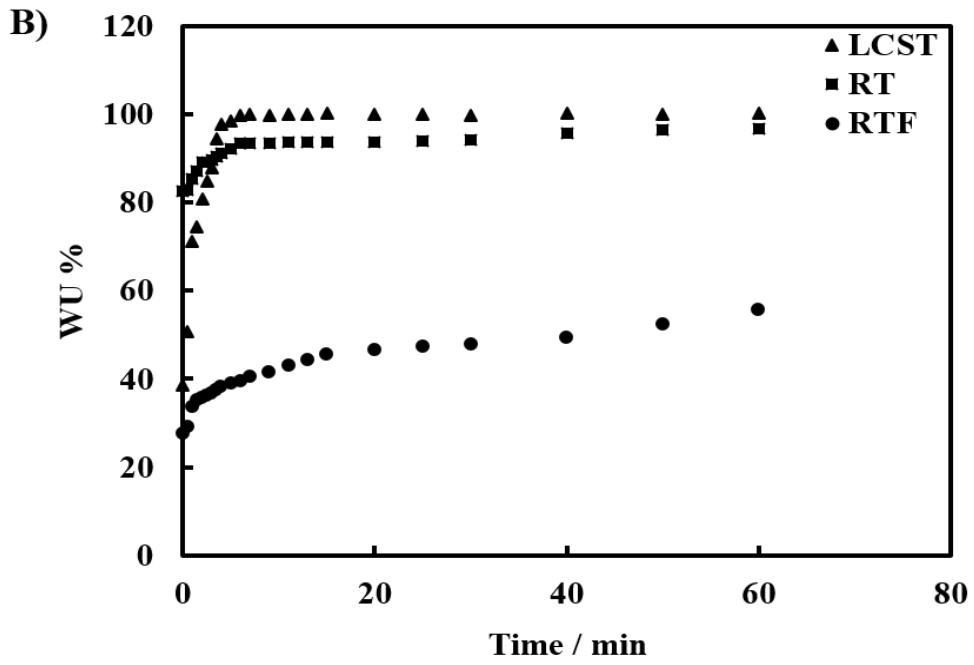

Figure 4.47. Kinetics of deswelling and swelling behaviour of HPC hydrogel prepared at different gelation temperature (LCST, RT, RTF) (A) Water retention ratio (WR) as a function of time for the HPC hydrogels, when plunged in a 50 °C water bath after initial equilibration at 15 °C (B) Water uptake ratio (WU) as a function of time for the HPC hydrogels, when plunged in a 15 °C water bath after initial equilibration at 50 °C.

It is clear that HPC LCST and HPC RTF hydrogels can shrink and lose water at temperatures above the LCST. These hydrogels can reach stable water retention in less than 10 min, although the level of stable water retention for each is different. Comparing the reswelling rate with deswelling rate for HPC LCST hydrogels, we find the deswelling rate is as fast as its swelling rate. However, the reswelling rate of the HPC RTF hydrogels is very slow and it only absorbs about 20% of the total reswelling water in 60 min. This suggested that the interconnected pores structure of HPC LCST allowed the gel to hold more water by capillary force and minimize water loss from the hydrogel.[60] This might be due to the porosity, pore structure and pore size of porous hydrogels changing with preparation approaches of hydrogels materials, such as phase separation and freeze-drying techniques.[61] The porosity within the hydrogels specially with open pores structure allowed for a quicker response to specific external stimuli due to rising further capillary absorption.[62] HPC RT hydrogels show negligible swelling and deswelling in compared with HPC LCST. In addition, experimentally it was found that many bubbles appeared on the surface of the HPC LCST hydrogel, but no bubbles appeared on the surface of the HPC RT hydrogel. As described above that might be because water in this type of HPC

hydrogel is prevented from diffusing out or in due to this hydrogel had close porous structure as mentioned early in SEM images in this chapter (Figures 4.7 and 4.8) and the thick wall of this hydrogel did not allow loose the water to diffuse in or out easily. Generally, the porosity of HPC hydrogels on the preparation techniques and it has a strong impact on their swelling and deswelling rate and found that the hydrogels with highly porous structure exhibited rapid swelling and deswelling rate.

4.2.11.3. Reversibility of swelling and deswelling processes.

The reversibility of the swelling-deswelling processes for HPC hydrogels was evaluated by performing cycles (one sample tested for each type of HPC hydrogel which prepared by different gelation condition). The samples were first equilibrated in distilled water at 15 °C for 24 h. Then, they were plunged in 50 °C distilled water for 10 min and were weighted at predetermined time intervals (every 30 s the first 4 min, then every 1 min for the last 6 min). They were then plunged back in 15 °C distilled water for another 10 min and were weighted at the same time intervals. The last two steps were repeated twice, for a total of three cycles for three samples prepared at LCST by TIPS method, at below LCST and at below LCST then freezing by liquid nitrogen as shown in Figure 4.48. It can be seen the HPC hydrogel prepared at LCST exhibits a dramatically fast response rate at temperatures cycled around the LCST. Whereas HPC RT, which prepared by gelation at temperature below the LCST shows slight or negligible swelling deswelling behaviour.

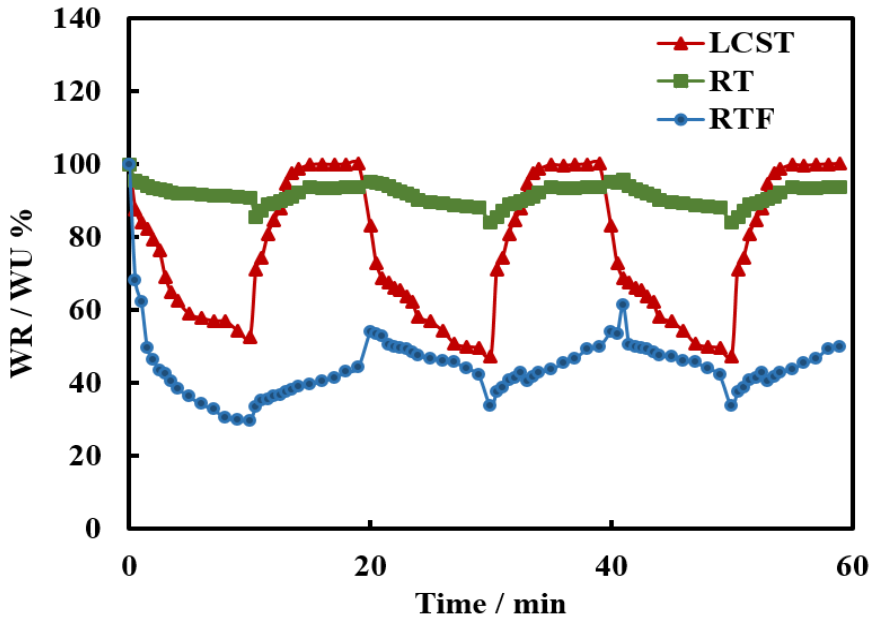

Figure 4.48. Deswelling and swelling cycles of HPC hydrogels at 15 and 50 °C, illustrating the reversibility of (red line) prepared at LCST by TIPS method (green line) at room temperature (blue line) at room temperature then freezing by liquid nitrogen.

The reversibility of the swelling/deswelling processes for HPC hydrogels was also evaluated by performing cycles. The samples were first equilibrated in distilled water at 15 °C for 24 h. Then, they were plunged in 50 °C distilled water for 1 hour and were weighted. They were then plunged back in 15 °C distilled water for another 1 hour and were weighted. The last two steps were repeated 10 times the swelling- deswelling reversibility cycle for the same above three samples as shown in Figure 4.49 shows

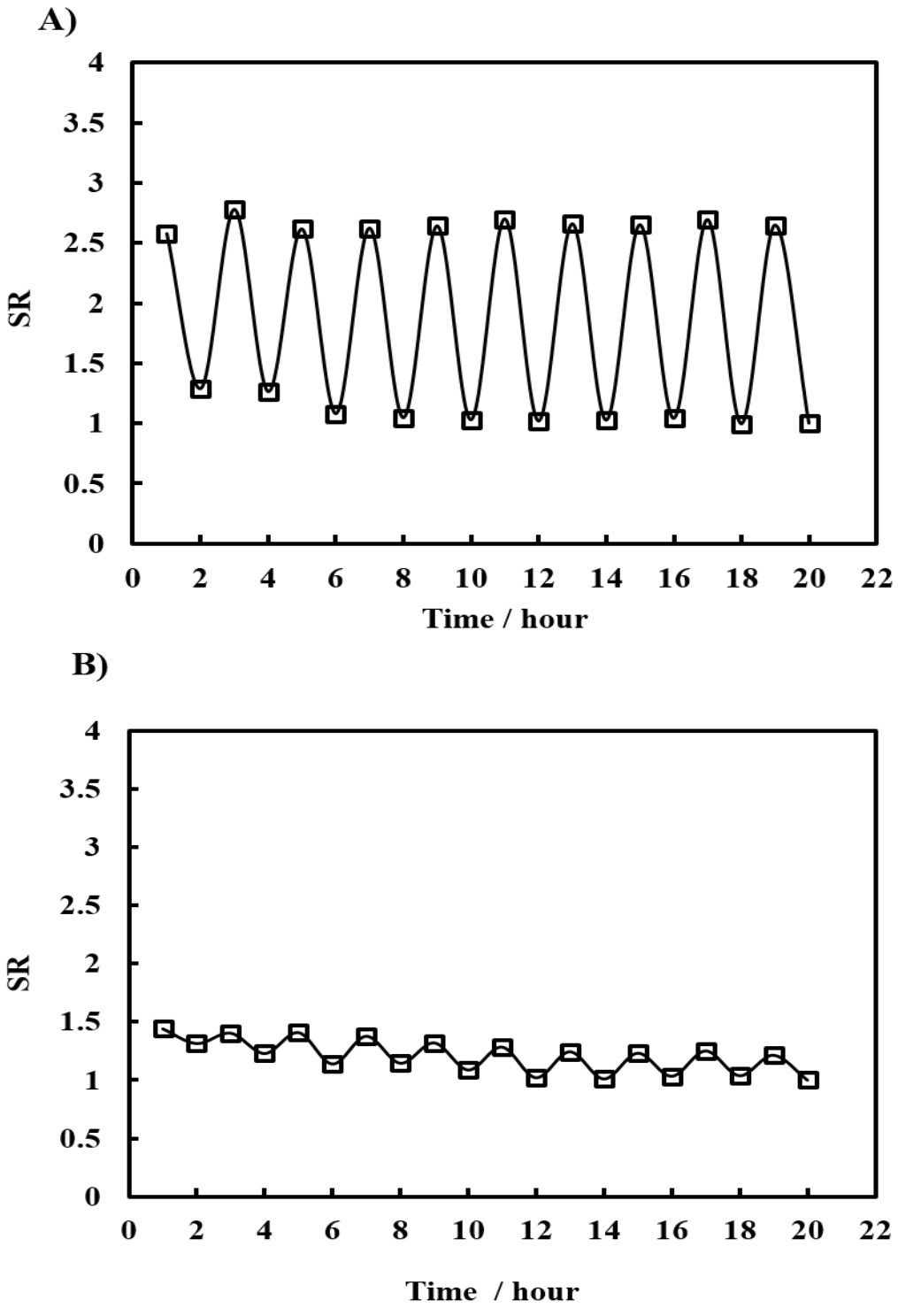

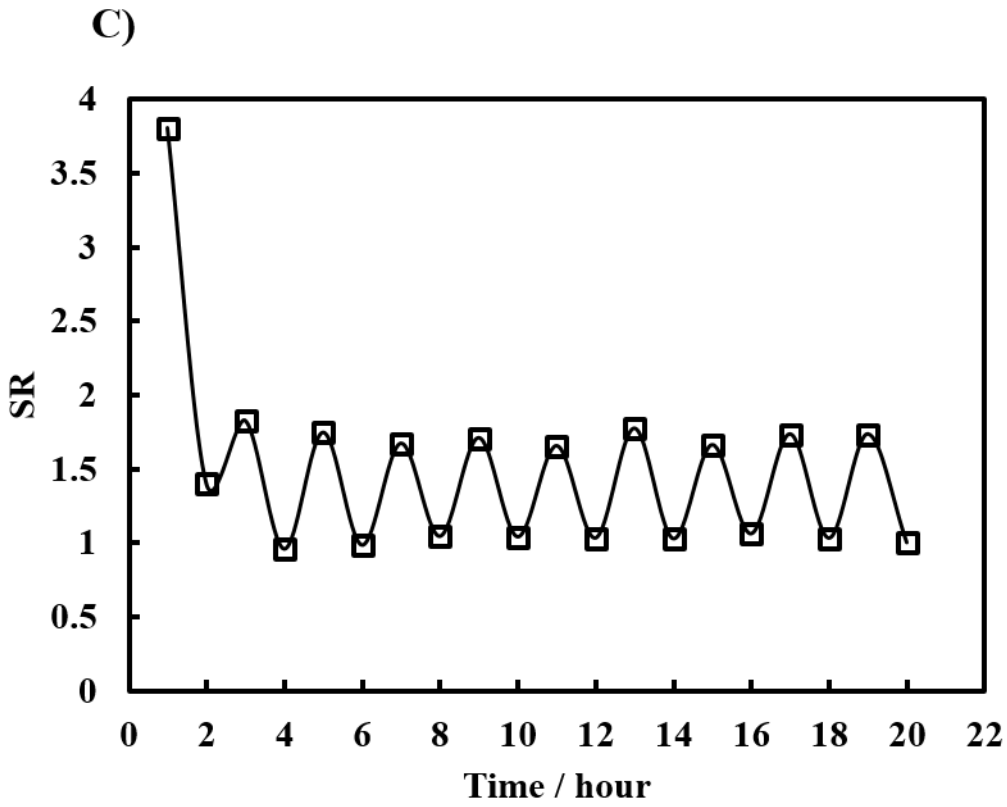

Figure 4.49. Reversibility cycle of swelling–deswelling as a function of time by varying the temperature from 15 to 50 °C of the HPC hydrogel prepared at (A) the LCST (LCST) (B) Below the LCST (RT) and (C) below the LCST and then freezing by liquid nitrogen (RTF).

The HPC hydrogel prepared at the LCST exhibited a dramatically fast response rate at temperatures cycled around the LCST in all reversibility of swelling and deswelling methods used.

The swelling reversibility of the HPC hydrogels in water at temperature between 15 and 50 ºC of HPC prepared at LCST showed the ability to quickly absorb and reabsorb the swelling medium upon changing the temperature. This could be due to the structure of the polymers with large numbers of pores connected to one another to form capillary channels causing rapid diffusion and releasing of the swelling medium into the network structure, thus, contributing to its quick response toward temperature change.[63]

HPC RTF displayed rapid loss of the water in the first cycle and then very slow swelling and deswelling in comparison with HPC LCST. This might be due to the porosity, pore structure and pore size of porous hydrogels changing with preparation approaches of hydrogels materials, such as phase separation and freeze-drying techniques.[61] Water uptake of HPC LCST, which was much higher than that of the hydrogel prepared at room temperature and then freezing. The porosity within the hydrogels with open pores

structure allowed for a quicker response to specific external stimuli due to increased capillary absorption.[62] Indeed, the porous network may allow for the solvent to flow simultaneously by convection and diffusion, finally reducing the swelling time and enhancing solvent uptake. Whereas HPC RT, prepared by gelation at room temperature showed slight or negligible swelling deswelling behaviour. The results indicated that the HPC hydrogel morphology significantly affected by the freeze drying preparation method.

4.2.12. Rheology

In order to obtain information about the mechanical properties of the HPC hydrogels prepared at LCST the rheology measurements were made of the HPC hydrogel with shear stress. The storage modulus (G′) describes the elasticity of polymers whereas the loss modulus (G″) reflects the dissipated energy as a characteristic of the viscous properties.[64] The behaviour of G′ and G″ was studied by increasing the stress at the same temperature and then increase the temperature with the same range of stress for the same HPC hydrogel sample. The stress dependence of G′, G″, for HPC hydrogels over the stress range of 1–400 pa as a function of temperature is depicted in Figures 4.50 and 4.51 respectively. For each temperature the G′ of HPC hydrogel firstly decreased slightly and then decreased dramatically with increasing stress, in contrast, the G″ of HPC increased continuously with increasing stress. Figure 4.52 shows a sudden decrease of G′ with increase the temperature at range 35–55 °C with different shear stress indicated the collapse of the HPC hydrogel due to the phase separation at the LCST. In addition to that the storage modules decrease with increase the shear stress from 100 to 400 pa.

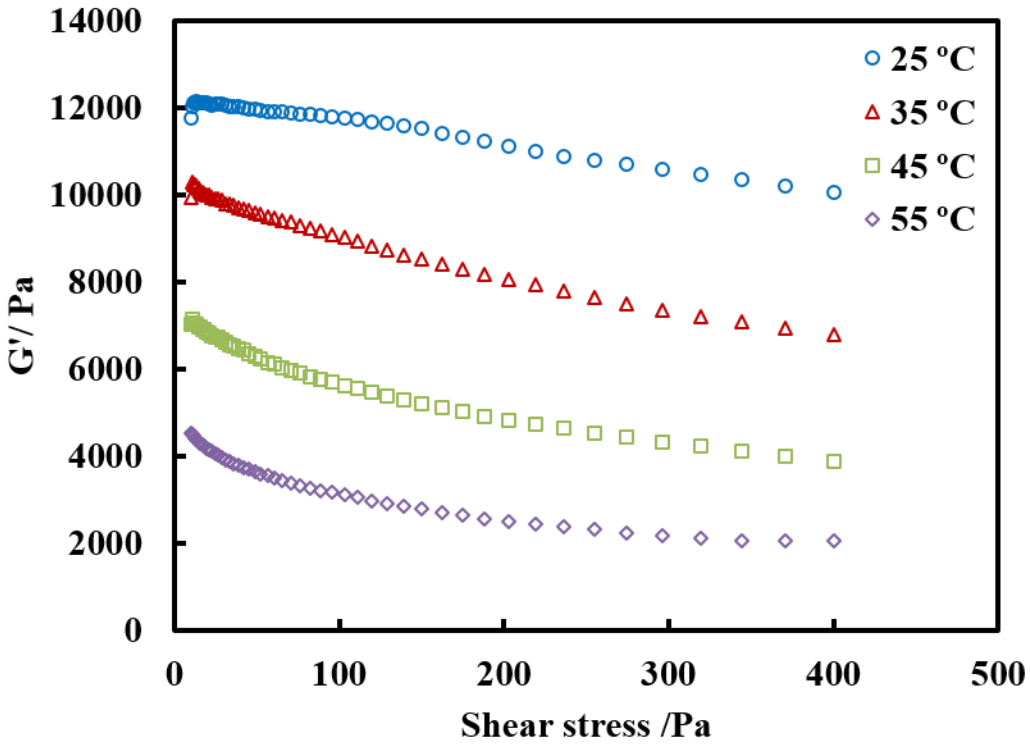

Figure 4.50. The storage modulus (G′) of HPC hydrogel as a function of temperature. The shear stresses from 10 Pa to 400 Pa. Note that the frequency used was constant and always 1 Hz.

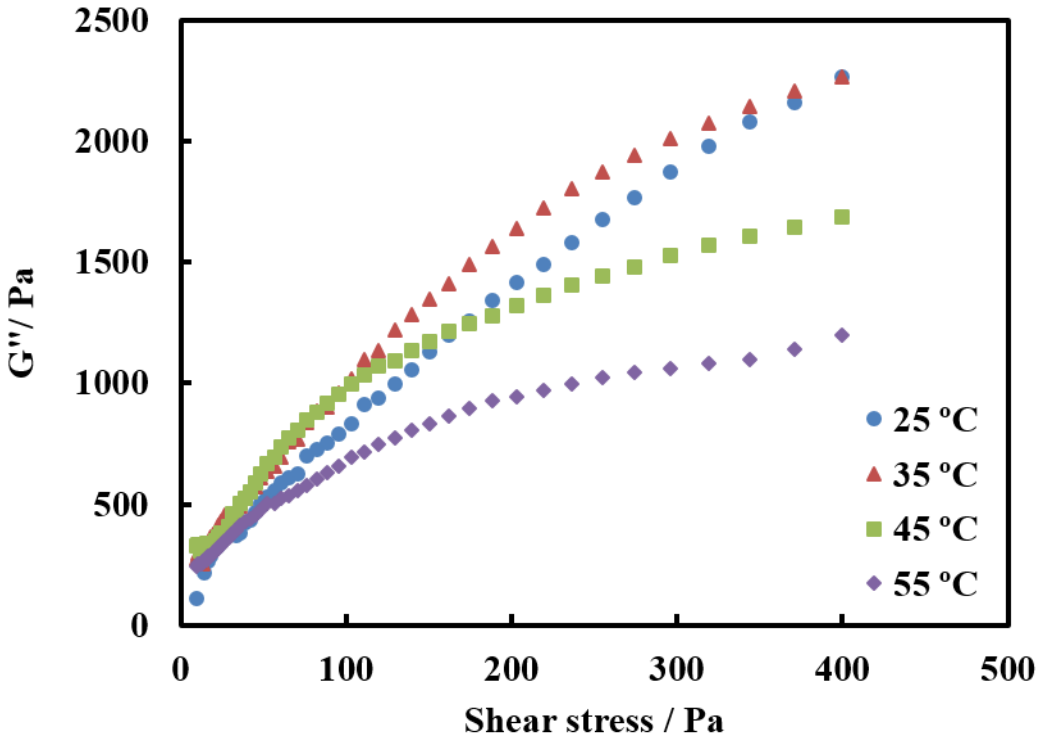

Figure 4.51. The Loss modulus (G″) of HPC hydrogel as a function of temperature. The shear stresses from 10 Pa to 400 Pa. Note that the frequency used was constant and always 1 Hz.

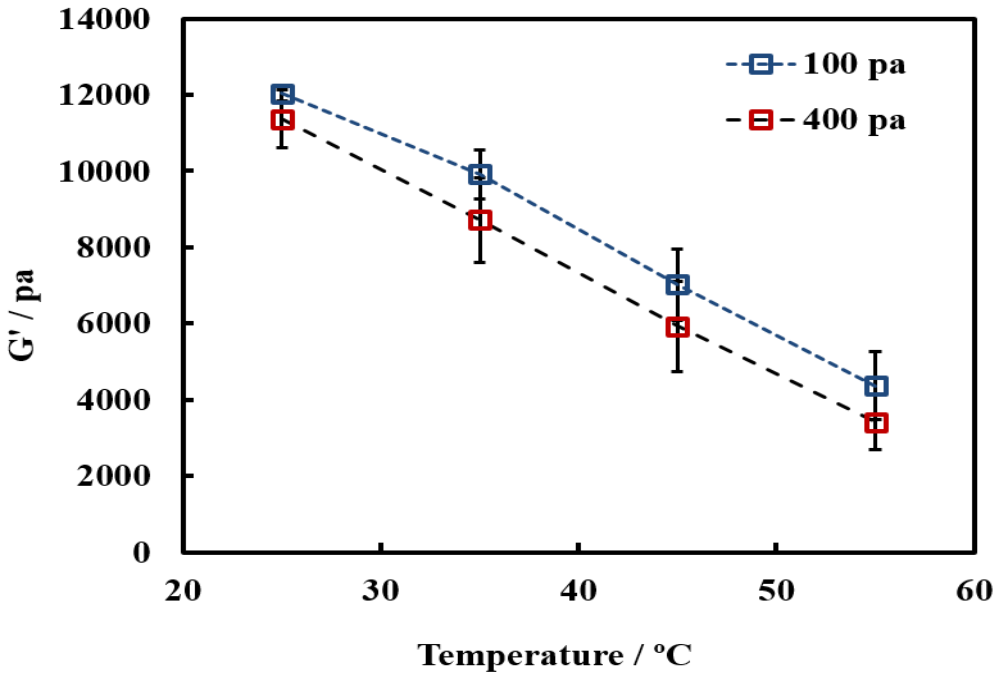

Figure 4.52. The storage modulus of HPC hydrogel as a function of temperature at shear stresses 100 and 400 Pa. Each sample was measured in triplicate and the error bars are the standard deviation.

The storage modules G′ decreased slightly with increase the temperature, but decreased with increasing temperature above the LCST due to the phase separation above this temperature.[32] As the temperature increased, the loss modulus (G″) increased and the storage modulus (G′) decreased. However, the storage modulus (G′) is still higher than the loss modules (G″) at all shear stress values, indicating the gel-like nature of the material. The HPC hydrogels do not reach to the cross-point (G′ and G″ assume the same value at the same shear stress). This implies the strength of the chemical crosslinking in the HPC hydrogels.[6]

4.3. Conclusions

In summary, a chemically cross-linked macroporous HPC hydrogel has been successfully synthesized by using DVS as cross linker in alkaline media. HPC a well-known a thermoresposive polymer exhibited LCST at 42 °C, thus the preparation of HPC hydrogel was influenced by gelation temperature, which impacts the properties of the resulting hydrogel. Firstly, the cross-linked HPC hydrogel was prepared at the LCST of HPC solution via modified TIPS method. Secondly, the porous HPC hydrogel the gelation was complete at temperatures below the LCST of HPC. In-depth investigations the characterization of HPC hydrogels were carried out to investigate parameters that affect the hydrogel properties. The cross-linked HPC hydrogel prepared by the TIPS method showed interconnected pores with pores size approximately 1–8 µm in diameter. This morphology arises from spinodal decomposition during the phase separation when complete gelation at the LCST in this method. The morphology of the HPC hydrogel with complete gelation at a single temperature, which is below the LCST connected honeycomb-like pores with bigger pore size. Originally at this gelation temperature the HPC hydrogel had closed pores as mentioned in the literatures.[31, 32] The main reason behind that pore structure was growth of relatively large ice crystals prior freeze-drying process. Furthermore, it is important to note that the HPC aerogel showed no observed shrinkage during the freeze drying process. This was attributed to the strength of the crosslinking in the polymer network. The mechanical properties of the HPC hydrogels prepared by both process were also investigated via compression test and rheology measurements. It was found that the Young modulus of the hydrogel prepared by TIPS method increased linearly with an increase in the polymer and cross linker concentrations. This hydrogel can be compressed to an approximately 20% height of the original size without fracture and exhibited the predominant mechanical properties of toughness and softness and were showed shape recovery, with approximately 100% of the original shape recovered within a few seconds maintained their structure during loading reloading. Rheological measurements confirmed a decrease in the Young modulus with increased the temperature which goes through a minimum when the temperature is 42 °C the LCST due to the phase separation of the HPC hydrogel at this temperature.

This chapter reported preparation and characterizations of temperature depend HPC hydrogel by different methods; firstly, by completing gelation at temperature below the LCST; second preparation method by developed TIPS process. Previous work in literature has shown the possibility of preparing interconnected HPC hydrogel via TIPS method by increasing the temperature at phase separation above the LCST of HPC. Here,

the heat setting of the phase separation keep at LCST of the polymer with adjust the pre-cross linking time. The mechanical properties of the HPC hydrogel by TIPS method controlled to the most desirable properties in our application by varying the gelation time before phase separation. Thus, this modification results interconnected macroporous HPC hydrogel with high mechanical properties of toughness and softness, this allowed to use this hydrogel for water purification for number of cycles.

4.4. References

1. Y. Hwang, J. Y. Park, O. S. Kwon, S. Joo, C.-S. Lee and J. Bae, *Applied Surface Science*, 2018, **429**, 258-263.
2. A. Olad, H. Zebhi, D. Salari, A. Mirmohseni and A. Reyhanitabar, *Journal of Porous Materials*, 2018, 1-11.
3. S. Garg and A. Garg, *Asian Journal of Biomaterial Research*, 2016, **2**, 163-170.
4. E. M. Ahmed, *Journal of advanced research*, 2015, **6**, 105-121.
5. A. Sannino, C. Demitri and M. Madaghiele, *Materials*, 2009, **2**, 353-373.
6. D. Pasqui, M. De Cagna and R. Barbucci, *Polymers*, 2012, **4**, 1517-1534.
7. X. Shen, J. L. Shamshina, P. Berton, G. Gurau and R. D. Rogers, *Green Chemistry*, 2016, **18**, 53-75.
8. W. A. Petka, J. L. Harden, K. P. McGrath, D. Wirtz and D. A. Tirrell, *Science*, 1998, **281**, 389-392.
9. C. Wang, R. J. Stewart and J. KopeČek, *Nature*, 1999, **397**, 417-420.
10. P. Matricardi, F. Alhaique and T. Coviello, *Polysaccharide Hydrogels: Characterization and Biomedical Applications*, CRC Press, 2016.
11. Z. Wang, S. Liu, Y. Matsumoto and S. Kuga, *Cellulose*, 2012, **19**, 393-399.
12. D. Klemm, B. Heublein, H. P. Fink and A. Bohn, *Angewandte Chemie International Edition*, 2005, **44**, 3358-3393.
13. A. Bashari, A. Rouhani Shirvan and M. Shakeri, *Polymers for Advanced Technologies*, 2018.
14. S. Jain, P. S. Sandhu, R. Malvi and B. Gupta, 2013.
15. C. Clasen and W. M. Kulicke, *Progress in Polymer Science*, 2001, **26**, 1839-1919.
16. N. A. Peppas, P. Bures, W. Leobandung and H. Ichikawa, *European Journal of Pharmaceutics and Biopharmaceutics*, 2000, **50**, 27-46.
17. A. E. Coukouma and S. A. Asher, *Sensors and Actuators B: Chemical*, 2018, **255**, 2900-2903.
18. M. Mahinroosta, Z. J. Farsangi, A. Allahverdi and Z. Shakoori, *Materials today chemistry*, 2018, **8**, 42-55.
19. X. Qiu and S. Hu, *Materials*, 2013, **6**, 738-781.
20. I. Roy and M. N. Gupta, *Chemistry & biology*, 2003, **10**, 1161-1171.
21. Y. Qiu and K. Park, *Advanced drug delivery reviews*, 2001, **53**, 321-339.
22. D. Schmaljohann, *Advanced drug delivery reviews*, 2006, **58**, 1655-1670.
23. M. A. Ward and T. K. Georgiou, *Polymers*, 2011, **3**, 1215-1242.

24. X. Liu, Y. Zhou, W. Nie, L. Song and P. Chen, *Journal of materials science*, 2015, **50**, 6113-6123.
25. R. Gottlieb, C. Kaiser, U. Gohs and K. F. Arndt, 2007.
26. S. Suto and M. Yoshinaka, *Journal of materials science*, 1993, **28**, 4644-4650.
27. C. Q. Song, M. H. Litt and I. Manas-Zloczower, *Macromolecules*, 1992, **25**, 2166-2169.
28. Y. Bai, Z. Zhang, M. Deng, L. Chen, C. He, X. Zhuang and X. Chen, *Polymer International*, 2012, **61**, 1151-1157.
29. X. Lu, Z. Hu and J. Schwartz, *Macromolecules*, 2002, **35**, 9164-9168.
30. S. M. O'Connor and S. H. Gehrke, *Journal of applied polymer science*, 1997, **66**, 1279-1290.
31. B. G. Kabra, S. H. Gehrke and R. J. Spontak, *Macromolecules*, 1998, **31**, 2166-2173.
32. S. G. Hirsch and R. J. Spontak, *Polymer*, 2002, **43**, 123-129.
33. J. Cai, S. Kimura, M. Wada, S. Kuga and L. Zhang, *Chemsuschem*, 2008, **1**, 149-154.
34. Y. Y. Han, X. X. Zhang, X. D. Wu and C. H. Lu, *ACS Sustain. Chem. Eng.*, 2015, **3**, 1853-1859.
35. H. Geng, *Carbohydrate polymers*, 2018, **186**, 208-216.
36. R. Bansil and G. Liao, *Trends in polymer science*, 1997, **5**, 146-154.
37. R. Yoshida, K. Sakai, T. Okano and Y. Sakurai, *Journal of Biomaterials Science, Polymer Edition*, 1995, **6**, 585-598.
38. R. Gavillon and T. Budtova, *Biomacromolecules*, 2007, **9**, 269-277.
39. R. H. Ras, X. Tian and I. S. Bayer, *Handbook of Nanocellulose and Cellulose Nanocomposites*, 2017, 731-760.
40. R. Subrahmanyam, P. Gurikov, P. Dieringer, M. Sun and I. Smirnova, *Gels*, 2015, **1**, 291-313.
41. C. Appaw, R. D. Gilbert, S. A. Khan and J. F. Kadla, *Cellulose*, 2010, **17**, 533-538.
42. N. Pircher, S. Veigel, N. Aigner, J.-M. Nedelec, T. Rosenau and F. Liebner, *Carbohydrate polymers*, 2014, **111**, 505-513.
43. E. In and H. Naguib, 2015.
44. K. S. Sing, *Pure and applied chemistry*, 1985, **57**, 603-619.
45. H. Sehaqui, Q. Zhou and L. A. Berglund, *Composites Science and Technology*, 2011, **71**, 1593-1599.

46. M. Chen, X. Zhang, A. Zhang, C. Liu and R. Sun, *Cellulose*, 2016, **23**, 1325-1334.
47. L. Yan, Q. Shuai, X. Gong, Q. Gu and H. Yu, *CLEAN–Soil, Air, Water*, 2009, **37**, 392-398.
48. M. W. Ellzy, J. O. Jensen and J. G. Kay, *Spectrochimica Acta Part A: Molecular and Biomolecular Spectroscopy*, 2003, **59**, 867-881.
49. K.-Y. Lee, T. Tammelin, K. Schulfter, H. Kiiskinen, J. Samela and A. Bismarck, *ACS applied materials & interfaces*, 2012, **4**, 4078-4086.
50. M. H. Mohamed, C. Wang, K. M. Peru, J. V. Headley and L. D. Wilson, *Molecular Pharmaceutics*, 2017, **14**, 2616-2623.
51. A. Gómez-Carracedo, C. Alvarez-Lorenzo, J. Gómez-Amoza and A. Concheiro, *Journal of Thermal Analysis and Calorimetry*, 2003, **73**, 587-596.
52. M. Trivedi, G. Nayak, S. Patil, R. M. Tallapragada and R. K. Mishra, 2015.
53. X. Yang and E. D. Cranston, *Chemistry of Materials*, 2014, **26**, 6016-6025.
54. C. Chang, K. Han and L. Zhang, *Polymers for Advanced Technologies*, 2011, **22**, 1329-1334.
55. C. Chang, B. Duan, J. Cai and L. Zhang, *European polymer journal*, 2010, **46**, 92-100.
56. X.-Z. Zhang and R.-X. Zhuo, *Langmuir*, 2001, **17**, 12-16.
57. L. Westman and T. Lindström, *Journal of Applied Polymer Science*, 1981, **26**, 2545-2559.
58. X.-Z. Zhang, Y.-Y. Yang and T.-S. Chung, *Langmuir*, 2002, **18**, 2538-2542.
59. J. Huang, X.-L. Wang, W.-S. Qi and X.-H. Yu, *Desalination*, 2002, **146**, 345-351.
60. N. V. Gupta and H. Shivakumar, *Iranian journal of pharmaceutical research: IJPR*, 2012, **11**, 481.
61. A. Salerno, R. Borzacchiello and P. A. Netti, *Journal of Applied Polymer Science*, 2011, **122**, 3651-3660.
62. N. Bodenberger, D. Kubiczek, I. Abrosimova, A. Scharm, F. Kipper, P. Walther and F. Rosenau, *Biotechnology Reports*, 2016, **12**, 6-12.
63. F. Dorkoosh, J. C. Verhoef, G. Borchard, M. Rafiee-Tehrani, J. Verheijden and H. Junginger, *International journal of pharmaceutics*, 2002, **247**, 47-55.
64. J. D. Ferry and J. D. Ferry, *Viscoelastic properties of polymers*, John Wiley & Sons, 1980.

Chapter Five

5. Preparation and characterization of functionally gradient porous HPC hydrogel

5.1 Introduction

Porous materials have been utilised for a massive range of applications over the decades because of their unique properties. Mostly, the pores of these materials are arranged uniformly across the materials. However, one group of porous materials consisting of different pore size, pore geometry or porosity across a certain dimension of the materials.[1] Functionally graded materials (FGM) have been developed with morphological, compositional and mechanical properties.[2]

FGM with multiscale pore size and porosity can be fabricated by either a stepwise (graded) or continuous (gradient).[3] The stepwise fabrication can be simply achieved by stacking material components into layers using a variety of methods, while in the continuous gradient structure the composition of material ingredients changes in a continuous way.[4] Nature has provided a range of hierarchical porous materials with interconnecting multi-scale pores structure. An excellent example is the human body which is made up of a number of functionally graded porosity materials such as bones and the teeth. The structure of bones and the teeth mainly contains a dense shell cover is covering a spongy structure. This structure can provide high mechanical stability and excellent permeability, but, these are the most replaced human body parts, as a result of the natural ageing process or as a result of damage to these parts.[5] With the increasing requirements of industry, gradient porous materials have been shown to be useful in a wide range of applications in different areas, such as the biomedical and environmental fields. A porosity gradient in functional materials is most commonly used in medical implants because their properties are very close to those of the parts they intend to replace, which helps to promote the new tissue growth with the desired mechanical properties.[6]

FGMs have also been used as filters for purification and separation applications.[7-8] Filters with hierarchy porosity which decreasing pores size with depth have been shown to have a high separation efficiency than filters with uniform pores.[9] Commonly filters with regular pore size capture the majority of the contaminants in the top layer of the filter while leaving the rest relatively unused, leading to premature clogging and reduced filtration efficiency.[10] While filters whose porosity decreases with depth can improve filtration efficiency due to the small pores trapping small particles within and not just on

the surface of the filter, thus, increase their efficiency due to the reduction of contaminant concentration with depth. Furthermore, the big pores improve mechanical proprieties and enhanced permeability.[11-12]

Production of gradient porous materials is more complicated than that of porous materials with uniform pore. Mainly, it requires further steps to introduce the gradient porosity structure.[1] Several approaches have been developed to fabricate a porous structure with a pore size gradient. For example, sintering of graded particles,[13] infiltration method,[14] multilayers multiple tape casting,[15] the emulsion centrifugation technique,[1] and ice-templating techniques.[3, 16] Most recently 3D printing technique has been also used to fabricate materials with gradient porosity.[17] Some of these techniques however have limitations because they are often time-consuming, size-limiting processes, not environmentally friendly, too costly, or just do not allow precise control over the final structure.[18-19] Among these processes, the ice-templating method including freeze-drying and freeze casting can overcome many of these limitations as the method is simple and can be used with a variety of materials to control the porosity and environmental friendly.[18-20] FGM also can be produced by varying the production processing parameters by using different preparation conditions to produce the required porosity gradient.[21] Responsive hydrogels with graded porosity have been prepared using stepwise methods to improve their mechanical properties.[22-23] There are however some disadvantages, which has produced a hydrogel less pore interconnectivity, which reduced mass transport causing a slow response to stimuli. A hydrothermal process has been introduced to fabricate thermoresponsive hydrogels with gradient porous construction in one step to address these issues.[24]

In this chapter, we report a new, simple method of forming a thermoresponsive hydrogel with gradient pore size which combing two methods. Hydroxypropyl cellulose (HPC) well-known thermo-responsive material was used as the polymer. In this method describes not only variation the temperature between the upper and lower part of the hydrogel depends on the LCST, which brings about a gradual change in pore geometry and pore size, but also the cryogenic treatment of the sample to obtain gradient porous HPC hydrogel with high permeability.

5.2 Results

5.2.1. Synthesis of gradient porous HPC hydrogels

A new method of creating an HPC functionally gradient porous materials has been developed whereby the shape and the size of the pore changed across the material. This method exploits the LCST of thermoresponsive HPC polymer to induce a graded porosity. The graded porosity HPC hydrogel was synthesised following the synthesis procedure developed its HPC hydrogel with uniform porous, which described in chapter four but the gelation temperature was varied for the same sample. As described previously HPC polymer exhibits a thermoresponsive behaviour with a reversible hydrophobic-hydrophilic transition at the LCST and below this temperature. Using this behaviour HPC hydrogel was prepared with DVS as a chemical crosslinker in an alkaline media at a different temperature. A schematic illustration of the generation method steps of the interconnected gradient porous HPC hydrogel (as described in chapter 2) is shown in Figure 5.1. It can be seen from Figure 5.2 photographic images of (A) HPC hydrogel was prepared at a temperature below the LCST, which shows a monolith HPC hydrogel with a light brown transparency colour. Whereas, the HPC hydrogel sample prepared via TIPS process as mentioned previously in chapter four shows white colour due to the HPC at the LCST turn to cloudy, which is named the cloud point as shown in Figure 5.2 (B). Figure 5.2 (C) presents an HPC hydrogel prepared at different temperatures across the sample. It is evident that the sharp limit between the two halves in the same sample in this image. The characterisation of sample A and B was performed in chapter four and as mentioned sample A shows close pores with big pore size and sample B demonstrated interconnected pores with small pore size. In this chapter, we will study the characterisation of sample C.

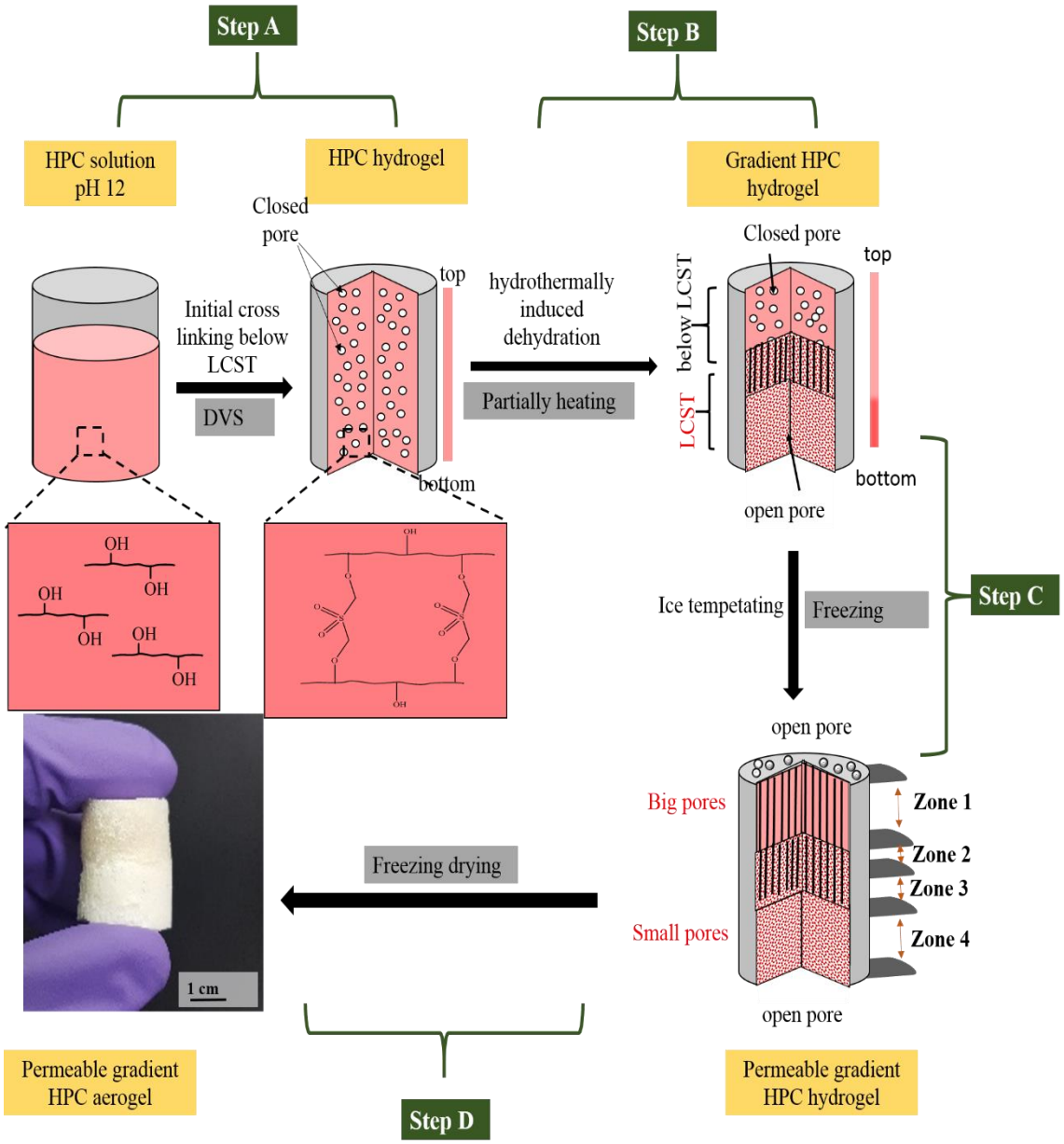

Figure 5.1. Scheme illustrating the preparation steps of gradient porous HPC hydrogel; (Step A) initial chemical crosslinking of HPC using DVS at room temperature (21±2 ºC, which is below the LCST) for 3 hours to form HPC hydrogel with close pores; (Step B) thermally forming of gradient porous HPC via partially heating HPC hydrogel (the bottom layer heat at LCST while the top layer left at temperature below the LCST) this step produces a gradient porous HPC hydrogel with different size and type of pores (close and open pores); (Step C) Ice templating method used to open the close pore of top layer by growing the ice crystals to form a permeable gradient porous HPC hydrogel; (Step D) freeze-drying the sample to produce a permeable gradient porous HPC aerogel.

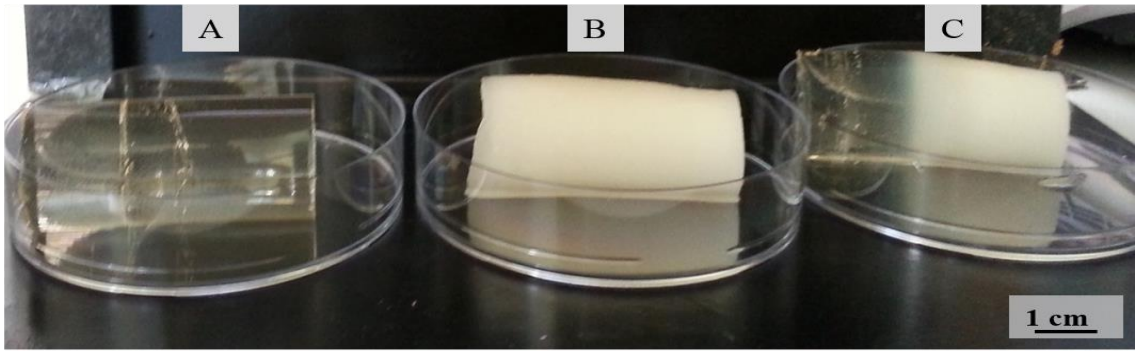

Figure 5.2. Photographic image of HPC hydrogel prepared by 7 w/v % HPC and 1.3 w/v % DVS at different temperature (A) at a temperature below the LCST (B) at LCST and (C) heating part of the sample at LCST and keeping the rest part at a temperature below LCST.

5.2.2. Characterisation of gradient porous HPC hydrogel

5.2.2.1. Morphology of FD-gradient porous HPC hydrogel

The morphology structural of the gradient porous HPC hydrogels under wet and dry conditions were observed. First, the surface morphology of the gradient porous freeze dried-HPC (FD-HPC) hydrogel was observed with a scanning electron microscope (JEOL JSM-6480 LV). The prepared hydrogel was quickly frozen in liquid nitrogen and then freeze-dried for 3 days to remove water thoroughly by sublimation. Before the SEM observation, the FD-HPC hydrogel was carefully sliced into four layers (as shown in the schematic in Figure 5.3) with random thickness and sputtered with gold.

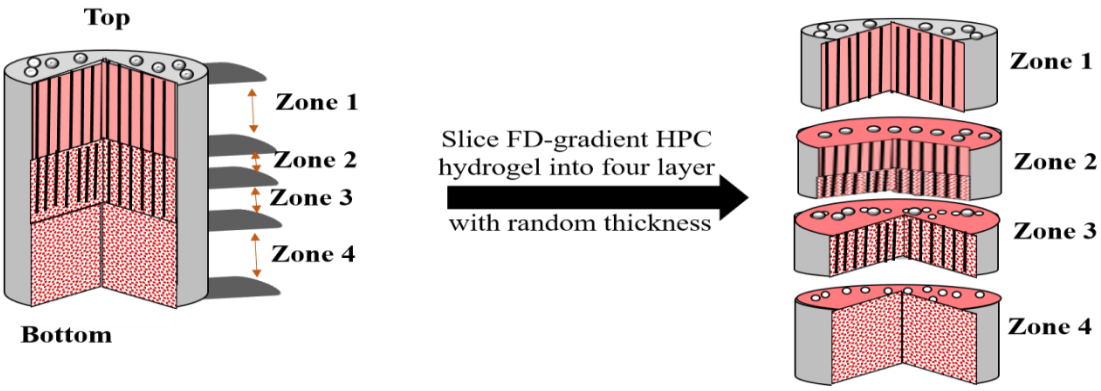

Figure 5.3. Schematic representation slice gradient porous HPC hydrogel into four sliced (zones); (zone 1) the top layer (left at a temperature below the LCST) with big and close a pores (as described in Chapter 4) and then open the pores by ice templating method; (zone 2) the midline layer between (below and at LCST) with a two different pores size and geometry; (zone 3) the layer below the midline layer, which is the top part of the layer heated at LCST; (zone 4) the bottom layer (at LCST) with small interconnecting pores.

Figures 5.4, 5.5, 5.6 and 5.7 show the SEM images of cross sections of the gradient porous HPC prepared from 7.0 w/v % HPC and 1.3 w/v % DVS at various temperature (below and at LCST) across the volume, which can be divided into four distinctive zones according to Figure 5.3. From these SEM images clearly show the internal porous structure of the FD-HPC gradient porous hydrogel and exhibit a different in pores structure and pores size from the top layer to bottom layer of the hydrogel. Each zone was exhibited different size and shape of the pores. Figure 5.4 shows the SEM image of the top layer (zone 1). The largest pores size with a thick wall with honeycomb shape in zone 1 can be clearly seen.

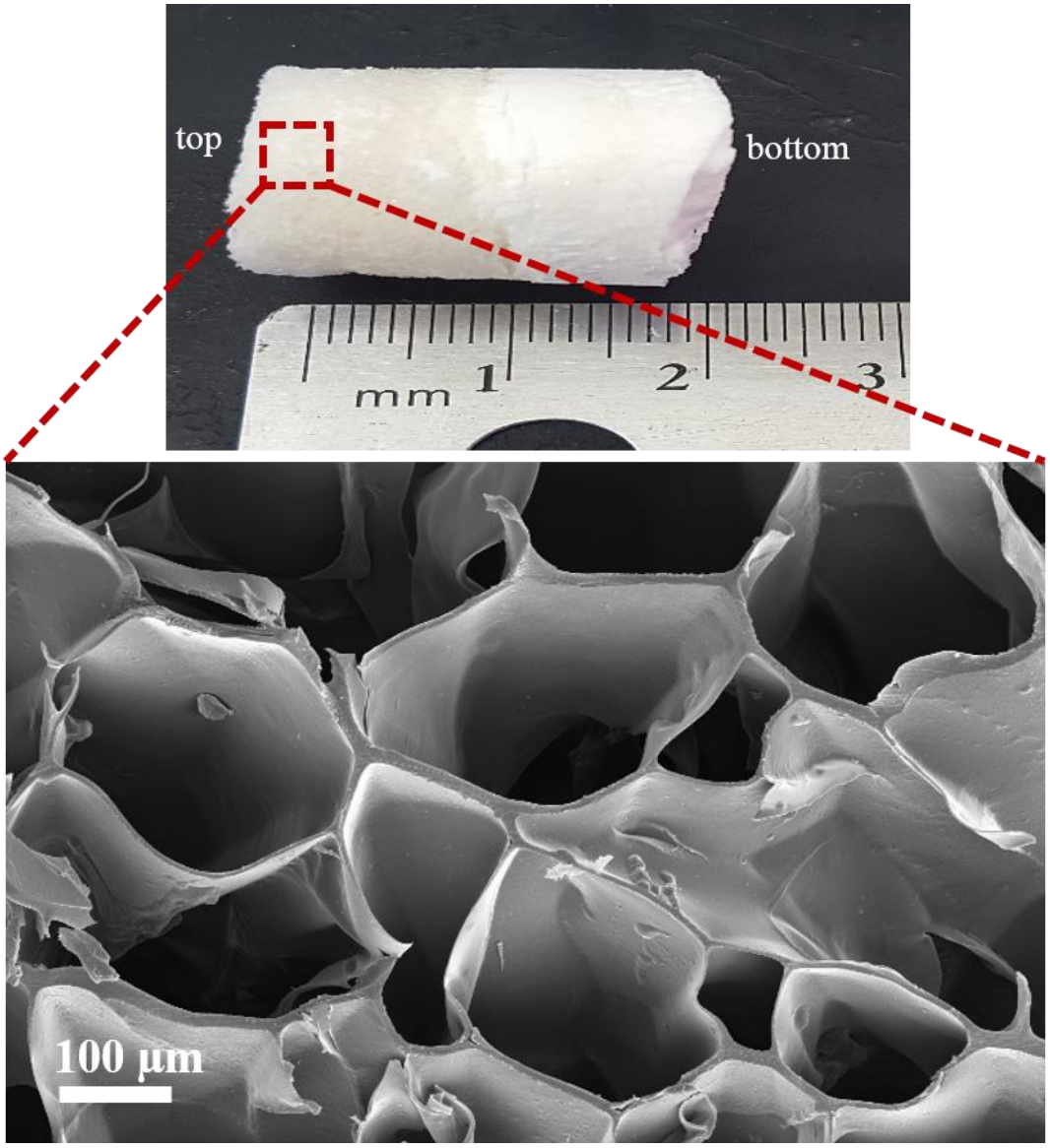

Figure 5.4. SEM image of cross sections of the top layer (zone 1) of FD-HPC hydrogel prepared at RT (22±2 ºC), which is below the LCST and then freeze-dried. The open big pores and the thick of the walls of the pores are observed in this image.

The SEM image in Figure 5.4 shows the top layer exhibits a macroporous structure with average pores pore around (100 µm). The big pore due to complete the crosslinking below the LCST.

Figure 5.5 shows the SEM image midline layer (zone 2) which is the layer between the different temperatures. In this zone, there is a sharp difference in the pore size from big pores to small pores from top to bottom.

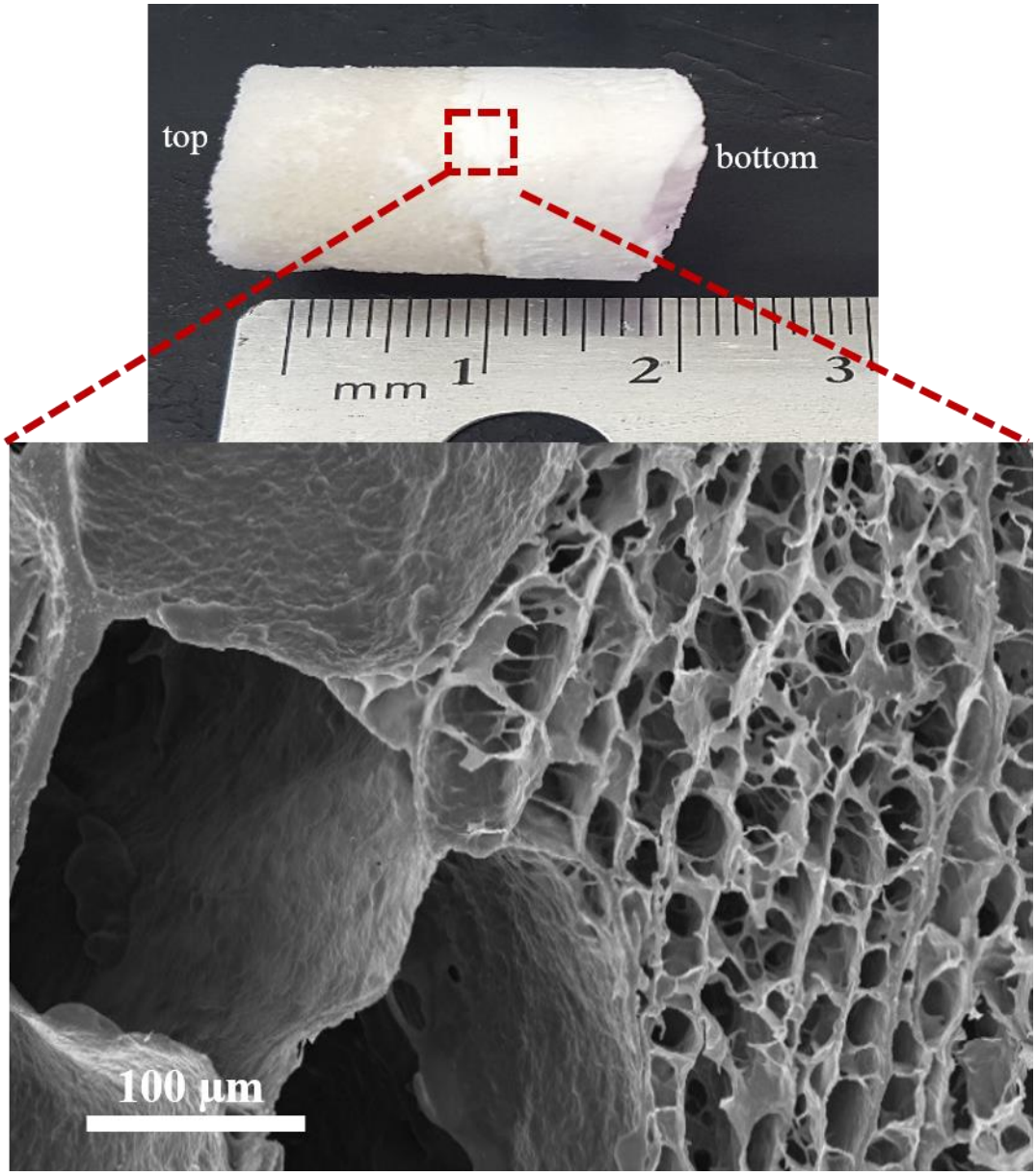

Figure 5.5. SEM image of cross sections of the midline layer (zone 2) of FD-HPC hydrogel, which is between two different temperatures below and at LCST and then freeze-dried. The difference in pore size from the top layer to the bottom layer of the hydrogel is very clear.

In zone 3 which is the top part of the bottom layer, the structure demonstrated lamellar pores with small interconnected pores between them. The bottom layer (zone 4) showed dense with small interconnected pores. SEM observations revealed reducing pores size along the cross-section of HPC hydrogel from top to bottom layer. In zone 3, the structure demonstrated lamellar pores with small interconnected pores between them. The bottom layer (zone 4) showed dense with small interconnected pores. SEM observations revealed reduced pores size along the cross-section of HPC hydrogel from top to bottom layer.

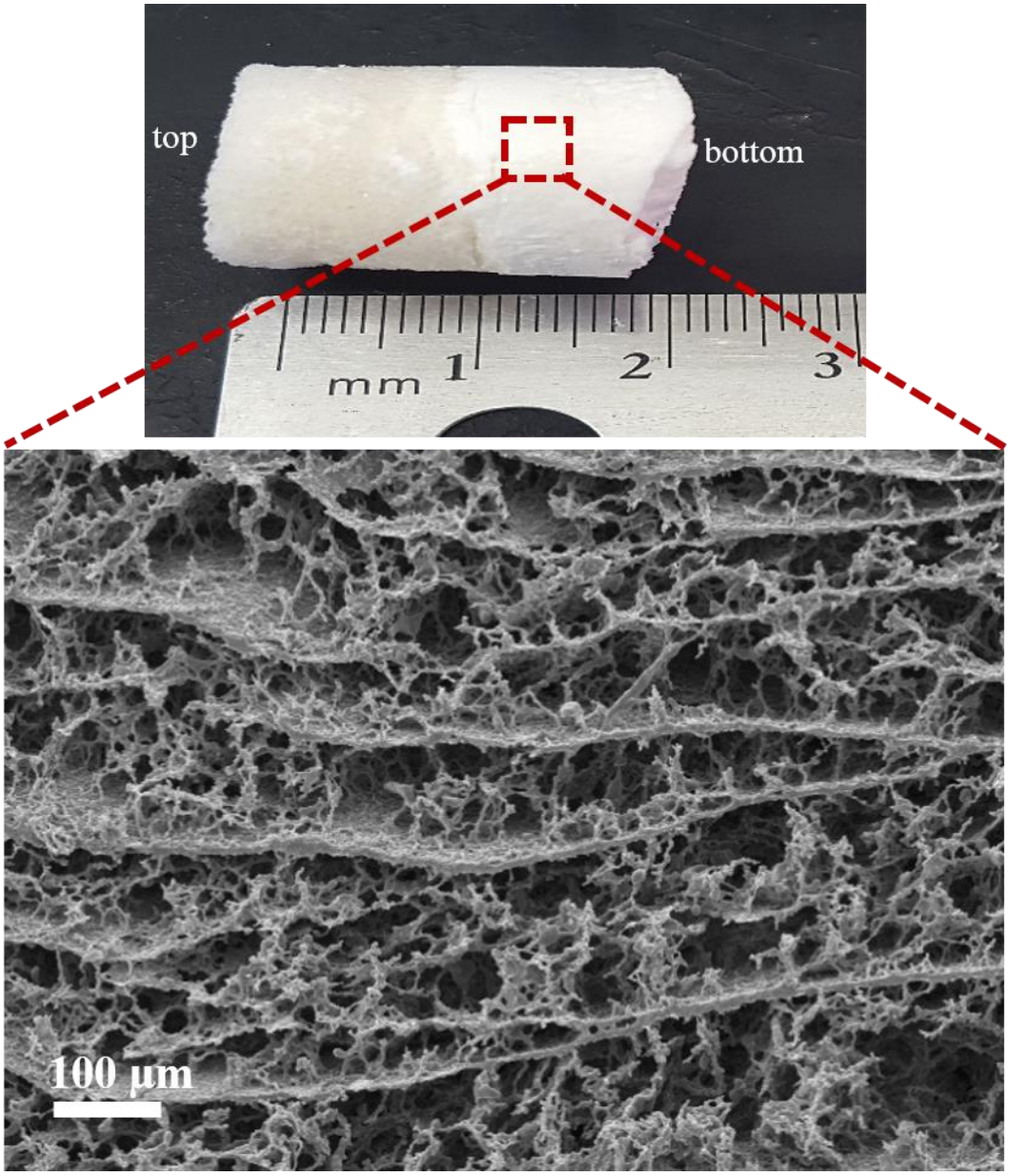

Figure 5.6. SEM image of cross sections of (zone 3) of FD-HPC hydrogel, which is the top part of LCST layer under the midline layer.

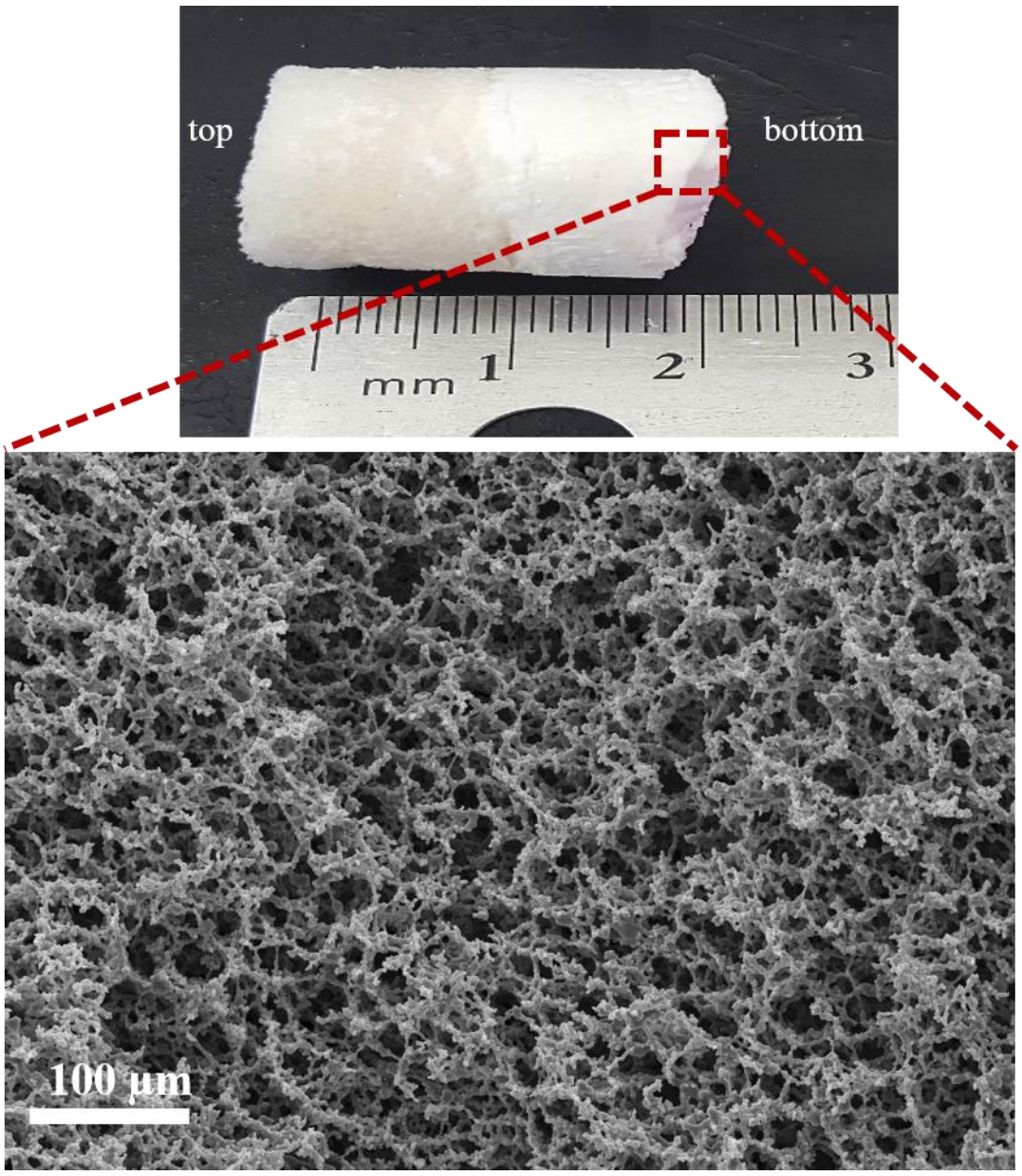

Figure 5.7. SEM image of cross sections of the bottom layer (zone 4) of FD-HPC hydrogel prepared at LCST. Showing a dense and highly interconnected matrix with small pores size.

The inverted SEM images clearly showed continuous gradient pores and the morphology structure of the top layer of the hydrogel was distinctly different from that of the bottom layer within the monolith hydrogel sample. The top layer exhibits a macroporous structure with pores with thick walls (Figure 5.4), whereas the bottom layer was dense with small pores (Figure 5.5), indicating the decreasing porosity from top to bottom layer of the HPC hydrogel. A gradual reduction in pore size from zone 1(100 µm) to zone 4(~ 1 µm) was observed, indicating the gradually changing pore size within the hydrogel. The small pores were formed as a result of decomposition of the HPC hydrogel during TIPS

method via complete the crosslinking at the LCST, while the big porous due to complete the crosslinking below the LCST (as described in Chapter 4).[25] The gradient pore structure of the HPC hydrogel can be therefore attributed to the different temperature between the top and bottom layer monolith sample. As mentioned in chapter four HPC hydrogel prepared at a temperature below LCST show close pore, while in SEM images show open pores. The reason behind that was growing ice crystals in the hydrogel via freezing the sample and phase separation of the ice to gas by sublimation during freeze-drying help to open the pores in this layer and leave behind large, interconnected pores system.[26] The lamellar pores in zone 3 (Figure 5.6) might be caused by growing ice crystals in both vertically and horizontally, thereby enabling aligned lamellar structures in this layer.

5.2.2.2. Morphology of gradient porous HPC hydrogel

As shown in Chapter 4 the morphology structure of HPC hydrogel in wet and dry status was different. The visualization of the porous structures of the top and bottom layers was also performed using cryo-SEM for the wet hydrogel to provide further information about the structural morphologies of wet gradient porous HPC hydrogel. The cryo-SEM images of HPC hydrogel prepared from 7.0 w/v % HPC and 1.3 w/v % DVS with different magnifications at a different temperature across the sample below the LCST and at LCST are shown in Figures 5.8 and 5.9 for the top layer and bottom layer respectively. The gradient hydrogel material showed no shrinkage in the top layer and slight shrinkage at the bottom part. Treatment of the bottom layer by heating at LCST of the polymer led to additional cross-linking and decomposition the network, as indicated by substantial shrinkage in this layer. In contrast, the top layer exhibited no volume change, suggesting saturation in cross-linking at a temperature below the LCST.

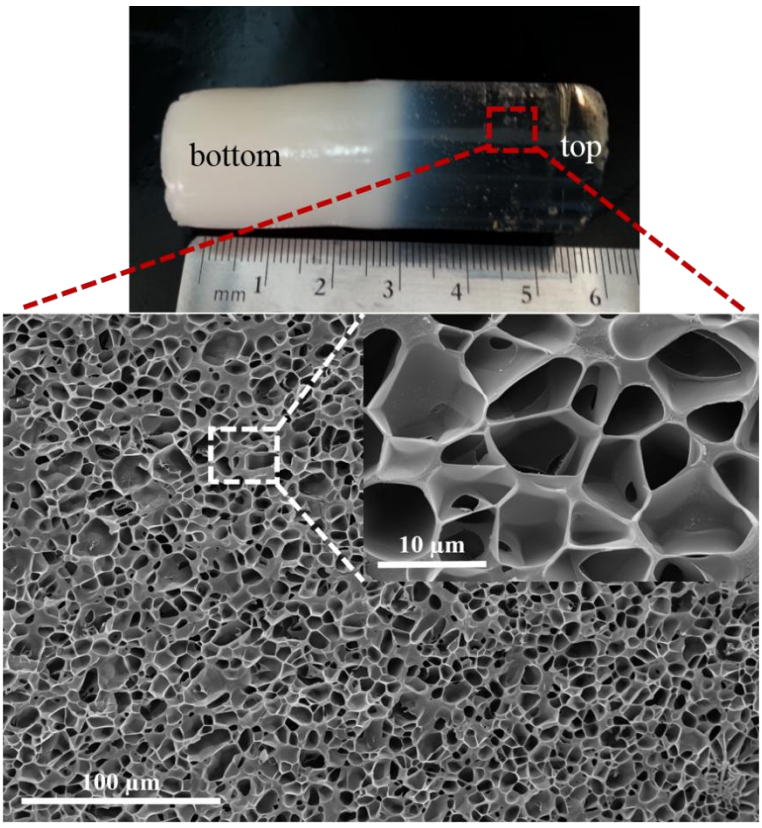

Figure 5.8. Cryo-SEM image of HPC hydrogel gelation at a temperature below LCST at different magnifications.

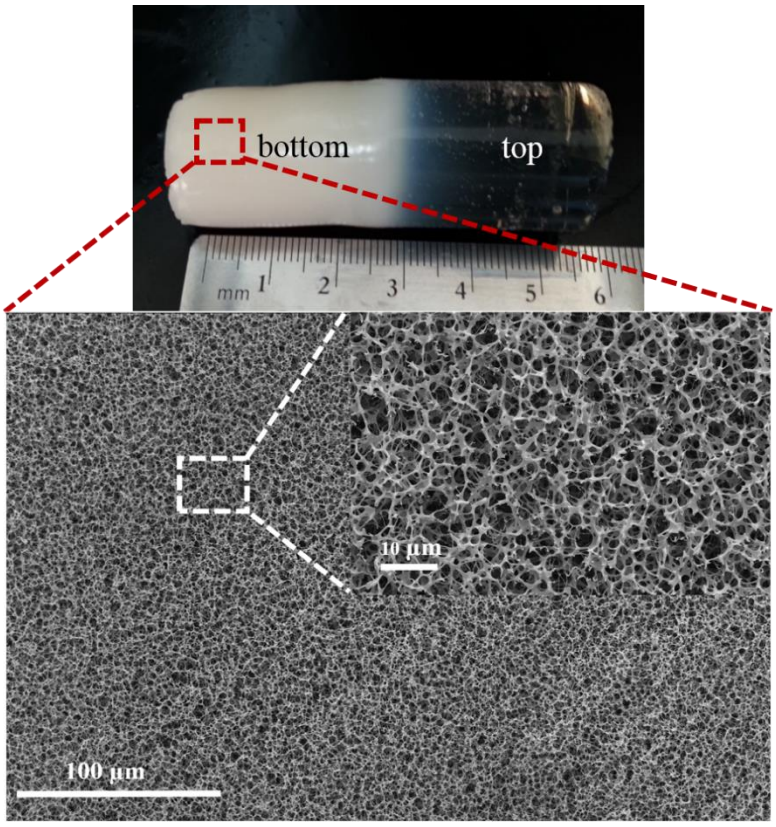

Figure 5.9. Cryo-scanning electron microscopy of HPC hydrogel prepared at 42 ºC at a different region at different magnifications.

Cryo-SEM images (Figure 5.8 and Figure 5.9) demonstrated the wet gradient porous HPC hydrogel gelation at different temperature across the volume consisted of different pore size macro-micro porous structure with varied pores geometry. SEM characterization of the porous HPC hydrogel gelation at LCST revealed small interconnected pores with sizes of 0.1-0.5 μm in the bottom layer. The pores in the HPC hydrogel are consistent with those that developed during decomposition at LCST. The interconnected pores and high porosity HPC hydrogel prepared at LCST showed high permeability to fluids like water. Nevertheless, the cryo-SEM of HPC hydrogel prepared at a temperature below the LCST demonstrated partially open big pores with thick walls and sizes of 10-20 μm as can be seen in Figure 5.8. The HPC hydrogel prepared below the LCST was not permeable to fluid. This can be explained as the top layer which prepared at below the LCST was initially have closed pores but at freezing the sample during the cryo-SEM the trapped water in this layer turns into large ice crystals with phase separation which causes open these pores in the HPC hydrogel. Figures 5.10 and 5.11 illustrate cryo-SEM of different regions from the surface of the top layer. The results in Figure 5.10 shows that this layer with closed pore due to this part no in the direction of growth the ice crystal by freezing the sample during cryo-SEM, while in Figure 5.11 shows the part with partially open pores.

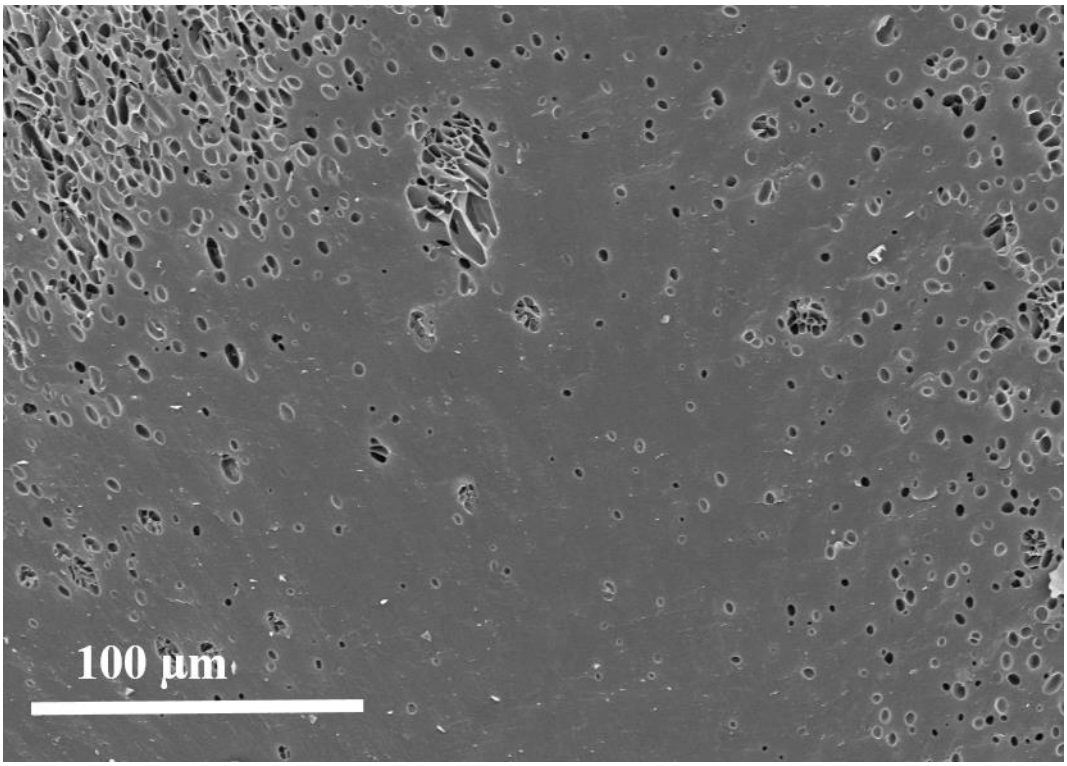

Figure 5.10. Cryo-SEM of the top layer of gradient porous HPC hydrogel. Shows the region which is showing almost plain non-porous surface morphology.

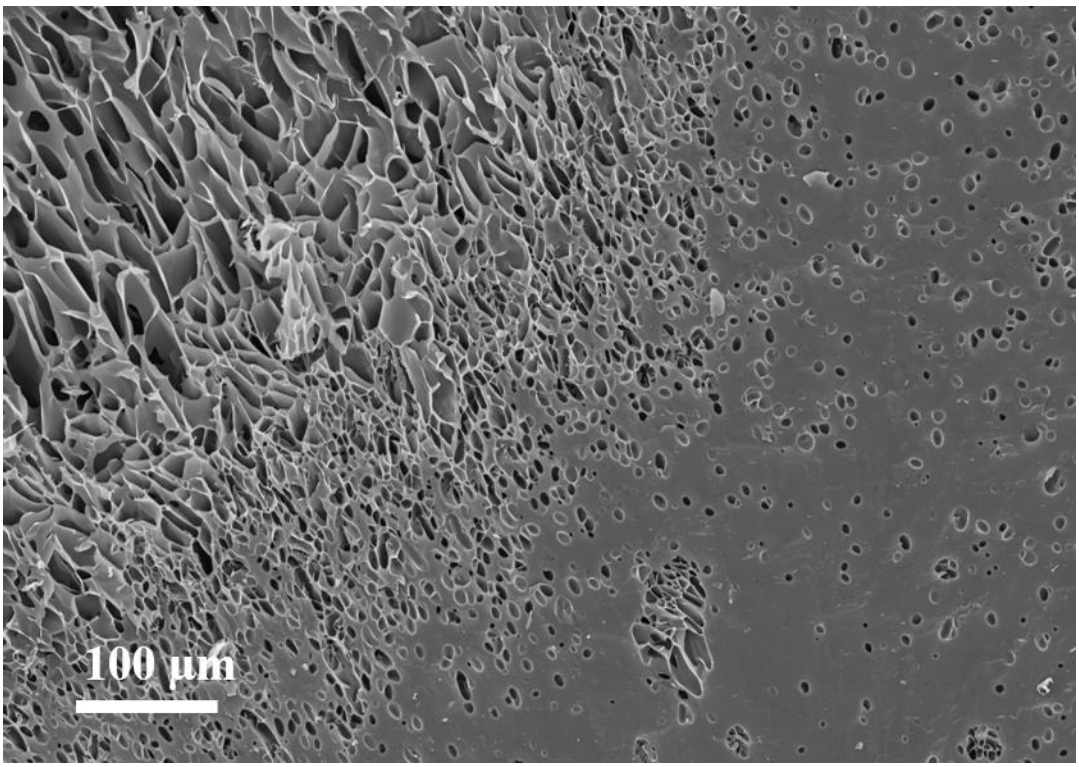

Figure 5.11. Cryo-SEM of the top layer of Gradient porous HPC hydrogel. Shows the region which is partially interconnected porous structures which may have resulted from the phase separation of ice during cryogenic treatment and due to this region located in the direction of Ice crystals growth.

Therefore, the permeability of this type of hydrogel was likely depended on freezing or freeze-drying the sample, which is probably due the solvent as ice crystals is then removed by sublimation under vacuum leaving behind open pores in the regions it previously occupied.[27] The pore sizes of the same layer show different measurement under wet and dry conditions and the pore size was larger in the dry state than the wet state, due to reduced swelling in the pore walls, once the water is removed.[17]

Freeze drying conditions have a significant influence on the shape and size of the pores. For example, the freezing temperature and rate affect the growth of ice nucleation, thus influence the total porosity of the hydrogel.[28] Slowing freezing at normal freezing temperature to allow larger solvent crystals to grow lower, thus produce materials with large macroporous pores. However, at lower temperatures (liquid nitrogen) and fast kinetics of ice-nucleation lead to fabricate hydrogel with smaller pore sizes due to quick freezing the gel samples are preventing any ice crystal growth.[29] The porosity decreased with the applied pressure during freeze-drying, thus the pore size was increased. During freeze-drying, ice sublimation causes great changes and create pores or voids with different pores geometry and size.[28, 30]

5.2.2.3. Test the permeability of gradient porous HPC hydrogel

Gradient porous HPC hydrogel was designed as a column due to is fast, flexible, easy to manage and can provide good evaluate of pore interconnectivity of this hydrogel.[31] The permeability is an important parameter for evaluation of the quality of porous materials filters. Tracer tests have been commonly used as benchmark experiments for evaluation of fluid transport behaviour within porous media.[32]This study was focused on the visualization recognition flow and transport of fluid through gradient porous HPC hydrogel to evaluate pore interconnectivity of this material using a dye tracer experiment method for this hydrogel. Fluorescent dye was used as tracers dye to mark diffusion of fluid through the hydrogel in this experiment, owing to their low toxicity, high solubility in the water and no adsorption behaviour of this dye in this column (will be explained later in Chapter 6).[33-34] A tracer test was performed at room temperature (22±1 °C) on two gradients porous HPC hydrogel column prepared with 7.0 w/v % HPC with 1.3 w/v % DVS, first without freezing and the second column with freezing at -20 ºC. Figure 5.12 shows a schematic diagram of the cryogenic treatment of the top layer to improve the permeability of the column.

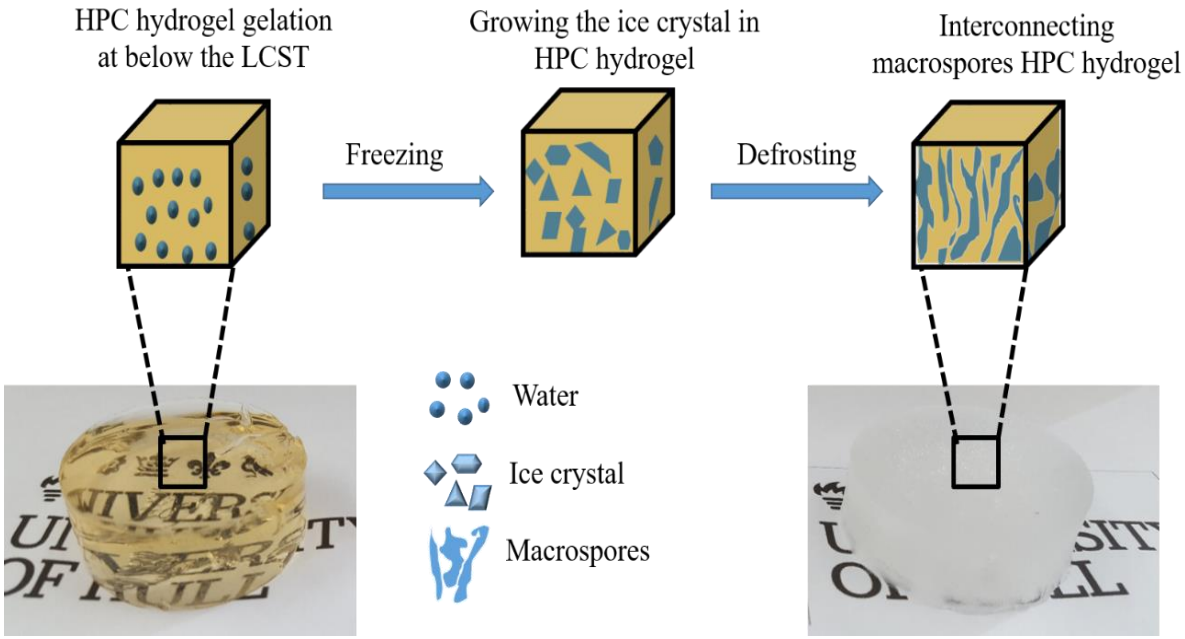

Figure 5.12. Schematic diagrams representation of ice templating method of the top layer of gradient porous HPC hydrogel, which is prepared at a temperature below LCST.

Figure 5.13 (A) shows photographic images of test the permeability of gradient porous HPC hydrogels column prepared without freezing. Figure 5.13 (B) shows the

photographic images of the trackers test of gradient porous HPC hydrogels columns after used ice templating method.

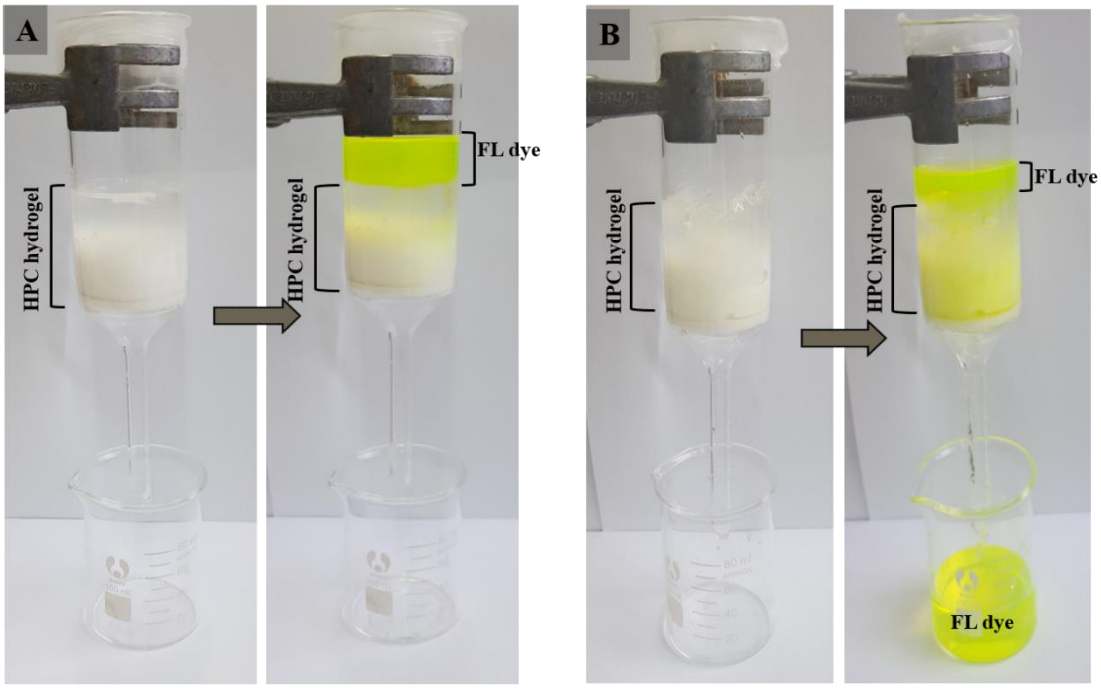

Figure 5.13. Evaluation of pore connectivity of the gradient porous HPC hydrogel (A) without cryogenic treatment (B) after freezing the column at -20 ºC for 2 days.

In Figure 5.13 (A) the hydrogel column without freezing treatment show that there is no diffusion of the dye through the hydrogel. Whereas, the column with freezing exhibited pore interconnectivity with gradient pore size with fast diffusion of the fluorescein dye within the hydrogel (Figure 5.13 (B). As a result, gradient porous HPC hydrogel with different pores size have been synthesised during the gradient temperature technique around the LCST. The disadvantage of this method produces nonpermeable gradient hydrogel due to the top layer had a closed pore. Therefore, ice templating method has been used to create hydrogels with gradient interconnected pores.[35-36] During freezing, the ice crystals nucleated grown and help to open the pores. The melting of these ice crystals at a temperature above the freezing temperature gives rise to interconnected macroporous networks.[37] Figure 5.14 demonstrates photographic images of the top layer, which is prepared at a temperature below the LCST before and after cryogenic treatment. Before freezing water cannot be released from the hydrogel upon compression, while after freezing released water can be seen after compression.

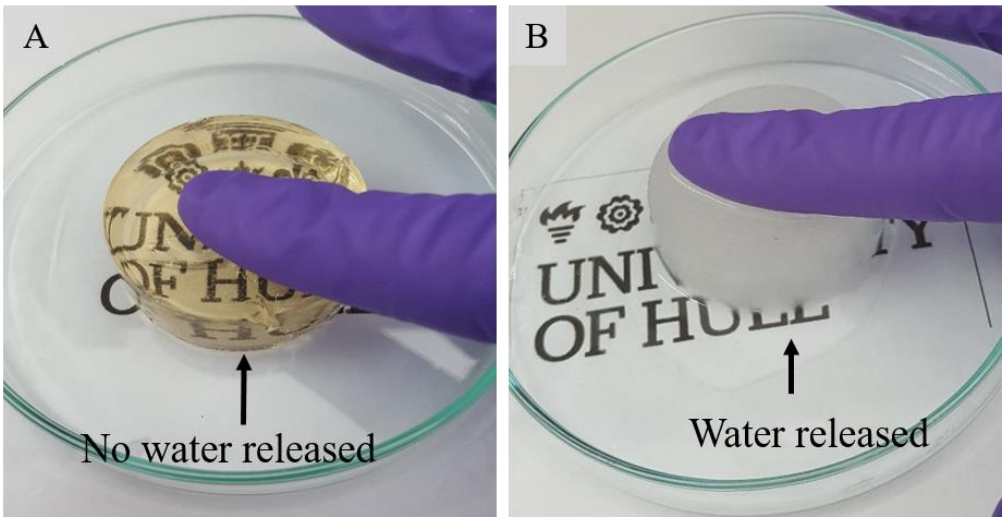

Figure 5.14. Photographic images of the top layer of gradient porous HPC hydrogel (A) without freezing, which shows no water released during compression the gel by a finger; (B) after freezing at -20 °C for three days, which the released water can be seen after compression the gel by finger.

5.2.2.3. Mechanical properties of gradient HPC hydrogel

5.2.2.3.1. Rheology

In order to obtain information about the mechanical properties of the gradient porous HPC hydrogels, rheology was used as a function of shear stress for zone 1 and zone 4 of the gradient HPC hydrogel, which is prepared below and at LCST respectively. Furthermore, the rheology test was performed for the top layer before and after cryogenic treatment. The storage modulus G′ was compared for those layers by increasing the stress over range 10–400 Pa and was carried out at room temperature (22±2 ºC). The results are shown in Figure 5.15 demonstrate the comparison between G′ of zone 1 and zone 4 layers at a various shear stress of gradient porous HPC hydrogels in addition to showing the difference in G′ for the top layer before and after freezing. The result showed that the storage modules of the Zone 4 was 13000 Pa, which is obviously higher than those of zone 1 (5000 Pa). Whereas the storage modules of zone 1 shows sharply increase after freezing the hydrogel. Furthermore, it can be also seen that zone 4 show decreases the storage modulus from 13000 Pa to 7000 Pa with an increase in the shear stress from 10-400 Pa, while zone 1 shows a sharp decrease in the storage modulus to reach about 400 Pa at the same shear stress range.

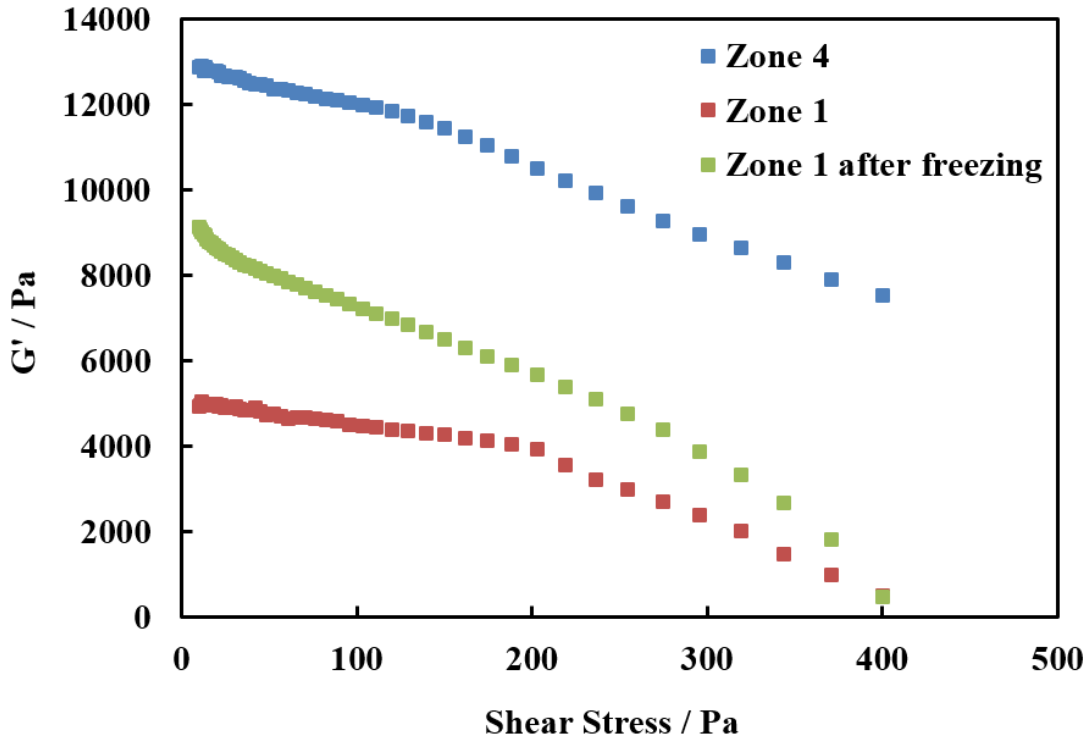

Figure 5.15. The storage modulus of gradient porous HPC hydrogel layers has been formulated by 7 w/v % HPC and 1.3 w/v % DVS at different temperature across the sample (LCST) the bottom layer, which gelation at the LCST; (RT) the top layer, which completed gelation at temperature below the LCST; (RTF) the top layer, which completed gelation at temperature below the LCST following freezing at -20 °C for three days.

It is obvious that the storage modulus of all the layers of the gradient hydrogels decreases as the shear stress was increased between 10– 400 Pa with a noticeable decrease above 100 Pa. The storage module of zone 4 was much higher than zone 1 upon decreasing the gelation temperature from bottom to top layer. Furthermore, it can be seen that the storage modules of zone 1 show significantly increases after cryogenic treatment compared with the same layer without treatment. It seems that the rheological properties of the frozen hydrogel improved due to the interconnected pores form during freezing the sample.

5.2.2.3.2. Compression test

The mechanical properties of the gradient porous HPC hydrogel was further investigated through an uniaxial compression testing. Figure 5.16 shows the compressive stress-strain curves of the top and bottom layer of the gradient hydrogel. The compression test was carried out for the top layer before and after freezing. From the curves, it can be seen that the bottom layer of the gradient porous hydrogel can be compressed to approximately 20%

of the height the original cylinder samples without fracture and exhibit the predominant mechanical properties of toughness and softness. The compressive stress of bottom layer of hydrogel (zone 4) gradually increased with increasing strain until the compressive strain was approximately 60%; above this point, it suddenly increased and showed typical ‘‘J’’ shape curves, indicating their high compressive strength.[38] Compared with a top layer of the gradient hydrogel, this layer shows remarkable fracture at a low deformation of about 47% with high elasticity, while, the same layer after freezing exhibited about 80% compression strain without mechanical destruction or permanent deformation. Figure 5.17 shows Young’s modulus of each zone calculated from the strain-stress curve. The top layer gives Young’s modulus of ~0.191 MPa in compression, whereas cryogels and the bottom layer show a dramatic reduction in the modulus, to ~0.053 MPa and ~0.105MPa respectively, as reported by Bencheri *etal*. that explains the cryogenic treatment reduce Young’s modulus of the hydrogel materials.[39]

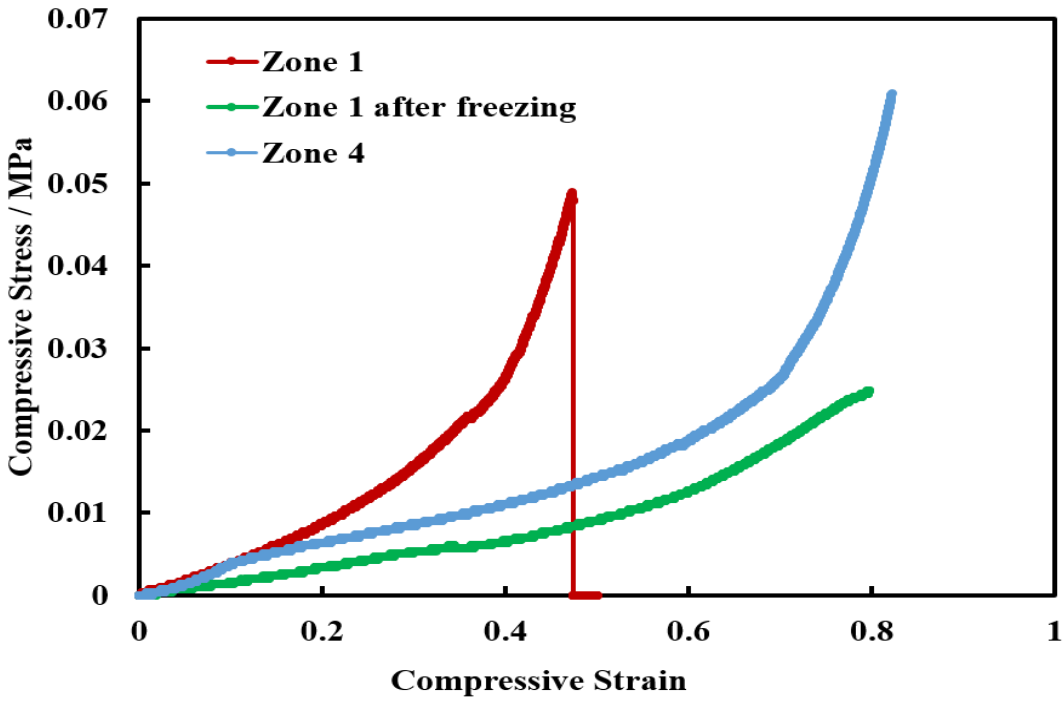

Figure 5.16. Compressive stress-strain curves of gradient porous HPC hydrogel layers has been formulated by 7 w/v % HPC and 1.3 w/v % DVS at different temperature across the sample (Zone 4) the bottom layer, which gelation at the LCST; (Zone 1) the top layer, which completed gelation at temperature below the LCST; (Zone 1 after freezing) the top layer, which completed gelation at temperature below the LCST following freezing at -20 °C for three days.

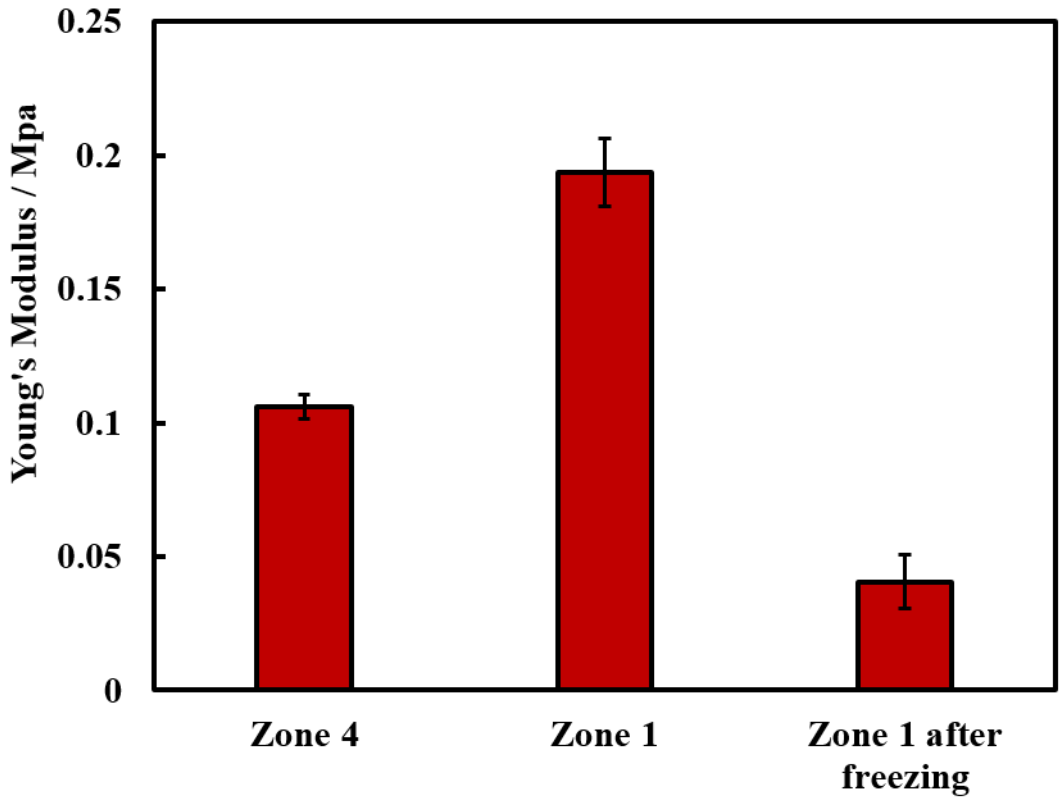

Figure 5.17. Young's modulus the top (zone 1) and bottom (zone 4) layers of the gradient porous HPC hydrogel and the top layer before and after freezing-thawing treatment. Each sample was measured in triplicate to calculate the error bars are the standard deviation.

Zone 1 after freezing exhibits less stiffness due to an increase in the interconnectivity of pores, which leads to reduce structural fracture upon compression. Typically, cryogels exhibit enhanced mechanical stability with larger interconnected macropores compared to traditional hydrogel structure.[40-41] Reasonably, we can conclude that cryogenic treatment leads to greater improvement in the mechanical property of the gradient hydrogel over without treatment.[37]

5.3. Conclusions

In summary, a novel, efficient approach was developed to produce interconnected gradient porous HPC hydrogel by taking advantage of thermoresponsive behaviour of HPC at the LCST. The temperature gradient between the top and the bottom layer within the monolith hydrogel sample during the chemical cross-linking step resulted in hydrogels with a graded pore size and vary pore geometry. SEM imaging revealed a reduced in pores size along the cross-section of the HPC hydrogel from a top layer which was the crosslinking was completed at a temperature below the LCST as compared to the bottom layer which the crosslinking was completed at the LCST. A gradual reduction in pore size from the top layer (100 μm) to the bottom layer (~ 1 μm) was observed, indicating the gradually changing pore size within the hydrogel. The small pores were formed as a result of decomposition of the HPC hydrogel during the TIPS method via completing the crosslinking at the LCST, whereas the big porous due to completing the crosslinking below the LCST. A tracers dye test was used to monitor the diffusion of fluid through the gradient HPC hydrogel column. The results showed nonpermeability of the column due to the top layer having close pores as mentioned in chapter 4. The cryogenic column showed high permeability of liquid through the column. Therefore, the thermal synthesis method of the gradient porous HPC hydrogel followed by the freeze-thawing method to provide high permeability. The mechanical properties of gradient porous HPC hydrogel layers were further investigated through uniaxial compression testing and rheology. It was found that the LCST layer compressed to approximately 80% without fracture and exhibited the predominant mechanical properties of toughness and softness, while the top layer showed fracture at about 47 %. The same top layer after freezing-thawing treatment however, exhibited about 80% compression strain and maintains its structure. Thus, it can be concluded that cryogenic treatment achieves greater improvement in the mechanical property and the permeability of the gradient porous HPC hydrogel.

This chapter is the first report of a gradient porous hydrogel made from hydroxypropyl cellulose depend on it LCST. Previous work in the literature has used *N* – isopropylacrylamide (NIPAM) as a thermoresponsive materials for forming gradient porous hydrogel by the hydrothermal process in a close system.[42] Furthermore HPC have been used to prepare porous hydrogel with uniform pores.[43-44] Here, the permeable gradient porous structure of the HPC hydrogel was prepared via changing the temperature between the top and bottom layer of the monolith sample in an open system.

5.4. References

1. Ahmed, A.; Smith, J.; Zhang, H., Gradient porous materials by emulsion centrifugation. *Chemical Communications* 2011, *47* (42), 11754-11756.

2. Suresh, S.; Mortensen, A., *Fundamentals of functionally graded materials*. The Institut of Materials: 1998.

3. Miao, X.; Sun, D., Graded/gradient porous biomaterials. *Materials* 2010, *3* (1), 26-47.

4. Suk, M.-J.; Choi, S., II; Kim, J.-S.; Kim, Y. D.; Kwon, Y.-S., Fabrication of a porous material with a porosity gradient by a pulsed electric current sintering process. *Metals and Materials International* 2003, *9* (6), 599-603.

5. Rho, J.-Y.; Kuhn-Spearing, L.; Zioupos, P., Mechanical properties and the hierarchical structure of bone. *Medical Engineering & Physics* 1998, *20* (2), 92-102.

6. Castillo, M.; Moore, J. J.; Schowengerdt, F. D.; Ayers, R. A.; Zhang, X.; Umakoshi, M.; Yi, H. C.; Guigne, J. Y., Effects of gravity on combustion synthesis of functionally graded biomaterials. *Advances in Space Research* 2003, *32* (2), 265-270.

7. Souzandeh, H.; Scudiero, L.; Wang, Y.; Zhong, W.-H., A Disposable Multi-Functional Air Filter: Paper Towel/Protein Nanofibers with Gradient Porous Structures for Capturing Pollutants of Broad Species and Sizes. *ACS Sustain. Chem. Eng.* 2017, *5* (7), 6209-6217.

8. Mopoung, S.; Sriprang, N.; Namahoot, J., Sintered filter materials with controlled porosity for water purification prepared from mixtures with optimal ratio of zeolite, bentonite, kaolinite, and charcoal. *Applied Clay Science* 2014, *88-89*, 123-128.

9. Vida-Simiti, I.; Jumate, N.; Thalmaier, G.; Sechel, N.; Moldovan, V., Study of gradual porous metallic membranes obtained by powder sedimentation. *Journal of Porous Materials* 2012, *19* (1), 21-27.

10. Datta, S.; Redner, S., Gradient clogging in depth filtration. *Physical Review E* 1998, *58* (2), R1203.

11. Barg, S.; Koch, D.; Grathwohl, G., Processing and Properties of Graded Ceramic Filters. *Journal of the American Ceramic Society* 2009, *92* (12), 2854-2860.

12. Dalwadi, M. P.; Griffiths, I. M.; Bruna, M., Understanding how porosity gradients can make a better filter using homogenization theory. *Proceedings of the Royal Society A: Mathematical, Physical and Engineering Sciences* 2015, *471* (2182), 20150464.

13. Thieme, M.; Wieters, K.-P.; Bergner, F.; Scharnweber, D.; Worch, H.; Ndop, J.; Kim, T.; Grill, W., Titanium powder sintering for preparation of a porous functionally

graded material destined for orthopaedic implants. *Journal of materials science: materials in medicine* 2001, *12* (3), 225-231.

14. Chabera, P.; Boczkowska, A.; Witek, A.; Oziębło, A., Fabrication and characterization of composite materials based on porous ceramic preform infiltrated by elastomer. *Bulletin of the Polish Academy of Sciences Technical Sciences* 2015, *63* (1), 193-199.

15. Werner, J.; Linner-Krčmar, B.; Friess, W.; Greil, P., Mechanical properties and in vitro cell compatibility of hydroxyapatite ceramics with graded pore structure. *Biomaterials* 2002, *23* (21), 4285-4294.

16. Zuo, K.-h.; Jiang, D.; Zeng, Y.-P. In *Gradient porous hydroxyapatite ceramics fabricated by freeze casting method*, IOP Conference Series: Materials Science and Engineering, IOP Publishing: 2011; p 182011.

17. Sultan, S.; Mathew, A. P., 3D printed scaffolds with gradient porosity based on a cellulose nanocrystal hydrogel. *Nanoscale* 2018, *10* (9), 4421-4431.

18. Deville, S.; Saiz, E.; Tomsia, A. P., Freeze casting of hydroxyapatite scaffolds for bone tissue engineering. *Biomaterials* 2006, *27* (32), 5480-5489.

19. Deville, S.; Saiz, E.; Nalla, R. K.; Tomsia, A. P., Freezing as a path to build complex composites. *Science* 2006, *311* (5760), 515-518.

20. Pawelec, K.; Husmann, A.; Best, S. M.; Cameron, R. E., Ice-templated structures for biomedical tissue repair: From physics to final scaffolds. *Applied Physics Reviews* 2014, *1* (2), 021301.

21. Mahamood, R. M.; Akinlabi, E. T., Modelling of Process Parameters Influence on Degree of Porosity in Laser Metal Deposition Process. In *Transactions on Engineering Technologies*, Springer: 2015; pp 31-42.

22. Asoh, T. a.; Matsusaki, M.; Kaneko, T.; Akashi, M., Fabrication of Temperature-Responsive Bending Hydrogels with a Nanostructured Gradient. *Advanced Materials* 2008, *20* (11), 2080-2083.

23. Zhang, E.; Wang, T.; Hong, W.; Sun, W.; Liu, X.; Tong, Z., Infrared-driving actuation based on bilayer graphene oxide-poly (N-isopropylacrylamide) nanocomposite hydrogels. *Journal of Materials Chemistry A* 2014, *2* (37), 15633-15639.

24. Luo, R.; Wu, J.; Dinh, N. D.; Chen, C. H., Gradient porous elastic hydrogels with shape- memory property and anisotropic responses for programmable locomotion. *Advanced Functional Materials* 2015, *25* (47), 7272-7279.

25. Bansil, R.; Guangdong, L., Kinetics of spinodal decomposition in homopolymer solutions and gels. *Trends in polymer science* 1997, *5* (5), 146-154.

26. Koshy, S.; Khademhosseini, A.; Dehghani, F., Controlling the Porosity and Microarchitecture of Hydrogels for Tissue Engineering.

27. Thomson, R.; Wake, M.; Yaszemski, M. J.; Mikos, A., Biodegradable polymer scaffolds to regenerate organs. In *Biopolymers Ii*, Springer: 1995; pp 245-274.

28. Qian, L.; Zhang, H., Controlled freezing and freeze drying: a versatile route for porous and micro-/nano-structured materials. *Journal of Chemical Technology & Biotechnology* 2011, *86* (2), 172-184.

29. Plieva, F. M.; Galaev, I. Y.; Mattiasson, B., Macroporous gels prepared at subzero temperatures as novel materials for chromatography of particulate-containing fluids and cell culture applications. *Journal of Separation Science* 2007, *30* (11), 1657-1671.

30. Oikonomopoulou, V. P.; Krokida, M. K.; Karathanos, V. T., The influence of freeze drying conditions on microstructural changes of food products. *Procedia Food Science* 2011, *1*, 647-654.

31. Banzhaf, S.; Hebig, K., *Use of column experiments to investigate the fate of organic micropollutants - A review*. 2016; Vol. 20, p 3719-3737.

32. Abbasi, M. Z., *An Experimental Study on Solute Transport in One-Dimensional Clay Soil Columns*. 2017; Vol. 2017, p 17.

33. Einsiedl, F.; Maloszewski, P., Tracer tests in fractured rocks with a new fluorescent dye—pyrene-1,3,6,8-tetra sulphonic acid (PTS) / Tests de traçage en roches fracturées avec un nouveau produit fluorescent—l'acide pyrène 1.3.6.8 tétra sulfonique (PTS). *Hydrological Sciences Journal* 2005, *50* (3), null-554.

34. Taylor, C. J. *Summary and interpretation of dye-tracer tests to investigate the hydraulic connection of fractures at a ridge-and-valley-wall site near Fishtrap Lake, Pike County, Kentucky*; 94-4189; 1994.

35. Plieva, F. M.; Galaev, I. Y.; Noppe, W.; Mattiasson, B., Cryogel applications in microbiology. *Trends in microbiology* 2008, *16* (11), 543-551.

36. Wang, C.; Chen, X.; Wang, B.; Huang, M.; Wang, B.; Jiang, Y.; Ruoff, R. S., Freeze-casting produces a graphene oxide aerogel with a radial and centrosymmetric structure. *ACS nano* 2018, *12* (6), 5816-5825.

37. Gun'ko, V. M.; Savina, I. N.; Mikhalovsky, S. V., Cryogels: morphological, structural and adsorption characterisation. *Advances in Colloid and Interface Science* 2013, *187*, 1-46.

38. Chang, C.; Han, K.; Zhang, L., Structure and properties of cellulose/poly(N-isopropylacrylamide) hydrogels prepared by IPN strategy. *Polymers for Advanced Technologies* 2011, *22* (9), 1329-1334.

39. Bencherif, S. A.; Sands, R. W.; Bhatta, D.; Arany, P.; Verbeke, C. S.; Edwards, D. A.; Mooney, D. J., Injectable preformed scaffolds with shape-memory properties. *Proceedings of the National Academy of Sciences* 2012, *109* (48), 19590-19595.

40. Lozinsky, V. I.; Galaev, I. Y.; Plieva, F. M.; Savina, I. N.; Jungvid, H.; Mattiasson, B., Polymeric cryogels as promising materials of biotechnological interest. *TRENDS in Biotechnology* 2003, *21* (10), 445-451.

41. Razavi, M.; Hu, S.; Thakor, A. S., A collagen based cryogel bioscaffold coated with nanostructured polydopamine as a platform for mesenchymal stem cell therapy. *Journal of Biomedical Materials Research Part A* 2018, *106* (8), 2213-2228.

42. Luo, R.; Wu, J.; Dinh, N.-D.; Chen, C.-H., Gradient Porous Elastic Hydrogels with Shape-Memory Property and Anisotropic Responses for Programmable Locomotion. *Advanced Functional Materials* 2015, *25* (47), 7272-7279.

43. Kabra, B. G.; Gehrke, S. H.; Spontak, R. J., Microporous, Responsive Hydroxypropyl Cellulose Gels. 1. Synthesis and Microstructure. *Macromolecules* 1998, *31* (7), 2166-2173.

44. Hirsch, S. G.; Spontak, R. J., Temperature-dependent property development in hydrogels derived from hydroxypropylcellulose. *Polymer* 2002, *43* (1), 123-129.

Chapter Six

6. Preparation and characterization of hydroxypropyl cellulose/calcium alginate double network HPC/CA DN hydrogel materials

In the previous chapters, the preparation and characterization of thermoresponsive macroporous HPC hydrogels and the permeable gradient porous HPC hydrogel with different pores size through variation the temperature between the upper and lower part of the hydrogel depends on the LCST and cryogenic treatment of the gradient porous hydrogel have been discussed. The thermally different process allows a gradual change in pore geometry and pore size, whereas the ice templating technique allows an improved permeability of the hydrogel across the volume. In this chapter, a novel promising route has been used to prepare hybrid DN hydrogel by mixing two types of crosslinked polymer: covalently crosslinked hydroxypropyl cellulose (HPC) and ionically crosslinked calcium alginate (CA) by a two-step method.

6.1. Introduction

Hydrogels materials have been widely used as adsorbents in the wastewater remediation field.[1-4]However, using hydrogels in adsorption process are often limited by their low adsorption capacity and poor mechanical properties (strength and toughness) leading to recycling difficulty.[5-7] Developing hydrogel materials with both good mechanical properties and high adsorption capacity is necessary for environmental application. Therefore, as one kind of high mechanical strength hydrogel, double network (DN) hydrogels have attracted considerable attention due to their good mechanical properties and provides plenty of active sites for adsorbing, which make them promising adsorbent for water treatment.[8]

DN hydrogel is a type of Interpenetrating Polymer Network (IPN) hydrogel. This consists of two types of polymer networks without covalent linkages.[9, 10] The properties of the two networks are very different due to their network density, molecular weight, cross-linking density and rigidity.[11] Generally, DN hydrogels have drawn much attention as an innovative material due to their superior properties such as higher mechanical strength and toughness in comparison with the corresponding single-network parent hydrogels.[12,13, 14, 15] The double-network structure can effectively improve the mechanical strength of hydrogels and it possesses good water permeability and excellent expansibility for easy access of guest molecules. DN hydrogel also introduces extra functional groups

into the network structures, these functional DN hydrogels are excellent adsorbents for wastewater treatment.[16]

DN hydrogels are usually synthesized via a classical method which includes a two-step polymerization process.[9, 15] The first step is to use strong polyelectrolytes to form a covalently cross-linked, rigid and brittle structure. Then, the first polyelectrolyte gel is immersed and swelled in a precursor solution containing the second network monomers, initiators and cross-linkers. During the swelling process, the second polymerization occurs to form the second network within the first network structure. The first DN hydrogel was fabricated using a two-step method by Gong *et al.* in 2003. They generated a DN hydrogel from two hydrophilic polymers separately crosslinked by two covalent bonds utilising a two-step method via free radical polymerization. The resulting hydrogel showed excellent mechanical strength and toughness as compared with single network hydrogels which are prepared from these polymers.[15] However, the chemically cross-linked DN hydrogels were damaged during stretching the hydrogel, due to the permanent breaking of chemical bonds in the first network and lack an ability to recover efficiently from this damage. [17]

To overcome this problem, the DN hydrogel can be created by different types of crosslinking.[18] Hybrid DN hydrogels always contain a physically cross-linked component and a chemically linked part.[19]The association forces between both networks and within the physical network are non-covalent linkages such as hydrophobic interactions, Van der Waals interactions, hydrogen bonding and electrostatic association. This is dependent on the intrinsic physicochemical properties of both individual polymers.[20] Suo and co-workers created DN hydrogels by mixing two types of cross-linked polymers which were covalently bound by polyacrylamide and ionically cross-linked with alginate having extremely stretchable and tough properties.[18] DN hydrogels with both covalent and ionic cross-links enable recoverable energy dissipating mechanisms. When the hydrogel is stretched, the covalent crosslinking chains do not rupture, whereas the ionic cross-links will break and dissipate energy. The ionic crosslinks can restructure after a period of time after the first loading.[21]

Here, a novel hybrid double network hydrogel was prepared by a simple two-step synthetic route with both chemically and physically cross-linking comprising of hydroxypropyl cellulose (HPC) and calcium alginate (CA) respectively to improve the mechanical properties of HPC hydrogel. The chemical cross-linked HPC hydrogel (the first network) was produced using DVS as chemical cross-linker during the same TIPS method as described in Chapter 4. While the second network formed by ionic crosslinking

of alginate chains through multivalent inorganic cations (Ca^{2+}), resulting in an alginate based hydrogel. Furthermore, alginate was selected to be the second network polymer due to the alginate with a carboxylate function groups is a suitable agent to remove cationic pollutant by electrostatic interactions which can improve the adsorption capacity of HPC SN hydrogel.[22] In addition to that this polymer naturally abundant, environmentally friendly, reusable and cheap materials.

6.2. Results and discussions

6.2.1. Preparation of HPC/CA DN hydrogel

Double network hydrogel (DN) strategy was developed to fabricate novel hydrogels composed of cellulose derivative HPC and sodium alginate. Various preparation methods were used to reach the target, which is a synthesis of HPC/CA DN hydrogels. In general, these methods can be classified into two types: Firstly the first network was prepared in present the polymer of the second network (one-step method).[23]Secondly, complete synthesis of the first network in the absence of the second network polymer with the second network polymer being diffused inside the first network and afterward cross-linked this polymer was occurred within the first network (two-step method).[24] Both those types were prepared at different gelation temperature at LCST and below the LCST of HPC as described in chapter two. Method four (M4) is a more favorable method in the synthesis of HPC/CA DN hydrogel due to its promising results. Therefore, Figure 6.1 illustrated the M4 method for preparing HPC/CA DN hydrogel by two steps approach and the estimated structure of the resulting DN hydrogel. The scheme shows how the diffusion of the second network polymer in the first network depends on the thermoresponsive behaviour of the first network hydrogel. The HPC chains collapse to a shrunken structure at the LCST freeing the surrounding water molecules due to entropic effects, thereby adding the second polymer at this temperature helps to improve diffusion of the second polymer when the mixture transfer to the swollen structure at a temperature below the LCST.[25] Figure 6.1 also shows the structures of chemical and physical crosslinking of the hybrid HPC/CA DN hydrogel.

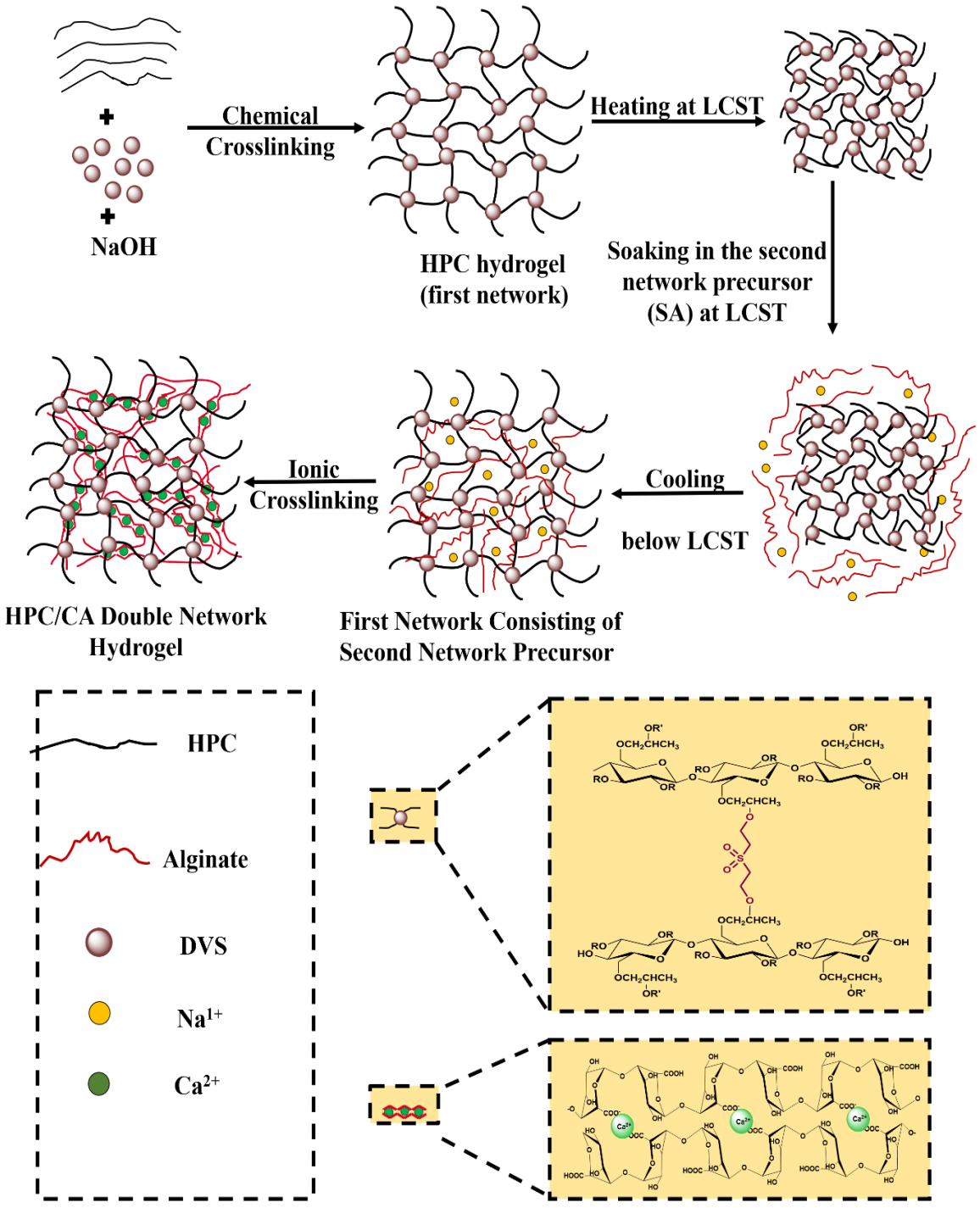

Figure 6.1. Schematic diagram illustrations design and fabrication of HPC/CA DN hydrogel by two steps method synthesis protocol and the possible structure of the first network (chemically cross-linked HPC) and the structure of the second network (ionically cross-linked CA).

6.2.2. Morphology of HPC/CA Double network hydrogel

6.2.2.1 Morphology of HPC/CA network hydrogel prepared via one-step method M1 and M2

Scanning Electron Microscopy (SEM) images of HPC/CA hydrogels which were prepared in the presence of the second network polymer during the preparation of the first network via chemical cross-linking at gelation temperature below the LCST (M1) are presented in Figure 6.2 shown the same area of the sample at different magnifications. The macroporous structure with different pores size (10-30 μm) are seen on the SEM image of the hydrogel prepared in this method. Whereas in Figure 6.3 SEM images of HPC/CA hydrogels obtained by gelation the sample at the LCST of HPC in one step are also shown at different magnifications. The SEM images show Sphere-like pores structure with different size (1-5 μm) and these images also show some nonporous smooth white spots, which is might be due to crosslinked of extra SA via calcium ions to form CA hydrogel.

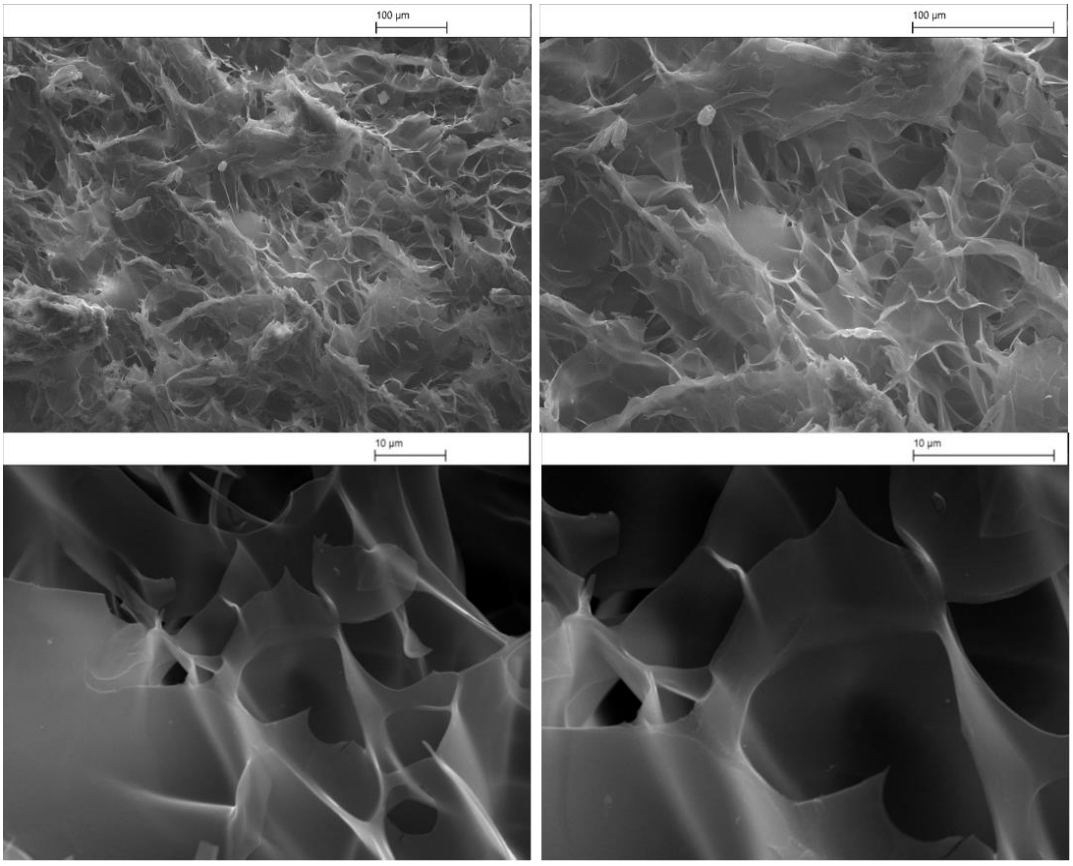

Figure 6.2. SEM images at different magnifications of FD-HPC/CA hydrogel sample (7.0 w/v % – 1.0 w/v % of HPC-SA) using 1.3 % w/v DVS as a chemical crosslinker for HPC at RT and 50 mmoles $CaCl_2$ as an ionic crosslinker for SA in one step method (M1). The scale bars correspond to 100 μm and 10 μm.

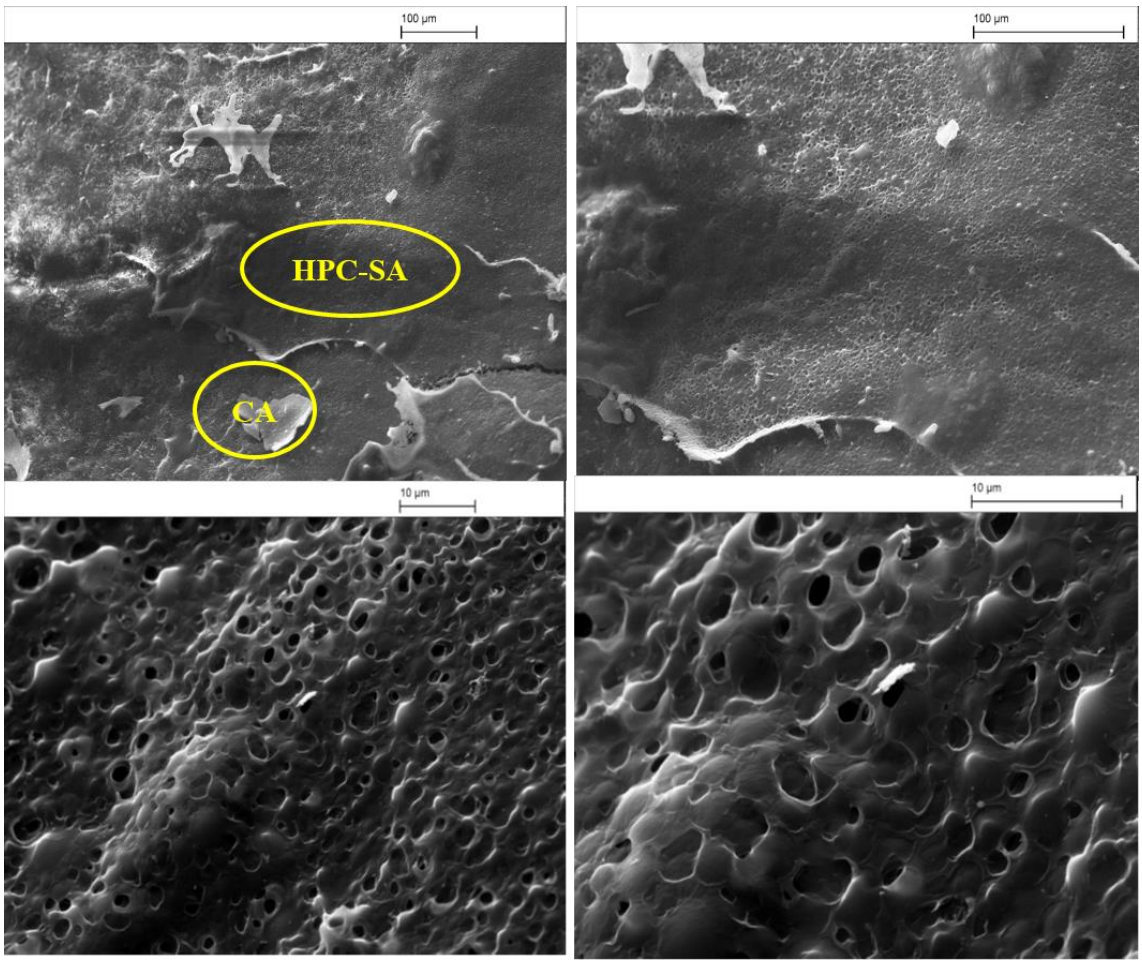

Figure 6.3. SEM images at different magnifications of FD-HPC/CA hydrogel sample (7.0 w/v % – 1.0 w/v % of HPC-SA) using 1.3 % w/v DVS as chemical crosslinker for HPC and 50 mmole $CaCl_2$ as ionic crosslinker for SA at LCST in one step method (M2). The scale bars correspond to 100 µm and 10 µm.

In both cases, the hydrogels produced in M1 and M2 show a single network structure as visualised by SEM images. From Figure 6.2 the SEM images of the freeze-dried HPC/CA hydrogel was prepared by mixing the SA with HPC during the preparation of the first network (one step method) at a temperature below the LCST (M1) has a heterogeneous interconnecting porous structure with big pore size. It also showed that the HPC/CA prepared by this method is not two independent networks. This was due to hydrogen bonding interactions between HPC and SA or might be because of the SA cross-linked with DVS during the gelation at this temperature resultant hydrogel with a single network of blend SA and HPC.[26, 27] Despite, FD-HPC/CA hydrogel prepared by mixing the SA with HPC during the preparation of the first network (one step method) and gelation at LCST (M2) also showed a single network of blend SA and HPC, but the morphology structure was different from HPC/CA hydrogel prepared by M1. The change in

morphology provided some evidence to the spinodal decomposition of the HPC/SA hydrogel during the phase separation at the LCST of HPC.[28]

EDX spectra of FD-HPC/CA hydrogels prepared by M1 and M2 via the one step method are presented in Figures 6.4 and 6.5 for M1 and M2 respectively. In both cases, the spectra detected atomic fractions of carbon, oxygen, sulfur, calcium and sodium elements. As shown in Figure 6.4 the atomic percentage of S element are 4.50%, while the atomic fraction of Ca element are just 0.24 % in the spectra. Approximately similar results were obtained for atomic % values of HPC/CA hydrogel prepared by M2, which are 4.05% of S element and 0.57% of Ca element as shown in Figure 6.5.

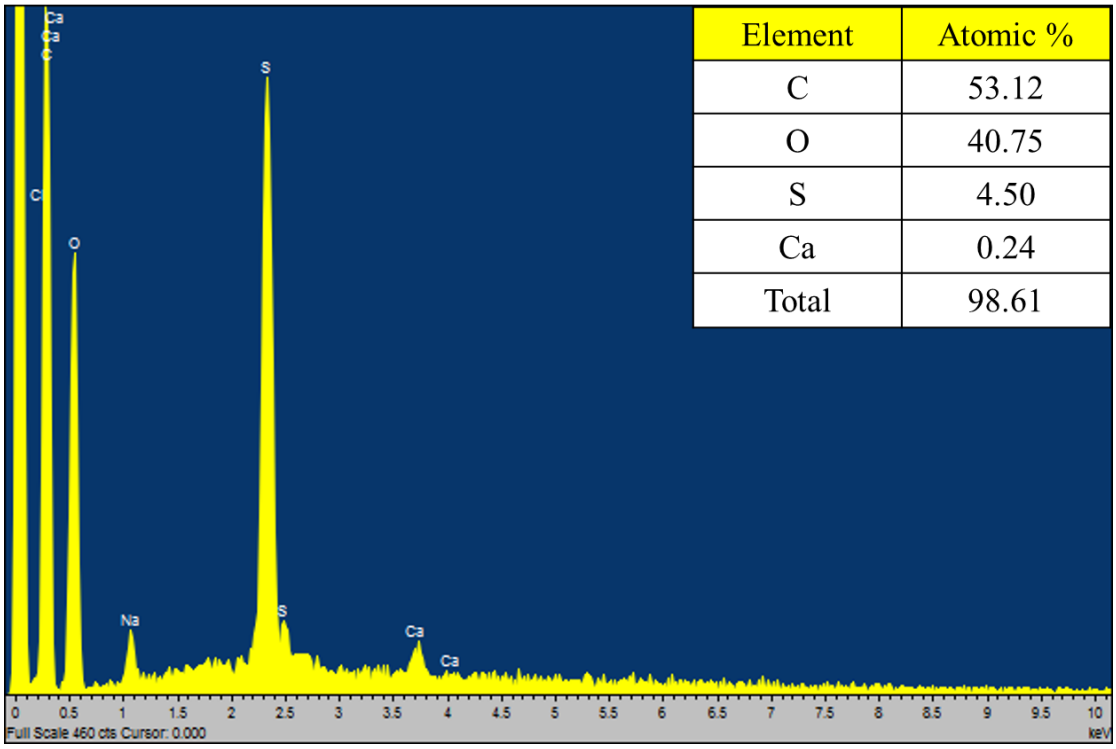

Element	Atomic %
C	53.12
O	40.75
S	4.50
Ca	0.24
Total	98.61

Figure 6.4. EDX of FD-HPC/CA hydrogel sample (7.0 w/v % – 1.0 w/v % of HPC-SA) using 1.3 % w/v DVS as a chemical crosslinker for HPC at RT and 50 mmoles $CaCl_2$ as an ionic crosslinker for SA in one step method (M1).

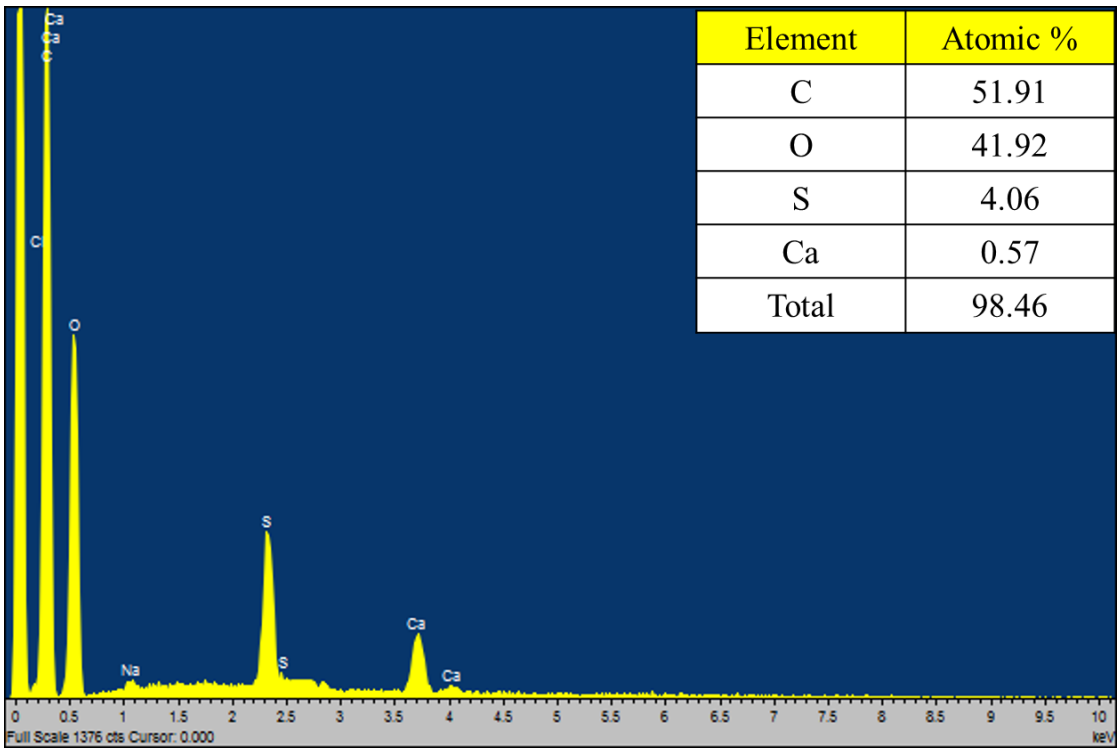

Element	Atomic %
C	51.91
O	41.92
S	4.06
Ca	0.57
Total	98.46

Figure 6.5. EDX of FD-HPC/CA hydrogel sample (7.0 w/v % – 1.0 w/v % of HPC-SA) using 1.3 % w/v DVS as chemical cross linker for HPC and 50 mmole $CaCl_2$ as ionic cross linker for SA at LCST in one step method (M2).

The results show the main element of the hydrogels were found to be carbon, oxygen and sulfur, which indicates that HPC reacted with DVS forming crosslinking covalent bonds as cross-linking also reveals the presented of sulfone group in the network structure.[29] While the amount of calcium is very small with a low peak intensity of Ca element at 3.7 keV.[30] The low percentage of Ca along with carbon, oxygen and sulfur peaks was confirmed that the covalent bonding between HPC and SA chains via DVS due to present the second network polymer during the initial crosslinking of the first network. Therefore, decreasing the ionic bonding between Ca^{2+} and second network polymer chains. From the EDX results, it could be concluded that the chemical crosslinking between HPC and the SA chains form a single network with high purity and the ionic crosslinking between the SA chains has failed. Thus, M1 and M2 failed to form DN hydrogels due to reacting the second network polymer with the crosslinker of the first network polymer during the initial cross-linking.[31]

6.2.2.2 Morphology of HPC/CA double network hydrogel prepared via two-step method M3 and M4

The cross-sectional morphology of the HPC/CA hydrogels, which prepared by complete gelation of the first network at LCST and followed by the adding of second network polymer (two steps method) at below the LCST of HPC (M3) was visualized by SEM images in Figure 6.6 at different magnifications for the same sample area. SEM micrographs showed that the HPC/CA DN hydrogel exhibited different morphologies from those of the hydrogel samples prepared in one step methods M1 and M2 in Figures 6.2 and 6.3 respectively. As shown in Figure 6.6, the HPC/CA DN hydrogels possessed an integrated reticulate architecture, which appeared as a combination of the chemically cross-linked HPC SN hydrogel structure and ionically cross-linked CA SN hydrogel structure.

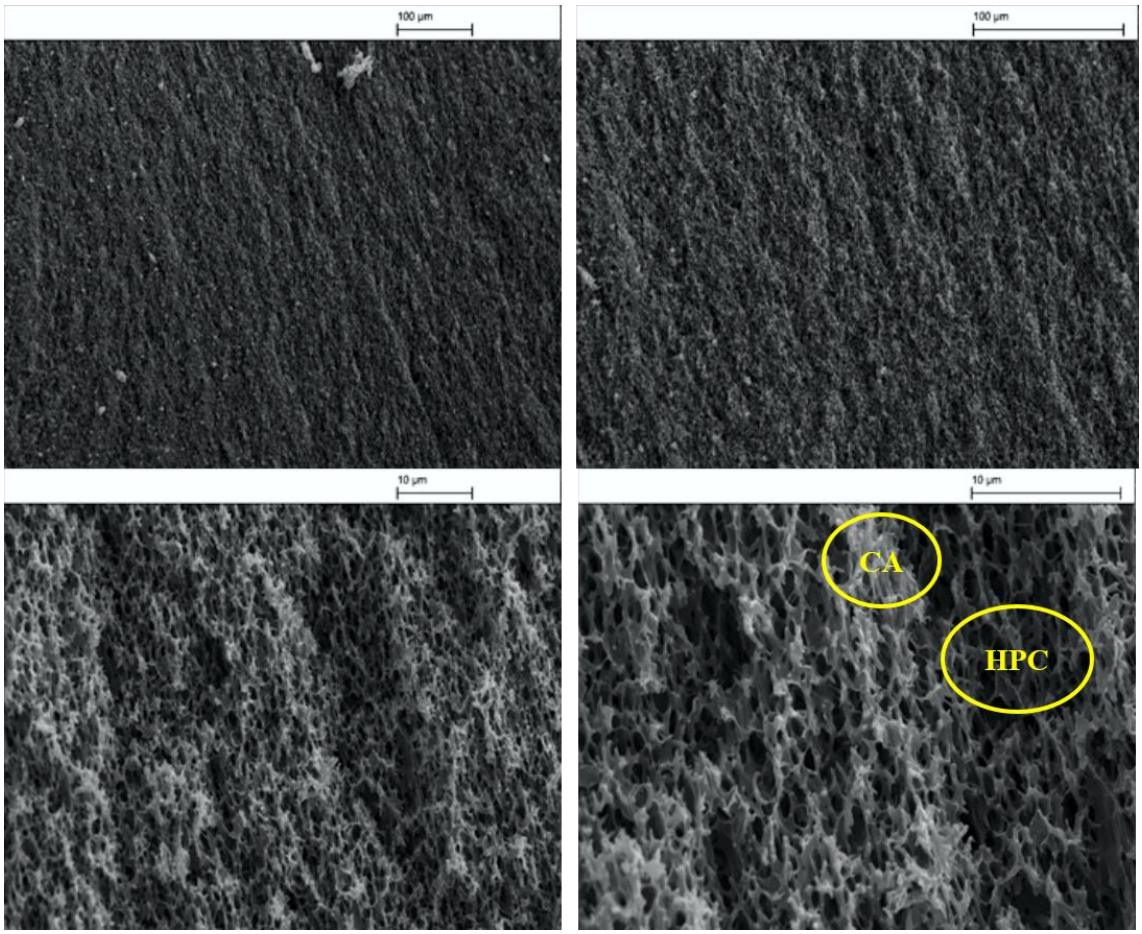

Figure 6.6. SEM images at different magnifications of FD-HPC/CA hydrogel prepared by using 7.0 w/v % HPC and 1.3 w/v % DVS as crosslinker at LCST and immersing HPC hydrogel in 1 w/v % SA solution at below the LCST (two steps method M3).

The combined architecture of the HPC/CA DN hydrogels indicated the interpenetration of two networks. SEM confirms that the HPC/CA DN hydrogels were successfully obtained by two-step method in M3 method. Successful incorporation of the second network within DN hydrogel is also cross-validated by energy dispersive X-ray analysis. Figure 6.7 shows the EDX spectrum of the selected area of HPC/CA DN hydrogel prepared in the two-step method by M3. In the preparation process, HPC effectively cross linked by DVS in alkaline media, suggested by sulfur peak at around 2.4 keV.[29] After preparation of the second network within the HPC hydrogel, a new cationic calcium characteristic peak appears at 3.7 keV, demonstrating the ionic cross-linking of the second network polymer.[30]

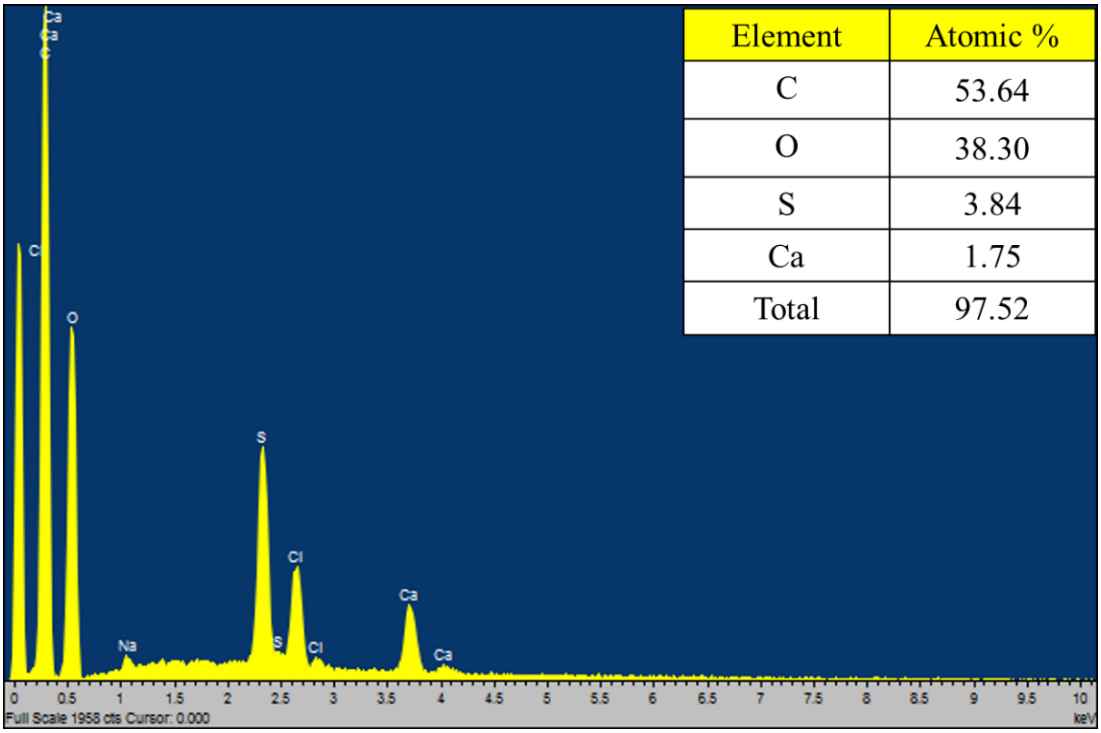

Element	Atomic %
C	53.64
O	38.30
S	3.84
Ca	1.75
Total	97.52

Figure 6.7. EDX of FD-HPC/CA DN hydrogel sample (7.0 w/v % – 1.0 w/v % of HPC-SA) using 1.3 % w/v DVS as chemical crosslinker for HPC and 50 mmole $CaCl_2$ as ionic crosslinker for SA at temperature below the LCST in two-step method (M3).

Despite, the above method was successful method for fabricating of HPC/CA DN hydrogel, but poorly diffusion the second polymer chains in the first network at the temperature below the LCST of HPC due to the swelling state of the first network at this temperature, the second network polymer will slowly trap into the 1st network leading to low present of the second network in the hydrogels.[20] Thus HPC/CA DN hydrogel prepared by this method shows heterogeneous structure with two networks and the second network just in the surface layer of the first network. This situation can be explained by

the fact that the ionic crosslinking occurred intensively on the surface. Thus the calcium cross-linking displaied lower percentage than the percentage of DVS chemical cross-linking as demonstrated in the EDX spectra in Figure 6.7.

To overcome the above problem HPC/CA DN hydrogel was also prepared by two steps method by complete gelation of the first network at LCST with add of the second network polymer at LCST via the M4 method as described in the schematic diagram in Figure 6.1. The microstructures of the hydrogel prepared by the M4 method at various mixing ratios of HPC were observed using SEM and the representative results are shown in Figures 6.8, 6.9 and 6.10 for 7.0 w/v %, 5.0 w/v % and 2.0 w/v % HPC respectively. As shown all these images confirmed the presence of two different crosslinked network structure with interconnected highly porous network structures. HPC/CA DN hydrogel prepared by M4 method showed an extremely different morphology structure from the DN hydrogels prepared by M3 method. A homogeneous porous structure was demonstrated with a small pore size. The alginate network showed lamellar structure while the HPC network was compact and dense. It was interesting to see that, at high HPC content (7.0 w/v % and 5.0 w/v %) the amount of CA network structures became less as shown in Figures 6.8 and 6.9 for 7.0 w/v% and 5.0 w/v% HPC respectively. Whereas, in the case of the HPC/CA DN hydrogel with 2.0 w/v % (Figure 6.8), it can be observed that there was a large amount of CA network located within the porous structure of the HPC network.

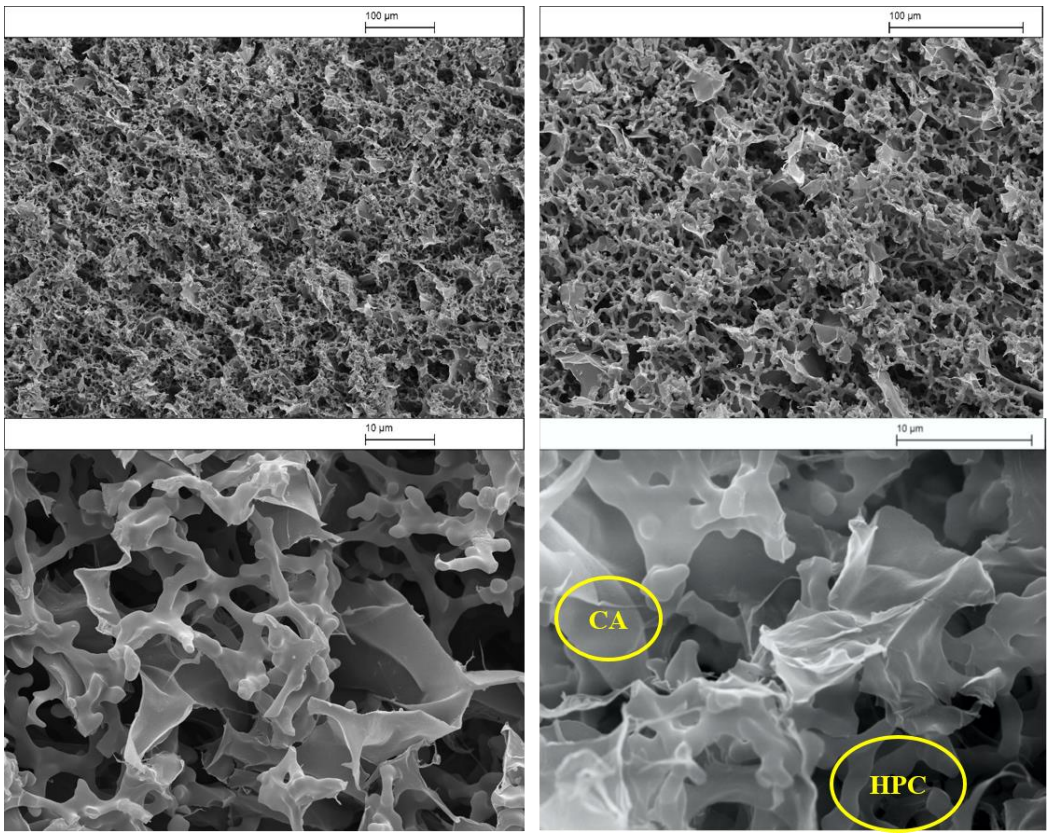

Figure 6.8. SEM images at different magnifications of FD-HPC/CA hydrogel prepared by using 7.0 w/v % HPC and 1.3 w/v % DVS as crosslinker at LCST and immersing HPC hydrogel in 1.0 w/v % SA solution at LCST (two steps method M4).

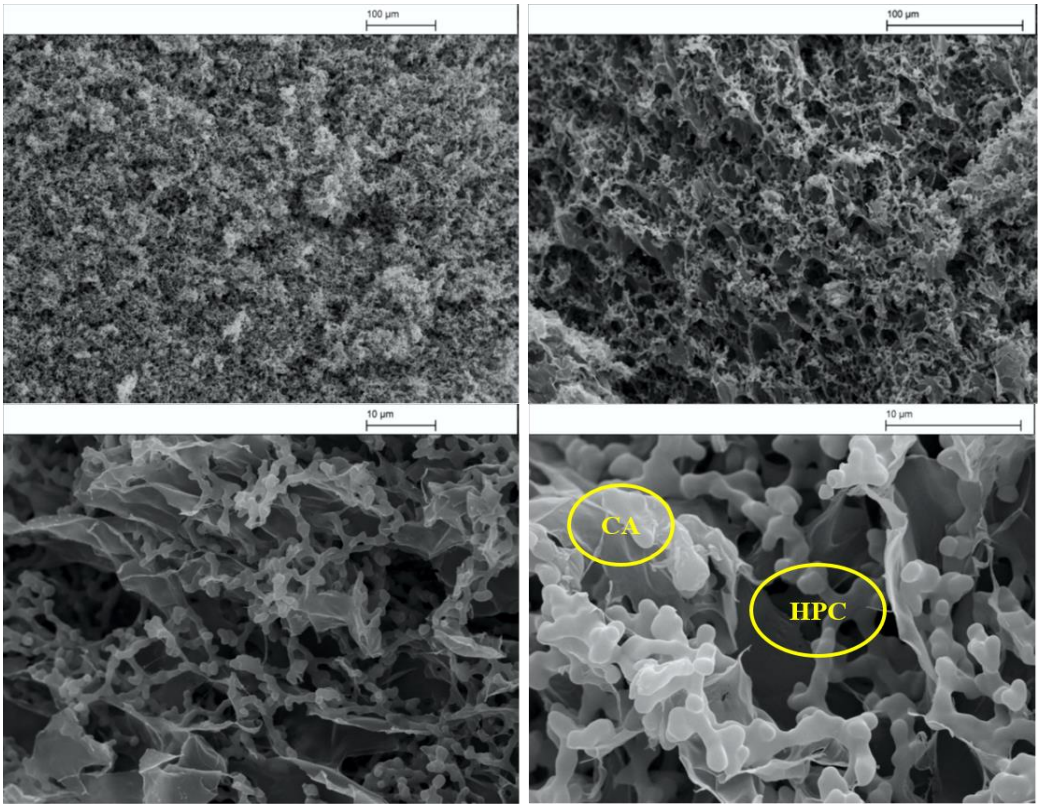

Figure 6.9. SEM images at different magnifications of FD-HPC/CA hydrogel prepared by using 5.0 w/v % HPC and 1.3 w/v % DVS as cross linker at LCST and immersing HPC hydrogel in 0.5 w/v % SA solution at LCST (two steps method M4).

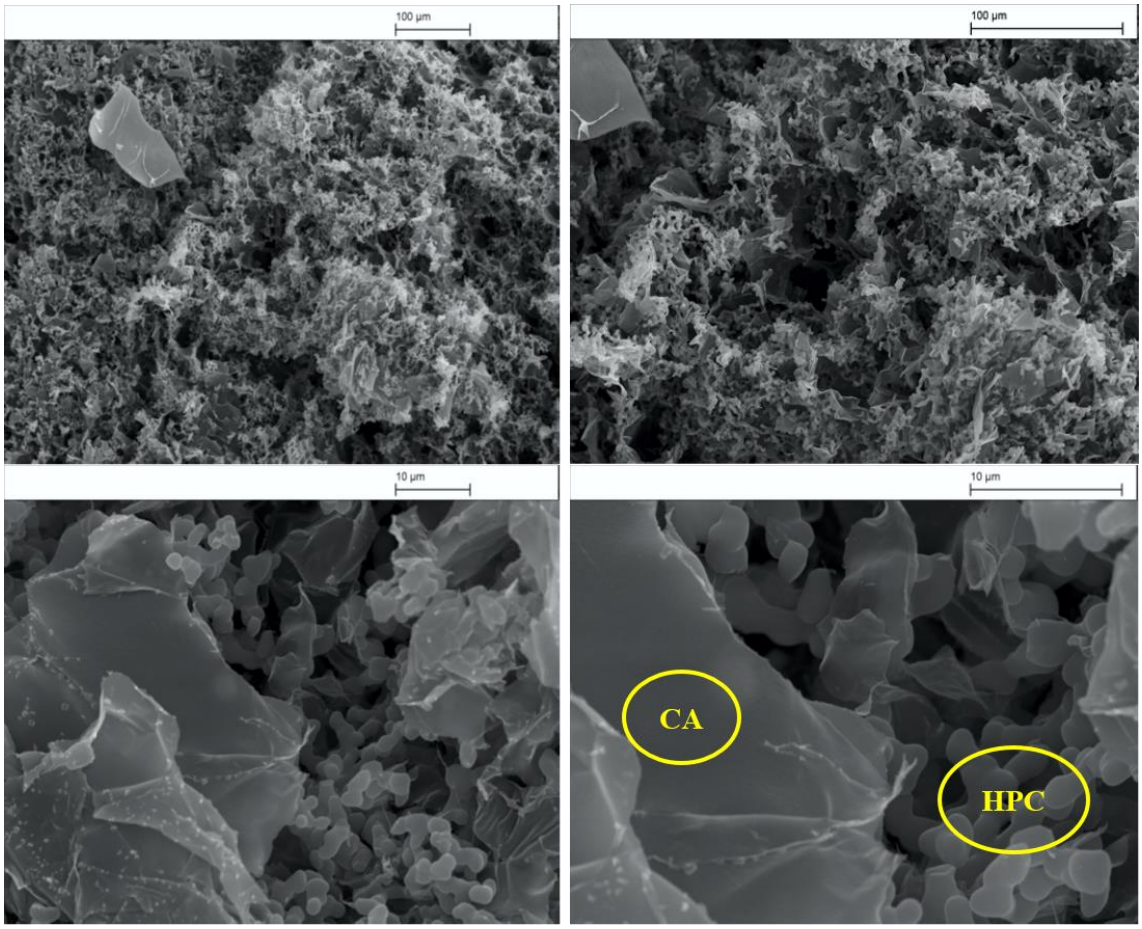

Figure 6.10. SEM images at different magnifications of FD-HPC/CA hydrogel prepared by using 2.0 w/v % HPC and 1.3 w/v % DVS as crosslinker at LCST and immersing HPC hydrogel in 1.0 w/v % SA solution at LCST (two steps method M4).

It was seen that the SEM images of the HPC/CA double networks, which prepared by two steps approach via M4 method showed extremely various morphologies from M1,M2 and M3 method. It was demonstrated the interconnecting porous structure was composed of two independently cross-linked networks with homogenous interpreting of CA network hydrogel within HPC network structure. The main reason behind that the dispersion of SA polymer inside the first network hydrogel matrix was improved during transfer the HPC hydrogel from two phase separation to one phase separation with the change in temperature. It has also partially prevented the formation of aggregates of the second network on the first network hydrogel surface.[32] So, the hydrophilic group in the HPC hydrogel structure formed an intermolecular hydrogen bond with surrounding water at low temperature (below the LCST), while above the LCST the hydrogen bonds are broken and the water molecules are expelled from the hydrogel.[33] This phenomenon makes it easy for the SA chain to distribute into the HPC hydrogel network structure when changing the temperature to below the LCST again.[34, 35] In addition, the increase of the

initial HPC concentrations induced a reduction in the size of the pores and increased the entanglements of the HPC hydrogel due to increase of the crosslinking density leading to the lower amounts of SA chain distributed in the hydrogel.[36]

In order to study in more detail the morphology structural of HPC/CA DN hydrogel, the morphology under wet conditions was also observed using cryo-SEM. The cryo-SEM images of HPC/CA DN hydrogels (2.0 w/v %/ 1.0 w/v % HPC/SA) prepared by the M4 method at different magnifications are shown in Figures 6.11. It can be seen that two interlocked crosslinked network structure with an interconnected highly porous network structures, HPC has a dense structure, while CA showed a lamellar structure. The domination of the results CA network was clear in this hydrogel due to the higher alginate content.

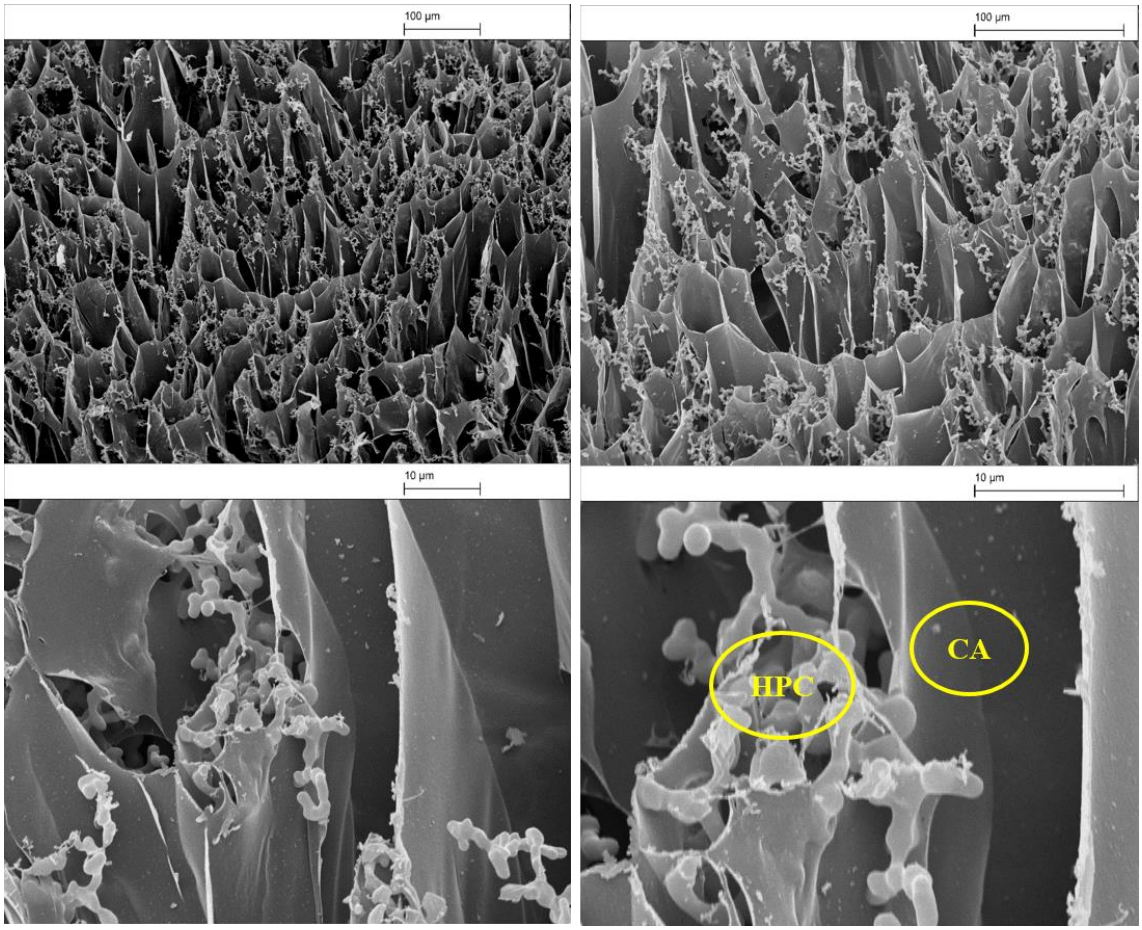

Figure 6.11. Cryo-SEM images at different magnifications of HPC/CA DN hydrogel prepared by M4 method with HPC-SA concentrations (2.0 w/v %/ 1.0 w/v % HPC/SA).

The morphological structure of HPC/CA DN hydrogels are different between wet and dry states as can be clearly observed in Figures 6.10 and 6.11. By comparing freeze-dried hydrogel (Figure 6.10) and the swollen hydrogels (Figure 6.11), it can be seen that freeze-dried hydrogel has a denser structure than wet hydrogel and the swollen hydrogels had a

bigger pore size with pore diameters ranging from 5 to 30 μm. This situation may be attributed to different polymeric chain conformation caused by the drying method and will result in shrinkage in the hydrogel network. The change in morphology provided some evidence of the swelling behaviours of the hydrogels in the wet state.[37]

EDX results give more information about the formation of double network by determining the quantitative analysis of the various elements present in the samples. Comparison of the EDX data in case of DN hydrogel prepared by M3 method (Figure 6.7) and M4 method (Figure 6.12) with HPC-SA concentrations (7.0 w/v %/ 1.0 w/v % HPC/SA) showed that calcium ion content has increased from (1.75 atomic % to 3.65 atomic %) in the HPC/CA DN hydrogels prepared by M4 method with respect to the present of carbon and oxygen. EDX analysis was also carried out for HPC/CA DN hydrogel with various concentration of the first network hydrogel. EDX spectra of HPC/CA DN hydrogels prepared by M4 method are shown in Figures 6.12, 6.13 and 6.14 for 7.0 w/v %, 5.0 w/v % and 2.0 w/v % HPC respectively. Obviously, the Ca content increased significantly with decreasing HPC concentration from 3.65 atomic % for 7.0 w/v % to 7.05 atomic % for 2 w/v % HPC.

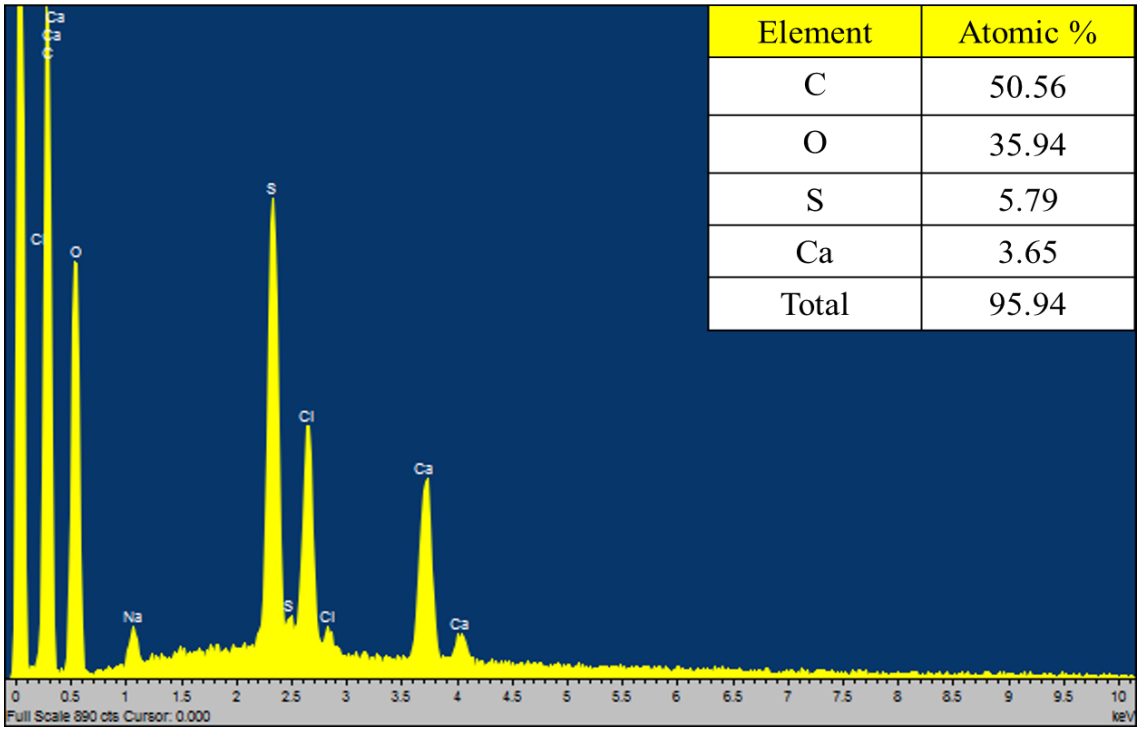

Element	Atomic %
C	50.56
O	35.94
S	5.79
Ca	3.65
Total	95.94

Figure 6.12. EDX of FD-HPC/CA DN hydrogel sample (7.0 w/v % – 1.0 w/v % of HPC-SA) using 1.3 % w/v DVS as chemical crosslinker for HPC and 50 mmole $CaCl_2$ as ionic cross linker for SA at the LCST in two step method (M4).

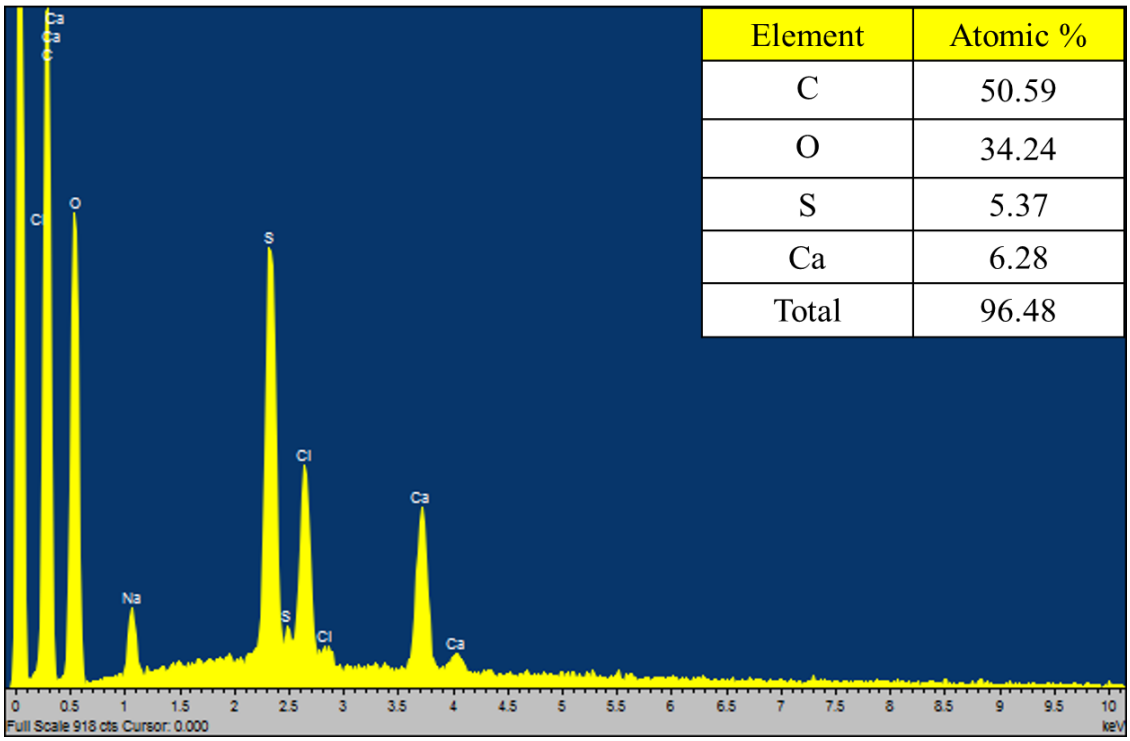

Element	Atomic %
C	50.59
O	34.24
S	5.37
Ca	6.28
Total	96.48

Figure 6.13. EDX of FD-HPC/CA DN hydrogel sample (5.0 w/v % – 1.0 w/v % of HPC-SA) using 1.3 % w/v DVS as chemical cross linker for HPC and 50 mmole $CaCl_2$ as ionic cross linker for SA at the LCST in two step method (M4).

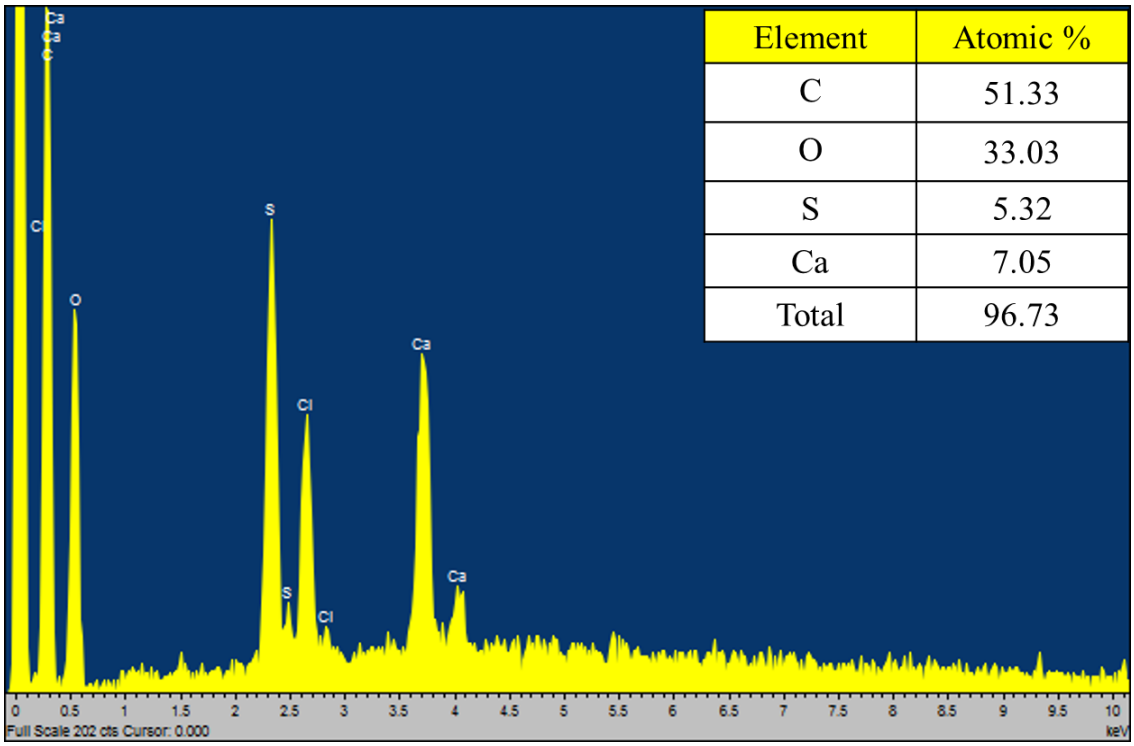

Element	Atomic %
C	51.33
O	33.03
S	5.32
Ca	7.05
Total	96.73

Figure 6.14. EDX of FD-HPC/CA DN hydrogel sample (2.0 w/v % – 1.0 w/v % of HPC-SA) using 1.3 % w/v DVS as chemical crosslinker for HPC and 50 mmole $CaCl_2$ as ionic cross linker for SA at the LCST in two step method (M4).

The contents of Ca element in the HPC/CA DN hydrogel prepared by the M4 method increased as compared to the HPC/CA DN hydrogel prepared by the M3 method. Calcium % increased after the addition of the SA at the LCST confirmed that the SA polymer is well distributed in the first network of the hydrogel.[38] Besides, it could be clearly seen that the calcium % of DN hydrogels prepared by M4 method with different concentration of HPC decreased significantly with increasing the concentration of the first network polymer from 2 w/v% to 7 w/v % HPC. As the content of HPC increased, the pore diameters of the HPC network became smaller and led to reduce the amounts of SA chains in the HPC network.[39] Therefore, calcium coordination in the second network decreased dramatically with an increase in the first network polymer ratios of HPC/CA DN hydrogels.

6.2.2.3. Morphology of HPC/CA DN hydrogel column prepared via two-step method M4

The morphology structural of HPC/CA DN hydrogel column for filtration prepared by M4 method was also studied. As seen in Figure 6.15 the cross-section images at different scales and magnifications of freeze-dried HPC/CA DN hydrogel column, which shows the formation of the homogeneous DN hydrogel networks with a ratio 6:1 hydroxypropyl cellulose to sodium alginate polymers and also demonstrates effective interlock between the two hydrogels networks.

As a result, hydrogels prepared according to M4 route as column present higher homogeneous between HPC and CA networks than those hydrogels prepared as monolith via the same route. This was due to long range ordered arrangement of the second crosslinked network in the first network structure that could enhance to the second network polymer (SA) was passed from the top of the column containing the HPC SN network until reaching the equilibrium and then cross-linked SA via passing calcium ion during the column. This morphology was provided some evidence that the HPC/CA DN hydrogels column exhibited an open and interconnected porous structure, thus these pores enabled easy passing the fluids during the column.

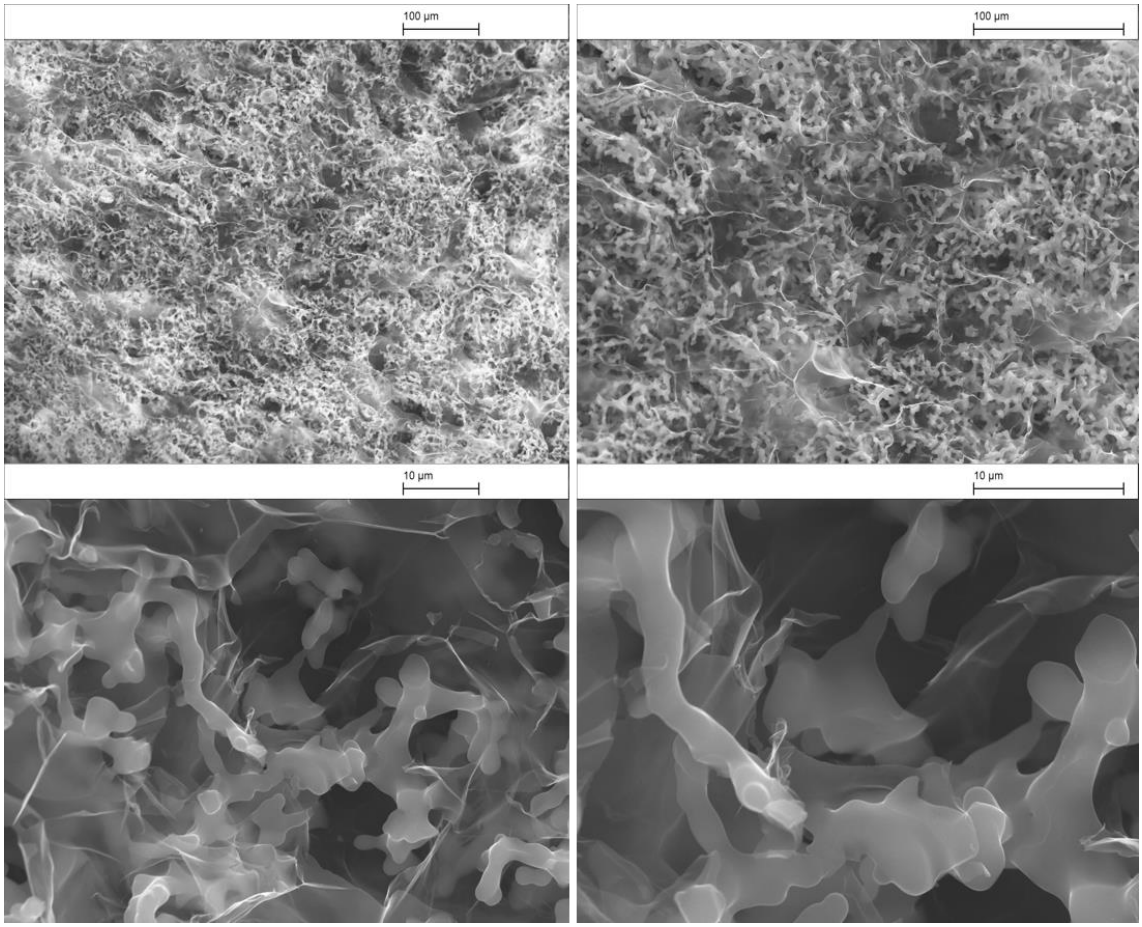

Figure 6.15. SEM images at different magnification of a freeze-dried column sample of HPC/CA DN hydrogel (7.0% w/v HPC and 1.0% w/v SA) prepared by two steps method via prepare the first network HPC with chemical cross-linking by DVS gelation at LCST of HPC and then added the polymer of the second network (SA) from the top of the column when it passes through the column adding the cross-linker $CaCl_2$ via M4 method.

The elemental analysis of HPC/CA DN hydrogel column sample was also determined by EDX as shown in Figure 6.16. The EDX pattern showed a high content of calcium ion (peak at 3.7 keV), which confirms that the ionic cross-linking of sodium alginate polymer successfully occurred within the first network.[30]

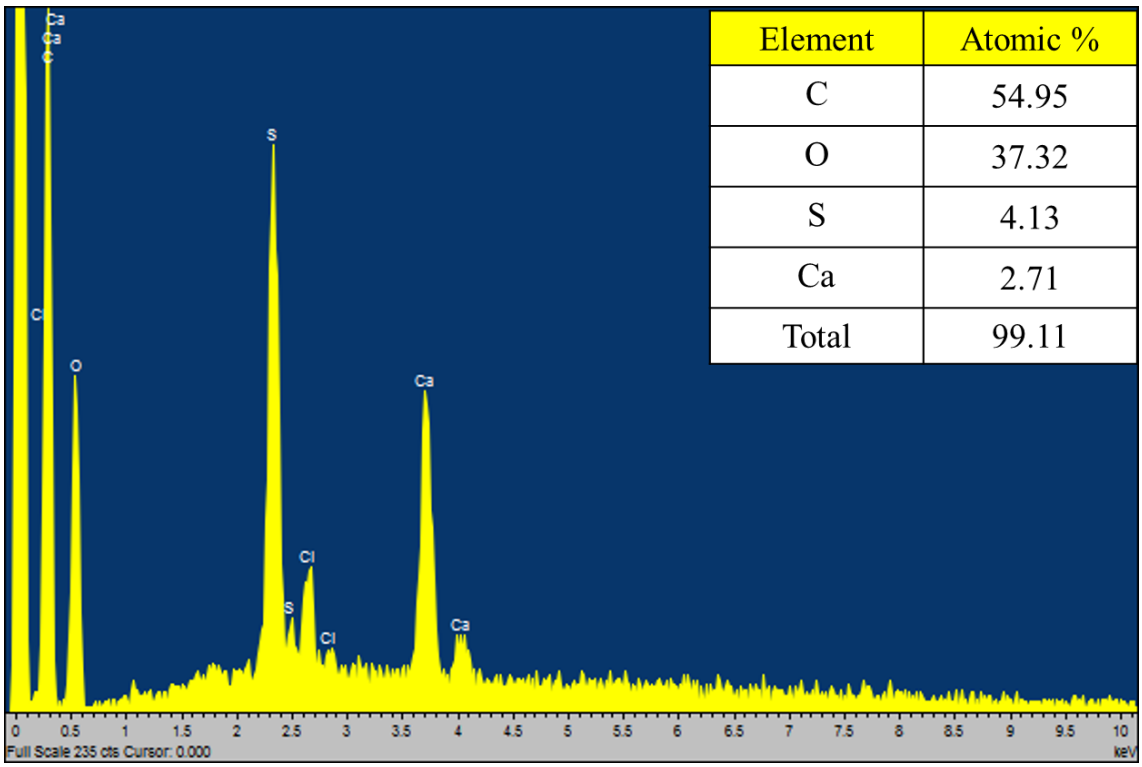

Element	Atomic %
C	54.95
O	37.32
S	4.13
Ca	2.71
Total	99.11

Figure 6.16. EDX of a freeze-dried column sample of HPC/CA DN hydrogel (7.0% w/v HPC and 1.0% w/v SA) prepared by two steps method via M4 by prepare the first network HPC with chemical cross-linking by DVS gelation at LCST of HPC and then added the polymer of the second network (SA) from the top of the column when it passes through the column adding the cross-linker $CaCl_2$.

6.2.3. BET surface area analysis

The BET surface area and porosity analysis was used to determine of the surface area and porosity of the FD-HPC/CA DN hydrogel and the results were compared with the values of the HPC SN hydrogel which demonstrated in Chapter 4. The textural properties of HPC SN and HPC/CA DN hydrogels are studied and listed in Tables 6.1, The results show that the BET surface area for the FD-HPC/CA DN hydrogel was found to be 35.4± 0.7 m^2. g^{-1}. The pore size distributions were calculated from the nitrogen sorption isotherm using the Barrett-Joyner-Halenda (BJH) model and were found to be 6.3 nm. Figure 6.18 displays the N_2 adsorption-desorption isotherms of the freeze-dried HPC/CA DN hydrogel prepared (6.0 w/v % HPC and 1.0 w/v % SA) by two steps method via M4 method, which was used to prepare the first network HPC with chemical cross-linking by DVS gelation at LCST of HPC and then added the polymer of the second network (SA) at the same temperature and cross-linked SA by $CaCl_2$ at temperature below the LCST. It can also be seen that as the pore diameter increased, the pore volume decreased,

indicating that well-developed pores led to a large surface area, which was beneficial for the adsorption efficiency.[40]

Table 6.1. Textural characterization of the FD-HPC SN and HPC/CA DN hydrogels.

Hydrogel types	BET surface area $m^2 g^{-1}$	Pore size nm	Pore volume $cm^3 g^{-1}$
HPC SN	5.1±0.1	9.2	0.0101
HPC/CA DN	35± 1.0	6.3	0.0137

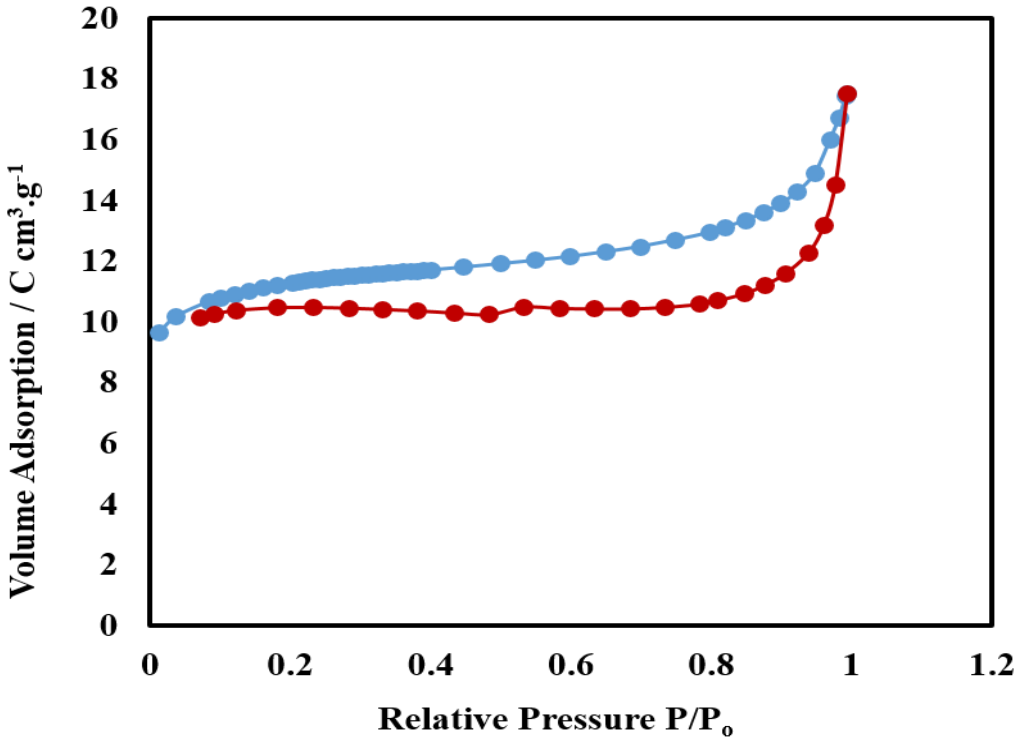

Figure 6.17. N_2 adsorption-desorption isotherm for FD-HPC/CA DN hydrogel sample (7.0 w/v % – 1.0 w/v % of HPC-SA) using 1.3 % w/v DVS as chemical crosslinker for HPC and 50 mmole $CaCl_2$ as ionic crosslinker for SA at the LCST in two-step method (M4) and degassing at 40 °C.

The sorption isotherms displayed type IV according to IUPAC with a hysteresis loop in the relative pressure P/P_o range of 0.5–1 P/P_o, indicating the FD-HPC/CA DN hydrogel had both mesoporous and macroporous structures.[41] The quantity of nitrogen sorption increased significantly at a P/P_o of 0.8, suggesting capillary condensation of nitrogen within the primary mesopores.[42] In comparison of the BET surface area values of HPC/CA DN hydrogel and HPC SN, the surface area increased from 5.1 ±0.1 $m^2.g^{-1}$ for SN hydrogel to 35.4 $m^2.g^{-1}$ for DN hydrogel and the average pore diameter decreased from 9.2 for SN to 6.3 nm for DN. This was due to the insertion of the second network

(CA hydrogel), which led to the increase of a specific surface area (SSA) with reduced the average pore diameter.[43] In contrast, the average pore diameter directly determined from SEM images was found around 5 µm. The mean reasons behind that there is error were happened for measuring the surface area and the pore diameter using nitrogen sorption method. As mentioned in the literature the specific surface area of macrospores materials obtained from nitrogen absorption method was approximately less than 1 m^2 /g, while for mesoporous materials measured by the same method was about 220 m^2 /g. This was due to the pores are very big compared with the adsorbed layers, thus there is no difference between open surface adsorption and macrosporous structure adsorption.

6.2.4. Fourier Transform Infrared Spectroscopy (FTIR)

The structural changes of calcium alginate, HPC hydrogel and the double network composited from CA and HPC were confirmed by FTIR spectroscopy. Figure 6.18 shows the ATR-FTIR spectrum and its characteristic peaks of HPC hydrogel (violet line), CA hydrogel (red line) and HPC/CA DN hydrogel (black line).

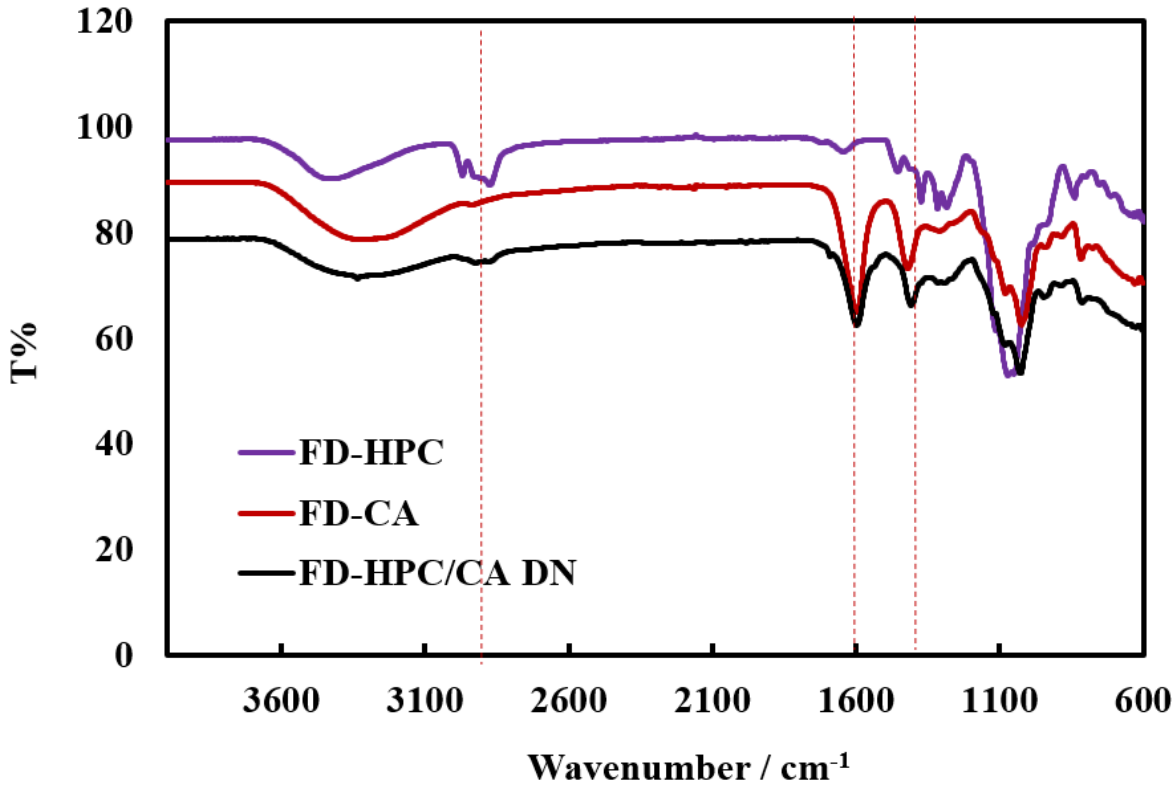

Figure 6.18. ATR-FTIR spectra of FD-HPC SN hydrogel (violent), FD-CA SN hydrogel (red), and HPC/CA DN hydrogel (black).

From Figure 6.18 the spectrum of the HPC SN hydrogel (violent) showed the peak at 3431 cm^{-1} which was assigned to the hydroxyl group in the HPC. Absorptions band at 2967 cm^{-1} and 2932 cm^{-1} was ascribed to CH_2 and CH stretching vibration. Stretching vibration peak of C=C was observed at 1533 $cm^{-1.}$ The strong peak at 1079 cm−1 belonged to C-O-C stretching vibration, which was consistent with the previous report.[44] Furthermore, the vibration bands that confirmed the chemical crosslinking between HPC chains via DVS appeared around 1300 cm^{-1} attributed to the asymmetric stretching of S=O in the sulfone cross-linker and the absorption band at approximately 700 cm^{-1} corresponds to thioether CH_2S (CS) stretching.[45] The spectrum of the CA SN hydrogel (Figure 6.18, (red line)) showed the absorption bands around 1610 cm^{-1}, 1416 cm^{-1}, are attributed to stretching vibrations of carboxylate anions and peak appeared at 3430 cm^{-1} corresponds to stretching vibrations of hydroxyl groups.[46] The data in Figure 6.18 (black line) show the characteristic peaks of both HPC and CA were present in the spectra of the HPC/CA DN hydrogel sample. These observations confirmed that DN hydrogel was composed successfully of both HPC and CA.

6.2.5. X-ray diffraction measurements

In order to confirm that the double network was successfully prepared from HPC and CA hydrogels, X-ray diffraction (XRD) was used. The X-ray diffraction pattern of HPC/CA DN hydrogel was performed and compared with that of HPC and CA single network hydrogels. The XRD patterns for three freeze-dried hydrogels samples; HPC SN hydrogel, CA SN hydrogel and HPC/CA DN hydrogel are shown in Figure 6.19. The X-ray diffraction patterns of the HPC SN hydrogel show semi-crystalline structure, which exhibited a peak in the region of 2θ =8.5° and a sharp diffraction peak located at 2θ =20° and a broad peak with a maximum at 2θ =43°. The X-ray diffraction patterns of CA hydrogel demonstrates a broad diffraction peak around 2θ =10°, indicating the defective crystals and low crystallinity of CA hydrogel.[47] Whereas in the HPC/CA DN hydrogel sample pattern a reduced intensity of the peak at 2θ =20° and 2θ =43°and the disappearance of the peak at 2θ =8.5°are observed. This clearly indicated that the second network hydrogel (CA) was well trapped in the HPC hydrogel matrix leading to the loss of crystallinity.[48]

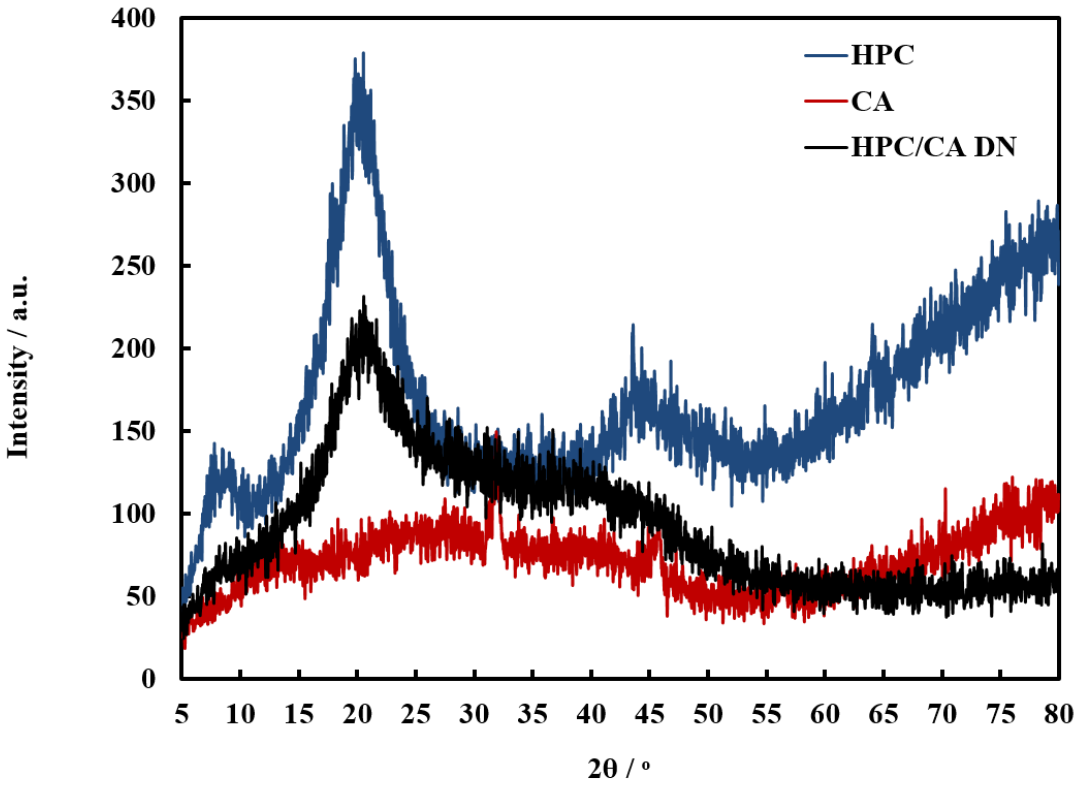

Figure 6.19. XRD analysis of FD-HPC SN hydrogel (7.0 w/v %) blue line, FD-CA SN (1.0 w/v %) red line and FD-HPC/CA DN double network hydrogel HPC-CA (7.0 – 1.0% w/v) black line.

6.2.6. Mechanical testing of HPC/CA DN

6.2.6.1. Compression test

The mechanical properties of the HPC/CA DN hydrogels prepared by M4 route were determined by using a uniaxial compression test. Figure 6.20 shows a comparison between the compressive stress-strain behaviour of HPC SN and HPC/CA DN hydrogels as freeze-dried hydrogels. The compressive stress of both hydrogels gradually increased with increasing strain until the compressive strain was approximately 70%; above this point, it suddenly increased and showed typical ‘‘J’’ shape curves, indicating their high compressive strength.[49] However, the HPC/CA DN hydrogel exhibits a higher degree of strength when compared to the HPC SN hydrogel. In contrast, their parent HPC SN hydrogel exhibited much weaker mechanical strength and a soft behaviour due to the flexible nature of the HPC hydrogels prepared by using the temperature induced phase separation (TIPS) method as mentioned in chapter four.

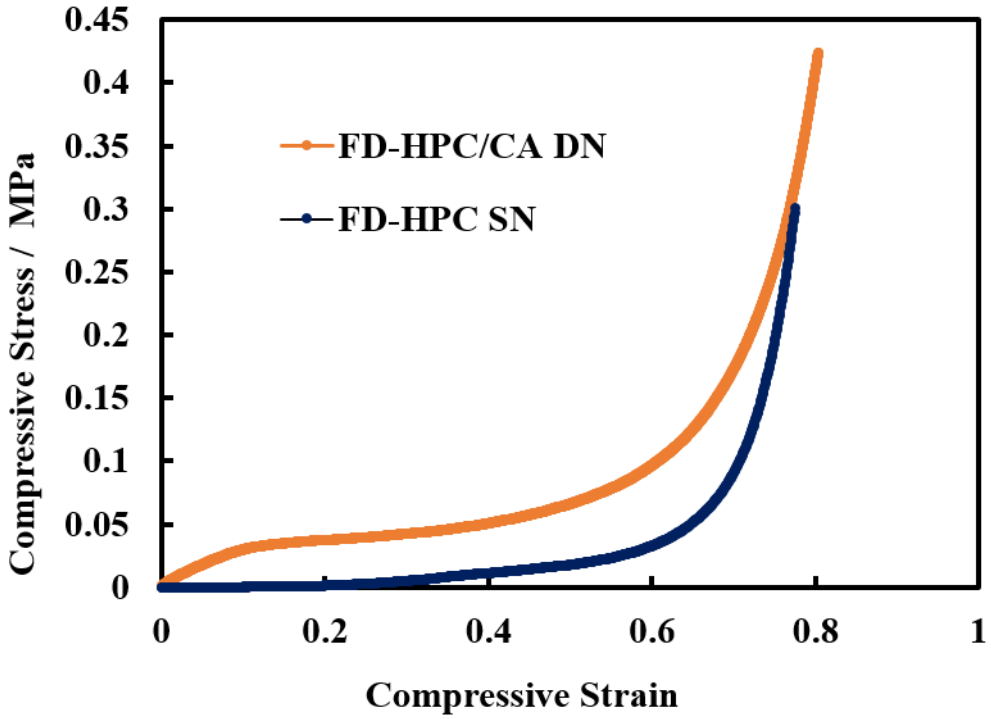

Figure 6.20. Compressive stress-strain curves of FD- HPC hydrogel prepared from 7.0 % w/v HPC and 1.3 % w/v DVS, FD-HPC/CA DN hydrogels prepared from 7.0 % w/v HPC and 1.3 % w/v DVS and 1% w/v SA at LCST (M4).

As depicted in the compressive stress-strain curves in Figure 6.20 the HPC/CA DN hydrogel and the HPC SN hydrogel could be compressed significantly without breakage, even at an extremely high strain it reached 80%. However, the combination of two networks significantly enhanced the mechanical strength of the HPC/CA DN hydrogel. The compressive elastic modulus values of HPC/CA DN hydrogel was1.28 MPa, which doubled compared to the HPC SN hydrogel (MPa). Thus, the double network structure led to a substantial improvement the mechanical properties. These results indicate that a denser network showed higher compressive strength in the presence of the CA hydrogel within the backbone structure of HPC hydrogel.

Compressive tests were also performed to investigate the compressive properties of the swollen HPC/CA DN hydrogel prepared by the same route with different HPC and SA concentrations. Compressive stress-strain curves of HPC/CA DN hydrogel with different concentrations of SA with 7 w/v % HPC are plotted in Figure 6.21. While Figures 6.22 demonstrated the compressive stress-strain curves of HPC/CA DN hydrogel prepared by 5 w/v% with different concentrations of SA. As shown the compressive strength of DN

hydrogels increases with the increasing the SA ratio with a fixed HPC concentration and also increase with the increasing the HPC ratio with fixed SA concentration.

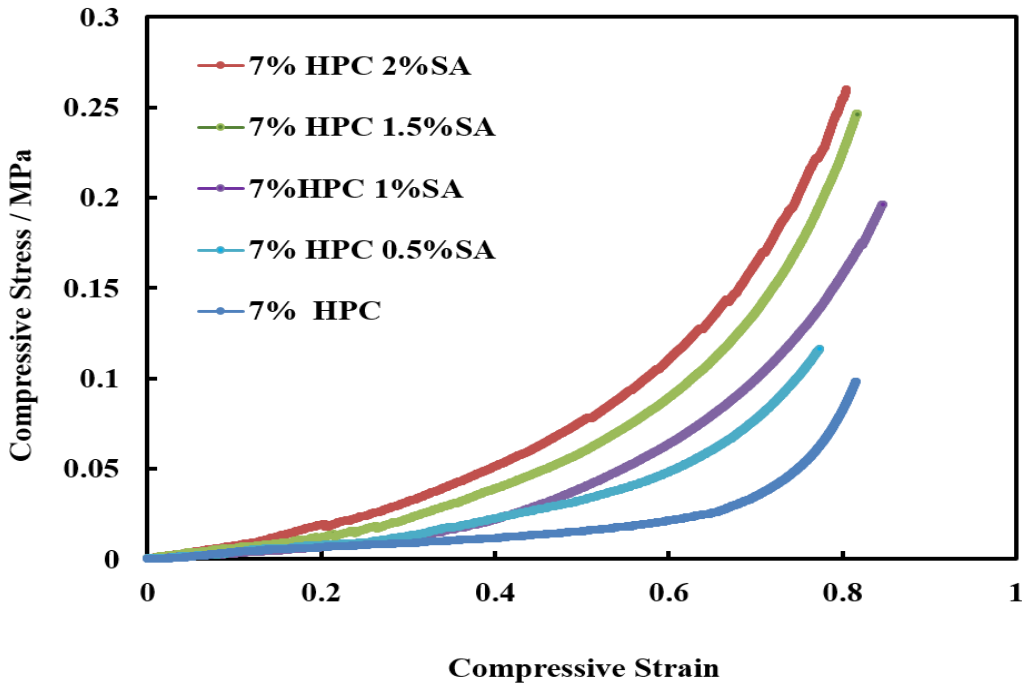

Figure 6.21. Compressive stress-strain curves of HPC/CA DN hydrogel prepared by 7.0 w/v % HPC and different concentration of SA (0.0, 0.5, 1.0, 1.5, 2.0 w/v %).

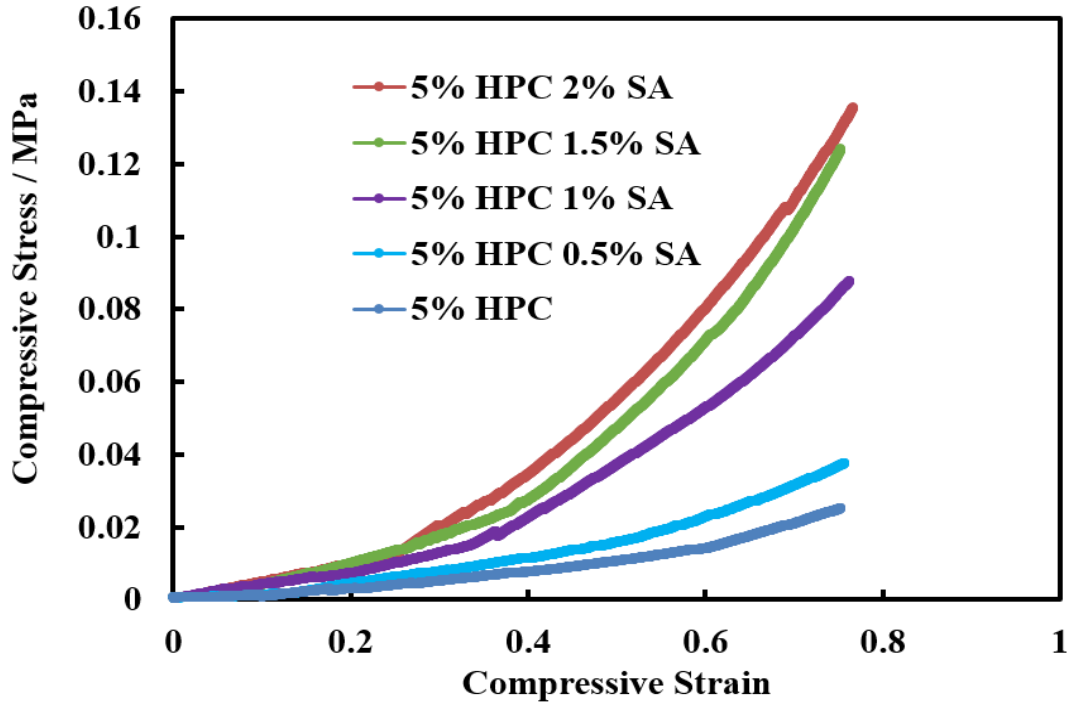

Figure 6.22. Compressive stress-strain curves of HPC/CA DN hydrogel prepared by 5.0 w/ v % HPC and different concentration of SA (0.0, 0.5, 1.0, 1.5, 2.0 w/v %).

From Figures 6.20 and 6.21 the compression strength and the Young modules of HPC/CA DN hydrogels as freeze dried hydrogel are much higher than swollen HPC/CA DN hydrogels. It could be due to the complex intermolecular competition between water–polymer and polymer-polymer interactions. On the one hand, water molecules can form hydrogen bonds with both networks with rich hydroxyl groups to enhance the mechanical properties of the gels. On the other hand, water fills the space voids between polymer chains that may reduce polymer interactions between and within the two networks, leading to the weakening of the gels.[50]

Furthermore, the results revealed that the increase of the second network polymer percentage obviously enhanced the mechanical properties of the DN hydrogels. HPC/CA DN hydrogel with higher sodium alginate content possessed relatively dense and strong networks, leading to higher compressive strength. Therefore, sodium alginate ratio played an important role in the improvement of the mechanical strength of these samples. As a result of that, the Young modules of HPC/CA DN hydrogels increased with the increase of the concentration of SA as shown in Figures 6.23 and 6.24 for 7.0 w/v% and 5.0 w/v% HPC respectively. It was found that the Young modulus value increased from 0.1 MPa to 0.33 MPa as the concentration of SA increased from 0.0 to 2.0 w/v %, which is three times higher than that of HPC SN. This can be attributed to the SA trapped into the HPC network and forming the DN hydrogel, which improves the mechanical properties of the hydrogel. Moreover, the formation of more extension alginate hydrogels networks in the DN hydrogel with the increased the weight percentage of SA polymer, which was used HPC network structure as a backbone of the hydrogels.

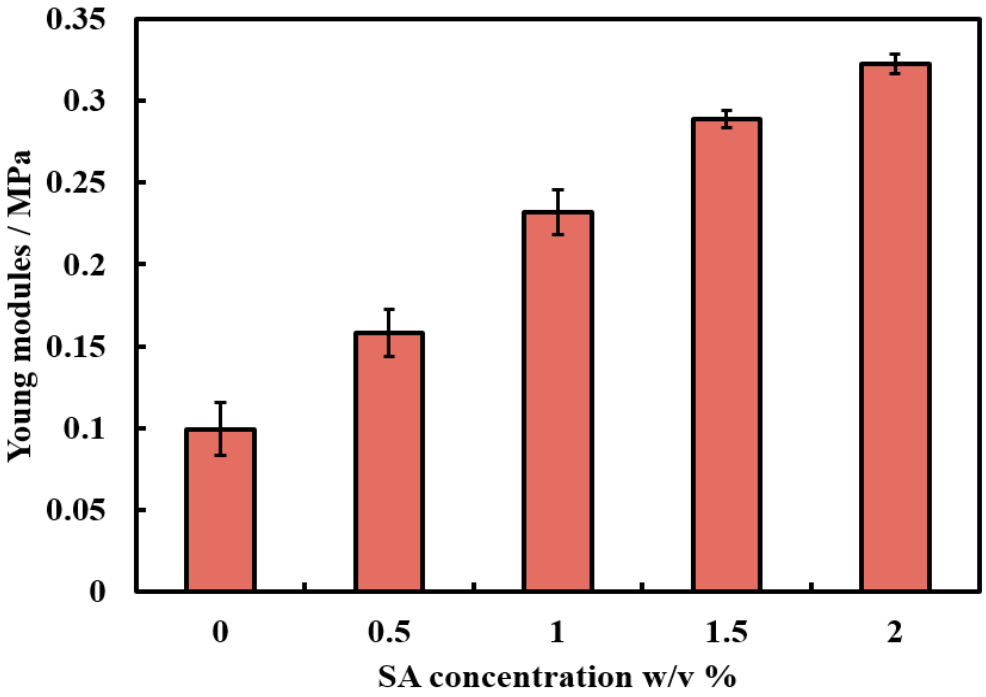

Figure 6.23. The effect of SA concentration on the Young Modules of HPC/CA DN hydrogels at constant concentration of HPC 7.0 % w/v. Each sample was measured in triplicate to calculate the error bars are the standard deviation.

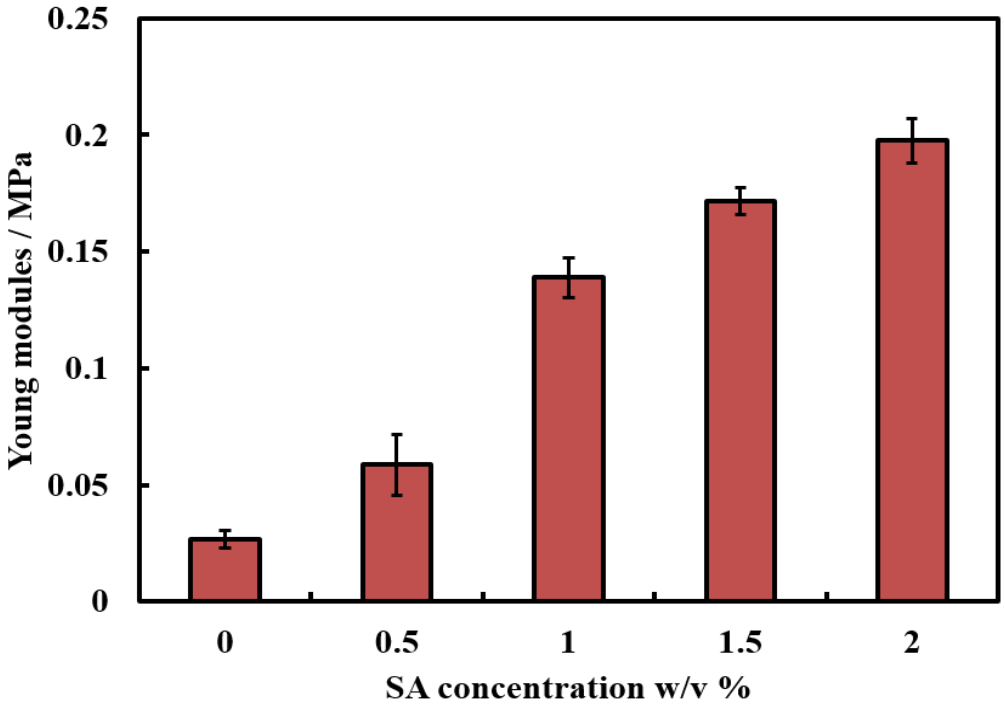

Figure 6.24. The effect of SA concentration on the Young Modules of HPC/CA DN hydrogels at a constant concentration of HPC 5.0 % w/v. Each sample was measured in triplicate to calculate the error bars are the standard deviation.

The compressive strength also increases with the increase of the concentration of the HPC polymer in the presence of a fixed concentration of SA polymer as shown above in Figures 6.21 and 6.22 for 7.0 w/v% and 5.0 w/v% HPC respectively. Moreover, it was found that Young modules of HPC/CA DN increased with the increase of HPC content from 5 w/v% to 7 w/v% with different concentrations of SA as shown in Figure 6.25. The result demonstrated that the Young modules of the DN with 7 w/v% hydrogel was 0.27 MPa, which is obviously higher than those of the DN with 5 w/v% (0.16 MPa) at 1 w/v % SA. These results indicate that the increase of HPC contents, leads to a denser network structure due to the increased degree of crosslinking, which showed higher compressive strength and the Young modules.[51]

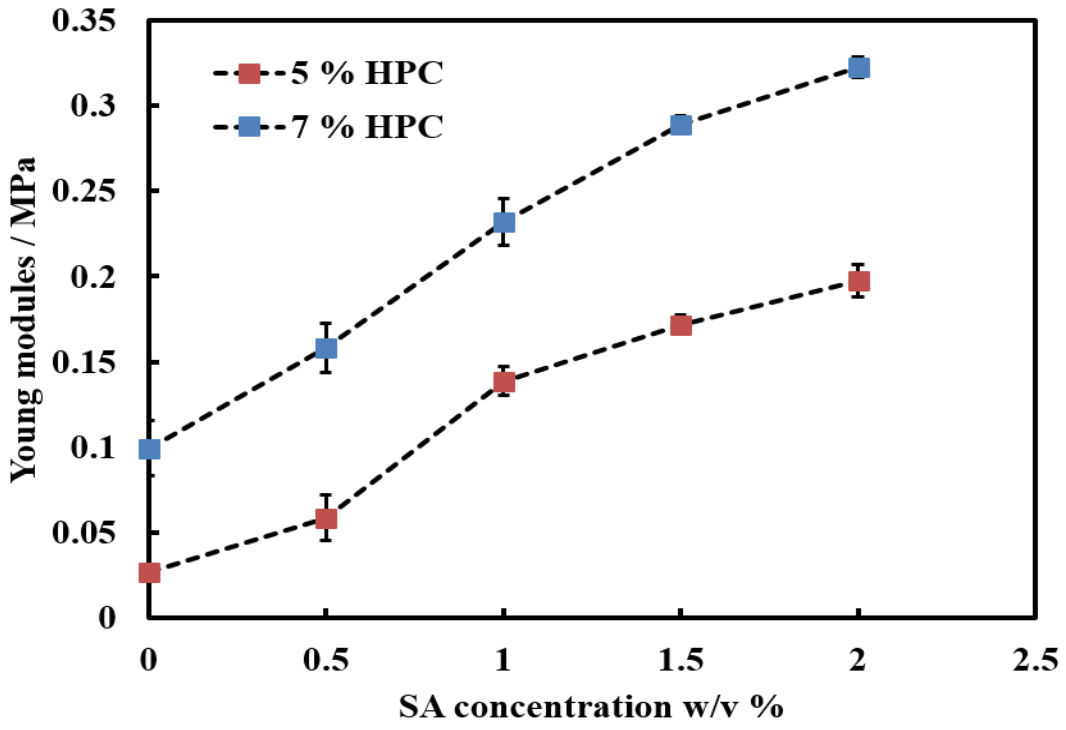

Figure 6.25. Compression between the young modules of HPC/CA DN hydrogels at different concentration of HPC and SA. Each sample was measured in triplicate to calculate the error bars are the standard deviation.

HPC/CA DN hydrogel samples prepared by (M4 method) showed a decrease in the height of the cylindrical sample and the water was released from the sample network as a compressive load is applied. The elastic modulus of HPC/CA DN hydrogels were calculated. The value of Young modulus increased from to 0.2 MPa to 0.3 MPa with an increase in the HPC concentration from 5.0 w/v % to 7.0 w/v % with the concentration

of SA 2.0 w/v % and increased from 0.1 MPa to 0.33 MPa with increase in the concentration of SA from 0.0 to 2.0 w/v %.

6.2.6.2. Rheology measurements

In order to investigate whether the incorporation of the second network would affect the rheological properties of the hydrogels, the rheological behaviour of the HPC/CA DN hydrogel was measured as a function of temperature. The effect of varying polymer concentration on the rheological properties of HPC/CA DN hydrogel was also investigated using different concentrations of the second network polymers. The rheology properties at varying temperatures and shear stress of four HPC/CA DN hydrogel samples prepared by M4 route in the constant HPC concentration (7.0 w/v %) with different concentrations of SA (0.5, 1.0, 1.5and 2.0 w/v %) was studied. In Figures 6.26, 6.27, 6.28 and 6.29, the evolution of the storage modulus as a function of temperature is shown for HPC/CA DN hydrogels of different concentrations of SA (0.5, 1.0, 1.5and 2.0 w/v % respectively). The HPC/CA DN hydrogel showed characteristics of both HPC and SA, depending on the temperature range. All the curves show almost the same behaviour. The results shows significant differences between the storage modulus at different temperatures and shear stress It can be seen that the storage modulus of the HPC/CA DN hydrogels decreases with increasing the temperature between 25 and 55 ºC over all these samples showing a minimum at 45 and 55 ºC, which is above the LCST of HPC. Furthermore, it can be seen that the HPC/CA DN hydrogel show decreases the storage modulus of the hydrogel with an increase in the shear stress from 10-400 Pa.

However, the storage modulus of HPC/CA DN sharply increased with the increase of the concentration of SA over a range of temperatures. The results shown in Figure 6.30 shows the effect of SA concentration on the storage modulus of HPC/CA DN hydrogels at a constant shear stress (400 Pa) and at varying temperatures. It can be seen that the storage modulus increased from 1000 Pa for 0.5 w/v % SA to 2300 Pa for 2.0 w/v % SA at 25 °C.

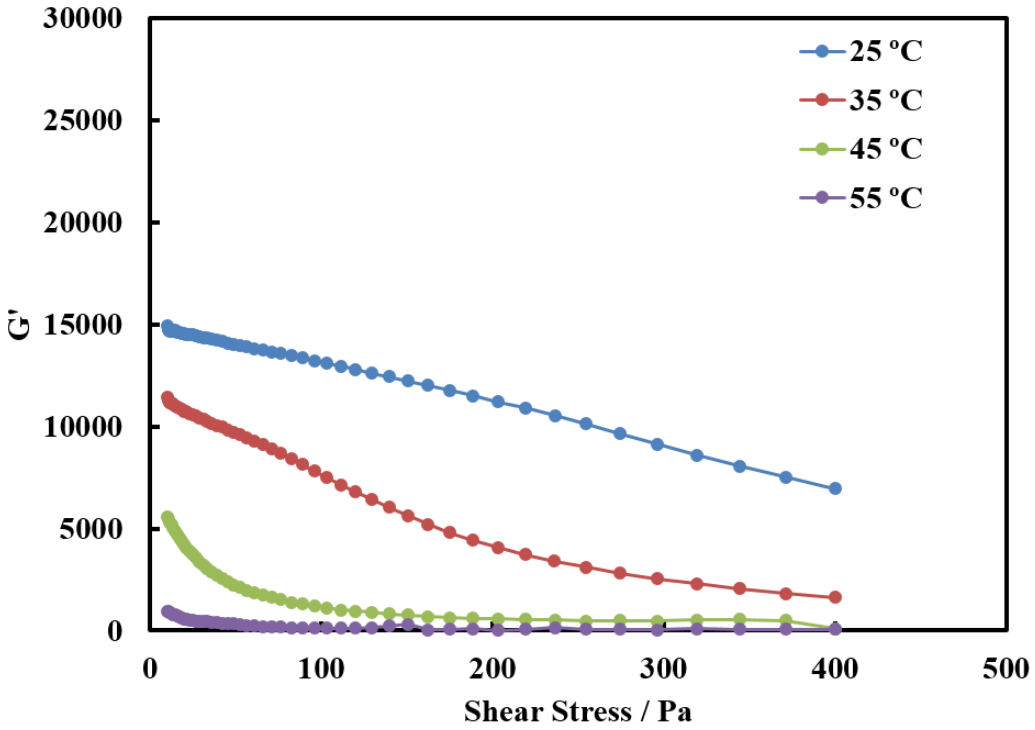

Figure 6.26. The storage modulus G′ as a function of temperature and shear stress in oscillation shear stress sweep tests at 1 Hz frequency (for HPC/CA DN hydrogel with 7% HPC and 0.5% SA).

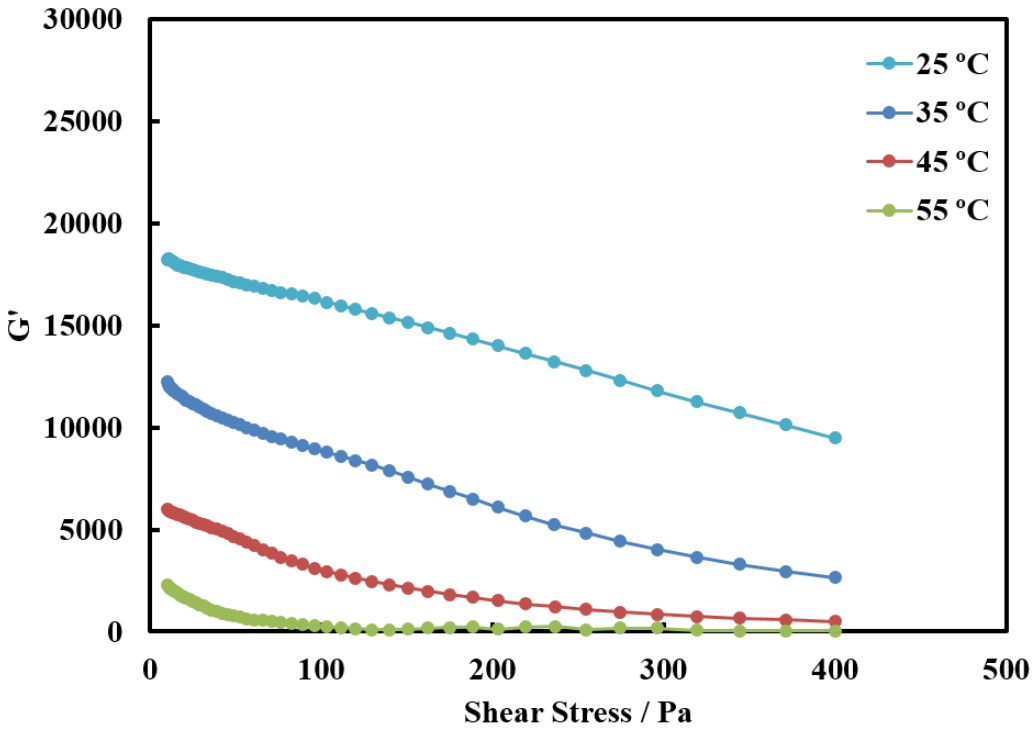

Figure 6.27. The storage modulus G′ as a function of temperature and shear stress in oscillation shear stress sweep tests at 1 Hz frequency (for HPC/CA DN hydrogel with 7% HPC and 1.0 % SA).

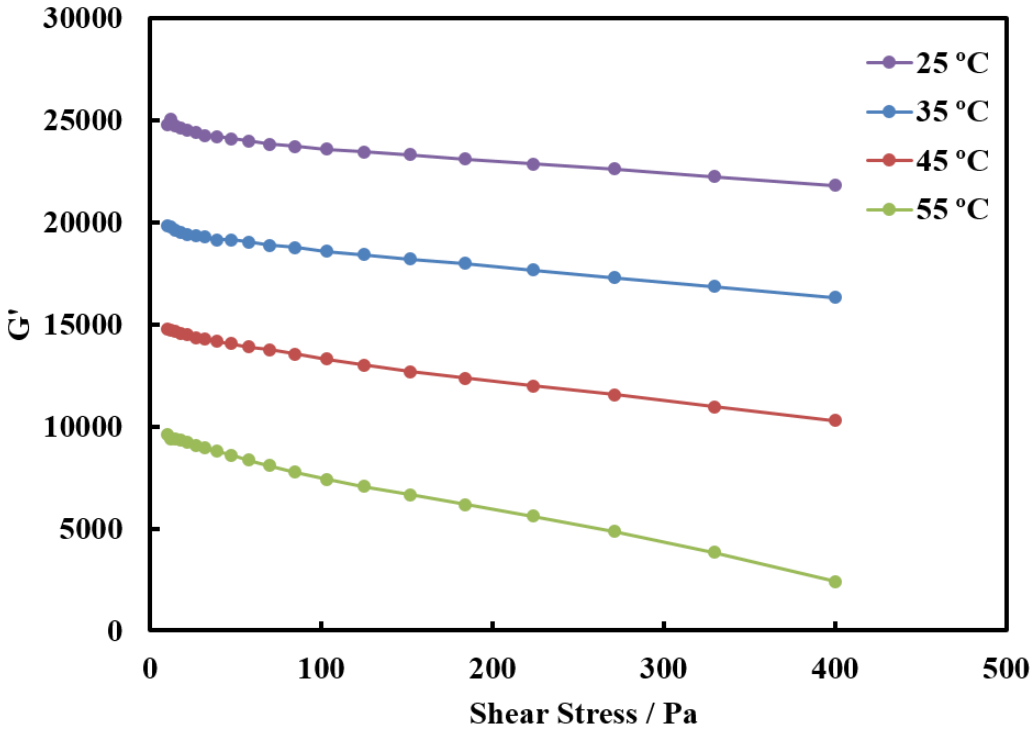

Figure 6.28. The storage modulus *G′* as a function of temperature and shear stress in oscillation shear stress sweep tests at 1 Hz frequency (for HPC/CA DN hydrogel with 7% HPC and 1.5% SA).

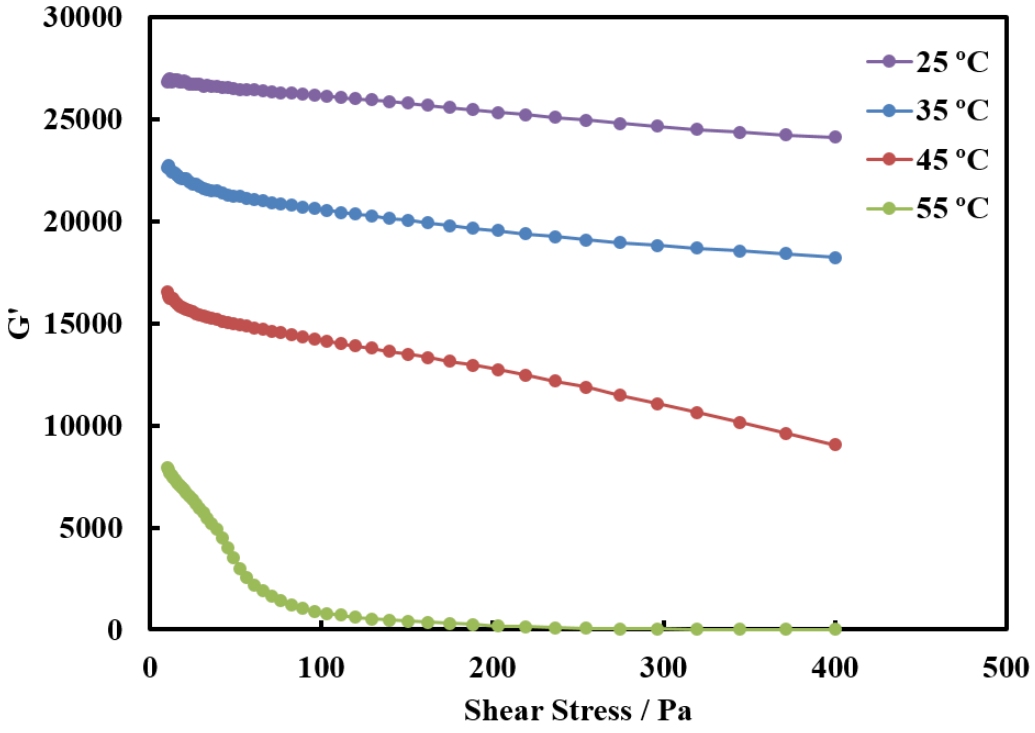

Figure 6.29. The storage modulus G′ as a function of temperature and shear stress in oscillation shear stress sweep tests at 1 Hz frequency (for HPC/CA DN hydrogel with 7% HPC and 2.0 % SA).

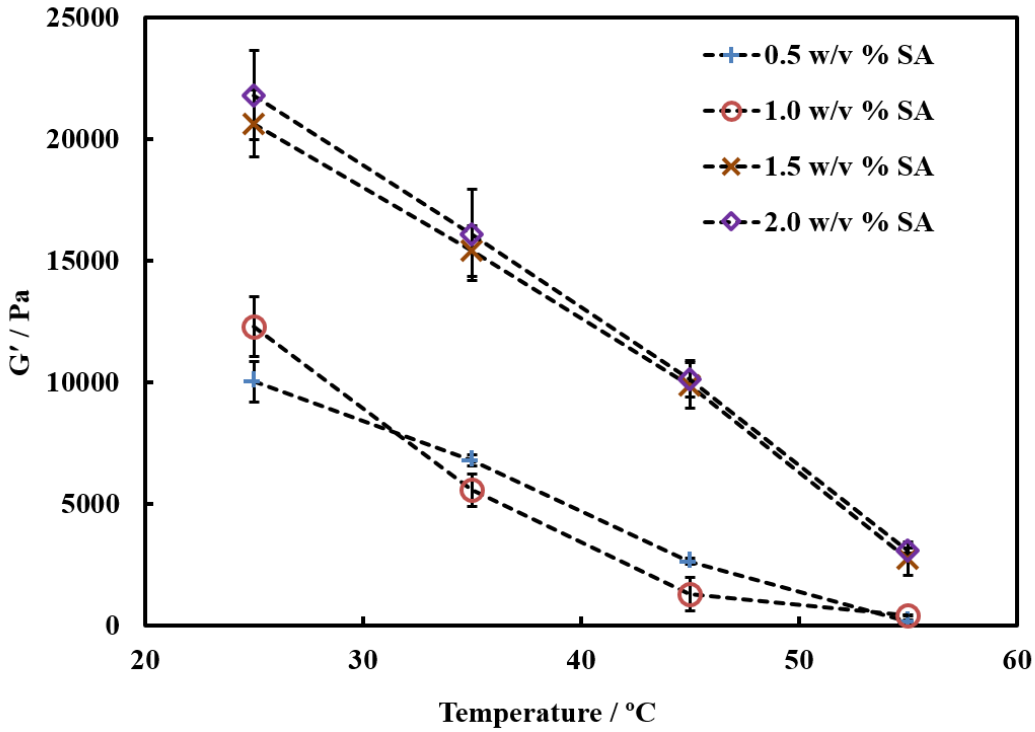

Figure 6.30. The storage modulus of HPC/CA DN hydrogel (7.0% w/v HPC), (0.5, 1.0, 1.5 and 2.0% w/v SA) as a function of temperature with constant shear stresses 400 Pa. Each sample was measured in triplicate and the error bars are the standard deviation.

It is noteworthy that the storage modules the HPC/CA DN hydrogels are significantly higher than HPC SN hydrogel over a range of temperature (Figure 4.52 in Chapter 4) at similar HPC polymer concentration under the same experimental condition. Furthermore, it can be seen that the HPC/CA DN hydrogels rheological characteristics are based on the concentration of SA polymer, shear stress and the temperature. As the shear stress increased from 10 to 400 Pa and combined with the elevated temperature, the storage modulus of HPC/CA DN hydrogels decreased. At low temperatures (25 and 35 °C), its storage modules slightly decrease with increase the share stress which is likely to be due to the partial weakening of HPC network, while this decrease was most noticeable at LCST and above this temperature, where the increased temperature has caused phase separation of the first network.

At temperatures below the LCST of HPC, the HPC/CA DN hydrogel showed characteristics of both HPC and CA, while at LCST and above this temperature the rheological properties are dominated mostly by the HPC network. At high temperatures, between 45 and 55 °C, depending on the SA concentration, the storage modulus decreased sharply. This decrease is related to the phase separation of the HPC network at LCST and

above this temperature. The separation of water from hydrogel due to the hydrophobic effect causes a loss of contact between the rheometer plates and the sample. This possibility causes an unpredictable decrease in the storage modulus values as a function of temperature and do not allow correct measurements of the rheological properties of HPC/CA DN hydrogel at a temperature above 42 °C. Finally, from Figure 6.30, it was seen that at a shear stress of 400 Pa, the mechanical strength and the storage modules of the HPC/CA DN hydrogels increased as the second network polymer concentration increased over a range of temperature. When the concentration of SA is increased from 0.5% w/v to 2.0 %w/v the storage modulus of the hydrogel increases due to the formation of stronger polymer networks.

6.3. Conclusions

Previous works reported that when fabricated hydrogel from hydroxypropyl cellulose (HPC) composited with graphene oxide (GO) or MoS_2 increase the surface area for adsorption, and confer negative electrostatic charges to the resulting hydrogel, thus aiding the adsorption of cationic dye. However, graphene oxide is relatively expensive, and requires careful preparation to ensure proper exfoliation. Similarly, the use of carboxylated MoS_2 nanosheets required additional preparative steps utilizing pyrophoric reagents.[52, 53] To overcome these problems, it is important to improve the adsorption capacity of HPC hydrogel by modifying this hydrogel with another polymer hydrogels and should be environmentally friendly, reusable and cheap materials. Here, a novel method was used to design and fabricate a new hybrid double network hydrogel through a two-step route. HPC/CA DN hydrogel was successfully synthesized consisting of a chemically linked HPC network, which was created through the covalent crosslinking between hydroxypropyl cellulose polymer chains by DVS in the alkaline media and second,by a physically crosslinked CA network, which was coordinated by alginate chains and Ca^{2+}. This method depends on immersion of the first network polymer in an aqueous solution of the second netwok polymer during the phase separation of the HPC hydrogel at the LCST. The SEM results showed that the DN hydrogel prepared by this method exhibited two networks with good compatibility and a homogeneous morphology in the hydrogel. Furthermore, FTIR, EDX and XRD analyses confirmed that the first network and the second network formed independently, and there was no chemical interaction between them. The mechanical properties of the HPC/CA DN hybrid hydrogels were investigated using a compression test and rheometry. The results have demonstrated that the HPC/CA DN hydrogel had superior mechanical properties which were dramatically improved compared with HPC SN hydrogel. In addition, the HPC/CA DN hydrogel demonstrated a flexible behavior without breakage under compression tests, even at an extremely high strain reached to 80% and showed substantial shape recovery after removing the compression, indicating easy recycling of this material. Through the combined advantages of both HPC and CA, the formed DN hydrogels not only exhibited higher mechanical properties but also provided a higher specific surface area than their parent HPC SN hydrogel. The combination of toughness and high mechanical properties and high surface area, an easy preparation method, along with the environmentally friendly material used for preparation, make this type of material an ideal candidate as adsorbents for wastewater treatment.

6.4. References

1. A.-C. Albertsson, J. Voepel, U. Edlund, O. Dahlman and M. Soderqvist-Lindblad, *Biomacromolecules*, 2010, **11**, 1406-1411.
2. D. R. Kioussis and P. Kofinas, *Polymer*, 2005, **46**, 9342-9347.
3. Y. Kong, Y. Zhuang, Z. Han, J. Yu, B. Shi, K. Han and H. Hao, *Journal of Environmental Sciences*, 2019, **78**, 81-91.
4. X. Qi, M. Chen, Y. Qian, M. Liu, Z. Li, L. Shen, T. Qin, S. Zhao, Q. Zeng and J. Shen, *International Journal of Biological Macromolecules*, 2019, **132**, 429-438.
5. Y. Zhuang, F. Yu, J. Ma and J. Chen, *Journal of Colloid and Interface Science*, 2017, **507**, 250-259.
6. J. Li, S. Zhang, C. Chen, G. Zhao, X. Yang, J. Li and X. Wang, *ACS Applied Materials & Interfaces*, 2012, **4**, 4991-5000.
7. Z. Wei, R. Xing, X. Zhang, S. Liu, H. Yu and P. Li, *ACS Applied Materials & Interfaces*, 2013, **5**, 598-604.
8. Y. Zhuang, F. Yu, H. Chen, J. Zheng, J. Ma and J. Chen, *Journal of Materials Chemistry A*, 2016, **4**, 10885-10892.
9. C. Chang, K. Han and L. Zhang, *Polymers for Advanced Technologies*, 2011, **22**, 1329-1334.
10. T. Nakajima, H. Furukawa, Y. Tanaka, T. Kurokawa, Y. Osada and J. P. Gong, *Macromolecules*, 2009, **42**, 2184-2189.
11. M. A. Haque, T. Kurokawa and J. P. Gong, *Polymer*, 2012, **53**, 1805-1822.
12. X. Yan, Q. Chen, L. Zhu, H. Chen, D. Wei, F. Chen, Z. Tang, J. Yang and J. Zheng, *Journal of Materials Chemistry B*, 2017, **5**, 7683-7691.
13. X. J. Liu, X. Y. Ren, S. Guan, H. Q. Li, Z. K. Song and G. H. Gao, *European Polymer Journal*, 2015, **73**, 149-161.
14. J. Wang, J. Wei, S. Su, J. Qiu and S. Wang, *Journal of Materials Science*, 2015, **50**, 5458-5465.
15. J. P. Gong, Y. Katsuyama, T. Kurokawa and Y. Osada, *Advanced Materials*, 2003, **15**, 1155-1158.
16. R. Xu, G. Zhou, Y. Tang, L. Chu, C. Liu, Z. Zeng and S. Luo, *Chemical Engineering Journal*, 2015, **275**, 179-188.
17. Q. M. Yu, Y. Tanaka, H. Furukawa, T. Kurokawa and J. P. Gong, *Macromolecules*, 2009, **42**, 3852-3855.
18. J.-Y. Sun, X. Zhao, W. R. K. Illeperuma, O. Chaudhuri, K. H. Oh, D. J. Mooney, J. J. Vlassak and Z. Suo, *Nature*, 2012, **489**, 133.

19. Q. Chen, D. Wei, H. Chen, L. Zhu, C. Jiao, G. Liu, L. Huang, J. Yang, L. Wang and J. Zheng, *Macromolecules*, 2015, **48**, 8003-8010.
20. Q. Chen, H. Chen, L. Zhu and J. Zheng, *Journal of Materials Chemistry B*, 2015, **3**, 3654-3676.
21. K. J. Henderson, T. C. Zhou, K. J. Otim and K. R. Shull, *Macromolecules*, 2010, **43**, 6193-6201.
22. L. Obeid, N. El Kolli, N. Dali, D. Talbot, S. Abramson, M. Welschbillig, V. Cabuil and A. Bée, *Journal of colloid and interface science*, 2014, **432**, 182-189.
23. F. Chen, Z. Tang, S. Lu, L. Zhu, Q. Wang, Q. Gang, J. Yang and Q. Chen, *Polymer*, 2019, **168**, 159-167.
24. S. Xiang, W. Qian, T. Li, Y. Wang, M. Chen, P. Ma and W. Dong, *New Journal of Chemistry*, 2017, **41**, 14397-14402.
25. J. Gao, G. Haidar, X. Lu and Z. Hu, *Macromolecules*, 2001, **34**, 2242-2247.
26. N. Astrini, L. Anah and A. Haryono, *Procedia Chemistry*, 2012, **4**, 275-281.
27. H. Li and G.-l. Gong, *e-Polymers*, 2010, **10**.
28. X. Lu, Z. Hu and J. Schwartz, *Macromolecules*, 2002, **35**, 9164-9168.
29. C. A. Castillo-Miranda, A. Beatriz Morales-Cepeda, C. F. Castro-Guerrero, H. Salas-Papayanopolos, H. A. Velasco-Ocejo, J. A. González-Sánchez, U. Paramo-Garcia and D. Alva-Salazar, *International Journal of Polymer Science*, 2016, **2016**.
30. S. Chen, J. Hu, J. Shi, M. Wang, Y. Guo, M. Li, J. Duo and T. Deng, *Journal of Hazardous Materials*, 2019, **371**, 694-704.
31. H. Li and X.-Y. Li, *Synthesis and Characterization of Temperature/pH Double-Sensitive Hydroxypropylcellulose/ Sodium Alginate Hydrogel*, 2009.
32. S. G. Kelmanovich, R. Parke-Houben and C. W. Frank, *Soft Matter*, 2012, **8**, 8137-8148.
33. M. R. Matanović, J. Kristl and P. A. Grabnar, *International Journal of Pharmaceutics*, 2014, **472**, 262-275.
34. S. Basu, H. S. Samanta and J. Ganguly, *Soft Materials*, 2018, **16**, 7-19.
35. K. M. Rao, B. Mallikarjuna, K. S. V. Krishna Rao, K. Sudhakar, K. C. Rao and M. C. S. Subha, *International Journal of Polymeric Materials and Polymeric Biomaterials*, 2013, **62**, 565-571.
36. Z. Zhang, L. Chen, C. Zhao, Y. Bai, M. Deng, H. Shan, X. Zhuang, X. Chen and X. Jing, *Thermo- and pH-responsive HPC g-AA/AA hydrogels for controlled drug delivery applications*, 2011.

37. D. J. Adams, *Gels*, 2018, **4**, 32.
38. M. V. A. Queirós, M. N. Bezerra and J. Feitosa, *Journal of the Brazilian Chemical Society*, 2017, **28**, 2004-2012.
39. J. Li and D. J. Mooney, *Nature Reviews Materials*, 2016, **1**, 16071.
40. Y. Zhang, D. Shao, J. Yan, X. Jia, Y. Li, P. Yu and T. Zhang, *Journal of Natural Gas Geoscience*, 2016, **1**, 213-220.
41. K. S. Sing, *Pure and applied chemistry*, 1985, **57**, 603-619.
42. T. Horikawa, D. Do and D. Nicholson, *Advances in colloid and interface science*, 2011, **169**, 40-58.
43. H. Mittal, V. Parashar, S. B. Mishra and A. K. Mishra, *Chemical Engineering Journal*, 2014, **255**, 471-482.
44. N. Eguchi, K. Kawabata and H. Goto, *Electrochemical Polymerization of 4,4-Dimethyl-2,2'-Bithiophene in Concentrated Polymer Liquid Crystal Solution*, 2017.
45. Y. Li, F. Liu, B. Xia, Q. Du, P. Zhang, D. Wang, Z. Wang and Y. Xia, *Journal of Hazardous Materials*, 2010, **177**, 876-880.
46. J. Nastaj, A. Przewłocka and M. Rajkowska-Myśliwiec, *Polish Journal of Chemical Technology*, 2016, **18**, 81-87.
47. L. Li, Y. Fang, R. Vreeker, I. Appelqvist and E. Mendes, *Biomacromolecules*, 2007, **8**, 464-468.
48. D. Han, L. Yan, W. Chen and W. Li, *Carbohydrate Polymers*, 2011, **83**, 653-658.
49. C. Chang, K. Han and L. Zhang, *Polymers for Advanced Technologies*, 2011, **22**, 1329-1334.
50. H. Chen, Q. Chen, R. Hu, H. Wang, B.-m. Z. Newby, Y. Chang and J. Zheng, *Journal of Materials Chemistry B*, 2015, **3**, 5426-5435.
51. Y. Piao and B. Chen, *International journal of biological macromolecules*, 2017, **101**, 791-798.
52. X. Liu, Y. Zhou, W. Nie, L. Song and P. Chen, *Journal of materials science*, 2015, **50**, 6113-6123.
53. P. Chen, X. Liu, R. Jin, W. Nie and Y. Zhou, *Carbohydrate polymers*, 2017, **167**, 36-43.

Chapter Seven

7. Adsorption and separation of dye mixtures by single and double network composite hydrogels based on hydroxypropyl cellulose and sodium alginate as renewable adsorbent and filters

The aims of the work in this chapter was to apply the single network and double network hydrogels prepared in Chapter 4 and Chapter 6 from hydroxypropyl cellulose and sodium alginate as adsorbents for the adsorption of dyes from aqueous solution (using methylene blue (cationic dye) and sodium fluorescein dyes (anionic dye) as representative dye). It was planning to use these hydrogels to form reusable columns for the adsorptive removal of cationic dyes and enable the separation of the two dyes from an aqueous solution of the dye mixtures by simple gravity filtration. The adsorption capacity of these materials was compared to determine which of these materials are more effective in the separation and the adsorption of the dyes by varying different parameters. HPC SN is anionic hydrogel with $–OH^-$ function group, which is assumed highly selective adsorption of cationic dye due to the electrostatic interaction. Whereas, HPC/CA DN hydrogel provides a dual function group ($-OH^-$ and $–COO^-$), which increase the negative charge density in the hydrogel. This was envisaged that the HPC/CA DN hydrogel has better adsorption capacity in comparison with HPC SN under the same condition due to increase the active sites for adsorption of cationic dye and then increase the electrostatic interaction between the cationic dye and anionic functional groups of HPC/CA DN hydrogel.

7.1. Introduction

Dyes have become a major polluting factor in wastewater, due to their use by the textile, paper, printing and plastic industries, whereby up to 200,000 tons of dye escapes into wastewater just from the textile industry alone.[1] Such dyes pose serious direct threats to the environment arising from their toxicity and mutagenicity. Indirectly, they also disrupt ecosystems by inhibit photosynthetic activity due to their absorption of sunlight. Of particular concern are synthetic dyes with high chemical stability, which accumulate in the environment due to their resistance to degradation.[2-4] Current strategies for dye removal include filtration,[5] chemical [6] and biological degradation [7, 8] as well as adsorption.[9] Of these methods, adsorption poses an attractive solution, particularly for

dyes with high stability and resistance to degradation.[10] Further, the simplicity and low cost of deployment of dye removal by adsorption enhances its feasibility.[11]

Adsorbents which have been investigated for dye removal include silica gel, activated carbon, synthetic polymers and even graphene oxide composites.[12] Activated carbons are generally the most commonly adsorbents used in adsorption process owing to their higher surface area and adsorption capacity. However, there are a number of problems with their use, mainly related to the fact that it is expensive and difficult regeneration, which limits their usage.[13, 14] In practice, the most researchers are focused to find adsorbents with a good stability and regeneration performance. Materials with porous structure are widely employed as adsorbents for removing harmful pollutants from the environment such as toxic metal ions and dyes.[15, 16] Among different materials used for adsorption pollutants from wastewater, materials with porous structures are engaging adsorbents owning to their thermal stability, high surface area and morphology structure.[17, 18] In addition, the interconnected porous system can simplify rapid transportation and diffusion of adsorbate molecules and promote access to the active sites.[19, 20] In this chapter, microporous hydroxypropyl cellulose single network hydrogel (HPC SN) was used for the selective adsorption and separation of cationic dyes from dye mixtures using a simple flow filtration method. Despite the ubiquity of HPC, there have been very few reports on the use of HPC hydrogels or composites for dye removal, [21, 22] and to our knowledge, no reports on selective dye separation. However, the HPC SN hydrogel shows low adsorption capacity. To overcome this problem novel double networks hydrogel from HPC and alginate have been proposed (as described in chapter six) to improve the adsorption capacity and the mechanical properties of HPC SN hydrogel. In this chapter adsorption of MB on HPC/CA DN hydrogel was studied through batch and column adsorption and compare with HPC SN hydrogel. In column study, the adsorbent reuse was investigated and the selective separation of dye mixture was also studied through ten cycles as shown in Figure 7.1.

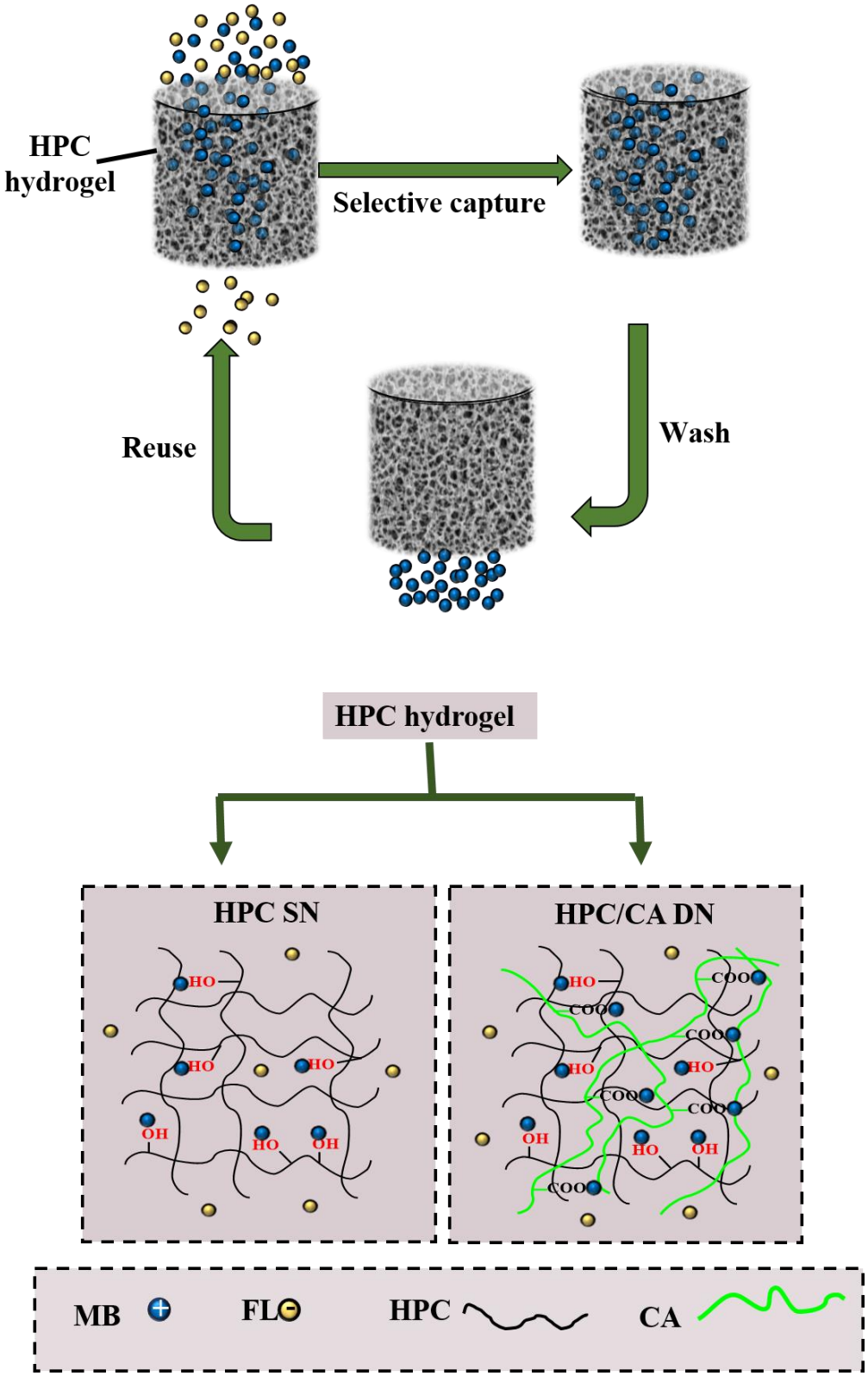

Figure 7.1. Schematic diagram illustrations the selective filtration of HPC/CA DN hydrogel column of MB/FL mixture dye solution and the regeneration of this column and also illustration of the possible interaction between HPC SN and HPC/CA DN hydrogels with methylene dye.

7.2. Results and discussion

7.2.1. Dyes adsorption onto HPC SN and HPC/CA DN hydrogels

As mentioned previously dyes are common water pollutants which are widely used to evaluate the adsorption efficiency of the adsorbent samples.[23] Methylene blue (MB) and sodium fluorescein (FL) water soluble dyes were selected as model contaminants to investigate the dye uptake characteristics of HPC SN and HPC/CA DN hydrogels and tested the removal efficiency of these dyes from aqueous solutions. MB and FL are cationic and anionic dyes, respectively, and their chemical structures are shown in Figure 7.2. Dyes uptake onto single and double network hydrogels prepared in Chapter 4 and 6 have been evaluated using batch and column adsorption.

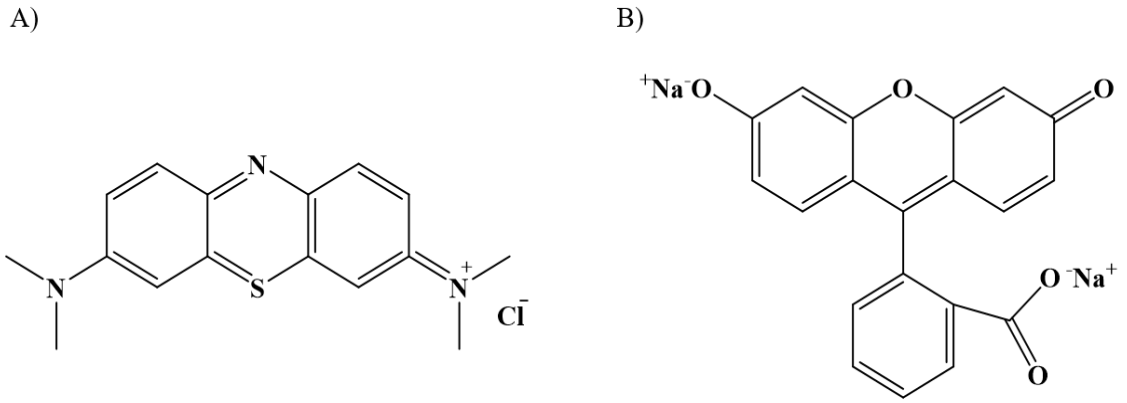

Figure 7.2. Drawings showing the molecular structures of (A) Methylene Blue (MB) and (B) Sodium Fluorescein (FL).

7.2.1.1. Batch adsorption study

7.2.1.1.1. Effect of contact time

The relationship between the adsorption behaviour of MB dye onto adsorbents HPC SN and HPC/CA DN hydrogels and the contact time were investigated (the method used described in Chapter 2) using an initial MB dye concentration of 40 mg/L and 300 mg/L at an optimum pH 6.4 and 298 K, the results are shown in Figures 7.3 and 7.4 respectively. It was found that the adsorption capacity of MB dye onto both hydrogels increased by increasing the time due to the existence of many adsorption sites for MB dye. The adsorption capacity rapidly increased at the initial adsorption stage then it was increased slowly with time until it remained constant reaching equilibrium. Furthermore, the adsorption equilibrium time of HPC/CA DN hydrogel was longer than that of HPC SN at all operating conditions. It was found that an equilibrium time of about 28 h was required for the HPCSN hydrogel, while HPC/CA DN was required around 40 hours.

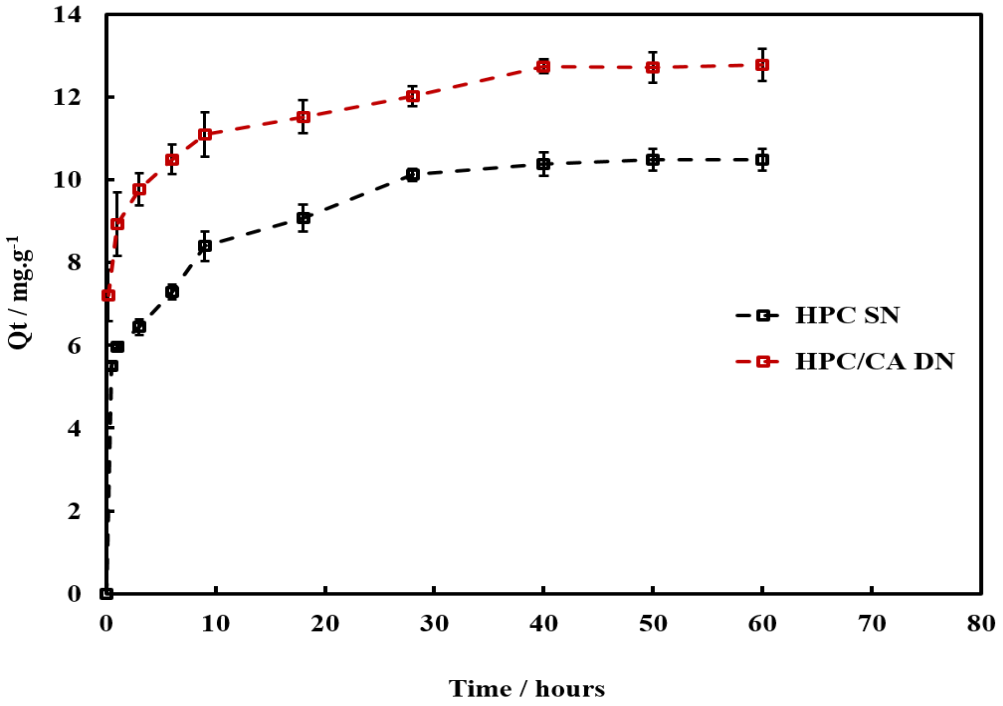

Figure 7.3. Effect of contact time on adsorption of MB dye onto HPC SN and HPC/CA DN hydrogels (initial MB concentration 40 mg/L, temperature 298 K, initial solution pH 6.4).

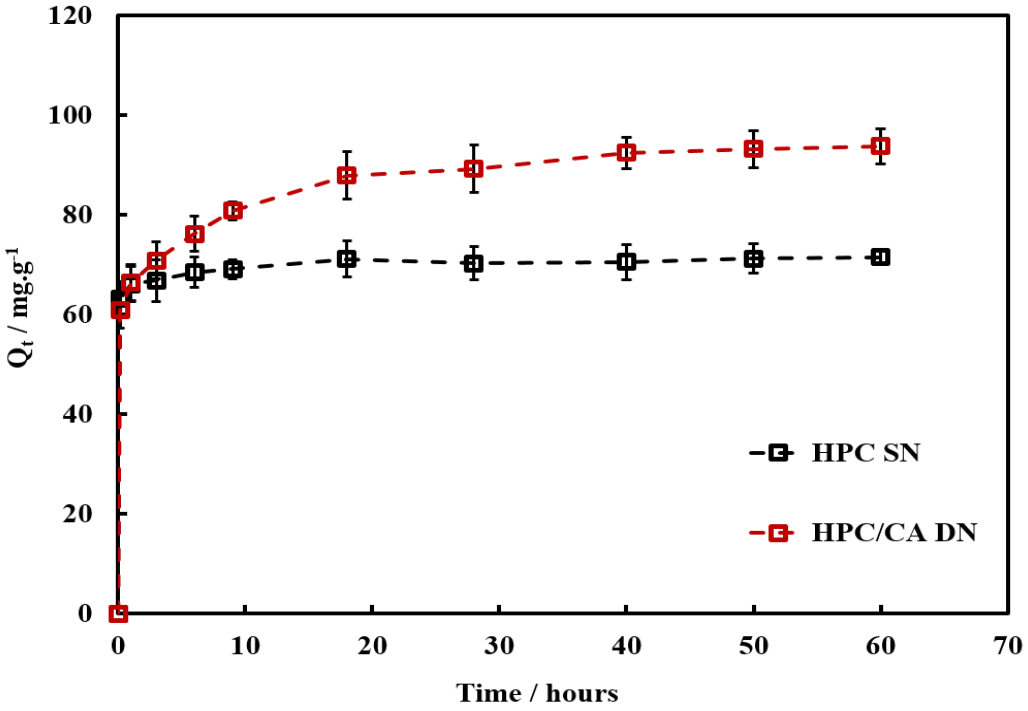

Figure 7.4. Effect of contact time on adsorption of MB dye onto HPC SN and HPC/CA DN hydrogels (initial MB concentration 300 mg/L, temperature 298 K, initial solution pH 6.4).

The results in Figures 7.3 and 7.4 demonstrate that the MB dye adsorption process on HPC/CA DN hydrogel is divided into three adsorption steps with time: adsorption on the surface of the hydrogel initially, rapidly diffusion in the pores of the hydrogel and then the adsorption equilibrium step. This might be attributed to the permeable microporous structure of HPC/SN and HPC/CA DN hydrogels which is provide the strong adsorption driving force and more the active adsorption sites due to capillary system of interconnected pores.[24] These results also showed that the removal of MB dye increased dramatically in the initial 30 min and then increased gradually until reached an equilibrium. The adsorption was very fast in the initial 30 min of the adsorption process, due to the high availability of unoccupied sites in the adsorbent provided the necessary driving force to enhance the adsorption rate. After that, the number of unoccupied sites decreased. Therefore, additional adsorption of the dye took more time and led to slower uptake rate until the adsorption equilibrium occurred. From Figure 7.4 the maximum adsorption capacities at the adsorption equilibrium were 70.5 and 93.7 mg/g for HPC SN and HPC/CA DN respectively. This was due to the relatively higher surface area of HPC/CA DN hydrogel.[25] Furthermore, MB dye adsorption on HPC SN hydrogel required about 28 h to achieve equilibrium, whereas the adsorption onto HPC/CA DN hydrogel at the same operating conditions attained equilibrium at a longer time (40 h). The mean reason behind that the adsorption capacity of HPC/CA DN was higher than that of HPC SN hydrogel due to the DN hydrogel providing more functional groups and a larger surface area hydrogel than the SN hydrogel.[26]

Figure 7.5 shows photographic images of adsorption of MB dye on the HPC/CA DN hydrogel. It was observed that the cylindrical DN hydrogel at time zero showed a white color, while after immersed into the MB solution within 40 h, the hydrogel takes on a deep blue color due to removed most of the MB from the solution and the solution has become a much lighter blue color compared to its original state. The cross-section of the hydrogel shows that the dye is diffused uniformly into the hydrogel core.

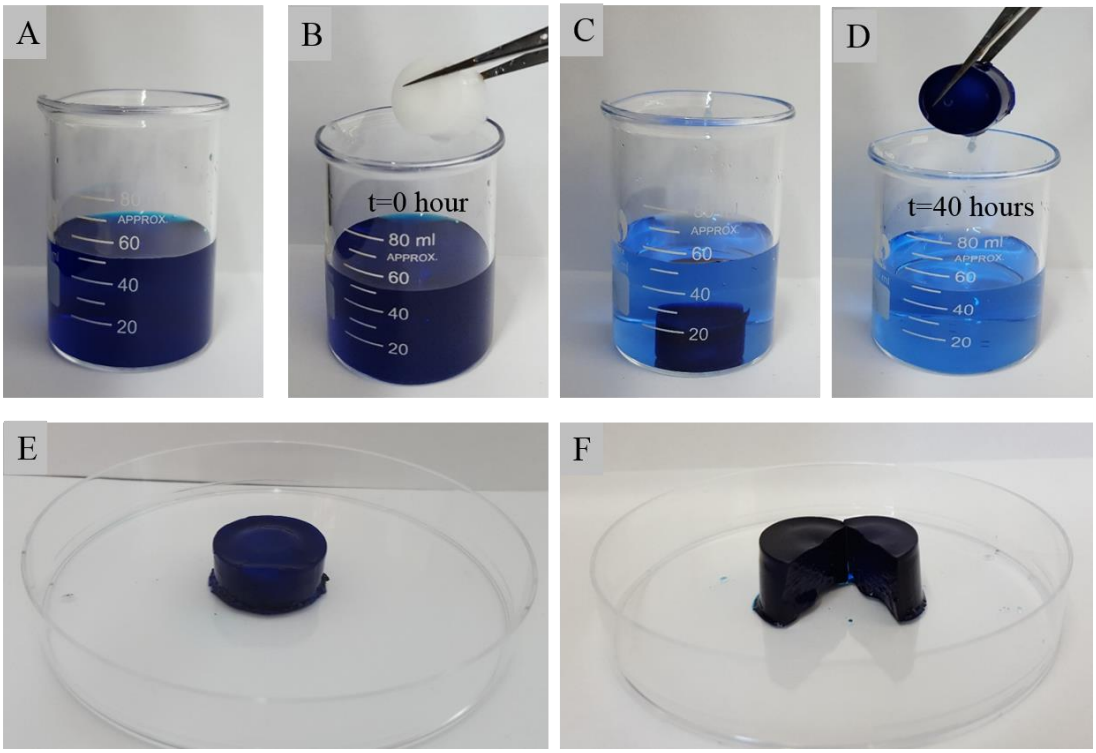

Figure 7.5. Photograph images show (A) 40 mg.L^{-1} of MB dye solution (B) 40 mg.L^{-1} of MB dye before added HPC/CA DN hydrogel (C) MB solution with HPC/CA DN hydrogel after 40 hours shaking (D) MB dye solution after adsorption (E) monolithic HPC/CA DN hydrogel after used for adsorption of MB dye (F) the internal surface of HPC/CA DN hydrogel after used for adsorption of MB dye.

7.2.1.1.2. Effect of dye concentration

The effect of MB dye concentration on the adsorption capacity of both HPC SN and HPC/CA DN hydrogels was evaluated by varying initial dye concentration from 5 to 40 mg/L and with constant operational parameters (pH = 6.4 and T = 298 K). The results are presented in Figure 7.6 showed that influence of the dye concentration on the adsorption capacity of HPC SN and HPC/CA DN hydrogels. It is obvious that the adsorption capacity increased almost linearly with the increase of the initial MB dye concentration. The adsorption capacity of HPC/CA DN hydrogel is higher than HPC SN hydrogel. The adsorption capacity of HPC/CA DN hydrogel increased from 1.6 to 13.1 mg.g^{-1} when the initial MB dye concentration increased from 5 to 40 mg.L^{-1}, while the adsorption capacity for HPC SN hydrogel increased from 1.6 to 9.9 mg g^{-1}. Figure 7.7 shows photographic images of MB dye solutions before and after adsorption by hydrogels with different MB dye concentrations and demonstrate a visual comparison between the hydrogel after used for adsorption. It was shown that the DN hydrogel which adsorbed

40 mg/L MB had a much darker blue color compared to the hydrogel which adsorbed 10 mg/L.

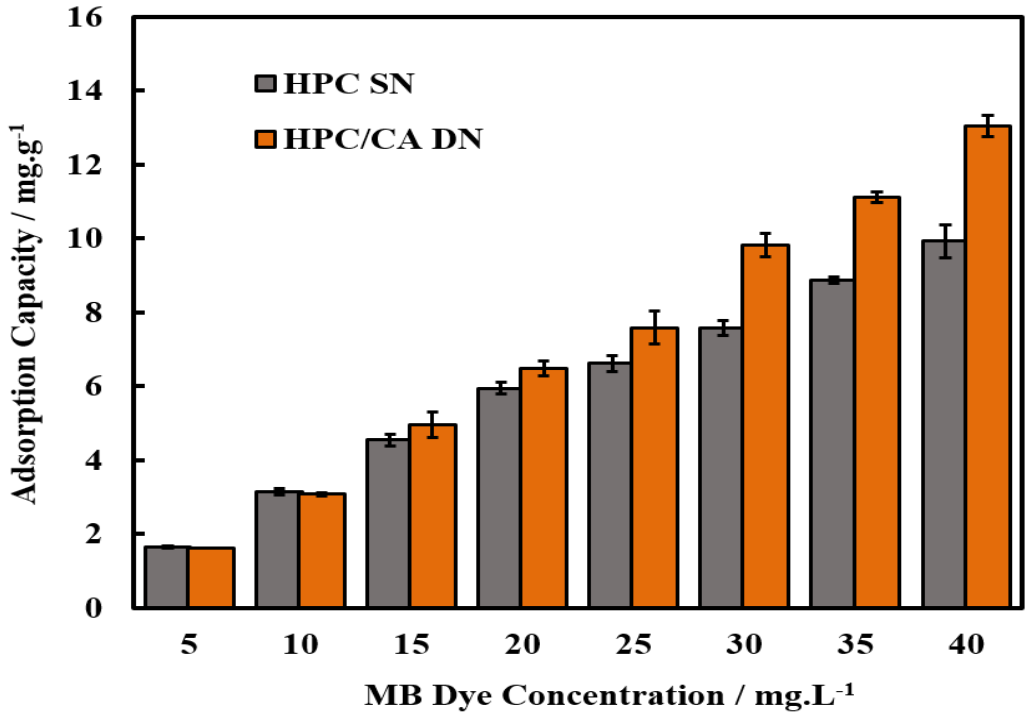

Figure 7.6. Effect of the initial MB dye concentration on the adsorption capacity of MB on HPC SN and HPC/CA DN hydrogels (Initial dye concentration = 5–40 mg/L; adsorbent dose 0.3 g/100 mL; pH 6.4; time 40 h; temperature 298 K; mole ratio of HPC to SA 7:0 and 6:1 for HPC SN and HPC/CA DN hydrogels respectively).

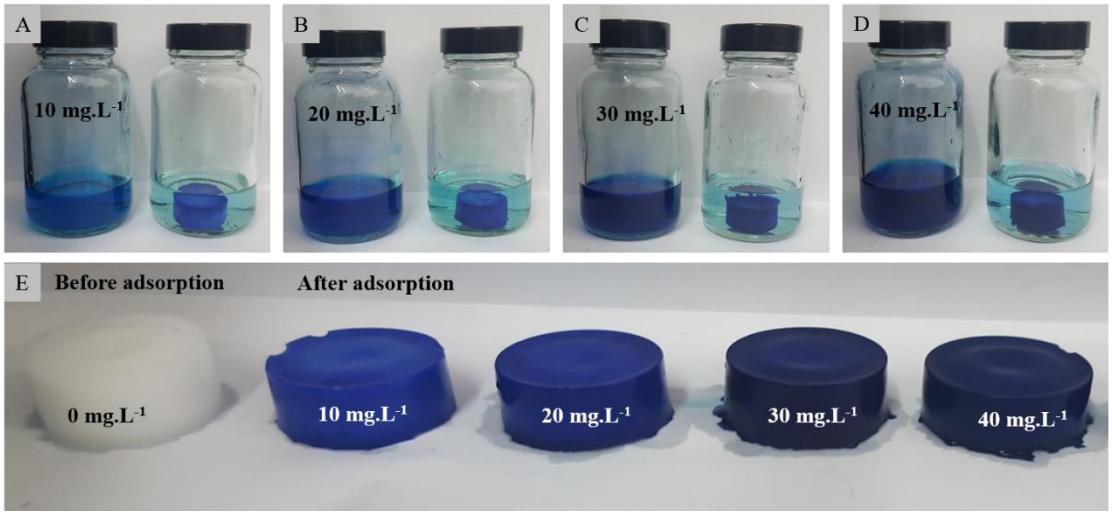

Figure 7.7. Photograph images show the change in colour of the aqueous solution after the adsorption process of different concentration of methylene blue dye (10 to 40 mg.L^{-1}) by HPC/CA DN hydrogels after 40 hours shaking (A), (B), (C) and (D) in the left

methylene blue dye solution before adsorption and in the right methylene blue dye solution after adsorption for 10, 20, 30 and 40 $mg.L^{-1}$ MB respectively.

From Figures 7.6 and 7.7 the uptake of MB dye in the HPC SN and HPC/CA DN hydrogels are be seen to be highly depend on the initial concentration of the dye. It is observed that the adsorption capacity of MB increases with the increase of the initial concentrations of both hydrogels in this study. This is likely to be due to the initial dye concentrations provide an important driving force to overcome the mass transfer resistance of the dye molecules between adsorption media and adsorbent.[27] Initially, the dye molecules diffuse onto adsorbent surface and then it diffuses into the porous structure of the hydrogel. It was also found that the adsorption capacity of HPC/CA DN hydrogel was higher than HPC SN. This was as expected due to interpreting the CA network within the HPC network could provide further active groups ($-COO^-$ groups) with the $–OH^-$ groups from HPC network, which provided large surface area (as confirmed in chapter six) and was advantageous for MB dye adsorption.[28] Therefore, the HPC/CA DN showed better adsorption performance than HPC SN. However, it was difficult to show the comparison between the adsorption capacity of HPC SN and HPC/CA DN hydrogels and comparison with the literature. Therefore, the adsorption capacity of both HPC SN and HPC/CA DN was evaluated using higher initial MB dye concentration (300 mg/L) as shown in Figure 7.8. It was found then the adsorption capacity of HPC SN hydrogel was 70.5 $mg.g^{-1}$, while it was found in HPC/CA DN hydrogel it was 92.4 $mg.g^{-1}$. Figure 7.9 presents images of MB dye solutions before and after adsorption by HPC SN and HPC/CA DN hydrogels and these hydrogels after have used for adsorption of 300 $mg.L^{-1}$ MB dye until the equilibrium occurred. It is clear that the cylindrical HPC/CA DN hydrogel after adsorption of MB dye has a dark blue color while the blue color of MB almost faded from the solution reflecting decrease the concentration of MB dye. Whereas, the HPC SN hydrogel shows lighter blue color still dark blue color.

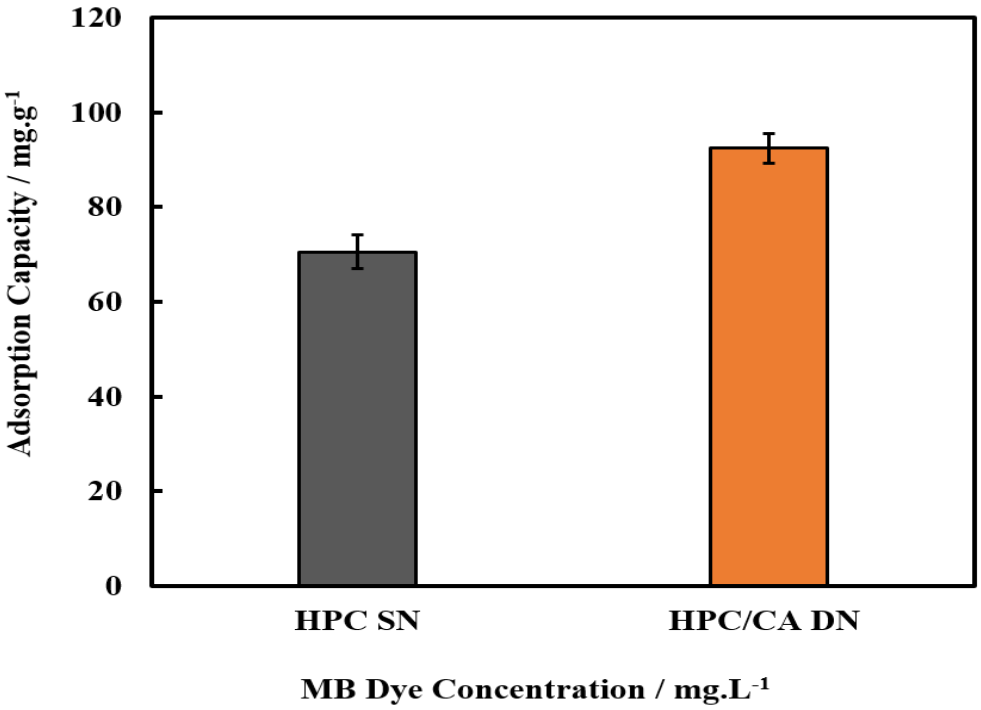

Figure 7.8. Comparison of the adsorption capacity of MB dye onto HPC SN and HPC/CA DN hydrogels (Initial dye concentration = 300 mg/L; adsorbent dose 0.3 g/100 mL; pH 6.4; time 40 h; temperature 298 K; mole ratio of HPC to SA 7:0 and 6:1 for HPC SN and HPC/CA DN hydrogels respectively).

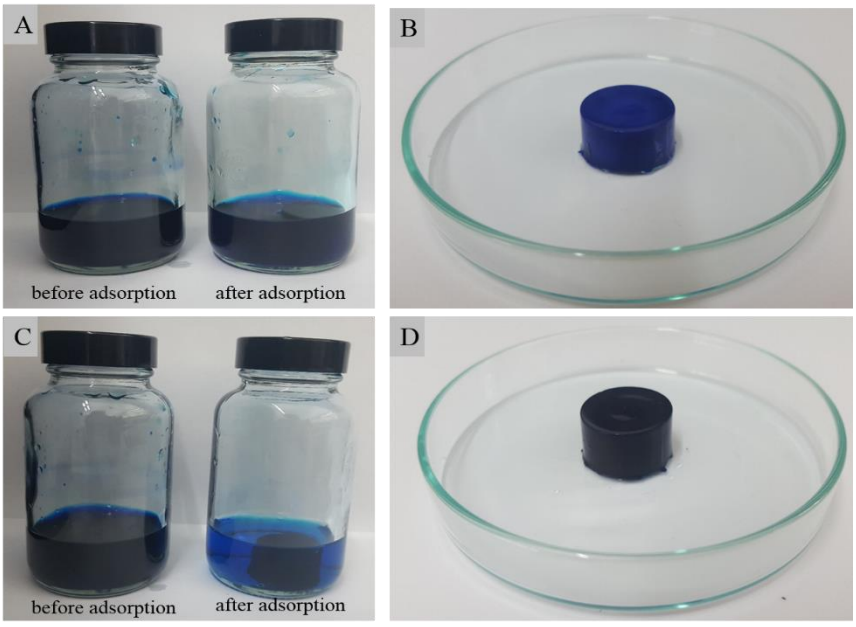

Figure 7.9. Photograph images show (A) 300 mg.L^{-1} of MB dye before and after adsorption by HPC SN hydrogel after 28 hours (B) HPC SN hydrogel after used for adsorption of 300 mg.L^{-1} of MB dye (C) 300 mg.L^{-1} of MB dye before and after adsorption by HPC/CA DN hydrogel after 28 hours shaking (D) HPC/CA DN hydrogel after used for adsorption of 300 mg.L^{-1} of MB dye.

The results from Figure 7.8 indicated that the adsorption capacity of MB increased with the increase of the initial MB concentrations. In the case of MB dye initial concentration 40 mg/L, the adsorption capacity reach to 9 mg /g for HPC SN hydrogel, while this adsorption capacity was possible to reach close to 70 mg/g with 300 mg/L MB dye solution. Therefore, MB dye uptake on to both hydrogels in this study greatly depends on the initial concentration of MB solution. The reason behind that is when the dye/ hydrogel ratio low, the dye adsorption involves the energy sites in the hydrogel. While in the high dye/ hydrogel ratio the energy sites are saturated and the adsorption begins on the lower energy sites, resulting increase in the adsorption capacity.[29] Furthermore, the results also show that the HPC/CA DN hydrogels exhibited higher MB dye uptake capacity than the HPC SN ones. This was due to double network hydrogel having an increased number of active sites available for adsorption and thus fixation of a large amount of solute dye molecules as long as an enough number of these molecules is available in solution in contact with the hydrogel.[26] A similar phenomenon was observed for the adsorption of MB dye from aqueous solution on alginate/graphene single and double-network hydrogel.[25] These interesting results confirm that the HPC/CA DN hydrogel exhibited better adsorption capacity than the HPC SN hydrogel. Hence, it can be considered an efficient adsorbent for the removal of cationic dye from aqueous solution.

7.2.1.1.3. Effect of pH

The impact of pH value is one of the most significant parameters that affects the adsorption process of different types of dye from aqueous solution, as pH affects the surface charges of adsorbent and dye molecules depending on the state of both materials, and affects the chemistry properties for both these materials. The concentration of the MB dye solution before and during the adsorption process was determined by UV−vis spectrometry at the maximum absorbance of MB dye (664 nm). Therefore the effect of the pH of the solution on the maximum absorption wavelength (λmax) of MB dye solution was carried out at pH range from 3.5 to 8.5 as shown in Figure 7.10. The UV-visible spectrum shows there was no impact on the maximum absorption of the MB dye solution with changing the pH value.

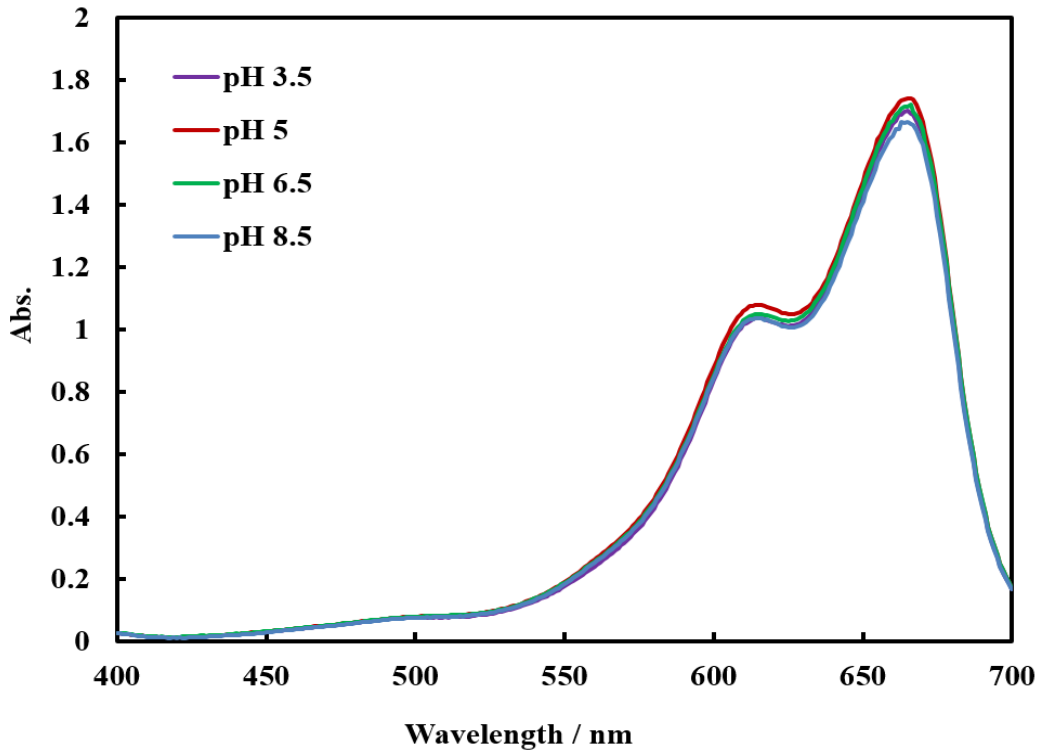

Figure 7.10. Visible spectrum of methylene blue in the range (400 -700 nm) at different pH.

The effect of initial solution pH on the adsorption of MB dye was investigated at different pH values using both HPC SN and HPC/CA DN at a constant dye concentration (40 mg/L) and adsorbent dosage (0.3 g) and the initial pH of the dye solutions was changed between 3 and 11 as present in Figure 7.11. The results obtained clearly showed that the adsorption efficiency of both hydrogels increases with the increase of the pH value from 3 to reach a maximum of pH 6.4, thereafter became nearly constant until pH 11. As can be seen, with increasing the pH values from 3 to 6.4, the removal efficiency of MB dye greatly increased from 45% to 80% and from 67% to 93% for HPC SN and HPC/CA DN hydrogels respectively. On the other hand, further increasing the pH values from 6.4 to 11, the adsorption capacity does not change. This is due to the presence of versatile oxygen-containing groups in DN hydrogels, such as hydroxyl and carboxyl groups.

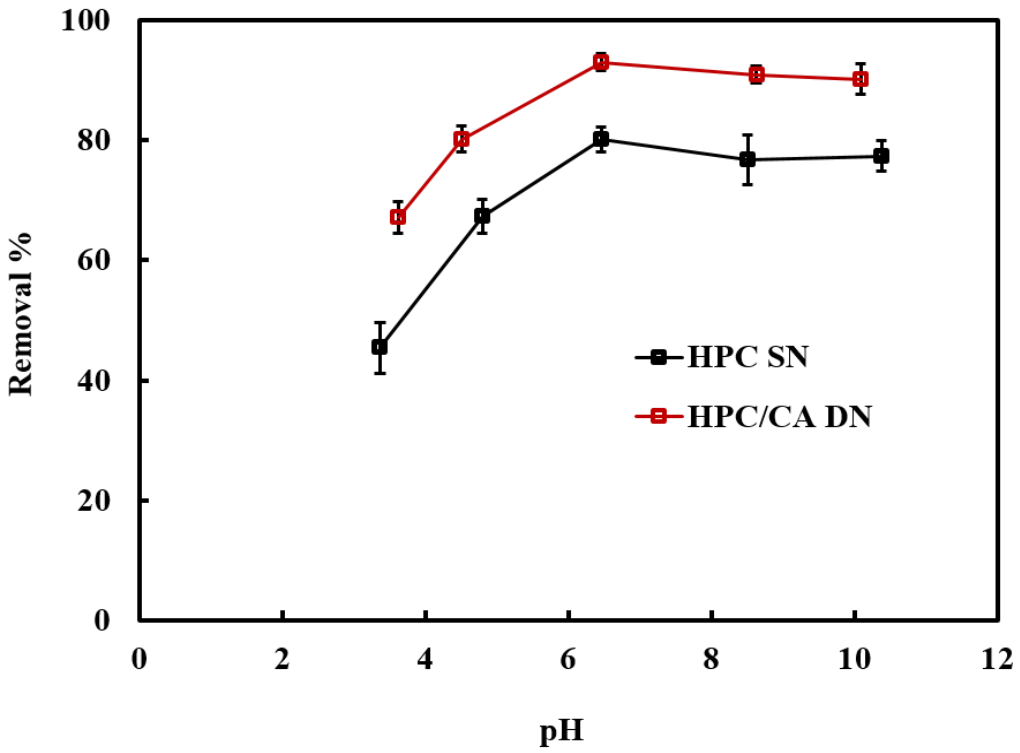

Figure 7.11. Effect of pH on adsorption of MB dye onto HPC SN and HPC/CA DN hydrogels (conditions: initial dye concentration = 40 mg/L; adsorbent dose 0.3 g/100 mL; time 40 h; temperature 298 K; mole ratio of HPC to SA 7:0 and 6:1 for HPC SN and HPC/CA DN hydrogels respectively).

As expected HPC/CA DN hydrogel exhibited higher adsorption capacity than HPC SN due to the carboxylate functional groups ($–COO^-$) and to hydroxyl groups ($–OH^-$), which provided plenty active sites for adsorption of cationic dye. However, both the HPC single and double network hydrogels exhibited maximum removal percentage at pH 6.4. This phenomenon can be explained by the electrostatic interaction between MB dye molecules charge and the hydrogel surface charge. At low pH values, the electrostatic repulsion between protonated adsorption sites on HPC/CA DN hydrogel and protonated dimethylamine group from MB increased, which prevented the interaction between HPC/CA DN hydrogel and MB molecules, so the adsorption capacity was less at low pH level. Whereas, with increasing pH values the level of deprotonation was increased and the electrostatic attraction enhanced, thus more MB was adsorbed onto the HPC hydrogel.[30] The zeta potential of HPC hydrogel was studied in order to determine the surface charge of this hydrogel. The point of zero charge (PZC) of the HPC hydrogel is calculated and it was found around 3.0 as shown in Figure 7.12.

As the pH of the solution increased the adsorption capacity of both hydrogels HPC SN and HPC/CA DN was found to be increasing; this was due to the removal of the

positive hydrogen ions thereby promoting activities of electrostatic interaction between the negative charges of both hydrogels and the MB dye molecules.[31] While at an acidic pH, the functional groups of HPC SN and HPC/CA DN become protonated, which are mainly the carboxylic groups (-$COOH^{2+}$) and hydroxyl groups (-OH^{2+}). At pH 3, the surface charge of HPC hydrogel becomes more positively charged, which enhances low adsorption capacity due to electrostatic repletion.

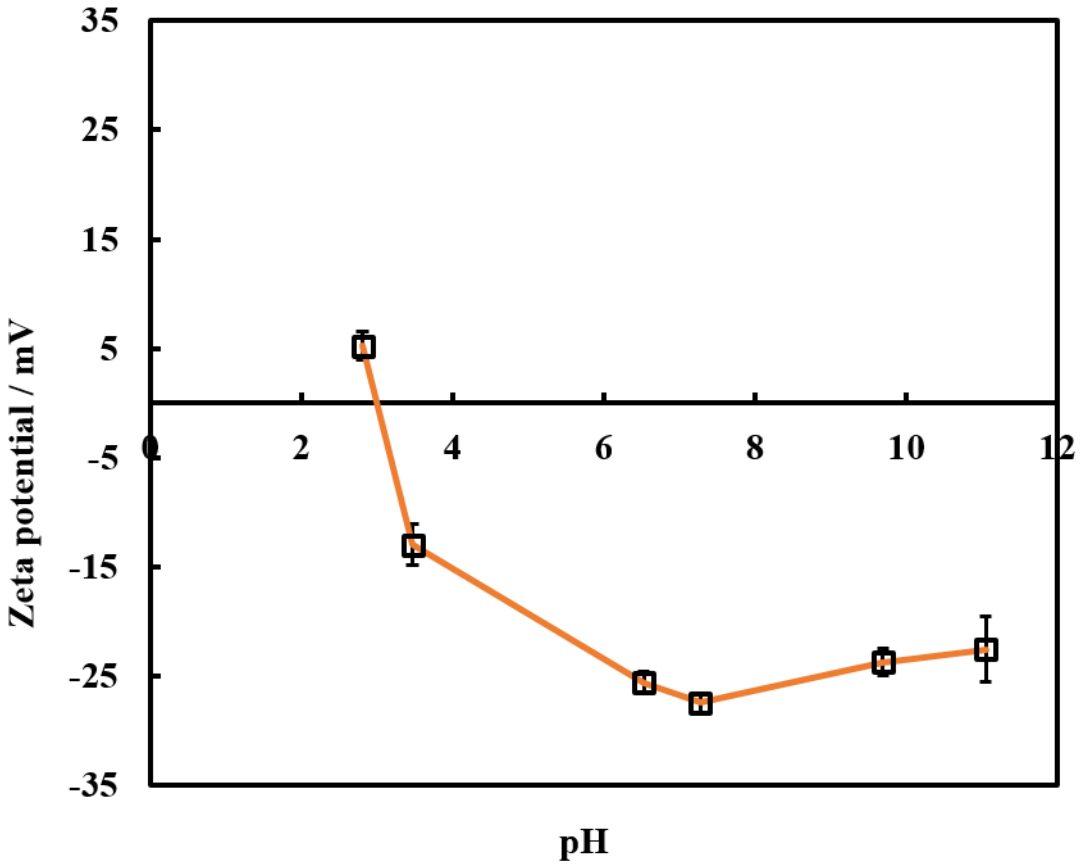

Figure 7.12. Zeta potential of HPC hydrogel dispersed in aqueous solution versus pH.

It is reasonable that, charges on the hydrogel surface are positive when of pH < pHpzc, since the protonation reactions happen during the process. Thus, at a low pH values MB dye are difficult to adsorb on the positively charged surface of HPC hydrogel due to the electrostatic repulsion and this decrease the uptake capacity. Whereas, above the pHpzc the surface charge of HPC hydrogel demonstrate a negative zeta potential. This was due to lack the concentration of protonated sites with increasing pH value because of the deprotonation reaction. [32]Thereby results in the increase of MB dye adsorption on the HPC hydrogel due to the electrostatic interaction.

7.2.1.1.4. Adsorption isotherms

Equilibrium adsorption isotherms are one of the most common ways to investigate the adsorption mechanism. The analysis of the isotherm data by fitting them to different isotherm models is an important step to find the suitable model that can be used to investigate how the adsorption molecules distribute between the liquid phase and the solid phase when the adsorption process reaches an equilibrium state. Langmuir and Freundlich adsorption isothermal equations are widely used to describe the adsorption behaviours. In the theoretical Langmuir model, it is assumed that the dye undergoes monolayer adsorption and that there is no interaction between the adsorbate molecules.[26]

$$\frac{C_e}{Q_e} = \frac{1}{Q_{max}K_L} + \frac{C_e}{Q_{max}} \qquad (7.1)$$

Where C_e (mg L^{-1}) is the equilibrium concentration of MB dye in solution, Q_e (mg g^{-1}) is the equilibrium capacity of MB on the adsorbent, Q_{max} (mg g^{-1}) is the maximum amount of MB on the adsorbent to form a complete monolayer on surface, K_L (L mg^{-1}) is the Langmuir constant that relates to the affinity of adsorption sites. The Freundlich model is an empirical model and more applicable at low adsorbate concentrations.[33]

$$\log Q_e = \log K_F + \frac{1}{n}\log C_e \qquad (7.2)$$

Where, Q_e (mg/g) is amounts of MB dye adsorbed at equilibrium, C_e (mg/L) is equilibrium MB dye concentration in the solution. K_F and (1/n) are Freundlich adsorption isotherm constants.

The equilibrium parameter or separation factor (RL) was used to determine the feasibility of adsorption in a given concentration range over adsorbent and can be evaluated by the following equation :[34]

$$R_L = \frac{1}{1 + K_L C_o} \qquad (7.3)$$

Where K_L (L/g) is the constant of Langmuir isotherm. C_o is the initial concentration.

Figures 7.13 and 7.14 show the adsorption isotherms, Langmuir and Freundlich isotherms of MB dye onto HPC SN and HPC/CA DN hydrogels respectively. The Langmuir and Freundlich models parameters and the correlation coefficients were calculated and summarized in Table 7.1. The adsorption isotherm of MB dye onto HPC SN and HPC/CA DN hydrogels were fitted to both the Langmuir and the Freundlich adsorption models. It can be seen that MB dye adsorption onto both hydrogels in this study better fitted the Langmuir model than Freundlich model, due to the larger correlation coefficient (R^2).

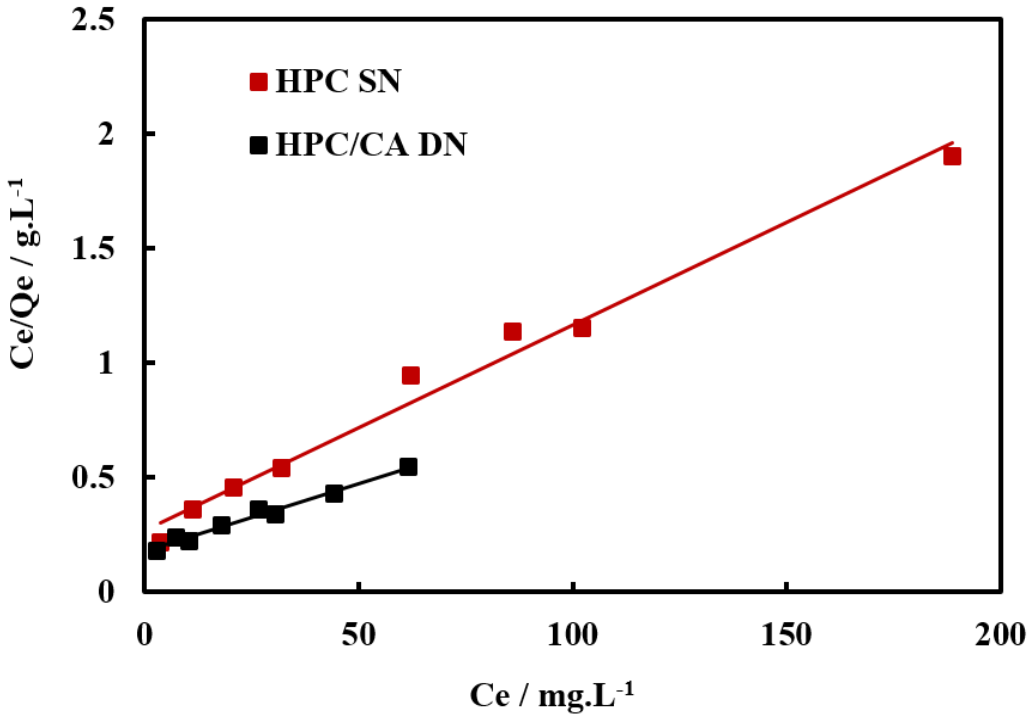

Figure 7.13. Adsorption isotherm models for MB on HPC SN hydrogel (A) Langmuir model (B), Freundlich model.

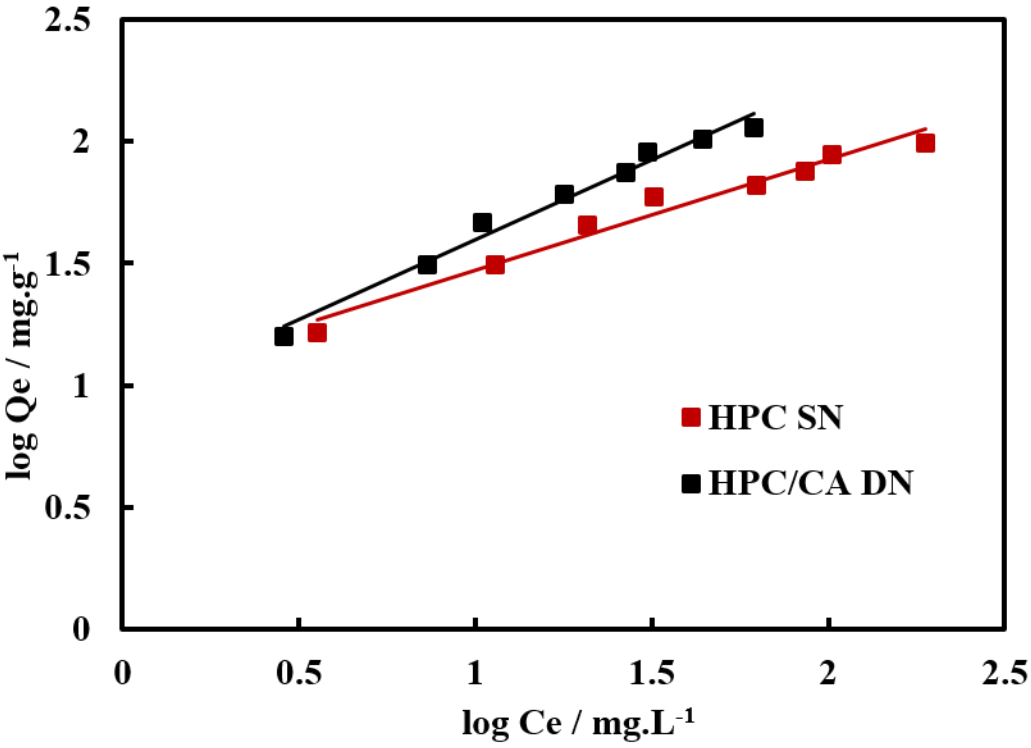

Figure 7.14. Adsorption isotherm models for MB on HPC/CA DN hydrogel (A) Langmuir model (B), Freundlich model.

Table 7.1. Adsorption isotherm parameters of Langmuir and Freundlich models

Isotherm model	Parameters	HPC SN hydrogel	HPC/CA DN hydrogel
Langmuir	q_{max} (mg/g)	112.359	169.491
	K_L (L/mg)	0.032	0.033
	R_L	0.092	0.090
	R^2	0.984	0.971
Freundlich	n	2.207	1.528
	K_F	10.456	8.747
	R^2	0.981	0.849

According to Figures 7.13, 7.14 and Table 7.1, A slightly better fit for MB adsorption onto the HPC hydrogel was found for the Langmuir model, with an R^2 value of 0.984 versus 0.981 for the Freundlich model, while the correlation coefficient values (R^2) of the Langmuir adsorption model was 0.971, which is larger than that of the Freundlich adsorption model (0.849) for HPC/CA DN hydrogels. Thus, the adsorption isotherms are fitted better by the Langmuir model in comparison with the Freundlich adsorption model, suggesting that MB dye adsorption onto HPC SN and HPC/CA DN hydrogels is mostly monolayer and there are no intermolecular interaction between the adsorbate molecules.[35] In addition, the RL values were found to be less than 1 and bigger than 0 for both HPC SN and HPC/CA DN hydrogels, indicating that MB is easily adsorbed onto the prepared hydrogels and the adsorption process is favourable. Based on the Langmuir model, HPC/CA DN hydrogel has a maximum adsorption capacity for MB 169.49 mg/g, which is higher than the adsorption capacity of HPC SN (112.35 mg/g) under the conditions used in this study. It can be noticed that the n values>1, which suggests that the adsorption of MB dye onto HPC SN and HPC/CA DN hydrogels is physical adsorption due to electrostatic interaction.[36, 37]

7.2.1.1.5. Adsorption kinetics

Kinetic study were also applied to provide information about the rate mechanism of MB adsorption onto HPC SN and HPC/CA DN hydrogels. Adsorption experiments were carried out by batch contact time at room temperature (22±1 °C) using 0.3 g of adsorbent and 100 mL of four different concentrations of the dye (10, 20, 30 and 40 $mg.L^{-1}$), while the contact time was changed between 30 min-28 hours . Both the pseudo-first-order

kinetic models and pseudo second- order kinetic models were used to fit the experimentally obtained adsorption data. The pseudo first- order and the pseudo-second-order rate equations were listed as follows:[31]

$$\frac{1}{q_t} = \left(\frac{k_1}{k_d}\right)\left(\frac{1}{t}\right) + \frac{1}{q_e} \qquad (7.4)$$

$$\frac{t}{q_t} = \frac{1}{k_2 q_e^2} + \frac{t}{q_e} \qquad (7.5)$$

Where q_e and q_t are the amount of MB dye adsorbed per unit mass of the adsorbent (mg/g) at equilibrium and time t (mins) respectively, k_1 (min^{-1}) is the first-order rate constant and k_2 ($g\ mg^{-1}\ min^{-1}$) is the pseudo second- order rate constant.

Figure 7.15 (A) and (b) showed the pseudo-first-order kinetic plots for the adsorption of MB dye by HPC SN and HPC/CA DN hydrogels respectively. The values of k_1 and q_e can be calculated from slope and intercept of the graph. Figure 7.15 (C) and (D) showed pseudo-second-order kinetics plots for the adsorption of MB dye by HPC SN and HPC/CA DN hydrogels respectively. The second-order sorption rate constant k_2, and q_e can be calculated from the slope and intercept of the graph. The parameters of both kinetic models were calculated and summarized in table 7.2.

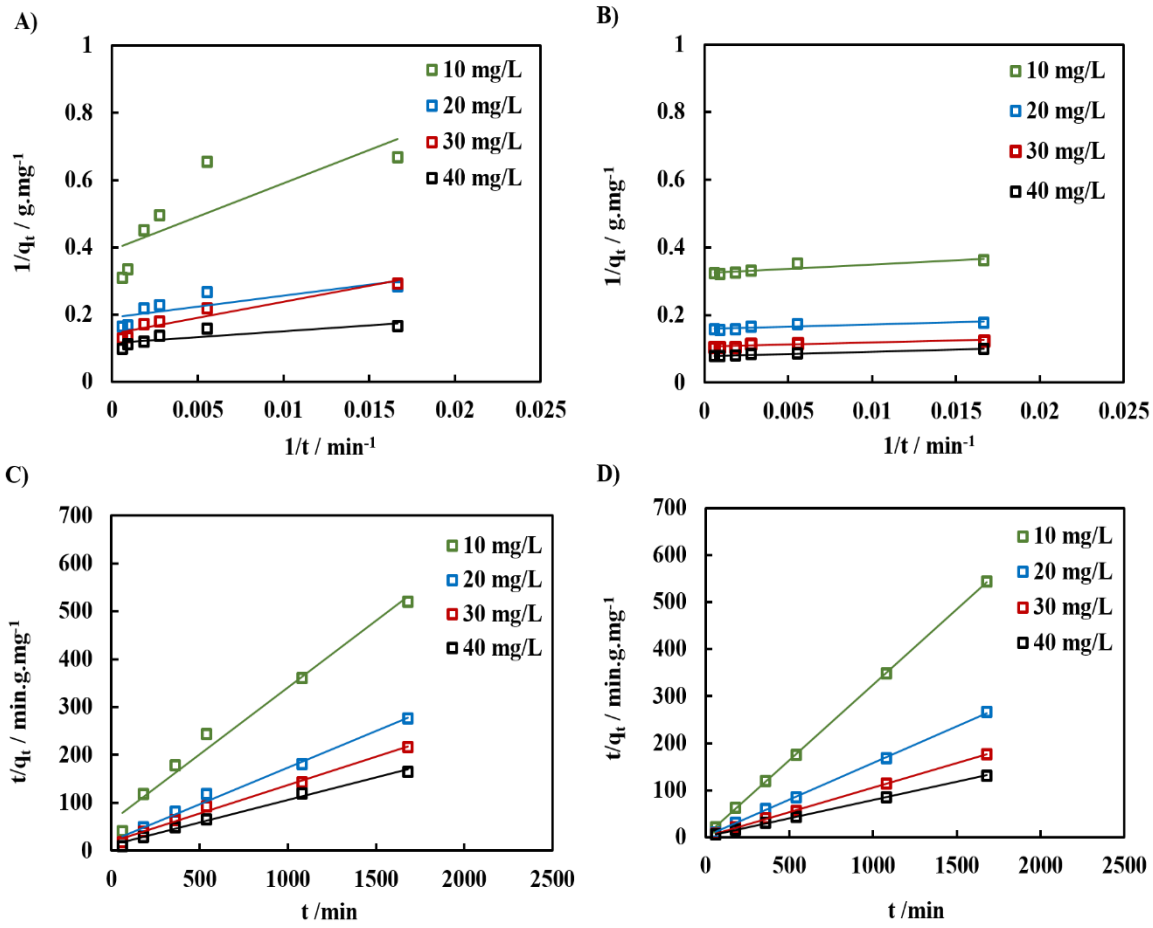

Figure 7.15. Kinetic curves (A) Pseudo-first-order plots, (B) pseudo-second-order plots for MB adsorption onto HPC SN hydrogel, and (C) Pseudo-first-order plots, (D) pseudo-second-order plots for MB adsorption onto HPC/CA DN hydrogel.

Table 7.2. Adsorption kinetic parameters of MB by HPC SN and HPC/CA DN hydrogels.

Pseudo-first-order model					
	C_o (mg.L^{-1})	R^2	K_1 (min^{-1})	$q_{e,cal}$(mg.g^{-1})	$q_{e,exp}$(mg.g^{-1})
HPC SN	10	0.625	61.804	2.551	3.121
	20	0.654	39.565	5.249	6.040
	30	0.914	65.528	7.047	7.887
	40	0.674	36.807	8.726	10.255
HPC/CA DN	10	0.838	7.826	3.085	3.106
	20	0.730	7.940	6.293	6.339
	30	0.843	11.340	9.425	9.563
	40	0.960	16.382	12.706	12.814
Pseudo-second-order model					
	C_o (mg.L^{-1})	R^2	k_2(g.mg^{-1} min^{-1})	$q_{e,cal}$(mg.g^{-1})	$q_{e,exp}$(mg.g^{-1})
HPC SN	10	0.981	0.084	3.585	3.121
	20	0.990	0.075	6.535	6.040
	30	0.992	0.058	8.445	7.887
	40	0.992	0.051	10.570	10.255
HPC/CA DN	10	0.999	0.097	3.115	3.106
	20	0.999	0.077	6.402	6.339
	30	0.999	0.051	9.643	9.563
	40	0.999	0.042	12.919	12.814

As can be seen in Table 7.2, the values of R^2 for the pseudo-second-order kinetic model for MB dye adsorption on both HPC SN and HPC/CA DN hydrogels showed better agreement with experimental data ($R^2 \geq 0.98$) than the pseudo-first-order model. Furthermore, the calculated q_e,cal values with different concentrations of MB dye were very close to the experimental q_e,exp values, while some different can was seen with the pseudo-first-order model. These results indicated that the adsorption of MB dye onto both HPC SN and HPAC/CA DN composite hydrogels was well described by the pseudo-second-order kinetic model.

The low values of the correlation coefficient (R^2) between the theoretical (q_{eq}) and the experimental ($q_{eq(exp)}$) values obtained for the pseudo-first-order model compared to that for the pseudo second- order kinetics is an indication that the adsorption of MB dye on

the HPC/CA DN hydrogel did not follow the pseudo-first-order reaction. The R^2 values were found to be close to unity for MB dye when the kinetic data were modelled with the pseudo-second-order equation.

The details of the diffusion mechanism of MB dye in the hydrogels materials cannot be descriped by the pseudo-first order and pseudo-second-order models. Therefore, an intraparticle diffusion model was employed to analyze the kinetic data to show the movement of the dye molecules from the aqueous solution into the pores of the hydrogels materials. The intraparticle diffusion model was expressed by the following equation:[38]

$$q_t = k_d t^{1/2} + C \qquad (7.6)$$

Where *qt* (mg/g) is the amount of dye adsorbed at time t (h), adsorbed at time *t* (mins), *kp* (mg g^{-1} $h^{-1/2}$) is the intra-particle diffusion rate constant, C (mg/g) is the adsorption capacity and calculate from intercept when *qt* is plotted against $t^{1/2}$. Figure 7.16 (A) and (B) shows the intraparticle diffusion plot (*qt* against $t^{1/2}$) for the adsorption of MB dye by HPC SN and HPC/CA DN hydrogels respectively. The values of intraparticle diffusion model parameters were calculated from the graph and summarized in Table 7.3.

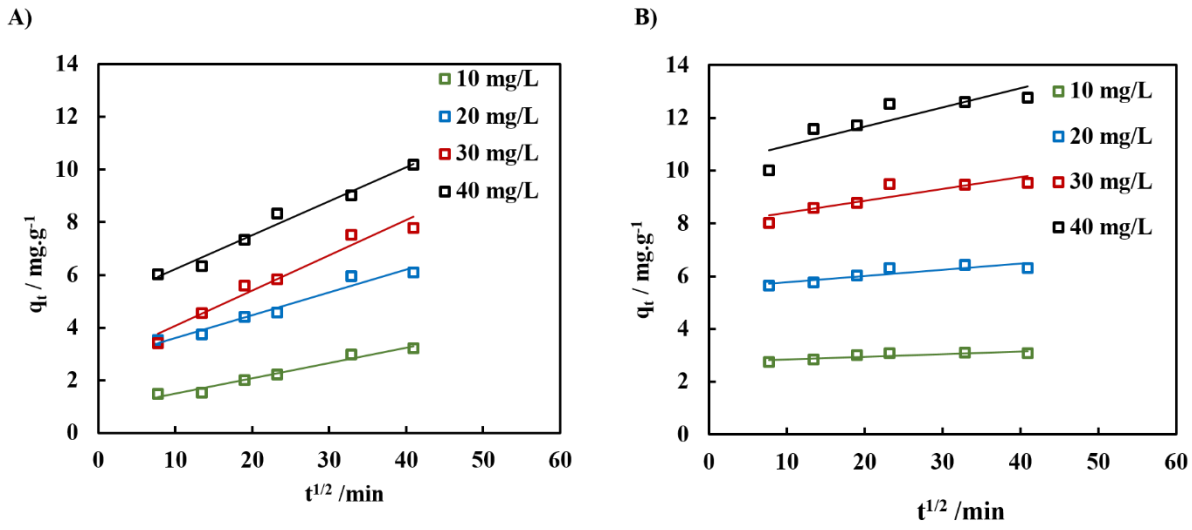

Figure 7.16. Intraparticle diffusion model of MB adsorption on (A) HPC SN hydrogel and (B) HPC/CA DN hydrogel.

Table 7.3. Intraparticle diffusion parameters for the adsorption of MB dye onto HPC SN and HPC/CA DN hydrogels.

	C_o (mg.L^{-1})	R^2	K_p(mg.g^{-1} min$^{-1/2}$)	C (mg.g^{-1})
HPC SN	10	0.9698	0.0582	0.9165
	20	0.9592	0.0865	2.7377
	30	0.9597	0.1335	2.7344
	40	0.9762	0.1287	4.9262
HPC/CA DN	10	0.7391	0.0101	2.7502
	20	0.7827	0.0235	5.5431
	30	0.7888	0.0447	7.9613
	40	0.7564	0.0725	10.2110

According to the intraparticle diffusion model, if the plot (q_t against $t^{1/2}$) gives a straight line passing through the origin, thus the adsorption process is controlled by the adsorbate molecules diffusion into the adsorbent pores, whereas if the plots do not pass through the origin, two or more steps effect the adsorption process.[39] The plots of both HPC SN and HPC/CA DN hydrogels the plot did not pass through the origin as showed in Figure 7.16 indicating that the processes rate-controlling are not depend totally on the MB dye molecules diffusion into the hydrogels pores. As mentioned above the adsorption process of MB on these hydrogels were divided into three adsorption regions with time. The first region relates to diffuse MB dye from the solution to the external surface of the hydrogel. The second region corresponds to the gradual MB dye adsorption inside the hydrogel pores and this stage reflecting intra-particle diffusion as the rate-controlling step. The equilibrium region is the final stage, which is relates to the intra-particle diffusion starts to slow down. These results suggested there are another steps controlling the adsorption rate along with intraparticle diffusion and confirmed that the pseudo-second order kinetic model was a suitable kinetic model used to describe the adsorption of MB by HPC SN and HPC/CA DN hydrogels.[40]

7.2.1.1.6. Thermodynamic studies

In order to investigate the impact of temperature on the adsorption process especially HPC hydrogel themoresponsive materials , an adsorption experiment was carried out for both HPC SN and HPC/CA DN hydrogels at 25, 35, 45 and 55 °C using 100 mL of 40 mg/L of the MB solutions at pH 6.4 and 0.3 g of the hydrogel. Figure 7.17 demonstrates the effect of temperature on the adsorption capacity of MB dye onto HPC SN and HPC/CA DN hydrogels. As shown the adsorption capacity of both hydrogels towards MB dye decreased slightly with the increase of the temperature from 25 to 35 °C. Whereas, the adsorption capacity sharply decreased with increase the temperature to 45 °C. The adsorption capacity of MB dye decreased from 8.34 to 6.01mg/g on the HPC SN hydrogel and from 12.31 to 9.62 mg/g on HPC/CA DN hydrogel.

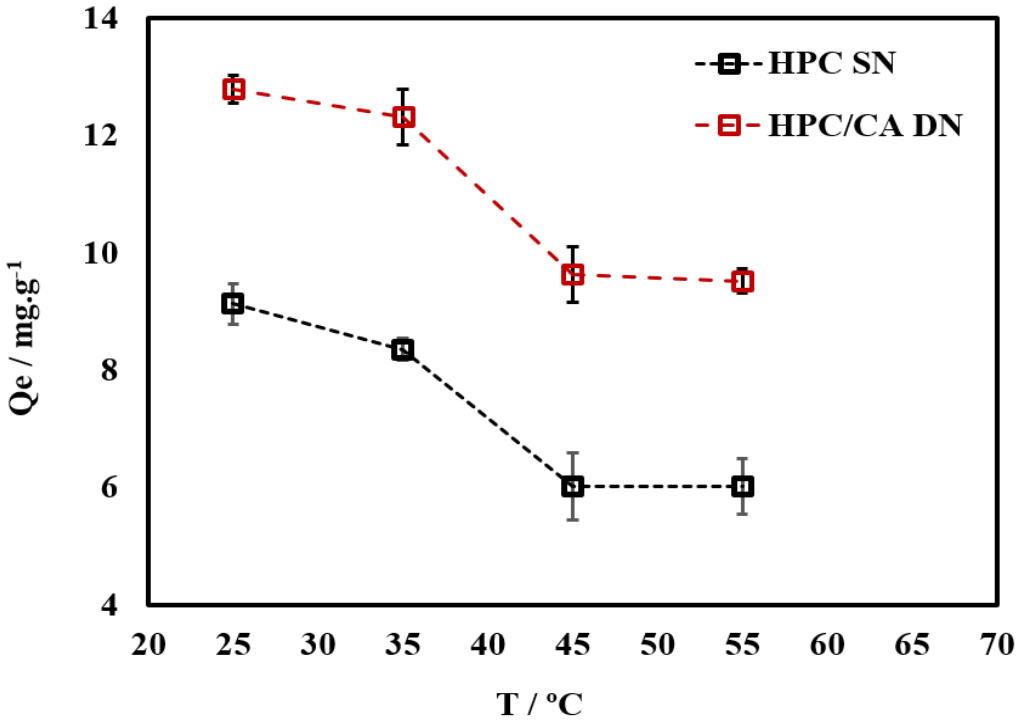

Figure 7.17. Effect of temperature on adsorption of MB dye by using HPC SN and HPC/CA DN hydrogels.

The adsorption capacity decreased with increase the temperature. Due to the reduce of the forces of adsorption between the MB dye molecules and the adsorption sites on the HPC SN and HPC/CA DN hydrogels surface causing a decrease in adsorption capacity. This results indicating the adsorption of MB dye onto HPC hydrogel an exothermic process.[41] The adsorption capacity of MB dye shows a high decrease at the temperatures above the LCST of HPC (42 °C), this might be due to the hydrophobic behaviour of HPC

hydrogel at this temperature causing phase separation between the hydrogel and the surrounding solution. Furthermore, high temperature might also lead to the breaking of existing intermolecular hydrogen bonding between HPC hydrogel and MB dye, which reduces the adsorption capacity.[42]

Study the thermodynamic parameters during the adsorption process is important because it shows the influence of temperature on the adsorption process nature in order to know the processes are spontaneous or nonspontaneous and prediction whether an adsorption process is endothermic or exothermic. The thermodynamic parameters include the standard free Gibbs energy (ΔG°), standard enthalpy change (ΔH°) and standard entropy change (ΔS°) can be calculated by the following equations:[28]

$$\Delta G^{O} = -RTlnK_{eq} \qquad (7.7)$$

$$\ln K_{eq} = \frac{\Delta S^{O}}{R} - \frac{\Delta H^{O}}{RT} \qquad (7.8)$$

Where R is the gas constant (8.314 J mol^{-1} K^{-1}), T is the absolute temperature (K), Keq is the equilibrium constant of the adsorption ($L.g^{-1}$) and can be calculated using the following equation:

$$K_{eq} = \frac{q_{eq}}{C_{eq}} \qquad (7.9)$$

Where q_{eq} ($mg.g^{-1}$) is the amount of MB dye adsorbed on the adsorbent from solution at equilibrium, C_{eq} ($mg.L^{-1}$) is the equilibrium concentration of metal ions in the solution.

Figure 7.18 demonstrates van't Hoff plots (lnK_{eq} against $1/T$) for MB dye adsorption onto HPC/CA DN hydrogel. The values of ΔH and ΔS of the adsorption of MB dye onto HPC/CA DN hydrogel were obtained from the slope (-ΔH /R) and intercept (ΔS /R)of the linear graph which is plotted between ln K_{eq} and 1/T. All the calculated thermodynamic parameters are summarised in Table 7.4. The data in this table shows that all the thermodynamic parameters have negative values at all temperatures studied and the negative ΔG values increased from −16.7 to −14.9 $kJ.mol^{-1}$ with increasing temperature from 25 to 55 ºC.

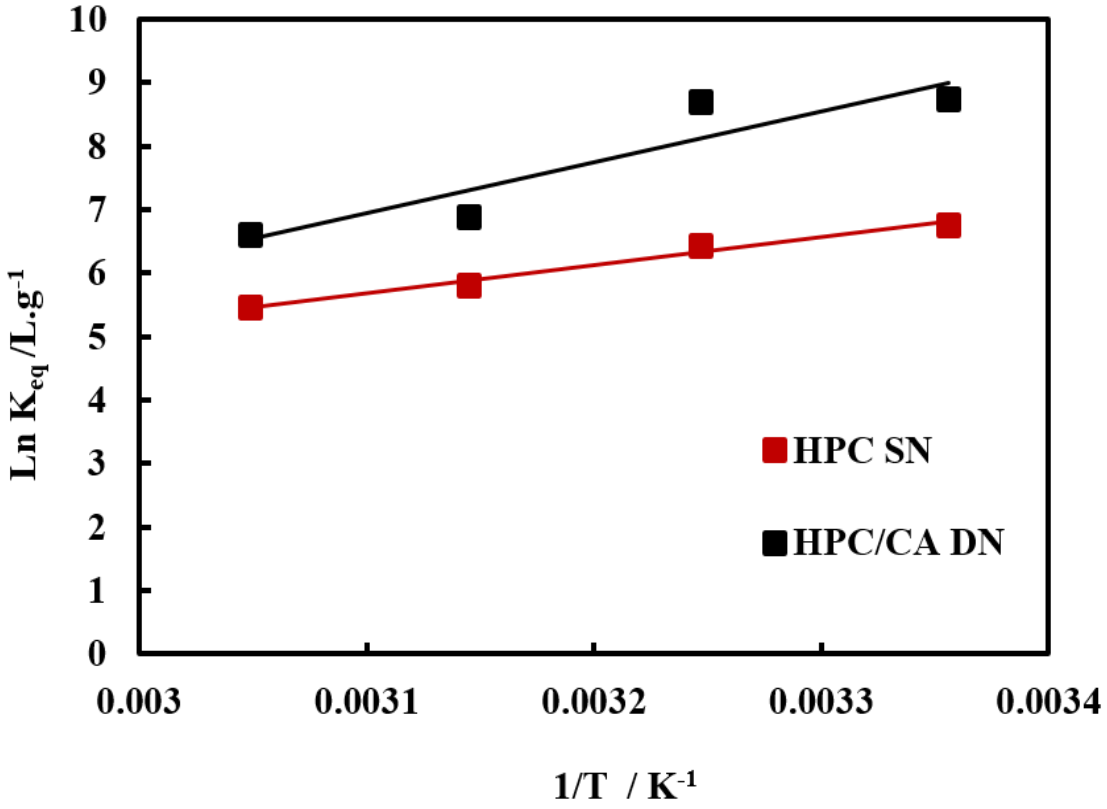

Figure 7.18. van't Hoff plot for MB dye adsorption onto HPC SN and HPC/CA DN hydrogels.

Table 7.4. Thermodynamic parameters for MB dye adsorption onto HPC SN and HPC/CA DN hydrogels at different temperatures.

	Temperature / K	ΔG° (KJ.mol^{-1})	ΔH° (KJ.mol^{-1})	ΔS° (J.mol^{-1}.K^{-1})
HPC SN	298	-16.771	-36.66	-66.36
	308	-16.501		
	318	-15.383		
	328	-14.923		
HPC/CA DN	298	-21.667	-66.58	-148.57
	308	-22.305		
	318	-18.219		
	328	-18.034		

The negative values of ΔG for the adsorption of MB dye onto both HPC SN and HPC/CA DN hydrogels at all studied temperatures indicates that the spontaneous nature of the adsorption process.[43] Furthermore, the negative values of ΔG were found to be increased with increasing the temperature indicates that the adsorption process of MB dye onto these adsorbents becomes more favourable at lower temperatures.[39, 44]The ΔH represented negative value, reflects that the adsorption reaction was exothermically driven.[45] It could be envisaged that the adsorption of MB dye onto both HPC SN and HPC/CA DN hydrogels was physical adsorption.[46] This is expected as an adsorption process shows spontaneously nature. However, ΔH values are lower than the chemical adsorption range, but still out the range assigned to physical adsorption. This results agreed with the suggestion that the adsorption of MB on both HPC SN and HPC/CA DN hydrogels being hydrogen bonding and/or electrostatic interactions between the adsorbent and the adsorbate molecules.[47] The entropy changes (ΔS) have also resulted in negative values indicates that the adsorption of MB dye on to both hydrogels in this study has resulted in decrease the degree of randomness which means that MB dye molecules were orderly adsorbed onto the hydrogel sample.[45]

7.2.2. Column adsorption study

7.2.2.1. MB and FL dyes filtration using HPC SN and HPC/CA DN hydrogel columns

The adsorption by monolithic columns with porous structures can provide better total efficiency due to their faster separation at low pressure and easy for regenration. To demonstrate the practical usage of the HPC SN and HPC/CA DN hydrogels, columns were fabricated from these hydrogels, thus allowing continuous liquid purification instead of requiring batch-wise operations. Elution experiments were carried out at room temperature (22 ± 2 °C) with hydrogels columns prepared in 20 mL syringe barrels. Aqueous solutions of MB (10 mg L^{-1}) were eluted through these columns. Adsorption of MB dye onto the prepared hydrogel columns and its removal from the aqueous solution was observed. Figure 7.19 and 7.20 show UV-vis spectrum before and after filtration by HPC/CA DN hydrogels column of MB and FL dyes respectively. UV-vis spectrum shows no detectable absorption bands for the MB dye in the solution after filtration. Similarly, aqueous solutions of FL dye (20 mg.L^{-1}) were eluted through separate sets of the columns. In contrast to MB, elution of FL dye solution led to no pronounced adsorption on the column, with little change in the UV-vis spectrum of the eluent from that of the loaded solution as shown in Figure 7.20.

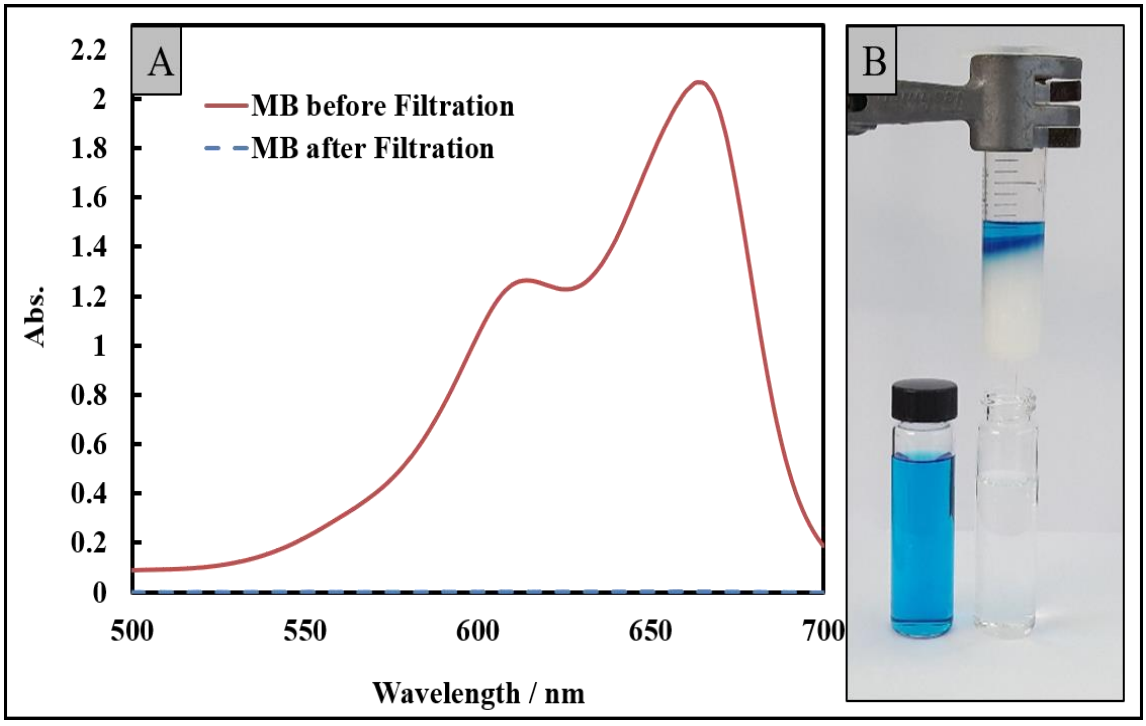

Figure 7.19. Elution of MB dye solutions through HPC hydrogel column; (A) UV-Vis spectrum of MB solution before and after filtration; (B) Image of the prepared column used for filtration MB dye and the solution before and after filtration. The filtered solution is colourless

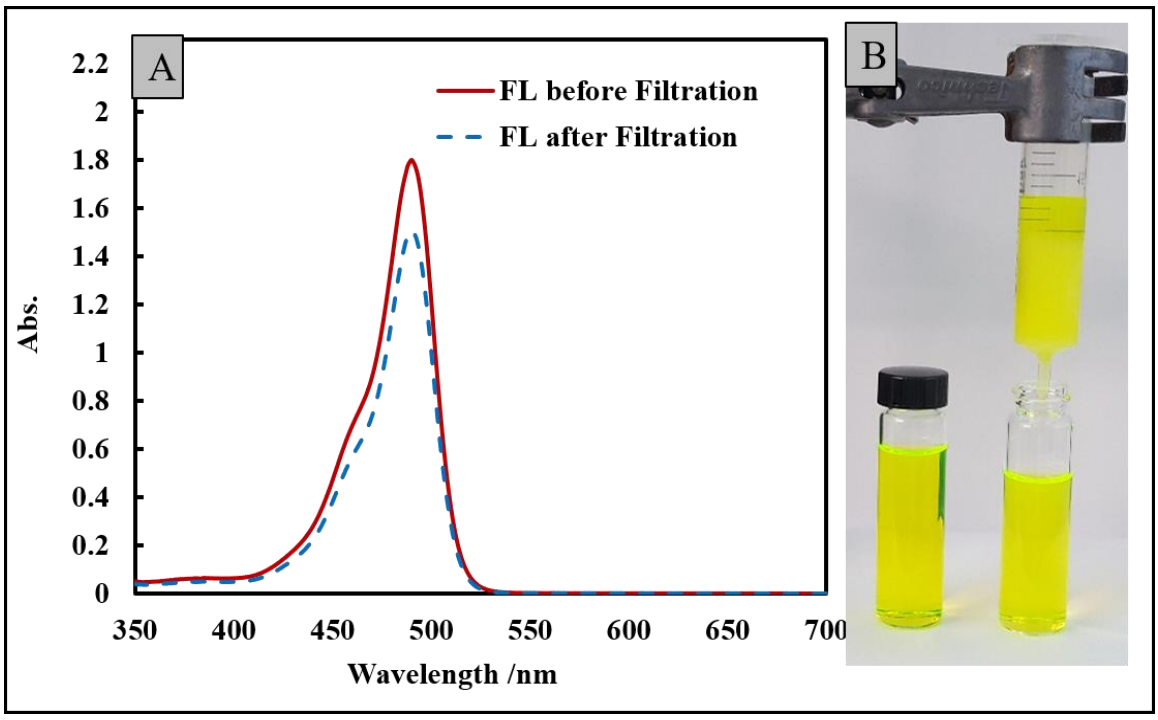

Figure 7.20. Elution of FL dye solutions through HPC hydrogel column; (A) UV-Vis spectrum of FL solution before and after filtration; (B) Image of the prepared column

used for filtration FL dye and the solution before and after filtration. The filtered solution is the same before filtration.

As can be seen from Figures 7.19 and 7.20, the HPC hydrogel columns showed a remarkable removal for MB dye, while extremely low removal of FL dye, indicating that the HPC hydrogel was an efficiently selective adsorbent for cationic dyes. It is obvious from the optical images in these Figures that the MB solution became clear and transparent after being filtrated by HPC hydrogel column, whereas the FL dye solution remained unchanged. The same results was also observed for HPC/CA DN hydrogel. The selectivity of the HPC SN and HPC/CA DN hydrogels columns for cationic dyes can be rational based on their chemical structures. There was a high density of negatively charged in HPC SN hydrogel with hydroxyl groups and with dual negatively functional groups in HPC/CA DN hydrogel (hydroxyl and carboxyl groups). Therefore, both HPC SN and HPC/CA DN hydrogels showed high adsorption capacity towards positively charged MB dye due to strong electrostatic interaction, whereas extremely low adsorption was observed for negatively charged FL dye due to electrostatic repulsion.

To compare the adsorption ability of the HPC SN and HPC/CA DN hydrogels columns, the removal percentage of MB and FL dyes for the outlet solution was recorded as a function of permeation volume during the filtration process. For FL dye the removal % was between 15-20 % for initial 10 mL eluted. This was due to dilution of the FL dye solution in the HPC hydrogel column. After that the removal percentage decreased rapidly and thereafter became nearly constant at about 5%. The small removal percentage of FL dye be HPC column was due to electrostatic repulsion between the HPC hydrogel and the anionic FL dye as mentioned above. MB solution with 10 $mg.L^{-1}$ concentration was eluted through these columns separately. As shown in Figure 7.21 (A), the removal percentage of HPC SN hydrogel column for MB dye of the first 200 effluent is kept approximately 100 %, although the removal % decreased gradually. Whereas, the removal % was kept 100% for the initial 450 mL then decreased slowly with the permeation volume as shown in Figure 7.21 (B).

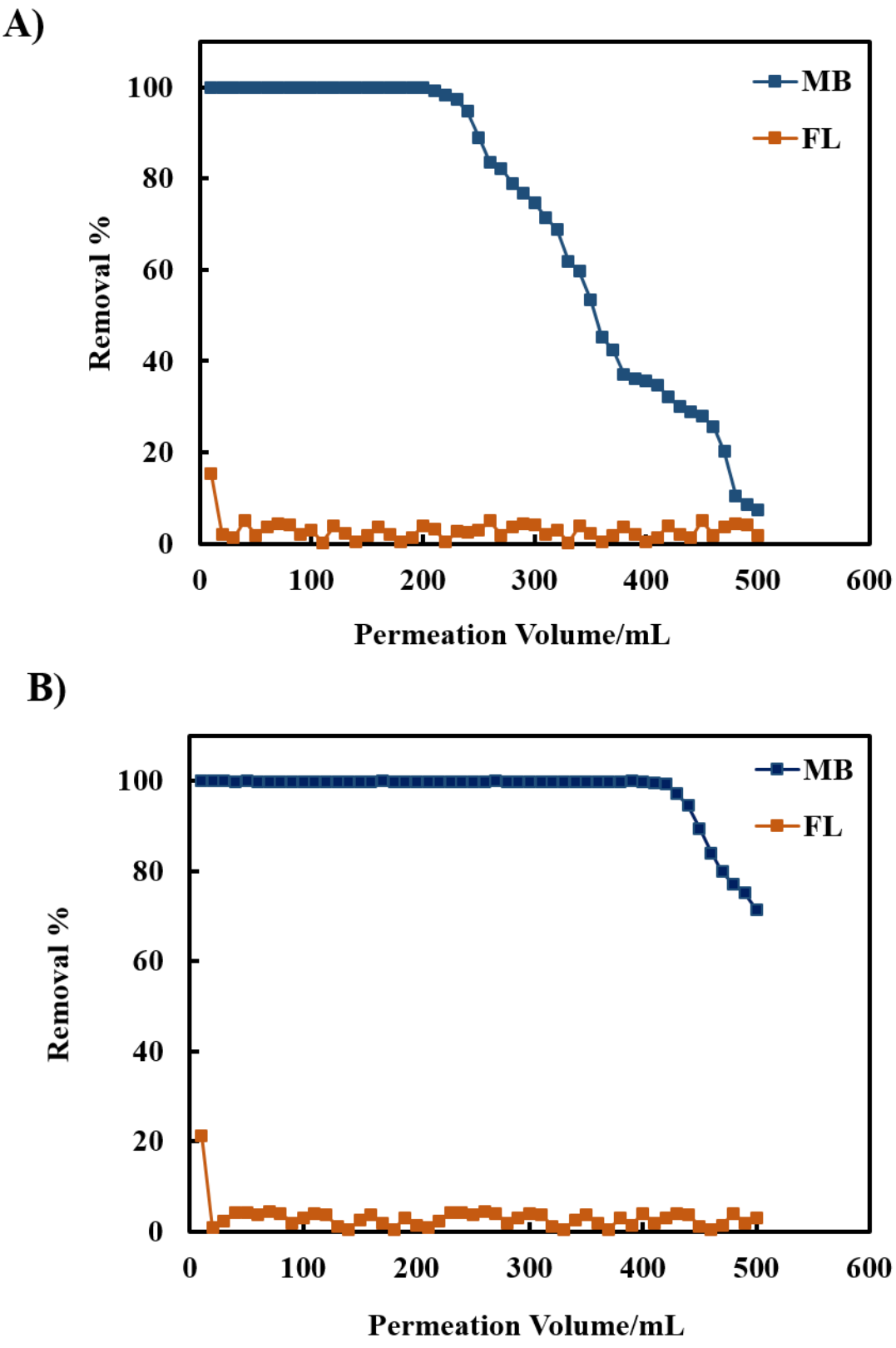

Figure 7.21. The removal percentage of MB and FL dyes by filtration of these dyes using (A) HPC SN (B) HPC/CA DN hydrogel as a function of permeation volume.

7.2.2.2. Regeneration study

Regeneration the used hydrogels is highly desirable for cost-effective practiced applications. In order to investigate the reusability of HPC SN and HPC/CA DN hydrogels the above dye filtration experiment was repeated with the regenerated column. The adsorption/regeneration cycles were repeatedly five times. FL dye could be easily desorbed from the columns by elution with deionized water, whereas MB-loaded columns were regenerated by elution with 0.01 M aq. HCl. This was due to HPC SN and HPC/CA DN hydrogels exhibit a relatively low adsorption efficiency at low pH values, which suggest that these hydrogels could be regenerated by acidic solutions As expected protonation decreases electrostatic attraction between the column and the positively charged dye.[48] After elution of the adsorbed dye, the hydrogel columns were further washed with deionized water and reused for MB dye removal. Figure 7.22 shows photographic images of desorption of FL and MB dyes from HPC hydrogel columns. It was found that HPC SN and HPC/CA DN hydrogels columns could be reused for several cycles, with only a 5% drop in MB uptake during the 5th cycle as shown in Figure 7.23.

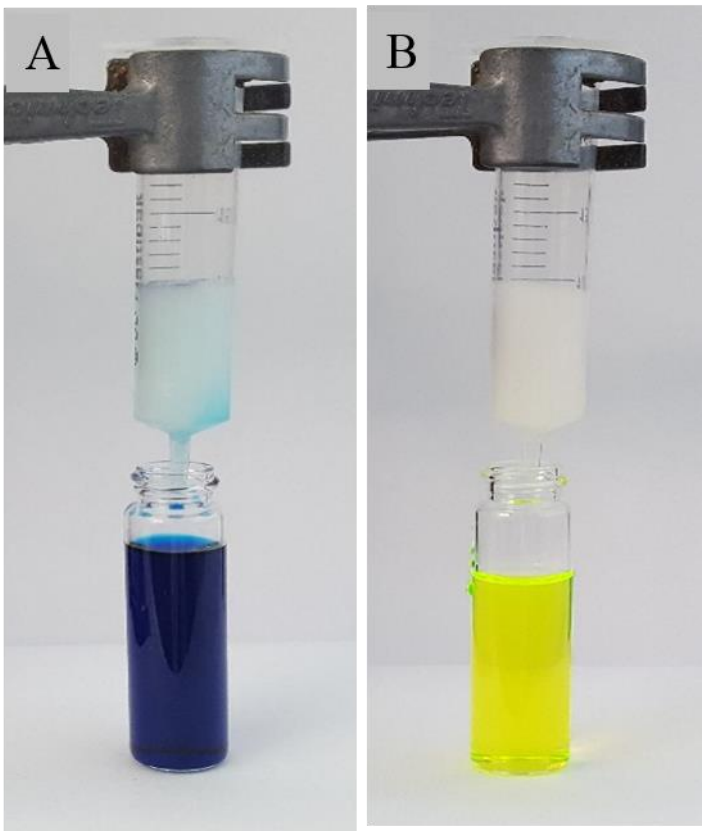

Figure 7.22. Photograph images show (A) desorption of MB dye from HPC hydrogel column by washing the column by 0.01 M aqueous HCl (B) desorption of FL dye from HPC hydrogel column by washing the column by water.

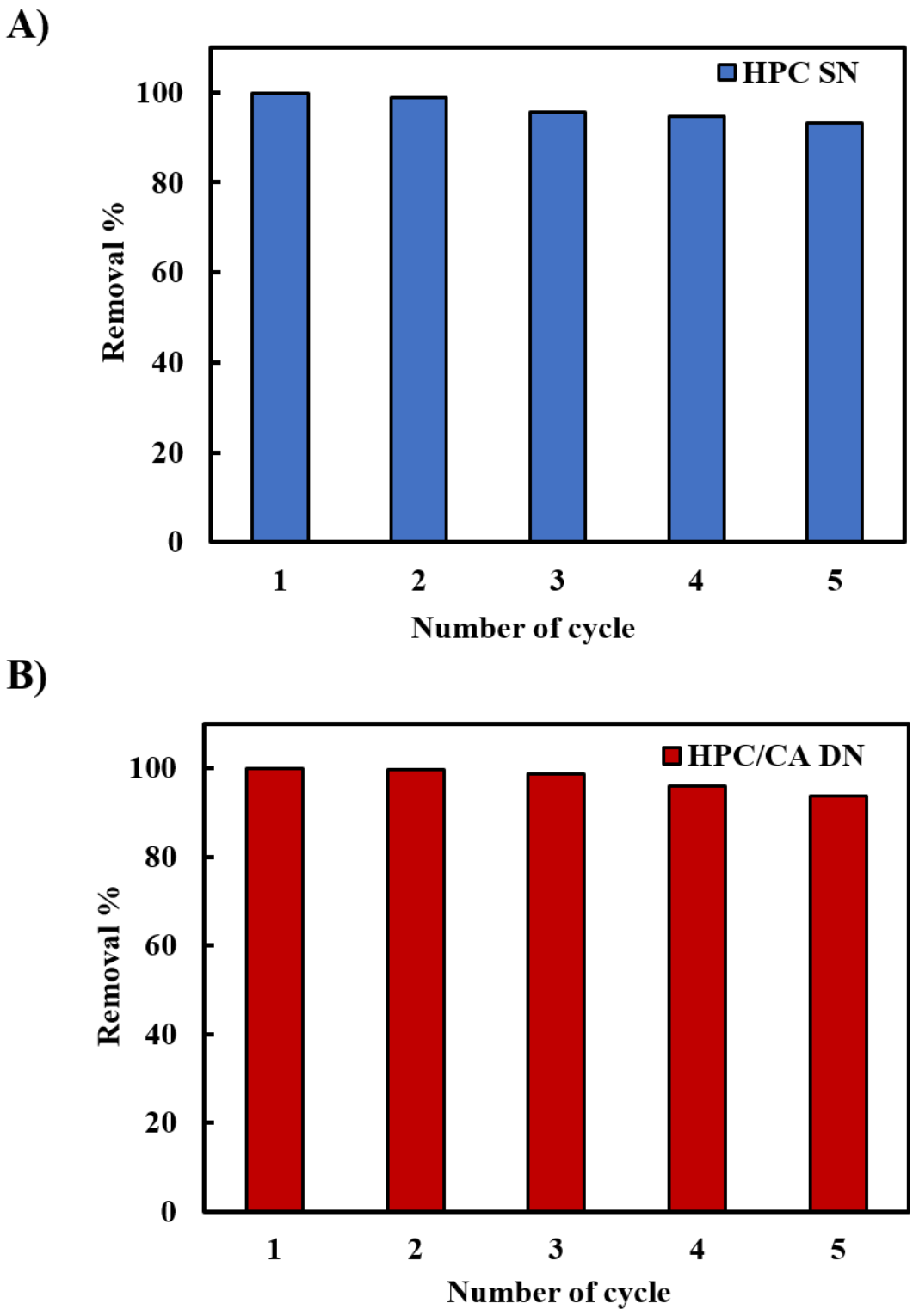

Figure 7.23. Bar chart showing extent of MB dye adsorption with each elution /regeneration cycle of (A) HPC SN hydrogel for adsorption of 200 ml of 10 mg.L^{-1} MB dye and (B) HPC/CA DN hydrogel for adsorption of 500 ml of 10 mg.L^{-1} MB dye.

The results demonstrated that protonation of the hydrogels by diluting HCl was a suitable candidate for regeneration the HPC hydrogels column. This was due to the adsorption capacity of MB dye onto both HPC SN and HPC/CA DN hydrogels showed a significant pH-dependent, which decreased dramatically as the pH solution decreased. This makes the MB adsorbed HPC hydrogel can be easily regenerated under acidic condition to recover both the hydrogel and MB dye. Therefore these columns could be facially regenerated and reused for several cycles, without significant drop in MB uptake during the 5^{th} cycle, thereby allowing multiple cycles of reuse. As shown in Figure 7.23 both HPC SN and HPC/CA DN hydrogels exhibits high recycling efficiency in removing MB dye without significant losses in the dye removal % was detected after these cycles. According to the above results, the use of these adsorbents for water purification results in reduced operating costs.

7.2.2.3. Filtration separation of MB/FL mixed dyes

Due to the marked difference in MB versus FL adsorption and filtration, the ability of HPC SN and HPC/CA DN hydrogels columns for separation of dye mixtures was investigate. Aqueous solutions containing MB and FL were gravity filtered through HPC single and double network hydrogels columns and the collected eluents were studied via UV-Vis spectroscopy. As shown in Figure 7.24(A), MB was selectively removed from the dye mixture, such that after filtration, the MB peak at 664 nm was barely observable by UV-Vis spectroscopy. However, the FL absorbance band at 490 nm remained high. Figure 7.24 (B) demonstrates photographic images of the prepared HPC hydrogel column used for separation of MB and FL dyes and the solution before and after filtration. The MB/FL mixture solution was green before the filtration reflecting the presence of both dyes and the color of the solution was changed from green to yellow after filtration, suggesting that MB dye was captured by HPC hydrogels column, but FL dye was left in the filtrate.

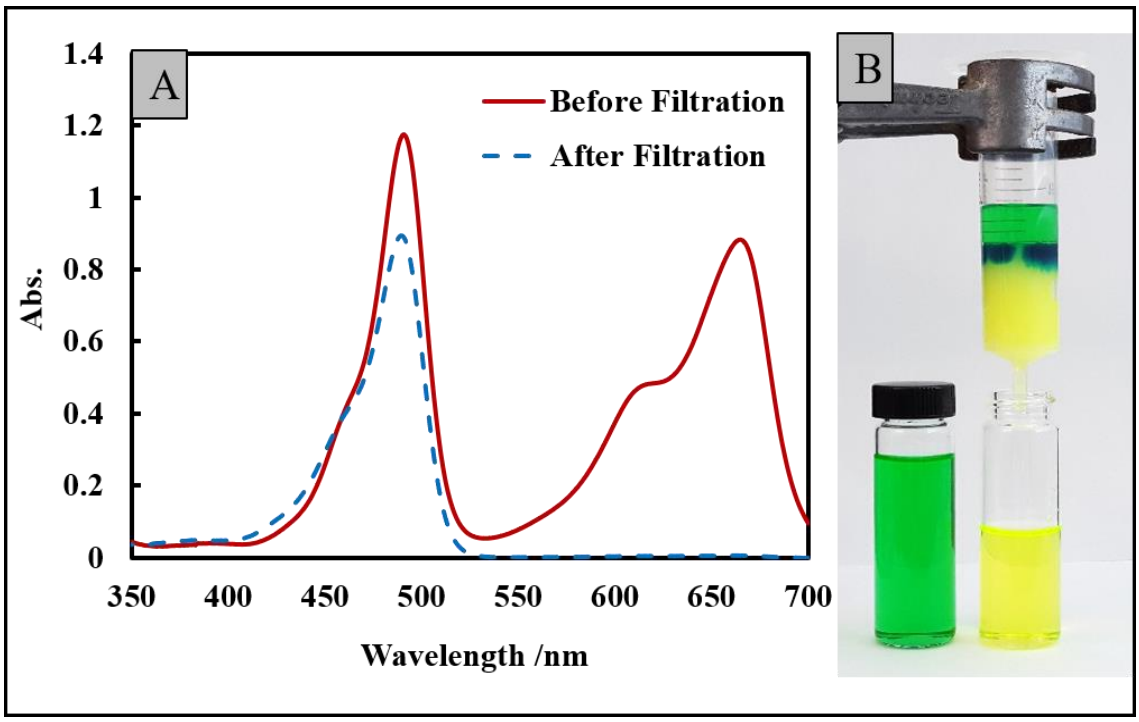

Figure 7.24. (A) UV-Visible spectrum of MB/FL mixture before and after filtration (B) Photographic images of MB/FL aqueous mixture and its elution through a HPC hydrogel column showing separation of MB from FL.

The separation efficiency, *S* (%) is used to evaluate the separation ability by the following equation:[49]

$$S\ (\%) = \frac{C(FL)_f}{C(FL)_f\ +\ C(MB)_f} \times\ 100\% \quad (7.10)$$

Where $C(MB)_f$ and $C(FL)_f$ are the concentration of MB and FL in the filtrate respectively.

It should be noted that HPC/CA DN hydrogel shows the same separation phenomenon for the MB/FL mixture. The results show the separation efficiency of HPC SN and HPC/CA DN hydrogels column for MB/FL mixture were 99.5% and 99.7% respectively. Thus, the results obtained indicate that the HPC SN and HPC/CA DN hydrogels columns can successfully separate the MB/FL mixture dyes by facile filtration method.

The recyclability of the columns for dye separation was also evaluated, HPC hydrogels columns was regenerated by washing with deionized water (10 mL) to remove FL dye and then washing with 0.01 M aqueous HCl (20 mL) and deionized water (50 mL). The above dye separation experiment was repeated on the regenerated columns to evaluate reusability. The separation/regeneration cycles were performed 10 times for HPC SN and HPC/CA DN hydrogels columns. As can be seen in Figure 7.25(A) there was little drop in the separation for the first six cycles for HPC SN hydrogel column, although the efficiency decreased to 86% by the 10th cycle for this column. Whereas, no

significant losses in the separation efficiency was detected even after ten cycles, the separation efficiency was decreased only 7% by the 10th cycle. (Figure 7.25 B)

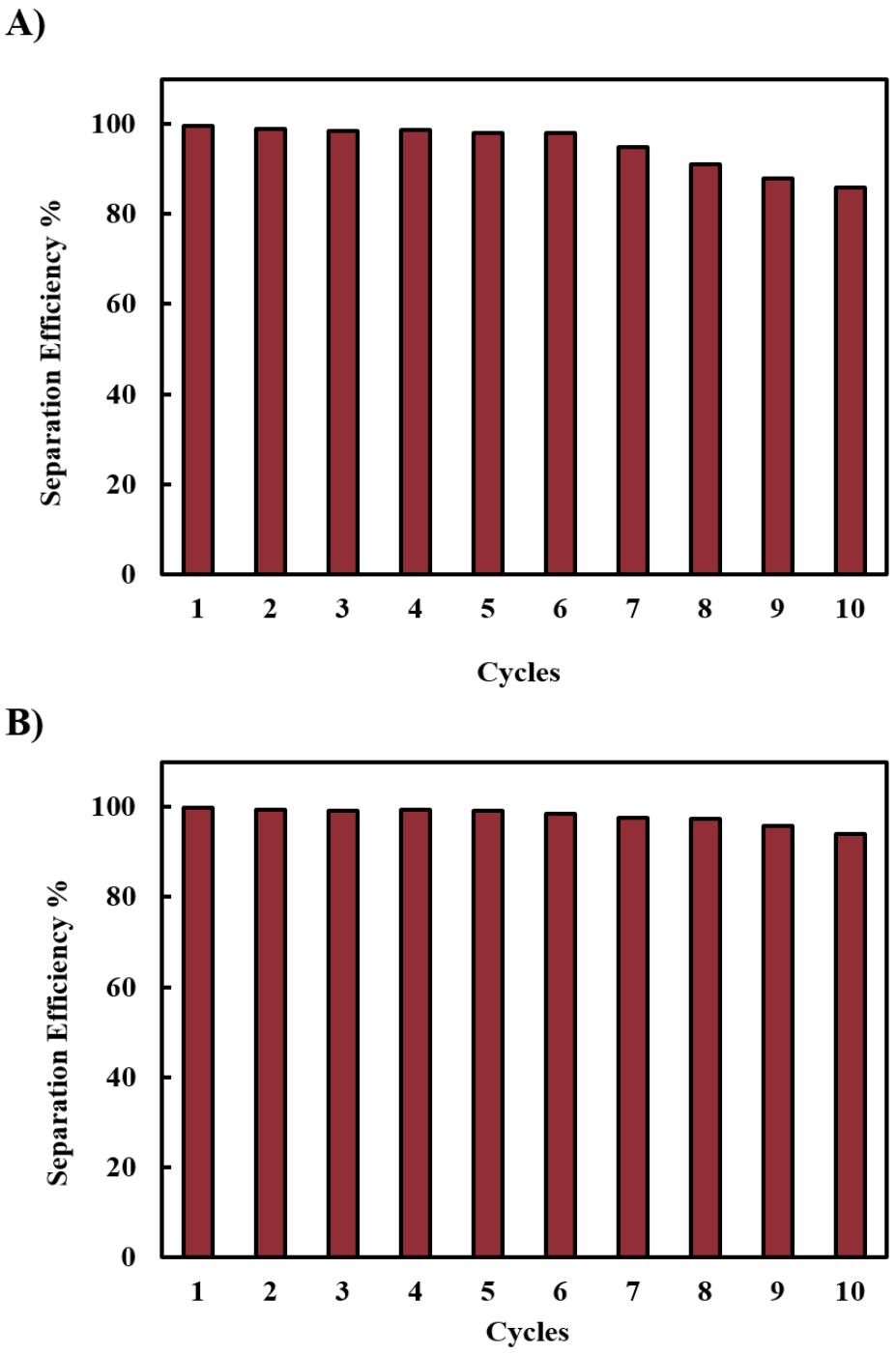

Figure 7.25. Separation efficiency of MB and FL from a mixture of both dyes by the regenerated hydrogel columns; (A) HPC SN and (B) HPC/CA DN hydrogels columns.

The results showed that HPC SN hydrogel column shows good reusablility without clogging and damge the network structure, and was also able to effectively separate MB from FL. However, as expected the prepared HPC/CA DN hydrogel has higher selective adsorption of MB dye in aqueous solutions than HPC SN.

7.3. Conclusions

In this chapter, DVS crosslinked HPC hydrogels prepared by the TIPS method (as described in chapter four) have been utilized as selective absorbents for removal of MB blue dye from aqueous solution. This hydrogel was showed selective adsorption towards MB dye was able to separate a mixed dyes solution. Despite the ubiquity of HPC, there have been very few reports on the use of HPC hydrogels or composites for dye removal,[50, 51] and to our knowledge, no reports on selective dye separation. However, the HPC hydrogel shows low adsorption capacity. Previous works reported that when fabricated hydrogel from hydroxypropyl cellulose (HPC) composited with graphene oxide (GO) or MoS_2 increase the surface area for adsorption, and negative electrostatic charges were confered to the resulting hydrogel, thus aiding the adsorption of cationic dye. However, graphene oxide is relatively expensive, and requires careful preparation to ensure proper exfoliation. Similarly, the use of carboxylated MoS_2 nanosheets required additional preparative steps utilizing pyrophoric reagents.[51, 52] To overcome these problems, it was important to improve the adsorption capacity of the HPC hydrogel by modifying this hydrogel with another polymer hydrogels and should be environmentally friendly, reusable and cheap.

In this study, to improve the adsorption capacity of HPC hydrogel, physical modification was made by including HPC with negatively charged renewable polymers to enhance the adsorption capacity of cationic dyes. Therefore, a new kind of porous HPC/CA double network hydrogel was prepared (as described in Chapter 6) and compared with the HPC single network hydrogel. The newly prepared HPC/CA double network hydrogel may be considered a good adsorbent due to this hydrogel achieved superior mechanical properties which were dramatically improved compared with HPC SN hydrogel (as described in Chapter 6), which allows it easy to regenerate and the HPC/CA DN hydrogel provides more functional groups than that of HPC SN hydrogel, this was due to HPC/CA DN hydrogel shows higher surface area than HPC SN because of the alginate network provides carboxyl groups beside hydroxyl groups from HPC hydrogel, which have great influence on the adsorption capacity. Both batch and column adsorption experiments of methylene blue (MB) onto HPC/CA DN hydrogel were studied to evaluate its adsorption performance and compared with HPC SN hydrogel. In batch adsorption, the results showed a significant pH-dependent equilibrium adsorption capacity of MB dye onto both hydrogels in this study, which decreased dramatically with decreasing the pH of MB dye solution. This makes the MB-loaded HPC hydrogel easy to regenerate under acidic conditions. The thermodynamic analysis of MB dye adsorption onto both HPC SN and

HPC/CA DN hydrogels were also studied and the process shows to be an exothermic and spontaneous process. Adsorption kinetic study were also applied and the obtained results show the adsorption of MB dye adsorption on both hydrogels were well described by the pseudo-second-order kinetic model and there are other steps controlling the adsorption rate along with intra-particle diffusion. Furthermore, both adsorption capacities increased by increasing of the initial solution concentration and the adsorption isotherms are well fitted by Langmuir model and the maximum adsorption capacity of HPC/CA DN hydrogel is 169.49 $mg.g^{-1}$, which is larger than HPC SN hydrogel (112.35 $mg.g^{-1}$).

Both hydrogels columns showed efficient selective adsorbent for cationic dyes, with very high removal of MB dye, while extremely low removal of FL dye. However, the HPC/CA DN hydrogels column exhibited a higher adsorption capacity than HPC SN hydrogel due to the dual functional groups (hydroxyl and carboxyl groups) in HPC/CA DN hydrogel provided by the higher density of negatively charge than HPC SN hydrogel with an only hydroxyl group. Furthermore, the dye-adsorbed HPC hydrogels columns can be easily regenerated in acidic solution (pH 1) and the regenerated hydrogel columns can be reused for MB dye adsorption with only 5% decrease in methylene blue uptake in the 5th adsorption cycle. Based on the selective adsorption towards cationic methylene blue over anionic sodium fluorescein dye, HPC SN and HPC/CA DN hydrogels columns could easily separate two dyes from aqueous solutions of dye mixtures by simple gravity filtration. Both HPC SN and HPC/CA DN hydrogel column showed high separation efficiency of more than 99%. It was also found that separation efficiency of HPC SN decreased to 86% by the 10th cycle for this column, while no significant losses in the separation efficiency was detected even after ten cycles for HPC/CA DN hydrogel column. Therefore, HPC/CA DN hydrogels not only greatly improves the adsorption capacity and the separation efficiency of MB dye, but also maintains good reusability even after many cycles of adsorption/regeneration of this dye. Thus, HPC/CA double network polymer hydrogels have great potential for improving the adsorption capacity with good reusability and would be a promising eco-friendly adsorbent for the treatment of dye wastewaters.

7.4. References

1. F. M. D. Chequer, G. A. R. d. Oliveira, E. R. A. c. Ferraz, J. C. Cardoso, M. V. B. Zanoni and D. P. d. Oliveira, in *Eco-Friendly Textile Dyeing and Finishing*, ed. M. Günay, InTech, Rijeka, 2013, DOI: 10.5772/53659, p. Ch. 06.
2. B. de Campos Ventura-Camargo and M. A. Marin-Morales, *Textiles and Light Industrial Science and Technology*, 2013.
3. B. Padhi, *International Journal of Environmental Sciences*, 2012, **3**, 940.
4. A. Ghaly, R. Ananthashankar, M. Alhattab and V. Ramakrishnan, *Journal of Chemical Engineering & Process Technology*, 2014, **5**, 1.
5. W. Jian, A. Kitanaka, W. Nishijima, A. U. Baes and M. Okada, *Water Research*, 1999, **33**, 1857-1863.
6. M. Hartmann, S. Kullmann and H. Keller, *Journal of Materials Chemistry*, 2010, **20**, 9002-9017.
7. J. D. Walker, R. R. Colwell and L. Petrakis, *Journal of Applied Microbiology*, 1975, **30**, 79-81.
8. A. Pasila, *Marine Pollution Bulletin*, 2004, **49**, 1006-1012.
9. M. J. Ayotamuno, R. B. Kogbara, S. O. T. Ogaji and S. D. Probert, *Applied Energy*, 2006, **83**, 1258-1264.
10. G. M. Shaul, T. J. Holdsworth, C. R. Dempsey and K. A. Dostal, *Chemosphere*, 1991, **22**, 107-119.
11. K. Periasamy and C. Namasivayam, *Chemosphere*, 1996, **32**, 769-789.
12. V. K. Gupta and Suhas, *Journal of Environmental Management*, 2009, **90**, 2313-2342.
13. P. Cooper, *Journal of the Society of Dyers and Colourists*, 1993, **109**, 97-100.
14. M. S. El-Geundi, *Adsorption science & technology*, 1997, **15**, 777-787.
15. Y. Lin, 2018.
16. G. Zhou, J. Luo, C. Liu, L. Chu and J. Crittenden, *Water research*, 2018, **131**, 246-254.
17. M. Chee Kimling, N. Scales, T. L. Hanley and R. A. Caruso, *Environmental science & technology*, 2012, **46**, 7913-7920.
18. J. E. Efome, D. Rana, T. Matsuura and C. Q. Lan, *Chemical Engineering Journal*, 2018, **352**, 737-744.
19. G.-R. Li, D.-L. Qu, L. Arurault and Y.-X. Tong, *The Journal of Physical Chemistry C*, 2009, **113**, 1235-1241.

20. Z. Ye, H. Chen, X. Cui, J. Zhou and J. Shi, *Materials Letters*, 2009, **63**, 2303-2305.
21. L. Yan, Q. Shuai, X. Gong, Q. Gu and H. Yu, *CLEAN – Soil, Air, Water*, 2009, **37**, 392-398.
22. P. Chen, X. Liu, R. Jin, W. Nie and Y. Zhou, *Carbohydr. Polym.*, 2017, **167**, 36-43.
23. M. G. Yazdi, M. Ivanic, A. Mohamed and A. Uheida, *RSC Advances*, 2018, **8**, 24588-24598.
24. G. Atun and T. Sismanoglu, *Journal of Environmental Science & Health Part A*, 1996, **31**, 2055-2069.
25. Y. Zhuang, F. Yu, J. Chen and J. Ma, *Journal of environmental chemical engineering*, 2016, **4**, 147-156.
26. J. Wang, N. Zhang, C. Jiang and C. Zhang, *Journal of Materials Research*, 2018, **33**, 3898-3905.
27. K. Bharathi and S. Ramesh, *Applied Water Science*, 2013, **3**, 773-790.
28. Y. Kong, Y. Zhuang, Z. Han, J. Yu, B. Shi, K. Han and H. Hao, *Journal of Environmental Sciences*, 2019, **78**, 81-91.
29. K. Kadirvelu, K. Thamaraiselvi and C. Namasivayam, *Separation and Purification Technology*, 2001, **24**, 497-505.
30. Y. Chen, Y. Long, Q. Li, X. Chen and X. Xu, *International journal of biological macromolecules*, 2019, **126**, 107-117.
31. S. Hassanpour, F. F. Azhar and M. Bagheri, *Polymer Bulletin*, 2019, **76**, 933-952.
32. R. Xu, G. Zhou, Y. Tang, L. Chu, C. Liu, Z. Zeng and S. Luo, *Chemical Engineering Journal*, 2015, **275**, 179-188.
33. C. Liu, H. Liu, T. Xiong, A. Xu, B. Pan and K. Tang, *Polymers*, 2018, **10**, 835.
34. N. M. Mahmoodi, *Journal of Chemical & Engineering Data*, 2011, **56**, 2802-2811.
35. Y. Zhuang, F. Yu, J. Ma and J. Chen, *Journal of colloid and interface science*, 2017, **507**, 250-259.
36. E. Serag, A. El Nemr and A. El-Maghraby, *Journal of Water and Environmental Nanotechnology*, 2017, **2**, 223-234.
37. A. T. Paulino, M. R. Guilherme, A. V. Reis, E. B. Tambourgi, J. Nozaki and E. C. Muniz, *Journal of hazardous materials*, 2007, **147**, 139-147.
38. A. E. Ofomaja, *Bioresource technology*, 2010, **101**, 5868-5876.

39. F. Deniz, *The Scientific World Journal*, 2013, **2013**.
40. Y. Hu, Y. Zhang, Y. Hu, C.-Y. Chu, J. Lin, S. Gao, D. Lin, J. Lu, P. Xiang and T.-H. Ko, *Journal of Chemistry*, 2019, **2019**.
41. R. Coşkun and A. Delibaş, *Polymer bulletin*, 2012, **68**, 1889-1903.
42. H. Li, G. Huang, C. An, J. Hu and S. Yang, *Industrial & Engineering Chemistry Research*, 2013, **52**, 15923-15931.
43. P. M. Pakdel and S. J. Peighambardoust, *Journal of environmental management*, 2018, **217**, 123-143.
44. A. Zaki, M. El-Sheikh, J. Evans and S. El-Safty, *Journal of colloid and interface science*, 2000, **221**, 58-63.
45. S. Umoren, U. Etim and A. Israel, *J. Mater. Environ. Sci*, 2013, **4**, 75-86.
46. P. Senthil Kumar, P. S. A. Fernando, R. T. Ahmed, R. Srinath, M. Priyadharshini, A. Vignesh and A. Thanjiappan, *Chemical Engineering Communications*, 2014, **201**, 1526-1547.
47. G. M. ElShafei, F. Al-Wadaani and A. A. Zahran, *Journal of Taibah University for Science*, 2018, **12**, 123-132.
48. C. H. Chan, C. H. Chia, S. Zakaria, M. S. Sajab and S. X. Chin, *Rsc Advances*, 2015, **5**, 18204-18212.
49. R. Zhao, Y. Wang, X. Li, B. Sun and C. Wang, *ACS applied materials & interfaces*, 2015, **7**, 26649-26657.
50. L. Yan, Q. Shuai, X. Gong, Q. Gu and H. Yu, *CLEAN–Soil, Air, Water*, 2009, **37**, 392-398.
51. X. Liu, Y. Zhou, W. Nie, L. Song and P. Chen, *Journal of materials science*, 2015, **50**, 6113-6123.
52. P. Chen, X. Liu, R. Jin, W. Nie and Y. Zhou, *Carbohydrate polymers*, 2017, **167**, 36-43.

Chapter Eight

8. Summary of the thesis and future work

8.1. Summary and conclusions

Water pollution is an important environmental problem, and is of major worldwide concern. Adsorption methods are regarded as a successful approach to treat water pollution because of the flexibility of the systems, low energy required and low cost operation. In practice, most researchers are focused on finding adsorbents with good stability, that are environmentally friendly and that have a good regeneration performance. Materials with the porous structure are widely employed as adsorbents for removing harmful pollutants from the environment, owning to their thermal stability, high surface area and morphology structure. In addition, the interconnected porous system can simplify rapid transportation and diffusion of adsorbate molecules and promote access to active sites. The primary goal of this project was to develop novel porous materials for pollution remediation, with the focus being on materials that could be produced economically. The work presented in the thesis contributes to this field as summarised below.

In Chapter 3, mesoporous carbon materials (OMC) and their magnetic counterparts (Fe/OMC, Co/OMC and Ni/OMC) were successfully prepared using resorcinol and formaldehyde as a carbon precursor and a triblock copolymer F127 as the template via the soft templating method. The characterisation results provided evidence that the template decomposed during the carbonization process to form the pores in the carbon materials. The mesoporous carbon monoliths obtained had a high surface area, narrow pore size, and high mechanical stability. In comparison with other methods for preparing mesoporous carbon monolith, this method was low cost and simple. However, there were some disadvantages of this method as the processing was time consuming, there were high operation cost when compare with biopolymer hydrogels materials, and the obtained OMC was hard and brittle and difficult to regenerate, which may is undesirable in the proposed application. Therefore, this study moved to the preparation of porous materials from cellulose owing to their natural abundance, being renewable, non-toxic and low-cost.

In Chapter 4, a microporous hydroxypropyl cellulose (HPC) hydrogel was successfully synthesized using DVS as chemical cross linker in alkaline media. HPC is a well-known thermoresposive polymer which exhibits a LCST at 42 °C, thus the preparation of HPC

hydrogel is influenced by gelation temperature, which impacts the properties of the resulting hydrogel. The thermoresponsivity behaviour of HPC was exploited to create cross-linked microporous hydrogels via modified Temperature Induced Phase Separation (TIPS) method. The advantages of this method include facile operating conditions, low costs and low energy requirements. In-depth investigations the characterization of HPC hydrogels were studied, the effect of preparation parameters on the hydrogel properties such as polymer and cross linker concentrations were also studied. SEM imaging revealed details of their microstructure of freeze-dried HPC hydrogel prepared by this method. The cross-linked HPC hydrogel shown interconnected pores with pores size are about 1–8 μm in diameter. This morphology arises from spinodal decomposition during the phase separation when complete gelation at the LCST in this method. Whereas, the morphology structure of HPC hydrogel complete gelation at a single temperature, which is below the LCST demonstrated connected honeycomb-like pores with bigger pore size. Furthermore, it is important to note that the HPC aerogel showed no observed shrinkage during the freeze-drying process due to the strength of the crosslinks in the polymer network. The mechanical properties of the HPC hydrogels were also investigated via compression test and rheology measurements. It was found that the Young modulus of the hydrogel prepared by TIPS method increased linearly with an increase in the polymer and cross linker concentrations. This hydrogel can be compressed to an approximately 20% height of the original size without fracture and exhibit the predominant mechanical properties of toughness and softness and was showed shape recovery, with approximately 100% of the original shape recovered within a few seconds maintained their structure during loading reloading. Compared with HPC hydrogel prepared at below the LCST, this hydrogel shows remarkable fracture at a low deformation of about 50% with high stiffness. Rheological measurements confirmed a decreasing in storage modulus with increased the temperature and goes through a minimum when the temperature is 42 °C the LCST due to the phase separation of the HPC hydrogel at this temperature. Previous work in the literature has shown the possibility of preparing interconnected HPC hydrogel via TIPS method by increase the temperature at phase separation above the LCST of HPC. Here, the heat setting of the phase separation keep at LCST of the polymer with adjusting the pre-cross linking time. The mechanical properties of this hydrogel controlled to the most desirable properties in our application by varying the gelation time before phase separation. Thus, this modification results interconnected microporous HPC hydrogel with high mechanical properties of toughness and softness, allowing its use for water purification for a number of cycles.

The a novel, efficient approach was developed to produce interconnected gradient porous HPC hydrogel by taking advantage of thermoresponsive behaviour of HPC at the LCST. This was the topic of Chapter 5. The temperature gradient between the top and the bottom layer within the monolith hydrogel sample during the chemical cross-linking step resulted in hydrogel with a graded pore size and vary pore geometry. SEM imaging provided details of the gradient microstructure under both dry and wet conditions, revealing a reduction in pores size along the cross-section of the HPC hydrogel from a top layer formed when the crosslinking was completed at a temperature below the LCST as compared to the bottom layer where the crosslinking was completed at the LCST. A gradual reduction in pore size from the top layer (100 μm) to the bottom layer (~ 1 μm) was observed, indicating the gradually changing pore size within the hydrogel. The small pores were formed as a result of decomposition of the HPC hydrogel during the TIPS method via completion of the crosslinking at the LCST, whereas the big porous were due to completion of the crosslinking below the LCST. A tracer dye test was used to monitor the diffusion of fluid through the gradient HPC hydrogel column developed. The results showed no permeability of the dye during the column due to the top layer having closed pores as mentioned in chapter four. This problem was overcome by using the thermal synthesis method for the gradient porous HPC hydrogel followed by a freeze-thawing method. The cryogenically treated column showed high permeability of liquid through the column. This chapter is the first report of a gradient porous hydrogel made from hydroxypropyl cellulose depend on it LCST. Previous work in the literature has been used HPC to prepare porous hydrogel with uniform pores.

The aim of In Chapter 6 was to further develop the material to obtain great adosorption properties and a better mechanical strength. This was achieved by fabricating a novel eco-friendly hybrid double network hydrogel through via a new two-step route. HPC/CA DN hydrogel was successfully synthesized consisting of a first, chemically linked HPC network, which created through the covalent crosslinking of hydroxypropyl cellulose polymer chains by DVS in alkaline media and secondly, by a physically crosslinked CA network, with coordination between sodium alginate chains and Ca2+. This method depended on immersing the first network in an aqueous solution of the second network polymer during the phase separation of the HPC hydrogel at LCST. The SEM results showed that the DN hydrogel prepared by this method exhibited two networks with good compatibility and homogeneous morphology in the hydrogel. Furthermore, FTIR, EDX and XRD analyses confirmed that the first network and the second network formed

independently, and there was no chemical interaction between them. The mechanical properties of the HPC/CA DN hybrid hydrogels were investigated using a compression test and rheometer. The results have demonstrated that the HPC/CA DN hydrogel achieved superior mechanical properties which were dramatically improved compared with HPC SN hydrogel. In addition, HPC/CA DN hydrogel demonstrated flexible t behaviour without breakage under compression tests. Even at an extremely high strain reached to 80% substantial shape recoverywas obtained after removing the compression, indicating easy recycling of this material. Through the combined advantages of both HPC and CA, the formed DN hydrogels not only exhibited higher mechanical properties but also provided a higher specific surface area than their parent HPC SN hydrogel. The combination of toughness and high mechanical properties and high surface area, an easy preparation method, along with the environmentally friendly material used for preparation, make this type of material an ideal candidate as adsorbents for wastewater treatment.

In Chapter 7, the application of the HPC SN and HPC/CA DN hydrogels developed in Chapter 6 and 4 for environmental remediation was demonstrated. DVS crosslinked HPC SN hydrogel prepared by the TIPS method was utilized as a selective adsorbent for removal of MB blue dye from aqueous solution. This hydrogel was showed to selectively adsorb MB dye allowing selective separation of a mixture of dye solutions. To the best of our knowledge, this is the first use of HPC hydrogel as filter for selective dye separation. However, the HPC hydrogel showed low adsorption capacity. Previous works reported that when fabricated hydrogel from hydroxypropyl cellulose (HPC) composited with graphene oxide (GO) or MoS_2 increase the surface area for adsorption, and confer negative electrostatic charges to the resulting hydrogel, thus aiding the adsorption of cationic dye. However, graphene oxide is relatively expensive and requires careful preparation to ensure proper exfoliation. Similarly, the use of carboxylated MoS2 nanosheets required additional preparative steps utilizing pyrophoric reagents. To overcome these problems, it is important to improve the adsorption capacity of HPC hydrogel by modifying this hydrogel with another polymer hydrogels and should be environmentally friendly, reusable and cheap materials.

In this study, to improve the adsorption capacity of HPC hydrogel, physical modification was achieved by including HPC with negatively charged renewable polymers to enhance the adsorption capacity of cationic dyes. Therefore, the new porous HPC/CA double network hydrogel as prepared in Chapter 6 was compared with the HPC single network

hydrogel. The HPC/CA DN hydrogel provided more functional groups than that of HPC SN hydrogel, due to the HPC/CA DN hydrogel showing a higher surface area than HPC SN because of the alginate network which provided carboxyl groups beside hydroxyl groups from the HPC hydrogel, which had a great influence on the adsorption capacity. Both batch and column adsorption experiments with methylene blue (MB) using the HPC/CA DN hydrogel were carried out to evaluate its adsorption performance and compared with the HPC SN hydrogel. The dye adsorption process for both hydrogels using batch adsorption or simple filtration, required no additional step such as centrifugation or sorbent separation unlike some methods that utilize particulate-based sorbents. In batch adsorption, the results showed a significant pH-dependent equilibrium adsorption capacity of MB dye for both hydrogels in this study, which decreased dramatically with decreasing the pH of MB dye solution. This uniqueness makes the MB-loaded HPC hydrogel easy to regenerate under acidic conditions. The thermodynamic analysis of the MB dye adsorption onto both HPC SN and HPC/CA DN hydrogels was also studied and the process was shown to be an exothermic and spontaneous process. Adsorption kinetic studies were carried out and results obtained showed the adsorption of MB dye on both hydrogels was well described by the pseudo-second-order kinetic model and there was another step controlling the adsorption rate along with intra-particle diffusion. Furthermore, both adsorption capacities increased by increasing the initial solution concentration and the adsorption isotherms fitted the Langmuir model well with the maximum adsorption capacity of HPC/CA DN hydrogel being 169.49 mg g^{-1}, which is larger than HPC SN hydrogel (112.35 mg g^{-1}). In column adsorption, both hydrogels columns showed efficient selective adsorption for cationic dyes, with a very high removal of MB dye and an extremely low removal of FL dye. However, the HPC/CA DN hydrogels column exhibited a higher adsorption capacity than HPC SN hydrogel due to the dual functional groups (hydroxyl and carboxyl groups) in HPC/CA DN hydrogel was provided a higher density of negative charge than HPC SN hydrogel with an only the hydroxyl groups. Furthermore, the dye-adsorbed HPC hydrogels columns could be easily regenerated in acidic solution (0.01 M HCl) and the regenerated hydrogel columns can be reused for MB dye adsorption with only 5% decrease in methylene blue uptake in the 5th adsorption cycle. Based on the unique selective adsorption towards cationic methylene blue over anionic sodium fluorescein dye, HPC SN and HPC/CA DN hydrogels columns could easily separate two dyes from aqueous solutions of dye mixtures by simple gravity filtration. Both HPC SN and HPC/CA DN hydrogel column showed high separation efficiency, of more than 99%. It

was also found that separation efficiency of HPC SN decreased to 86% by the 10th cycle for this column, while no significant losses in the separation efficiency were detected even after ten cycles for the HPC/CA DN hydrogel column. Therefore, the HPC/CA DN hydrogel not only had greatly improved the adsorption capacity and separation efficiency for MB dye, but also maintained good reusability even after many cycles of adsorption/regeneration of this dye. Thus a combination of the unique characteristics of both networks in the HPC/CA double network hydrogel have great potential for improving the adsorption capacity with good reusability and would be a promising eco-friendly adsorbent for the treatment of dye wastewaters.

8.2. Future work

In the future work, the HPC and HPC/CA hydrogels monolith and column would apply for the adsorption of dyes in real samples. In addition to that development of these materials to increase the adsorption capacity and improve the separation selectivity. Due to the functional groups in the adsorbent materials are very important to ensure interactions with the adsorbate. Therefore, the future work related to the HPC single network hydrogel in Chapter 4 would functionalise with MOFs to create hybrid materials with capacity for catalysis or sensing and pollution remediation via post-synthetic treatment of hydrogel with MOF precursor solution or blending of HPC with MOF crystals to create hierarchical materials. Furthermore, this hydrogel could be applied to selective oil adsorption by hydrophobic modification of this hydrogel by a simple Chemical Vapor Deposition (CVD). Other work could involve functionalisation of the HPC SN hydrogel with acrylate to increase the adsorption capacity of this hydrogel.

The permeable graded porous structure of the HPC hydrogel column described in Chapter 5 should be further controlled to avoid clogging the pores specially when use this column for particle filtration. This could be achieved by controlling the freezing direction and rate.

In addition to that examination of the possibility of using HPC SN and HPC/CA DN hydrogels to adsorb potentially toxic elements from water such as cadmium (Cd^{2+}) and Lead (Pb^{2+}), using ICP-OES measurements to determine the difference in the concentration of these metals before and after adsorption.